UNIVERSIDADE DE LISBOA

INSTITUTO SUPERIOR TÉCNICO

Spin Structure of the Proton at Low x and Low Q^2 from the COMPASS Experiment at CERN

Ana Sofia da Silva Nunes

Supervisor: Doctor Sérgio Eduardo de Campos Costa Ramos
Co-supervisor: Doctor Maria Paula Frazão Bordalo e Sá

Thesis approved in public session to obtain the PhD Degree in
Technological Physics Engineering
Jury final classification: Pass with Distinction

2017

UNIVERSIDADE DE LISBOA

INSTITUTO SUPERIOR TÉCNICO

Spin Structure of the Proton at Low x and Low Q^2 from the COMPASS Experiment at CERN

Ana Sofia da Silva Nunes

Supervisor: Doctor Sérgio Eduardo de Campos Costa Ramos
Co-supervisor: Doctor Maria Paula Frazão Bordalo e Sá

Thesis approved in public session to obtain the PhD Degree in
Technological Physics Engineering
Jury final classification: Pass with Distinction

Jury

Chairperson: Doctor Mário João Martins Pimenta (Instituto Superior Técnico da Universidade de Lisboa)

Members of the Committee:

Doctor João Manuel Coelho dos Santos Varela (Instituto Superior Técnico da Universidade de Lisboa)

Doctor Pedro José de Almeida Bicudo (Instituto Superior Técnico da Universidade de Lisboa)

Doctor José Ricardo Morais Silva Gonçalo (Laboratório de Instrumentação e Física Experimental de Partículas, Lisboa)

Doctor Nuno Teotónio Viegas Guerreiro Leonardo (Laboratório de Instrumentação e Física Experimental de Partículas, Lisboa)

Doctor Sérgio Eduardo de Campos Costa Ramos (Instituto Superior Técnico da Universidade de Lisboa)

Doctor Marcin Stolarski (Laboratório de Instrumentação e Física Experimental de Partículas, Lisboa)

Funding Institution
Fundação para a Ciência e a Tecnologia

2017

Abstract

This thesis describes the analysis of data collected by the COMPASS experiment at CERN in 2007 and 2011, using a muon beam with 160 GeV/c and 200 GeV/c momenta, respectively, with the purpose of studying the process of inelastic scattering of longitudinally polarised muons off longitudinally polarised protons. A solid state target of ammonia was used in both years as a source of protons.

The events studied in this work belong to the phase-space region of low values of the Bjorken scaling variable x and low values of the exchanged photon virtuality Q^2, that probe the nucleon at high densities of quarks and gluons and offer an opportunity to test theoretical models that make the connection from the photo-production regime, *i.e.* $Q^2 \to 0$ (GeV/c)^2, to the DIS regime, *i.e.* $Q^2 \gtrsim 1$ (GeV/c)^2. Using a large sample of about 700 million events in the non-perturbative region, the virtual photon-nucleon spin asymmetry A_1^p and the spin-dependent structure function g_1^p have been extracted as functions of the Bjorken scaling variable x and of the energy of the virtual photon ν, and as functions of pairs of variables (x, Q^2), (ν, Q^2), (x, ν) and (Q^2, x). The last grid differs from the first one in the numbers of bins chosen per variable. The following kinematic region was investigated: $4 \times 10^{-5} < x < 4 \times 10^{-2}$, 0.001 (GeV/$c$)$^2 < Q^2 < 1$ (GeV/c)^2 and 14 GeV $< \nu <$ 194 GeV. The details of the extraction are given in this thesis. The sample is 150 times larger than the similar low x, low Q^2 sample from the previous experiment Spin Muon Collaboration (SMC), that took data in the 1990's at CERN, which allowed the measurement in COMPASS, for the first time, of small but significantly positive spin asymmetries A_1^p at very low x. The results were confronted with models, in particular the Regge model and phenomenological models that describe g_1^p in the low Q^2 region as a linear combination of a (generalised) vector meson dominance ((G)VMD) term and a partonic term, with reasonable agreement between data and model predictions.

As a complement to this data analysis, the COMPASS Detector Control System, which is a full and exclusive responsibility of the LIP group participating in the COMPASS Collaboration, of which the author is a member, is presented and some of its implementations are detailed.

Keywords: COMPASS, detector control system, spin, structure function, low Q^2.

Resumo

Esta tese descreve a análise de dados colectados pela experiência COMPASS do CERN em 2007 e 2011, usando um feixe de muões com momentos de 160 GeV/c e 200 GeV/c, respetivamente, com o objetivo de estudar o processo de difusão inelástica de muões polarizados longitidinalmente por protões polarizados longitudinalmente. Um alvo de estado sólido de amónia foi usado em ambos os anos como fonte de protões.

Os eventos estudados neste trabalho pertencem à região do espaço de fases de baixos valores da variável de escala de Bjorken x e baixos valores da virtualidade do fotão trocado Q^2, que sondam o nucleão a elevadas densidades de quarks e gluões e oferecem uma oportunidade para testar modelos teóricos que fazem a ligação do regime de fotoprodução, *i.e.* $Q^2 \to 0$ (GeV/c)^2, ao regime de dispersão inelástica profunda, *i.e.* $Q^2 \gtrsim 1$ (GeV/c)^2. Usando uma grande amostra de cerca de 700 milhões de eventos na região não perturbativa, foram extraídas a assimetria de spin fotão virtual-nucleão A_1^p e a função de estrutura dependente do spin g_1^p como funções da variável de escala de Bkorken x e da energia do fotão virtual, ν, e como funções de pares de variáveis (x, Q^2), (ν, Q^2), (x, ν) e (Q^2, x). A última grelha difere da primeira nos números de intervalos escolhidos por variável. Foi investigada a seguinte região cinemática: $4 \times 10^{-5} < x < 4 \times 10^{-2}$, 0.001 (GeV/$c$)^2 $< Q^2 <$ 1 (GeV/c)^2 e 14 GeV$< \nu <$ 194 GeV. Os detalhes da extração são apresentados nesta tese. A amostra é 150 vezes mais extensa do que a amostra similar, com baixo x e baixo Q^2, da experiência SMC, que tomou dados nos anos 1990's no CERN, o que tornou possível a medição em COMPASS, pela primeira vez, de simetrias de spin A_1^p pequenas mas significativamente positivas a muito baixo x. Os resultados foram comparados com modelos, em particular com o modelo de Regge e com modelos fenomenológicos que descrevem g_1^p na região de baixo Q^2 como uma combinação linear de um termo de dominância mesão-vetor (generalizada) (G)VMD e um termo partónico, tendo-se verificado um acordo razoável entre dados e previsões dos modelos.

Como complemento a esta análise de dados, o Sistema de Controlo de Detetores (DCS) de COMPASS, que é responsabilidade total e exclusiva do grupo do LIP que participa na Colaboração COMPASS, de que a autora é membro, é apresentado e algumas das suas implementações são detalhadas.

Palavras-chave: COMPASS, sistema de controlo de detetores, spin, função de estrutura, baixo Q^2.

Acknowledgements

This thesis could not have been done without the collaboration of a number of people, to whom I am very grateful.

First of all, I would like to thank the members of the juri for accepting to participate in my Ph.D. defence, for the interest and the detailed comments about my work, and in particular to Prof. João Varela and Dr. Marcin Stolarski for their reports.

I would like to thank Prof. Paula Bordalo and Prof. Sérgio Ramos for giving me the opportunity to integrate the group of LIP in COMPASS working in its Detector Control System (DCS) and to develop a Ph.D. project in COMPASS.

I would also like to thank Dr. Catarina Quintans for her patience and rigour introducing me to the COMPASS DCS.

To Dr. Marcin Stolarski I thank for having suggested me the topic of data analysis that I developed and for sharing his knowledge with me.

In the context of the DCS work I also profitted from the collaboration with my colleague Dr. Christophe Pires.

CERN's controls group (with different names over the years) has always provided a reliable support for the COMPASS DCS, and the same can be said about its databases group. Thank you!

I thank all the COMPASS Collaboration members for running the experiment in a constructive and friendly environment. I am especially grateful to Prof. Eva Kabuss, Prof. Barbara Badełek, Dr. Yann Bedfer, Dr. Claude Marchand, Prof. Jan Friedrich, Dr. Alain Magnon and Dr. Reiner Geyer for their support. I am particularly grateful to my cross-checker, Dr. Malte Wilfert, for our successful collaboration, his programming skills and his pacience, and to Dr. Vincent Andrieux for the considerable work of producing the bad spill list that was a very important input to the performed data analysis.

I am very grateful for the support at the IN2P3/CNRS computing center at Lyon, where most of the data analysis of this thesis was performed, and in particular to the contact colleagues Dr. Damien Neyret and Dr. Yann Bedfer.

Moreover, I would like to thank the remaining members of the COMPASS group in Lisbon, Prof. Luís Silva, Dr. Celso Franco and Dr. Márcia Quaresma, for the friendly environment.

I thank again Dr. Catarina Quintans, Dr. Márcia Quaresma and Prof. Luís Silva for reading and commenting previous versions of this thesis.

I am indebted to the very efficient LIP secretariat and LIP IT group.

As a colleague of a neighbouring office and healthy lunches, Dr. Helena Santos has been a great model of an enthusiastic scientist!

I am very grateful to my family and friends for their continuous support.

This work was partly financed by the FCT grant SFRH/BD/84590/2012.

Contents

List of Figures

List of Tables

Abbreviations and acronyms

ADC	Analog to Digital Converter
API	Application Programming Interface
BNL	Brookhaven National Laboratory, in the USA
BMS	Beam Momentum Station(s), a set of detectors in the beam line placed before and after a bending magnet, used to measure the momentum of each muon of the beam
CAN	Controller Area Network
CEBAF	Continuous Electron Beam Accelerator Facility, at the Jefferson Laboratory, in the USA
CERN	European Organisation for Nuclear Research, formerly Conseil Européen pour la Recherche Nucléaire, located in the Geneva region, in Switzerland
CEDAR	ČErenkov Differential counter with Achromatic Ring focus
CHEOPS	CHarm Experiment with OmniPurpose setup
CMF	Computer Management Framework
CNGS	CERN Netrinos to Gran Sasso
CNIC	CERN's Computing and Network Infrastructure for Controls
CRON	Command Run ON, a job scheduler in Linux
CSV	Comma-Separated Values
COMPASS	COmmon Muon Proton Apparatus for Structure and Spectroscopy
CORAL	COmpass Reconstruction and Analysis Library
DAQ	Data Acquisition system
DC	Saclay Drift Chamber
DCS	Detector Control System

DGLAP	Dokshitzer, Gribov, Lipatov, Altarelli, Parisi
DIM	Distributed Information Management System
DIP	Data Interchange Protocol
DIS	Deep Inelastic Scattering
DNP	Dynamic Nuclear Polarisation
DVCS	Deeply Virtual Compton Scattering
DY	Drell-Yan (process)
ECAL	Electromagnetic CALorimeter
EIC	Electron-Ion Collider
ELIC	ELectron-Ion Collider, a possible implementation of the EIC project at the Jefferson Laboratory, in the USA
ELMB	Embedded Local Monitoring Board
EN/ICE	CERN's Engineering department, Industrial Controls and Engineering
EPICS	Experimental Physics and Industrial Control System
eRHIC	Electron-Relativistic Heavy Ion Collider, a possible implementation of the EIC project at the Brookhaven National Laboratory, in the USA
FSM	Finite State Machine
GEM	Gaseous Micropattern detector
GPD	Generalised Parton Distribution
GUI	Graphical User Interface
HCAL	Hadronic Calorimeter
HMC	Hadron Muon Collaboration
IT/CO	CERN's Information and Technology department, Controls group (replaced by EN/ICE)
LHC	Large Hadron Collider at CERN, Geneva, Switzerland
JCOP	LHC experiments Joint Controls Project
JLAB	Jefferson Laboratory, in the USA
LINAC 2	Linear Accelerator 2

MM	Micromegas or Micromesh Gaseous Structure
MWPC	Multi-wire Proportional Chamber
mDST	Mini Data Summary Tables
mySQL	Database management system implementing the SQL standard
NMR	Nuclear Magnetic Resonance
OLE	Object Linking and Embedding
OPC	OLE for Process Control
PCI	Peripheral Component Interconnect
PDF	Parton Distribution Function
PHAST	COMPASS PHysics Analysis Software Tools
PhyDB	CERN's Physics Databases service
PLC	Programmable Logic Controllers
pQCD	Perturbative Quantum CromoDynamics
PVSS	Prozessteuerung und Prozessvisualisierung (Process control and visualization), the SCADA used in the COMPASS DCS
QCD	Quantum ChromoDynamics
RHIC	Relativistic Heavy Ion Collider, at the Brookhaven National Laboratory
RICH	Ring-Imaging CHerenkov detector, used for particle identification
SCADA	Supervisory Control and Data Acquisition system
SIDIS	Semi-Inclusive Deep Inelastic Scattering
SLiC	SLow Control
SM1	COMPASS Spectrometer Magnet 1
SM2	COMPASS Spectrometer Magnet 2
SMC	Spin Muon Collaboration
SPS	Super Proton Synchrotron at CERN
SQL	Structured Query Language, a language for managing data in relational database management systems (RDBMS)
TMD	Transverse Momentum Dependent (Parton Distribution Function)

UI User Interface

VME VERSAmodule Eurocard

WinCC-OA SIMATIC WinCC Open Architecture (new name of PVSS)

Chapter 1

Introduction

The atomic nucleus is made of nucleons: the protons and the neutrons. It is now known that these have internal structure, namely they are made of quarks and gluons. To our best knowledge, quarks and gluons don't have internal structure. Among hadrons, that is, particles that interact via the strong interaction, the nucleons fall in the category of baryons, because they are made of three constituent or valence quarks and have half-integer spin. In particular, it was found out in 1927 that the proton is a fermion of spin $\frac{1}{2}$ [1].

The concept of spin has been introduced in 1925 by S.A. Gouldsmit and G.E. Uhlenbeck to explain the measurements done some years earlier by O. Stern and W. Gerlach. The latter had measured the non-zero magnetic moment of silver atoms, which have zero orbital angular momentum. Gouldsmit and Uhlenbeck proposed that this was originated by a different kind of angular momentum, spin. The hypothesis of the spin of the electron also explained many other phenomena in atomic spectroscopy, such as the Zeeman effec, *i.e.* changes in the spectra in the presence of a magnetic field, but also doublet lines in the spectra of alkali elements, and the fine structure of the hydrogen spectrum, consisting of doublet and triplet lines.

In 1933, Estermann and Stern measured the proton's anomalous magnetic moment [2], $k_{\mathrm{p}} = 1.79$ Bohr magnetons, which indicated that the proton is not point-like but rather has an internal structure.

The scattering of different kinds of probes off protons or heavier nuclei is an experimental technique that has played a decisive role in the discovery and study of the atomic nucleus and of the proton and its internal structure. The nucleus was discovered by scattering alpha particles off gold nuclei [3,4] and a strong evidence for the internal structure of the proton was observed in the elastic scattering of electrons off protons, using an electron beam with an energy of a few MeV [5].

In the decade of the 1960's, experiments of deep inelastic scattering (DIS) began being done at SLAC. In such experiments, the virtuality of the photon exchanged between the leptonic probe and the nucleon is large ($Q^2 \gg M_p$), and the mass of the hadronic final state is also large ($W^2 \gg M_p^2$). These experiments demonstrated the presence of point-like scattering objects with which the leptonic probes interacted, because they exhibited a behaviour called scaling, that had been predicted by J.D. Bjorken [6]. Those point-like objects were identified with the

quarks that had been introduced by theorists [7, 8] to explain a multitude of hadronic bound states that were being discovered in laboratory and cosmic ray experiments.

The Quark Parton Model (QPM) developed by M. Gell-Mann, G. Zweig and R. Feynman [7–9] allowed to describe the properties of baryons at low energies as systems with three constituent quarks. The proton consists of two *up* quarks with electrical charge $+2/3e$ and one *down* quark with electrical charge $-1/3e$. In the naïve QPM, the constituent quarks have spin 1/2 that align either parallel or anti-parallel to the nucleon spin, thus explaining the total spin 1/2 of the nucleons (two quarks spins being aligned parallel and one quark spin begin aligned anti-parallel to the spin of the nucleon).

The naïve QPM did not take into consideration the transient quark-antiquark pairs (sea quarks) and gluons which bind the valence quarks by the strong interaction. To accommodate these, the QPM was improved to include a Quantum Chromodynamic (QCD) description for the strong interaction between the quarks through the exchange of gluons.

Experimentally, the spin-independent structure functions of the proton and of the neutron have been extensively studied in scattering experiments, namely by experiments at SLAC, DESY and CERN.

On the other hand, in 1988, the EMC experiment at CERN studied the spin-dependent structure of nucleons, namely the contribution to their spin 1/2 of their constituent quarks, with (then) surprising results: this contribution was measured to be very small, even compatible with zero [10, 11], at contrast with the naïve theoretical predictions. This situation became known as the "proton spin crisis".

The well known value of 1/2 of the spin of nucleons can be divided into its contributions from quarks, gluons and their orbital angular momentum as

$$S = \frac{1}{2} = \frac{1}{2}\underbrace{\Delta\Sigma}_{\text{quarks}} + \underbrace{\Delta G}_{\text{gluons}} + \underbrace{L_q + L_g}_{\text{orbital angular momenta}} \quad . \tag{1.1}$$

The contribution from the quarks can be further decomposed into individual flavours, as $\Delta\Sigma = \Delta u + \Delta d + \Delta s$, or separating valence and sea quarks, as $\Delta\Sigma = \Delta u_v + \Delta d_v + 2\Delta\bar{u} + 2\Delta\bar{d} + \Delta s + \Delta\bar{s}$. The last two terms allow for an asymmetry in the contribution from the strange quarks and antiquarks. The notation of the helicities is sometimes not well defined, but in general, for each flavour, the helicities represent the balance from the contribution from quarks that have spins parallel to the nucleon spin and quarks that have spins anti-parallel to the nucleon spin. Often, for a given flavour, both quarks and anti-quarks are considered, that is, $\Delta q = q^+ - q^-$ is the quark helicity distribution for given flavour, given by the difference of those with spin parallel (+) or antiparallel (−) to the nucleon spin. The spin-independent PDFs are then given by $q = q^+ + q^-$.

A need to measure the contribution to the nucleon spin of the gluons in the nucleon arose. At the same time, the contribution of the quarks should be more precisely determined. This was tackled by different experiments, such as experiments at SLAC, SMC and COMPASS at CERN, HERMES at DESY, Halls A, B, and C at JLab, and later PHENIX and STAR at RHIC.

The most recent results point to quarks spin contributing only about 30% to the nucleon spin: COMPASS measured $\Delta\Sigma(Q^2 = 3\ (\mathrm{GeV}/c)^2)) = 0.32 \pm 0.02_{\mathrm{stat}} \pm 0.04_{\mathrm{syst}} \pm 0.05_{\mathrm{evol}}$ [12]. The gluon contribution is constrained only for a limited x range; the most recent COMPASS results point to a small positive contribution: $\langle \Delta g/g \rangle = 0.113 \pm 0.038_{\mathrm{stat}} \pm 0.036_{\mathrm{syst}}$ at $\langle x_{\mathrm{g}} \rangle \approx 0.1$ ($\mu = 3\ (\mathrm{GeV}/c)^2$) [13].

Different parametrisations for the helicity distributions have been attempted, as is the case with the recent ones by the JAM collaboration [14]. In all the parametrisations, the quarks contribution to the nucleon spin is about 30% with an uncertainty of 10%-20%, and the Δu and Δd distributions don't change much among different parametrisations. The strange quark helicity distribution is constrained mainly by the assumptions used, and has small and negative values (except for the DSSV09 parametrisation). The gluon helicity distribution is small but has large uncertainties, and is known only in a limited region of phase-space. A more detailed discussion on the current status of the "nucleon spin puzzle" can be found, *e.g.*, in Ref. [15].

Finally, very few experimental results were obtained on the orbital angular momentum: *e.g.* the transverse-spin-dependent azimuthal asymmetries measured in the polarised Drell-Yan process at COMPASS for the first time validate the TMD approach to the description of the nucleon spin [16].

Quantum chromodynamics allows to explain the composition of hadrons as bound states of quarks, held together by the mediators of the strong force, the gluons, and their interactions. In contrast to what happens to the mediators of the electromagnetic and weak forces, gluons interact with other gluons, with dramatic consequences, namely the asymptotic freedom of quarks inside hadrons and the confinement of quarks in hadrons. When describing the high energy scattering of nucleons by leptons, the theory of QCD is calculable in terms of perturbative series of the strong coupling constant, for high enough exchanged momentum between the leptonic probe and the nucleon. When that kinematic condition is not fulfilled, we enter in the non-perturbative region, which is a less known region both theoretically and experimentally. In that region, and in the conditions of the COMPASS measurements, the Regge model [17,18] is expected to be applicable. Attempts to reconcile the perturbative and non-perturbative regions have been done, and need experimental testing. Some tests will be discussed in the present work. The approach of Lattice QCD should be able to calculate the different contributions to the total nucleon spin in the non perturbative region, and there have been some attempts in that respect; see, *e.g.*, Refs. [19–23] and references therein.

The description of the differential cross-section of the high energy scattering of leptons by nucleons can be done, in its simplest form, in terms of four structure functions that need to be determined experimentally: the spin-independent structure functions F_1 and F_2 and the spin-dependent structure functions g_1 and g_2.

A first step to the determination of the structure function g_1^p of the proton done in this thesis is the extraction from data of the spin asymmetry A_1^p, which is a ratio of the difference of cross sections of different spin configurations to the unpolarised cross section.

The extraction of the spin-dependent structure function of the proton g_1^p is done in the framework of the collinear approximation, where transverse degrees of freedom of quarks are

neglected (being either considered small or calculations doing integrations over them). However, while being small, these do exist and they were measured in COMPASS and in other experiments. More complete ("3D") views of the nucleon structure make use of transverse momentum dependent parton distribution functions (TMDs) or generalised parton distribution functions (GPDs), which take into account more degrees of freedom of the nucleon; they can, in turn, be considered as the result of averaging over some of the degrees of freedom of even more general entities that describe the nucleon, the so called Wigner distributions [24].

Some of the information needed for the performed analysis, such as the beam and target polarisations, the dilution and the depolarisation factors, and the quantities F_2 and R, was obtained from the official COMPASS analysis software package, PHAST (PHysics Analysis Software Tools) [25]. The author programmed the code for the determination of spin asymmetries A_1^p and of the structure function g_1^p, their statistical and systematic uncertainties, and the systematic studies performed for investigation of possible sources of reproducible and random false asymmetries.

The author performed data analysis in the COMPASS Collaboration, being the first author of two COMPASS internal peer-reviewed release notes [26, 27]. The author produced the code to extract the spin asymmetries A_1^p and the spin structure function g_1^p, and to calculate their statistical and systematic errors, as well as for the test to investigate possible sources of reproducible false asymmetries. Some of the information used as input fr the analysis was obtained from the COMPASS official software package for data analysis, PHAST. The results of the analysis were shown on behalf of the Collaboration at the largest international conferences of the field, both by herself [28–31] and by other COMPASS members [32–34], and were submitted for publication as a COMPASS paper to Physics Letters B [35].

One of the important subsystems that are essencial for running the experiment is the Detector Control System, which is an exclusive responsibility of the LIP-Lisbon group since 2003. The author has been a member of the COMPASS DCS group since 2007. The DCS was presented in a IEEE pear-reviewed international conference by the author [36], on behalf of the COMPASS DCS team, and she participated in the drafting of the DCS part of the article describing the COMPASS hadron setup [37].

The structure of this thesis is the following. In Chapter 2, a literature review is presented. The variables needed to describe the interactions are introduced and the experimental results directly connected to the performed data analysis are shown. In Chapter 3, a description of the COMPASS experiment is presented, and in Chapter 4 the Detector Control System of the experiment is described. In Chapter 5, the method used for the extraction of the spin asymmetries A_1^p and of the spin-dependent structure function of the proton g_1^p is introduced and the necessary external inputs for their computation are presented. In Chapters 6 and 7, the extractions of A_1^p and of g_1^p in unidimensional and in bidimensional bins, respectively, are discussed. The thesis ends with a chapter on conclusions.

Chapter 2

Theoretical and Experimental Overview

2.1 Overview

This chapter contains the theoretical framework for the data analysis presented in this work. It reviews the description of the proton, firstly independent of spin, and afterwards with spin taken into account; both in the perturbative region of QCD and in the non-perturbative region.

Subsequently, an experimental overview of the current knowledge of the spin structure of the nucleon, focusing on the experimental results related to the analysis of the A_1^p and g_1^p at low x and low Q^2, is given.

2.2 Theoretical Overview

2.2.1 Deep Inelastic Scattering

One of the important tools to study the structure of the nucleon is the process of deep inelastic scattering (DIS), that is, the scattering of a lepton by a nucleon in which the nucleon is destroyed (a so called "inelastic" process), creating a hadronic final state with an energy much larger than the mass of the nucleon and of the nuclear resonances, *i.e.* larger than about 1 GeV/c^2 ("deep"), while the lepton in the final state remains the same as the lepton in the initial state:

$$l + N \to l + X. \tag{2.1}$$

Experimentally, there are two possibilities:

- to observe only the scattered lepton l, commonly also denoted l' (then called an inclusive process);
- to observe the scattered lepton and at least one final state hadron (called a semi-inclusive process, $l + N \to l + h + X$).

Figure 2.1 depicts the diagram that describes the process of deep inelastic scattering.

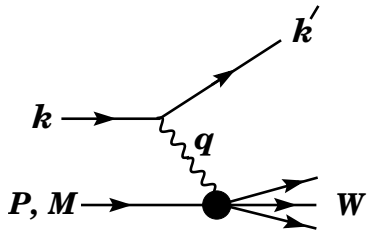

Figure 2.1: Diagram of the process of deep inelastic scattering of a lepton off a nucleon through the exchange of a virtual photon. The quantities k and k' are the four-momenta of the incoming and outgoing leptons, P is the four-momentum of a nucleon with mass M, and W is the mass of the recoiling system X. The exchanged particle is a γ, $W^{\pm}$, or Z; it transfers a four-momentum $q = k - k'$ to the nucleon.

In Table 2.1, the most important kinematic variables used to describe the inclusive processes are listed.

2.2.2 Cross Sections, Asymmetries and Structure Functions

Spin Independent and Spin-dependent DIS Cross Sections

Let us consider the definitions and formalism needed to describe the deep inelastic scattering of polarized leptons on polarised nucleons [38]. In the following expressions, the leptonic mass terms (which are usually ignored) are taken into account. Consider that m is the mass of the lepton, $k(k')$ is the initial (final) lepton 4-momentum, $s(s')$ is the covariant spin 4-vector, such that $s \cdot k = 0 (s' \cdot k' = 0)$ and $s \cdot s = 1 (s' \cdot s' = -1)$; the nucleon mass is M and P and S are the nucleon 4-momentum and the nucleon spin 4-vector, respectively. Admitting, as usual, the exchange of one photon, the differential cross-section to detect the final polarised photon in the solid angle $d\Omega$ and in the final energy range $(E', E' + dE')$ in the laboratory frame, and $P = (M, \mathbf{0})$, $k = (E, \mathbf{k})$, $k' = (E', \mathbf{k}')$, can be written as

$$\frac{d^e\sigma}{d\Omega dE'} = \frac{\alpha^2}{2Mq^4}\frac{E'}{E} L_{\mu\nu} W^{\mu\nu} \tag{2.2}$$

where $q = k - k'$ and α is the fine structure constant.

The leptonic tensor $L_{\mu}\nu$ (summed over the unobserved lepton final spin) is given by

$$L_{\mu\nu}(k, s; k') = \sum_{s'} [\bar{u}(k', s')\gamma_\mu u(k, s)] * [\bar{u}(k', s')\gamma_\nu u(k, s)] \tag{2.3}$$

and can be split between symmetric (S) and antisymmetric (A) parts by exchange of μ, ν:

$$L_{\mu\nu}(k, s; k') = 2\{L^{(S)}_{\mu\nu}(k; k') + \mathrm{i} L^{(A)}_{\mu\nu}(k, s; k')\} \tag{2.4}$$

Variable	Description
$M(m)$	nucleon (lepton) mass
$k(k')$	four momentum vector of the incoming (outgoing) lepton
$s(s')$	spin four vector of the incoming (outgoing) lepton
p	four momentum vector of the nucleon in the initial state
S	spin four vector of the nucleon in the initial state
p_X	four momentum vector of the hadronic final state
$E = \frac{p\cdot k}{M}$	energy of the incoming lepton in the laboratory system
$E' = \frac{p\cdot k'}{M}$	energy of the outgoing lepton in the laboratory system
θ	scattering angle of the lepton in the laboratory system
θ_γ	angle of the virtual photon with respect to the
	incoming lepton in the laboratory system
$q = k - k'$	four momentum transfer
$Q^2 = -q^2$	four momentum transfer squared
$\simeq 4EE' \sin^2 \frac{\theta}{2}$	if lepton mass neglected
$\nu = \frac{p\cdot q}{M}$	energy transfer in the laboratory system
$= E - E'$	
$W^2 = (p+q)^2$	mass of the hadronic final state squared
$x = \frac{Q^2}{2p\cdot q} = \frac{Q^2}{2M\nu}$	Bjorken variable ($0 \leq x \leq 1$)
$y = \frac{p\cdot q}{p\cdot k} = \frac{\nu}{E}$	relative energy transfer in the laboratory system ($0 \leq y \leq 1$)
$\gamma^2 = \frac{2Mx}{Ey} = \frac{Q^2}{\nu^2}$	
m_h	mass of the observed hadron
p_h	four momentum vector of the observed hadron
$E_h = \frac{p\cdot p_h}{M}$	energy of the hadron in the laboratory frame
$z = \frac{p\cdot p_h}{p\cdot q} = \frac{E_h}{\nu}$	fraction of the virtual photon energy
	carried by the hadron in the laboratory frame ($0 \leq z \leq 1$)
$p_{h\|\|} = \frac{\vec{p_h}\cdot\vec{q}}{\|q\|}$	momentum of hadron parallel to photon momentum $\vec{q}$
$p_T = \sqrt{\vec{p_h}^{\,2} - p_{h\|\|}^2}$	transverse momentum of hadron
$\vec{q*}(\vec{p*}_h)$	three momentum vector of the virtual photon (hadron)
	in the photon-nucleon rest frame
$p^*_{h\|\|}$	momentum of the hadron parallel to the photon momentum
	in the photon-nucleon c.m. system
$x_F = \frac{2}{W}\frac{\vec{q*}\cdot\vec{p*}_h}{\|\vec{q*}\|} = 2\frac{p^*{}_{h\|\|}}{W}$	Feynman variable ($-1 \leq x_F \leq 1$)

Table 2.1: Definition of kinematic variables used to describe the process of deep inelastic scattering (top) and of semi-inclusive deep inelastic scattering (bottom).

where

$$L^{(S)}_{\mu\nu}(k;k') = k_\mu k'_\nu + k'_\mu k_\nu g_{\mu\nu}(k\cdot k - m^2)$$
$$L^{(A)}_{\mu\nu}(k,s;k') = m\epsilon_{\mu\nu\alpha\beta}s^\alpha q^\beta. \tag{2.5}$$

The hadronic tensor $W_{\mu\nu}$ describes the interaction between the virtual photon and the nucleon and depends on four scalar structure functions: the unpolarised functions F_1 and F_2 and the polarised functions g_1 and g_2 (ignoring parity violating interactions). These must be measured and can then be studied in theoretical models, such as the QCD-modified quark-parton model, in which they can be written as functions of the two scalar quantities q^2 and $q\cdot P$ (as there are only two independent kinematic variables in DIS). Usually, one works with

$$Q^2 \equiv -q^2 \qquad \text{and} \qquad x_{\mathrm{Bj}} \equiv Q^2/2q\cdot P = Q^2/2M\nu \tag{2.6}$$

where $\nu = E - E'$ is the energy of the virtual photon energy in the laboratory frame. x_{Bj} is known as "Bjorken x", and is usually abreviated as x. The invariant mass of the unobserved final state (in DIS) is $W = \sqrt{(P+q)^2} = \sqrt{M^2 + 2M\nu - Q^2}$. The hadronic tensor can likewise be split in symmetric and antisymmetric parts.

$$W_{\mu\nu}(q;P,S) = W^{(S)}_{\mu\nu}(q;P) + \mathrm{i}W^{(A)}_{\mu\nu})(q;P,S). \tag{2.7}$$

The symmetric part is relevant for unpolarised DIS, and is given by

$$W^{(S)}_{\mu\nu}(q;P) = 2\left[\frac{q_\mu q_\nu}{q^2} - g_{\mu\nu}\right]F_1(x,Q^2) + \frac{2}{M\nu}\left[P_\mu - \frac{P\cdot q}{q^2}q_\mu\right]\left[P_\nu - \frac{P\cdot q}{q^2}q_\nu\right]F_2(x,Q^2). \tag{2.8}$$

The antisymmetric part is relevant for polarised DIS, and is given by

$$W^{(A)}_{\mu\nu}(q;P,s) = 2\epsilon_{\mu\nu\alpha\beta}q^\alpha\left\{M^2S^\beta G_1(\nu,Q^2) + \left[M\nu S^\beta - (S\cdot q)P^\beta\right]G_2(\nu,Q^2)\right\} \tag{2.9}$$

or, as a function of the scaling functions g_1 and g_2

$$g_1(x,Q^2) = M^2\nu G_1(\nu,Q^2), \qquad g_2(x,Q^2) = M\nu^2 G_2(\nu,Q^2), \tag{2.10}$$

$$W^{(A)}_{\mu\nu}(q;P,s) = \frac{2M}{P\cdot q}\epsilon\mu\nu\alpha\beta q^\alpha\left\{S^\beta g_1(q,Q^2) + \left[S^\beta - \frac{(S\cdot q)P^\beta}{(P\cdot q)}\right]g_2(x,Q^2)\right\}. \tag{2.11}$$

In the Bjorken limit or deep inelastic scattering regime, *i.e.* for $Q^2 > 1$ (GeV/c)^2),

$$-q^2 = Q^2 \to \infty, \qquad \nu = E - E' \to \infty, \qquad x \text{ fixed} \tag{2.12}$$

the structure functions F_1, F_2, g_1 and g_2 approximately scale, that is, they change very slowly with Q^2 for a fixed x - in the simple parton model, they scale exactly; in QCD, their Q^2 evolution can be calculated perturbatively.

The difference of cross sections with targets with opposite spins are given by

$$\left[\frac{d^2\sigma}{d\Omega\, dE'}(k,s,P,-S;k') - \frac{d^2\sigma}{d\Omega\, dE'}(k,s,P,S;k')\right] = \frac{\alpha^2}{2Mq^4}\frac{E'}{E}4L^{(A)}_{\mu\nu}W^{\mu\nu(A)}. \tag{2.13}$$

After some algebra, one obtaines the following expressions for the differences of polarised cross sections.

- For longitudinally polarised lepton and nucleon, that is, spin along or opposite to the direction of the leptonic beam, the difference of cross sections for the two directions of the nucleon spin direction (indicated by the double arrow) is given by:

$$\frac{d^2\sigma^{\overrightarrow{\Leftarrow}}}{dx\, dy} - \frac{d^2\sigma^{\overrightarrow{\Rightarrow}}}{dx\, dy} = \frac{16\pi\alpha^2}{Q^2}\left[\left(1 - \frac{y}{2} - \frac{y^2(M^2x^2+m^2)}{Q^2}\right)g_1 - \frac{2M^2x^2y}{Q^2}g_2\right]. \tag{2.14}$$

- For transversely polarised nucleons one obtains:

$$\frac{d^2\sigma^{\rightarrow\Uparrow}}{dx\, dy} - \frac{d^2\sigma^{\rightarrow\Downarrow}}{dx\, dy} = \frac{16\alpha^2}{Q^2}\left(\frac{2Mx}{Q}\right)\sqrt{1 - y - \frac{M^2x^2y^2}{Q^2}}\left[\frac{y}{2}\left(1 + \frac{2m^2y}{Q^2}\right)g_1 + g_2\right] \tag{2.15}$$

where

$$y \equiv \frac{\nu}{E} = \frac{P\cdot q}{P\cdot k}. \tag{2.16}$$

The two independent observables give access to the extraction of both g_1 and g_2. However, the transverse cross section is usually smaller because of kinematic factors. Only recently has it been possible to obtain precise measurements of g_2, which is usually smaller that g_1 in DIS.

It is common to present results of spin asymmetries, *i.e.* ratios of the differences in cross section to unpolarised cross sections, together or as the first step to the extration of the polarised structure functions. The unpolarised cross section is

$$\frac{d^2\sigma_{unpold}}{dx\, dy} = \frac{4\pi\alpha^2}{xyQ^2}\left\{xy^2\left(1 - \frac{2m^2}{Q^2}\right)F_1 + \left[1 - y - \frac{M^2x^2y^2}{Q^2}\right]F_2\right\}. \tag{2.17}$$

Since it is not simple to obtain independent information about F_1 and F_2, the results are usually given for F_2 and R, where

$$R \equiv [1+\gamma]\left(\frac{F_2}{2xF_1}\right) - 1 \tag{2.18}$$

and

$$\gamma^2 = \frac{4M^2x^2}{Q^2}. \tag{2.19}$$

In the Bjorken limit, where $\gamma = 0$ and $R = 0$, the Callan-Gross relation is recovered: $F_2 = 2xF_1$. In case of a target that is longitudinally polarised, the asymmetry measured is

$$A_{||} \equiv \frac{d\sigma^{\overrightarrow{\Leftarrow}} - d\sigma^{\overrightarrow{\Rightarrow}}}{2d\sigma_{unpold}} \tag{2.20}$$

and, in the case of target that is transversely polarised, it is

$$A_{\perp} \equiv \frac{d\sigma^{\rightarrow\Uparrow} - d\sigma^{\rightarrow\Downarrow}}{2d\sigma_{unpold}}. \tag{2.21}$$

One may now define the virtual photon-nucleon asymmetries A_1 and A_2,

$$A_1 = \frac{g_1 - \gamma^2 g_2}{F_1} \qquad A_2 = \gamma \left[\frac{g_1 + g_2}{F_1}\right]. \tag{2.22}$$

We can write

$$A_{||} = D(A_1 + \eta A_2) \qquad A_{\perp} = d(A_2 - \xi A_1) \tag{2.23}$$

with

$$D = \frac{y[(1+\gamma^2 y/2)(2-y) - 2y^2 m^2/Q^2]}{y^2(1-2m^2/Q^2)(1+\gamma^2) + 2(1+R)(1-y-\gamma^2 y^2/4)} \tag{2.24}$$

$$d = \left[\frac{[1+\gamma^2 y/2(1+2m^2 y/Q^2)]\sqrt{1-y-\gamma^2 y^2/4}}{(1-y/2)(1+\gamma^2 y/2) - y^2 m^2/Q^2}\right] D \tag{2.25}$$

$$\eta = \gamma \frac{[1-y-y^2(\gamma^2/4 + m^2/Q^2)]}{(1-y/2)(1+\gamma^2 y/2) - y^2 m^2/Q^2} \tag{2.26}$$

$$\xi = \gamma \frac{1 - y/2 - y^2 m^2/Q^2}{1 + \gamma^2 y/2(1+2m^2 y/Q^2)}. \tag{2.27}$$

Taking $R = \sigma_L/\sigma_T$, the ratio of cross sections for absortion of longitidinally and transversally polarised photons, and F_1 from parametrisation, simultaneous measurements of $A_{\perp}$ and $A_{||}$ allow the extraction of the values of g_1 and g_2 directly but, in practice, most of the past experiments only measured $A_{||}$. Those experiments where used to measure g_1, by neglecting or correcting for the terms with g_2. Although we now know that g_2 is small, there is no *a priori* reason for this, which asks for a method that neglects a quantity for which we know an upper limit. For instance, $A_{\perp} \leq 1$ could be used, but a better approach involves using the virtual photon-nucleon asymmetries, because there are upper limits for A_2: the so called positivity limit, $A_2 < \sqrt{R}$, and the so called Soffer limit:

$$|A_2| \leq \sqrt{R(1+A_1)/2}. \tag{2.28}$$

With g_2 written as a function of g_1 and A_2, one gets

$$\frac{A_{||}}{D} = (1+\gamma^2)\left[\frac{g_1}{F_1}\right] + (\eta - \gamma)A_2, \tag{2.29}$$

with $\eta - \gamma$ being very small. One can use a parametrisation for A_2 or neglect it, which yields

$$A_1 \simeq \frac{A_{||}}{D} \simeq (1+\gamma^2)\left[\frac{g_1}{F_1}\right] \tag{2.30}$$

in order to estimate g_1, while A_2 is used to obtain an upper limit for the uncertainty of g_1.

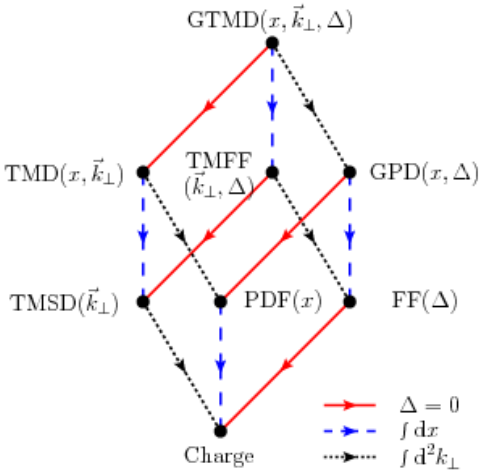

Figure 2.2: Representation of the projections of the Generalised Transverse Momentum Dependent Parton Distribution Functions (GTMDs) into parton distributions and form factors. The arrows correspond to different reductions in the hadron and quark momentum space: the solid (red) arrows give the forward limit in the hadron momentum, the dotted (black) arrows correspond to integrating over the quark transverse-momentum and the dashed (blue) arrows project out the longitudinal momentum of quarks [39]. The different distributions resulting from these operations are explained in the text.

2.2.3 Wigner Distributions

The structure of the nucleon can be described in terms of the six dimensions of space and momentum of its constituent partons using the so called Wigner distributions, $W(\vec{r}, \vec{k})$, where $\vec{r}$ and $\vec{k}$ are, respectively, the position and the 3-momentum vectors of a parton in a nucleon. In the infinite momentum frame, any parton motion is slowed down by time dilation, and the nucleon charge distribution is Lorentz-contracted, which results in incoming particles being scattered instantaneously and incoherently. In this frame, the Wigner distributions can be reduced to five-dimensional distributions, $W(x, k_\perp, b_\perp)$, with x, $k_\perp$ and $b_\perp$ being, respectively, the longitudinal momentum, the momentum in the transverse plane and the position in the transverse plane (*i.e.* the impact parameter) for any given parton. By integrating or making projections with respect to some of those kinematic variables, one obtains the probability distributions that can be accessed in experiments.

In Fig. 2.2, such operations are illustrated. There, Δ is the Fourier conjugate of $b_\perp$ and making it zero is equivalent to integrating over $b_\perp$. By integrating over $b_\perp$, one obtains the TMDs, $f(x, k_\perp)$, that can be seen as quark density distributions in the 3-dimensional momentum space. On the other hand, by integrating over $k_\perp$, one obtains the GPDs, $f(x, b_\perp)$, which can be accessed experimentally by the processes of Deeply Virtual Compton Scattering (DVCS) or Deeply Virtual Meson Production (DVMP). The form factors, $F(b_\perp)$ can be seen as the electric charge and electric current distributions in space (related to the electric form factor G_E and the magnetic form factor G_M); these can be expressed in terms of the spin-independent structure functions F_1, F_2 and F_3. Integrating over $k_\perp$ and $b_\perp$ results in one

dimensional distributions $f(x)$ called Parton Distribution Functions (PDFs).

In the perturbative regime, *i.e.*, for $Q^2 > 1$ GeV, the DGLAP equations [40–42] can be used to relate a PDF at a given hard-scale μ, that is $f(x, \mu)$, to that PDF at another hard-scale. This allows to gather experimental world data at any given common hard scale, and perform global phenomenological fits of the PDFs.

2.2.4 Regge Model

The region of low x and low Q^2 is the Regge limit of deep inelastic scattering where the Regge pole exchange model should be applicable. The Regge model [17, 18] has predictions for g_1, in particular for its singlet $g_1^{\mathrm{S}} = g_1^p + g_1^n$ and non-singlet $g_1^{\mathrm{NS}} = g_1^p - g_1^n$ components. In this model, the shape of g_1 for $x \to 0$ (that is, at $Q^2 \ll W^2$) is parametrised as

$$g_1^i(x, Q^2) \sim \beta(Q^2) \cdot x^{-\alpha_i(0)}, \qquad i = \mathrm{S,NS} \tag{2.31}$$

with $\alpha_i(0)$ being the Regge trajectory function at zero momentum transfer. It is expected that $\alpha_i(0) \lesssim 0$ and $\alpha_s(0) \approx \alpha_{\mathrm{NS}}(0)$ [43–45].

2.2.5 Other Models

Other models have been developed to allow a smooth transition from the perturbative regime to the non-perturbative one. The preditions of those models for g_1 are shown in Figs. 2.3 to 2.5.

For instance, the model of Badełek et al. [47], whose predictions are depicted in Fig. 2.4 describes the calculation of theoretical predictions for g_1^p at low values of Q^2 in the framework of generalised vector dominance model. Both light and heavy vector meson contributions were evaluated. The generalised vector meson dominance model was very sucessful in describing the behaviour of the unpolarised structure function F_2^p in the same kinematic region. The g_1^p structure function was considered to be originated from two components: a perturbative one, related to the heavy vector mesons, and a non-perturbative contribution, related to the light vector mesons. This last part was parametrised using the partonic distributions then available of GRSV2000 at a fixed Q^2 or using simple phenomenological distributions almost independent of x. In the photoproduction limit, the first moment of g_1^p is related to the static properties of the nucleon via the Drell-Hearn-Gerasimov-Hosoda-Yamamo sum rule. This was used to fix the magnitude of the light vector mesons contribution to g_1, using the then available measurements of barionic resonances. The values for g_1^p where evaluated assuming that the structure function

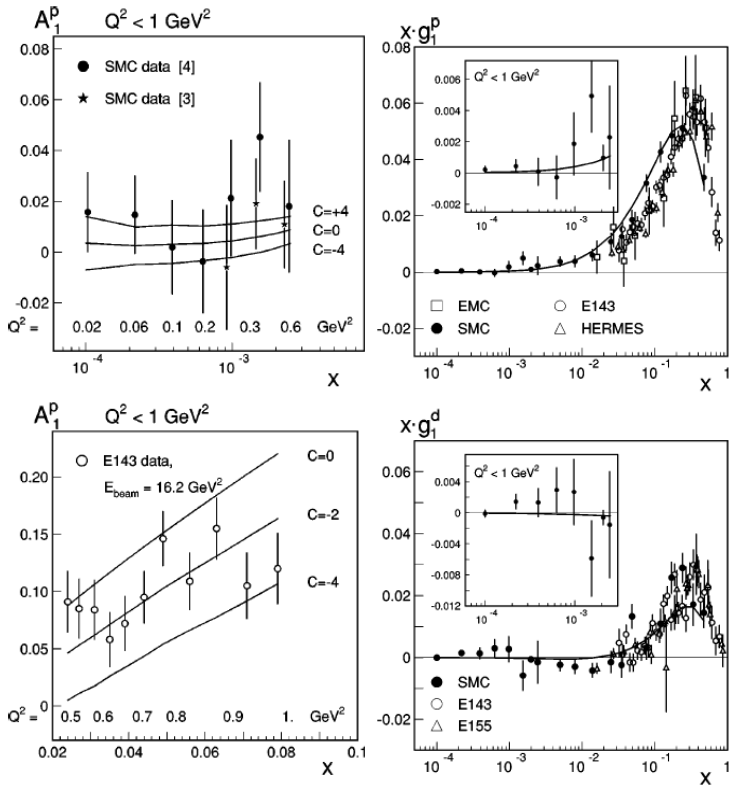

Figure 2.3: Predictions from the model of Badelek *et al.* [46].

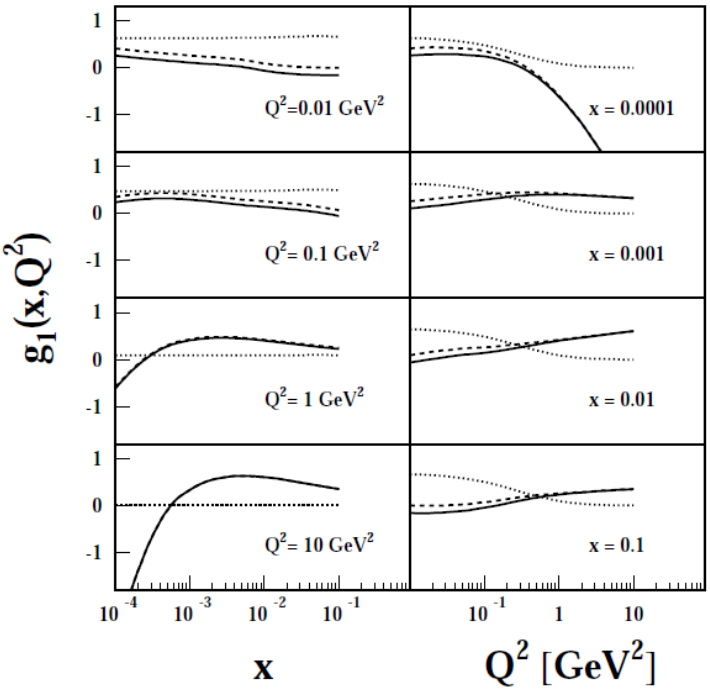

Figure 2.4: Predictions from the model of Badelek *et al.* [47]. The continuous curves indicate the predictions for g_1^p, which in the model is the result of a sum of a VDM contribution, indicated as dotted lines, and an asymptotic contribution, indicated as broken lines.

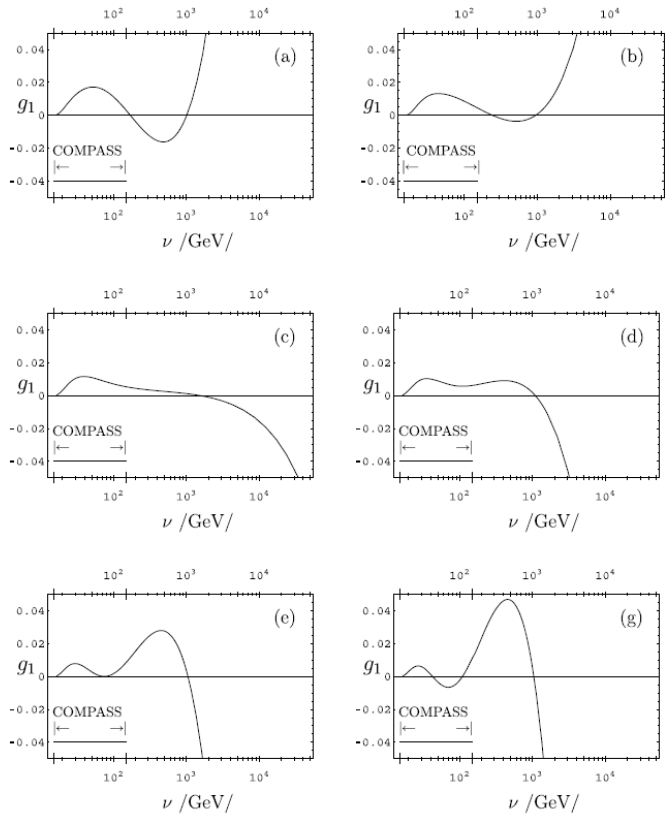

Figure 2.5: Predictions from the model of Ermolaev *et al.* [48]. Notice the large dependence of g_1 with ν, even in the region covered by COMPASS. The different plots correspond to different values of a parameter of the model.

can be written as

$$\begin{aligned} g_1^p(x,Q^2) &= g_1^{\mathrm{L}}(x,Q^2) + g_1^{\mathrm{AS}}(\bar{x},Q^2+Q_0^2) \\ &= C\left[\frac{4}{9}(\Delta u_{\mathrm{val}}^{(0)} + \Delta\bar{u}^{(0)}(x)) + \frac{1}{9}(\Delta d_{\mathrm{val}}^{(0)} + \Delta\bar{d}^{(0)}(x))\right]\frac{M_\rho^4}{(Q^2+M_\rho^2)^2} \\ &+ C\left[\frac{1}{9}(2\Delta\bar{s}^{(0)}(x))\right]\frac{M_\phi^4}{(Q^2+M_\phi^2)} \\ &+ g_1^{\mathrm{AS}}(\bar{x},Q^2+Q_0^2). \end{aligned} \tag{2.32}$$

It was found that the factor C, measuring the contribution of the non-perturbative part of g_1, is negative and equal to about 0.24–0.30, depending on the parametrisation used. This value was found to change at most by 13% in the range $1.0 < Q^2 < 1.6$ GeV^2, where such change was studied.

2.3 Experimental Overview

The analysis presented in this thesis involves the extraction of the spin asymmetry A_1^p and of the spin-dependent structure function g_1^p of the proton at low x and low Q^2. The phase-

space coverage of the data obtained in 2007 is show in Fig. 2.6[1]. Several different previous experimental measurements are related to that analysis and will be briefly summarised in this section:

(a) DIS ($Q^2 > 1$ (GeV/c)^2) F_2^p - unpolarised measurement, complementary phase-space;

(b) low x and low Q^2 F_2^p - unpolarised measurement, similar phase-space;

(c) DIS ($Q^2 > 1$ (GeV/c)^2) A_1^p and g_1^p - similar measurement and complementary phase-space;

(d) COMPASS low x and low Q^2 A_1^d and g_1^d - complementary measurement and similar phase-space;

(e) DIS ($Q^2 > 1$ (GeV/c)^2) A_1^d and g_1^d - complementary measurement and complementary phase-space;

(f) SMC low x and low Q^2 A_1^p and g_1^p - similar measurement and similar phase-space, less statistics.

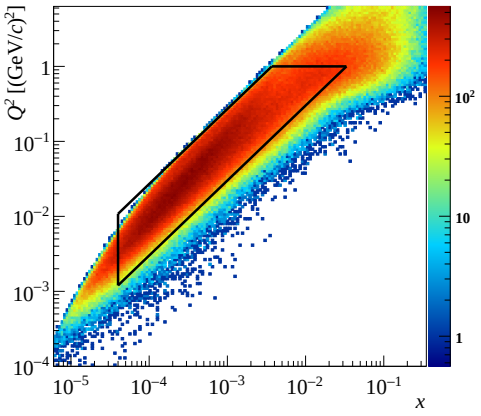

Figure 2.6: COMPASS phase-space coverage and low x low Q^2 region of used for the analysis presented in this work (delimited by polygon).

In Fig. 2.7, measurements of F_2^p and F_2^d (top) and g_1^p and g_1^d (bottom) in the perturbative region, *i.e.* for $Q^2 > 1$ (GeV/c)^2, are shown. For F_2, a typical expected behaviour is seen: at intermediate values of x, F_2 is approximately constant with Q^2; for the highest values of x, F_2 decreases with Q^2; finally, for the lowest values of x, F_2 increases with Q^2. In the case of g_1^p, a mild scaling violation is observed for the lowest values of x. For the g_1 plots, also the COMPASS QCD fit results on world data are shown, and it can be seen that the fits describe the data very well. With its latest measurements in the DIS regime, COMPASS extended the region accessed by the SMC and improved the precision of the measurements, in particular at intermediate and low x.

[1]The inclusive acceptance was estimated with the Monte Carlo event generator AROMA (see Fig. 8(a) of Ref. [49]), but for the setup of 2004, where a target soleinoid with a smaller polar aperture was in use in the experiment, and not for the setup used to collected the data studied in this thesis, which has a wider acceptance.

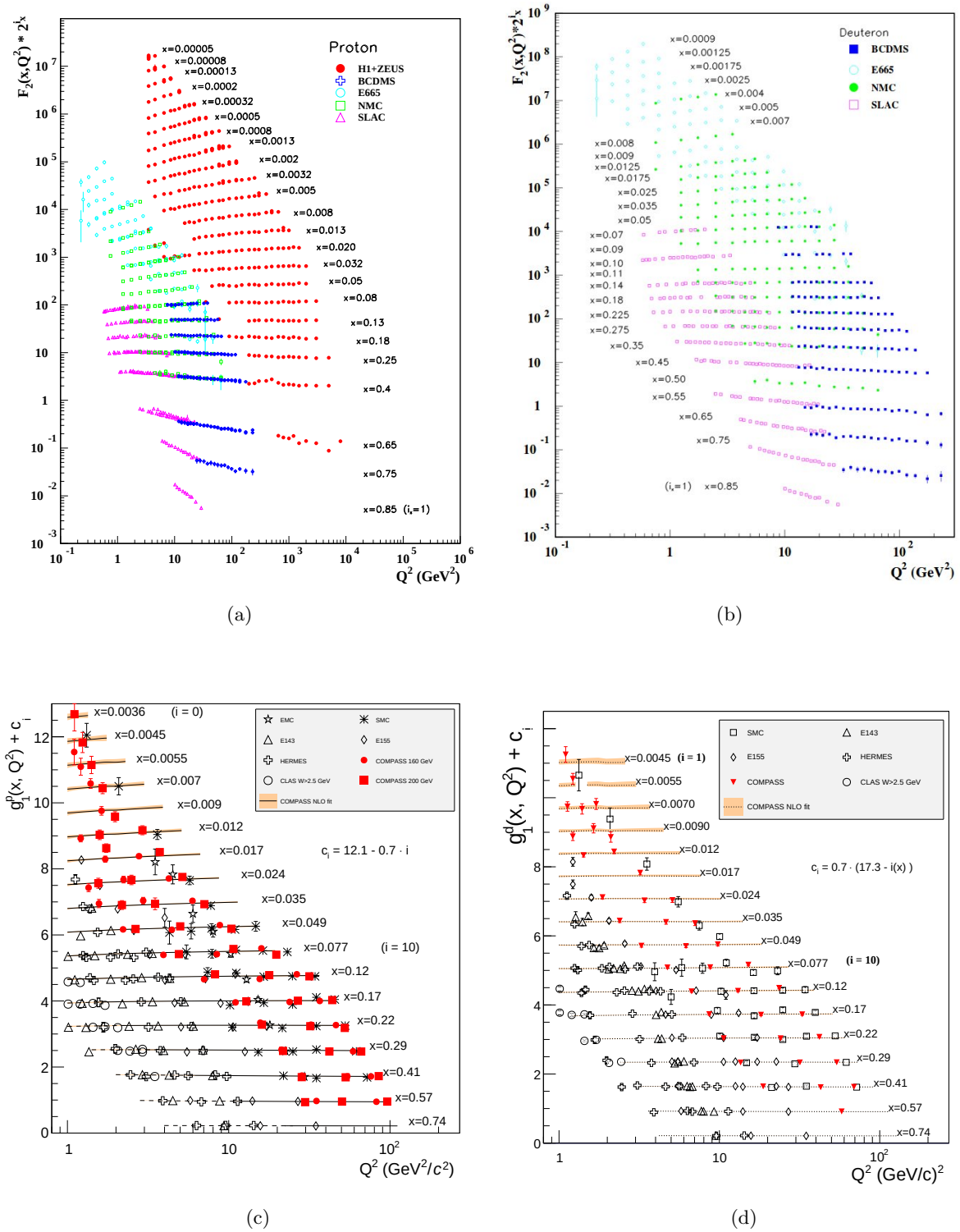

(a) (b)

(c) (d)

Figure 2.7: F_2^p and F_2^d (top) and g_1^p and g_1^d (bottom) in the perturbative region, *i.e.* for $Q^2 > 1$ (GeV/c)^2, from world data. Plots from Refs. [12, 50, 51]. The COMPASS data points in (c) were extracted using a similar method as the one detailed in this thesis, but for the perturbative region of phase space.

In Figs. 2.8 and 2.9, $F_2^p(x)$ results from different experiment at low x and low Q^2 are shown. In Fig. 2.8, the peculiar behaviour of F_2^p as a function of x is visible: not very sensitive to Q^2

down to about $x \sim 0.1$ and then increasing much with decreasing x, and more for higher values of Q^2. In that figure and in Fig. 2.9, curves of the so called ZEUS Regge fit are shown.

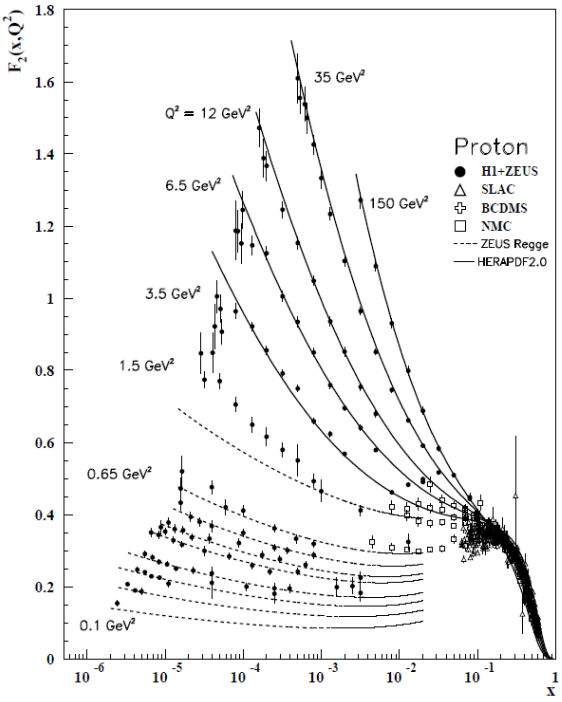

Figure 2.8: $F_2^p(x)$ results at low x from different experiments. Plot from [50].

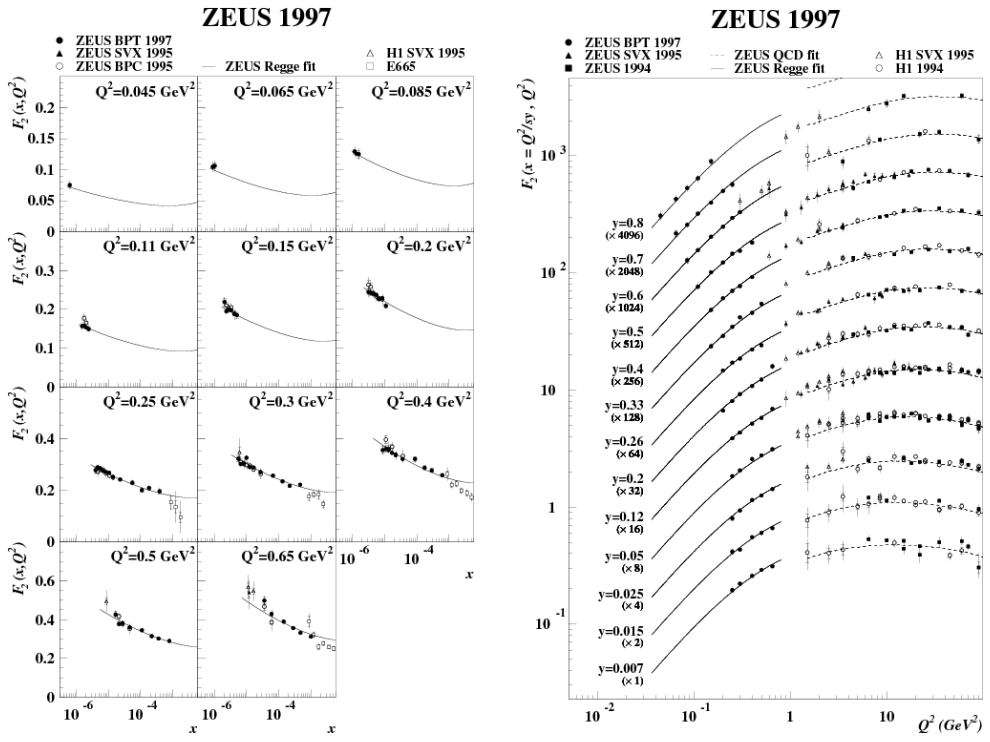

(a) (b)

Figure 2.9: F_2^p results from ZEUS at low x and low Q^2 [52].

The Regge-type fits of ZEUS [52] were done on data that could be described by Regge theory with a constant logarithmic slope $\partial \ln F_2 / \partial \ln(1/x)$. On the other hand, the dependence of F_2 on Q^2 was seen to be stronger than at higher Q^2 values, aproaching, at the lowest Q^2 values of this measurement, a region where F_2 becomes nearly proportional to Q^2. The fit functional form was based on the combination of a simplified version of the generalized vector meson dominance model for the description of the Q^2 dependence and Regge theory for the description of the x dependence of F_2 and has the form:

$$F_2(x, Q^2) = \left(\frac{Q^2}{4\pi^2\alpha}\right) \cdot \left(\frac{M_0^2}{M_0^2 + Q^2}\right) \cdot \left(A_{\mathbb{R}} \cdot \left(\frac{Q^2}{x}\right)^{\alpha_{\mathbb{R}}-1} + A_{\mathbb{P}} \cdot \left(\frac{Q^2}{x}\right)^{\alpha_{\mathbb{P}}-1}\right) \tag{2.33}$$

assuming $R = 0.165 \cdot Q^2/m_\rho^2$, with $m_\rho = 0.77$ GeV $\Rightarrow F_L = 0$, and $\alpha_{\mathbb{R}} = 0.5$. The parameters obtained from the fit were: $A_{\mathbb{R}} = 147.8 \pm 4.6$ μb, $A_{\mathbb{P}} = 62.0 \pm 2.3$ μb, $\alpha_{\mathbb{P}} = 1.102 \pm 0.007$ and $M_0^2 = 0.52 \pm 0.04$ GeV^2.

In Fig. 2.10, the world data on A_1^p for $Q^2 > 1$ (GeV/c)^2 is presented. One can see that COMPASS extended the region accessed by the SMC and improved the precision of the measurements, in particular at intermediate and low x.

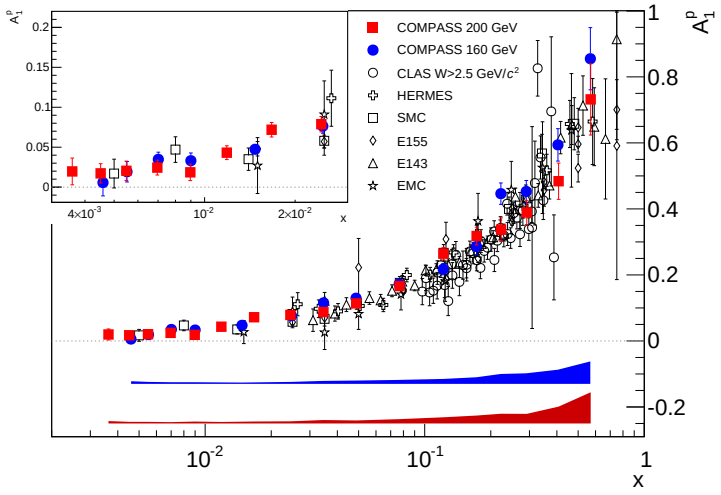

Figure 2.10: World data on A_1^p for $Q^2 > 1$ (GeV/c)^2 [51]. The blue and red bands in the bottom of the figure represent the systematic uncertainties of the COMPASS data.

In Fig. 2.11, the results from COMPASS A_1^p for $Q^2 > 1$ (GeV/c)^2 as a function of x and Q^2 are show. The data taken in 2011 with a 200 GeV/c beam allowed to access lower values of x and gain statistics. It is possible to observe that the results of the two beam energies used are compatible within uncertainties. Furthermore, the asymmetries increase at larger x, but in each bin of x there is no strong dependence on Q^2 (it is possible to fit the values by constants).

In Fig. 2.12, the double longitudinal spin asymmetries for the deuteron are depicted, including data points both from the DIS regime and from the low x and low Q^2 regime. Notoriously, COMPASS reached the lowest x values for the deuteron. Note that, at low x, the deuteron

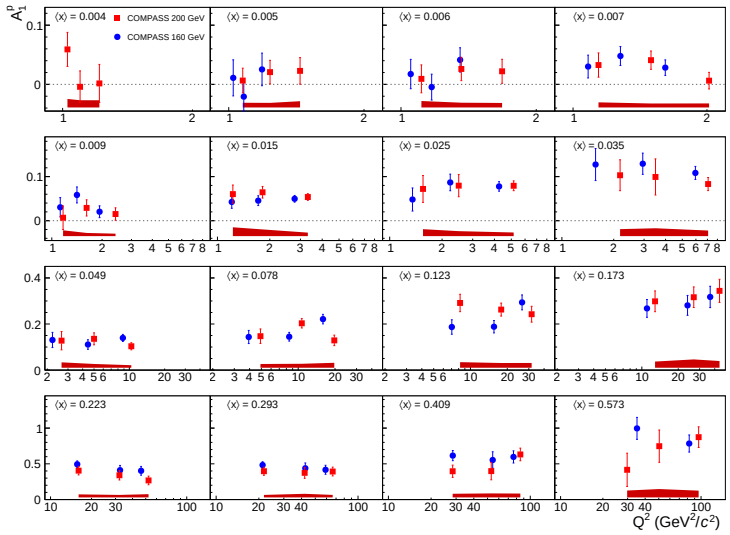

Figure 2.11: COMPASS A_1^p for $Q^2 > 1$ (GeV/c)^2 as a function of x and Q^2 [51]. The red bands in the bottom of the figure represent the systematic uncertainties of the 200 GeV data.

COMPASS data is compatible with zero within uncertainties.

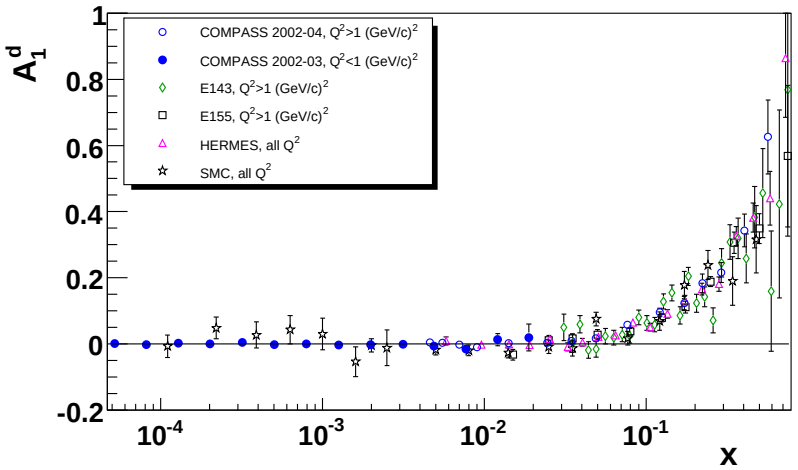

Figure 2.12: World data on double longitudinal spin asymmetry of the deuteron, A_1^d [53].

In Fig. 2.13, the world data results on g_1 (multiplied by x) for the proton, the deuteron and the neutron are shown. It can be seen that SMC reached the lowest values of x for the proton so far, and COMPASS reached the lowest x for the deuteron. At low x, the deuteron COMPASS data is compatible with zero within uncertainties. Moreover, at low x, the proton SMC data is compatible with zero within uncertainties. The neutron g_1 is negative between $x \sim 10^{-2}$ and $x \sim 2 \times 10^{-1}$.

In Fig. 2.14, the COMPASS data and the COMPASS QCD fits for g_1^p an g_1^d are shown. It can be seen that the fit agrees well with the COMPASS data and that the uncertainties increase at the lowest values of x, because there is less data available in that region and in the DIS regime.

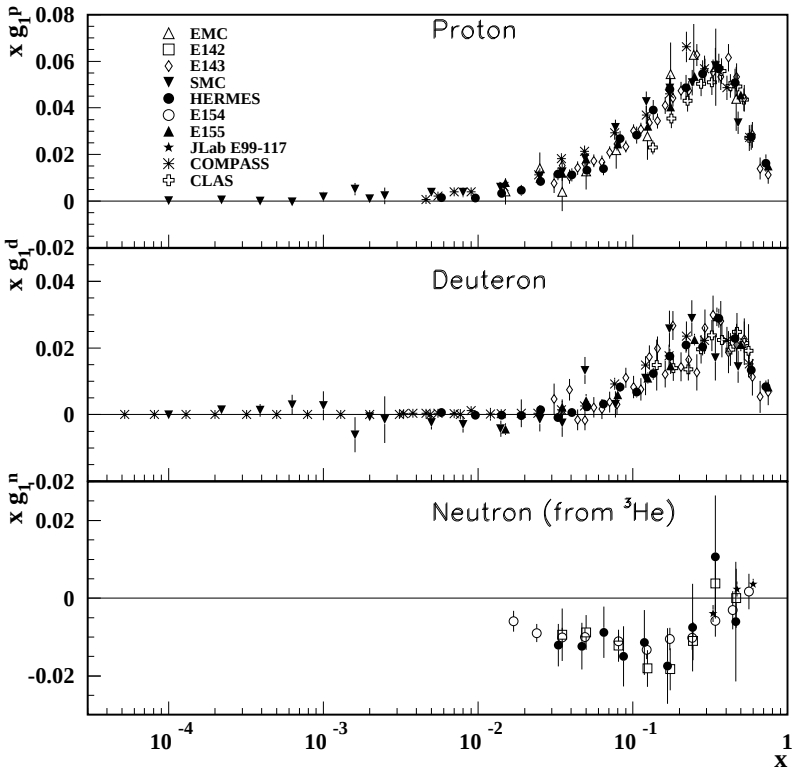

Figure 2.13: World data results on g_1 (multiplied by x) for the proton, the deuteron and the neutron. Plot from [50].

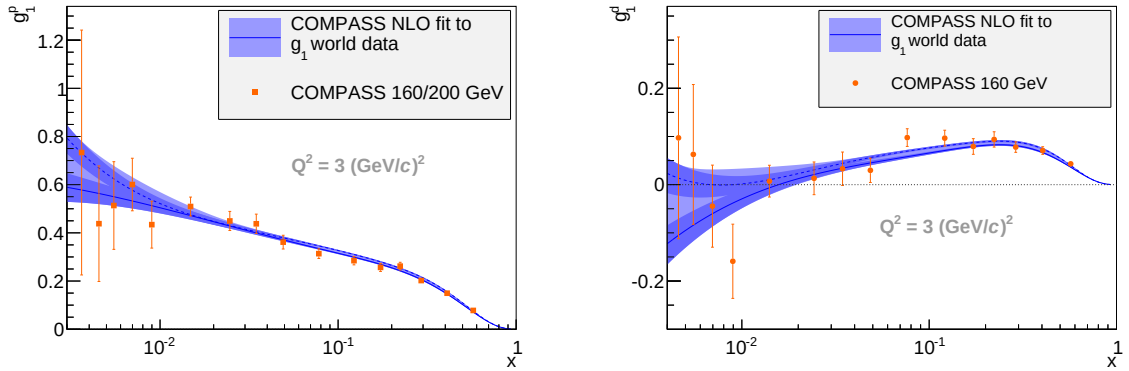

(a) (b)

Figure 2.14: Spin dependent structure function g_1^p (a) and g_1^d (b), with the COMPASS QCD fit of world data at $Q^2 = 3$ (GeV/c)^2 superimposed [51]. The curves correspond to two sets of funtional shapes used. The dark bands represent the statistical uncertainties associated to each curve and the light bands, which overlap the dark bands, represent the total systematic and statistical uncertainties added in quadrature.

The results of the QCD fits on world data for unpolarised and polarised PDFs are shown in Fig. 2.15. The polarised PDFs are much less constrained as compared to the unpolarised ones. The valence quarks dominate at high values of x, whereas the sea dominates at low x, with a significant increase of the gluons in the unpolarised distributions. Note that the distributions are defined for a given scale (and the DGLAP evolution equations allow to translate results

between different scales).

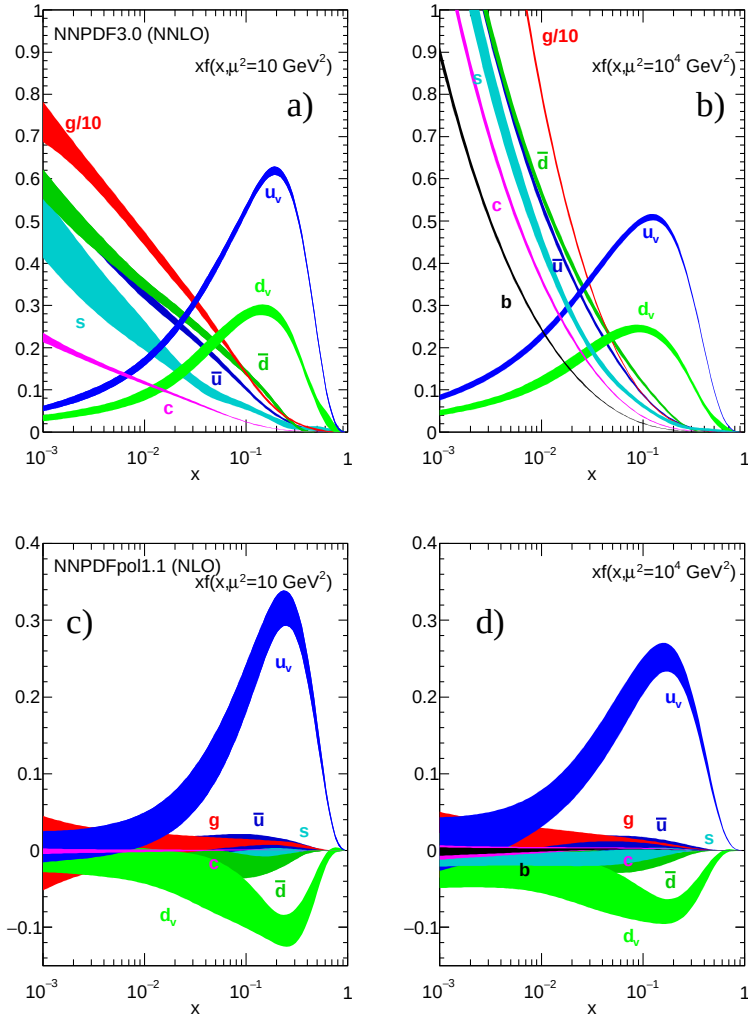

Figure 2.15: (a,b) Unpolarised parton distributions (u_v, d_v, $\bar{u}$, $\bar{d}$, $s \simeq \bar{s}$, $c = \bar{c}$, g) multiplied by x obtained with the NNLO NNPDF3.0 global analysis [54] at the scales $\mu^2 = 10$ GeV^2 (left) and $\mu^2 = 10^4$ GeV^2 (right), with $\alpha_s(M_Z^2) = 0.118$. (c,d) Polarised parton distributions, obtained in NLO with NNPDFpol1.1 [55]. Plot from [50].

The most recent results from a QCD fit to g_1 world data (of the proton, deuteron or neutron) done by COMPASS is show in Fig. 2.16. On the top row, the quarks and the gluons helicities, multiplied by x, are shown as functions of x. The quark helicity distributions are relatively well constrained, but that is not the case for the gluon helicity distribution, for which two solutions (one positive and one negative) are still possible. On the bottom row, one can see that the helicity distributions associated with the flavours u and d are quite well constrained, but the same is not true for the flavour s.

In Fig. 2.17, the quark helicity distributions obtained from a QCD fit perfomed by COMPASS on the world available data is show, obtained both with a proton and a deuteron target. The measured data points are superimposed. While the integrated value of the flavour asymmetry of the helicity distribution of the light-quark sea, $\Delta\bar{u} - \Delta\bar{d}$ is found to be slightly positive, about 1.5 standard deviations away from zero, the sea quark distributions are small and do not

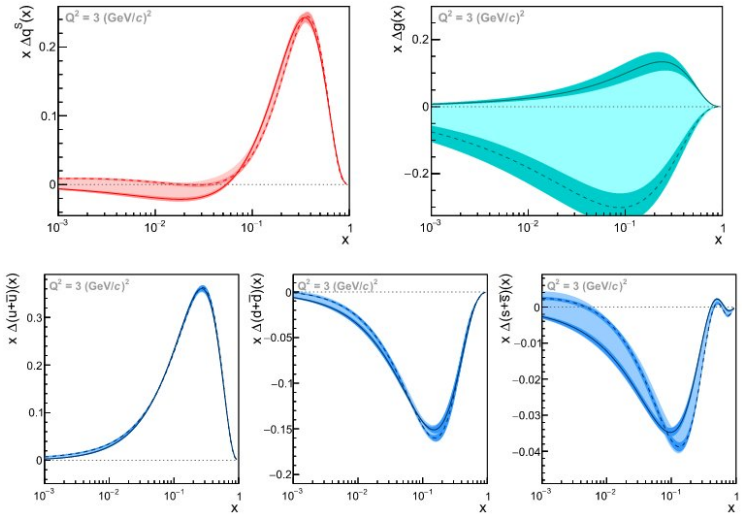

Figure 2.16: Results of the QCD fit at $Q^2 = 3$ (GeV/c)^2 performed by COMPASS on world data for the polarised PDFs [56]. The two curves in each figure represent different sets of functional forms used. Top: singlet $x\Delta q^S(x)$ and gluon distribution $x\Delta g(x)$. Bottom: distributions of $x[\Delta q(x) + \Delta\bar{q}(x)]$ for the light flavours u, d and s. The dark bands represent the statistical uncertainties, whereas the light bands, that overlay the dark ones, represent the total systematic and statistical uncertainties added in quadrature.

show any sizable dependence on x in the range of the measurements. No significant difference is observed between the strange and antistrange helicity distributions, both compatible with zero.

Flavour Separated PDFs from COMPASS and Fits

Quark helicity distributions resulting from the COMPASS QCD fit of world data are shown in Fig. 2.17. The resulting values of the sea quark distributions are small and do not show any sizeable dependence on x in the range of the measurements. Furthermore, the integrated value of the flavour asymmetry of the helicity distribution of the light-quark sea, $\Delta\bar{u} - \Delta\bar{d}$, is found to be slightly positive, about 1.5 standard deviations away from zero.

COMPASS Low x and Low Q^2 Double Longitudinal Spin Asymmetries in Single Hadron Quasi-real Photoproduction at High p_T

COMPASS has published data based on its low x and low Q^2 proton and deuteron samples, in particular for its subsample with single hadron quasi-real photoproduction at high p_T [58]. More specifically, the following kinematic range was used: $p_T > 1$ GeV/c, $Q^2 < 1$(GeV/c)^2, $0.1 < y < 0.9$, $0.2 < z < 0.8$. The experimental asymmetries were compared to next-to-leading order pQCD calculations, being sensitive to the gluon polarisation ΔG inside the nucleon in the range of the nucleon momentum fraction carried by gluons $0.05 < x_g < 0.2$. Results for the longitudinal spin asymmetry $A_{LL}(p_T)$ on polarised protons and deuterons were extracted

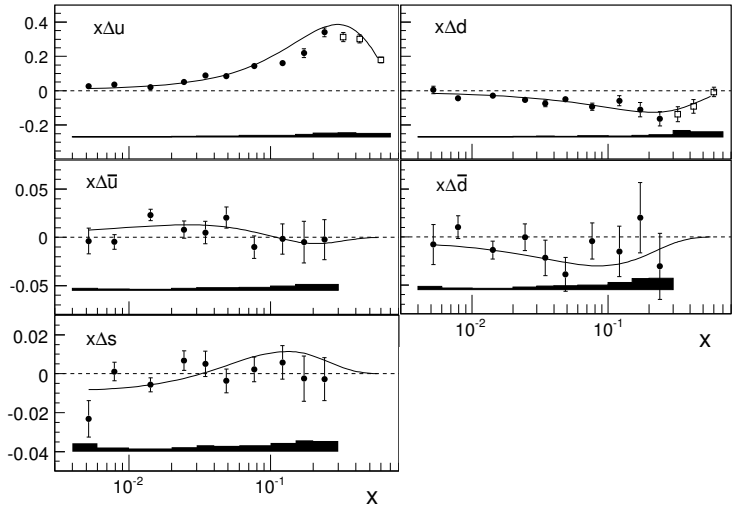

Figure 2.17: Quark helicity distributions resulting from the COMPASS QCD fit of world data. The data from COMPASS, SMC and HERMES are superimposed [57]. Flavour speparation requires the use of semi-inclusive data and hadron identification. The dark bands in the bottom of each plot represent the systematic uncertainties of the data.

separately for positively and negatively charged hadrons, and in three rapidity bins. They were compared to theoretical calculations at NLO without threshold resummation and an overall agreement was found with the calculations based on earlier GRSV$_{std}$ and recent DSSV14 polarised parton distribution functions (PDF) sets, and using the most recent fragmentation functions (FF) set. Nevertheless, calculations including full threshold resummation at next-to-leading-logarithm (NLL) are needed before a meaningful result on ΔG can be extracted quantitatively from this data.

SMC Low x and Low Q^2 A_1^p and g_1^p

The low x and low Q^2 A_1^p and g_1^p results obtained by SMC are shown in 2.18. That experiment developed a special trigger to cover the low x (and therefore low Q^2) region. The asymmetries obtained with the low x trigger show a similar behaviour to the asymmetries obtained with standard triggers in their common region and extend the x range covered by a decade, down to $x = 10^{-4}$. Both the results of A_1^p and $x \cdot g_1^p$ were found to be compatible with zero in the region of the lowest accessed values of x.

The low x and low Q^2 region encompasses the transition from the non-perturbative regime of photoproduction to the perturbative regime of deep inelastic scattering, and several predictions were formulate. Some of these use first principles, like Refs. [48, 60], but there are also predictions for g_1^p based in GVMD ideas, from two works: (1) B. Badełek *et al.* [47]; and (2) W. Zhu and J. Ruan [61].

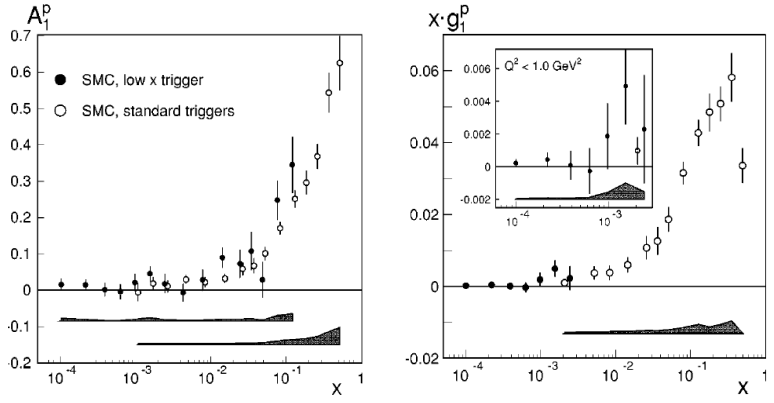

(a) (b)

Figure 2.18: Low x and low Q^2 A_1^p and g_1^p analysis of SMC [59]: (a) results for A_1^p; (b) Results for g_1^p. The bands in the bottom of the plots represent the systematic uncertainties of the data.

2.4 Summary

In this chapter, a review of the framework used to describe the high energy scattering of leptons by nucleons was done. Furthermore, the experimental results that are related to the analysis discribed in this thesis are briefly referred. While the spin dependent structure function F_2 is already quite well known in the perturbative regime, the measurements at low x and low Q^2 only reach Q^2 values as low as 0.2 $(\mathrm{GeV}/c)^2$. The efforts to solve the "proton spin puzzle" persist, the measurements of the gluon contribution and of the strange quark contribution are still not satisfactorily known. The spin dependent structure functions g_1^p and g_1^d in DIS and g_1^d in the non perturbative regime; a precise measurement of g_1^p in the non perturbative regime was not yet published by COMPASS, and the analysis for its extraction is the subject of the thesis. Finally, some of the phenomenological models that make predictions for A_1^p and g_1^p in the region of low x and low Q^2 were presented; they will be compared to the data obtained from the analysis.

Chapter 3

The COMPASS Experiment

3.1 Overview

In this chapter, the COMPASS experiment as it was operated in 2007 and in 2011 is described, focusing on the elements necessary for the low x and low Q^2 A_1^p and g_1^p extractions. These were the years when the muon programme was pursued with a longitudinally polarised target of protons. The muon beam energy was 160 GeV in 2007 and 200 GeV in 2011.

For the analysis of spin asymmetries at low x and low Q^2 studied in this thesis, a scattered muon is detected at small polar angles, and therefore mostly in the (second) small angle spectrometer, whereas the additional hadron required in the interaction vertex is detected at larger polar angles, and therefore mostly in the (first) large area spectrometer. Consequently, the complete spectrometer is effectively used for the detection and reconstruction of the tracks in the events here studied.

3.2 Introduction

The COMPASS experiment at CERN [37,62,63] is a fixed target experiment on the M2 beamline of the CERN Super Proton Synchrotron that uses high intensity and high energy secondary hadron beams or tertiary muon beams. Electron beams of low intensity can also be produced. The data-taking started in 2002. The experimental apparatus is described in detail in Ref. [63] (muon program) and [37] (hadron program).

The experimental apparatus is a large angular and momentum acceptance two-stage forward spectrometer, *i.e.* it uses two dipole magnets, SM1 and SM2, in order to reconstruct trajectories and measure the momenta of particles emitted from the target volume either at larger or smaller polar angles in the laboratory frame, or with smaller or larger momentum, respectively. The total field integrals of the two magnets are 1.0 Tm for SM1 and 4.4 Tm for SM2, for its nominal current of 4000 A.

The apparatus is multi-purpose, allowing for different Physics programmes to be pursued with only some small changes. During the first phase of the experiment, the data-taking was divided into a hadron program using hadron beams, to study hadron spectroscopy and to measure the polarisability of the pion, and a muon program, to study the spin structure of

the nucleon and to access fragmentation functions by studying the process of inclusive and semi-inclusive deep inelastic scattering. The latter program was further subdivided in two, corresponding to having the polarised target with either longitudinal or transverse polarisation with respect to the direction of the beam. Two materials were used in the target: deuterated lithium, ^{6}LiD, as an isoscalar target (the ^{6}Li nucleus being approximated to a non-polarisable alpha particle and a polarisable deuteron), and ammonia, NH_3, as a source of polarised protons. In 2006, the experiment was significantly upgraded by the replacement of the target solenoid magnet by a new one with wider angular aperture.

A summary of the conditions of data-taking in the years of 2007 and 2011 is presented in Appendix A.

3.3 Experimental Setup for the Muon Program

3.3.1 Polarised Beam

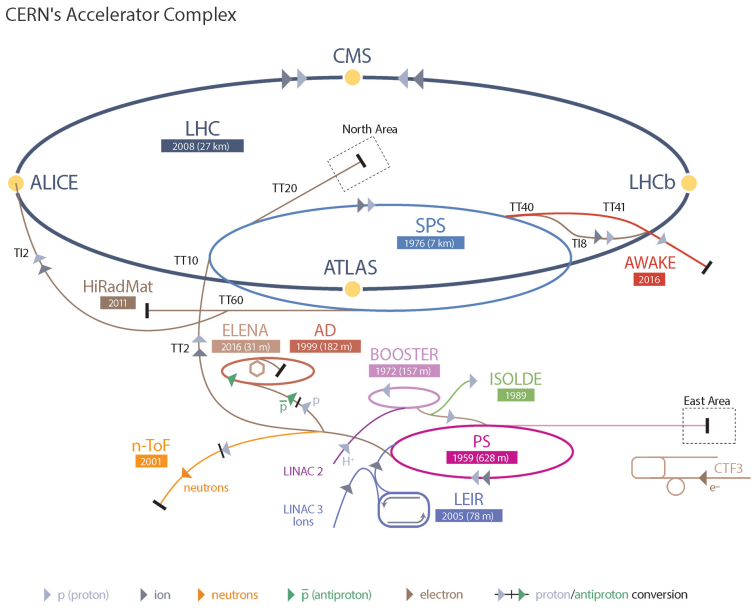

Figure 3.1: CERN accelerator complex. The COMPASS experiment is located in the North Area, at ground level (in contrast to the SPS ring, which is 40 m underground). The LINAC 2 accelerates protons up to energies of 50 MeV, then the Booster accelerates them up to 1.4 GeV, followed by the PS that accelerates them to 26 GeV and the SPS which acelerates them up to 450 GeV. Currently the LHC accelerates protons further up to 6.5 TeV.

The CERN accelerator complex, as presented in Fig. 3.1, circulates and accelerates, among other particles, protons in a series of accelerators (LINAC2 and PS Booster), until they reach the Super Proton Synchrotron (SPS).

To obtain beam particles in the COMPASS hall, there must first be an extraction of protons from the SPS using a technique called slow extraction, in spills or packets of beam particles with flat tops of 4.8 or 9.6 s, in supercycles with varying length, depending on other users of

the acellerators complex but usually of the order of tens of seconds. This kind of extraction allows to have a constant beam flux of particles (*i.e.* a debunched beam) over many seconds, *i.e.* lower rates of events, that the experiment's front-end electronics and the DAQ can handle. Usually, 300×10^{11} protons are extracted from the SPS per spill, of which a fraction, of the order of 250×10^{11}, impinge on the CERN North Area T6 target. The T6 primary target is a beryllium target with a length of 500 mm. The material and the length of this target are optimised for the maximum intensity of the secondary beam, composed of hadrons. The final hadron beams that arrive at COMPASS are, in the case of negative hadron beams, composed mostly by pions, with a small percentage of kaons and antiprotons, while the positive hadron beams are mixes of protons and pions, with a small percentage of kaons. The muon beams from the CERN M2 beam line consist of muons that are polarised as a result of the parity violating process of their production in pion decays ($\pi^+ \to \mu^+\nu_\mu$) or, to a lesser extent, in kaon decays ($K^+ \to \mu^+\nu_\mu$). The decay products of a pion, and in particular the correlation between their momentum and their spin, are shown in Fig. 3.2. For DIS and SIDIS measurements, a

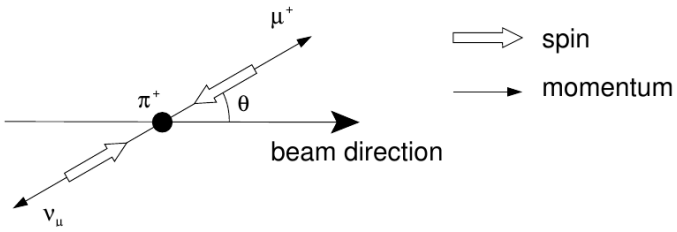

Figure 3.2: Decay products of a pion. Momentum and spin of the neutrino and of the muon are shown.

positive muon beam is used because of the higher intensity that can be achieved as compared to a negative muon beam. In the center-of-mass frame of the decay process, the polarisation is 100%. In the laboratory frame, in the direction of the beam, the polarisation is smaller, and given by

$$P_\mu \approx \pm \frac{m_\pi^2 + (1 - 2\frac{E_\pi}{E_\mu})m_\mu^2}{m_\pi^2 - m_\mu^2}. \tag{3.1}$$

The dependence of the beam polarisation and of the beam intensity on the beam momentum is shown in Fig. 3.3. The maximum intensity is reached at about 120 GeV/c momentum for a 80% polarisation. The value of 160 GeV/c used in most of the years of data-taking was chosen to minimise the statistical uncertainty of the main measurement of the experiment, *i.e.* spin asymmetries, which means to maximise the figure of merit of the measurement, that which involves the product of the number of events and the square of the beam polarisation, NP_b^2 where N is the number of events.

In 2011, a beam momentum of 200 GeV/c was used in order to access a phase-space region with lower x. The beam intensity was consequently reduced to about one half with respect to the 160 GeV/c beam.

The beam spot at the polarised target has a width of 7.8 mm and a divergency of 0.4 $\times$

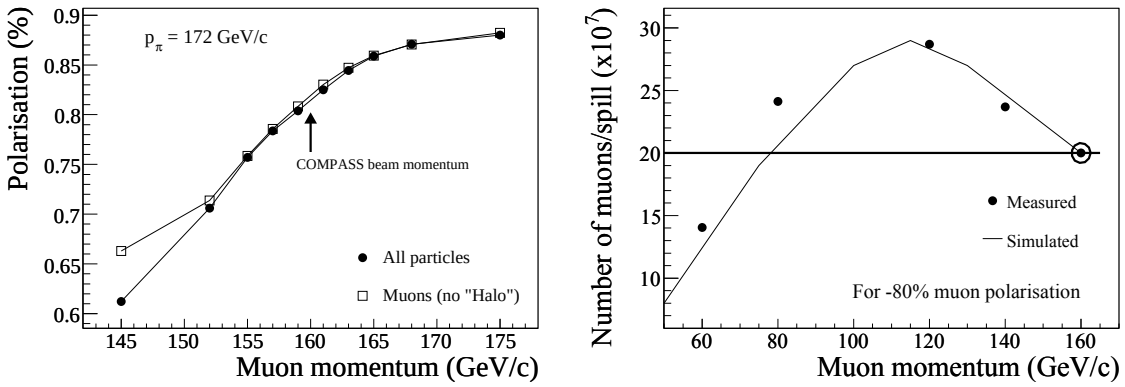

(a) (b)

Figure 3.3: (a) Beam polarisation versus momentum; (b) beam intensity versus momentum [63]. More details can be found in [64].

0.8 mrad. A beam intensity of 200×10^6 muons per spill can be reached with the nominal primary beryllium target of $500 \times 3 \times 3$ mm^3. The transverse dimensions of the primary target must be adequate for the operations of the subsequent beam line. Shorter lenghts of targets can be used for specific purposes, such as the alignment of the spectrometer tracking detectors.

3.3.2 Beam Momentum Station

In COMPASS, it is possible to measure the momentum of each individual muon of the beam, using the beam momentum station (BMS). In fact, in order to make maximum use of the incident flux, the momentum spread of the beam as defined by the beam optics is large and can reach 5%, thus making the measurement necessary. Fig. 3.4 shows the detectors that are part of the BMS. There are six detectors of scintillating material, three before and three after the bending magnet Bend6 that bends the beam in the vertical plane. The measurement of the bending angle allows to calculate the momentum of the muons.

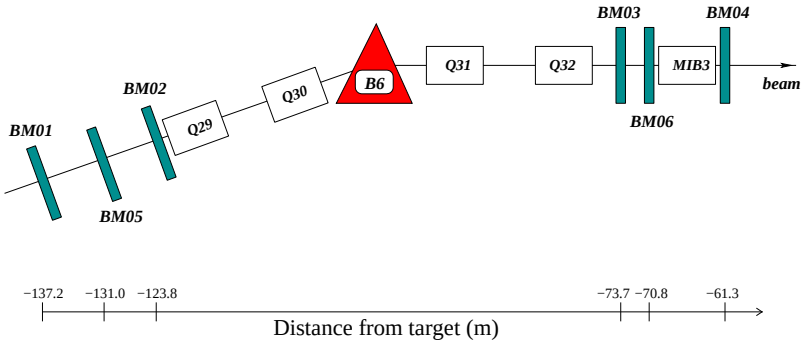

Figure 3.4: Layout of the beam momentum station for the COMPASS muon beam.

3.3.3 Polarised Target

The polarised target is one of the most important components of the COMPASS experiment. It is represented in Fig. 3.5. In order to build and maintain the polarisation of the target material,

Material	Polarisation (%)	Dilution factor f (%)
^{6}LiD	50	40
NH_3	85	16

Table 3.1: Characteristics of the two polarised target materials used in COMPASS.

it includes a superconducting solenoid magnet that can reach a very uniform magnetic field of 2.5 T, with spatial variations of the field within the target material smaller than 0.01%. The target material has to be kept at very low temperatures, as low as 60 mK, which is achieved using a large ^{3}He-^{4}He dilution refrigerator.

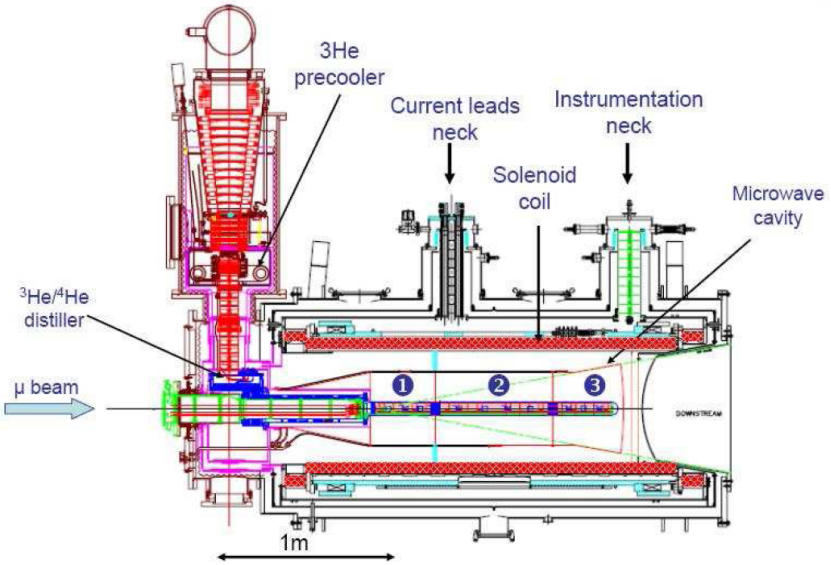

Figure 3.5: Polarised target system, in the configuration with three target cells. The numbers 1, 2 and 3 indicate the location of the cells, inside a cylindrical target holder.

Two different materials are used in the polarised target of COMPASS. From 2002 to 2006, ^{6}LiD was used to study the deuteron. From 2007 onward NH_3 was used to study the proton. In ammonia, the ^{14}N is only slightly polarisable, and this small contamination is corrected for in the data analysis.

The protons in ammonia reach polarisations of about 85%, a value higher that the polarisation that can be reached by ^{6}LiD, which is about 50%. On the other hand, the fraction of material that is polarisable, measured by the dilution factor f, is smaller in the case of ammonia, as can be seen in Table 3.1. More details on the calculation of the dilution factor are given in Section .

The length of the three cells used from 2006 to 2011 is, respectively, 30, 60 and 30 cm, with a 5 cm gap between each consecutive cells. In Fig. 3.6, the polarization of the three target cells is shown. both one cycle and a full year of a data-taking campaign. Polarisations between 80% and 90% are reached.

The physical process that is used to polarise the target protons is called dynamic nuclear polarisation (DNP), and consists of irradiating the paramagnetic centers of the target material

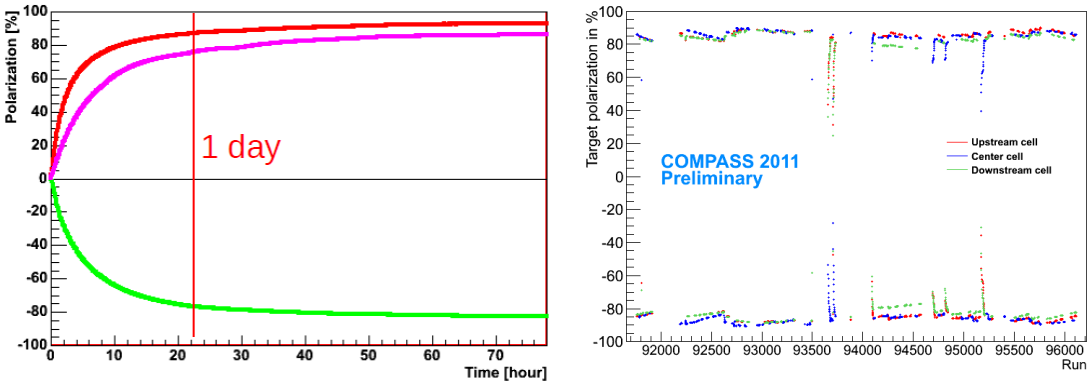

(a) (b)

Figure 3.6: Polarisation of the three target cells: (a) during one cycle and (b) during 2011, using an ammonia target with three longitudinally polarised cells. Several polarisation built-up processes are seen, as well as the frequent polarisation rotations, about every 24 hours [65].

with microwaves, with a magnetic field applied. A schematic view of the whole process is shown in Fig. 3.7.

1. A longitudinal magnetic field of 2.5 T is applied using a superconducting solenoid. At a temperature of the order of 1 K, only the lower energy states are populated. Due to their higher magnetic moments, electrons in the target material anti-align more easily with the external magnetic field than protons. The electron-proton systems occupy both of the lower levels in Fig. 3.7.

2. By applying microwaves of a well defined frequency (in the range $\sim 70.2 - 70.3$ GHz) to the target material a simultaneous flip of the electron spin and its companion proton spin is induced, leaving the electron aligned with the magnetic field. Consecutive target cells are irradiated with different frequencies, for them to end up with opposite polarisations. For a final state with proton spins parallel to the magnetic field $\vec{B}$, a frequency $\omega_e - \omega_p$, as indicated in the figure, is applied. For a final state with proton spins antiparallel to the magnetic field $\vec{B}$, a frequency $\omega_e + \omega_p$, is applied. Each of these cases corresponds to one of the top energy levels in Fig. 3.7 the first case to the level on the left and the second case to the level on the right.

3. Finally, since the electron relaxation time is much shorter than the one of the proton, their spins will spontaneously become antialigned with the magnetic field. the net effect is the polarisation of proton spins either parallel or anti-parallel to the direction of the external magnetic field, depending on the value of the frequency applied. The two final cases corresponds to one of the bottom energy levels in Fig. 3.7 the first case to the level on the left and the second case to the level on the right.

he applied microwaves are further modulated with a frequency of about 5 MHz to enhance the polarisation. In frozen spin mode, with temperatures of the order of 60 mK, the relaxation rate

of the polarisation is $(0.05-0.10)\%$ per day in a 2.5 T field. During the physical measurements with the target magnetic field in longitudinal mode, the relaxation time was about 9000 hours for the field of 1.0 T in 2007 and also with 2.5 T in 2011 (in this latter case, with a new material) [66].

In Fig. 3.6, the values of the polarisation for the three target cells is shown (a) for one cycle and (b) for a whole data-taking campaign (2011).

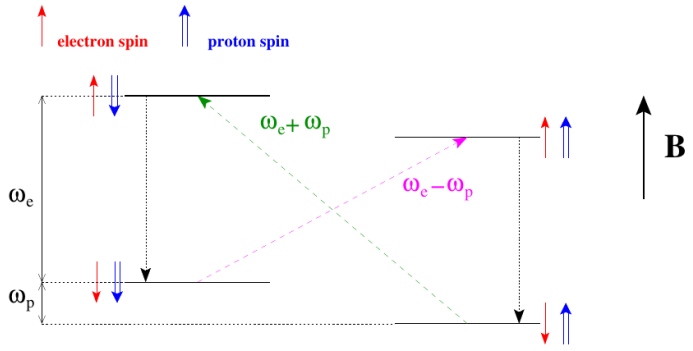

Figure 3.7: Illustration of the process of dynamic nuclear polarisation.

The direction of the polarisation of the target cells is changed regularly (typically every 24 hours), by rotation of the magnetic field of the target solenoid, and using the dipole magnet during the rotation as an auxiliary in order not to loose the polarisation. The idea is to keep the magnetic field vector with an almost constant magnitude, changing only its direction. The rotation procedure takes about 30 minutes and is accompanied by a small loss of polarisation. It allows to collect data with the two spin configurations and similar acceptances

At least once each year, the direction of the polarisation of each cell with respect to the solenoid field is changed. This allows the cancelation of possible systematic effects that may arise if only one such "microwave settings" is used.

In Fig. 3.8, the four cases of polarisation of the target cells and direction of the solenoid field are shown. The transition from the top figures to the lower ones is usually called a solenoid field reversal or rotation and is typically done every 24 hours. It reverses the cells polarisation directions by reversing the solenoid field direction. The transition from the figures on the left to the ones on the right is a microwave setting reversal. It requires bringing the polarisation to zero, and introduces an opposite relative direction of the cells polarisation with respect to the solenoid field direction.

3.3.4 Spectrometer

COMPASS uses a high intensity beam and a spectrometer with a large angular and momentum acceptance. This requires the use of very different detector technologies: silicon detectors and scintillating fiber detectors are used in the beam telescope before the target; scintillating fiber detectors, Micromegas (and Pixel Micromegas) and GEMs (and Pixel GEMs) cover particle trajectories emitted at small angles; and drift chambers and multi-wire proportional chambers are used to cover particle trajectories emitted at large angles with respect to the beam

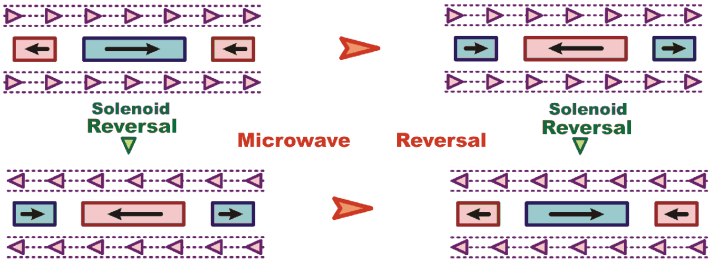

Figure 3.8: Illustration of the four possible different cases for the target cell polarisation and solenoid field direction, for data-taking with a longitudinally polarised target. The small pink arrows indicate the direction of the solenoid field.

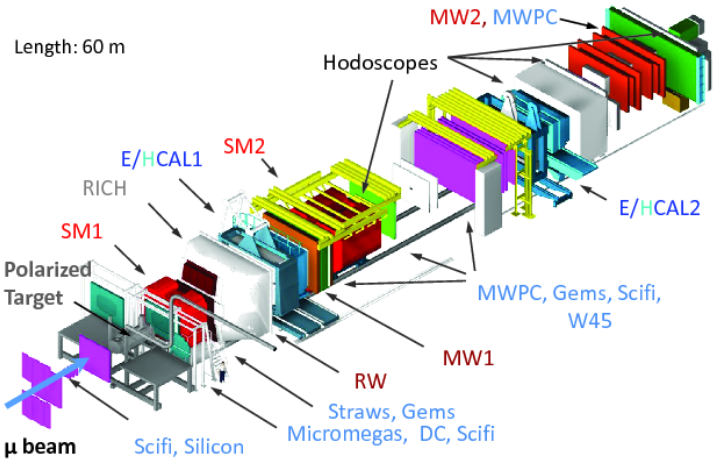

Figure 3.9: Illustration of the COMPASS spectrometer in its setup for the muon programme. The beam enters the experimental hall from the bottom left in the picture, to impinge the polarised target, represented in dark grey. The two dipole magnets of the spectrometer, SM1 and SM2 are represented in red.

direction. Finally, for particle identification, a RICH detector, electromagnetic and hadronic calorimeters, and drift chambers placed before and after the so called muon walls (iron in the first spectrometer and concrete in the second spectrometer) are used. The setup is shown in Figs. 3.9 and 3.10.

3.3.5 Tracking Detectors

Several types of tracking detectors are used in the experiment, in order to handle the expected incident rate, required space resolution and solid angle to be covered.

Along the beam line, in the so called "beam telescope", scintillating fiber detectors are used for their time resolution and rate capability, together with silicon detectors, for their spacial resolution. In the spectrometer, at intermediate angles, Micro-Pattern Gas Detectors (MPGD), in particular the Gas Electron Multiplier (GEM) detectors and the Micro-Mesh Gaseous Structure (Micromegas) detectors, had pioneering usage in the COMPASS experiment. Furthermore, for larger angles, drift chambers, straw drift tubes, and multiwire proportional chambers are used.

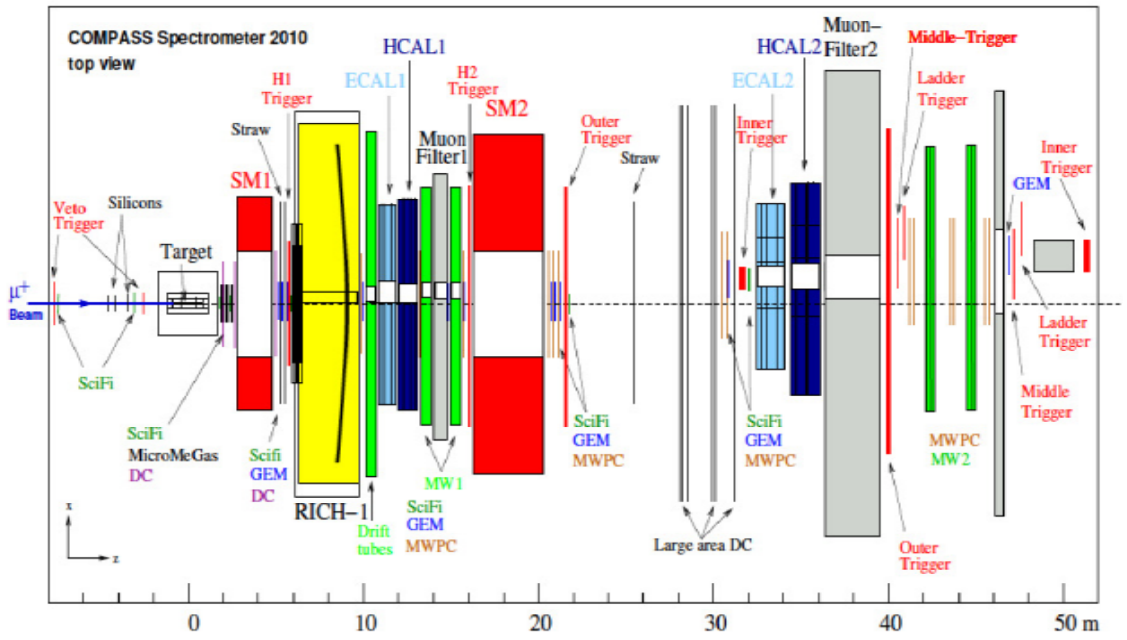

Figure 3.10: Top view of the COMPASS spectrometer in 2010, which is similar to 2011. In 2007, the H1 and H2 hodoscopes that are part of the LAST trigger, where not installed.

3.3.6 Detectors for Particle Identification

The experiment has three types of detectors for particle identification: the RICH, a ring imaging Cherenkov detector; the electromagnetic and the hadronic calorimeters; and the Muon Walls.

In an inclusive analysis, only muon identification is required. There is one Muon Wall at the downstream end of each of the two spectrometers of the experiment. They consist of a massive wall either of iron (in the first spectrometer) or of concrete (in the second spectrometer), that is located in between tracking detectors located immediately before and after it. The passage of particles through such walls is an indication that they are muons, and the trackers associated to it allow to reconstruct their trajectories.

While for other analyses the RICH and the calorimeters are extensively used, that is not the case in the analysis described in this thesis. The calorimeters are used in the trigger, turning some of its sub-triggers into semi-inclusive as, in addition to coincidences of signals in hodoscope slabs, also energy depositions (presumably from a hadron) above a certain threshold are required for the trigger to fire. This is done to have events with a well reconstructed primary vertex.

3.3.7 Detector Control System

The Detector Control System is a set of hardware and software components that allows to efficiently control and monitor the experiment's data-taking, from high voltage and low voltage crates to VME crates, gas flows, temperatures, pressures, humidity and magnetic fields. It is discussed in detail in Chapter 4.

3.3.8 Data Acquisition

The high energy and high intensity beams and solid state targets require data handling with high rate capability, which is provided by the COMPASS Data Acquisition System (DAQ). In Fig. 3.11, the general architecture of the DAQ system that was in use in the 2007 and 2011 data-taking is presented.

The number of detector channels is of the order of 250000 and the total amount of data recorded per year is of the order of 580 TB. With beam particle fluxes of 2×10^8 muons per spill of 9.6 s, the typical event sizes are 35 kB and the typical trigger rates are of the order of 10 kHz for the muon beam.

There has been an upgrade of the DAQ system for the second phase of COMPASS; the new DAQ is based on FPGAs. For details, see [67].

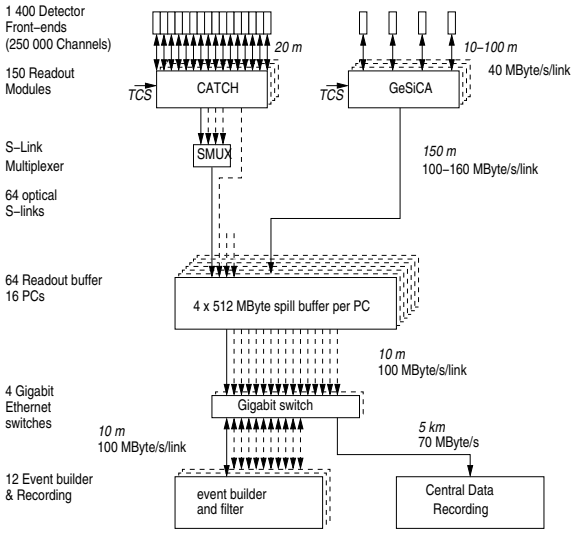

Figure 3.11: General architecture of the DAQ system during the 2007 and 2011 data-taking. Digitised data from the detector front-ends are combined on the readout modules named CATCH and GeSiCa (developed by different groups in the collaboration) close to the detectors. The storage of the data during the spill and the event buildind are performed locally. The data are recorded at the CERN computer center.

3.3.9 Triggers of the Muon Program

The muon triggers of COMPASS are based on hodoscopes made of scintillators. The scattered muon produces a coincidence of signals in a pair of hodoscopes, one of which is after a wall of iron (in the first spectrometer) or concrete (in the second spectrometer), in the activated elements of a coincidence matrix that is set up electronically. The dipole magnets of the experiment bend the trajectories of charged particles only horizontally; therefore, for hodoscopes with horizontal slabs, it is possible for the trigger matrix to have only the diagonal activated, thus allowing target pointing, whereas for hodoscopes that have vertical slabs, half of the coincidence matrix elements need to be activated, and hence all the events with energy loss in the target larger than a predefined minimum will be selected.

Most of the uninteresting halo muon tracks that accompany the beam and that produce coincidences in the trigger hodoscopes are rejected because suitably placed veto hodoscopes are used. One may further require a minimum energy deposition in the calorimeters, corresponding to the detection of one hadron, to increase the purity of the triggers, but transforming them into semi-inclusive triggers. The trigger concept is presented in Fig. 3.12. The different trigger components are complementary with respect to the kinematic coverage they provide, as is shown in Fig. 3.13. More details about the COMPASS trigger for the muon programme are given in Ref. [68].

For the study of the low x and low Q^2 region, the triggers that are most relevant are the Inner Trigger, the Calorimetric Trigger, the Ladder Trigger, the Middle Trigger and the Inclusive Middle Trigger.

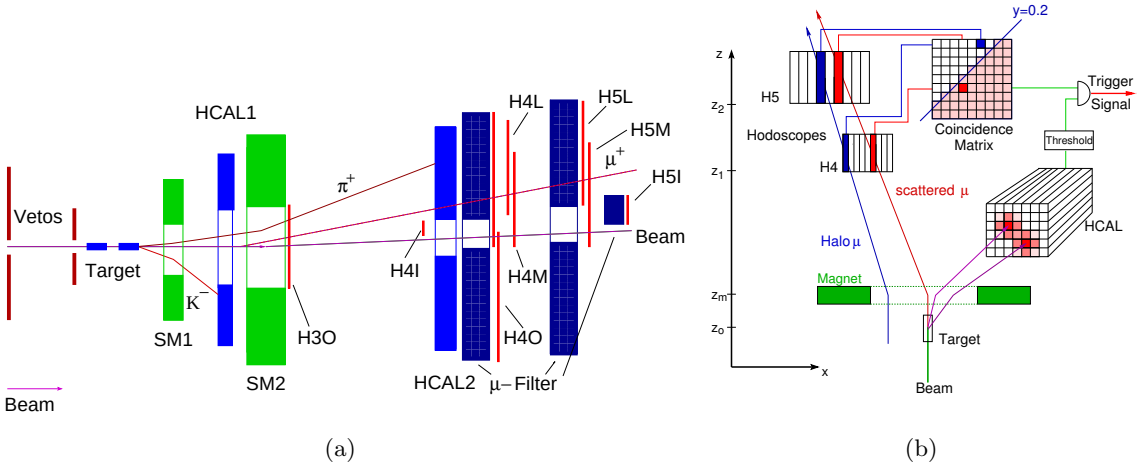

(a) (b)

Figure 3.12: Trigger concept. Along the spectrometer, pairs of hodoscopes constituted by slabs of scintillating material are positioned to detected the passage of the scattered trigger stemming out of the target region. For each pair, one hodoscope is located before and the other is located after a muon filter, that is a thick material, either concrete or iron, that stops other particles but lets the muons pass. When two signals in two slabs of two hodoscopes of one pair are detected in coincidence, given a time window, a trigger is fired and the information collected by the different detectors for the event is recorded by the DAQ. A trigger matrix defined by slabs of the two hodoscopes in a pair is defined in order to only have a trigger if the geometry of the two slabs indicates that the muon track originated in the target.

In Tables 3.2 and 3.3, rates per trigger for two typical runs of 2007 and 2011 data taking are shown. The definition in the DAQ of the bits for the different triggers in 2007 and 2011, respectively, the prescaling factors applied to each trigger, and typical trigger rates (per spill) before the prescaling is applied are shown. Note that the Inner Veto, the Halo Trigger and the Beam Trigger are auxiliary triggers, used *e.g.* for the alignment runs, and are therefore very much prescaled (*i.e.* only a small fraction is selected to be saved by the DAQ) during the Physics runs. The random triggers are also auxiliary triggers and are either prescaled or not, in this last case because they are truly random triggers generated by a radioactive source whose intensity was tuned beforehand.

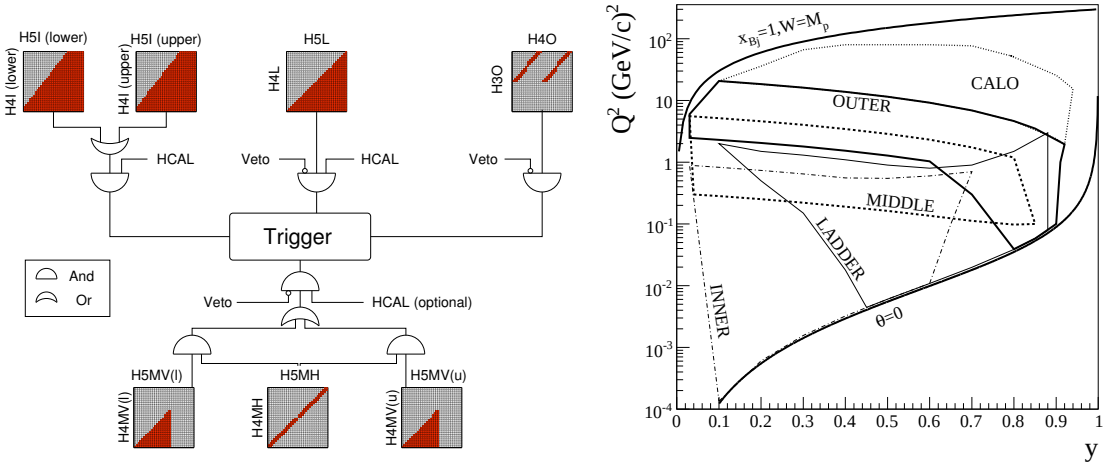

(a) (b)

Figure 3.13: (a) Trigger logic. Since the two spectrometer magnets deflect charged particle tracks only in the horizontal plane, it is possible for triggers defined with horizontal slabs to check for the condition of target pointing, and thus the trigger matrix is only occupied in the diagonal (as seen for the Middle Trigger and its hodoscope slabes H4MH and H5MH). For triggers with vertical slabs, apart from the diagonal, also one side of the matrix is occupied. (b) Kinematic coverage of the different components of the trigger system.

Trigger element	Short name	Trigger bits	Nr. (dec)	Nr. (hex)	Division factor	In rate (1st spill)
Inner Trigger	IT	000000000001	1	0x1	1	20890
Middle Trigger	MT	000000000010	2	0x2	1	2066
Ladder Trigger	LT	000000000100	4	0x4	1	8794
Outer Trigger*	OT	000000001000	8	0x8	1	12691
Calorimeter Trigger	CT	000000010000	16	0x10	1	29071
Inner Veto	VI	000000100000	32	0x20	40000	14495518
Halo Trigger (VO ∧ H4O)	Halo	000001000000	64	0x40	10000	2578929
Beam Trigger	BT	000010000000	128	0x80	99999	51737608
Inclusive Middle Trigger*	inclMT	000100000000	256	0x100	1	21710
Large-Q^2 Trigger	LargeQ2	001000000000	512	0x200	1	0
Low rate random Trigger	lowrandom	010000000000	1024	0x400	1	479
Random Trigger	random	100000000000	2048	0x800	4000	515347

Table 3.2: Trigger bits, so called "prescaling factors" and trigger rates for the run 60363, a typical run of 2007 in longitudinal configuration of the target magnetic field. Triggers marked with an asterisk are inclusive, *i.e.* they don't have include any calorimeter in the definition of the trigger condition.

3.3.10 Event Reconstruction

The large amount of data collected by COMPASS requires the availability of computing power to reconstruct the events at a rate comparable or faster to the data acquisition rate. The reconstruction is performed using a object oriented program with modular architecture and

Trigger element	Short name	Nr. (binary)	Nr. (dec)	Nr. (hex)	Division factor	In rate (1st spill)
Inner Trigger	IT	000000000001	1	0x1	1	13710
Middle Trigger	MT	000000000010	2	0x2	1	1977
Ladder Trigger*	LT	000000000100	4	0x4	1	25975
Outer Trigger*	OT	000000001000	8	0x8	1	16771
Calorimeter Trigger	CT	000000010000	16	0x10	1	65038
Inner Veto	VI	000000100000	32	0x20	40000	10562964
Halo Trigger (VO $\wedge$ H4O)	Halo	000001000000	64	0x40	10000	2909500
Beam Trigger	BT	000010000000	128	0x80	99999	69245931
Middle Trigger Inclusive*	MTincl	000100000000	256	0x100	1	20979
Large Angle Spectrometer Trigger	LAST	001000000000	512	0x200	1	4354
True Random	TRand	010000000000	1024	0x400	1	5297
Noise Random	NRand	100000000000	2048	0x800	4000	333578

Table 3.3: Trigger bits, so called "prescaling factors" and trigger rates for the run 91905, a typical run of 2011. Triggers marked with an asterisk are inclusive, *i.e.* they don't have include any calorimeter in the definition of the trigger condition.

written in C++, called CORAL. The schematic representation of the reconstruction software, describing the steps performed and their mutual connections, is shown in Fig. 3.14. In Fig. 3.15, the relative track resolution obtained for tracks reconstructed in the different parts of the spectrometer is shown.

3.4 Changes of the Setup for other Physics Programmes

The COMPASS setup has been adapted to the requirements of the different Physics programmes in different years, with the corresponding changes in the DAQ and DCS systems. A new set of trigger hodoscopes in the first spectrometer was used since 2010 to have a large-Q^2 trigger. Moreover, the hadron programme setup includes a liquid hydrogen and nuclear targets, cryogenic silicon detectors, a recoil proton detector, different trigger elements (multiplicity trigger, sandwich veto, beam trigger, CEDARs). For the DVCS programme, which uses both positive and negative muon beams, a large recoil proton detector (CAMERA) and a 4-meter liquid hydrogen target were used; a new electromagnetic calorimeter, ECAL0, was built to cover large angles of emission of the photon. The Drell-Yan programme data-taking in 2014 and 2015 implied the use of an intense hadron beam, a modified polarised target, a dedicated hadron absorber, a new vertex detector using scintillating fibres, modified trigger components, and CEDAR detectors were also installed. Moreover, a new large area drift chamber detector was constructed and installed for this Physics programme.

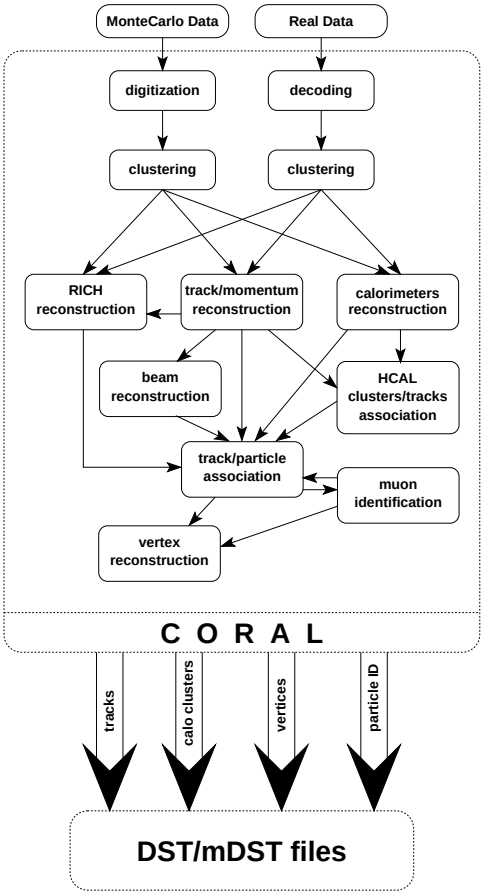

Figure 3.14: Schematic representation of the COMPASS reconstruction software.

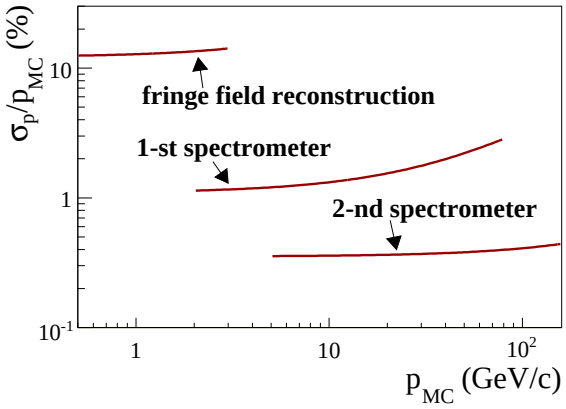

Figure 3.15: Relative track momentum resolution σ_p/p versus p, as obtained by Monte Carlo simulations. The fringe field mentioned is the field between the target solenoid and the first dipole magnet of the experiment.

3.5 Summary

The COMPASS experiment is a flexible, multi-purpose apparatus that can be adjusted to different Physics programmes. It has been optimised to make use of the unique high intensity muon and hadron beams of the CERN M2 beam line. Its muon beam which is naturally polarised and its solid state polarised target enable the measurement of double spin asymmetries.

The trigger configuration allows to access events in which muons were emitted from the interaction vertex at very small polar angles in the laboratory frame. The experiment uses multiple technologies of detectors for different requirements of rate, angle and time and space resolutions, with some degree of redundancy, which is useful to maintain the overall acceptance and efficiency constant over time. The triggers covering smaller polar angles allow for the detection of scattered muons in events with low x and low Q^2. The inclusion of a calorimetric condition in the trigger definition, and therefore of a hadron, allows to have still well defined primary vertices and kinematic variables.

Chapter 4

The COMPASS Detector Control System

4.1 Overview

The measurement of spin asymmetries, often of small magnitudes, with the COMPASS apparatus, which involves field rotations that can only be done about once every 24 hours, rely strongly on the stability of the apparatus, complemented by some redundancy of the detectors. The Detector Control System (DCS), is in this respect, an important tool to ensure the nominal operation of its many components, to detect malfunctioning parts and to allow for their fast recovery. In addition, the DCS is also a useful tool during the commissioning phase of each data-taking campaign, where nominal settings can be easily changed *e.g.* for calibration purposes. Finally, the DCS is still operational during the shut-down periods, to monitor temperatures, humidities, gas flows and any equipment that needs to continue to be monitored.

Since 2003, the COMPASS DCS is a full and exclusive responsibility of the LIP group participating in the COMPASS Collaboration. It is a work of a team of one to three people in permanence at CERN, including the author, who was at permanently at CERN accompanying the preparation and data-taking periods from 2007 to 2011, inclusive. The team is usually reinforced in the months of preparation and commissioning of each new yearly campaign of data-taking.

In this chapter, the COMPASS DCS is described.

4.2 Introduction

The COMPASS experiment is taking data since 2002, around seven months per year, and has shutdown periods in between, in which operations of maintenance and preparation of the following data-taking period take place. The detector devices and the experiment's environmental parameters are monitored and controlled using an experiment-wide Detector Control System (DCS). This system must ensure a coherent, efficient and safe operation of the experiment, by providing clear and prompt information for the shift crew and detector experts

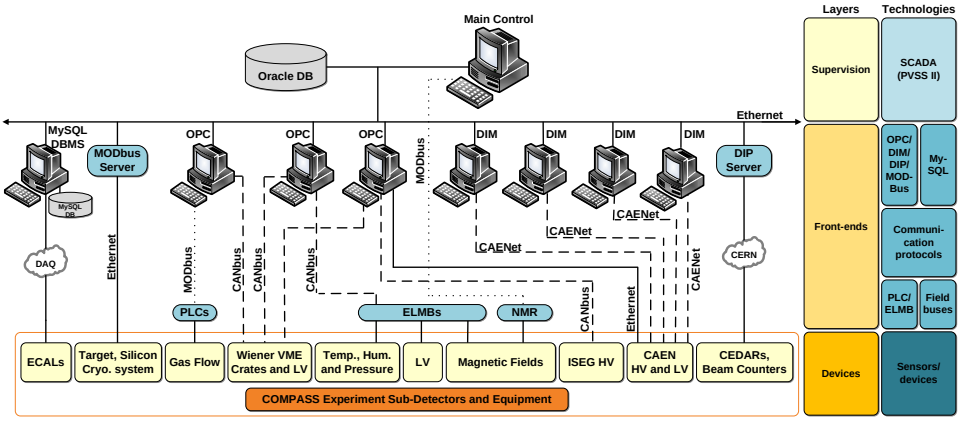

Figure 4.1: The COMPASS Detector Control System architecture, comprising a devices layer, a front-ends layer and a supervision layer. The technologies used in each layer are indicated in the rightmost column. The direction of updates on the status of the equipment (values and alarm flags) is from bottom to top, whereas the direction of commands is from top to bottom.

in the COMPASS control room. Some complex subsystems of the experiment have dedicated stand-alone control systems. These systems communicate with the DCS, providing it the most relevant information. The COMPASS DCS is unified in only one PVSS/WinCC-OA project developed and maintained, both hardware and software-wise, by only one group participating in the Collaboration. This structure and organisation is at contrast with the one of the big LHC experiments, which have a bigger dimension and hence a hierarchical structure, with distributed responsibilities [69–72].

The DCS provides a graphical user interface (GUI) to access all the relevant parameters monitored, their alert state (normal or in alert - indicated visually by use of a color code and acoustically) and their history, and a straightforward way to change their state, their settings, and the thresholds that define their state of alert.

The architecture of the DCS is shown in Fig. 4.1. It can be divided in three different layers: the supervisory layer, the front-ends layer and the devices layer. These will be detailed in the following sections.

4.3 The Supervisory Layer

On the supervisory layer, all the data collected, managed and published by the different kinds of servers or made available in databases are gathered, analysed, displayed to the end user and stored in an external database. It includes visual and sound alarms in case of states of alarm. Settings of high and low voltage channels and of VME channels, and alarm limits are also managed by the system.

The program previouly called PVSS-II[1], the commercial SCADA system that was chosen by CERN to use in the LHC experiments, after a thorough evaluation process, is now designated SIMATIC WinCC Open Architecture. Some of the aspects taken into account in that process

[1]Prozessteuerung und Prozessvisualisierung. See http://www.etm.at

that led to its selection were: openness of the code, scalability, cross-platform capability (*i.e.* to run in Windows and Linux) and long-term support.

The COMPASS experiment has adopted PVSS/WinCC-OA early in its development phase and has been a benchmark for other experiments at CERN since, before the LHC experiments started their data-taking in 2010, COMPASS was the biggest experiment operating at CERN. Over the years, several versions of PVSS/WinCC-OA were used in COMPASS. These were always previously tested and validated both by CERN and by the COMPASS DCS group. The installation of security patches during the data-taking periods is done only after a careful evaluation.

The JCOP Framework [73] is a CERN project to develop common software tools for High Energy Physics related equipment and operations, to be used with PVSS/WinCC-OA. It provides templates of datapoint types, panels, functions and mass configuration tools for different classes of equipments (*e.g* divided by brand) and for different functionalities, providing, for instance, tools for the management of privileges or for trending plots.

The objects provided by PVSS/WinCC-OA and the JCOP Framework have sometimes to be adapted to meet COMPASS' needs. In addition, other solutions had to be developed independently for custom devices. This includes the control of devices accessed using their serial (RS232) interfaces or their web servers, or the monitoring of items from dedicated control systems, developed in other platforms such as EPICS, LabView, etc.[2], which are made available by various means, including ascii files and mySQL (from the DAQ system) and Oracle databases (*e.g.* from the polarised target control system).

The PVSS/WinCC-OA production system of the DCS of COMPASS is both distributed and scattered. Historically, it started as a scattered project, meaning that it was constituted by a main PVSS/WinCC-OA project running in a Linux machine, and 3 associated PVSS/WinCC-OA projects running on Windows machines, that had PVSS/WinCC-OA processes running as OPC[3] clients (7 clients in total). As the DCS developed, the main project was split into two distributed projects, for performance reasons.

In Fig. 4.2, the structure of a PVSS/WinCC-OA project is shown in terms of its individual processes. The most important processes are the Event Manager, that manages all the other processes, and the Database Manager, that manages the connection with the database where historical values and alerts are stored. The Driver Managers can directly connect to devices, or to OPC or DIM servers, and take care of subscription of parameter values and commands. The Control Managers run scripts, for instance to permanently sum alerts on nodes, or for occasional use. The graphical User Interfaces (GUIs) allow end users to have information about the state of the system, namely actual values of parameters, historical values (that can be seen in trending plots showing evolution over time) and alert states, both actual and past ones. It is also possible to use the GUIs to send commands to devices that are controlled by the DCS (*e.g.* changing the settings of nominal voltage or switching on or off a high voltage channel).

[2]See http://www.aps.anl.gov/epics, http://www.ni.com/labview
[3]OLE (Object Linking and Embedding) for Process Control. See http://www.opcfoundation.org

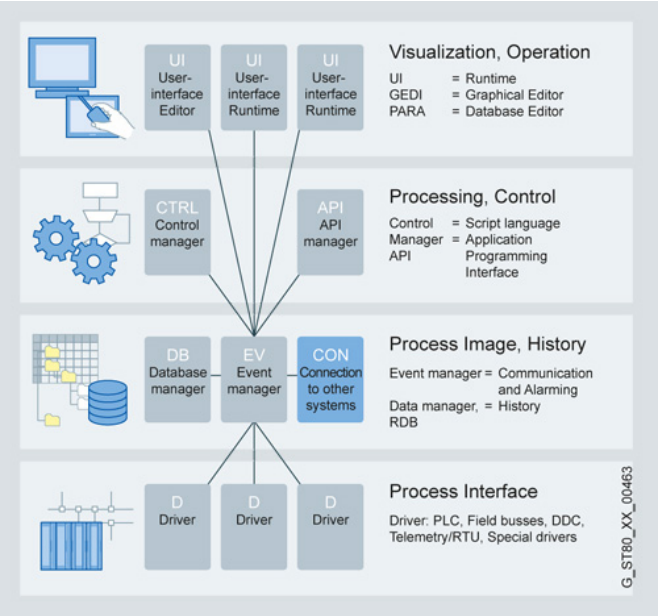

Figure 4.2: Structure of a PVSS/WinCC-OA project. Each grey rectangle represents a process running in the PC.

PVSS/WinCC-OA works with objects called *datapoints*, which are structures, *i.e.* they have a tree structure that can include branches and where the leaves are the monitored and controlled parameters (and can have different types, such as floats, integers, booleans, strings, etc., or the corresponding array types).

Presently, the project comprises over 20000 datapoints. Close to 17000 parameter values have alert handling, whereas almost 19000 parameters have their values archived.

The polling rates are adapted to the rate of changes of the parameters, and range from one reading every 1.5 seconds (for fast varying parameters, sensitive to the beam, such as some high voltage channels' currents) to one reading every 2 minutes (for slowly varying parameters, such as high voltage channels' settings, or detector positions). For any given type of equipment, the items are grouped in PVSS/WinCC-OA subscription data sets according to these rates.

The access to the PVSS/WinCC-OA project is made available to the users upon login. There is a general user name for the shift crew, user names for each of the detector experts, and a user name for guests. For each user or group of users, there is an authorisation policy associated: certain operations are restricted (such as switching on or off the high voltage channels for guest users), or selectively allowed (such as saving recipes or reference files of high voltage settings; see details later in this text).

The graphical user interface (GUI) is the main way for users to interact with the DCS. It is composed of multiple subpanels, organised in a hierarchical way, as can be seen in Fig. 4.3. One can see, on the top, the alerts table and, on the left, the buttons to access dedicated detector panels and, below them, a table with the summary status of the experiment. In the larger area of the panel, a synoptic view of the spectrometer is displayed. This area is also used for navigation in the subsystems controlled and to display the actual data of the monitored parameters.

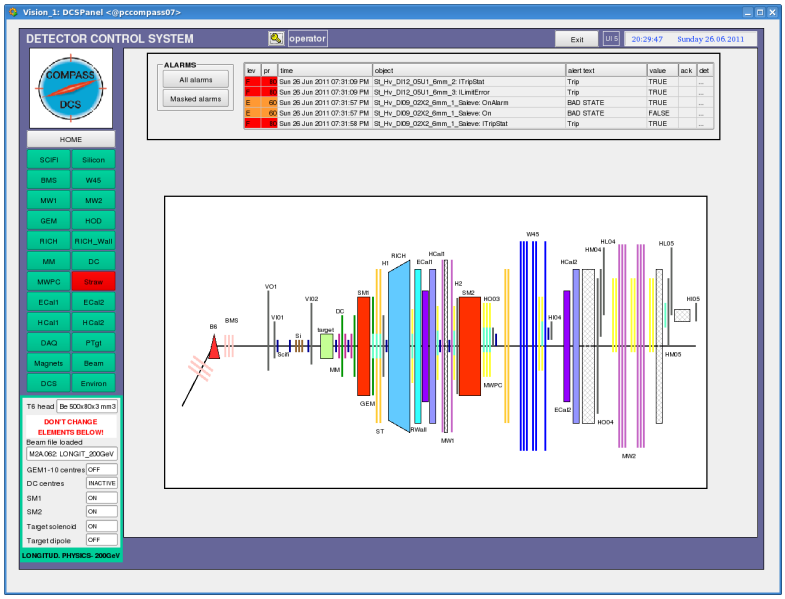

Figure 4.3: The graphical user interface (GUI) of the COMPASS DCS. One can see, on the top, the alert panel and, on the left, the buttons to access dedicated detector panels and, below them, a table with the summary status of the experiment.

The parameters' values history is also made available in the GUI. In fact, PVSS/WinCC-OA trending plots (namely values over time) are one of the more useful and more used features of the DCS. In the user interface panels, customised buttons were created for the items that have numerical values, so that their history can be easily accessed by users. The JCOP Framework provides its own trending plot widget, that was further customised for COMPASS, to make it simple to use. Users can choose the time range they want to visualise, see a time interval in the past, change the scale (between linear and logarithmic) or zoom in or out the abscissa or the ordinate by using the mouse scroll wheel or choosing a rectangular region for zooming in by simply indicating two opposite vertices of the region of interest with the cursor. Templates can be created to allow, with one click, to see related parameters all at once with *a priori* adjusted ranges for each of them. It is also possible for the users to include additional parameters to a predefined plot as well as to print the trending plots being displayed, or to save them to a file, not only as an image, but also in CSV (comma separated values) format.

One of the most important functionalities of the DCS is the display of visual and audio alarms, when predefined conditions are met, namely, when parameter values beyond predefined thresholds are reached for parameters with numerical values or when devices send alarm flags. The visual display of alarms follows a colour code that indicates its severity. The colour code used in the DCS of COMPASS is indicated in Table 4.1. For the most relevant parameters, it is important to assure that the operator didn't fail to notice the alarm condition, even if it has disappeared in the meantime; in this case, it is requested that the alarms are acknowledged by the operator in the graphical user interface. Furthermore, upon activation of some predefined alarms, the implicated detector experts are warned by email or SMS of those states of alert of their detectors.

Since the DCS has both a relatively fast knowledge of the state of the parameters it mon-

Colour	Meaning
GREEN	all OK
ORANGE	some alert is present
RED	some fatal alert is present
DARK GREY	an alert has come, but state went back to normal again.
	The grey color is displayed until a user **"acknowledges"** the alert.
LIGHT GREY	no alert limits defined, or they exist but the alerts were masked
WHITE	no alert limits defined

Table 4.1: Colour code of alert states in the DCS.

itors and also the ability to send commands to the devices, it is used to ensure software-wise protections to several equipments. For instance, some detectors have components that are sensitive to magnetic field gradients; for this reason, when a trip of one of the spectrometer magnets (SM1 or SM2) occurs, or when these are switched off with the detectors high voltage channels still switched on, the DCS issues a switch-off command, so that the time interval during which the gradient is felt is minimised. In addition, for some detectors, the high voltage channels should only be switched on or off in pairs; hence, if a trip is detected in only one member of a pair, the DCS sends a switch-off command to the other member of the pair.

Furthermore, some detectors have front-end cards that are refrigerated by a water circuit. When this circuit stops for some reason, the temperature of the cards increases and can reach a value above a predefined threshold. If this happens, the DCS issues a switch-off command to the low voltage power supplies that power them, thus preventing these sensitive and sophisticated cards to be damaged. A hardware interlock is activated at a higher temperature, but the recovery from the interlocked state implies access to the experimental area, thus implying longer beam time losses, which are to be avoided.

A configurations database associated to the project was implemented. It is based in a JCOP Framework package, which was adapted for the COMPASS needs. It is an independent Oracle database, that has two main purposes. On the one hand, it allows to save and to retrieve the so called "recipes", *i.e.* sets of thresholds for alarms of groups of parameters. The recipes can be created, or its values committed in the PVSS/WinCC-OA project using the DCS GUI, provided that the user has the privileges to change the respective detector items.

The second important purpose of the configuration database is to store so called "configurations", *i.e.* the mapping of hardware names vs. logical names (*i.e.* PVSS/WinCC-OA datapoint element names and respective aliases), for snapshots of stable states of the PVSS/WinCC-OA project. These configurations are used to keep track of changes of the aforementioned mapping. These changes can happen either because, for instance, a high voltage channel gets broken and the same part of the detector (*i.e.* same alias) is then powered by a different channel (*i.e.* different datapoint), or because channels are reused when switching *e.g.* between the data-taking of the muon and the hadron Physics programmes.

For storage of settings of high voltage channels (set voltage, maximum current allowed, ramp up speed, ramp down speed and trip time), ascii files are used, for convenience. Detector experts can access the files from the DCS GUI, edit them, and send the values to be used to

the equipment using the DCS GUI. In case of problems, the shift crew can access the reference files of the different detectors from the GUI to send the nominal values back to the equipment, thereby recovering the normal state of the equipment.

Only a subset of all the data that PVSS/WinCC-OA receives and manages is actually saved. For this to happen, the PVSS/WinCC-OA datapoints need to have an archiving policy defined. This is chosen according to the known changes of each datapoint and the relevance of its history. For instance, it may be useful to store the readings of a temperature every ten minutes or if the change with respect to the previous reading exceeds one degree. This smoothing condition, called dead-band, is adjusted for each datapoint group or even per datapoint, if needed. The rates of storage range from one value for every ∼10 seconds (corresponding to the beam spill time interval) for beam-related quantities, to one value for every half an hour (for the positions of detectors). For commissioning of detectors, an archiving rate of 1 value every second has been accepted.

Currently, there are about 4×10^9 values stored (*i.e.* about 600 GB of data including indexes), comprising the project history since 2006. The DCS historical data that had been saved in PVSS/WinCC-OA internal format (during its first years of operation, until the end of 2008) was copied to a CERN central Oracle database, and the new data archived since then was all stored in this database. This way of storing data has all the advantages of Oracle and makes their access independent of PVSS/WinCC-OA. The data is continuously replicated to a second database, to ensure that the access to the data by offline users never compromises the performance of the production database. The data can also be provided in other formats, such as ascii or ROOT [74] trees.

In Fig. 4.4 the accumulated values stored in database associated to the WinCC-OA project as a function of time are presented. After the transition to the external database (indicated by a red line), it was possible to store data of more datapoints with higher archiving frequencies, if needed.

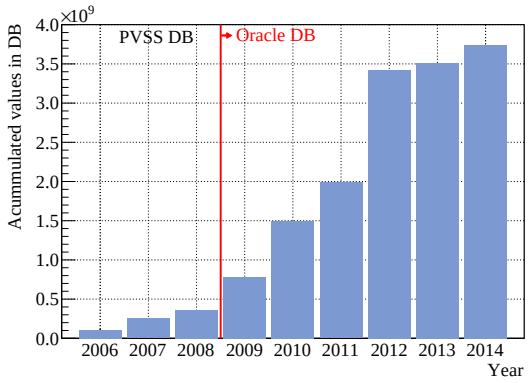

Figure 4.4: Accumulated stored values in the Oracle external database. Note that in 2013 there was no data-taking and that in 2014 there was a data-taking period of only three months.

The DCS data is important for studies of the spectrometer stability. Some particularly relevant parameters are regularly copied to the experiment's mySQL conditions database in

the DAQ, for offline Physics data analysis, using a cron job. Other data relevant for the estimation of detectors efficiencies are retrieved from the DCS database at the end of each year's data-taking. The history of alerts of all the datapoint elements that have alert handling is also saved and made available by PVSS/WinCC-OA. This includes the timestamps of their arrival and departure, and of eventual acknowledgements done, among other data.

The knowledge of malfunctioning of parts of the experiment relies substantially on the DCS, namely on the display of alarms. Hence, it is important to assure its integrity and availability, ideally, at all times. Some of the mechanisms used are heart-beats and watch-dogs, back-ups of the PVSS/WinCC-OA project, a strict security policy and the issuing of regular ping commands from other machines.

The managers of PVSS/WinCC-OA's main project, which are independent processes running in Linux, may, for a number of reasons, either block or stop running. On the other hand, the servers – including OPC [75] servers – may stop delivering meaningful data. For this reason, for each manager in PVSS/WinCC-OA that acts as a client, a heart-beat item was created to record the timestamp of the last meaningful data it received, so that an alert can be raised when a problem occurs.

Moreover, to verify that PLCs[4] are sending meaningful data at all times, a mechanism of watch-dogs is implemented by an OPC server. It marks as invalid values sent by a PLC in case the values of the items published for this purpose (which have, during normal operation, varying integer values) stop being updated.

The communication with individual VME[5] crates or power supplies is also monitored, by continuously checking for selected equipment items that the timestamp of the latest value read is more recent than a predefined time interval.

To ensure the integrity of the project if a software corruption occurs in the PVSS/WinCC-OA project and associated software, the data is copied every twenty-four hours to a central repository at CERN. Furthermore, local copies are periodically made.

A thorough security policy is implemented. All the computers that integrate the DCS belong to a dedicated experimental domain, that communicates with the CERN network using the experiment's gateways. All the PCs in use have firewalls implemented. In addition, all the user interfaces, with the exception of the one in the control room that should be permanently accessible, have a users auto-logout mechanism after one hour.

The project should be available in the network at all times, for instance to diagnose eventual DCS problems remotely. For this to happen, the gateways of the COMPASS domain have to be switched on and accessible via the CERN network. To check that this is the case at all times, regular ping commands are issued (every fifteen minutes) from an external server and the response is monitored; a notification is sent to the DCS experts in case those gateways are not reachable.

[4] Programmable logic controllers.
[5] VERSAmodule Eurocard bus.

4.4 The Front-ends Layer

The experiment devices that are monitored and controlled by the DCS are spread over nearly two hundred meters, including the spectrometer and the beam tunnel. To communicate with all the devices, different field buses and communication protocols are used, namely CANbus[6] (8 daisy-chains), CAENet (6 daisy-chains), ModBus[7], Profibus[8] (4 daisy-chains) and Ethernet. The general baud rate used for monitoring in the COMPASS CAN buses is 125 kbits/s[9], which is the recommended baud rate for the length of the daisy-chains used. These field buses transmit the information about the measurements of sensors to the front-end PCs (and commands to actuators in the opposite direction). In the front-end PCs, front-end PCI-type [10] cards, either from Kvaser or from CAEN, are installed to collect the information carried by the field buses. The data is transmitted to the supervisory layer using a server-client model. An exception to this model is the three-layer model which is used when a database is included as an intermediate between the server and PVSS/WinCC-OA. This is the case for the monitoring of the calorimeters, beam and trigger rates, and part of the polarised target system.

In addition, specialised devices are used as intermediates between the devices and some of the front-end PCs, namely ELMBs (Embedded Local Monitoring Boards) and PLCs (Programmable Logic Controllers).

The ELMBs, described in Ref. [76], are multi-purpose multiplexed ADCs (Analog to Digital Converters) each with 64-analog input channels with 16 bit-resolution which were developed by the ATLAS experiment. The communication of the ELMBs with the front-end PCs is done with the CAN field bus, using the CANopen protocol. The ELMB was designed and tested to be radiation- and magnetic field tolerant: its tolerance ranges up to about 5 Gy and 3×10^{10} neutrons/cm^2 for a period of 10 years and to a magnetic field up to 1.5 T. In Fig. 4.5, photos of the two sides of the ELMB are shown.

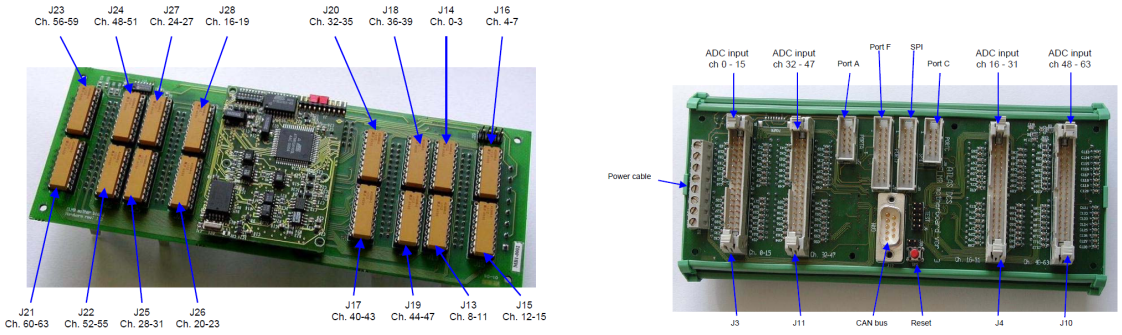

(a) (b)

Figure 4.5: The ELMB (Embedded Local Monitor Board): (a) back side, showing the adapter connectors; (b) front side, showing the connectors.

[6] Controller area network. ISO standard 11898, see e.g. www.iso.org
[7] See http://www.modbus.org
[8] See http://www.profibus.com
[9] A baud rate of 100 kbits/s has been implemented in the chains controlling VME crates to solve problems with invalid readings.
[10] Peripheral Component Interconnect.

The PLCs are stand-alone, very robust, reliable and relatively fast devices that allow, among many other uses, to regulate flows of gases and their percentage in mixtures, according to predefined settings and tolerance intervals, as well as to regulate cryogenic systems, *e.g.* by regulating valve openings. The measurement of gas flows or gas percentages in mixtures is provided by the PLCs by ModBus to the DCS front-end PCs.

Manufacturer's OPC servers are used when available and stable. This is the case for the modern CAEN equipment (high and low voltage) and for Iseg equipment (high voltage). In order to communicate with PLCs, an OPC server from Schneider[11], is used. Moreover, an OPC server was developed at CERN to control relatively old Wiener equipment, as the one used in COMPASS. To communicate with ELMBs, a CANopen OPC server, described in Ref. [77], is used.

The Distributed Information Management system (DIM) was developed at CERN and allows the implementation of a server-client model of publishing lists of items and their actual values. The SLiC[12] DIM server developed at CERN allows the control of the six CAENet lines used in COMPASS for the older type of CAEN crates. Each server has different groups of items with individually tunable speed reading cycles, thus permitting the separation of fast reading cycles (comprising voltages, currents and channels status) with reading frequencies as high as 1 Hz, thus allowing a fast detection of high voltage trips and failures; and of slow cycles, used for the read-back of settings.

The DIM protocol is also used to monitor other systems, namely temperatures and disk occupancy of servers, and processes of data transfer from the DAQ machines to the central storage system of CERN, CASTOR.

DIP[13] is a protocol developed at CERN, based on DIM, but allowing exclusively read-only parameters, which are, in practical terms, those related to the CERN infrastructure (such as beam line magnet currents and the last beam file loaded, the primary target head inserted, the parameters to allow the monitoring of the CEDAR detectors, data relative to the liquid nitrogen supply, and information about measured radiation levels in the COMPASS experimental hall).

One PLC from the polarized target system is monitored using the S7 driver provided by PVSS/WinCC-OA, thereby avoiding the use of an OPC server.

PVSS/WinCC-OA provides functions to access relational databases such as mySQL and Oracle. This allows the access of information from the experiment conditions database (a set of mySQL databases), such as the calorimeter calibration event amplitudes, the beam and trigger rates, and parameters related with the polarised target.

The high voltage system of some of the detectors (Micromegas and the so called Saclay Drift Chambers) have special requirements with regards to its monitoring, and thus had a dedicated control system based on EPICS. This system published the most relevant data of the high voltage channels, which were read by a specially developed PVSS/WinCC-OA API (Application Programming Interface).

[11] See http://www.schneider-electric.com
[12] See http://j2eeps.cern.ch/wikis/display/EN/SLiC
[13] See http://en-dep.web.cern.ch/en-dep/Groups/ICE/Services/DIP

The Profibus protocol is used to transmit the data coming from the PLCs that monitor the detector gas systems to the PC that runs the Schneider OPC server.

In addition, the magnetic field of the SM2 magnet is measured with an NMRmeter that has a serial interface which allows the communication with a standard PC by use of the Profibus protocol. In the PC, a custom C program reads the information transmitted, writes it in an ascii file and thereby makes it available for a PVSS/WinCC-OA API that finally collects the values and writes them into a datapoint.

4.5 The Devices Layer

Many different types of devices need to be controlled or simply monitored by the DCS, from high and low voltage crates and VME crates, to gas systems and to sensors for measurement of temperature, humidity, pressure and magnetic field.

COMPASS uses CAEN crates of different models to power most of its high voltage channels and for part of its low voltage channels. About twenty CAEN crates of older models (with CAENet interface) are in use, together with eleven crates of newer models (with Ethernet interface). Presently, eight Iseg high voltage modules are also in use and integrated in the DCS via their CAN interfaces. In addition, fourteen Wiener low voltage power supplies are controlled, of which four are of type UEP6000, eight of type PL6021 and two of type PL508L. Twenty VME crates are integrated in the DCS, both of older models (power supplies of type UEP5021) and newer models (power supplies of type UEP6021), the former being the majority. Both the low voltage power supplies and the VME crates are controlled by use of their CAN interface.

In detector's subsystems where PLCs are used, such as the gas systems, the DCS only monitors the values that are published by them. The same happens for the CEDAR detectors, and for systems that have dedicated control systems, namely the cryogenic systems of the polarized target, liquid hydrogen target and cold silicon detectors [78, 79].

A wide range of devices are monitored by use of the ELMBs. More recently, some low voltage power supply channels are also controlled via ELMBs.

Hundreds of sensors were installed to monitor specific components of detectors or the experimental hall environment. For temperature monitoring, PT100 sensors (see Fig. 4.6) in a 4-wire configuration are extensively used, and their output (electrical resistances) is read using the ELMBs.

Some of the low voltage power supplies used in the experiment only have an interface for monitoring channel voltages or currents by means of voltage signals that are linear functions of the monitored parameters, which are also read by ELMBs. In such cases, a calibration formula is used in the configuration of the CANopen OPC server, to provide the conversion to the real values delivered by the channels.

Moreover, two of the most important magnets of the experiment, SM1 and Bend6, have their magnetic field monitored by Hall probes, whose output signals are read by ELMBs.

In the case of the second dipole magnet of the experiment, an NMRmeter is used. The NMRmeter has a serial interface, which allows the communication with a PC, as described earlier.

Six custom power switches are also controlled, using the web servers and drivers provided with the equipment.

Figure 4.6: Temperature sensor of type PT100, widely used in COMPASS.

The DCS has an indirect monitoring of the powering system and read-out chain of the calorimeters of the experiment, based on the calibration signals of a laser system (for ECAL1) or a LED system. A component of the DAQ system calculates a spill-average amplitude of the signal read-out by each of the ∼4500 channels and saves this information in a mySQL conditions database [80], that is subsequently accessed by a PVSS/WinCC-OA script. For the more recent ECAL0, there is an autonomous monitoring system, whose values are made available to the DCS using a web server. In the DCS, a reference is chosen by the detector experts; afterwards, the DCS calculates, for each beam spill (using a synchronisation scheme with the DAQ), the state of alert of each channel, based on the relative difference of the actual amplitude of the calibration amplitudes with respect to the reference values. The conditions to indicate alarms in the main panel are specified for the sums of channels with given alert states.

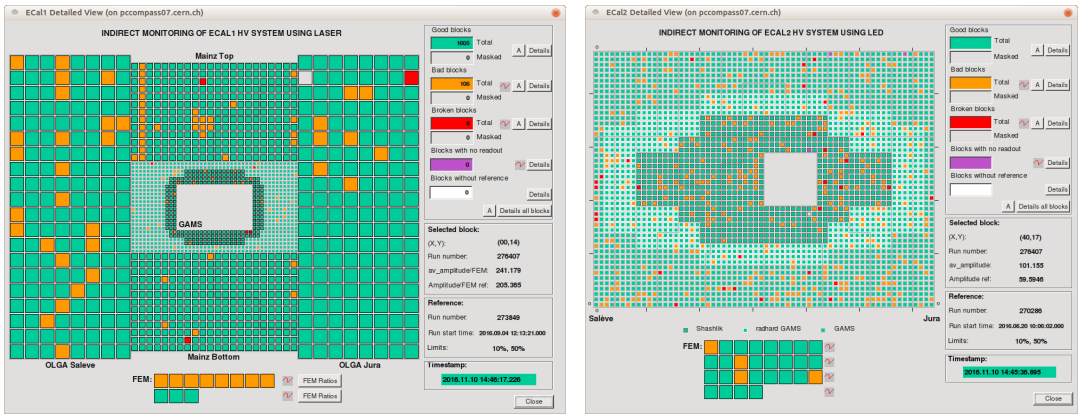

(a) (b)

Figure 4.7: Panels for monitoring of the powering systems of (a) ECAL1 and (b) ECAL2, comprising around 1500 and 3000 channels, respectively.

In Fig. 4.7, the sub-panels displaying the alert states of the electromagnetic calorimeters ECAL1 and ECAL2 are shown. The sums of channels in the predefined categories are displayed ("good blocks", "bad blocks", "broken blocks", "blocks with no readout" and "blocks without reference"). These alert states are calculated taking into account information introduced by the detector experts, which can be a reference run, or *e.g.* an edited version of the set of values of a reference run. In each spill, the values of the actual amplitudes of the monitoring signals (either LED or laser signals), read from a mySQL database from the DAQ system, are compared to the reference values of amplitudes, for each calorimeter cell. If the deviation to the reference is below a given threshold (*e.g.* $< 5\%$ deviation with respect to the reference)

the cell is marked as a "good cell" and displayed in green, if it is between that threshold and a second one (*e.g.* between 5% and 25% deviation with respect to the reference), the cell is marked as a "bad cell" and is displayed in orange, and if the deviation is larger that that second threshold, the cell is marked as a "broken cell" and is displayed in red. The FEM signals of the laser monitoring system of ECAL1 are themselves monitored. If a given block of cells show up with a given color, the geometry of the block can be identified by the detector experts as corresponding to a given element of the powering or readout chain that is malfunctioning. In the dedicated DCS panels, each channel can be double-clicked to give access to a trending plot that shows the monitoring amplitudes over time, as well as the reference values which may also have been changed over time by the detector experts. In Fig. 4.8, examples of trending plots of amplitudes as functions of time are shown.

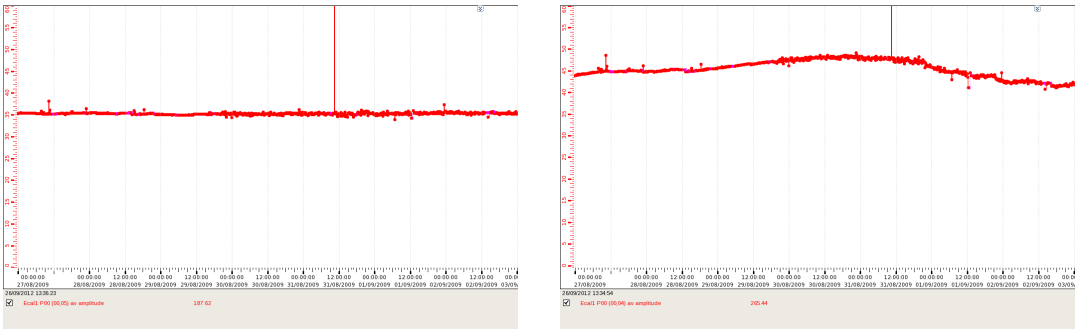

(a) (b)

Figure 4.8: Trending plots of two cells of one of electromagnetic calorimeters (ECAL1) during seven days. The left (right) plots are examples of a stable (unstable) cell.

The main power supplies powering the electromagnetic calorimeters, their monitoring systems, and the subgroups distributor voltages are monitored by use of ELMBs.

The positions and movement of the electromagnetic calorimeters are controlled by CAMAC[14] modules, from whose readings the detector positions are calculated and read by the DCS.

A recent integration in the main PVSS/WinCC-OA project is the direct monitoring of the most relevant parameters of the complex Polarised Target system. The communication with the devices required the usage of different protocols and front-end solutions: PLC S7, ModBus, DIP and ODBC (for mySQL and Oracle database connection).

The rates of the different triggers of the experiment, monitored online by the shift crew, are stored in a DAQ mySQL conditions database read by the DCS, which calculates rates normalised to the beam flux, and triggers alarms when those normalised rates fall outside predefined ranges.

The servers used in the DAQ run DIM servers to publish data related to internal temperatures, occupancy of their disks and status of important processes.

The beam line M2 belongs to CERN's infrastructure and thus is monitored and controlled by dedicated programs. The most important parameters, such as magnet currents, collimator

[14] Computer Automated Measurement And Control.

positions, the primary target head or the beam file loaded are made available via DIP, thus providing alarms and historical values of these important parameters. Note that although there is a dedicated control system for the beam line elements, it doesn't provide audio alarms nor historical values in trending plots.

Moreover, the CEDAR detectors (ČErenkov Differential counters with Achromatic Ring focus), used in the hadron program of the experiment, are a responsibility of CERN, and its relevant parameters are published using a DIP server. For the operation of these detectors in previous years, the density of the gas used should be within a predefined range. When this didn't happen, the DCS displayed a state of alarm, allowing the shift crew to start a procedure to refill the detectors. The high voltage system and the motors are also monitored.

4.6 Summary

The DCS of the COMPASS experiment at CERN was presented in detail. In COMPASS, this is a centralized system that displays to the end user in a homogeneised graphical user interface many different subsystems that use a wide range of devices and thus require the use of very different front-end solutions. Note however that systems requiring more reliable monitoring and control, because of security reasons, such as gas systems, cryogenic systems, radiation monitoringare dealt by other dedicated systems that are a responsiblity of CERN. These systems make relevant summary information available to be monitored in the DCS.

The external database for storage of historical values and alerts allowed to extend significantly the number of parameters monitored and controlled.

The DCS has played a particularly important role in the monitoring of the experiment's calorimeters, giving a first online image of the instabilities of these very complex and sensitive detectors.

The author was deeply involved in the transition of the DCS to an external Oracle archiving scheme, in the monitoring of the calorimeters, in integration of sensors to be monitored by ELMBs, and in maintenance and DSC-related permanent support to the COMPASS control room during the data-taking campaings.

Chapter 5

Method and Inputs for the Extraction of A_1^p and g_1^p

5.1 Overview

In this chapter, the method used for extraction of the longitudinal double spin asymmetry of the proton A_1^p and of the spin dependent structure function of the proton g_1^p are detailed. In addition, the external inputs needed for their computation is presented.

5.2 Extraction of the Proton Spin Asymmetry A_1^p

The number of events measured in a given target cell or set of cells with the same polarisation, N_i, in a given time interval is related to the double spin longitudinal photon-nucleon asymmetry A_1^p by

$$N_i \simeq a_i \phi_i n_i \bar{\sigma}(1 - P_b P_t f D A_1^p). \tag{5.1}$$

In the equation, a_i is the acceptance, ϕ_i is the integrated beam flux, n_i is the number of nuclei per unit area in the target cell, $\bar{\sigma}$ is the spin independent cross-section, P_b and P_t are the beam and the target polarisations, respectively, f is the dilution factor that takes into account the fact that not all the material in the target is polarisable, D is the depolarisation factor, that accounts for the fraction of the muon polarisation that is transfered to the virtual photon and is obtained from Eq. 2.24 and A_1^p is the asymmetry being measured, the spin asymmetry relating cross-sections in different virtual-photon-proton spin configurations,

$$A_1^p = \frac{\sigma_{1/2} - \sigma_{3/2}}{\sigma_{1/2} + \sigma_{3/2}} \tag{5.2}$$

where the subscripts refer to the total angular momentum of the virtual photon-nucleon system in the direction of the nucleon spin assuming one photon exchange. Note that the minus sign in Eq. 5.1 allows for a conventionally positive spin asymmetry A_1^p for the case where the beam and target polarisations have opposite sign, *i.e.* using a similar convention of sign as in Eq. 5.2, which also yiels positive values of A_1^p in case of a larger cross section when the spins of the quark

and of the virtual photon are antiparallel; experimentally, one effectively finds A_1^p positive in the DIS regime, *cf.*Fig. 2.10.

The asymmetries were obtained using the second order weighting method [81–83], where the asymmetry is the unknown in a second order equation where all the other terms are known a priori or measured, and using a weight $\omega = fD|P_b|$ per event to optimise the statistical uncertainty of the result.

The second order weighted method gathers the advantages of the two methods used in by the SMC, namely the "fD-method" and the "second order method". The "fD-method" weights each event by the product of the dilution factor and of the depolarisation factor (hence its name), and yields the smallest possible statistical uncertainty to the asymmetries; the disadvantage of the method is that it relies on the assumption that the asymmetries are small. The "second order method" does not yield the smallest statistical uncertainty but is valid even if the asymmetries are not small.

5.3 Number of Events and Cross Section

The relation between the number of collected events and the virtual photon-nucleon asymmetry is given.

The total number of observed interactions N of the muon beam in the target is the product of the total cross-section σ, the integrated luminosity L and the acceptance. In a fixed target experiment, the luminosity is defined using the integrated beam flux ϕ and the density of the nucleons n in the target, which are the scattering centers. We can thus express N as

$$N = \int a\phi n \left(\frac{d^2\sigma}{dx\, dQ^2} \right) d\vec{\xi}, \tag{5.3}$$

where $\vec{\xi}$ represents all integration variables, like Q^2, x, time t, position of the interaction point $\vec{v}$, etc. In Eq. 5.3 the total spectrometer acceptance a was taken into account; this is the probability that an interaction which occureed in the target volume has been observed and reconstructed. Time-dependent variations of the spectrometer acceptance and of the target position (the position of the target affects the number of the scattering centers illuminated by the beam) can lead to false asymmetries.

The beam and the target material are polarised and therefore Eq. 5.3 should be expressed in terms of the helicities of the beam and target. To simplify the formula the differential cross-section $d^2\sigma/dx\, dQ^2$ will be denoted by σ. Since the proton has spin 1/2, 2 states with spin projections $+1/2$ and $-1/2$ on the reference axis have to be considered. The arrows in $\phi^{\rightarrow}$, $\phi^{\leftarrow}$, $n^{\Rightarrow}$ and $n^{\Leftarrow}$ indicate the orientation of the spin of the beam and the target relative to the beam direction: parallel or anti-parallel. As only the relative spin orientation between the beam and the nucleon matters, the followin expressions hold: $\sigma^{\Leftarrow} = \sigma^{\Rightarrow}$, $\sigma^{\Leftarrow} = \sigma^{\Rightarrow}$. Thus we

can write

$$N = \int a d\vec{\xi} \left[(\phi^{\rightarrow} n^{\Rightarrow} + \phi^{\leftarrow} n^{\Leftarrow}) \sigma^{\vec{\Rightarrow}} + (\phi^{\rightarrow} n^{\Leftarrow} + \phi^{\leftarrow} n^{\Rightarrow}) \sigma^{\vec{\Leftarrow}} + (\phi^{\rightarrow} + \phi^{\leftarrow}) \sum_i n_i \bar{\sigma}_i \right], \quad (5.4)$$

where $\bar{\sigma}$ is the spin averaged cross-section $\bar{\sigma} = (\sigma^{\vec{\Rightarrow}} + \sigma^{\vec{\Leftarrow}})/2$ and the $\sum_i n_i \bar{\sigma}_i$ is the sum over all elements in the target other than the proton. Most of these elements are not polarised and for them the spin averaged cross-section is used. We can now introduce the beam and the proton target polarisations

$$P_b = \frac{\phi^{\rightarrow} - \phi^{\leftarrow}}{\phi}; \qquad P_t = \frac{n^{\Rightarrow} - n^{\Leftarrow}}{n} \quad (5.5)$$

and define the measured asymmetry as

$$A = (\sigma^{\vec{\Leftarrow}} - \sigma^{\vec{\Rightarrow}})/(\sigma^{\vec{\Leftarrow}} + \sigma^{\vec{\Rightarrow}}). \quad (5.6)$$

The total beam flux is $\phi = \phi^{\rightarrow} + \phi^{\leftarrow}$ and the total density of scattering centers is $n = n^{\Rightarrow} + n^{\Leftarrow}$. Using the above definitions we can rewrite Eq. 5.4 in the following form

$$N = \int d\vec{\xi} a \left[\phi n \bar{\sigma} - \phi n \bar{\sigma} P_b P_t A + \sum_i n_i \bar{\sigma}. \right] \quad (5.7)$$

Taking into account the dilution and the depolarisation factors we come to the final form of Eq. 5.4,

$$N = \int d\vec{\xi} a \phi n \bar{\sigma} [1 - f D P_b P_t A]. \quad (5.8)$$

which gives the total number of events observed in a given configuration of polarisations of beam and target.

5.3.1 The First Order Method

In COMPASS it is not practical to use directly Eq. 5.8 to extract the cross-section asymmetry because the incoming muon flux is known with a precision of $\sim 10\%$, which would translate to a large uncertainty on the derived asymmetry. Instead, a counting rate asymmetry is defined as

$$A_N = \frac{N^{\vec{\Rightarrow}} - N^{\vec{\Leftarrow}}}{N^{\vec{\Rightarrow}} + N^{\vec{\Leftarrow}}} = \frac{N_o - N_c}{N_o + N_c}, \quad (5.9)$$

where N_o, N_c are the number of events observed in the outer and central target cells respectively. Here the outer cells have nucleons polarised anti-parallel to the beam ($P_b P_t < 0$) while for the central cell the opposite happens ($P_b P_t > 0$). The flux is secured to be the same for both target cells by selecting events with the extrapolated beam trajectory crossing the full lenght of the target. Furthermore by considering small intervals in x, Q^2 the product $\phi\sigma$ in Eq. 5.8 can be approximated by a product which allows for the cancellation of the beam flux and the

cross-section. The expression for the counting rate asymmetry becomes

$$A_N = \frac{r - 1 - \omega A(rP_o - P_c)}{r + 1 - \omega A(rP_o + P_c)}, \tag{5.10}$$

where $r = a_o n_o / a_c n_c$ and $\omega = fDP_b$. As usually $\omega A \ll 0.1$ and $P_o \approx -P_c$ (the target cells, both the outer cells and the central cell, have similar polarization), then, assuming that the difference between the acceptances is small ($r \approx 1$), the term $\omega A(rP_o + P_b)$ in the denominator can be neglected. This leads to a linear dependence of A on the counting rate asymmetry. For this reason this method is called the first order method. The obtained expression for A is

$$A = \frac{1}{\omega} A_N - \frac{1}{\omega} \left(\frac{r-1}{r+1} \right). \tag{5.11}$$

The acceptances and the density of scattering centers are not the same for the outer and the central cells. Therefore, $r \neq 1$, which means that the A_N is an estimator of A which is biased by the term $(r-1)/(r+1)$, which is called the apparatus asymmetry. In order to eliminate this bias, the polarisations in the target cells are reversed periodically. We can distingish the configurations before and after reversal by introducing an apostrophe for the configuration after the reversal. The counting rate asymmetry after the field reversal is defined as

$$A_N = \frac{N'^{\Rightarrow} - N'^{\Leftarrow}}{N'^{\Rightarrow} + N'^{\Leftarrow}} = \frac{N'_c - N'_o}{N'_c + N'_o} = -\frac{N'_o - N'_c}{N'_o + N'_c} = -\frac{r' - 1 - \omega A(r'P'_o - P'_c)}{r' + 1 - \omega A(r'P'_o - P'_c)}. \tag{5.12}$$

Then data collected with two configurations of target spins are combined

$$\frac{A_N + A'_N}{2} = \frac{1}{2} \left[\frac{r - 1 - \omega A(r - P_o - P_c)}{r+1} - \frac{r' - 1 - \omega A(r'P'_o - P'_c)}{r'+1} \right]. \tag{5.13}$$

The spin orientation of nucleons in outer (central) cells is defined to be parallel (anti-parallel) to the beam direction, similarly after the polarisation reversal the orientation in outer (central) cells is anti-parallel (parallel). Thus we can use the absolute values of the polarisations

$$\begin{aligned} |P_b||P_o| = -P_b P_o, |P_b||P'_o| = -P_b P'_o, \\ |P_b||P_c| = P_b P_c, |P_b||P'_c| = P_b P'_c. \end{aligned} \tag{5.14}$$

Hence we obtain

$$\frac{A_N + A'_N}{2} = \frac{1}{2} \left[\frac{r-1}{r+1} - \frac{r'-1}{r'+1} \langle \omega \rangle A \left(\frac{r|P_o| + |P_c|}{r+1} + \frac{r'|P'_o| + |P'_c|}{r'+1} \right) \right], \tag{5.15}$$

where $\langle \omega \rangle$ is defined as $\langle \omega \rangle = \langle f \rangle \langle D \rangle \langle |P_b| \rangle$ with $\langle f \rangle$ and $\langle D \rangle$ being average values of f and D in the (x, Q^2) bin and $\langle |P_b| \rangle$ is the average of the absolute value of the beam polarisation. Using the average target polarisation

$$\langle P_t \rangle = \frac{1}{2} \left[\frac{r|P_o| + |P_c|}{r+1} + \frac{r'|P'_o| + |P'_c|}{r'+1} \right], \tag{5.16}$$

we obtain the followin expression for the cross-section asymmetry and its statistical uncertainty

$$A = \frac{1}{\langle\omega\rangle\langle P_t\rangle}\left(\frac{A_N + A'N}{2}\right) - \underbrace{\frac{1}{2\langle\omega\langle P_t\rangle\rangle}\left(\frac{r-1}{r+1} - \frac{r'-1}{r'+1}\right)}_{A_{\text{false}}} \tag{5.17}$$

$$\sigma(A) \simeq \frac{1}{2\langle\omega\rangle\langle P_t\rangle\sqrt{\frac{1}{N_o+N_c} + \frac{1}{N'_o+N'_c}}}. \tag{5.18}$$

The statistical uncertainty for the asymmetry is determined assuming that $r \approx 1$ and that the number of collected events is large ($\sigma(N_i) = \sqrt{N_i}$). The false asymmetry A_{false} vanishes provided that the ratio r is stable over time ($r = r'$). Another thing to notice is that r is "hidden" in the definition of $\langle P_t\rangle$, and therefore should be known for the correct asymmetry extraction. The determination of r with high precision is difficult and therefore other methods for extraction of the asymmetries were developed, including an improved first order method and the *second order method*.

5.3.2 The Improved First Order Method

If no terms are neglected in the denominator of 5.12, a less biased asymmetry can be obtained. If, additionally, the raw asymmetry is redefined as

$$\Delta_{raw} = \frac{N_o - \tilde{r}N_c}{N_o + \tilde{r}N_c} \tag{5.19}$$

where $\tilde{r}$ is an estimator of r, one can reduce the false asymmetries to a large extent. The expressions of the asymmetry and of its uncertainty become:

$$A_1 = \frac{(1 + r/\tilde{r})^2}{4r/\tilde{r}} \frac{1}{2\langle f\rangle\langle D\rangle\langle P_b\rangle\langle P_t\rangle}\left(\frac{N_o - \tilde{r}N_c}{N_o + \tilde{r}N_c} - \frac{N'_o - \tilde{r}N'_c}{N'_o + \tilde{r}N'_c}\right) \tag{5.20}$$

$$\delta A_1 = \sqrt{\frac{(1 + r/\tilde{r})^2}{4r/\tilde{r}}} \frac{1}{\langle f\rangle\langle D\rangle\langle P_b\rangle\langle P_t\rangle}\sqrt{\frac{1}{N_o + \tilde{r}N_c} + \frac{1}{N'_o + \tilde{r}N'_c}}. \tag{5.21}$$

This method can be therefore be used in a wide range of r and A_1, at the cost of having an expression that is no longer intuitive and of the requirement that $\tilde{r}$ is known *a priori*.

5.3.3 The Weighted First Order Method

The two methods of asymmetry extraction described before use averages for f, D, P_b and P_t, and therefore some information is lost, which can be recovered if those quantities are taken event by event. If one divides each kinematic bin into sub-bins, in particular, sub-bins as small that contain only one event, and adds up the asymmetries obtained in all the sub-bins, the resulting expression looks like each event is being weighted by a weight $\omega = fDP_bP_t$. This would be an optimal choice from the point of view of reducing the statistical uncertainty, but is not viable because the average value of P_t is not the same before and after the field reversal. For this reason, a weight $\omega = fDP_b$ is used for each event, and the averages of P_t (before and

after the field reversal) need to be used. The expressions for the asymmetry and its uncertainty are:

$$A_1 = \frac{1}{2}\left(\frac{\sum_j^{N_o}(\omega)_j - \sum_j^{N_c}(\omega)_j}{\sum_j^{N_o}(\omega)_j^2 + \sum_j^{N_c}(\omega)_j^2} - \frac{\sum_j^{N'_o}(\omega)_j - \sum_j^{N'_c}(\omega)_j}{\sum_j^{N'_o}(\omega)_j^2 + \sum_j^{N'_c}(\omega)_j^2}\right) \tag{5.22}$$

$$\delta A_1 = \frac{1}{2}\sqrt{\frac{1}{\sum_j^{N_o}(\omega)_j^2 + \sum_j^{N_c}(\omega)_j^2} + \frac{1}{\sum_j^{N'_o}(\omega)_j^2 + \sum_j^{N'_c}(\omega)_j^2}} \tag{5.23}$$

5.3.4 The Improved Weighted First Order Method

The advantages of the improved first order method and of the weighted first order method can be used together, with intuitive replacement of quantities in the expressions for the asymmetries at their uncertainties.

5.3.5 The Second Order Method

In this section, a second order method for asymmetry extraction is introduced. We start from the expression for the total numbers of events collected in the two classes of target cells for the two spin configurations.

$$N_o = \int d\vec{\xi} a_o \phi n_o \bar{\sigma}(1 - P_b P_o f_o D A) = \int \vec{\xi}\alpha_o(1 - \beta_o A), \tag{5.24}$$

$$N_c = \int d\vec{\xi} a_c \phi n_c \bar{\sigma}(1 - P_b P_c f_c D A) = \int \vec{\xi}\alpha_c(1 - \beta_c A), \tag{5.25}$$

$$N'_o = \int d\vec{\xi} a'_o \phi n'_o \bar{\sigma}(1 - P_b P'_o f'_o D A) = \int \vec{\xi}\alpha'_o(1 - \beta'_o A), \tag{5.26}$$

$$N'_c = \int d\vec{\xi} a'_c \phi n'_c \bar{\sigma}(1 - P_b P'_c f'_c D A) = \int \vec{\xi}\alpha'_c(1 - \beta'_c A), \tag{5.27}$$

where $\alpha_i \equiv a_i \phi n_i \bar{\sigma}$ and $\beta_i \equiv P_b P_i f_i D$ and the $\vec{\xi}$ denotes, as before, all variables (x, Q^2, $\vec{v}$, etc.) involved in the integration. The above integrals are equivalent to

$$N_i = \langle a_i \rangle (1 - \langle \beta_i \rangle) A \int \phi n_i \bar{\sigma} d\vec{\xi}, \tag{5.28}$$

with the average acceptance

$$\langle a_i \rangle = \frac{\int a_i \phi n_i \bar{\sigma} d\vec{\xi}}{\int \phi n_i \bar{\sigma} d\vec{\xi}} \tag{5.29}$$

and the average β

$$\langle \beta_i \rangle = \frac{\int \beta_i \alpha_i d\vec{\xi}}{\int \alpha_i d\vec{\xi}} \overset{N_i \text{ large}}{\approx} \frac{\sum_{j=1}^{N_i} \beta_i^j}{N_i}, \tag{5.30}$$

where β_i^j is the value of β_i for event j with $j = 1 \ldots N_i$.

In the first order method we have defined the counting rate asymmetry. This time the

interesting quantity will be the double ratio of counting rates

$$\delta \equiv \frac{N_o N_c'}{N_c N_o'} = \frac{\langle a_o \rangle \langle a_c' \rangle}{\langle a_o' \rangle \langle a_c \rangle} \frac{\int \phi n_o \bar{\sigma} d\vec{\xi} \int \phi n_c' \bar{\sigma} \vec{\xi}}{\int \phi n_o' \bar{\sigma} d\vec{\xi} \int \phi n_c \bar{\sigma} \vec{\xi}} \frac{(1 - \langle \beta_o \rangle A)(1 - \langle \beta_c' \rangle A)}{(1 - \langle \beta_o' \rangle A)(1 - \langle \beta_c \rangle A)}. \tag{5.31}$$

Assuming that the target position does not change between the spin reversals we obtain

$$\frac{\int \phi n_o \bar{\sigma} d\vec{\xi} \int \phi n_c' \bar{\sigma} \vec{\xi}}{\int \phi n_o' \bar{\sigma} d\vec{\xi} \int \phi n_c \bar{\sigma} \vec{\xi}} = 1. \tag{5.32}$$

In addition we assume that the ratio of acceptances is equal to 1

$$\frac{\langle a_o \rangle \langle a_c' \rangle}{\langle a_o' \rangle \langle a_c \rangle} = 1. \tag{5.33}$$

This leads to a second order equation for the asymmetry A

$$aA^2 + bA + c = 0 \tag{5.34}$$

with $a = \delta \langle \beta_o' \rangle \langle \beta_c \rangle - \langle \beta_o \rangle \langle \beta_c' \rangle$, $b = -\delta(\langle \beta_o' \rangle + \langle \beta_c \rangle) + (\langle \beta_o \rangle + \langle \beta_c' \rangle)$ and $c = \delta - 1$. If $a \neq 0$, $A = \frac{-b \pm \sqrt{b^2 - 4ac}}{2a}$ and for $a = 0$, $A = -\frac{c}{b}$.

The uncertainty of the asymmetry is given by

$$\sigma(A) = \frac{1}{\langle \beta \rangle \sqrt{N_{\text{tot}}}}, \tag{5.35}$$

where we assume that $\frac{N_{\text{tot}}}{4} \equiv N_o \simeq N_c \simeq N_o' \simeq N_c'$ and $\langle \beta \rangle \equiv \langle \beta_o \rangle \simeq \langle \beta_c' \rangle \simeq -\langle \beta_o' \rangle \simeq -\langle \beta_c \rangle$. One of the solutions of Eq. 5.34 yields $A \gg 1$ which is non-physical, thus it is rejected. An important observation is that in the case of the second order method the asymmetry does not depend on r in contrast to the first order method.

5.3.6 The Second Order Weighted Method

In both the first order method and the second order method only mean values $\langle f \rangle$, $\langle D \rangle$, $\langle P_b \rangle$ and $\langle P_t \rangle$ were considered. This is not an optimal solution as far as the statistical uncertainty is concerned. An estimator that gives the smallest variance is the weighted mean. In this section a method for asymmetry extraction based on such estimator is presented.

In this approach the values of f, D, P_b and P_t are calculated on an event-by-event basis and then they are used in a weight. To introduce the weight into the second order method a few modifications of the formalism are necessary. Here we define p_i as

$$p_i = \int \omega N_i \vec{\xi} = \int \phi n_i \bar{\sigma} d\vec{\xi} \langle a_i \rangle_\omega (1 - A \langle \beta_i \rangle_w), \tag{5.36}$$

where

$$\langle a_i \rangle_\omega = \frac{\int a_i \omega \phi n_i \bar{\sigma} d\vec{\xi}}{\int \omega \phi n_i \bar{\sigma} d\vec{\xi}}, \tag{5.37}$$

$$\langle \beta_i \rangle_\omega = \frac{\int \beta_i \omega \phi n_i \bar{\sigma} d\vec{\xi}}{\int \omega \phi n_i \bar{\sigma} d\vec{\xi}} \overset{N_i \text{ large}}{\simeq} \frac{\sum_{j=1}^{N_i} \omega_j \beta_i^j}{\sum_{j=1}^{N_i} \omega_j} \tag{5.38}$$

where β_j^i being the value of β_i for the event j. Then the double ratio δ from Eq. 5.31 is redefined as

$$\delta = \frac{p_o p_c'}{p_o' p_c}. \tag{5.39}$$

Using similar assumptions as in the previous section we obtain the equation $aA^2 + bA + c = 0$ with $a = \delta\langle\beta_o'\rangle_\omega\langle\beta_c\rangle_\omega - \langle\beta_o\rangle_\omega\langle\beta_c'\rangle_\omega$, $b = -\delta(\langle\beta_o'\rangle_\omega + \langle\beta_c\rangle_\omega) + (\langle\beta_o\rangle_\omega + \langle\beta_c'\rangle_\omega)$, $c = \delta - 1$. With the assumptions that

$\frac{N_{\text{tot}}}{4} \equiv N_o \simeq N_c \simeq N_o' \simeq N_c'$ and $\langle\beta\rangle \equiv \langle\beta_o\rangle \simeq \langle\beta_c'\rangle \simeq -\langle\beta_o'\rangle \simeq -\langle\beta_c\rangle$ the statistical uncertainty of the asymmetry is given by

$$\sigma(A) = \sqrt{\frac{\langle\omega^2\rangle}{\langle\omega\beta\rangle^2}\frac{1}{N_{\text{tot}}}}. \tag{5.40}$$

The optimal weight, which gives the smallest statistical uncertainty $\sigma(A) = \sqrt{\frac{1}{\langle\beta^2\rangle N_{\text{tot}}}}$ is $\omega = \beta = fDP_bP_t$. The uncertainty for this estimator is reduced by a factor of $\sqrt{\langle\beta^2\rangle/\langle\beta\rangle^2}$ compared to the one for the not-weighted second order method.

However, such weight is not optimal as far as the systematic uncertainty is concerned. This happens because the mean value of the weight should be the same before and after the spin reversal. If this is not the case, then a false asymmetry appears. Indeed, in the COMPASS case, P_t is often different between the spin reversals. For instance, data is sometimes collected when the polarised target is not yet in "frozen spin mode", but is rather still being polarised. For this we choose the weight $\omega = fDP_b$ and for the target polarisation we use its mean value $\langle P_t\rangle$.

In the main analysis developed in this work, the second order weigthed method is used. The weighting allows the reduction of the uncertainty bars of the asymmetries by about 10%. It should be stressed that this analysis does not rely on Monte Carlo simulations, which is a strenght of the analysis, because in this case the extraction of A_1^p and of g_1^p is a clean and not dependent on models that would need to be used for generators and in an eventual limited knowledge in the description of the detector materials to extract acceptances.

5.4 Inputs for the Extraction of A_1^p

The extraction of the spin asymmetries and of the structure function g_1 rely on inputs from different sources. They are: the beam and the target polarisations, the dilution factor, the depolarisation factor, the spin-independent structure function F_2^p and the function R.

5.4.1 Beam Polarisation

The beam polarisation is calculated using the beam particle measurement on an event by event basis, using a parametrisation. Its relative uncertainty is estimated to be 5%.

5.4.2 Target Polarisation

The target polarisation is measured by different NMR coils in the target volume, several times per run. Averages per run and per cell are calculated and used in the analysis. A relative uncertainty of 2.5% or 3% is estimated, respectively, for 2007 and 2011 data.

5.4.3 Dilution Factor

The dilution factor, usually denoted by f, takes into account the fraction of material in the target that is polarisable, in order to apply an apropriate correction to the measured spin asymmetry. There are different non-polarised materials in the target,namely ^{3}He and ^{4}He, used for the cooling of the target material, but also ^{14}N (in ammonia) and C, F, Ni and Cu from the NMR coils. Both the number of such atoms and their interaction cross-sections with muons, which depend on kinematic variables, are taken into account in the computation of the dilution factor. The nuclei of ^{14}N are polarisable, but to a small extent, and the small effect to the spin asymmetries introduced by them are corrected for, as will be described later, in 6. The dilution factor is given by [84]

$$\begin{aligned} f_{\text{bare}}(x,Q^2) &= \frac{n_p\sigma_p(x,Q^2)}{n_p\sigma_p(x,Q^2)+\Sigma_A n_A\sigma_A(x,Q^2)}, \\ &= \frac{n_p}{n_p+\Sigma_A n_A\frac{\sigma_A}{\sigma_p}} \end{aligned} \tag{5.41}$$

where n_i are the numbers of nuclei of type i in the target material, σ_p and σ_A are the unpolarised cross-sections for the muon-proton and muon-nucleus scattering, respectively. The dilution factor is computed using a parametrisation of the cross-section ratios measured by the NMC and EMC and the COMPASS target material composition. The factor f_{bare} is multiplied my a factor ρ that takes into account unpolarised radiative corrections calculated using the program TERAD [85]. The used dilution factor is thus

$$f = \rho f_{\text{bare}} \tag{5.42}$$

The relative uncertainty of the dilution factor in the COMPASS kinematic domain is 5%.

In Fig. 5.1, the average value of the dilution factor f as function of x or ν is shown. Typical values range from 0.14 to 0.18. Since this variable is used event by event, contour plots are also shown.

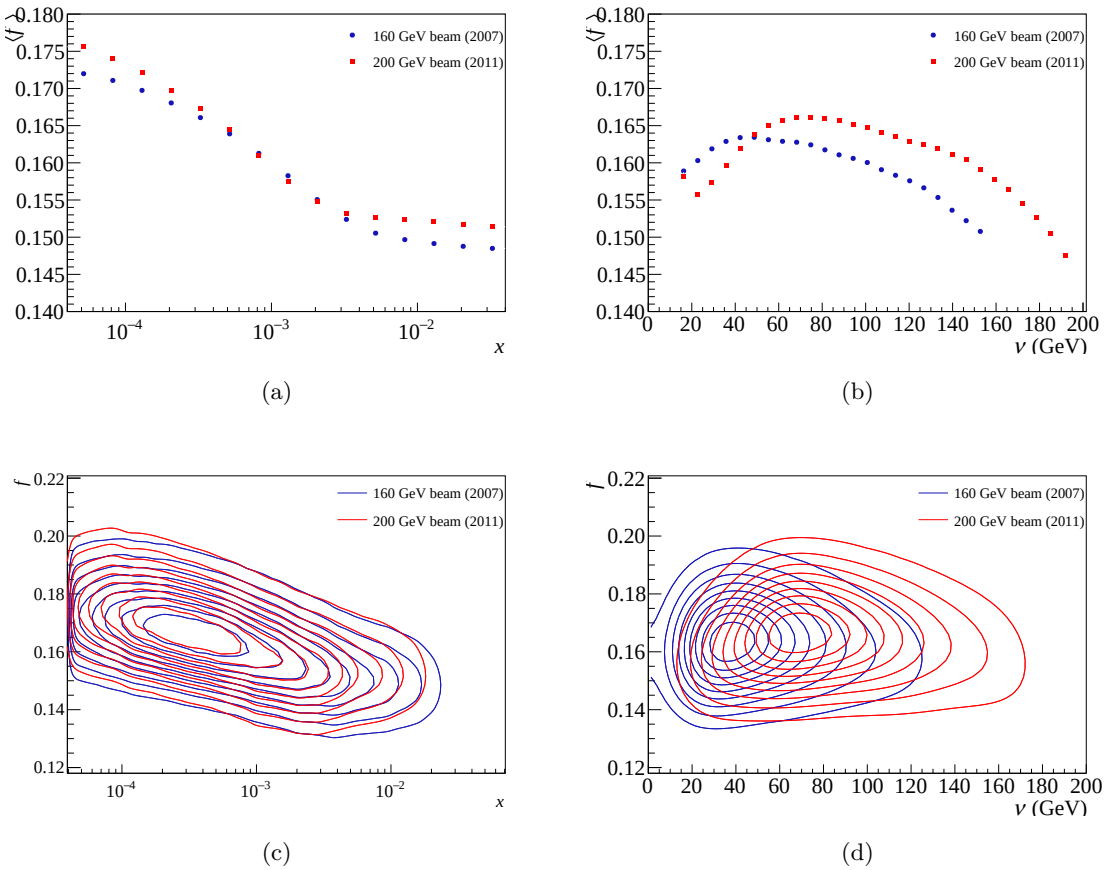

Figure 5.1: Distributions characterising the final sample used for extraction of asymmetries: the dilution factor f vs. (a and c) x and (b and d) ν.

5.4.4 Depolarisation Factor

The depolarisation factor, D, takes into account that the virtual photon polarisation is only a fraction of the incident muon polarisation, and is given by

$$D = \frac{y[(1+\gamma^2 y/2)(2-y) - 2y^2 m^2/Q^2]}{y^2(1-2m^2/Q^2)(1+\gamma^2) + 2(1-y-\gamma^2 y^2/4)(1+\gamma^2)(1+R)}, \tag{5.43}$$

with

$$\gamma = \frac{2Mx}{\sqrt{Q^2}} = \frac{\sqrt{Q^2}}{\nu}. \tag{5.44}$$

In Fig. 5.2, the depolarisation factor D as function of x and Q^2 is shown. Again, this variable is used in the analysis event by event and, for that reason, also contour plots are shown.

The depolarisation factor D increases with increasing y, *i.e.* events at lower values of y will have less diluted spin asymmetries. In the kinematic domain relevant to this work, $Q^2 < 1$ (GeV/c)^2, the dependence of the depolarisation factor D with the function $R = \sigma_L/\sigma_T$, as can be seen in its definition in Eq. 2.24, has important consequences: the large relative uncertainty of R at low values of Q^2 implies also large relative uncertainties of the depolarisation factor, up to 39%, as can be seen in Tables 6.7 and 6.8 for the one dimensional analysis and in

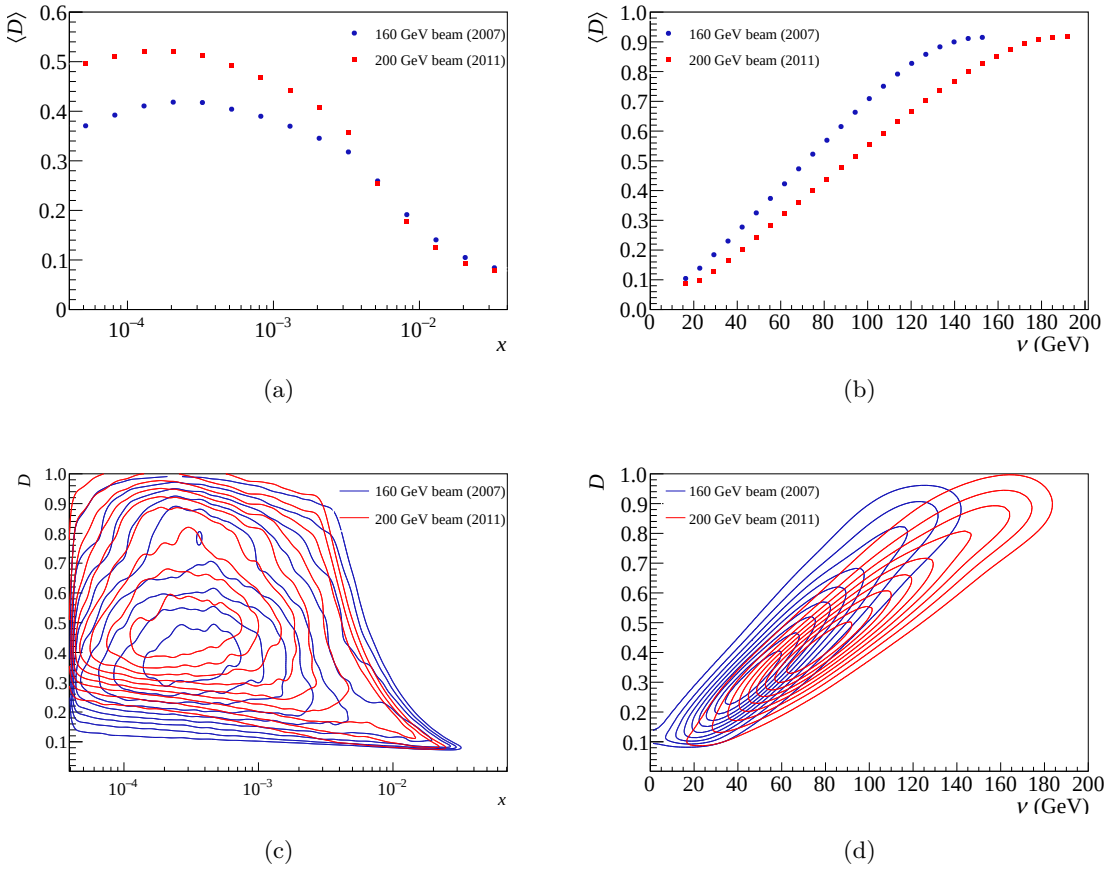

(a) (b)

(c) (d)

Figure 5.2: Distributions characterising the final sample used for extraction of asymmetries: the depolarisation factor D vs. x and ν.

Tables 7.2, 7.3, 7.4 and 7.5, being the largest multiplicative contribution to the asymmetries systematic uncertainty.

5.5 Inputs for the Extraction of g_1^p

5.5.1 The Spin-independent Structure Function F_2^p

In Fig. 5.3, four different parametrisations of F_2^p available in PHAST are shown. They are:

- a model including saturation (GBW) [86], valid for $x \in [10^{-6}, 0.1]$ and $Q^2 \in [10^{-5}, 10^3]$ $(\mathrm{GeV}/c)^2$;
- a GVDM model (JKBB) [87,88], valid for $x \leq 0.1$ and any Q^2;
- a fit to the world data made by the SMC collaboration (Tulay) [89], valid for $x \in [3.5 \times 10^{-5}, 0.85]$ and $Q^2 \in [0.2, 220]$ $(\mathrm{GeV}/c)^2$;
- a parametrisation of the proton world data (ALLM97) [90], valid for $x \in [3 \times 10^{-6}, 0.85]$ and $Q^2 \in [0, 5 \times 10^3]$ $(\mathrm{GeV}/c)^2$.

There is another parametrisation available in PHAST, MRS99, but its validity range doesn't include the phase space region of the present analysis. In this analysis, the SMC fit (Tulay), is used for the region where it is available; in the remaining phase space region, the model of JKBB is used.

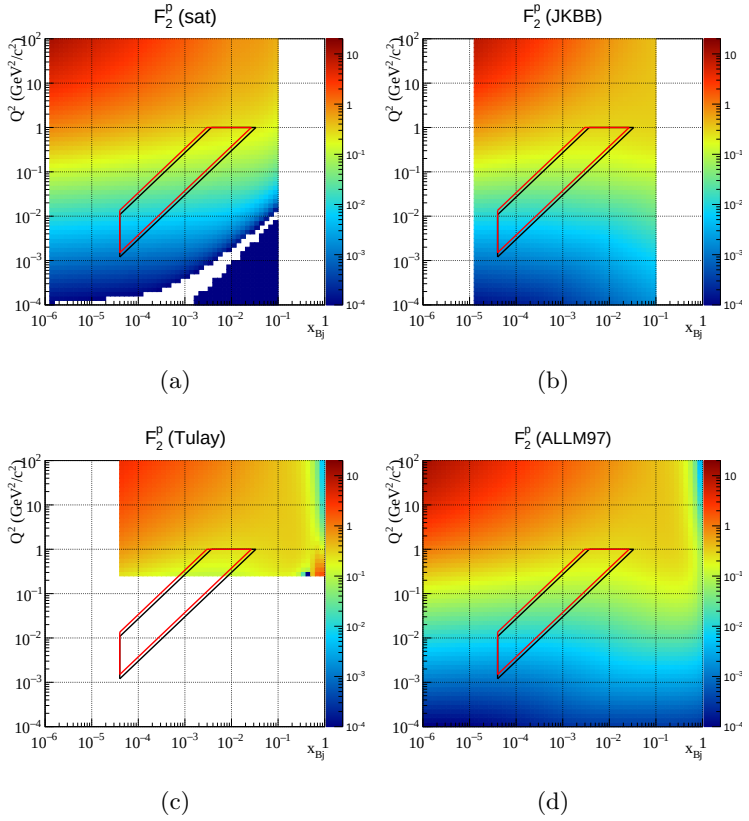

Figure 5.3: Four different parametrisations of F_2^p available in PHAST. The regions of interest for this analysis are marked by polygons (black for 2007 and red for 2011 data).

In Figs. 5.4 and 5.5, F_2^p as function of x and ν is presented. Note that there is a small discontinuity at $Q^2 = 0.2$ (GeV/c)^2, related to the transition from the region of validity of the Tulay parametrisation for F_2^p to the region where it is necessary to rely on models.

In Fig. 5.4, the values of F_2^p as a function of x for the (x, Q^2) grid are shown. One can see the steps when moving to higher values of x, caused by the transition at $Q^2 = 0.2$ (GeV/c)^2 from the SMC/Tulay fit to the JKBB parametrisation; this is taken into account in the systematic uncertainty of F_2^p. In the right plot, the transition occurs around $\nu = 130$ GeV for the 2007 data and around $\nu = 160$ GeV for the 2011 data.

5.5.2 The Function R

The spin-dependent structure function g_1^p is obtained from the double longitudinal spin asymmetries using

$$g_1^p = \frac{F_2^p}{2x(1+R)} A_1^p. \tag{5.45}$$

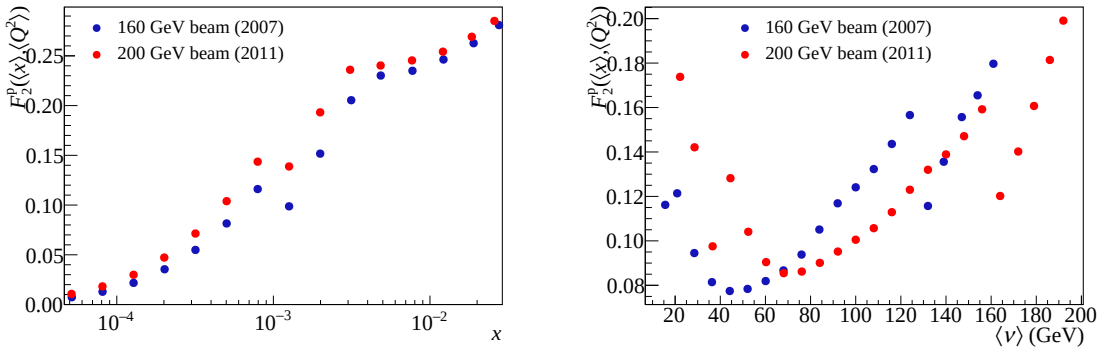

(a) (b)

Figure 5.4: Values of F_2^p for the final samples, as a function of (a) x or (b) ν. In the left plot, it is possible to observe a transition from the region where parametrisations of F_2^p to data where used, for $x > 10^{-3}$, and the region where a model was used, for $x < 10^{-3}$.

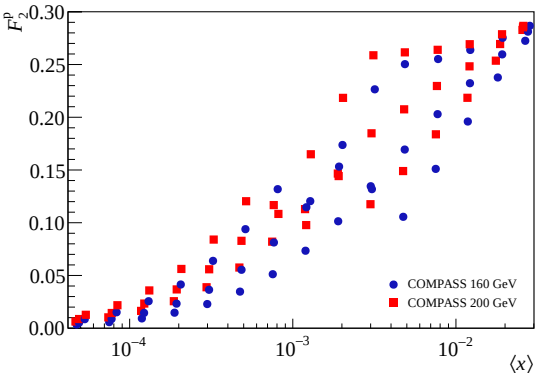

Figure 5.5: Values of F_2^p as function of x for the (x, Q^2) grid used in the bidimensional analysis described in Chapter 7. For each x bin, there are three Q^2 bins for each year of data-taking (2007 and 2011); F_2^p grows both with x and with Q^2.

The statistical uncertainty of g_1^p is estimated simply by propagation of the the statistical uncertainty of A_1^p. The remaining uncertainties on R and on F_2^p are included in the systematic uncertainty of g_1^p. We take advantage of the correlation of the depolarisation factor D, entering in the computation of A_1^p, with R, to reduce the term of the systematic uncertainty of g_1^p coming from $D \cdot (1 + R)$. In fact, the depolarisation factor is a function of R, as indicated in Eq. 5.43.

In Fig. 5.6, R as function of x and ν is presented.

In Fig. 5.7, the values of R as function of x for the (x, Q^2) grid, without and with the associated uncertainties.

5.6 Summary

In this chapter, the method used for extraction of the double spin longitudinal asymmetries A_1^p and the spin-dependent structure function g_1^p and the external inputs needed for their

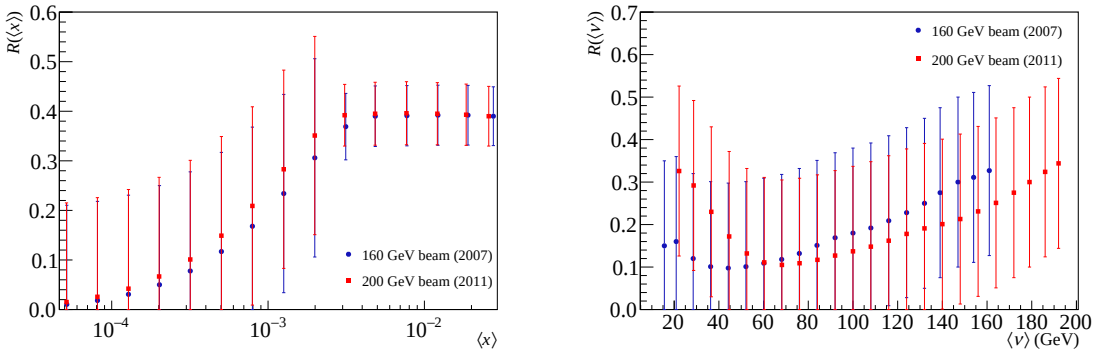

(a) (b)

Figure 5.6: Values of R for the final samples, as a function of x or ν, with their statistical uncertainty.

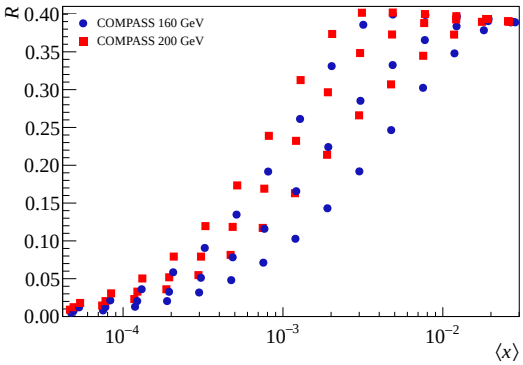

Figure 5.7: Values of R as function of x for the (x, Q^2) grid used in the bidimensional analysis described in Chapter 7. For each x bin, there are three Q^2 bins for each year of data taking (2007 and 2011); R grows both with x and with Q^2. The statistical uncertainties have been omitted for clarity.

computation were explaind. These methods are standard in COMPASS, having been used in the previous extractions of g_1^p (in the DIS regime) and of g_1^d. They were validated by toy Monte Carlo simulations.

Chapter 6

Unidimensional Extraction of A_1^p and g_1^p

6.1 Overview

In this chapter, the extraction of the longitudinal double spin asymmetry of the proton A_1^p and of the spin dependent structure function of the proton g_1^p as functions of the scaling variable x and, independently, of the energy lost by the interacting muon ν are detailed. The quality tests and the event selection of the studied samples are explained. The obtained results are presented and discussed, including comparisons with previous experimental results and with models.

6.2 Initial Sample

The data studied here were taken by COMPASS in its 2007 and 2011 data taking campaigns with a longitudinally polarised target of ammonia, that provided polarised protons, and the naturally polarised positive muons from CERN's M2 beam line, with nominal momenta of 160 and 200 GeV/c, respectively, in 2007 and 2011.

The most recent COMPASS official data productions were used, namely the production slot 2 for most of 2007 data, except for period 07W45, in which the slot 3 was used; for 2011 data, the production slot 1 was used.

The integrated muon in 2007 and 2011 returned by the two methods available in PHAST is given in Table 6.1.

For practical reasons, the event selection was divided into two steps. In the first step,

PHAST method for flux estimation	2007 data	2011 data
method #1 ("last-in-spill" minus "first-in-spill")	3.06×10^{13}	1.16×10^{13}
method #2 (counting "from previous processed event")	3.00×10^{13}	1.13×10^{13}

Table 6.1: Estimation of the integrated muon beam flux corresponding to the initial sample of events stored in mDSTs and processed by PHAST.

PHAST, the official COMPASS software to read mini Data Summary Trees (mDSTs) and perform analysis, used as input the mDSTs and produced as output ROOT trees with the most relevant parameters of each event. The PHAST version 7.136, patched with the most updated values of the beam polarisation and of the target polarisation [91, 92] was used.

In the second step of the analysis, a cut of $Q^2 < 1$ (GeV/c)^2 was applied, in order to have a sample that is complementary to the one with $Q^2 > 1$ (GeV/c)^2, whose results have been published in Refs. [51, 56]. An additional cut on x was applied, namely $\log_{10}(x) \geq -4.4$. This cut is the same as the one used for the $Q^2 < 1$ (GeV/c)^2 COMPASS deuteron analysis [93, 94]. It was motivated by the presence of a bias in the measurement of $\langle x \rangle$ at very low x, large relative uncertainties of the values of x as they become very small.

The data is divided according to microwave settings, *i.e.* the relative direction of the target cells polarisation with respect to the magnetic field of the target solenoid; their labeling is merely conventional but must be consistent for all the years of data because that is relevant in the discussion of systematic uncertainties. The data is also grouped in so called "periods", that approximately correspond to weeks of data-taking. Finally, the smaller, fundamental, groups of data are called configurations, corresponding to data taken close in time (in order to have a constant efficiency and acceptance), and with two different solenoid orientations, to be able to calculate spin asymmetries with such data. The composition of the data sets is indicated in Table 6.2.

Year	MW−	MW+	# Runs	Configs.
2007	W35, W36, W37, W38	W32, W33, W34, W44, W45	1112	23
2011	W25, W27, W30, W31, W32, W33	W36, W38, W39, W41, W43	1529	39

Table 6.2: Periods of data grouped by microwave settings in 2007 and 2011 data taking, where the sign here attributed is the sign of the product of the polarisation in the upstream cell (where the beam direction defines the positive orientation) and of the solenoid current as written in the COMPASS Run Logbook. On the last two columns, the number of runs and the number of configurations (data sets collected close in time with the two different solenoid orientations) are also indicated.

The initial sample has many events that are not relevant to the proposed analysis, including some backgrounds: events with elastic $\mu - e$ scattering, events including beam halo tracks, events resulting from interactions with a particle other than a proton in the target material and radiative events. The $\mu - e$ elastic events are removed with a cut described later in more detail. Halo tracks are removed by quality criteria imposed on the reconstructed kinematic variables. The non-proton particles in the target are corrected for using a dilution factor. Finally, the radiative events are avoided by a cut to remove high y events, and applying radiative corrections as a multiplicative factor in an effective dilution factor and at the level of spin asymmetries.

6.3 Data Stability Studies

When measuring spin asymmetries, it is important to ensure that the data-taking conditions for the two spin configurations are similar, and this implies in particular that the spectrometer is stable over time. In addition to the efforts put in operating the spectrometer as stably as possible, including redundancy of detectors, in the offline analysis several kinematic variables are monitored over time, per spill or per run, and spills with outlying values of those variables are marked as bad spills, ending up in lists of bad spills or bad runs, that are rejected from the subsequent analysis. In Fig. 6.1, an illustration of the method used to identify bad spills [96]

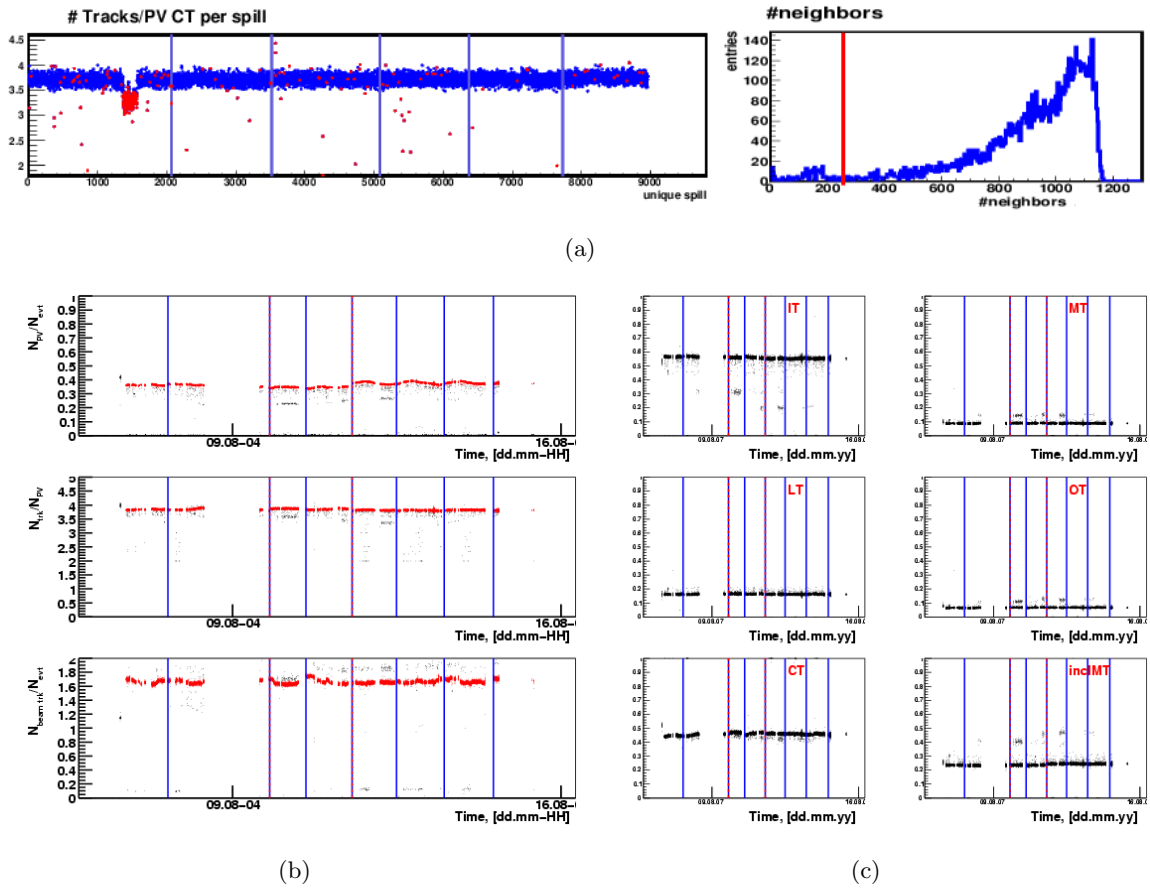

Figure 6.1: (a) Illustration of the method used for the identification of bad spills. (See details in the text.) (b) Example of analysis for the determination of the bad spills, for period 07W32 [95], together with the defined run limits for each configuration. The vertical lines show, in blue, the target polarisation reversals and, in magenta, the group limits. (c) Example of analysis performed for the determination of the bad spills for period 07W32 [95], done per trigger, where some instabilities become more obvious. The vertical lines show, in blue, the target polarisation reversals and, in magenta, the group limits.

is shown. For each period of data, that usually lasted one week, several kinematic quantities are plotted versus spill number. Examples of such quantities are:

- integrated flux;
- trigger rates;

- average number of primary vertices per event;
- average number of beam tracks per event;
- average number of tracks per event;
- average number of tracks per primary vertex;
- average χ_r^2 of primary vertices per vertex;
- average χ_r^2 of track per track;
- average number of hits per track;
- likelihoods per track;
- average number of charged clusters per event;
- energy of clusters in calorimeters per event.

Assuming the spectrometer was stable during the whole period of data taking, the distributions should be constant over time. Spills were rejected if they deviate in at least one of the distributions from the criterion to define a good spill according to a standard method. To allow fluctuations on a timescale of a couple of hours the interval for counting the number of neighbours was restricted to 600 to the left and 600 to the right of a given spill. The counting of the number of good neighboring spills that each spill has is based on the computed RMS of each distribution for the 1200 spills around the considered spill. Based on the RMS of each distribution, an appropriate threshold for the deviation from the mean in multiples of the RMS is chosen to achieve the best separation of good spills (with many good neighbors) and bad spills (with only a few good neighbors). For instance, in Fig. 6.1, spills are rejected if they have less than 250 good neighbors, where these are those that deviate less than *e.g.* $3 \times$ RMS. These bad spill thresholds can be tuned period wise. In adition, spills with less than a given number of muons are empty spills and are classified as bad by definition.

If problems with detectors or the beam line elements, or different trigger settings, were present for long periods of time, the corresponding spills are labeled bad spills by hand. For the 2011 data, the bad spill analysis was performed trigger by trigger, and dedicated bad spill lists were produced for the data with all Q^2 values. The overview of the data rejection rates using the bad spill labeling procedure is presented in Table 6.3.

Furthermore, other bad runs may be identified using information from the COMPASS Run Logbook by hand, or by offline analyses, by monitoring well known physical quantities, such as the mass of produced K^0 particles over time, or by monitoring the fitted centroid in the x distribution of the $\mu - e$ elastic scattering events over time. Three runs were removed according to the official bad runs list for 2007 while in 2011 the use of a bad run list is not required after the bad spill list.

The runs are subsequently grouped in configurations containing data collected with two different target spin configurations and with similar conditions of data-taking. For data with

2007 data				2011 data			
Period	Spills	Bad Spills	Reduction %	Period	Spills	Bad Spills	Reduction %
W32	24844	2701	10.9	W25	9439	3538	37.5
W33	19778	1447	7.3	W27	23706	4378	18.5
W34	8291	765	9.2	W30	9403	1034	11.0
W35	23006	2244	9.8	W31	7870	2949	37.5
W36	26618	2379	8.9	W32	6910	2552	36.9
W37	22627	1860	8.2	W33	1941	214	11.0
W38	5352	1092	20.4	W36	14511	2319	16.0
W44	26351	1847	7.0	W38	7498	819	10.9
W45	4875	348	7.1	W39	18899	1975	10.4
				W41	16436	1976	12.0
				W43	11511	1142	9.9

Table 6.3: Overview of the rejection rates because of the identification of bad spills.

longitudinal target polarisation taken in 2007 and 2011, each period of data (taken roughly during one calendar week) has between one and five configurations. The official COMPASS data grouping was used. In total, the analysed 2007 data consists of 23 configurations, whereas the 2011 data consists of 39 configurations.

For both 2007 and 2011 data, the official COMPASS bad spill lists and runs grouping into configurations were applied [95].

6.4 Event Selection

The criteria used for the event selection are similar to the ones used in the deuteron target data analysis, described in Ref. [93], mostly aiming at eliminating backgrounds and improving the quality of the reconstructed kinematic variables. They are listed hereafter.

1. A Physics trigger must have fired. For 2007, the Physics triggers were the inclusive Outer and Inclusive Middle Triggers and the semi-inclusive Inner, Middle, Ladder and Calorimetric Trigger. For 2011, the Physics triggers were the inclusive Ladder, Outer and Inclusive Middle Triggers and the semi-inclusive Inner, Middle, Calorimetric and Large Angle Spectrometer Triggers. This selection criterion excludes the events from auxiliary triggers: Veto Inner Trigger, Beam Trigger, Halo Trigger, True Random Trigger, Noise Random Trigger. For 2007, the LargeQ2 Trigger was not used for the analysis because it was not put to the mDSTs during the data production step. For more details on the Trigger, in particular the kinematic coverage of the different triggers, see Appendix A.

2. The event has at least one primary vertex (PV), *i.e.* a beam track and one outgoing reconstructed track. A beam track is a track with momentum reconstructed in the BMS; if several valid BMS-tracks are compatible in time with a given SciFi/Si track or vice-versa or both the backtracking algorithm is used to resolve ambiguities; the track is reconstructed in the scintillating fibres and silicon microstrip detectors starting upstream

	2007	2011
x_U	-0.15	-0.0073
y_U	0.39	-0.1680
$z_{U,1}$	$-62.5+2$	$-61.7-1.2$
$z_{U,2}$	-32.5	$-32.4-1.2$
$z_{C,1}$	$-27.5+2$	-26.5
$z_{C,2}$	32.5	32.1
x_D	0.02	0.1261
y_D	0.23	-0.1796
$z_{D,1}$	$37.5+0$	37.2
$z_{D,2}$	67.5	66.5

Table 6.4: Target fiducial volume definition resulting from the procedure to determine its position. The indices U, C, D indicate, respectively, the upstream, central and downstream cells and the z coordinate is along the beam direction. The indices $1, 2$ indicate the starting and the ending coordinates of a cell along the beam direction. The units are centimeters. The cells are cylindrical with a radius $R = 2.0$ cm. For the low x and low Q^2 analysis, a radial cut at $R = 1.8$ cm is applied.

of the target; and, finally, the track time is within 3 sigmas of BMS and trigger time. This condition ensures the presence of an interaction of interest with a beam particle.

3. A scattered muon was identified in the best primary vertex (BPV). This condition further selects the event type of interest, *i.e.* the scattering of a beam muon. A particle/track is identified as belonging to a scattered muon if: (a) it crossed more than 30 radiation lengths; (b) has the last measured point after the Muon Filter 1; (c) has the same charge as the beam particle (checked based on SM2 polarisation); (d) belongs to a primary vertex that does not contain other outgoing muon tracks (μ track passing the three previous requirements); (e) its extrapolation goes through the active area of the pair of hodoscopes that fired the trigger; (f) it does not cross the yoke of SM2; (g) it belongs to an event that does not contain a track which goes through the hole in the absorber system.

4. At least one additional track besides the track of the scattered muon is associated to the best primary vertex. This condition is used to have a good reconstruction of the vertex, as was done in the analysis of the COMPASS deuteron data at low x and low Q^2 and also in SMC data in a similar kinematic domain. Removing this condition wouldn't significantly change the final sample, because there are other quality criteria applied to the vertex reconstruction, as described below.

5. The best primary vertex is inside the target region (using the COMPASS official position of the target encoded in PHAST and further requiring that the distance to the fiducial axis of the target, r, is smaller than 1.8 cm). The position of the target was found by carefully studying distributions of the primary vertices and identifying in them pieces of the mechanical support of the target material whose relative positioning is well described in technical drawings.

6. The beam particle has reconstructed momentum and the primary vertex is well recon-

structed: $\sigma_{Z_{BPV}} < 5\,\text{cm}$ and $\chi^2_{BPV} \leq (\text{NDF} + 3 \cdot \sqrt{2 \cdot \text{NDF}})$ (3σ). This condition ensures a good reconstruction of the primary vertex.

7. The fraction of the energy lost by the muon, y, is between 0.1 and 0.9. The events with very low values of y have poorly reconstructed vertices, and are thus rejected. The events with high values of y are the most affected by radiative corrections, which are especially uncertain, and therefore they are removed from further analysis.

8. The beam momentum is within a window centered at the nominal beam momentum $140 < p_{\text{beam}} < 180\,\text{GeV}/c$ (2007) or $185 \leq p_{\text{beam}} \leq 215\,\text{GeV}/c$ (2011), and the track momentum must be well reconstructed: $0.5 \times 10^{-9} < \sigma^2_{|q|/p} < 20 \times 10^{-9}$ $(c/\text{GeV})^2$. These cuts remove events without reconstructed beam momentum.

9. No candidate of elastic μe scattering is found in the event. The following conditions were imposed:

   - $-3.6 < \log_{10}(x) < -3.0$; and
   - $-0.005 < q\theta^* < 0.002$ for events w/ 1 hadron candidate (two outgoing particles in the primary vertex), or
   - $-0.001 < q\theta^* < 0.000$ for events w/ 2 hadron candidates (three outgoing particles in the primary vertex).

   Here, $q\theta^*$ is the product of the charge of the particle and the angle formed by the hadron candidate track and the virtual photon direction in the laboratory frame. Of course that the "hadron candidate" is in the case of the spurious background of the $\mu - e$ events, an electron (or a positron), while it can be a hadron in the other event types. Note that there is a significant conversion of photons emitted by the electron, namely in the target material, which explains that particles of positive charge (positrons) show up in events of elastic $\mu - e$ scattering, where one would expect only negatively charged particles (electrons) stemming out of the vertex besides the scattered muon.

10. There is at least one "good hadron". The following conditions were imposed:

    - the hadron candidate has a reconstructed track;
    - it has reconstructed momentum;
    - the fraction of the energy lost by the muon that is carried by the hadron candidate is $0.1 < z_h < 1$;
    - the track has $p_{\text{track}} < 140.0$ GeV/c (2007) or $p_{\text{track}} < 180.0$ GeV/c (2011);
    - the track is not identified as a muon, which is ensured by imposing that the last measured point has $350 < Z_{\text{last}} < 3500$ cm and that the number of radiation lenghts travelled are $X/X_0 < 15$.

11. The beam particle track or its extrapolation crosses all the target cells ($R \leq 1.8$ cm). This condition ensures that the fiducial cell volumes with the two different spin configurations are impinged by the same beam flux.

This data analysis makes use of the so called "hadron method", *i.e.* the requirement of at least one hadron in the event (cut #4), in contrast to the data analysis of the $Q^2 > 1$ (GeV/c)^2 sample. This method was first used by the SMC, and allows to improve the primary vertex resolution, in order to distinguish between two contiguous target cells. This distinction is difficult because of the very small polar angles of the scattered muon in the laboratory frame in this sample. The disadvantage of the method is that the sample is not strictly inclusive, but most of COMPASS triggers are already semi-inclusive. The bias in the asymmetries introduced by the "hadron method" was shown to be small at low values of x by Monte Carlo simulations [89], as can be seen in Fig. 6.2.

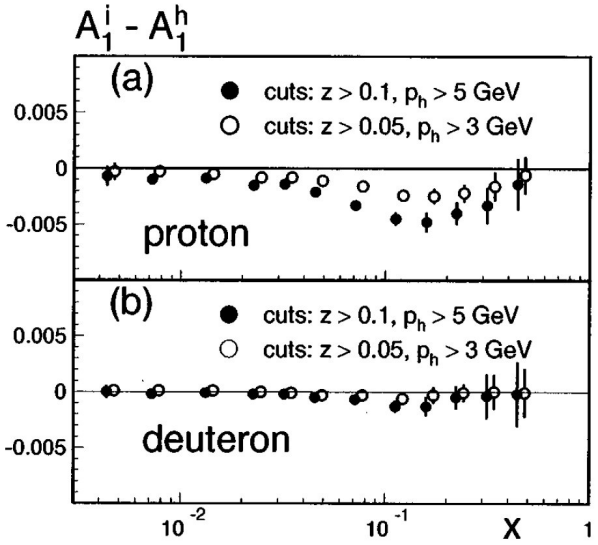

Figure 6.2: The differences of inclusive asymmetries and hadron asymmetries, $A_1^i - A_1^h$, calculated from Monte Carlo by the SMC [89] for generated DIS events (A_1^i) and for events with at least one forward hadron surviving cuts on z and on the hadron momentum (A_1^h). The results are shown for two sets of cuts for the proton and for the deuteron.

The stricter cut on the radial coordinate of the primary vertex is motivated by the intention to be free of possible misalignments of the target with respect to the spectrometer.

The cut on the highest values of y removes events with expected large radiative corrections and low momentum muons resulting from pion decays. The cut on the lowest values of y removes poorly reconstructed scattered muons and halo muons misidentified as scattered muons.

The distributions of the variable $q\theta^*$, the product of the charge of the particle associated to the track with the angle of the hadron candidate track and the virtual photon direction in the laboratory frame, for 2007 and 2011, are presented in Figures 6.3 and 6.4.

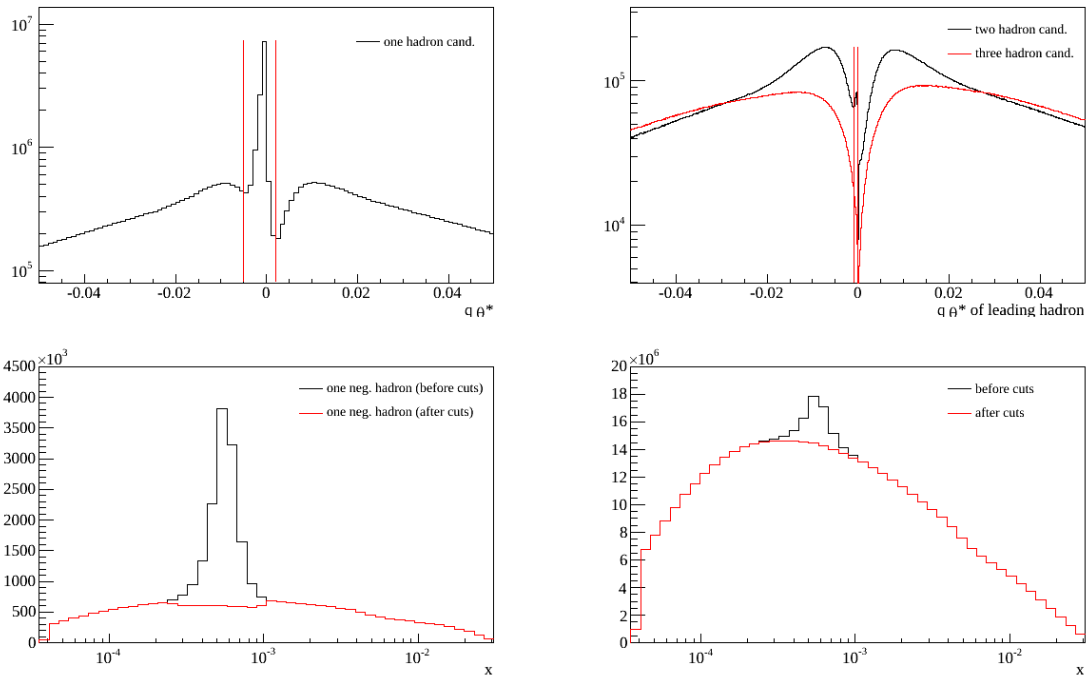

Figure 6.3: Top left: Distribution of the variable $q\theta^*$ (see definition in the text) for 2007 events with one "hadron candidate" (with one additional track in the primary vertex beside the muon) in the primary vertex. Events between vertical lines were removed from further analysis. Top right: same as the previous plot, but for events with one or two hadron candidates. A cut was applied for events with two hadron candidates in the primary vertex. Bottom left: x distribution of events with one negative hadron candidate before and after the μe rejection. Bottom right: same as the previous plot, but for the whole sample.

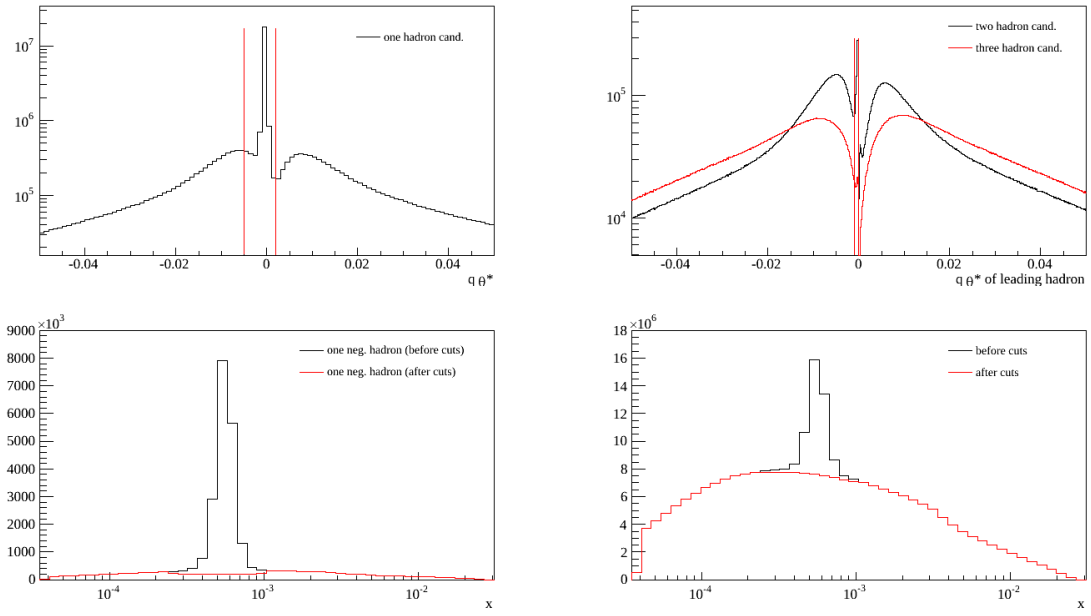

Figure 6.4: Same as in Fig. 6.3, but for 2011 data. The cut was not optimised for the 2011 data.

The effect of the cuts on the number of events is given in the Table 6.5 and is also shown if Fig 6.5.

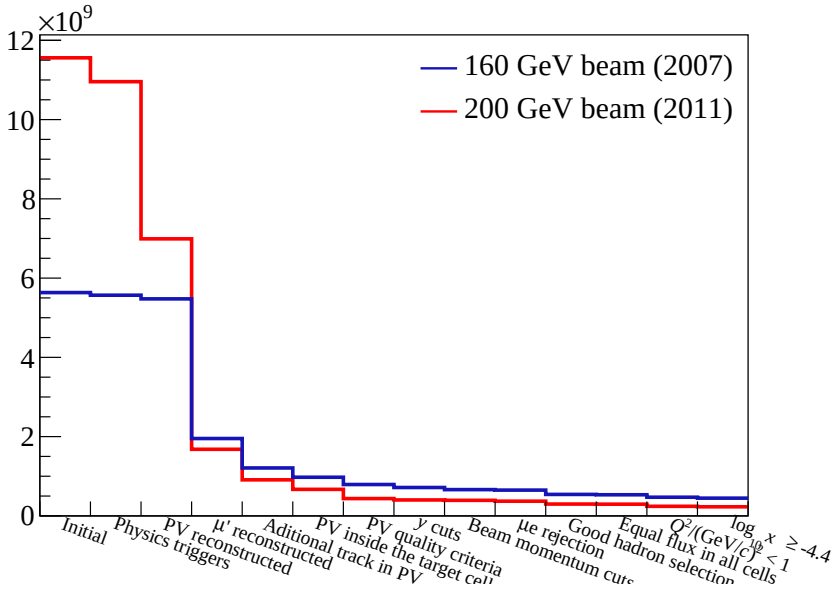

Figure 6.5: Event number reduction after each selection criterion applied.

Take note that, for the 2011 data, all sorts of events were kept in the production of the mDSTs, whereas for the 2007 data, only events with at least one reconstructed vertex were saved in the mDSTs. This explains that only 60.5% of the initial sample of 2011 pass the cut #2, requiring a reconstructed primary vertex, in contrast with the corresponding 97.2% in the 2007 data sample. Note also that although the beam intensity in 2011 was about half of the

		2007 data			2011 data		
#	**Criterion**	**Nr. events**	**%prev**	**%init**	**Nr. events**	**%prev**	**%init**
	Initial w/o bad spills/runs	5 634 708 006	–	100.0	11 558 898 030	–	100.0
1	W/ phys. trig.	5 568 358 198	98.8	98.8	10 956 941 316	94.8	94.8
2	PV reconstructed	5 475 928 162	98.3	97.2	6 990 966 363	63.8	60.5
3	μ' reconstructed (iMuPrim)	1 951 632 662	35.6	34.6	1 680 138 907	24.0	14.5
4	Additional track(s) in BPV	1 208 959 217	61.9	21.4	909 397 741	54.1	7.9
5	BPV inside the target cells	974 647 377	80.6	17.2	669 017 875	73.6	5.8
6	BPV quality criteria	791 138 915	81.2	14.0	436 279 892	65.2	3.8
7	y cuts	715 679 394	90.5	12.7	401 458 648	92.0	3.5
8	Beam momentum cuts	662 290 591	92.5	11.8	391 748 374	97.6	3.4
9	μe events rejection	649 824 306	98.1	11.5	370 449 195	94.6	3.2
10	Good hadron selection	541 234 853	83.3	9.6	297 682 626	80.4	2.6
11	Equal flux in all cells	532 432 728	98.4	9.4	294 950 110	99.1	2.6
12	$Q^2 < 1$ (GeV/c)^2	470 545 684	88.4	8.4	241 027 684	81.7	2.1
13	$\log_{10}(x) \geq -4.4$	447 036 988	95.0	7.9	228 950 419	95.1	2.0
TOTAL final sample 2007+2011 :		$\sim 676 \times 10^6$ events					

Table 6.5: Event number reduction after each selection criterion applied.

one of 2007, the data-taking time range in 2011 was about two times longer, and therefore the final number of events in 2011 is somewhat unexpected. Three possible effects may have contributed to this: the supercycle length was larger in 2011 (about 50 s in contrast to the length of 40 s in 2007); the criteria for bad spill rejection were stricter in 2011, leading to larger rates of rejection of spills for this year of data; finally, some triggers were slightly changed from 2007 to 2011.

6.5 Final Sample

The distributions of kinematic variables that characterise the final sample are presented in Figs. 6.6 to 6.8.

Fig. 6.6 shows the kinematic coverage in x and Q^2 of the final sample. It is clear that the low x and low Q^2 region represent most of the data taken by COMPASS, and that there is a strong correlation between x and Q^2. Furthermore, one observes that the use of a 200 GeV/c in 2011 allowed to extend the kinematic coverage, namely by covering lower values of x for a given Q^2. The black polygons mark the region used for the analysis. The diagonal lines mark the cuts $y > 0.1$ (the lower right one) and $y < 0.9$ (the upper left one), the horizontal lines mark the cut $Q^2 < 1$ (GeV/c)^2 and the vertical lines mark the cut $x > 4.4 \times 10^{-5}$.

In Fig. 6.7, the distributions of the interaction vertices along the beam direction coordinate, z_{PV} are shown, both for samples where that cut was applied and for samples where it was not. For the latter, the three target cells are clearly visible, together with the location of target windows and detectors. The cuts on this variable further ensure no wrong vertex cell attribution.

Figure 6.8 exhibits distributions of several kinematic variables for the final sample used for

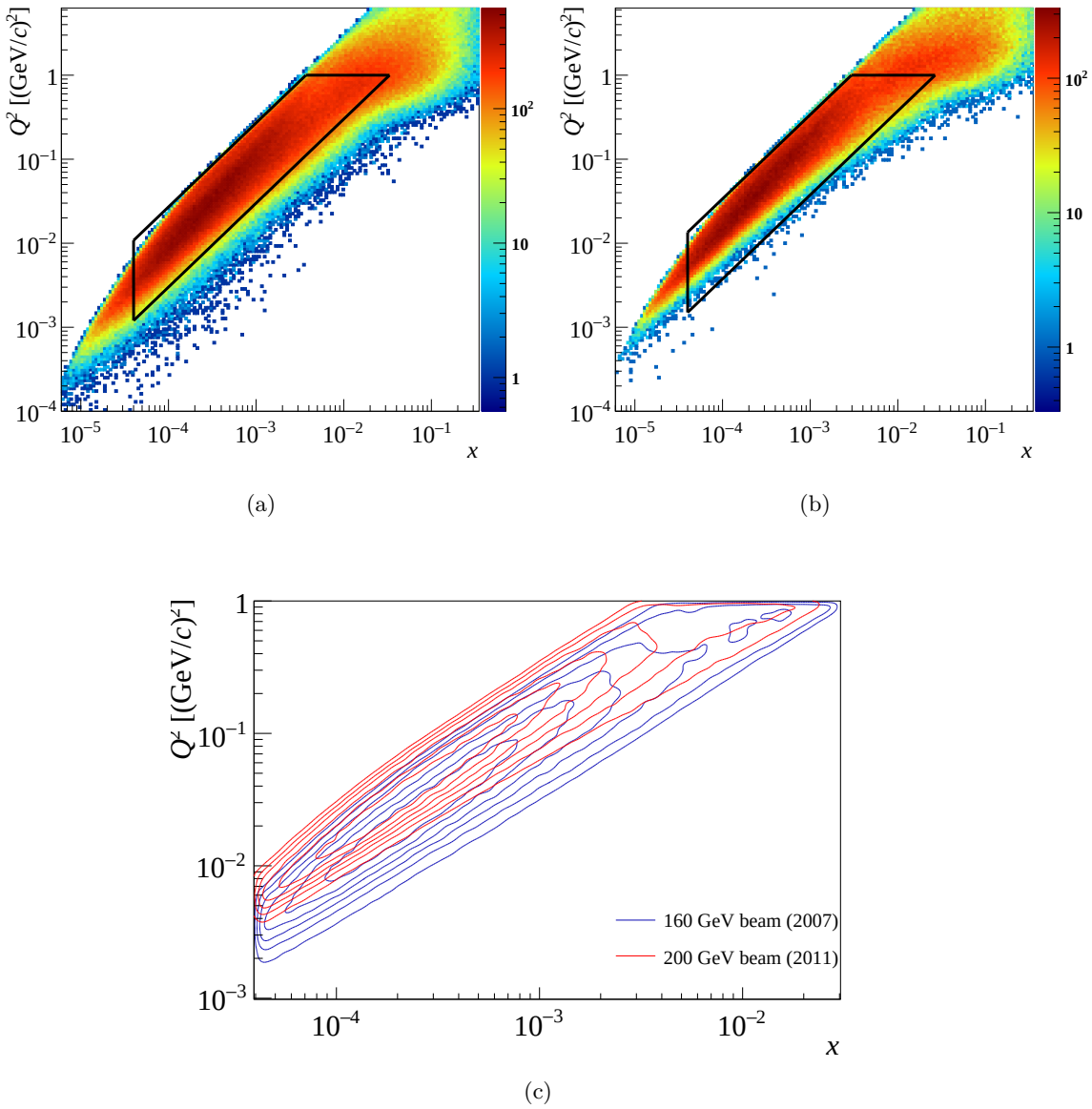

Figure 6.6: COMPASS phase-space coverage in the (x, Q^2) plane, for (a) the 2007 sample and (b) the 2011 sample. The polygons indicate the regions selected for this analysis. With the 200 GeV beam used in 2011, it was possible to access smaller values of x for any given Q^2. In (c), it is possible to see the displacement in phase space coverage of 2011 data with respect to 2007 data, towards lower values of x at any given Q^2 or to higher values of Q^2 at any given x.

the analysis: x, Q^2, ν, W, y and the polar angle of the scattered muon in the laboratory frame, $\theta_{\mu'}$. In Subfigure 6.8 (a), one observes the range of x covered in the analysis, from 4.0×10^{-5} to 4.0×10^{-2}, *i.e.* along three decades. In Subfigure (b), one observes the distribution of Q^2, extending to values of Q^2 of 1.0×10^{-3}. Subfigure (c) shows the distribution of ν, which extends to larger values for the 2011 data, as expected from the larger beam momentum. Note that the borders of each distribution are determined by the cuts $0.1 < y < 0.9$, which also explains that the distribution of the 2011 data starts at larger values of ν. Overall, the data is within

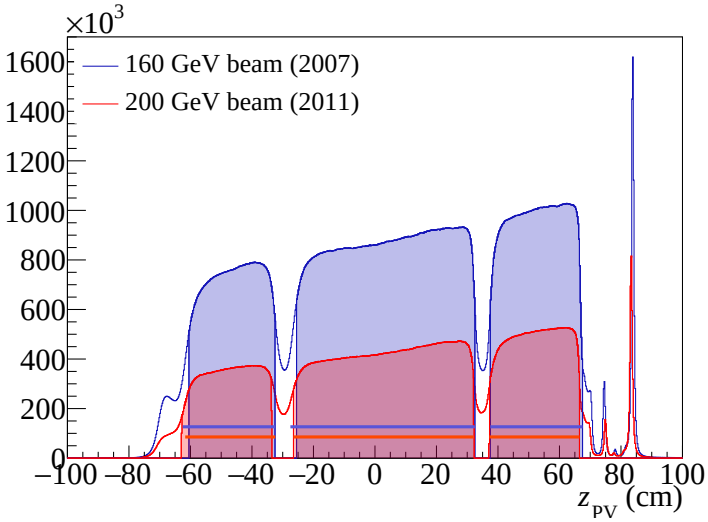

Figure 6.7: Longitudinal spatial coordinate of the interaction vertices, for the 2007 and 2011 final samples used for extraction of asymmetries. All event selection criteria were applied except the one on z_{PV} (unfilled histograms) and with all event selection criteria applied (filled histograms). The superimposed lines at the bottom indicate the positions of the target cells. The slope of the distributions is caused by the difference of acceptance along the beam direction, mostly constrained by the target solenoid aperture.

$14 < \nu < 194$ GeV. In Subfigure (d), the distribution of W is shown. Note that this quantity is always larger than 5 GeV, *i.e.* well above the region of production of the nucleon and delta resonances. Subfigure (e) shows the distribution of the variable y, the fraction of energy lost by the muon; the cuts on low and high values of this variable are also shown. Finally, Subfigure (f), exhibits the distribution of the polar angle of the scattered muon in the laboratory frame; typical values are around 2 mrad.

The effect of the successive cuts is shown in Fig. 6.9 for the 2007 data. In Fig. 6.10, some kinematic distributions are shown per trigger, also for the 2007 data: x, Q^2, ν and W. Moreover, in Fig. 6.11, the kinematic coverage per trigger is shown in the plot with Q^2 vs. x.

In Fig. 6.12, the kinematic coverage of the different triggers for the 2007 and 2011 runs is shown in the plots with Q^2 vs. x, Q^2 vs. y, and ν vs. x. The increase of beam momentum to 200 GeV/c beam in 2011, resulted in lower values of x being accessed for any given Q^2. Note that in 2011, a new trigger was present, the LAST or Large Angle Spectrometer Trigger. Also in 2011, the calorimeter mix condition and the calorimetric trigger condition used a common low threshold (while in 2007 and in other years the calo trigger condition threshold was higher than the calo mix trigger condition threshold).

6.6 One Dimensional Analyses

In this section, details will be shown on the results of the extraction of the spin asymmetry A_1^p and of the structure function g_1^p as functions of x, the traditional variable used in previous experimental studies, and as functions of ν, to test possible dependences on this variable. In

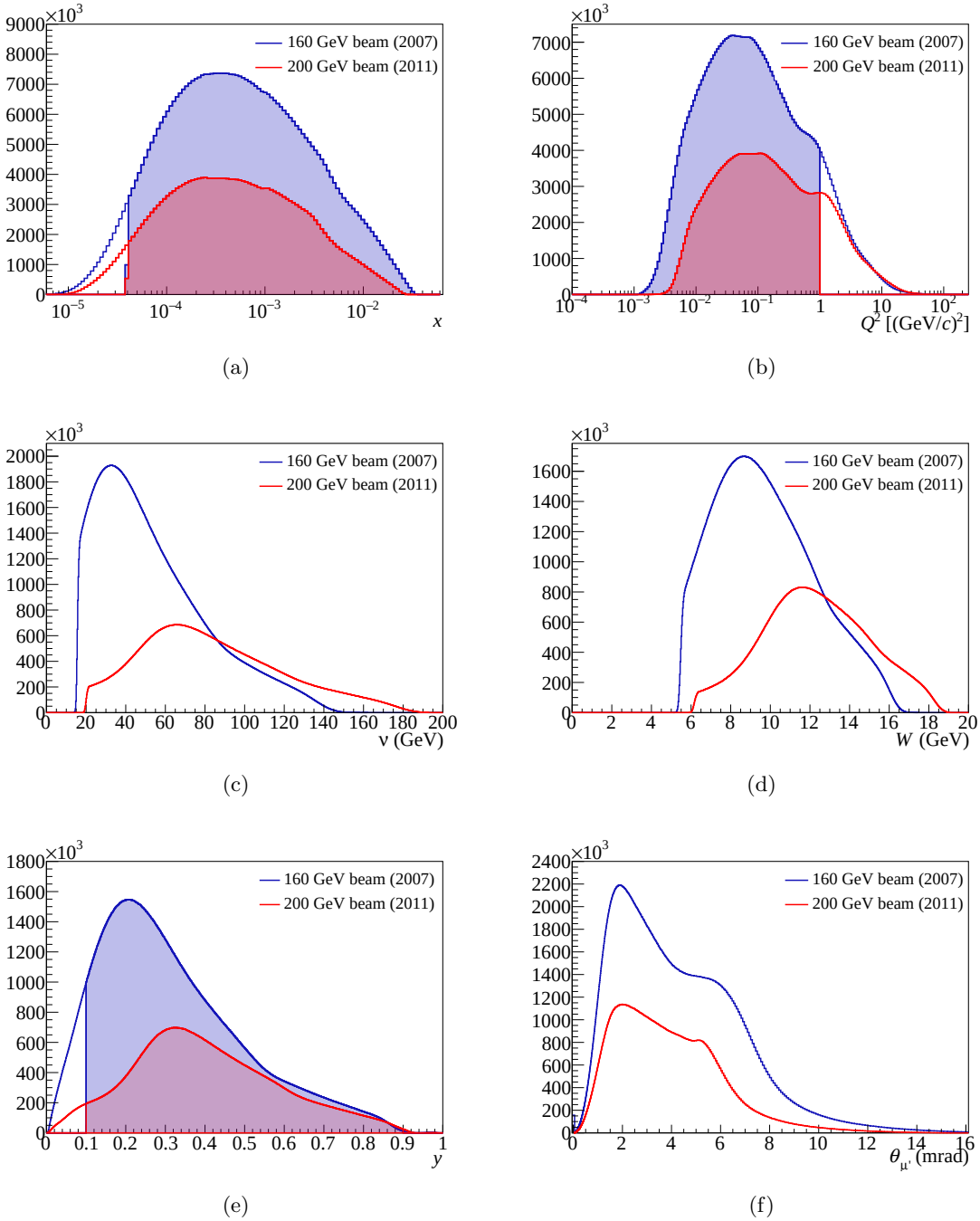

Figure 6.8: Kinematic distributions characterising the final sample used for extraction of asymmetries: (a) x, (b) Q^2, (c) ν, (d) W, (e) y and (f) $\theta_{\mu'}$. For x, Q^2 and y, the distributions with events before and after all cuts but the one in the displayed variable are shown.

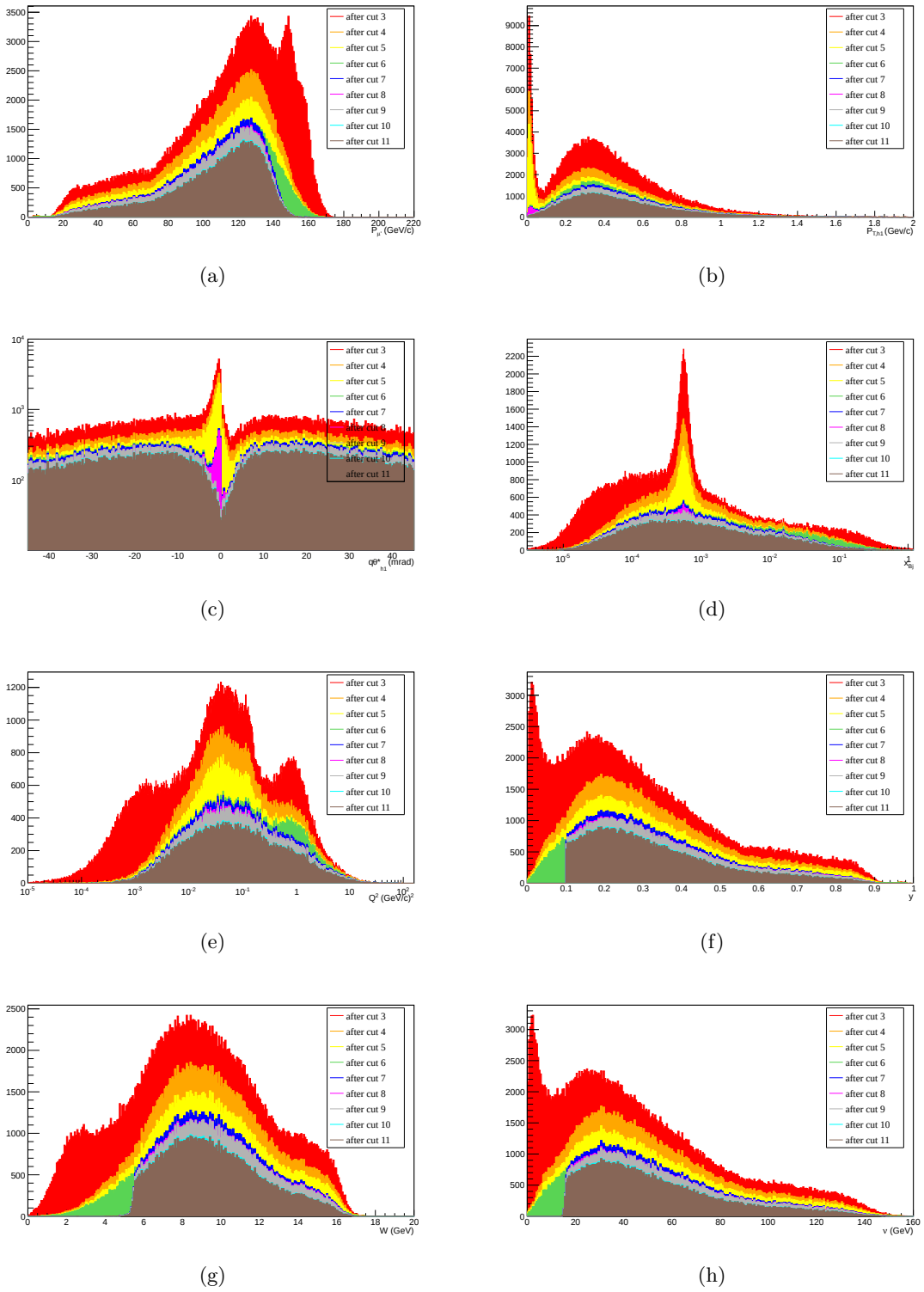

Figure 6.9: Effect of the successive selection criteria on selected kinematic variables for the 2007 data. In subfigure (a), the peak in the scattered muon momentum distribution that is still present after the cut #3 (the requirement of a reconstructed scattered muon), but is removed by the cut #4 (the requirement of an additional track in the primary vertex) at around 155 GeV/c can be intepreted as coming from muons resulting from the decay of pions. (See Table 6.5 and text for other details.)

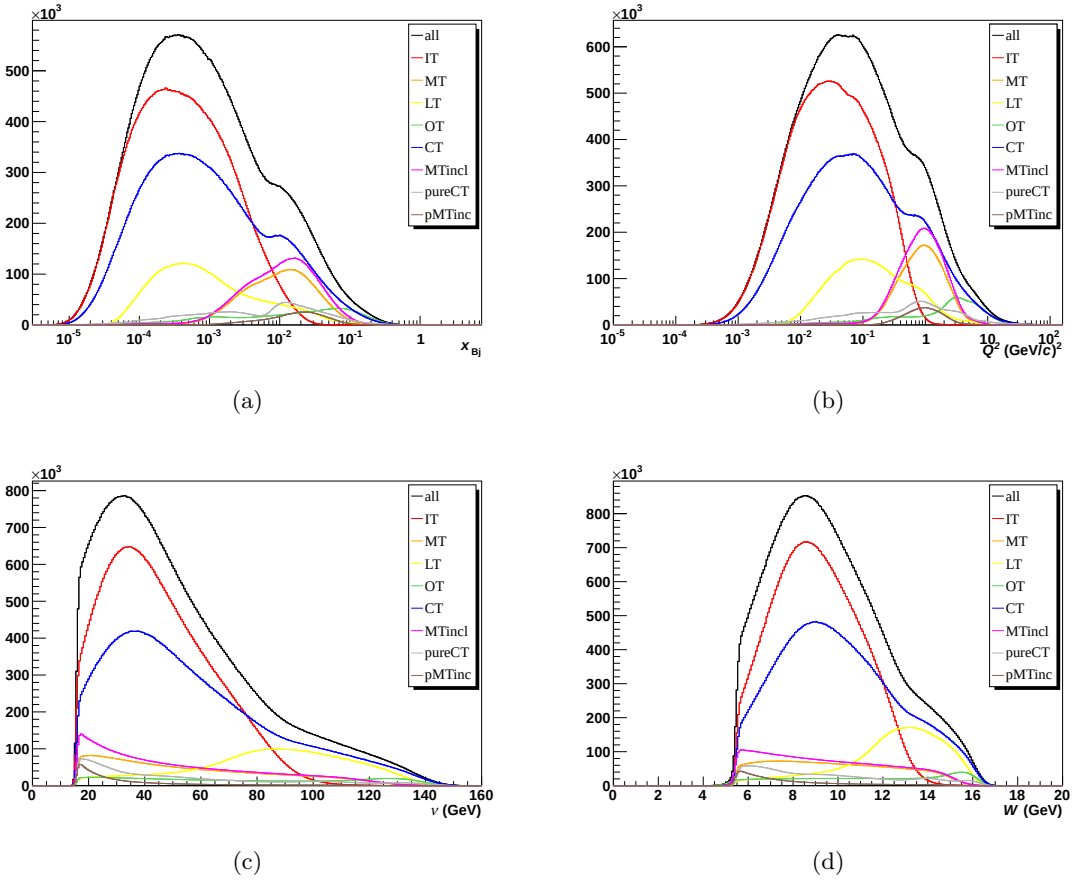

(a) (b)

(c) (d)

Figure 6.10: Kinematic distributions for 2007 data trigger by trigger: (a) x, (b) Q^2, (c) ν and (d) W.

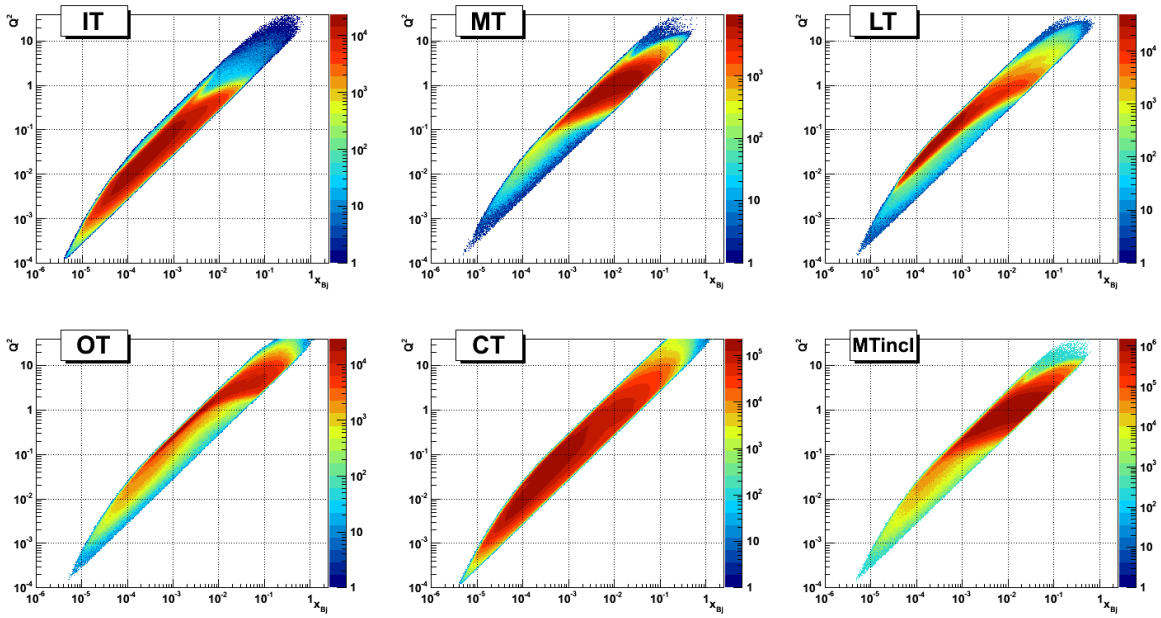

Figure 6.11: Kinematic coverage of the different triggers, for the final 2007 data sample.

Fig. 6.13, the averagevalues of the kinematic variables x and Q^2 or ν and x, respectively, for the the bins used in the extractions (a) of $A_1^p(x)$ and $g_1^p(x)$; and (b) of $A_1^p(\nu)$ and $g_1^p(\nu)$ are depicted.

6.6.1 Correction to the Asymmetries for the Presence of ^{14}N

The spin asymmetry measured using an ammonia target NH_3 includes a term related to the presence of the polarisable nucleons in ^{14}N, that has to be subtracted to obtain the spin asymmetry caused only by the presence of polarisable protons.

The measured asymmetry is related to A_1^p as

$$A_{1,\text{meas}} = A_1^p + \frac{N_N}{N_p}\frac{P_{^{14}\text{N}}}{P_p}\frac{\sigma_{^{14}\text{N}}}{\sigma_p}A_1(^{14}\text{N}). \tag{6.1}$$

The ratio N_N/N_p accounts for the number of ^{14}N with respect to H. The ratio $P_{^{14}\text{N}}/P_p$ accounts for the fact that the nucleon spin is aligned anti-parallel to the ^{14}N one third of the time. Finally the ratio $\sigma_{^{14}\text{N}}/\sigma_p$ gives the relative polarisation of the ^{14}N with respect to the protons [56, 97].

In the shell model, the nitrogen can be modeled as a carbon spinless core plus a proton and a neutron [98] so that the nitrogen contribution can be rewritten as $A_1(^{14}\text{N})\sigma_{^{14}\text{N}} = \beta_{^{14}\text{N}} g_{^{14}\text{N}}(A^p\sigma_p + A^n\sigma_n)$, where $\beta_{^{14}\text{N}}$ and $g_{^{14}\text{N}}$ are corrections resulting from nuclear effects and the EMC effect [99] in the nitrogen, respectively. The proton and the neutron contributions can also be extressed in terms of deuteron asymmetry according to $A^d\sigma_d = \gamma_d(A^p\sigma_p + A^n\sigma_n)$, where γ_d corrects for the D-state of the deuteron. Rewriting the equations, one obtains the

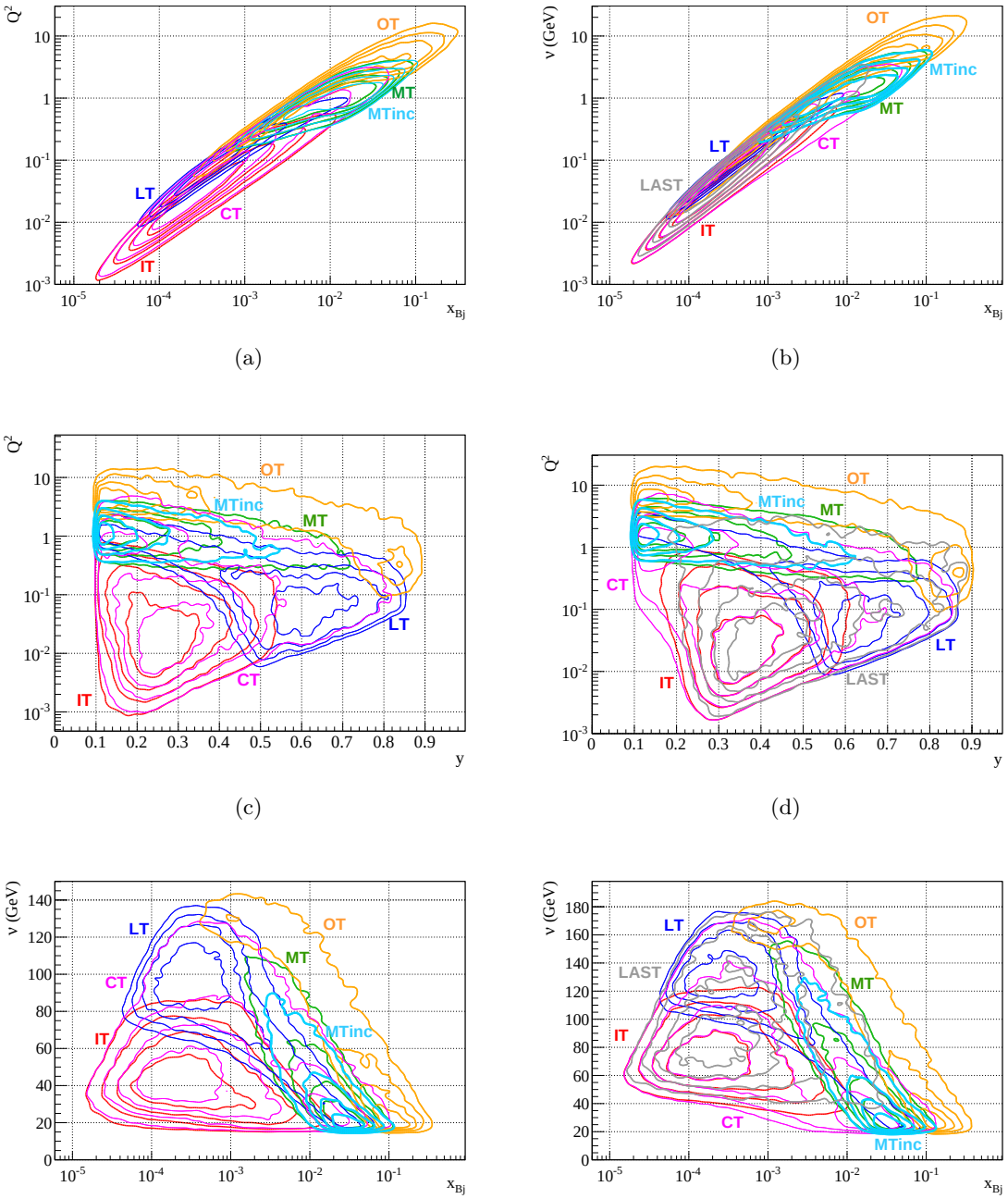

Figure 6.12: Kinematic coverage of the different triggers of COMPASS, in 2007 (a,c,e) and 2011 (b,d,f).

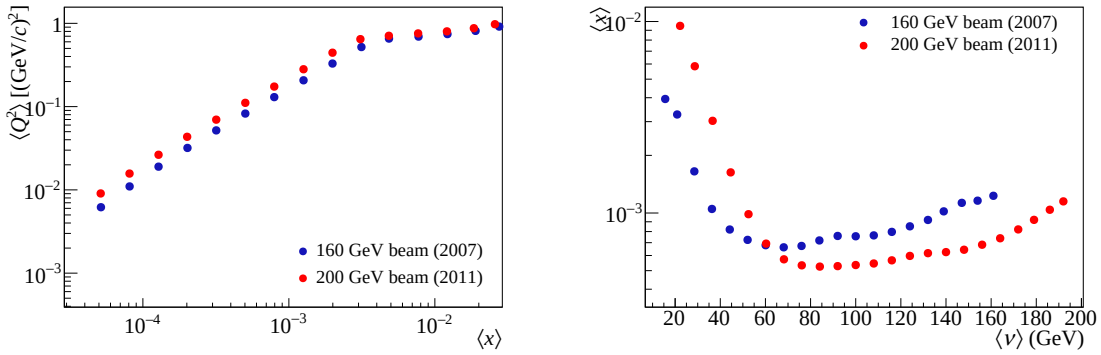

(a) (b)

Figure 6.13: Mean Q^2 and x for the analysis in x bins and mean x and ν for the analysis in bins of ν.

correction to subtract to the measured asymmetry given by

$$\Delta A_1^p(^{14}\mathrm{N}) = \left(\frac{1}{3}\right) \cdot \left(-\frac{1}{3}\right) \cdot \left(\frac{1}{6}\right) \frac{\sigma_d}{\sigma_p} A_1^d = -\frac{1}{54} \frac{\sigma_d}{\sigma_p} A_1^d \tag{6.2}$$

The approximation $\sigma_d/\sigma_p \sim F_2^d/F_2^p$ is used, with F_2^d and F_2^p being taken from [100]. The values of F_2^p and F_2^d were obtained using the SMC/Tulay fits, within their range of validity, and otherwise using the model of [101] with an asymptotic function given by GRV94 NLO $\overline{\mathrm{MS}}$ with charm. Note that for $Q^2 < 0.2$ /GeV/$c)^2$ no unpolarised experimental data were ever published. The values of A_1^d can be estimated using the parametrisation from COMPASS of the world data [102],

$$A_1^d(x) = (x^\alpha - \gamma^\alpha)(1 - e^{-\beta x}) \tag{6.3}$$

with $\alpha = 1.158 \pm 0.024$, $\beta = 125.1 \pm 115.7$, and $\gamma = 0.018 \pm 0.0038$. The values of the corrections are presented in Tables F.1, F.2, F.3 and F.4 .

6.6.2 Polarised Radiative Corrections to the Asymmetries

To calculate the asymmetries that are associated to radiative events, the program POLRAD 1.4 [103] was used, in a version adapted for the COMPASS conditions. The corrections are presented in Tables F.1, F.2, F.3 and F.4.

6.7 Systematic Studies

6.7.1 Internal Consistency Between 2007 and 2011 Results

The results of the experimental asymmetries from the 2007 and 2011 data takings were confronted, and found to be compatible within uncertainties (see Figures 6.14 to 6.15).

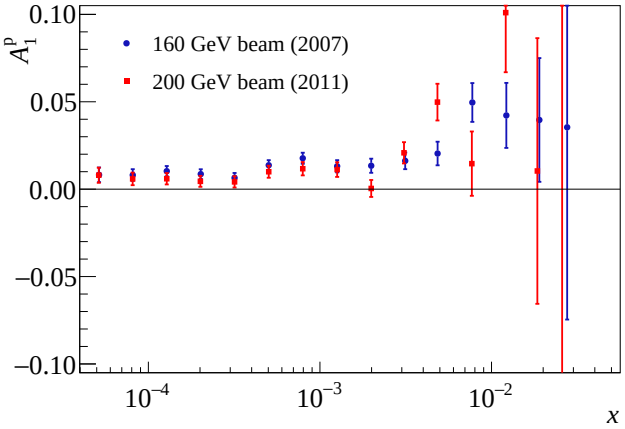

Figure 6.14: Experimental $A_1^p(x)$ obtained from 2007 and 2011 data, before corrections resulting from the polarised radiative asymmetry and the presence of ^{14}N in the ammonia target. An homogeneity χ^2-test using $\chi^2 = \sum[(A_{2007} - A_{2011})^2/(\sigma^2_{2007} + \sigma^2_{2011})]$ yields $Prob(\chi^2 = 20.2749, \mathrm{NDF} = 15) = 0.16$.

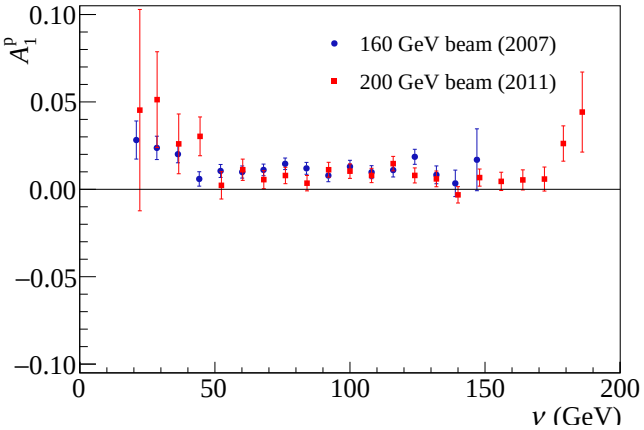

Figure 6.15: Experimental $A_1^p(\nu)$ obtained from 2007 and 2011 data, before corrections resulting from the polarised radiative asymmetry and the presence of ^{14}N in the ammonia target. A χ^2-test using $\chi^2 = \sum[(A_{2007} - A_{2011})^2/(\sigma^2_{2007} + \sigma^2_{2011})]$ yields $Prob(\chi^2 = 26.5437, \mathrm{NDF} = 20) = 0.15$.

6.7.2 Systematic Studies on Asymmetries

The measured asymmetries are small, of the order of half a percent. It is therefore very important to ensure that they are not produced by the apparatus (in which case oreproduciblene would be measuring "false asymmetries"). This was done in two ways. In the first way, the global sample is divided into subsamples, to verify if the (true, physical) asymmetries obtained from such subsamples are stable with respect to the investigated factor. In the second way, asymmetries which are expected to be zero are calculated and their compatibility with zero is verified.

For the purpose of detection of possible sources of false (*i.e.* non-physical, apparatus-related) reproducible asymmetries, physical asymmetries were calculated for the following pairs

of data subsamples:

- different methods of asymmetry extraction (see note [104] for a description of the methods);
- global vs consecutive configurations;
- day vs night;
- different microwave settings;
- top vs bottom scattered muon;
- left vs right scattered muon;
- upstream vs downstream primary vertex;
- inner vs outer primary vertex.

On the other hand, also for detection of possible sources of reproducible false asymmetries, (or "fake asymmetries") – expected to be zero – were calculated for the following subsamples and configurations:

- false consecutive ("fake") configurations;
- false asymmetries C-C & U-D;
- false asymmetries C-C & U-D for different microwave settings.

The results of the systematic tests on possible sources of false asymmetries which were done for the 2007 and 2011 data, and for $A_1(x)$ and for $A_1^p(\nu)$ are presented in the Appendix C, namely in Figs. C.1 to C.15. The tests done and the reasoning behind them is given hereafter.

Different methods of asymmetry extraction Either first order, first order improved (taking into account the differences in acceptance of the different target cells) or second order; standard or weighted by $w = fD|P_b|$. The asymmetries were extracted with these six methods. The results of the tests are shown Figs. C.1, C.17, C.33 and C.49.

Global vs. consecutive configurations Whereas in the standard grouping (consecutive configurations) one uses in each group data taken in a limited period of time with the two possible target spin configurations to calculate asymmetries per configuration that are later combined, in the global configuration all the data are used in one single configuration. The results of the tests are shown in Figs. C.2, C.18, C.34 and C.50, the results using the global and the consecutive configuration are shown.

Fake configurations The groups are in this case obtained from data collected within limited intervals of time, but all taken with the same target spin configuration. The asymmetries are calculated between two halves of each group, and the results of these groups are combined to get a result for the full year. Such grouping should lead to a zero asymmetry. The results of the tests are shown in Figs. C.3, C.19, C.35 and C.51.

C-C/U-D The upstream and downstream target cells always have the same spin projection, and the same is true for the two halves of the central cell. Therefore, measuring asymmetries using events with primary vertices in the upstream and the downstream cells should result in a null asymmetry; the same is true for the two halves of the central cell. The results of the tests are shown in Figs. C.4, C.20, C.36 and C.52.

Day/night The COMPASS hall is at ground level, which makes the spectrometer very sensitive to temperature and humidity effects. This might affect the asymmetry extraction. The simplest test one can do is to evaluate separately the asymmetries obtained from data taken in the two halves of the day with highest and lowest temperatures, which were found to be the time intervals 00:00-12:00 and 12:00-24:00. The results of the tests are show in Figs C.5, C.21, C.38 and C.53.

Microwave settings The direction of the target solenoid magnetic field can be changed to rotate the spin alignment of the target cells, and this is done regularly to ensure constant acceptance conditions within each group of data. Nevertheless the field direction of the solenoid is always aligned in the same way with the spin direction of the target cells. To circumvent this possible source of false asymmetries, within each year of data taking, at least once the polarisation is rebuilt from zero in the opposite setting of these fields, which is done by changing the microwave frequencies applied to the different cells during the polarisation process. The results of the tests are show in Figs C.7, C.23, C.39 and C.55.

Top/bottom μ' One checks if the events with the scattered muon directed to the upper part of the spectrometer lead to the same asymmetries as the events where the scattered muon is directed to the lower part of the spectrometer. The results of the tests are show in Figs C.9, C.25, C.41 and C.57.

Left/right μ' One checks if the events with the scattered muon directed to the left (Salève) of the spectrometer lead to the same asymmetries as the events with the scattered muon is directed to the right (Jura) of the spectrometer, with the angle taken in the primary vertex. The results of the tests are show in Figs C.11, C.27, C.43 and C.59.

Inner/outer PV One checks if the events with the primary vertex in the innermost part of the target cells yield the same asymmetries as those with the primary vertex in the outermost part of the target cells. The results of the tests are show in Figs C.13, C.29, C.45 and C.61.

Upstream/downstream PV One checks if the asymmetries obtained with events with the primary vertex in the upstream cell and the upstream half of the central cell are compatible with those obtained with events in the downstream half of the central cell and the downstream cell. The results of the tests are show in Figs C.15, C.31, C.47 and C.63.

While the vast majority of the tests done showed no possible sources of false asymmetries, two possible effects that might lead to false asymmetries were found. They are shown in

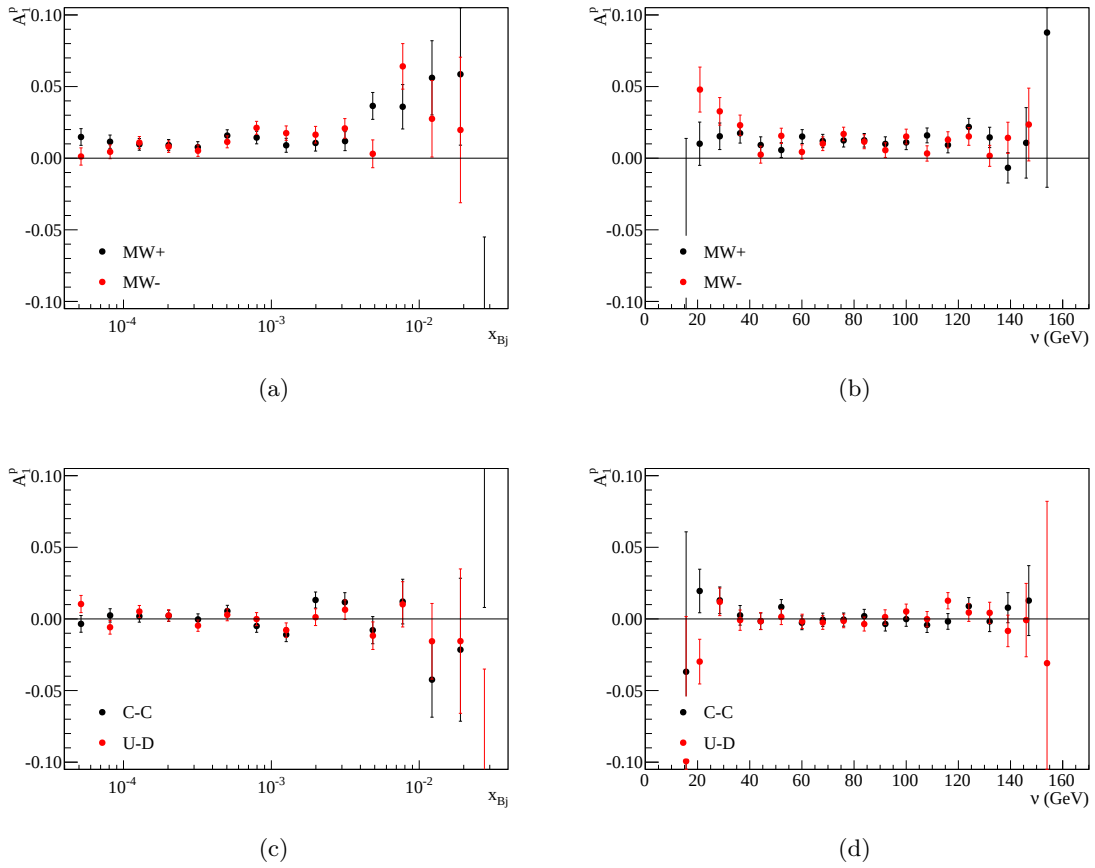

Figure 6.16: Selected tests for search of possible sources of reproducible false asymmetries on 2007 data, for $A_1^p(x)$ (left) and $A_1^p(\nu)$ (right). Top: Asymmetries were calculated with two subsamples collected with different microwave settings to check if the results are compatible within uncertainties. Bottom: (false) asymmeties were calculated either with the two halves (upstream and downstream as if they had opposite polarisation) of the central cell or with the upstream and the downstream cells, as if they had opposite polarisation, to check if the results are compatible with zero.

Figs. 6.16 and 6.17. However, the experimental procedures are expected to be enough to reduce their impact to a minimum.

The first effect was a possible reproducible false (*i.e.* non-physical) asymmetry at very low x, visible when calculating the (true) asymmetries with the two different microwave settings. This problem is overcome by the selection criteria that rejects data with very low x, and with the use of two microwave settings with similar number of events each.

The second effect was seen when calculating the false asymmetries with the upstream and downstream cells and with the two halves of the central cell. This was only visible in the 2011 data, and thus it is probably related to the fact that in 2011 a target solenoid field of 2.5 T was used, instead of the usual 1.0 T (used in 2007). This suspicion was supported by the fact that the effect reverses sign when doing the test for the two microwave settings. To quantify the amplitude of this effect, a test was done, by artificially injecting false asymmetries in the 2007 data, thus mimicking a change in acceptance in the different cells for different solenoid currents.

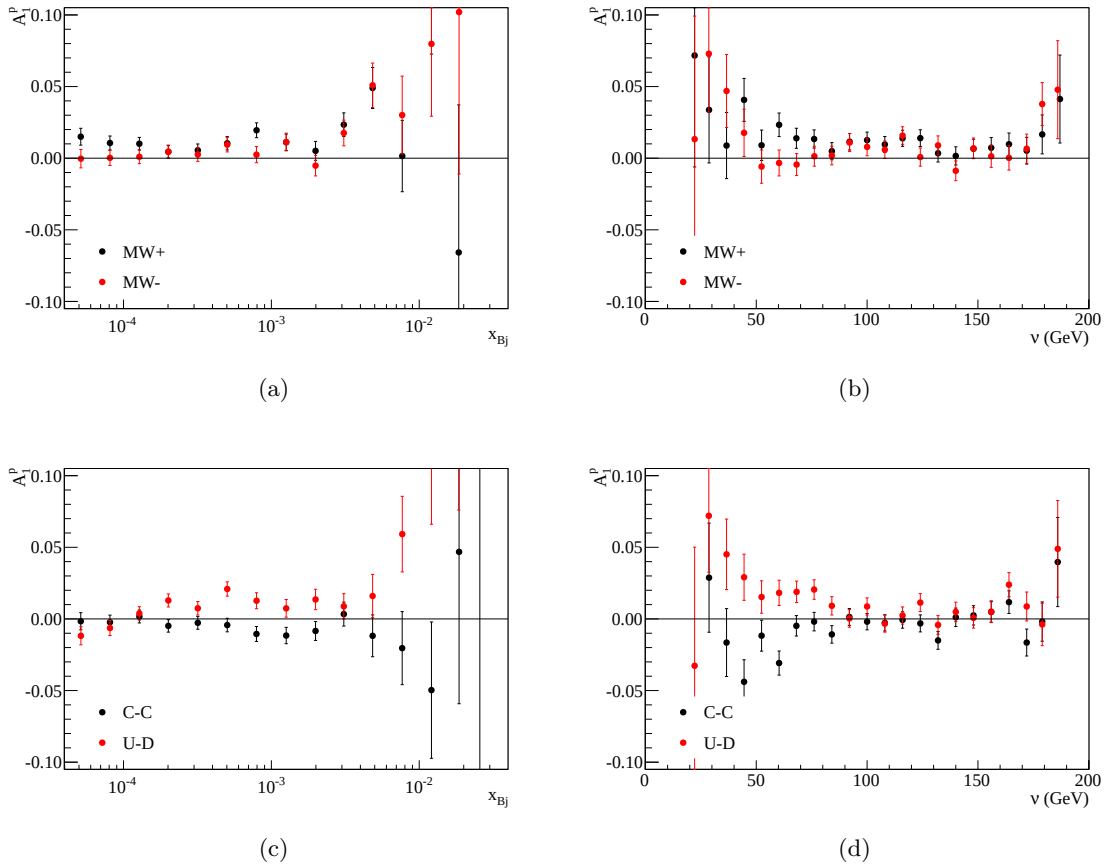

Figure 6.17: Selected tests for search of possible sources of false asymmetries on 2011 data, for $A_1^p(x)$ (left) and $A_1^p(\nu)$ (right). Top: Asymmetries were calculated with two subsamples collected with different microwave settings to check if the results are compatible within uncertainties. Bottom: (false) asymmeties were calculated either with the two halves (upstream and downstream as if they had opposite polarisation) of the central cell or with the upstream and the downstream cells, as if they had opposite polarisation, to check if the results are compatible with zero.

This can be done by changing the weights attributed to events in the second order weighted method. The weights were adjusted until the false asymmetries observed in 2011 data were reproduced. With these new weights, the true asymmetries were extracted. The difference to the standard extraction can be used as an estimation of the false asymmetry. It was found that these residual false asymmetries amount to, at most, 20% of the statistical uncertainties, and were thus ignored from the subsequent analysis.

In Table 6.6, the results of two tests are shown, namely on the compatibility of the asymmetry results obtained from the two years of data and with subsamples of data corresponding to the two microwave settings. A reasonable compatibility of the results is found.

	2007				2011			
	x		ν		x		ν	
NDF	15		20		20		23	
	χ^2	p	χ^2	p	χ^2	p	χ^2	p
microwave settings	22.4564	0.096	14.9047	0.729	$24.0935^{\mathrm{NDF}=19}$	0.064	21.082	0.576
	2007 vs. 2011							
	x				ν			
NDF	15				19			
	χ^2		p		χ^2		p	
	20.2013		0.164		20.7753		0.349	

Table 6.6: Summary of values of χ^2 and their probability for the concerned degrees of freedom (χ^2 homogeneity test), for selected studies: the compatibility of the results obtained with the two different microwave settings, and of the compatibility of the 2007 and the 2011 results. In both cases, there is a reasonable compatibility of the results. Values below 0.05 are conventionally considered suspicious, even if there is a 5% probability of them showing up even in the case of compatible distributions.

6.8 Total Systematic Uncertainty

The statistical uncertainties of the asymmetries result from uncertainty propagation of the uncertainties of the quantities used in the extractions. The systematic uncertainties, on the other hand, rely on assumptions based on different studies performed with the objective of identifying possible sources of asymmetries, for instance by setting upper limits to such possible false asymmetries.

The systematic uncertainty has multiplicative contributions, *i.e.* possible biases that are proportional to the asymmetries themselves, and additive contributions, which don't depend on the amplitude of the asymmetries. The additive contributions can be expressed in terms of their relative values with respect to the statistical uncertainties.

The systematic uncertainty can be decomposed in a multiplicative term and in an additive term, as

$$\Delta A_1^{mult} = A_1 \sqrt{\left(\frac{\delta P_b}{P_b}\right)^2 + \left(\frac{\delta P_t}{P_t}\right)^2 + \left(\frac{\delta D(R)}{D(R)}\right)^2 + \left(\frac{\delta f}{f}\right)^2} \tag{6.4}$$

and

$$\Delta A_1^{add} = \sqrt{\left(\frac{\eta}{\rho}\Delta A_2\right)^2 + (\Delta A_1^{RC})^2 + (\Delta A_{false})^2}, \tag{6.5}$$

where ΔA_2 is the bias associated to neglecting A_2, ΔA_1^{RC} is the uncertainty associated to radiative corrections, and ΔA_{false} is the uncertainty due to (random) false asymmetries. The two components of the systematic uncertainty of the asymmetries (multiplicative and additive) are added in quadrature,

$$\Delta A_1^{syst} = \sqrt{(\Delta A_1^{mult})^2 + (\Delta A_1^{add})^2}. \tag{6.6}$$

A summary with the different contributions is given in Tables 6.7 and 6.8.

Note that, in contrast to the DIS case, the depolarisation factor gives a very big contribution to the systematic uncertainty in this analysis, up to 39% of the asymmetries.

The value taken as an upper limit to A_2^p was the measurement at the lowest x included in HEPDATA [105, 106].

No significant sources of (reproducible) false asymmetries were identified in extensive studies performed for that purpose. Hence, upper limits for the (random) false asymmetries are estimated from the pulls of asymmetries obtained from different configurations. The idea is that an excess in the width of the pulls distributions is possibly caused by instabilities of the spectrometer. In 2007, there were 23 configurations and in 2011 there were 39 configurations. For each configuration, the following quantity was estimated:

$$\Delta r = \frac{A_{1,i} - \bar{A}_1}{\sqrt{\sigma^2_{A_{1,i}} - \sigma^2_{\bar{A}_1}}}. \tag{6.7}$$

This upper limit to the systematic uncertainty contribution is estimated to be:

$$\sigma^{syst}_{\Delta r} = \sqrt{(max\{1, \sigma_{\Delta r}\} + \delta_{\sigma_{\Delta r}})^2 - 1}. \tag{6.8}$$

Here $\sigma_{\Delta r}$ is the width of the pulls distribution and $\delta_{\sigma_{\Delta r}}$ is the uncertainty of that width. The full set of pulls for (random) false asymmetries calculations are presented in Appendix D. The deviation from zero of the centroid of the pulls distribution could be used as input to an estimation of the systematic uncertainty. However, the distributions are centered at zero within uncertainties and for that reason the information about the centroid value was not used.

The statistical uncertainty of g_1^p results only from the propagation of the statistical uncertainty of A_1^p, while the remaining uncertainties, on $D(1+R)$ and on F_2^p are included in the systematic uncertainty. For the extraction of g_1^p as a function of x or of ν, the relative uncertainty of F_2^p, $\Delta F_2^p/F_2^p$ takes values between 19% and 34%, whereas the relative uncertainty of the quantity $\Delta(D(1+R))/(D(1+R))$ ranges from 5.3% to 10%.

Taking into account that g_1^p can be written as $g_1^p = F_2^p A_{LL}/[2x \cdot D(1+R)]$, the systematic uncertainty of g_1^p is obtained from three components: (1) the systematic uncertainty of $A_{LL} \equiv A_1^p \times D$, (2) the systematic uncertainty of F_2^p, and (3) the systematic uncertainty of the product $D(1+R)$. The systematic uncertainty of A_{LL} was already discussed. The systematic uncertainty of F_2^p comes from the fact that the values of F_2^p available come either from the parametrisation from SMC (the so called "Tulay fit") [89] or from models [86, 87, 90]. In this analysis, the parametrisation from SMC is used in its range of validity (namely $Q^2 > 0.2$ (GeV/c)^2) and the model of [86, 88] is used in the remaining phase space region. The systematic uncertainty of F_2^p is taken as half of the maximum of the absolute differences between the used parametrisation or model and the remaining parametrisation or models. For $Q^2 > 0.2$) (GeV/c)^2, this is always the absolute value of the difference between the SMC parametrisation and the model of [86, 87]. As for the systematic uncertainty of R, it is taken as a constant value of 0.2 for $Q^2 < 0.5$ (GeV/c)^2.

Uusing $A_{LL} = A_1^p \cdot D$, we can write

$$g_1^p = \frac{F_2^p A_{LL}}{2x \cdot D \cdot (1+R)}, \tag{6.9}$$

the systematic uncertainty of g_1^p, $\sigma^2_{syst}(g_1^p)$, can be obtained from the systematic uncertainties of the three contributing systematic uncertainties, $\sigma^2_{syst}(A_{LL})$, $\sigma^2_{syst}(F_2^p)$, and $\sigma^2_{syst}(D\cdot(1+R))$:

$$\frac{\sigma^2_{syst}(g_1^p)}{(g_1^p)^2} = \frac{\sigma^2_{syst}(A_{LL})}{(A_{LL})^2} + \frac{\sigma^2_{syst}(F_2^p)}{(F_2^p)^2} + \frac{\sigma^2_{syst}(D\cdot(1+R))}{[D\cdot(1+R)]^2}. \tag{6.10}$$

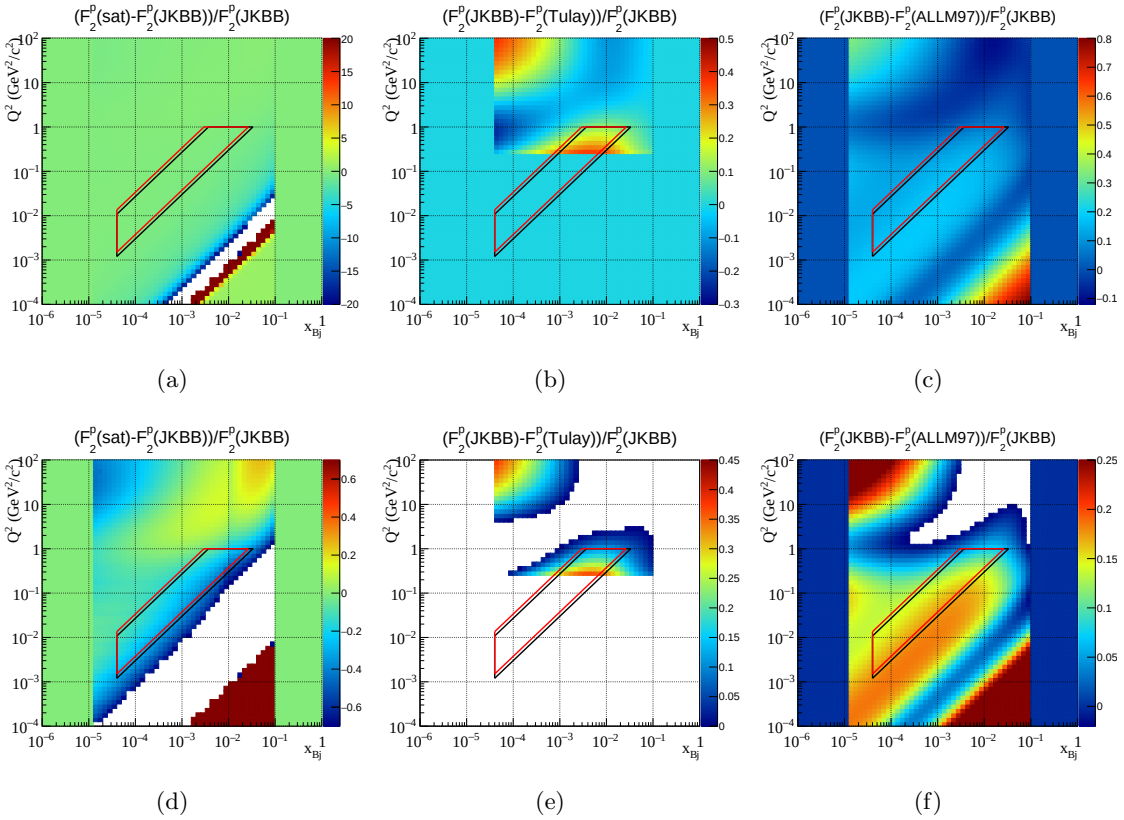

Figure 6.18: Differences between $F_2^p(JKBB)$ and other parametrisations or fits. On the top plots, the z scale was chosen to cover most of the phase-space. In the bottom plots, the z scale was chosen in order to see details in the region of interest for this analysis. The regions of interest for this analysis are marked by polygons (black for 2007 and red for 2011 data). N.B.: monocromatic bands don't have a physical meaning.

The systematic uncertainty of F_2^p was taken as half of the maximum absolute difference between $F_2^p(JKBB)$ and the other three parametrisations (see Fig. 6.18). Note that for $Q^2 > 0.2$ (GeV/c)^2, the maximum absolute difference between any two parametrisations is the difference between $F_2^p(JKBB)$ and $F_2^p(Tulay)$.

In Fig. 6.19, 6.20 and 6.21 we can see the relative uncertainties of D, R and $D(R)\cdot(1+R)$,

respectively as functions of x, ν and Q^2, where

$$\delta^+[D\cdot(1+R)] \equiv |D(R+\delta R)\cdot(1+R+\delta R) - D\cdot(1+R)| \tag{6.11}$$

and

$$\delta^-[D\cdot(1+R)] \equiv |D(\max\{0,R-\delta R\})\cdot(1+\max\{0,R-\delta R\}) - D\cdot(1+R)|. \tag{6.12}$$

We can see that dependence of D upon R allows to significantly reduce the uncertainties. Only for the largest values of ν the uncertainties are increased, as can be seen in Fig. 6.20. In Fig. 6.21, the decrease of δ^+ and δ^- close to $Q^2 \sim 0.02$ is a consequence of how they were defined: the quantities inside the modulus signs changes sign in this region.

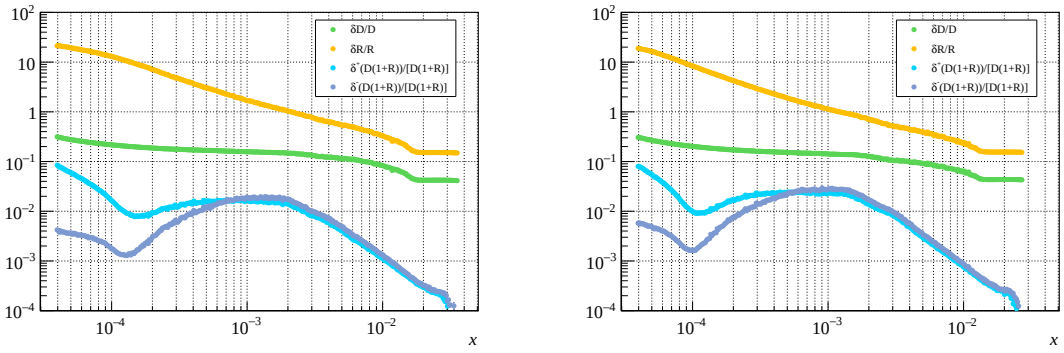

(a) (b)

Figure 6.19: Relative uncertainties as functions of x of D, R and $D\cdot(1+R)$ for the 2007 case (left) and for the 2011 case (right).

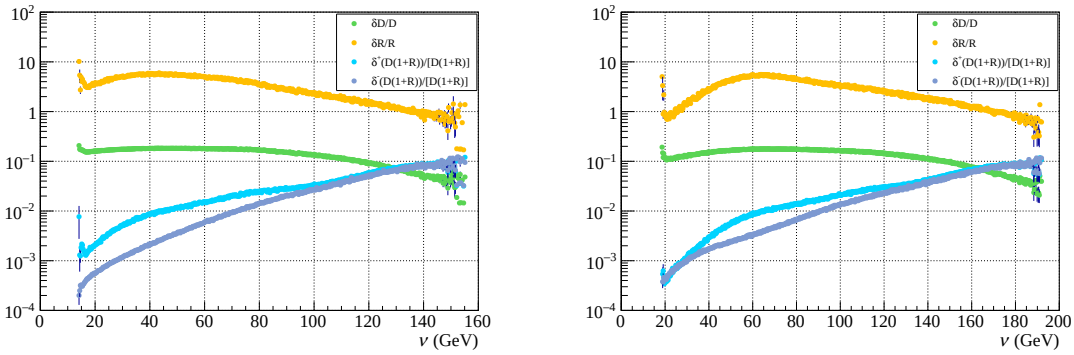

(a) (b)

Figure 6.20: Relative uncertainties as functions of ν of D, R and $D\cdot(1+R)$ for the 2007 case (left) and for the 2011 case (right).

The systematic uncertainty of $D\cdot(1+R)$ was taken to be the average of δ^+ and δ^-.

In Figs. 6.22 to 6.24, the contributions of the different partial systematic uncertainties to the total systematic uncertainty of the asymmetries is shown. The systematic uncertainties

			2007	2011
Multiplicative variables uncertainty	Beam polarisation	$\delta P_B/P_B$	5%	5%
	Target polarisation	$\delta P_T/P_T$	2%	3.5%
	Depolarisation factor	$\delta D(R)/D(R)$	4-32%	4-29%
	Dilution factor	$\delta f/f$	5%	5%
Additive variables uncertainty	Transverse asymmetry	$\eta/\rho \cdot \delta A_2$	$< 0.022 \cdot \delta A_1^{stat}$	$< 0.026 \cdot \delta A_1^{stat}$
	Radiative corrections	δA_1^{RC}	$< 0.025 \cdot \delta A_1^{stat}$	$< 0.020 \cdot \delta A_1^{stat}$
	False asymmetry	A_{false}	$< 1.2 \cdot \delta A_1^{stat}$	$< 1.2 \cdot \delta A_1^{stat}$
		$\delta F_2^p/F_2^p$	30%	19%
		$\delta[D(1+R)]/[D(1+R)]$	5.8%	5.3%

Table 6.7: Decomposition of the systematic uncertainty of $A_1^p(x)$ into multiplicative and additive variables contributions, for the extraction of $A_1^p(x)$, and further contributions to the systematic uncertainty of $g_1^p(x)$ in the last two lines.

			2007	2011
Multiplicative variables uncertainty	Beam polarisation	$\delta P_B/P_B$	5%	5%
	Target polarisation	$\delta P_T/P_T$	2%	3.5%
	Depolarisation factor	$\delta D(R)/D(R)$	10-92%	9-92%
	Dilution factor	$\delta f/f$	5%	5%
Additive variables uncertainty	Transverse asymmetry	$\eta/\rho \cdot \delta A_2$	$< 0.014 \cdot \delta A_1^{stat}$	$< 0.012 \cdot \delta A_1^{stat}$
	Radiative corrections	δA_1^{RC}	$< 0.25 \cdot \delta A_1^{stat}$	$< 0.01 \cdot \delta A_1^{stat}$
	False asymmetry	A_{false}	$< 1.2 \cdot \delta A_1^{stat}$	$< 3.3 \cdot \delta A_1^{stat}$
		$\delta F_2^p/F_2^p$	24%	34%
		$\delta[D(1+R)]/[D(1+R)]$	10%	8.7%

Table 6.8: Decomposition of the systematic uncertainty of $A_1^p(\nu)$ into multiplicative and additive variables contributions, for the extraction of $A_1^p(\nu)$, and further contributions to the systematic uncertainty of $g_1^p(\nu)$ in the last two lines.

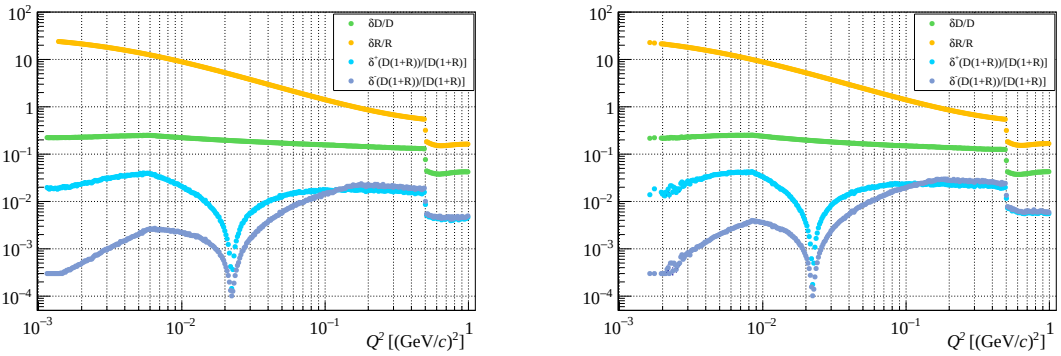

(a) (b)

Figure 6.21: Relative uncertainties as functions of Q^2 of D, R and $D \cdot (1 + R)$ for the 2007 case (left) and for the 2011 case (right).

rise for higher x. The systematic uncertainty is dominated by the uncertainty associated to false asymmetries, followed by the uncertainty coming from uncertainty on D. Moreover, the systematic uncertaities are of the same order of magnitude as the statistical uncertainties. In the analysis as function of ν, we can see that the lower and the higher values of ν have larger systematic uncertainties. In this case, the uncertainties resulting from false asymmetries and to the depolarisation factor are dominant.

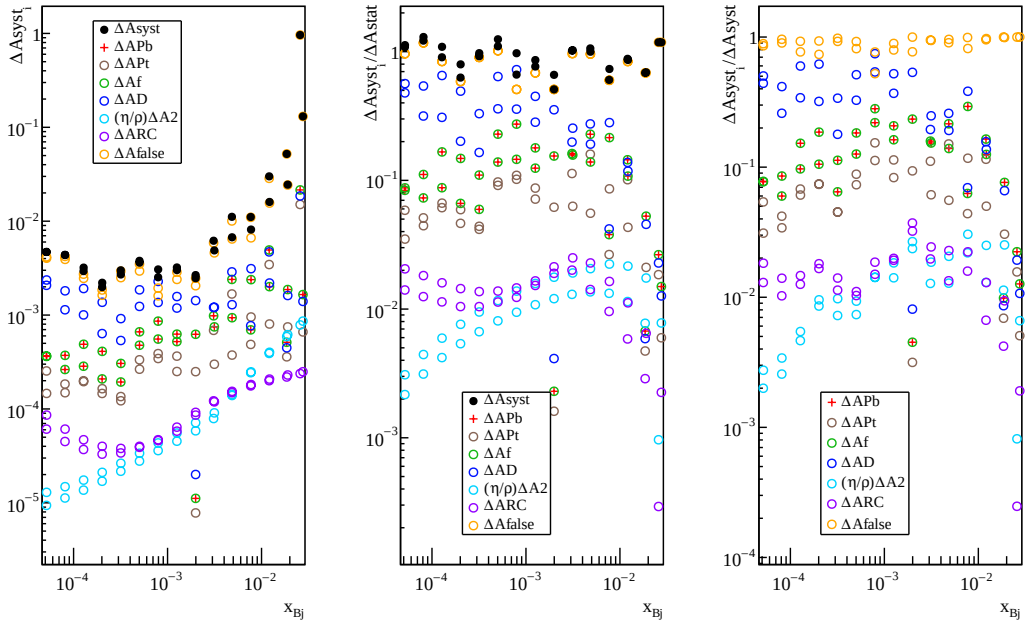

Figure 6.22: The contributions for the total systematic uncertainty of $A_1^p(x)$: (left) their absolute values; (middle) their values normalised to the total statistical uncertainty; (right) their values normalised to the total systematic uncertainty.

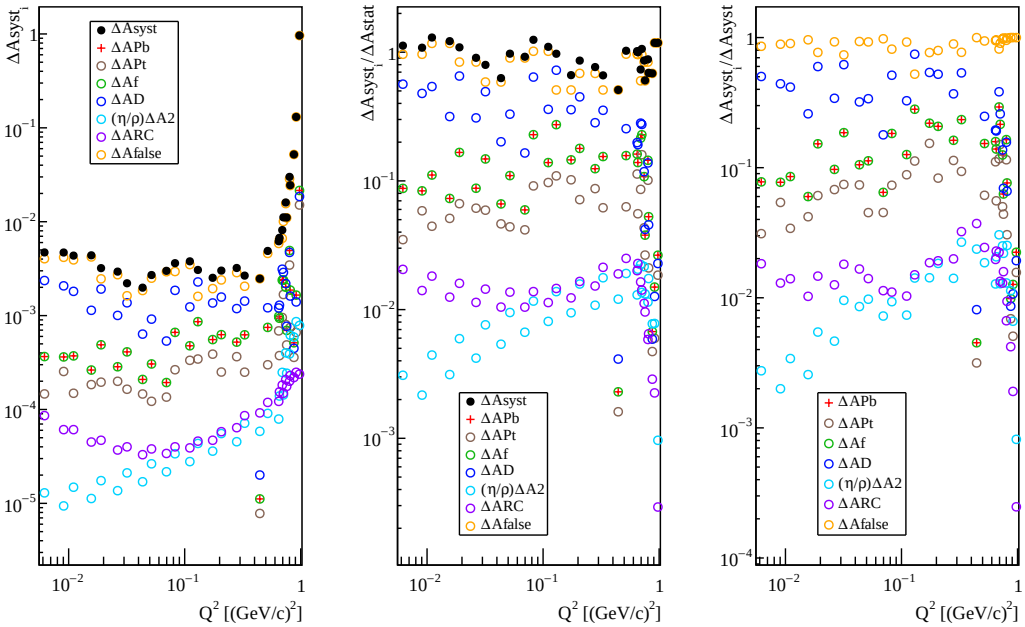

Figure 6.23: The contributions for the total systematic uncertainty of $A_1^p(x)$, but displayed as a function of Q^2: (left) their absolute values; (middle) their values normalised to the total statistical uncertainty; (right) their values normalised to the total systematic uncertainty.

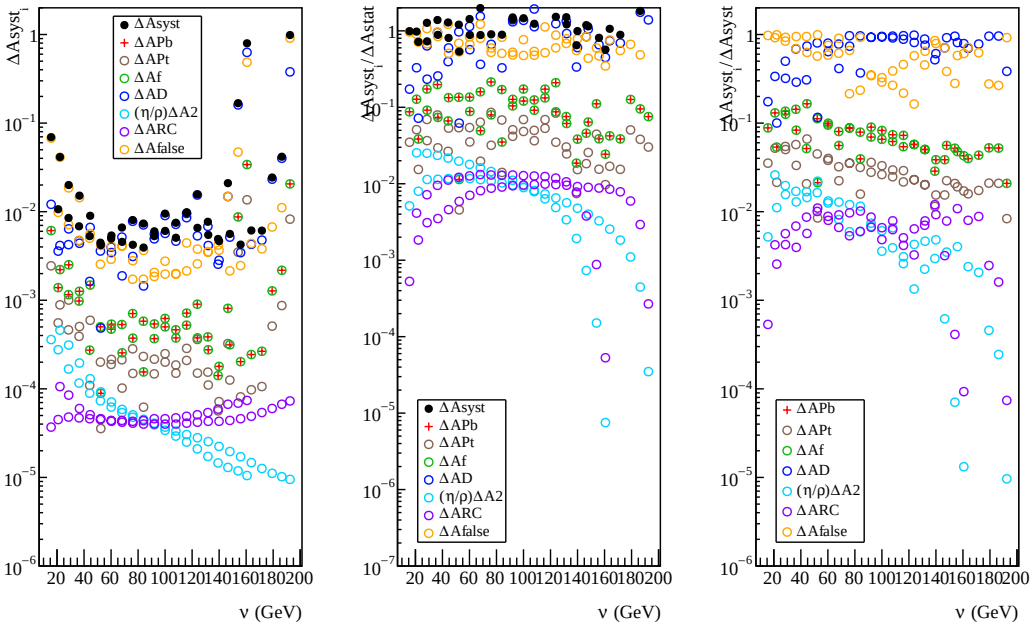

Figure 6.24: The contributions for the total systematic uncertainty of $A_1^p(\nu)$: (left) their absolute values; (middle) their values normalised to the total statistical uncertainty; (right) their values normalised to the total systematic uncertainty.

6.8.1 Results

The results for $A_1^p(x)$, $A_1^p(\nu)$, $g_1^p(x)$ and $g_1^p(\nu)$ are presented in Tables 6.9 and 6.10. In Appendix F, the auxiliary quantities used for the extraction are also presented. The results are also shown in Figures 6.25, 6.26, 6.27 and 6.28. Note that the averages of kinematic variables are weighted averages, using as weights the same weights used to weight events in the extraction of asymmetries:

$$\langle x \rangle = \frac{\sum x_i \omega_i^2}{\sum \omega_i^2}. \tag{6.13}$$

x range	$\langle x \rangle$	$\langle Q^2 \rangle$ (GeV$^2/c^2$)	$\langle y \rangle$	A_1^p	g_1^p
$E_{beam} = 160$ GeV (2007 sample)					
0.00004–0.000063	0.000052	0.0062	0.40	$0.0073 \pm 0.0042 \pm 0.0047$	$0.51 \pm 0.29 \pm 0.29$
0.000063–0.0001	0.000081	0.011	0.45	$0.0074 \pm 0.0034 \pm 0.0044$	$0.58 \pm 0.26 \pm 0.31$
0.0001–0.00016	0.00013	0.019	0.49	$0.0098 \pm 0.0029 \pm 0.0032$	$0.81 \pm 0.24 \pm 0.22$
0.00016–0.00025	0.00020	0.032	0.53	$0.0082 \pm 0.0028 \pm 0.0022$	$0.69 \pm 0.23 \pm 0.15$
0.00025–0.0004	0.00032	0.052	0.54	$0.0061 \pm 0.0028 \pm 0.0027$	$0.49 \pm 0.22 \pm 0.21$
0.0004–0.00063	0.00050	0.082	0.55	$0.013 \pm 0.0029 \pm 0.0036$	$0.96 \pm 0.21 \pm 0.24$
0.00063–0.001	0.00079	0.13	0.55	$0.017 \pm 0.0032 \pm 0.0031$	$1.1 \pm 0.20 \pm 0.16$
0.001–0.0016	0.0013	0.21	0.55	$0.012 \pm 0.0035 \pm 0.0030$	$0.40 \pm 0.11 \pm 0.15$
0.0016–0.0025	0.0020	0.33	0.55	$0.012 \pm 0.0040 \pm 0.0027$	$0.36 \pm 0.12 \pm 0.095$
0.0025–0.004	0.0031	0.52	0.55	$0.015 \pm 0.0048 \pm 0.0049$	$0.36 \pm 0.11 \pm 0.12$
0.004–0.0063	0.0048	0.66	0.46	$0.019 \pm 0.0067 \pm 0.0067$	$0.32 \pm 0.12 \pm 0.12$
0.0063–0.01	0.0077	0.69	0.30	$0.048 \pm 0.011 \pm 0.0081$	$0.52 \pm 0.12 \pm 0.096$
0.01–0.016	0.012	0.74	0.21	$0.040 \pm 0.019 \pm 0.016$	$0.29 \pm 0.14 \pm 0.12$
0.016–0.025	0.019	0.81	0.14	$0.037 \pm 0.035 \pm 0.024$	$0.18 \pm 0.18 \pm 0.12$
0.025–0.04	0.028	0.91	0.11	$0.033 \pm 0.11 \pm 0.13$	$0.12 \pm 0.40 \pm 0.48$
$E_{beam} = 200$ GeV (2011 sample)					
0.00004–0.000063	0.000051	0.0091	0.46	$0.0073 \pm 0.0043 \pm 0.0044$	$0.74 \pm 0.44 \pm 0.40$
0.000063–0.0001	0.000081	0.016	0.51	$0.0053 \pm 0.0036 \pm 0.0023$	$0.58 \pm 0.39 \pm 0.22$
0.0001–0.00016	0.00013	0.026	0.54	$0.0057 \pm 0.0032 \pm 0.0021$	$0.64 \pm 0.37 \pm 0.22$
0.00016–0.00025	0.00020	0.043	0.57	$0.0042 \pm 0.0032 \pm 0.0019$	$0.46 \pm 0.35 \pm 0.21$
0.00025–0.0004	0.00032	0.070	0.58	$0.0039 \pm 0.0033 \pm 0.0025$	$0.39 \pm 0.33 \pm 0.25$
0.0004–0.00063	0.00050	0.11	0.58	$0.0095 \pm 0.0034 \pm 0.0024$	$0.86 \pm 0.31 \pm 0.20$
0.00063–0.001	0.00079	0.17	0.58	$0.011 \pm 0.0038 \pm 0.0028$	$0.83 \pm 0.29 \pm 0.20$
0.001–0.0016	0.0013	0.28	0.59	$0.010 \pm 0.0042 \pm 0.0027$	$0.45 \pm 0.18 \pm 0.14$
0.0016–0.0025	0.0020	0.44	0.59	$-0.022 \pm 0.0049 \pm 0.0037$	$-0.0080 \pm 0.17 \pm 0.13$
0.0025–0.004	0.0031	0.65	0.56	$0.020 \pm 0.0061 \pm 0.0038$	$0.54 \pm 0.17 \pm 0.11$
0.004–0.0063	0.0048	0.71	0.39	$0.048 \pm 0.010 \pm 0.0086$	$0.85 \pm 0.19 \pm 0.16$
0.0063–0.01	0.0077	0.76	0.26	$0.014 \pm 0.018 \pm 0.010$	$0.16 \pm 0.21 \pm 0.12$
0.01–0.016	0.012	0.80	0.18	$0.099 \pm 0.034 \pm 0.025$	$0.75 \pm 0.26 \pm 0.19$
0.016–0.025	0.018	0.87	0.13	$0.010 \pm 0.076 \pm 0.046$	$0.053 \pm 0.40 \pm 0.24$
0.025–0.04	0.026	0.98	0.10	$-0.43 \pm 0.81 \pm 0.61$	$-1.7 \pm 3.2 \pm 2.4$

Table 6.9: Values of A_1^p and g_1^p with their statistical and systematic uncertainties as functions of x with the corresponding average values of x, Q^2 and y, for the 2007 and 2011 samples. The maximum Q^2 cut is 1 (GeV/c)^2. Bins in x are of equal width in $\log_{10} x$.

ν range (GeV)	$\langle\nu\rangle$ (GeV)	$\langle Q^2\rangle$ (GeV$^2/c^2$)	$\langle y\rangle$	A_1^p	g_1^p
$E_{beam} = 160$ GeV (2007 sample)					
8–16	15.6	0.12	0.103	$-0.12 \pm 0.070 \pm 0.069$	$-1.4 \pm 0.82 \pm 0.84$
16–24	20.9	0.14	0.133	$0.028 \pm 0.011 \pm 0.011$	$0.41 \pm 0.16 \pm 0.16$
24–32	28.5	0.098	0.181	$0.023 \pm 0.0067 \pm 0.0085$	$0.52 \pm 0.15 \pm 0.18$
32–40	36.3	0.082	0.229	$0.020 \pm 0.0049 \pm 0.0068$	$0.59 \pm 0.15 \pm 0.17$
40–48	44.2	0.078	0.278	$0.0055 \pm 0.0041 \pm 0.0053$	$0.20 \pm 0.15 \pm 0.19$
48–56	52.1	0.079	0.327	$0.010 \pm 0.0037 \pm 0.0045$	$0.44 \pm 0.16 \pm 0.13$
56–64	60.1	0.083	0.377	$0.0094 \pm 0.0035 \pm 0.0050$	$0.47 \pm 0.17 \pm 0.16$
64–72	68.0	0.089	0.427	$0.011 \pm 0.0033 \pm 0.0066$	$0.59 \pm 0.18 \pm 0.24$
72–80	76.0	0.099	0.476	$0.014 \pm 0.0033 \pm 0.0080$	$0.85 \pm 0.20 \pm 0.17$
80–88	83.9	0.11	0.525	$0.012 \pm 0.0034 \pm 0.0073$	$0.73 \pm 0.21 \pm 0.16$
88–96	92.0	0.13	0.576	$0.0074 \pm 0.0035 \pm 0.0053$	$0.49 \pm 0.23 \pm 0.14$
96–104	100	0.14	0.627	$0.012 \pm 0.0036 \pm 0.0095$	$0.87 \pm 0.25 \pm 0.22$
104–112	108	0.16	0.676	$0.0093 \pm 0.0037 \pm 0.0075$	$0.67 \pm 0.27 \pm 0.17$
112–120	116	0.17	0.725	$0.010 \pm 0.0039 \pm 0.0097$	$0.78 \pm 0.29 \pm 0.34$
120–128	124	0.20	0.774	$0.018 \pm 0.0043 \pm 0.016$	$1.4 \pm 0.32 \pm 0.25$
128–136	132	0.23	0.817	$0.0077 \pm 0.0051 \pm 0.0077$	$0.39 \pm 0.26 \pm 0.20$
136–144	139	0.27	0.850	$0.0028 \pm 0.0076 \pm 0.0049$	$0.15 \pm 0.40 \pm 0.22$
144–152	147	0.31	0.873	$0.016 \pm 0.018 \pm 0.021$	$0.86 \pm 0.94 \pm 0.80$
152–160	154	0.33	0.882	$0.17 \pm 0.079 \pm 0.17$	$9.5 \pm 4.3 \pm 3.1$
160–168	161	0.37	0.895	$-0.68 \pm 1.4 \pm 0.80$	$-37 \pm 77 \pm 27$
$E_{beam} = 200$ GeV (2011 sample)					
16–24	22.2	0.40	0.111	$0.044 \pm 0.058 \pm 0.041$	$0.30 \pm 0.40 \pm 0.29$
24–32	28.6	0.32	0.144	$0.050 \pm 0.027 \pm 0.020$	$0.46 \pm 0.25 \pm 0.29$
32–40	36.6	0.22	0.184	$0.025 \pm 0.017 \pm 0.015$	$0.31 \pm 0.21 \pm 0.21$
40–48	44.5	0.15	0.224	$0.030 \pm 0.011 \pm 0.0090$	$0.89 \pm 0.33 \pm 0.21$
48–56	52.4	0.11	0.262	$0.0018 \pm 0.0078 \pm 0.0042$	$0.070 \pm 0.31 \pm 0.16$
56–64	60.3	0.094	0.301	$0.011 \pm 0.0061 \pm 0.0054$	$0.51 \pm 0.29 \pm 0.21$
64–72	68.1	0.088	0.339	$0.0051 \pm 0.0052 \pm 0.0046$	$0.28 \pm 0.29 \pm 0.23$
72–80	76.1	0.089	0.378	$0.0075 \pm 0.0047 \pm 0.0042$	$0.46 \pm 0.29 \pm 0.18$
80–88	84.1	0.094	0.417	$0.0031 \pm 0.0044 \pm 0.0039$	$0.21 \pm 0.30 \pm 0.25$
88–96	92.1	0.10	0.456	$0.011 \pm 0.0042 \pm 0.0060$	$0.78 \pm 0.31 \pm 0.18$
96–104	100	0.11	0.495	$0.010 \pm 0.0041 \pm 0.0061$	$0.77 \pm 0.32 \pm 0.18$
104–112	108	0.11	0.534	$0.0075 \pm 0.0041 \pm 0.0051$	$0.61 \pm 0.33 \pm 0.18$
112–120	116	0.12	0.573	$0.014 \pm 0.0041 \pm 0.0098$	$1.2 \pm 0.35 \pm 0.24$
120–128	124	0.14	0.613	$0.0075 \pm 0.0043 \pm 0.0066$	$0.66 \pm 0.38 \pm 0.34$
128–136	132	0.15	0.652	$0.0055 \pm 0.0045 \pm 0.0055$	$0.50 \pm 0.40 \pm 0.32$
136–144	140	0.16	0.692	$-0.0036 \pm 0.0047 \pm 0.0046$	$-0.33 \pm 0.43 \pm 0.34$
144–152	148	0.18	0.731	$0.0063 \pm 0.0049 \pm 0.0056$	$0.59 \pm 0.46 \pm 0.21$
152–160	156	0.20	0.770	$0.0041 \pm 0.0052 \pm 0.0042$	$0.38 \pm 0.50 \pm 0.24$
160–168	164	0.23	0.807	$0.0049 \pm 0.0058 \pm 0.0061$	$0.32 \pm 0.38 \pm 0.30$
168–176	172	0.26	0.841	$0.0053 \pm 0.0069 \pm 0.0061$	$0.36 \pm 0.46 \pm 0.26$
176–184	179	0.31	0.866	$0.026 \pm 0.010 \pm 0.024$	$1.7 \pm 0.68 \pm 0.55$
184–192	186	0.36	0.885	$0.044 \pm 0.023 \pm 0.042$	$2.9 \pm 1.5 \pm 0.87$
192–200	192	0.42	0.898	$-0.41 \pm 0.27 \pm 0.99$	$-27 \pm 18 \pm 59$

Table 6.10: Values of A_1^p and g_1^p with their statistical and systematic uncertainties as functions of ν with the corresponding average values of ν, Q^2 and y, for the 2007 and 2011 samples. The maximum Q^2 cut is 1 (GeV/c)^2. Bins in ν are of equal width.

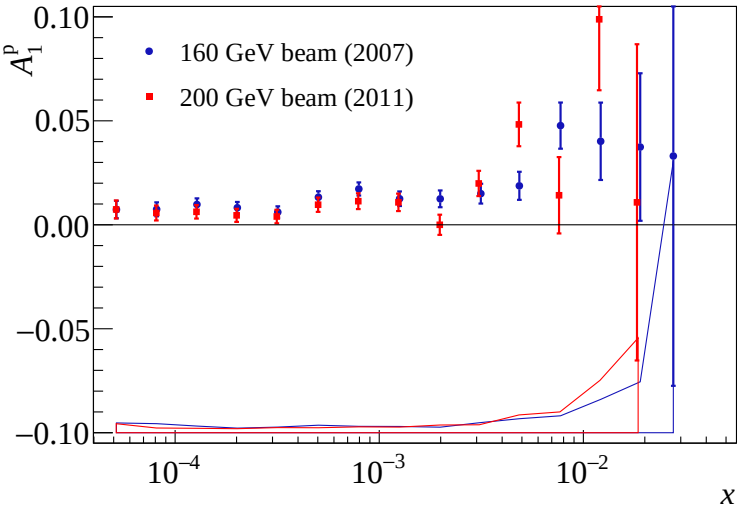

Figure 6.25: Results for $A_1^p(x)$ obtained from 2007 and 2011 data, after corrections resulting from the polarised radiative asymmetry and the presence of ^{14}N in the ammonia target. The bands in the bottom of the figure represent the systematic uncertainties of the data.

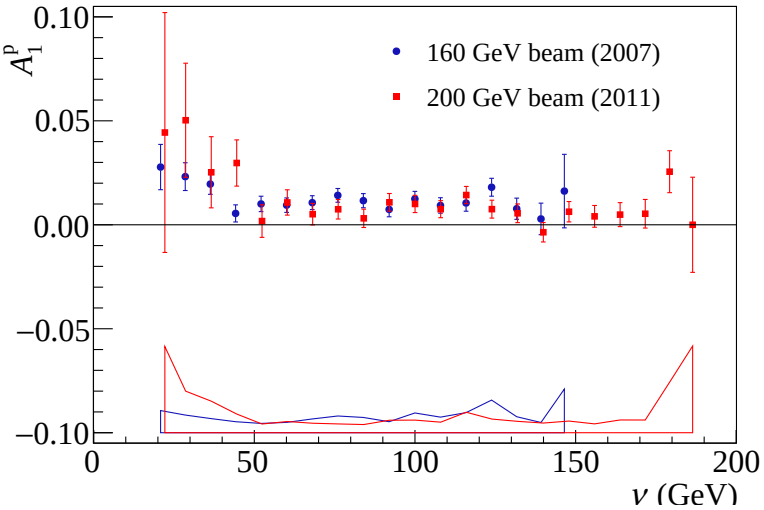

Figure 6.26: Results for $A_1^p(\nu)$ obtained from 2007 and 2011 data, after corrections resulting from the polarised radiative asymmetry and the presence of ^{14}N in the ammonia target. The bands in the bottom of the figure represent the systematic uncertainties of the data.

6.8.2 Discussion

The data is more precise than the SMC data, as expected from the larger size of the sample. Moreover, the results from both years are compatible within uncertainties. The asymmetries were found to be mostly positive and incompatible with zero at the lowest values of x. For

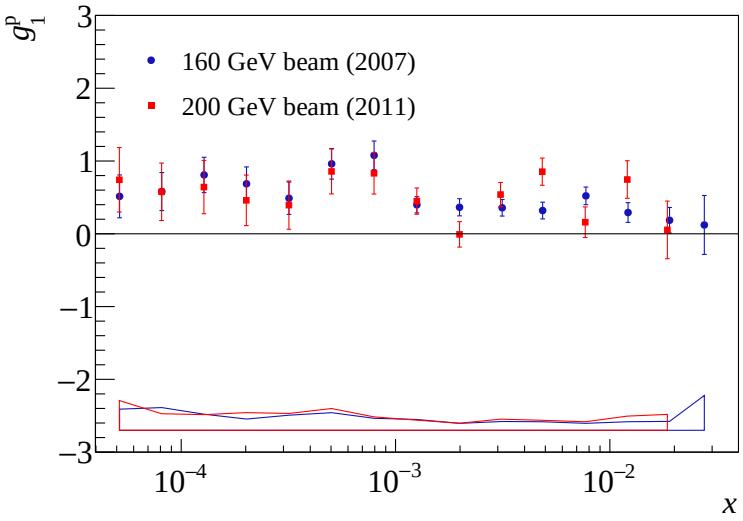

Figure 6.27: Results for $g_1^p(x)$ obtained from 2007 and 2011 data. The bands in the bottom of the figure represent the systematic uncertainties of the data.

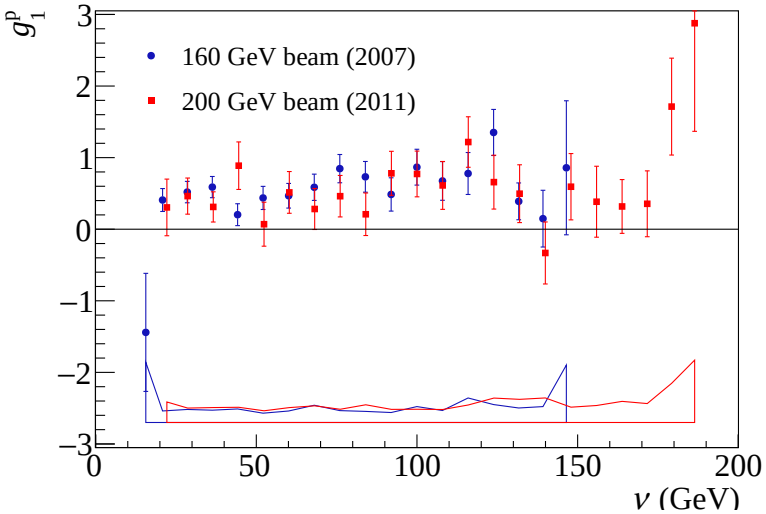

Figure 6.28: Results for $g_1^p(\nu)$ obtained from 2007 and 2011 data. The bands in the bottom of the figure represent the systematic uncertainties of the data.

$x < 10^{-3}$, one obtains a weighted average for the spin asymmetry of

$$\langle A_1^p \rangle = 0.0084 \pm 0.0009 \tag{6.14}$$

if only statistical uncertainties are used in the calculation. If systematic uncertainties are added in quadrature to the statistical one, the weighted average spin asymmetry for $x < 10^{-3}$ becomes $\langle A_1^p \rangle = 0.0081 \pm 0.0012$.

The asymmetries show no specific dependence on ν.

For g_1^p, the weighted average, for all x, taking only statistical uncertainties into account, is

$$\langle g_1^p \rangle = 0.458 \pm 0.035 \tag{6.15}$$

while adding in quadrature statistical and systematic uncertainties yields $\langle g_1^p \rangle = 0.458 \pm 0.046$.

The results on $A_1^p(x)$ and $g_1^p(x)$ can be confronted with theoretical predictions, such as the Regge model and the generalised vector meson dominance model (GVMD). In addition, the results on $g_1^p(x)$ can be combined with the $g_1^d(x)$ to obtain $g_1^{\mathrm{NS}}(x)$, to be compared with theoretical models, taking into account that $g_1^d \simeq (g_1^p + g_1^n)/2$.

Comparison with Previous Results

In Fig. 6.29, the spin asymmetries obtained from the COMPASS data at low x and low Q^2 as a function of x are compared with the results from previous experiments, namely the SMC and the Hermes results. The measurement from different experiments are clearly compatible within uncertainties. The COMPASS results are much more precise than the ones from SMC, as expected. Hermes has made some measurements in the region of $Q^2 < 1$ (GeV/c)^2, but not probing the lower values of x as SMC and COMPASS. In addition, while the SMC results were still compatible with zero in the low x region, the better precision of COMPASS, allows to measure small but significantly positive spin asymmetries down to the lowest values of x probed.

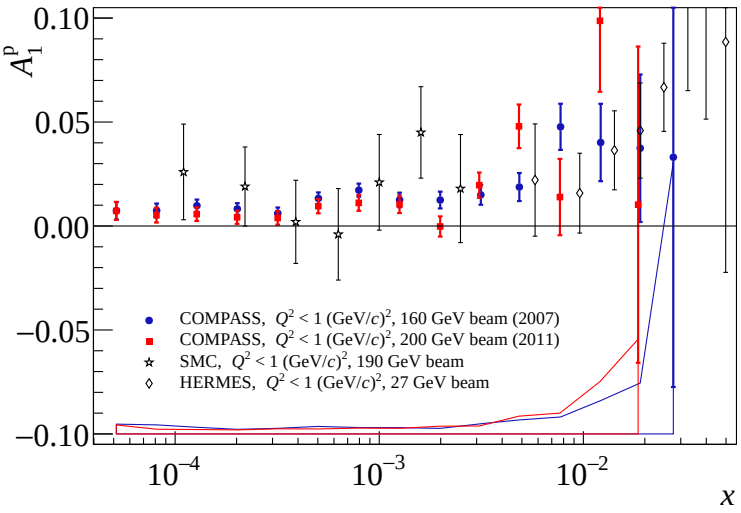

Figure 6.29: Comparison of the spin asymmetry results in bins of x with previous experiments' results. The bands in the bottom of the figure represent the systematic uncertainties of the COMPASS data.

Comparison with Models

In Fig. 6.30, the obtained results for $g_1^p(x)$ are compared with the predictions from [47] and [61,107]. The first model assumes that in the low x and low Q^2 region, g_1^p results from the sum

of two contributions: a so called asymptotic contribution, obtained from a DGLAP evolution together with double logarithmic terms resummation, and a VMD contribution,

$$g_1^p = g_{1,asym}^p + C \cdot g_{1,VMD}^p \tag{6.16}$$

In this model, the non-perturbative parton distributions were evaluated at a fixed Q_0^2 using either:

1. the GRSV2000 parametrisation, or
2. a simple "flat" input:

$$\Delta p_j^{(0)}(x) = N_i(1-x)^{\eta_i} \tag{6.17}$$

with $\eta_{u_v} = \eta_{d_v} = 3$, $\eta_{\bar{u}} = \eta_{\bar{s}} = 7$, $\eta_g = 5$.

For those two different hypotheses and applying phenomenological constraints, two different values for the parameter C were found: -0.30 and -0.24, respectively. The second model uses a similar approach, but is more recent. Both sets of predictions are roughly compatible with the data. However, one cannot draw a definitive conclusion because the model does not provide associated uncertainties.

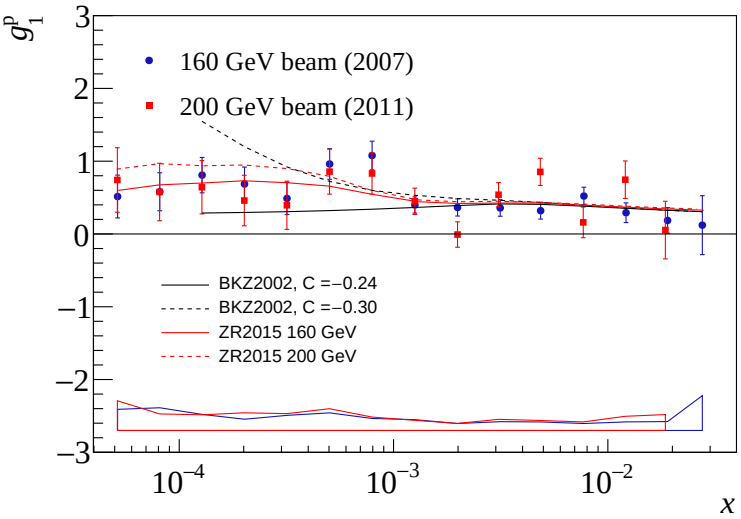

Figure 6.30: Comparison of the obtained results for $g_1^p(x)$ with model predictions from [47] and [61,107]. The bands in the bottom of the figure represent the systematic uncertainties of the data.

6.9 Summary

The double longitudinal spin asymmetry A_1^p and the spin-dependent structure function g_1^p were extracted as functions of the Bjorken scaling variable x, which is the traditional extraction, but also as functions of the energy lost by the muon ν, because a strong dependence on ν is predicted for $g_1^{NS} = g_1^p - g_1^n$. The results show a compatibility within uncertainties of the

results with the two beam energies. Furthermore, strong dependences are not observed, neither as a function of x nor as a function of ν.

A spin effect – small positive asymmetries – is observed for the first time at the very low x probed. This is to be confronted with the results obtained with the COMPASS deuteron data at this region of phase-space, which are compatible with zero. The COMPASS results are also an order of magnitude more precise than the SMC results, which were still compatible with zero.

It is possible to combine the obtained proton results with the deuteron results to calculate the non-singlet structure function $g_1^{NS} = g_1^p - g_1^n$ which can be fit with a Regge-type functional form, namely $g_1^{NS}(x, Q^2) = \beta(Q^2)x^{-\alpha_0}$. This topic will be discussed in more detail in Section 7.2.9.

Chapter 7

Bidimensional Extraction of A_1^p and g_1^p

7.1 Overview

In this chapter, the bidimensional extraction of A_1^p and g_1^p is detailed. Four grids of two variables were used: (x, Q^2), (ν, Q^2), (x, ν) and (Q^2, x), where the fourth grid differs from the first one in the number of bins per variable.

7.2 Bidimensional Analysis

Having found no specific dependences on x nor on ν, there was the possibility that it was hidden by looking solely at dependences on one variable. To test this possibility and make use of the large size of the sample recorded, a two dimensional analysis was performed. No more variables can be studied in a multidimensional analysis, since in deep inelastic scattering, there are only two independent kinematic variables.

The sections on event selection, stability studies, selection criteria, event number reduction discussed in the chapter on the one dimensional analysis are valid for this analysis. The asymmetries were extracted, as in the one-dimensional analysis, using the second order weighting method [81, 82]. The beam polarisation and the target polarisation are not the ones included in the PHAST distributions, as described in Ref. [104]. As in the one-dimensional analysis, the asymmetries were corrected for the presence of ^{14}N, for unpolarised radiative corrections from TERAD (included in an effective dilution factor f available as a PHAST function PaAlgo::GetDilutionFactor()), and for polarised radiative corrections using POLRAD. The spin dependent structure function g_1^p is obtained from A_1^p using the expression

$$g_1^p = \frac{F_2^p}{2x(1+R)} A_1^p.$$

It must be stressed that neither F_2^p nor R were measured for the lowest values of x and Q^2, and it is necessary to estimate them from models.

7.2.1 Binning

The x or ν bins from the one-dimensional analysis were subdivided, respectively, in three Q^2 equipopulated bins and in five Q^2 equipopulated bins in order to obtain the first two grids (x, Q^2) and (ν, Q^2). To obtain the third grid, the x bins were subdivided in equipopulated ν bins. Finally, to obtain the fourth grid, regular bins in Q^2 were subdivided in three equipopulated x bins. The purpose of the fourth grid is to allow Regge type fits (functions of x) while keeping Q^2 constant.

The average values of the pairs of independent variables of each of the four grids used in the present analysis are shown in Fig. 7.1.

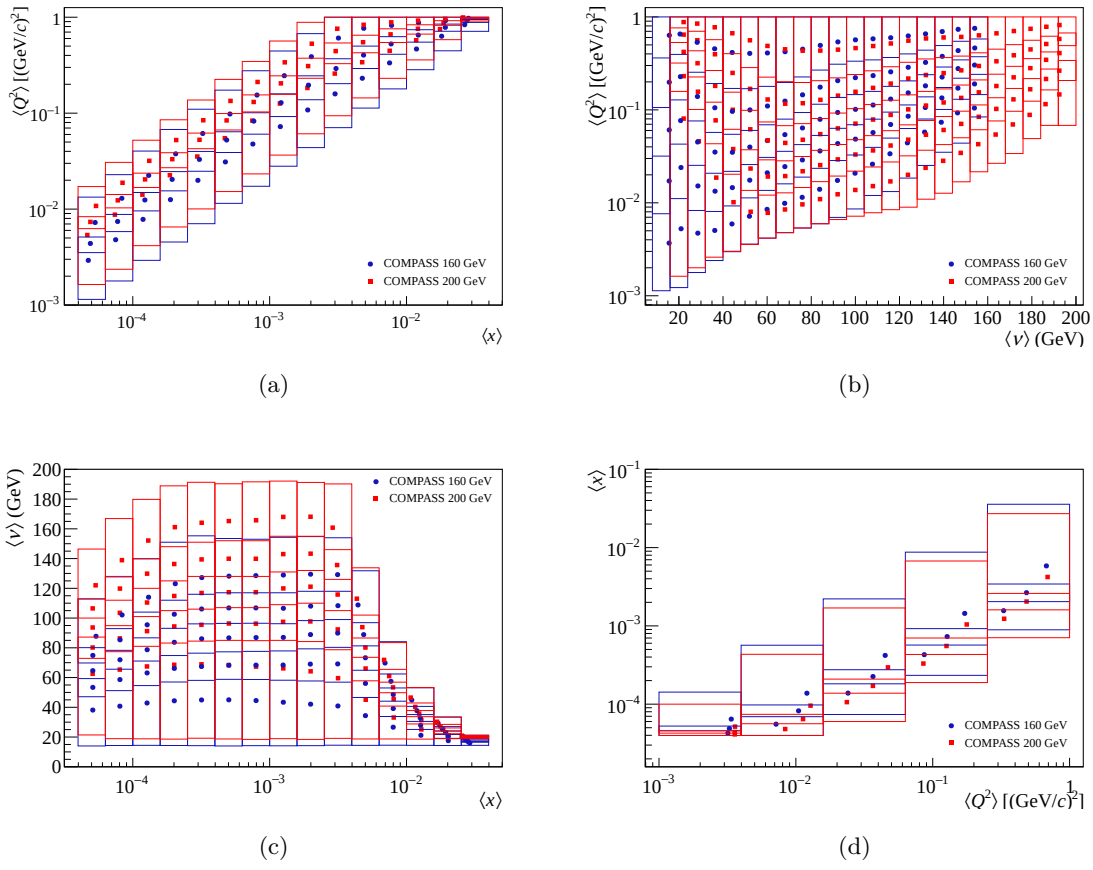

Figure 7.1: Average values of the pairs of independent variables for each of the four grids used. The limits of each bin are also shown.

7.2.2 Systematic Studies

7.2.3 Systematic Studies on Asymmetries

As in the one-dimensional case, the full sample was subdivided in pairs of sub-samples and true asymmetries were extracted for each subsample, in search for systematic effects caused by the experimental apparatus [108]. Furthermore, asymmetries expected to be zero were calculated with the same purpose.

Study \ grid	$A(x, Q^2)$	$A(\nu, Q^2)$	$A(x, \nu)$	$A(Q^2, x)$
Different methods of asymmetry extraction	NA, OK	NA, OK	NA, OK	NA, OK
Global vs consecutive configurations	NA, OK	NA, OK	NA, OK	NA, OK
False consecutive ("fake") configurations	**0.01651**	0.09723	**0.04444**	0.10024
False asymmetries C-C	1.0×10^{-1}	$\mathbf{1.2 \times 10^{-2}}$	$\mathbf{6.1 \times 10^{-2}}$	4.9×10^{-1}
False asymmetries U-D	$\mathbf{2.3 \times 10^{-7}}$	$\mathbf{8.6 \times 10^{-4}}$	$\mathbf{5.9 \times 10^{-5}}$	$\mathbf{1.7 \times 10^{-5}}$
Day vs night	**0.02008**	0.44972	0.08937	**0.00301**
Different microwave settings	**0.00271**	0.07936	0.12166	**0.02528**
Top vs bottom scattered muon	0.49146	0.05289	0.82459	0.95258
Left vs right scattered muon	0.10970	**0.02806**	0.16445	0.08006
Upstream vs downstream primary vertex	0.06622	0.12223	0.05523	0.47545
Inner vs outer primary vertex	0.88968	0.84627	0.66096	0.15225

Table 7.1: Summary of the p-values of the χ^2 homogeneity test obtained for systematic studies done. The p-value is the probability that, under the null hypothesis (that the two distributions of asymmetries from the two subsamples are the same), the χ^2 value will be greater than the value obtained from the data. The p-values lower than 0.05 are highlighted in bold.

The same tests were done as for the one-dimensional analysis. In Table 7.1, the p-values obtained are indicated. For the first two lines, no p-values were computed as they aren't directly applicable, but a visual inspection was done to the plots and no problems were identified.

As in the one-dimensional analysis, some systematic effects were found for the different microwave settings and for the false asymmetries upstream-downstream and center-center. A study was made to try to correlate those two types of effects, but the correlation is not as evident as discussed for the one-dimensional analysis, for which an upper limit to the systematic effect (of 20% of the statistical uncertainty) could be estimated for the 2011 data. For this analysis, we rely on the cancelation of the effects with the use of the two microwave settings.

7.2.4 Internal Consistency Between 2007 and 2011 Asymmetries

The data of 2007 and of 2011 were taken with different beam energies (160 GeV and 200 GeV) and with different solenoid fields (1 T in 2007 and 2.5 T in 2011). For this reason, the compatibility of the results from the two data sets was studied. To summarize, the results of the two years were found to be compatible.

7.2.5 Total Systematic Uncertainty of Asymmetries

The systematic uncertainty was estimated as in the one-dimensional analysis, detailed in Section 6.8. The full set of pulls for false asymmetries calculations are presented in Appendix E. A summary with the different contributions for the total systematic uncertainty is given in Tables 7.2, 7.3, 7.4 and 7.5 and show in Figs. 7.2 to 7.5.

7.2.6 Relative Contributions to the Systematic Uncertainty of g_1^p

The systematic uncertainty of g_1^p was calculated as for the one-dimensional analysis. The main contribution is the systematic uncertainty of $A_1^{LL} = A_1^p \cdot D$, which in turn is dominated by the false asymmetries due to the instability of the asymmetries results over time.

			2007	2011
Multiplicative variables uncertainty	Beam polarisation	$\delta P_B/P_B$	5%	5%
	Target polarisation	$\delta P_T/P_T$	2%	3.5%
	Depolarisation factor	$\delta D(R)/D(R)$	3.8%-35%	3.2%-29%
	Dilution factor	$\delta f/f$	5%	5%
Additive variables uncertainty	Transverse asymmetry	$\eta/\rho \cdot \delta A_2$	$< 0.015 \cdot \delta A_1^{stat}$	$< 0.010 \cdot \delta A_1^{stat}$
	Radiative corrections	δA_1^{RC}	$< 0.023 \cdot \delta A_1^{stat}$	$< 0.018 \cdot \delta A_1^{stat}$
	False asymmetry	A_{false}	$< 1.33 \cdot \delta A_1^{stat}$	$< 1.27 \cdot \delta A_1^{stat}$
		$\delta F_2^p/F_2^p$	31%	31%
		$\delta[D(1+R)]/[D(1+R)]$	6.4%	6.5%

Table 7.2: Decomposition of the systematic uncertainty of A_1^p into multiplicative and additive variables contributions, for the extraction of A_1^p, in bins of (x, Q^2), and further contributions to the systematic uncertainty of $g_1^p(x, Q^2)$ in the last two lines.

			2007	2011
Multiplicative variables uncertainty	Beam polarisation	$\delta P_B/P_B$	5%	5%
	Target polarisation	$\delta P_T/P_T$	2%	3.5%
	Depolarisation factor	$\delta D(R)/D(R)$	1.4%-28%	1.2%-25%
	Dilution factor	$\delta f/f$	5%	5%
Additive variables uncertainty	Transverse asymmetry	$\eta/\rho \cdot \delta A_2$	$< 0.20 \cdot \delta A_1^{stat}$	$< 0.010 \cdot \delta A_1^{stat}$
	Radiative corrections	δA_1^{RC}	$< 0.012 \cdot \delta A_1^{stat}$	$< 0.0086 \cdot \delta A_1^{stat}$
	False asymmetry	A_{false}	$< 1.3 \cdot \delta A_1^{stat}$	$< 1.3 \cdot \delta A_1^{stat}$
		$\delta F_2^p/F_2^p$	31%	31%
		$\delta[D(1+R)]/[D(1+R)]$	24%	19%

Table 7.3: Decomposition of the systematic uncertainty of A_1^p into multiplicative and additive variables contributions, for the extraction of A_1^p, in bins of (ν, Q^2), and further contributions to the systematic uncertainty of $g_1^p(\nu, Q^2)$ in the last two lines.

			2007	2011
Multiplicative variables uncertainty	Beam polarisation	$\delta P_B/P_B$	5%	5%
	Target polarisation	$\delta P_T/P_T$	2%	3.5%
	Depolarisation factor	$\delta D(R)/D(R)$	2.2%-39%	2.2%-31%
	Dilution factor	$\delta f/f$	5%	5%
Additive variables uncertainty	Transverse asymmetry	$\eta/\rho \cdot \delta A_2$	$< 0.016 \cdot \delta A_1^{stat}$	$< 0.011 \cdot \delta A_1^{stat}$
	Radiative corrections	δA_1^{RC}	$< 0.014 \cdot \delta A_1^{stat}$	$< 0.0097 \cdot \delta A_1^{stat}$
	False asymmetry	A_{false}	$< 1.32 \cdot \delta A_1^{stat}$	$< 1.22 \cdot \delta A_1^{stat}$
		$\delta F_2^p/F_2^p$	31%	28%
		$\delta[D(1+R)]/[D(1+R)]$	8.8%	9.2%

Table 7.4: Decomposition of the systematic uncertainty of A_1^p into multiplicative and additive variables contributions, for the extraction of A_1^p in bins of (x, ν), and further contributions to the systematic uncertainty of $g_1^p(x, \nu)$ in the last two lines.

			2007	2011
Multiplicative variables uncertainty	Beam polarisation	$\delta P_B/P_B$	5%	5%
	Target polarisation	$\delta P_T/P_T$	2%	3.5%
	Depolarisation factor	$\delta D(R)/D(R)$	6.3%-32%	6.6%-35%
	Dilution factor	$\delta f/f$	5%	5%
Additive variables uncertainty	Transverse asymmetry	$\eta/\rho \cdot \delta A_2$	$< 0.031 \cdot \delta A_1^{stat}$	$< 0.020 \cdot \delta A_1^{stat}$
	Radiative corrections	δA_1^{RC}	$< 0.037 \cdot \delta A_1^{stat}$	$< 0.028 \cdot \delta A_1^{stat}$
	False asymmetry	A_{false}	$< 1.51 \cdot \delta A_1^{stat}$	$< 1.08 \cdot \delta A_1^{stat}$
		$\delta F_2^p/F_2^p$	17%	15%
		$\delta[D(1+R)]/[D(1+R)]$	6.6%	7.3%

Table 7.5: Decomposition of the systematic uncertainty of A_1^p into multiplicative and additive variables contributions, for the extraction of A_1^p in bins of (Q^2, x), and further contributions to the systematic uncertainty of $g_1^p(Q^2, x)$ in the last two lines.

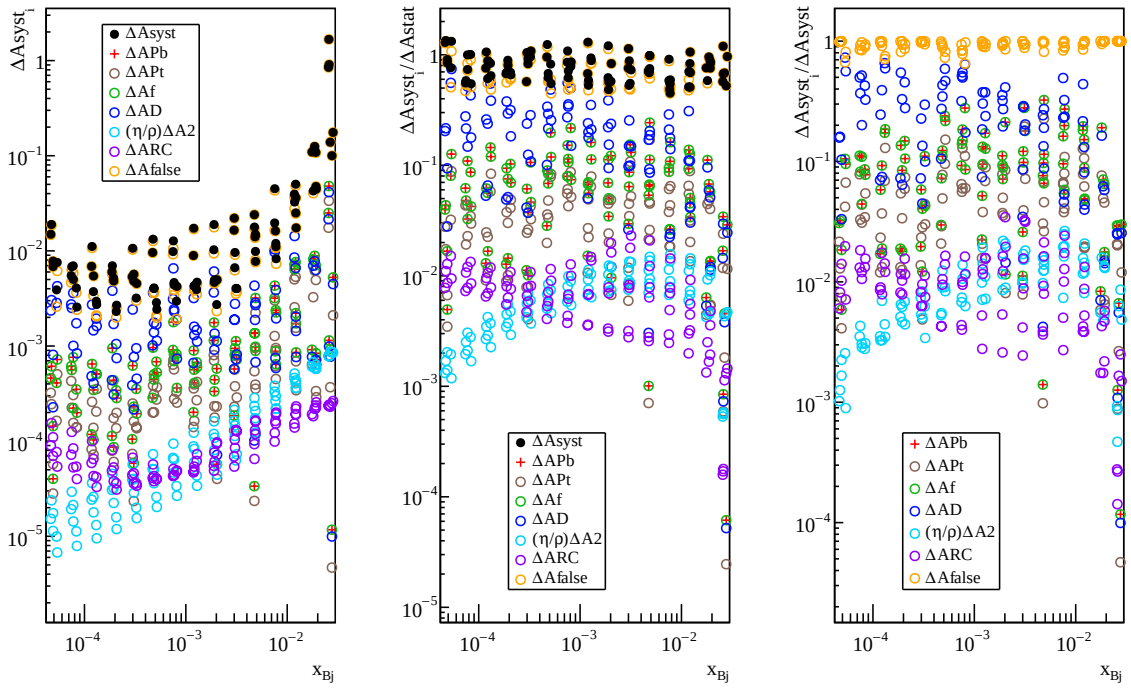

Figure 7.2: Contributions to the systematic uncertainty of $A_1^p(x, Q^2)$.

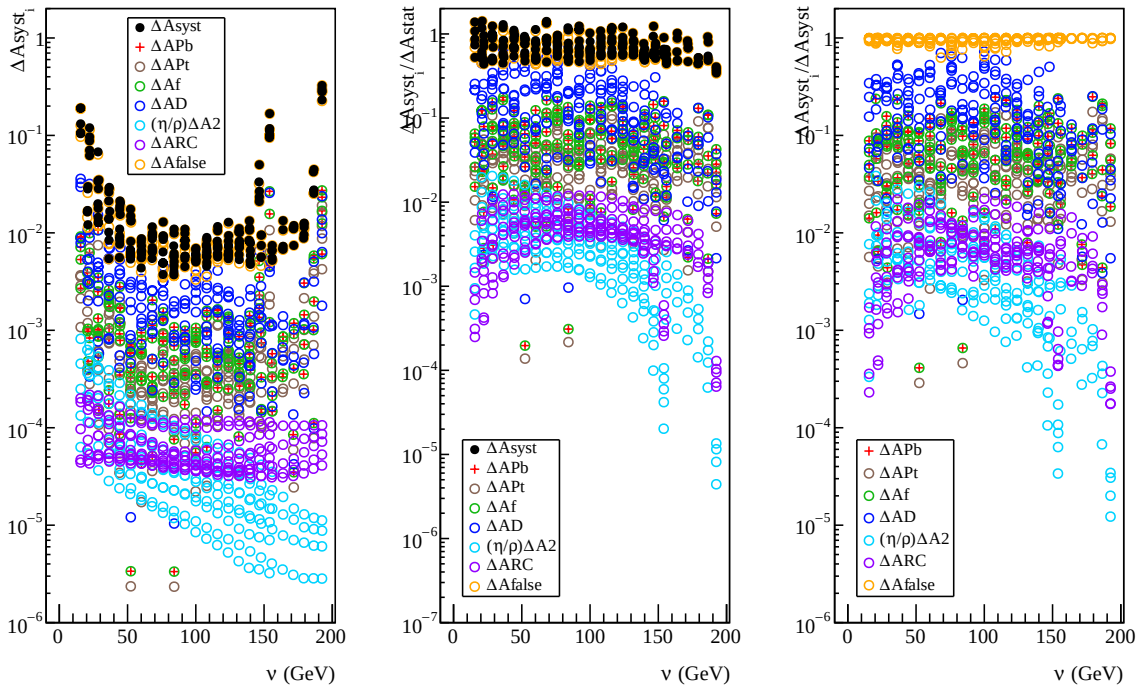

Figure 7.3: Contributions to the systematic uncertainty of $A_1^p(\nu, Q^2)$.

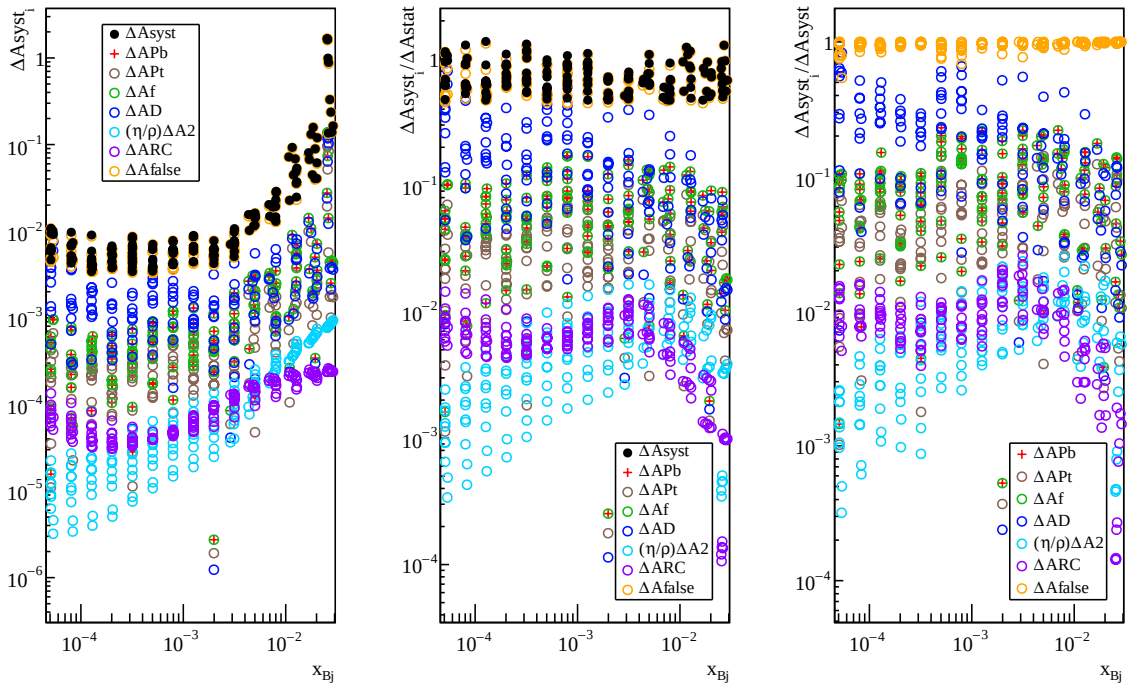

Figure 7.4: Contributions to the systematic uncertainty of $A_1^p(x, \nu)$.

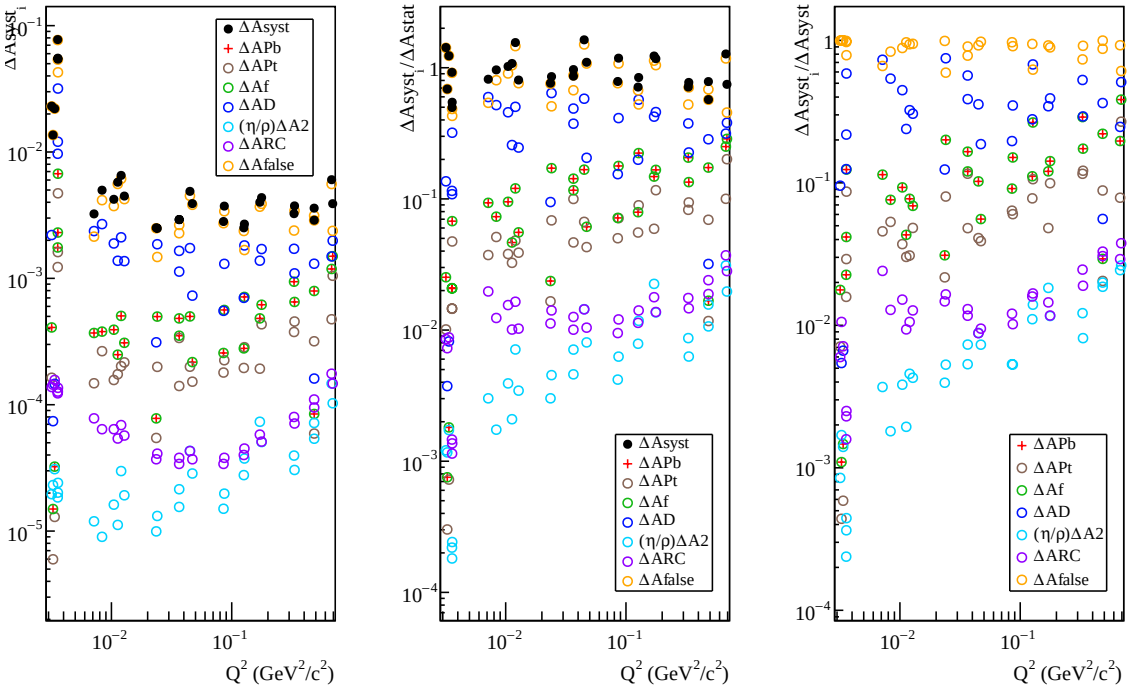

Figure 7.5: Contributions to the systematic uncertainty of $A_1^p(Q^2, x)$.

7.2.7 Results

The results for $g_1^p(x, Q^2)$ are shown in Tables 7.6 and 7.7 and, for all the grids, in Figs. 7.6 to 7.12. All the intermediate quantities used are shown in Appendix F.

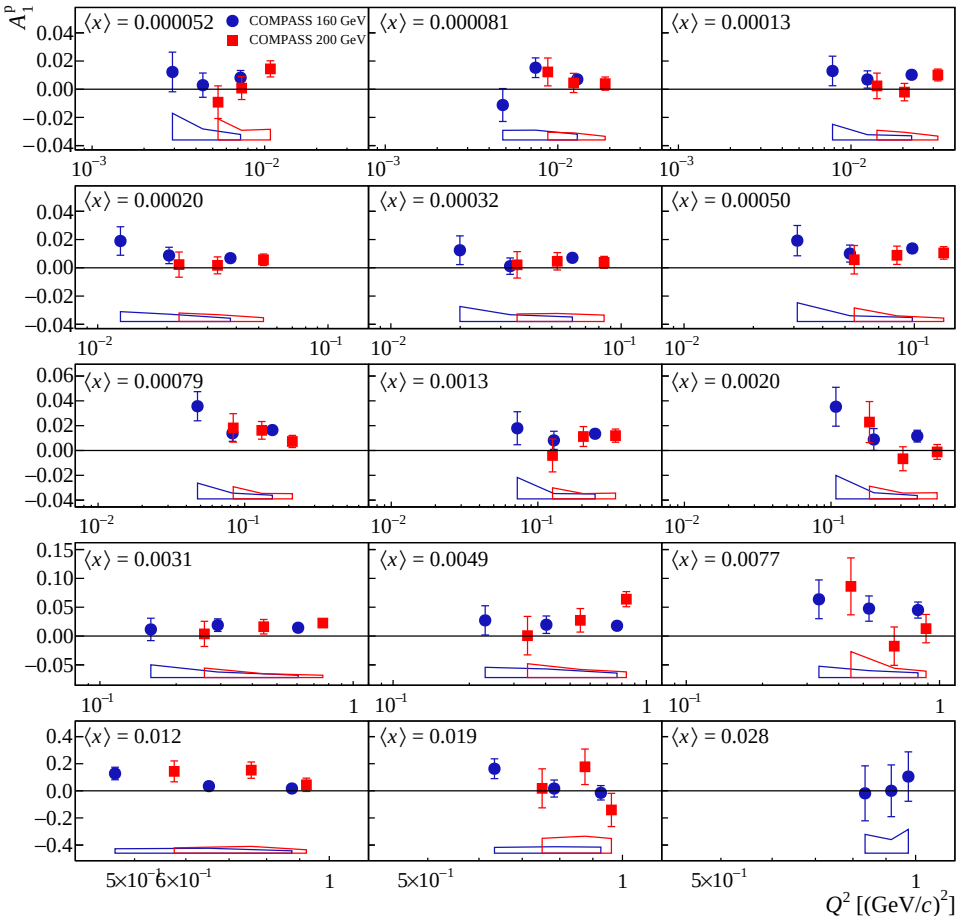

Figure 7.6: Results for $A_1^p(x, Q^2)$ from 2007 and 2011 data. The bands in the bottom of the plots represent the systematic uncertainties of the data.

7.2.8 Discussion

As expected, no significant differences are seen between the results obtained with the two different beam energies used. The small positive asymmetries are still visible, although their significance is smaller than in the unidimensional extraction of A_1^p. Furthermore, there is no strong dependence with the kinematic variables studied.

7.2.9 Comparison with Models

The Regge model predicts that the non-siglet structure function $g_1^{NS} = g_1^p - g_1^n$ can be written as

$$g_1^{NS}(x, Q^2) = \beta(Q^2) \cdot x^{-\alpha_0}. \tag{7.1}$$

Taking into account that g_1^d was found by COMPASS to be compatible with zero at low x and low Q^2 [93], such a dependence on x and Q^2 may be valid also for g_1^p. Under this assumption,

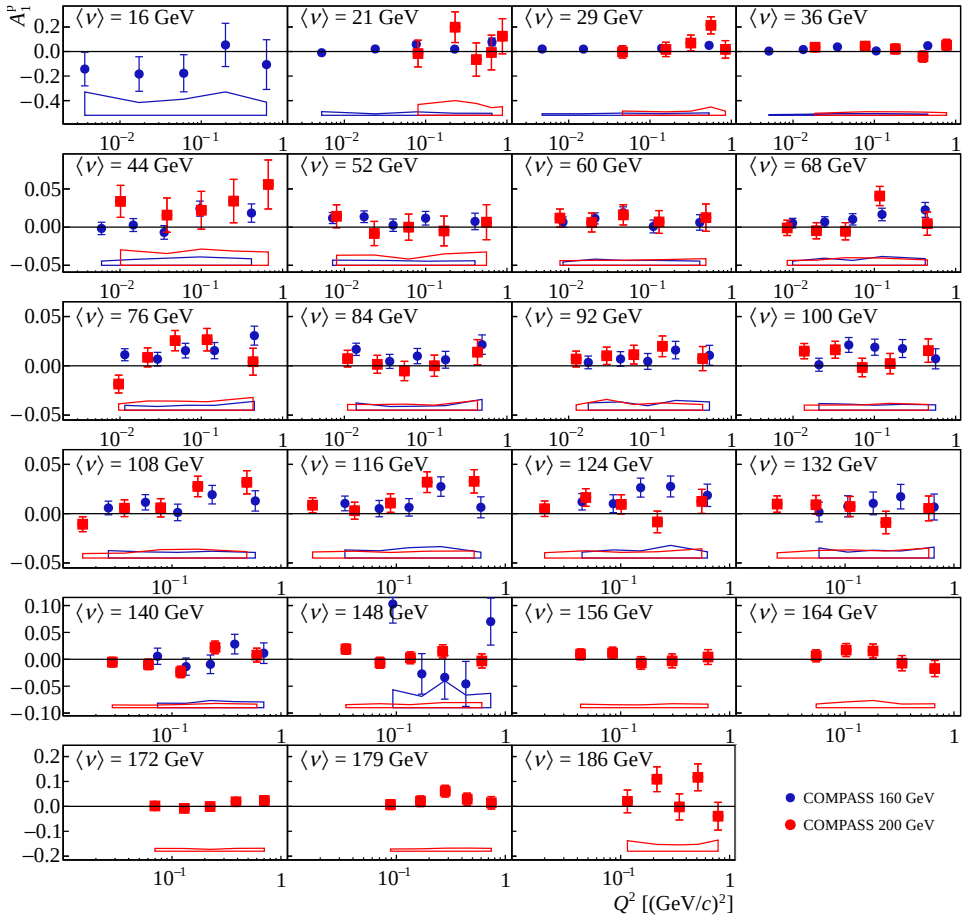

Figure 7.7: Results for $A_1^p(\nu, Q^2)$ from 2007 and 2011 data. The bands in the bottom of the plots represent the systematic uncertainties of the data.

a χ^2 scan was done by letting α_0 vary, assuming that $\beta(Q^2)$ is a constant and trying to obtain the α_0 which minimises the χ^2. The results are shown in Fig. 7.13. A value of α_0 is obtained:

$$\alpha_{0,scan} = 0.31 \pm 0.14\,. \tag{7.2}$$

In Figs. 7.14, 7.15, 7.16 and 7.17, the results obtained for the spin asymmetry A_1^p are compared with the prediction from the model of Ref. [47]. The model has predictions for g_1^p, which were translated to predictions for A_1^p for each of the COMPASS points using the same R and F_2^p that was used to obtain g_1^p from the measured A_1^p.

The model is in reasonable agreement with the data. Nevertheless, letting the parameter C free, and doing χ^2 scans of the parameter in order to determine a new value that would better describe the COMPASS data led to inconclusive results. In fact, the first type of distributions result in lower χ^2 for three of the grids, namely (x, Q^2), (x, ν) and (Q^2, x), the second type of distributions (the so called "flat" distributions) are favored in the case of the (ν, Q^2) grid. The eight values obtained for C are not compatible among them. The model should be upgraded to include more modern parametrisations for the parton distributions, since the GRSV2000 is quite old and has been substituted by a more recent one, based on more data and obtained with different techniques and hypotheses.

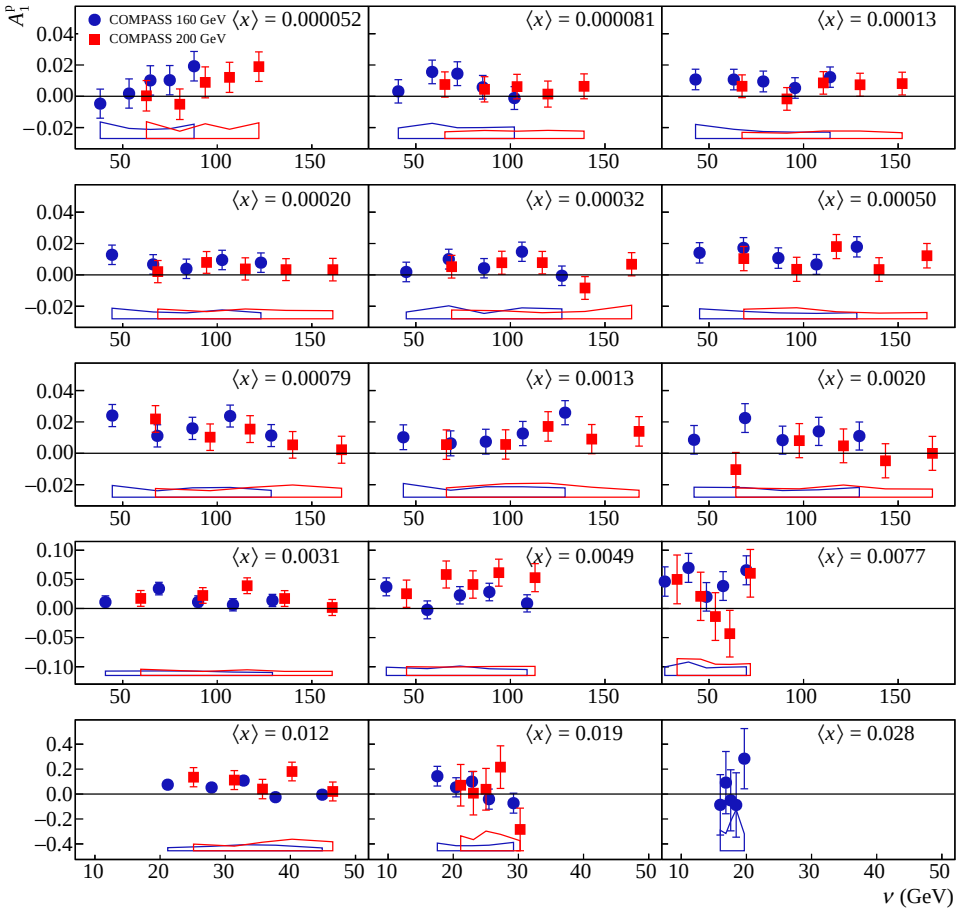

Figure 7.8: Results for $A_1^p(\nu, x)$ from 2007 and 2011 data. The bands in the bottom of the plots represent the systematic uncertainties of the data.

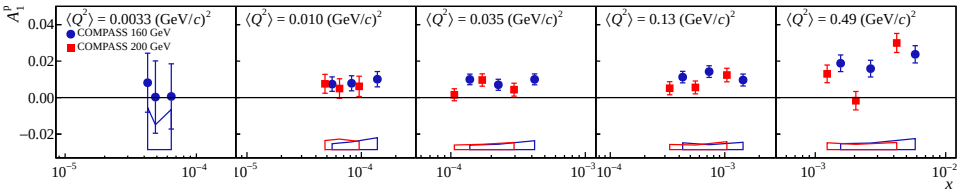

Figure 7.9: Results for $A_1^p(Q^2, x)$ from 2007 and 2011 data. The bands in the bottom of the plots represent the systematic uncertainties of the data.

In Fig. 7.18, in addition to the model already described of Ref. [47], the predictions of a similar, although more recent, model are also shown. All the model predictions are compatible with the data. Nevertheless, the model of Ref. [47] gives predictions for g_1^d that are different from zero in the low x and low Q^2 region, contrarily to what was observed by COMPASS [93].

7.3 Summary

The spin asymmetries A_1^p and the structure function g_1^p have been extracted in four grids with bins of two kinematic variables (two is the number of independent variables in DIS). While the first grid (x, Q^2) is the traditional one, the others were also used to provide ready-to-use

results for theoreticians, and to test the possibility of dependences with any given variable that would be hidden by averaging on the others. No strong dependences with the studied variables were observed. The results in grids of pairs of variables allows to test functional forms with two variables.

The data was confronted with models, and the comparisons show reasonable agreement of data and models. Nevertheless, the data does not allow the rejection of any of those models.

x range	$\langle x \rangle$	$\langle Q^2 \rangle$ (GeV$^2/c^2$)	$\langle y \rangle$	A_1^p	g_1^p
$E_{beam} = 160$ GeV (2007 sample)					
0.00004–0.000063	0.000047	0.0029	0.21	$+0.012 \pm 0.014 \pm 0.019$	$+0.45 \pm 0.52 \pm 0.69$
0.00004–0.000063	0.000049	0.0044	0.30	$+0.0029 \pm 0.0086 \pm 0.0078$	$+0.15 \pm 0.46 \pm 0.41$
0.00004–0.000063	0.000053	0.0073	0.45	$+0.0082 \pm 0.0051 \pm 0.0039$	$+0.65 \pm 0.41 \pm 0.22$
0.000063–0.0001	0.000075	0.0048	0.22	$-0.011 \pm 0.012 \pm 0.007$	$-0.43 \pm 0.44 \pm 0.24$
0.000063–0.0001	0.000077	0.0074	0.33	$+0.0153 \pm 0.0070 \pm 0.0070$	$+0.85 \pm 0.39 \pm 0.34$
0.000063–0.0001	0.000083	0.013	0.52	$+0.0070 \pm 0.0040 \pm 0.0041$	$+0.62 \pm 0.36 \pm 0.33$
0.0001–0.00016	0.00012	0.0078	0.22	$+0.013 \pm 0.010 \pm 0.011$	$+0.50 \pm 0.40 \pm 0.42$
0.0001–0.00016	0.00012	0.012	0.35	$+0.0069 \pm 0.0061 \pm 0.0037$	$+0.40 \pm 0.36 \pm 0.20$
0.0001–0.00016	0.00013	0.022	0.57	$+0.0102 \pm 0.0035 \pm 0.0030$	$+0.97 \pm 0.33 \pm 0.22$
0.00016–0.00025	0.00019	0.013	0.23	$+0.019 \pm 0.010 \pm 0.007$	$+0.72 \pm 0.39 \pm 0.23$
0.00016–0.00025	0.00019	0.020	0.36	$+0.0087 \pm 0.0058 \pm 0.0052$	$+0.51 \pm 0.34 \pm 0.29$
0.00016–0.00025	0.00021	0.038	0.61	$+0.0068 \pm 0.0033 \pm 0.0023$	$+0.65 \pm 0.32 \pm 0.20$
0.00025–0.0004	0.00030	0.020	0.23	$+0.012 \pm 0.010 \pm 0.011$	$+0.46 \pm 0.38 \pm 0.39$
0.00025–0.0004	0.00031	0.033	0.37	$+0.0012 \pm 0.0058 \pm 0.0048$	$+0.07 \pm 0.33 \pm 0.27$
0.00025–0.0004	0.00032	0.061	0.63	$+0.0071 \pm 0.0033 \pm 0.0032$	$+0.64 \pm 0.30 \pm 0.28$
0.0004–0.00063	0.00047	0.031	0.22	$+0.019 \pm 0.011 \pm 0.013$	$+0.67 \pm 0.37 \pm 0.45$
0.0004–0.00063	0.00048	0.053	0.37	$+0.0101 \pm 0.0060 \pm 0.0041$	$+0.53 \pm 0.31 \pm 0.20$
0.0004–0.00063	0.00051	0.098	0.64	$+0.0137 \pm 0.0035 \pm 0.0029$	$+1.11 \pm 0.28 \pm 0.21$
0.00063–0.001	0.00075	0.048	0.22	$+0.036 \pm 0.012 \pm 0.013$	$+1.13 \pm 0.37 \pm 0.37$
0.00063–0.001	0.00077	0.083	0.37	$+0.0139 \pm 0.0065 \pm 0.0046$	$+0.66 \pm 0.31 \pm 0.20$
0.00063–0.001	0.00081	0.15	0.64	$+0.0165 \pm 0.0038 \pm 0.0030$	$+1.13 \pm 0.26 \pm 0.19$
0.001–0.0016	0.0012	0.072	0.21	$+0.018 \pm 0.013 \pm 0.017$	$+0.50 \pm 0.37 \pm 0.48$
0.001–0.0016	0.0012	0.13	0.36	$+0.0082 \pm 0.0073 \pm 0.0043$	$+0.33 \pm 0.30 \pm 0.17$
0.001–0.0016	0.0013	0.25	0.64	$+0.0135 \pm 0.0042 \pm 0.0039$	$+0.50 \pm 0.16 \pm 0.18$
0.0016–0.0025	0.0019	0.11	0.19	$+0.035 \pm 0.016 \pm 0.019$	$+0.82 \pm 0.37 \pm 0.43$
0.0016–0.0025	0.0019	0.20	0.35	$+0.0089 \pm 0.0088 \pm 0.0050$	$+0.29 \pm 0.29 \pm 0.16$
0.0016–0.0025	0.0020	0.39	0.64	$+0.0116 \pm 0.0047 \pm 0.0027$	$+0.37 \pm 0.15 \pm 0.10$
0.0025–0.004	0.0030	0.16	0.18	$+0.012 \pm 0.019 \pm 0.022$	$+0.22 \pm 0.36 \pm 0.41$
0.0025–0.004	0.0031	0.29	0.33	$+0.019 \pm 0.011 \pm 0.010$	$+0.32 \pm 0.18 \pm 0.17$
0.0025–0.004	0.0032	0.61	0.64	$+0.0144 \pm 0.0055 \pm 0.0040$	$+0.37 \pm 0.14 \pm 0.11$
0.004–0.0063	0.0048	0.23	0.17	$+0.027 \pm 0.025 \pm 0.018$	$+0.24 \pm 0.23 \pm 0.17$
0.004–0.0063	0.0049	0.40	0.28	$+0.020 \pm 0.015 \pm 0.015$	$+0.26 \pm 0.20 \pm 0.20$
0.004–0.0063	0.0049	0.77	0.54	$+0.0178 \pm 0.0079 \pm 0.0078$	$+0.33 \pm 0.15 \pm 0.14$
0.0063–0.01	0.0075	0.33	0.15	$+0.064 \pm 0.034 \pm 0.020$	$+0.49 \pm 0.26 \pm 0.16$
0.0063–0.01	0.0077	0.53	0.23	$+0.048 \pm 0.022 \pm 0.012$	$+0.46 \pm 0.21 \pm 0.12$
0.0063–0.01	0.0078	0.82	0.36	$+0.045 \pm 0.014 \pm 0.008$	$+0.53 \pm 0.16 \pm 0.10$
0.01–0.016	0.012	0.47	0.13	$+0.128 \pm 0.046 \pm 0.033$	$+0.79 \pm 0.28 \pm 0.21$
0.01–0.016	0.012	0.65	0.18	$+0.035 \pm 0.034 \pm 0.036$	$+0.24 \pm 0.24 \pm 0.25$
0.01–0.016	0.012	0.88	0.24	$+0.017 \pm 0.025 \pm 0.018$	$+0.13 \pm 0.20 \pm 0.13$
0.016–0.025	0.018	0.63	0.12	$+0.163 \pm 0.073 \pm 0.043$	$+0.78 \pm 0.35 \pm 0.21$
0.016–0.025	0.019	0.78	0.14	$+0.017 \pm 0.063 \pm 0.048$	$+0.08 \pm 0.30 \pm 0.23$
0.016–0.025	0.019	0.93	0.16	$-0.014 \pm 0.053 \pm 0.045$	$-0.07 \pm 0.27 \pm 0.23$
0.025–0.04	0.027	0.84	0.11	$-0.02 \pm 0.20 \pm 0.14$	$-0.07 \pm 0.75 \pm 0.51$
0.025–0.04	0.028	0.92	0.11	$+0.00 \pm 0.19 \pm 0.10$	$+0.00 \pm 0.70 \pm 0.37$
0.025–0.04	0.028	0.97	0.12	$+0.11 \pm 0.18 \pm 0.18$	$+0.38 \pm 0.66 \pm 0.64$

Table 7.6: Values of A_1^p and g_1^p with their statistical and systematic uncertainties as functions of x and Q^2, with the corresponding average values of x, Q^2 and y, for the 2007 sample. The maximum Q^2 cut is 1 (GeV/c)^2. Bins in x are of equal width in $\log_{10} x$.

x range	$\langle x \rangle$	$\langle Q^2 \rangle$ (GeV$^2/c^2$)	$\langle y \rangle$	A_1^p	g_1^p
$E_{beam} = 200$ GeV (2011 sample)					
0.00004–0.000063	0.000047	0.0054	0.31	$-0.009 \pm 0.012 \pm 0.015$	$-0.6 \pm 1.0 \pm 1.0$
0.00004–0.000063	0.000049	0.0074	0.40	$+0.0008 \pm 0.0081 \pm 0.0068$	$+0.07 \pm 0.71 \pm 0.60$
0.00004–0.000063	0.000054	0.011	0.53	$+0.0144 \pm 0.0057 \pm 0.0076$	$+1.67 \pm 0.66 \pm 0.74$
0.000063–0.0001	0.000074	0.0087	0.32	$+0.0123 \pm 0.0099 \pm 0.0055$	$+0.84 \pm 0.68 \pm 0.33$
0.000063–0.0001	0.000078	0.012	0.43	$+0.0044 \pm 0.0068 \pm 0.0050$	$+0.40 \pm 0.63 \pm 0.45$
0.000063–0.0001	0.000084	0.019	0.59	$+0.0040 \pm 0.0047 \pm 0.0026$	$+0.50 \pm 0.59 \pm 0.31$
0.0001–0.00016	0.00012	0.014	0.32	$+0.0024 \pm 0.0091 \pm 0.0069$	$+0.16 \pm 0.62 \pm 0.47$
0.0001–0.00016	0.00012	0.020	0.45	$-0.0021 \pm 0.0062 \pm 0.0055$	$-0.19 \pm 0.57 \pm 0.50$
0.0001–0.00016	0.00013	0.032	0.64	$+0.0101 \pm 0.0042 \pm 0.0027$	$+1.30 \pm 0.54 \pm 0.30$
0.00016–0.00025	0.00019	0.023	0.32	$+0.0023 \pm 0.0089 \pm 0.0060$	$+0.15 \pm 0.59 \pm 0.40$
0.00016–0.00025	0.00019	0.033	0.46	$+0.0017 \pm 0.0060 \pm 0.0048$	$+0.16 \pm 0.54 \pm 0.43$
0.00016–0.00025	0.00021	0.052	0.67	$+0.0057 \pm 0.0041 \pm 0.0027$	$+0.71 \pm 0.51 \pm 0.33$
0.00025–0.0004	0.00030	0.035	0.32	$+0.0021 \pm 0.0093 \pm 0.0053$	$+0.13 \pm 0.58 \pm 0.33$
0.00025–0.0004	0.00031	0.053	0.46	$+0.0046 \pm 0.0062 \pm 0.0057$	$+0.39 \pm 0.52 \pm 0.48$
0.00025–0.0004	0.00033	0.084	0.68	$+0.0039 \pm 0.0042 \pm 0.0045$	$+0.45 \pm 0.48 \pm 0.52$
0.0004–0.00063	0.00047	0.055	0.31	$+0.006 \pm 0.010 \pm 0.010$	$+0.32 \pm 0.57 \pm 0.54$
0.0004–0.00063	0.00048	0.084	0.46	$+0.0089 \pm 0.0065 \pm 0.0040$	$+0.68 \pm 0.49 \pm 0.29$
0.0004–0.00063	0.00052	0.13	0.69	$+0.0105 \pm 0.0044 \pm 0.0024$	$+1.04 \pm 0.44 \pm 0.23$
0.00063–0.001	0.00075	0.084	0.30	$+0.018 \pm 0.012 \pm 0.010$	$+0.89 \pm 0.56 \pm 0.47$
0.00063–0.001	0.00076	0.13	0.46	$+0.0162 \pm 0.0071 \pm 0.0044$	$+1.06 \pm 0.46 \pm 0.26$
0.00063–0.001	0.00082	0.21	0.69	$+0.0073 \pm 0.0049 \pm 0.0042$	$+0.39 \pm 0.26 \pm 0.25$
0.001–0.0016	0.0012	0.13	0.28	$-0.004 \pm 0.013 \pm 0.010$	$-0.16 \pm 0.54 \pm 0.36$
0.001–0.0016	0.0012	0.20	0.45	$+0.0113 \pm 0.0080 \pm 0.0042$	$+0.37 \pm 0.26 \pm 0.17$
0.001–0.0016	0.0013	0.34	0.70	$+0.0120 \pm 0.0053 \pm 0.0047$	$+0.58 \pm 0.26 \pm 0.24$
0.0016–0.0025	0.0019	0.18	0.26	$+0.023 \pm 0.016 \pm 0.010$	$+0.73 \pm 0.53 \pm 0.32$
0.0016–0.0025	0.0019	0.31	0.44	$-0.0067 \pm 0.0097 \pm 0.0047$	$-0.19 \pm 0.28 \pm 0.14$
0.0016–0.0025	0.0020	0.53	0.69	$-0.0011 \pm 0.0060 \pm 0.0050$	$-0.04 \pm 0.23 \pm 0.19$
0.0025–0.004	0.0030	0.26	0.23	$+0.004 \pm 0.022 \pm 0.016$	$+0.06 \pm 0.34 \pm 0.26$
0.0025–0.004	0.0030	0.44	0.39	$+0.016 \pm 0.013 \pm 0.007$	$+0.36 \pm 0.28 \pm 0.15$
0.0025–0.004	0.0031	0.76	0.65	$+0.0225 \pm 0.0073 \pm 0.0040$	$+0.67 \pm 0.22 \pm 0.13$
0.004–0.0063	0.0047	0.34	0.19	$+0.001 \pm 0.033 \pm 0.024$	$+0.01 \pm 0.40 \pm 0.29$
0.004–0.0063	0.0048	0.55	0.31	$+0.027 \pm 0.020 \pm 0.014$	$+0.42 \pm 0.32 \pm 0.22$
0.004–0.0063	0.0049	0.83	0.46	$+0.064 \pm 0.013 \pm 0.010$	$+1.23 \pm 0.25 \pm 0.20$
0.0063–0.01	0.0075	0.45	0.16	$+0.086 \pm 0.049 \pm 0.045$	$+0.78 \pm 0.45 \pm 0.41$
0.0063–0.01	0.0076	0.66	0.23	$-0.018 \pm 0.033 \pm 0.016$	$-0.19 \pm 0.36 \pm 0.18$
0.0063–0.01	0.0077	0.88	0.31	$+0.013 \pm 0.025 \pm 0.011$	$+0.16 \pm 0.30 \pm 0.14$
0.01–0.016	0.012	0.58	0.13	$+0.144 \pm 0.077 \pm 0.040$	$+0.97 \pm 0.52 \pm 0.28$
0.01–0.016	0.012	0.76	0.17	$+0.15 \pm 0.060 \pm 0.050$	$+1.12 \pm 0.44 \pm 0.38$
0.01–0.016	0.012	0.92	0.20	$+0.044 \pm 0.049 \pm 0.025$	$+0.35 \pm 0.39 \pm 0.20$
0.016–0.025	0.018	0.75	0.11	$+0.018 \pm 0.14 \pm 0.11$	$+0.10 \pm 0.75 \pm 0.57$
0.016–0.025	0.019	0.88	0.13	$+0.18 \pm 0.13 \pm 0.13$	$+0.92 \pm 0.68 \pm 0.65$
0.016–0.025	0.019	0.96	0.13	$-0.14 \pm 0.12 \pm 0.11$	$-0.74 \pm 0.64 \pm 0.57$
0.025–0.04	0.026	0.95	0.10	$-0.5 \pm 1.5 \pm 0.8$	$-2.0 \pm 5.9 \pm 3.4$
0.025–0.04	0.026	0.98	0.10	$-1.0 \pm 1.4 \pm 1.7$	$-3.8 \pm 5.6 \pm 6.7$
0.025–0.04	0.026	0.99	0.10	$+0.0 \pm 1.4 \pm 0.9$	$+0.1 \pm 5.4 \pm 3.6$

Table 7.7: Values of A_1^p and g_1^p with their statistical and systematic uncertainties as functions of x and Q^2, with the corresponding average values of x, Q^2 and y, for the 2011 sample. The maximum Q^2 cut is 1 (GeV/c)^2. Bins in x are of equal width in $\log_{10} x$.

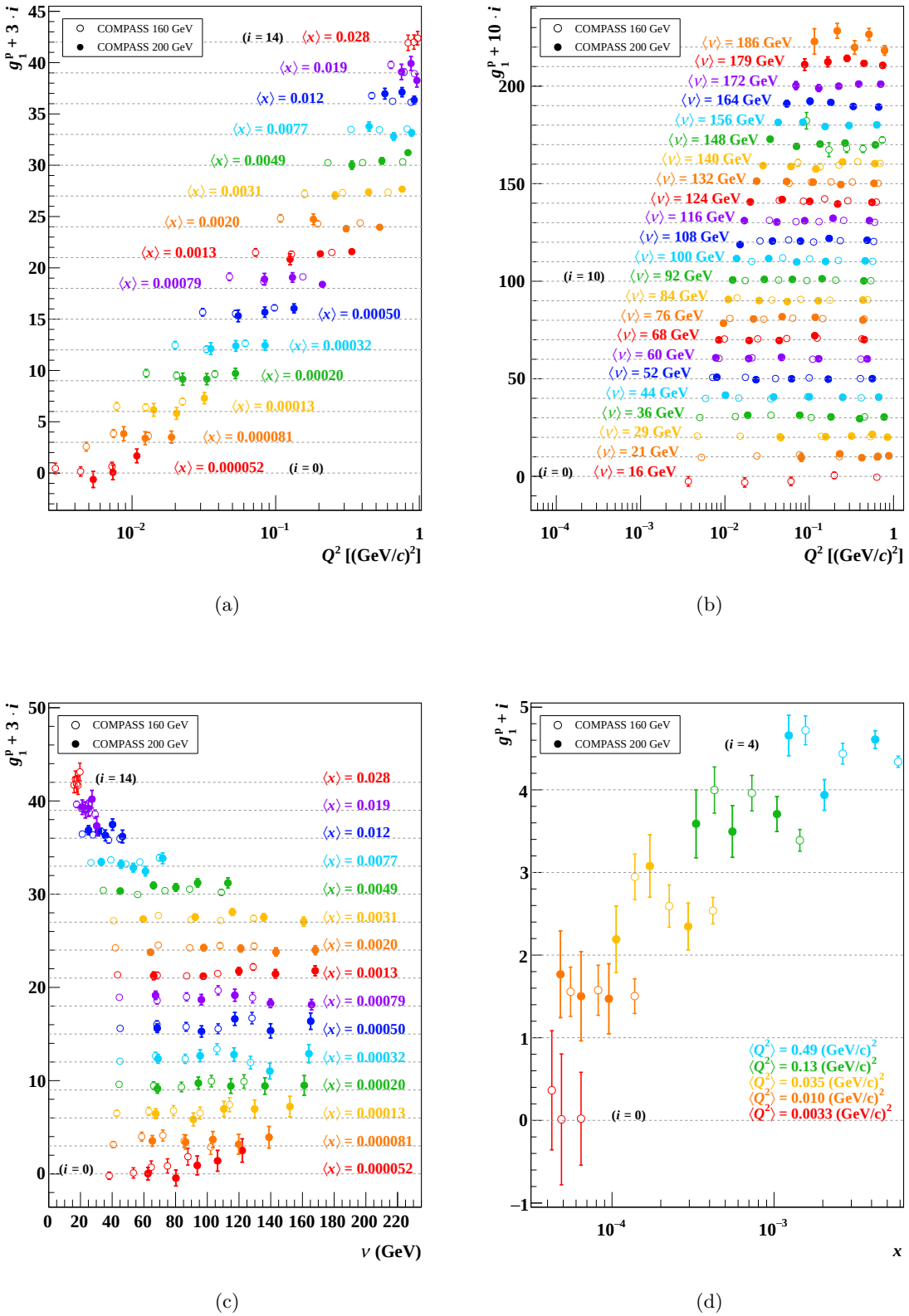

Figure 7.10: Results for (a) $g_1^p(x, Q^2)$, (b) $g_1^p(\nu, Q^2)$, (c) $g_1^p(\nu, x)$ and (d) $g_1^p(Q^2, x)$, from 2007 and 2011 data. The filled and the open circles represent, respectively, the results from 2007 data and from 2011 data.

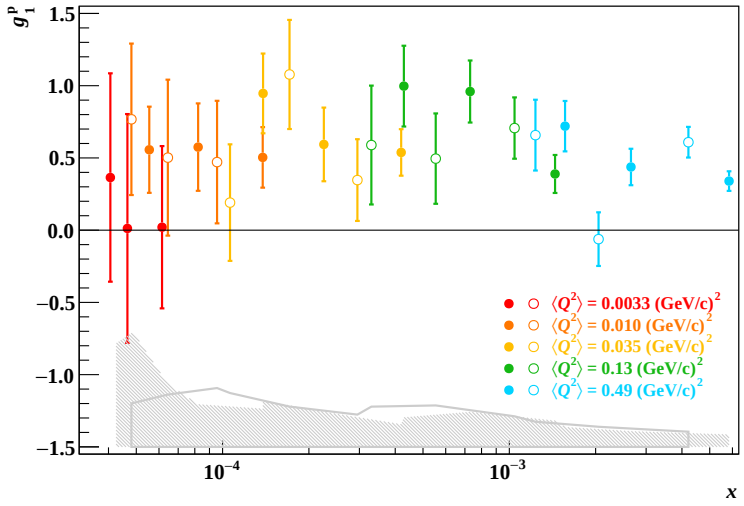

Figure 7.11: Results for $g_1^p(Q^2, x)$ from 2007 and 2011 data (without staggering). The filled and the open circles represent, respectively, the results from 2007 data and from 2011 data. The bands in the bottom of the figure represent the systematic uncertainties of the data (filled for 2007 data and open for 2011 data).

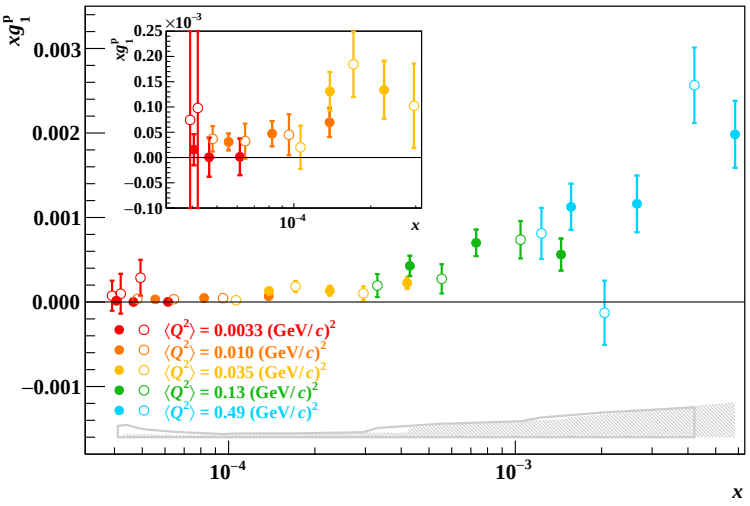

Figure 7.12: Results for $xg_1^p(Q^2, x)$ from 2007 and 2011 data. The filled and the open circles represent, respectively, the results from 2007 data and from 2011 data. The bands in the bottom of the figure represent the systematic uncertainties of the data (filled for 2007 data and open for 2011 data).

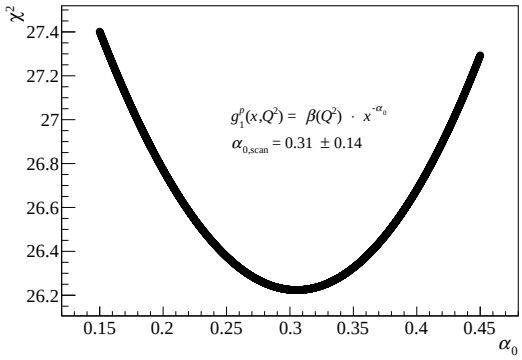

Figure 7.13: Results of a χ^2 scan to a combined fit of the type $g_1^p(Q^2, x) = \beta \cdot x^{-\alpha_0}$ to determine the value of α_0

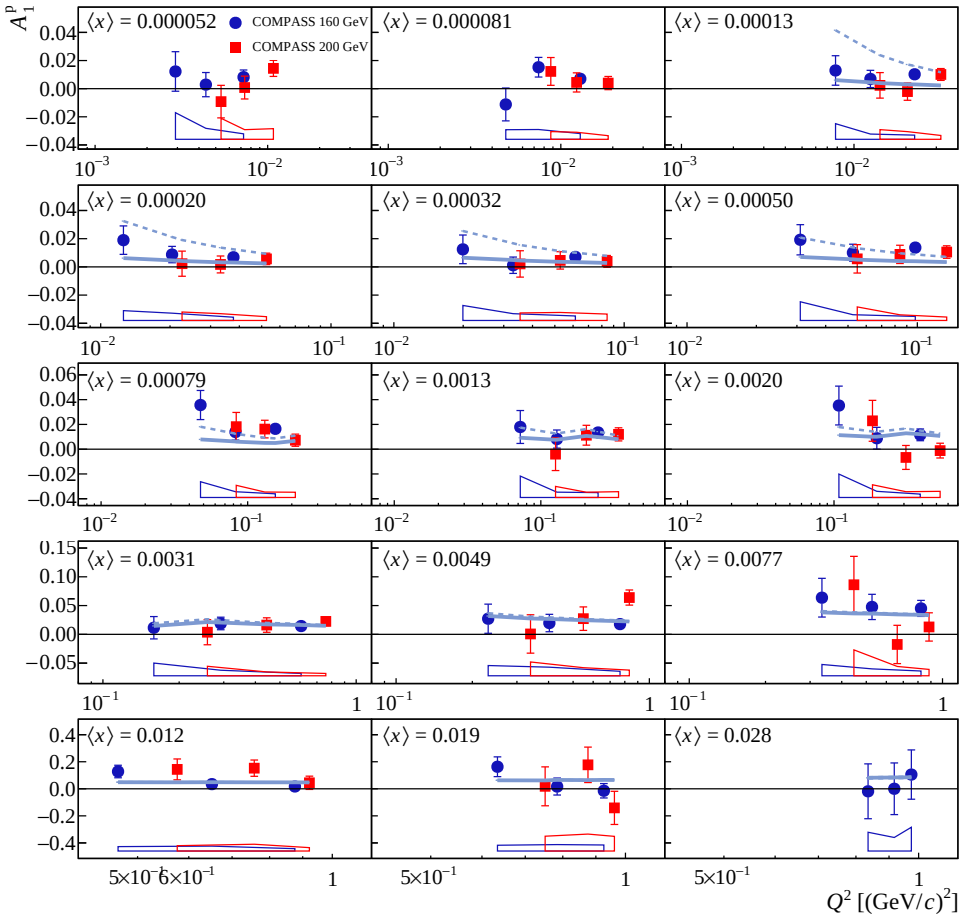

Figure 7.14: Results for $A_1^p(x, Q^2)$: comparison with the model of Ref. [47]. The solid light blue curve corresponds to the first scenario of the model (associated to a value of its parameter $C = -0.24$), while the dashed light blue curve corresponds to the second scenario of the model (associated to a value of its parameter $C = -0.30$). The bands in the bottom of the plots represent the systematic uncertainties of the data.

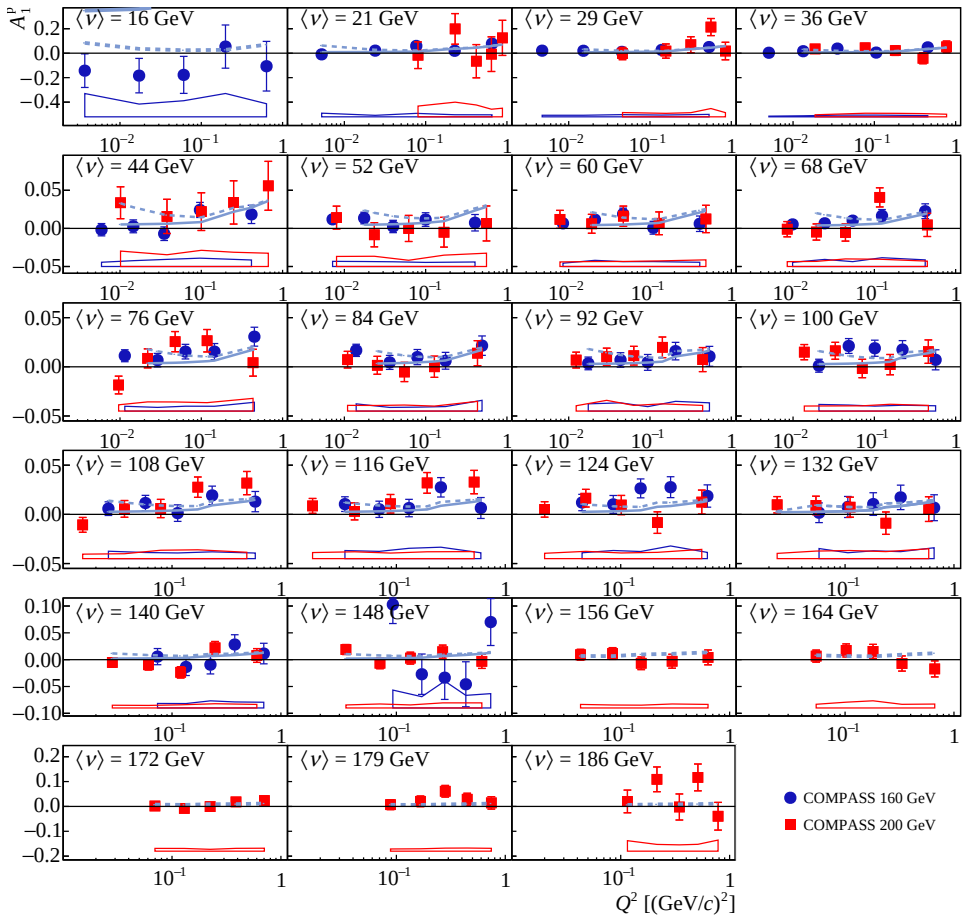

Figure 7.15: Results for $A_1^p(\nu, Q^2)$: comparison with the model of Ref. [47]. The solid light blue curve corresponds to the first scenario of the model (associated to a value of its parameter $C = -0.24$), while the dashed light blue curve corresponds to the second scenario of the model (associated to a value of its parameter $C = -0.30$). The bands in the bottom of the plots represent the systematic uncertainties of the data.

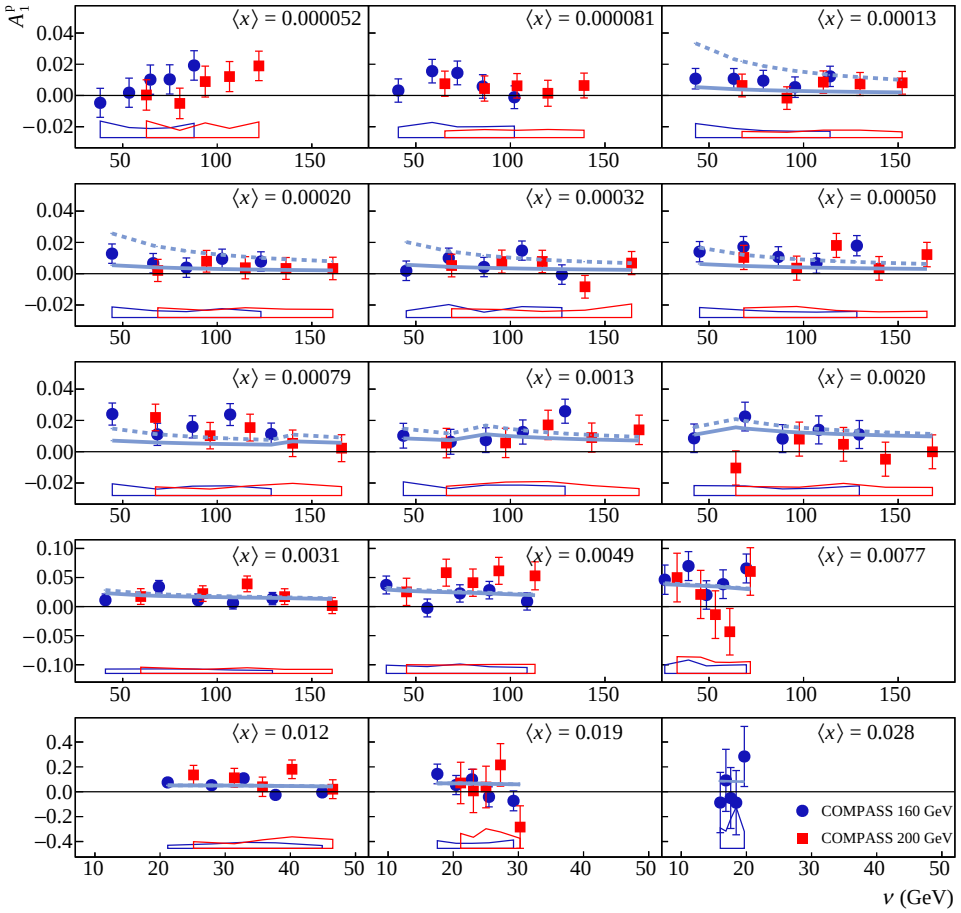

Figure 7.16: Results for $A_1^p(\nu, x)$: comparison with the model of Ref. [47]. The solid light blue curve corresponds to the first scenario of the model (associated to a value of its parameter $C = -0.24$), while the dashed light blue curve corresponds to the second scenario of the model (associated to a value of its parameter $C = -0.30$). The bands in the bottom of the plots represent the systematic uncertainties of the data.

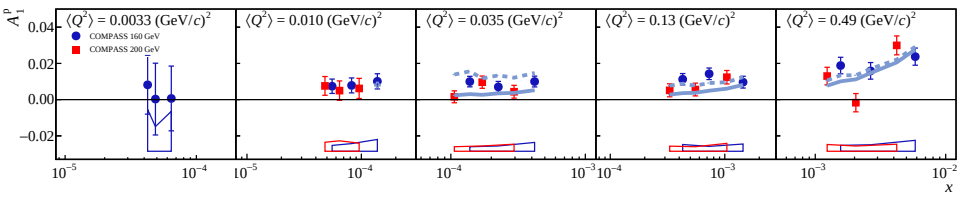

Figure 7.17: Results for $A_1^p(Q^2, x)$: comparison with the model of Ref. [47]. The solid light blue curve corresponds to the first scenario of the model (associated to a value of its parameter $C = -0.24$), while the dashed light blue curve corresponds to the second scenario of the model (associated to a value of its parameter $C = -0.30$). The bands in the bottom of the plots represent the systematic uncertainties of the data.

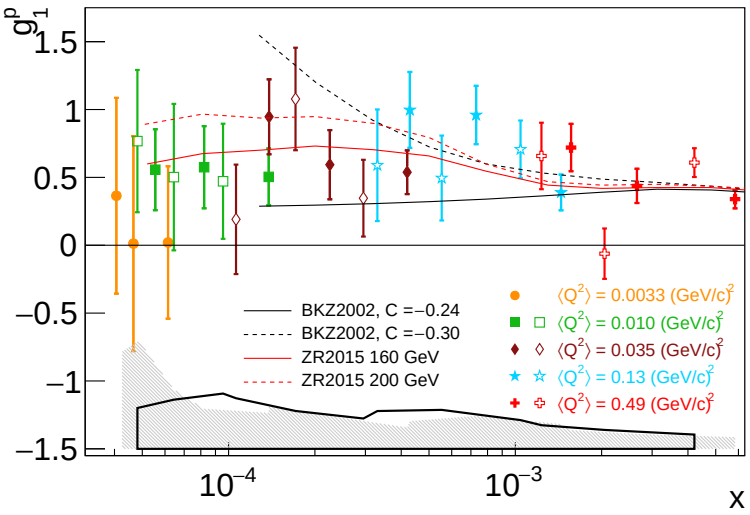

Figure 7.18: Results for $g_1^p(Q^2, x)$: comparison with the models of Ref. [47] and of Ref. [61, 107]. Closed (open) symbols represent 160 (200) GeV data. The bands in the bottom of the figure represent the systematic uncertainties of the data (filled for 2007 data and open for 2011 data).

Chapter 8

Conclusions and Outlook

This thesis began with a theoretical and experimental overview on the subject of the spin structure of the nucleon, in particular at low x and low Q^2. The variables used to describe the process of deep inelastic scattering can still be used in the non-perturbative region studied in this thesis. However, perturbative QCD cannot be directly applied, and fenomenological models have been developed to describe the available data and make preditions in the kinematic domain in the transition from photoproduction, *i.e.* $Q^2 \to 0$ $(\mathrm{GeV}/c)^2$, to the deep inelastic scattering regime, *i.e.* $Q^2 \gtrsim 1$ $(\mathrm{GeV}/c)^2$.

The COMPASS experiment as it operated in 2007 and 2011 was presented. It makes use of a unique naturally polarised muon beam and of a solid state polarised target to measure double spin longitudinal asymmetries. Its trigger system allows to detect scattered muons emitted from the target at very low polar angles, thereby reaching low values of x and Q^2, down to 4×10^{-5} and 10^{-3}, respectively. The detection of an additional particle (hadron) stemming from the interaction vertex permits to reconstruct this vertex with an acceptable precision. This so called "hadron method" was first used by SMC, which also showed that the inclusive asymmetries at low x are not biased by this selection criteria. While the scattered muon is mostly detected in the second spectrometer, the hadron is mostly emitted at large polar angles and is detected in the first spectrometer.

The Detector Control System (DCS) of COMPASS, which is a full and exclusive responsibility of the LIP group participating in the COMPASS Collaboration, was described. The author has been a member of the COMPASS DCS team since 2007. It was shown that the DCS is a complex system comprising elements of software and hardware, and using a multitude of communication protocols, thereby contributing to the efficient operation of the experiment. In what concerns the DCS, an external database as a solution for the storage of the historical values and alerts was one of the developments that allowed to increase the number of monitored and controlled parameters. The DCS has played an important role in the monitorisation of the experiment's calorimeters, giving a first online alert and visualisation of eventual instabilities in these very complex and sensitive detectors. The DCS is an ever changing complex system that has become more and more reliable and a source of information for the experiment operation; the monitoring of its own processes with watchdog mechanisms and monitoring of radiation

levels by subscription to CERN DIP publications are two examples of improvements developed after it started operating.

The measurement of the spin structure of the proton at low x and low Q^2, namely the double longitudinal spin asymmetry A_1^p and the spin-dependent structure function g_1^p, was detailed. The author was the main analyst of this data analysis in the COMPASS Collaboration. The measurement greatly improves the precision as compared to the previous pioneering experiment in that region, the SMC. COMPASS has extended the studied region to lower values of x, accessing *e.g.* three units of $\log_{10} x$. For the first time, non-zero, positive virtual photon-nucleon spin asymmetries A_1^p were measured at such low values of x. All these aspects can be observed in Figs. 8.1 and 8.2.

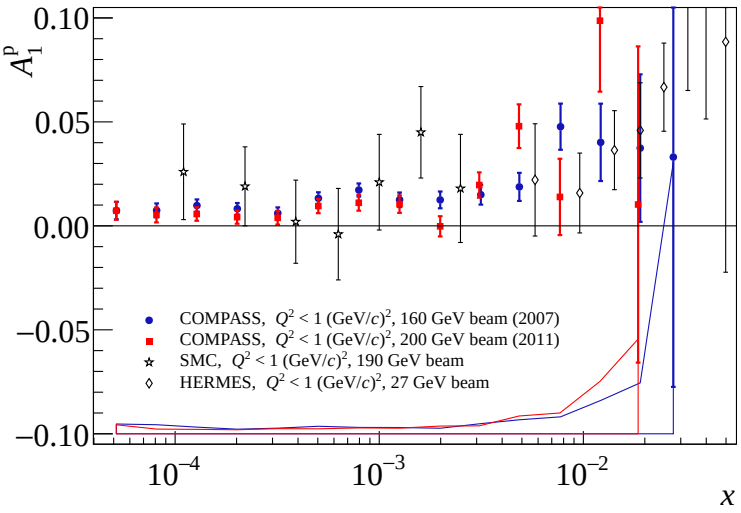

Figure 8.1: Comparison of the spin asymmetry results in bins of x with previous experiments' results. The bands in the bottom of the figure represent the systematic uncertainties of the COMPASS data.

The extraction of A_1^p and g_1^p in the region of low values of x and Q^2 was done for the first time in to two-dimensional bins, as asked by theoretical works. The results of A_1^p and g_1^p as functions of x and Q^2 is shown again in Figs. 8.3 and 8.4. Strong dependencies with the DIS variables predicted by those works were not confirmed by the observations.

Even if the studied region cannot be described simply by perturbative QCD, it was shown that a model that extends perturbative QCD to that region adding also a component to g_1^p in the framework of the GVMD model can describe the data reasonably well, as can be seen in Fig. 8.3.

The future extraction of g_1^d as a function of two kinematic variables from COMPASS data on tape would allow to calculate g_1^{NS} also as a function of two variables and confront the results with theoretical predictions.

There are no measurements of the spin-independent structure function F_2^p nor of the ratio $R = \sigma_L/\sigma_T$ in the region accessed, namely for $Q^2 < 0.2$ (GeV/c)^2, and it thus was necessary to use predictions from a model to extract the structure function g_1^p. One important improvement

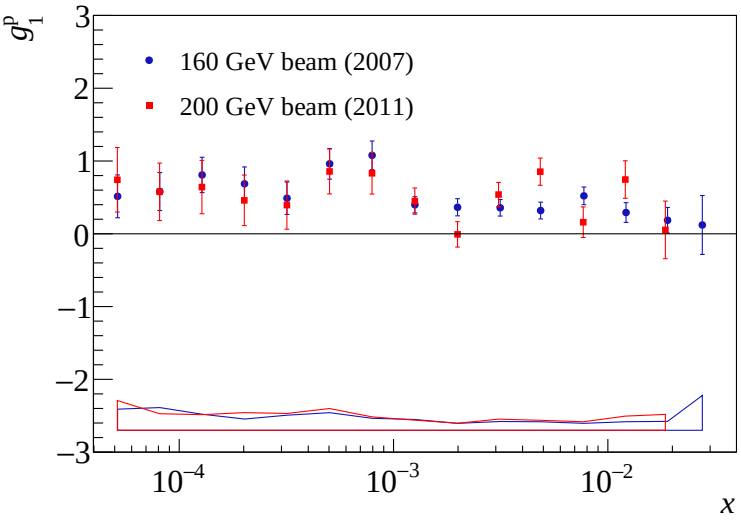

Figure 8.2: Results for $g_1^p(x)$ obtained from 2007 and 2011 data. The bands in the bottom of the figure represent the systematic uncertainties of the data.

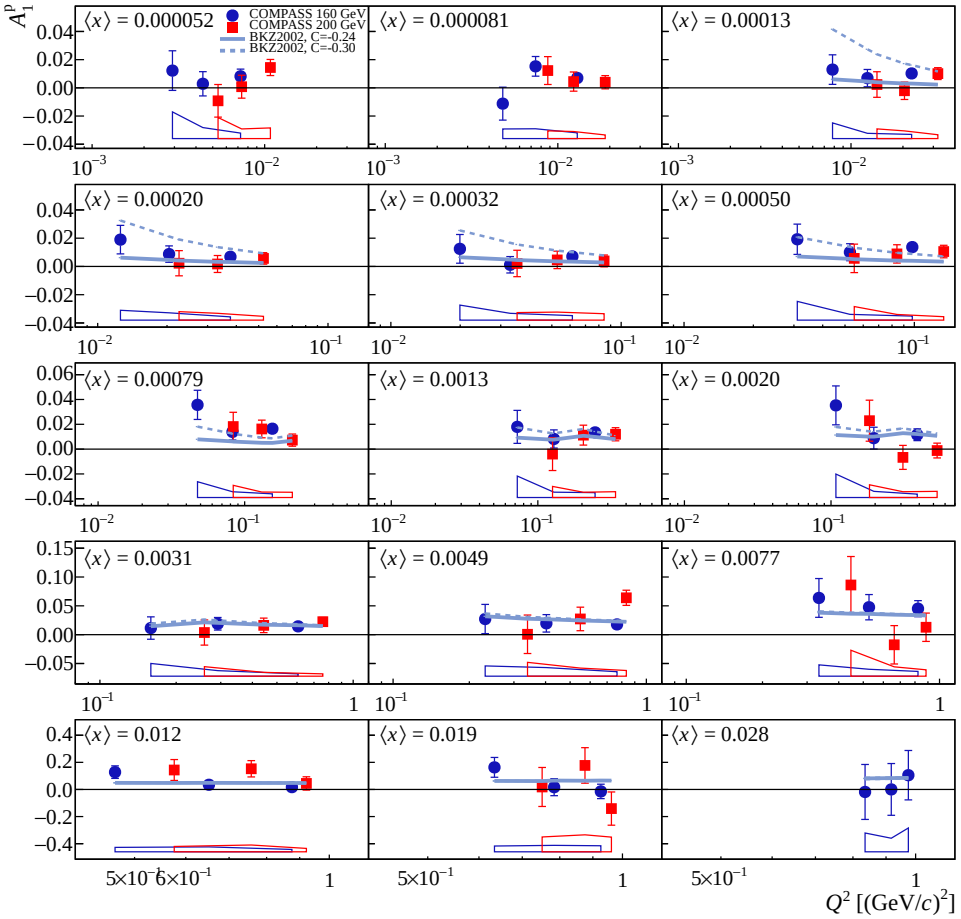

Figure 8.3: Results for $A_1^p(x, Q^2)$ from 2007 and 2011 data and comparison with the model of Ref. [47]. The bands in the bottom of the plots represent the systematic uncertainties of the data.

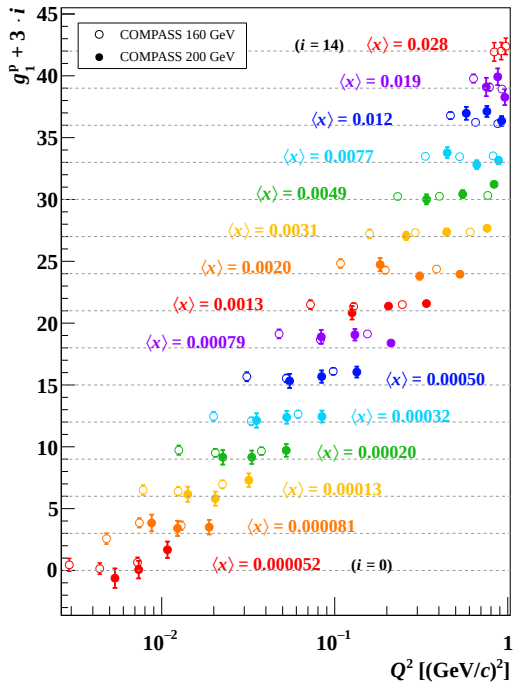

Figure 8.4: Results for $g_1^p(x, Q^2)$ from 2007 and 2011 data.

to the measurement of g_1^p in this region would be to measure those two quantities experimentally in the region of low x and low Q^2. However, they are not easily accessible in COMPASS in the low x and low Q^2 region of the analysis here described, because the triggers covering that phase-space region are mostly semi-inclusive. In addition, one would need measurements at different beam energies, which would require a dedicated data-taking campaing for that purpose.

Furthermore, now that experiments have entered a high precision era with respect to the most fundamental quantities that describe the nucleons, the extraction of A_2 and g_2 becomes a needed ingredient in order to reach a full description of the nucleon dynamics.

The project for a future electron-ion collider (EIC) [109], expected to be built in the USA in the next few years, will allow to further explore the nucleon structure in the low x region of phase space, eventually entering the region where the phenomenon known as parton saturation may occur. This may be relevant to describe extreme astrophysical scenarios, and shed light into unknown aspects of QCD. The actual implementation of the project can be either an eRHIC (a new electron beam colliding with already available high-energy polarised proton or nuclear beams at RICH) at the Brookhaven National Laboratory (BNL) or an ELIC (a new ELectron-Ion Collider working together with the 12 GeV upgraded CEBAF) at the Jefferson Laboratory.

Bibliography

[1] D.M. Dennison. A note on the specific heat of the hydrogen molecule. *Proc. R. Soc. London, Ser. A*, 115:483, 1927. (Cited on page 1.)

[2] I. Estermann and O. Stern. Über die magnetische Ablenkung von Wasserstoffmolekülen und das magnetische Moment des Protons. ii. *Z. Physik*, 85, 1933. (Cited on page 1.)

[3] Geiger H. and Marsden E. On a diffuse reflection of the α-particles. *Proc. R. Soc. A*, 82:495, 1909. (Cited on page 1.)

[4] E. Rutherford. The scattering of alpha and beta particles by matter and the structure of the atom. *Phil. Mag. Ser.6*, 21:669, 1911. (Cited on page 1.)

[5] R. Hofstadter and R.W. McAllister. Electron Scattering From the Proton. *Phys. Rev.*, 98:217–218, 1955. (Cited on page 1.)

[6] J.D. Bjorken. Asymptotic Sum Rules at Infinite Momentum. *Phys. Rev.*, 179:1547–1553, 1969. (Cited on page 1.)

[7] M. Gell-Mann. A Schematic Model of Baryons and Mesons. *Phys. Lett.*, 8:214–215, 1964. (Cited on page 2, 2.)

[8] G. Zweig. An SU(3) model for strong interaction symmetry and its breaking. Version 2. In D.B. Lichtenberg and Simon Peter Rosen, editors, *Developments in the Quark Theory of Hadrons, Vol. 1. 1964 - 1978*, pages 22–101. 1964. (Cited on page 2, 2.)

[9] R.P. Feynman. Very high-energy collisions of hadrons. *Phys. Rev. Lett.*, 23:1415–1417, 1969. (Cited on page 2.)

[10] J. Ashman *et al.* (Spin Muon Collaboration). A Measurement of the Spin Asymmetry and Determination of the Structure Function g_1 in Deep Inelastic Muon-Proton Scattering. *Phys. Lett.*, B206:364, 1988. (Cited on page 2.)

[11] J. Ashman *et al.* (European Muon Collaboration). An Investigation of the Spin Structure of the Proton in Deep Inelastic Scattering of Polarized Muons on Polarized Protons. *Nucl. Phys.*, B328:1, 1989. (Cited on page 2.)

[12] C. Adolph et al. Final COMPASS results on the deuteron spin-dependent structure function g_1^{d} and the Bjorken sum rule. *Phys. Lett.*, B769:34–41, 2017, 1612.00620. (Cited on pages 3, 16.)

[13] C. Adolph et al. Leading-order determination of the gluon polarisation from semi-inclusive deep inelastic scattering data. *Eur. Phys. J.*, C77(4):209, 2017, 1512.05053. (Cited on page 3.)

[14] Nobuo Sato, W. Melnitchouk, S. E. Kuhn, J. J. Ethier, and A. Accardi. Iterative Monte Carlo analysis of spin-dependent parton distributions. *Phys. Rev.*, D93(7):074005, 2016, 1601.07782. (Cited on page 3.)

[15] E.-M. Kabuss. Progress in Spin and 3D Nucleon Structure. *PoS*, DIS2017:018, 2018. (Cited on page 3.)

[16] M. Aghasyan et al. First measurement of transverse-spin-dependent azimuthal asymmetries in the Drell-Yan process. *Phys. Rev. Lett.*, 119(11):112002, 2017, 1704.00488. (Cited on page 3.)

[17] T. Regge. Introduction to complex orbital momenta. *Nuovo Cim.*, 14:951, 1959. (Cited on pages 3, 12.)

[18] P.D.B. Collins. *An Introduction to Regge Theory and High-Energy Physics*. Cambridge Monographs on Mathematical Physics. Cambridge Univ. Press, Cambridge, UK, 2009. (Cited on pages 3, 12.)

[19] C. Alexandrou, K. Cichy, V. Drach, E. Garcia-Ramos, K. Hadjiyiannakou, K. Jansen, F. Steffens, and C. Wiese. Lattice calculation of parton distributions. *Phys. Rev.*, D92:014502, 2015, 1504.07455. (Cited on page 3.)

[20] C. Alexandrou, M. Constantinou, K. Hadjiyiannakou, C. Kallidonis, G. Koutsou, K. Jansen, C. Wiese, and A.V. Avilés-Casco. Nucleon spin and quark content at the physical point. *PoS*, LATTICE2016:153, 2016, 1611.09163. (Cited on page 3.)

[21] H.-W. Lin et al. Parton distributions and lattice QCD calculations: a community white paper. 2017, 1711.07916. (Cited on page 3.)

[22] G. Bali et al. The spin content of the nucleon, Lattice 2017, Granada, June 21, 2017, https://makondo.ugr.es/event/0/session/95/contribution/377. (Cited on page 3.)

[23] S. Collins. Hadron Structure, Lattice 2016, Southampton, 26th July, https://conference.ippp.dur.ac.uk/event/470/session/1/contribution/118. (Cited on page 3.)

[24] C. Lorce and B. Pasquini. Quark Wigner Distributions and Orbital Angular Momentum. *Phys. Rev.*, D84:014015, 2011, 1106.0139. (Cited on page 4.)

[25] PHysics Analysis Software Tools. (Cited on page 4.)

[26] A.S. Nunes, M. Wilfert, V. Andrieux and B. Badełek for the SIDIS subgroup. COMPASS internal release note: Extraction of A_1^p and of g_1^p for $Q^2 < 1$ (GeV/c)^2. September 2013. (Cited on page 4.)

[27] A.S. Nunes, M. Wilfert, M. Stolarski, B. Badełek and the SIDIS subgroup. COMPASS internal release note: Extraction of A_1^p and g_1^p for $Q^2 < 1$ (GeV/c)^2 in two-dimensional bins from the 2007 and 2011 longitudinal data. November 2015. (Cited on page 4.)

[28] A.S. Nunes. Longitudinal double spin asymmetry A_1^p and spin-dependent structure function g_1^p of the proton at low x and low Q^2 from COMPASS. In *Proceedings, 15th Workshop on High Energy Spin Physics (DSPIN-13): Dubna, Russia, Oct 8-12, 2013*, 2014, 1405.5811. (Cited on page 4.)

[29] A.S. Nunes. First results on A_1^p and g_1^p at low x and low Q^2 from COMPASS. *PoS*, DIS2014:221, 2014. (Cited on page 4.)

[30] A.S. Nunes. New COMPASS results on A_1^p and g_1^p and QCD fit. *Nucl. Part. Phys. Proc.*, 258-259:65–68, 2015. (Cited on page 4.)

[31] A.S. Nunes. The spin structure of the proton at low x and low Q^2 in two-dimensional bins from COMPASS. *PoS*, DIS2016:229, 2016, 1606.06612. (Cited on page 4.)

[32] M. Stolarski. Latest Results from the COMPASS Experiment. *Int. J. Mod. Phys. Conf. Ser.*, 40:1660006, 2016. (Cited on page 4.)

[33] B. Badelek. Final COMPASS results on the spin-dependent structure functions g_1^p and g_1^d in the deep-inelastic and nonperturbative regions. *PoS*, DIS2017:247, 2016. (Cited on page 4.)

[34] V. Andrieux. The spin structure function of the proton at low x and low Q^2 from COMPASS. In *22nd International Symposium on Spin Physics (SPIN 2016) Urbana, IL, USA, September 25-30, 2016*, 2016. (Cited on page 4.)

[35] M. Aghasyan *et al.* (COMPASS Collaboration). Longitudinal double-spin asymmetry $A_1^{\rm p}$ and spin-dependent structure function $g_1^{\rm p}$ of the proton at small values of x and Q^2. http://arxiv.org/abs/1710.01014v1. (Cited on page 4.)

[36] P. Bordalo, A.S. Nunes, C. Pires, C. Quintans, and S. Ramos. Control Systems: an Application to a High Energy Physics Experiment (COMPASS). In *Proceedings of the 2012 IEEE International Conference on Automation, Quality and Testing, Robotics (AQTR 2012) 20-25*, 2012, 1206.3709. (Cited on page 4.)

[37] P. Abbon *et al.* (COMPASS Collaboration). The COMPASS Setup for Physics with Hadron Beams. *Nucl. Instr. and Meth. A*, 779:69–115, 2015, 1410.1797. (Cited on pages 4, 25, 25.)

[38] S. E. Kuhn, J.-P. Chen, and E. Leader. Spin Structure of the Nucleon - Status and Recent Results. *Prog. Part. Nucl. Phys.*, 63:1–50, 2009, 0812.3535. (Cited on page 6.)

[39] C. Lorce, B. Pasquini, and M. Vanderhaeghen. Unified framework for generalized and transverse-momentum dependent parton distributions within a 3Q light-cone picture of the nucleon. *JHEP*, 05:041, 2011, 1102.4704. (Cited on page 11.)

[40] Yuri L. Dokshitzer. Calculation of the Structure Functions for Deep Inelastic Scattering and e+ e- Annihilation by Perturbation Theory in Quantum Chromodynamics. *Sov. Phys. JETP*, 46:641–653, 1977. [Zh. Eksp. Teor. Fiz.73,1216(1977)]. (Cited on page 12.)

[41] G. Altarelli and G. Parisi. Asymptotic Freedom in Parton Language. *Nucl. Phys.*, B126:298–318, 1977. (Cited on page 12.)

[42] V. N. Gribov and L. N. Lipatov. Deep inelastic e p scattering in perturbation theory. *Sov. J. Nucl. Phys.*, 15:438–450, 1972. [Yad. Fiz.15,781(1972)]. (Cited on page 12.)

[43] R.L. Heimann. Spin dependent high frequency inelastic electron scattering and helicity flip couplings. *Nucl. Phys.*, B64:429–463, 1973. (Cited on page 12.)

[44] J.R. Ellis and M. Karliner. An Analysis of the Angular Momentum of the Proton. *Phys. Lett.*, B213:73–80, 1988. (Cited on page 12.)

[45] B.L. Ioffe, V.A. Khoze, and L.N. Lipatov. *Hard Processes. Vol. 1: Phenomenology, Quark Parton Model*. 1985. (Cited on page 12.)

[46] B. Badelek, J. Kiryluk, and J. Kwiecinski. (Cited on pages xv, 13.)

[47] B. Badełek *et al.* Spin structure function $g_1(x, Q^2)$ and the DHGHY integral $I(Q^2)$ at low Q^2: Predictions from the GVMD model. *Eur.Phys.J. C*, 26:45, 2002. (Cited on pages xv, xviii, xviii, xviii, xviii, xviii, xviii, 12, 13, 23, 104, 105, 115, 116, 116, 122, 123, 124, 124, 125, 129.)

[48] B.I. Ermolaev *et al.* Comment on the recent COMPASS data on the spin structure function g_1. *Eur.Phys.J. C*, 58:29, 2008. (Cited on pages xv, 14, 23.)

[49] C. Adolph et al. D* and D Meson Production in Muon Nucleon Interactions at 160 GeV/c. *Eur. Phys. J.*, C72:2253, 2012, 1211.1575. (Cited on page 15.)

[50] C. Patrignani *et al.* (Particle Data Group). Review of Particle Physics. *Chin. Phys.*, C40(10):100001, 2016. (Cited on pages 16, 17, 20, 21.)

[51] C. Adolph *et al.* (COMPASS Collaboration). The spin structure function g_1^{p} of the proton and a test of the Bjorken sum rule. *Phys. Lett.*, B753:18–28, 2016, 1503.08935. (Cited on pages 16, 18, 19, 20, 70.)

[52] J. Breitweg *et al.* (ZEUS Collaboration). Measurement of the proton structure function F_2 at very low Q^2 at HERA. *Phys. Lett.*, B487:53–73, 2000, hep-ex/0005018. (Cited on pages 17, 18.)

[53] E.S. Ageev *et al.* (COMPASS Collaboration). Spin asymmetry A_1^d and the spin-dependent structure function g_1^d of the deuteron at low values of x and Q^2. *Phys. Lett.*, B647:330–340, 2007, hep-ex/0701014. (Cited on pages xv, 19.)

[54] R.D. Ball *et al.* (NNPDF Collaboration). Parton distributions for the LHC Run II. *JHEP*, 04:040, 2015, 1410.8849. (Cited on page 21.)

[55] E. R. Nocera, R.D. Ball, S. Forte, G. Ridolfi, and J. (NNPDF Collaboration) Rojo. A first unbiased global determination of polarized PDFs and their uncertainties. *Nucl. Phys.*, B887:276–308, 2014, 1406.5539. (Cited on page 21.)

[56] M.G. Alekseev *et al.* (COMPASS Collaboration). The Spin-dependent Structure Function of the Proton g_1^p and a Test of the Bjorken Sum Rule. *Phys. Lett.*, B690:466–472, 2010, 1001.4654. (Cited on pages 22, 70, 85.)

[57] M.G. Alekseev *et al.* (COMPASS Collaboration). Quark helicity distributions from longitudinal spin asymmetries in muon-proton and muon-deuteron scattering. *Phys. Lett.*, B693:227–235, 2010, 1007.4061. (Cited on page 23.)

[58] C. Adolph *et al.* (COMPASS Collaboration). Longitudinal double spin asymmetries in single hadron quasi-real photoproduction at high p_T. *Phys. Lett.*, B753:573–579, 2016, 1509.03526. (Cited on page 22.)

[59] B. Adeva *et al.* (Spin Muon Collaboration). Erratum: Spin asymmetries A_1 of the proton and the deuteron in the low x and low Q^2 region from polarized high-energy muon scattering [Phys. Rev.D60,072004 (1999)]. *Phys. Rev.*, D62:079902, 2000. [Erratum of: Phys. Rev.D60,072004(1999)]. (Cited on page 24.)

[60] B.I. Ermolaev *et al.* Overview of the spin structure function g_1 at arbitrary x and Q^2. *Riv.Nuovo Cim.*, 33:57, 2010. (Cited on page 23.)

[61] W. Zhu and J. Ruan. Nucleon spin structure. *Int. J. Mod. Phys.*, E24(10):1550077, 2015, 1503.02250. (Cited on pages xviii, 23, 104, 105, 125.)

[62] G. Baum *et al.* (COMPASS Collaboration). Proposal for a common muon and proton apparatus for structure and spectroscopy, March 1996. (Cited on page 25.)

[63] P. Abbon *et al.* (COMPASS Collaboration). The COMPASS experiment at CERN. *Nucl. Instr. and Meth. A*, 577:455–518, 2007, hep-ex/0703049. (Cited on pages 25, 25, 28.)

[64] N. Doble, L. Gatignon, G. von Holtey, and F. Novoskoltsev. The Upgrated muon beam at the SPS. *Nucl. Instrum. Meth.*, A343:351–362, 1994. (Cited on page 28.)

[65] V. Andrieux, A. Ivanov, M. Wilfert and E. Zemlyanichkina. Compass release note for the asymmetry A_1^p and the structure g_1^p. September 2012. (Cited on page 30.)

[66] G. Nukazuka. Target polarisation in 2015. COMPASS Analysis Meeting, 22/06/2016. (Cited on page 31.)

[67] Y. Bai *et al.* FPGA based event building and data acqiusition system for the COMPASS experiment. In *Proceedings, 2015 IEEE Nuclear Science Symposium and Medical Imaging*

Conference (NSS/MIC 2015): San Diego, California, United States, page 7581844, 2016. (Cited on page 34.)

[68] C. Bernet *et al.* The COMPASS trigger system for muon scattering. *Nucl. Instrum. Meth.*, A550:217–240, 2005. (Cited on pages 35, 139.)

[69] G. Aad *et al.* (ATLAS Collaboration). The ATLAS Experiment at the CERN Large Hadron Collider. *JINST*, 3:S08003, 2008. (Cited on page 42.)

[70] S. Chatrchyan *et al.* (CMS Collaboration). The CMS experiment at the CERN LHC. *JINST*, 3:S08004, 2008. (Cited on page 42.)

[71] K. Aamodt *et al.* (ALICE Collaboration). The ALICE experiment at the CERN LHC. *JINST*, 3:S08002, 2008. (Cited on page 42.)

[72] A.A. Alves Jr. *et al.* (LHCb Collaboration). The LHCb Detector at the LHC. *JINST*, 3:S08005, 2008. (Cited on page 42.)

[73] O. Holme *et al.* The JCOP framework. In *Proceedings of the 10th International Conference on Accelerator and Large Experimental Physics Control Systems (ICALEPCS 2005)*, CERN-OPEN-2005-027, Geneva, 2005. (Cited on page 43.)

[74] R. Brun and F. Rademakers. ROOT - An Object Oriented Data Analysis Framework. In *Proceedings of AIHENP'96 Workshop, Nucl. Inst. & Meth. in Phys. Rev. A 389* 1997 *81-86*, Lausanne, 1996. (Cited on page 47.)

[75] OPC Foundation. OLE for Process Control (OPC). (Cited on page 48.)

[76] B.H̃allgren *et al.* The embedded local monitoring board (ELMB) in the LHC front-end I/O control system. In *Proceedings of the Seventh Workshop on Electronics for the LHC Experiments*, CERN 2001-005, CERN/LHCC/2001-034, page 325, Stockholm, 2001. (Cited on page 49.)

[77] G. Gruhler and B. Dreider. CANopen Implementation Guidelines, 1997. (Cited on page 50.)

[78] V.˜*et al.* Baggiolini. The CESAR Project - Using J2EE for Accelerator Controls. In *Proceedings of ICALEPCS2003*, Gyeongju, Korea, 2003. (Cited on page 51.)

[79] CEA-Saclay. Anibus^{TM}. (Cited on page 51.)

[80] R. Konopka. Real time data processing and feature extraction of calorimeter data in COMPASS, 2009. Diploma Thesis. (Cited on page 52.)

[81] J. Pretz. A new method of asymmetry extraction. COMPASS note 2004-11. (Cited on pages 56, 107.)

[82] J.-M. le Goff. Asymmetry extraction. COMPASS note 2004-3. (Cited on pages 56, 107.)

[83] J. Pretz. Comparison of methods to extract an asymmetry parameter from data. *Nucl.Instrum.Meth. A*, 659, 2011. (Cited on page 56.)

[84] K. Gustafsson. Computation of the Dilution Factor for the Year 2002 COMPASS Data. COMPASS note 2003-3. (Cited on page 63.)

[85] A.A. Akhundov *et al. Fortschr. Phys.*, 44:373, 1996. (Cited on page 63.)

[86] J. Bartels, K. J. Golec-Biernat, and H. Kowalski. A modification of the saturation model: DGLAP evolution. *Phys. Rev.*, D66:014001, 2002, hep-ph/0203258. (Cited on pages 65, 94, 94, 94.)

[87] J. Kwiecinski and B. Badelek. Analysis of the Electroproduction Structure Functions in the Low Q^2 Region Combining the Vector Meson Dominance and the Parton Model With Possible Scaling Violation. *Z. Phys.*, C43:251, 1989. (Cited on pages 65, 94, 94.)

[88] B. Badelek and J. Kwiecinski. Electroproduction structure function F_2 in the low Q^2, low x region. *Phys. Lett.*, B295:263–268, 1992. (Cited on pages 65, 94.)

[89] B. Adeva *et al.* (SMC Collaboration). Spin asymmetries A_1 and structure functions g_1 of the proton and the deuteron from polarized high energy muon scattering. *Phys.Rev. D*, 58:112001, 1998. (Cited on pages 65, 76, 76, 94.)

[90] H. Abramowicz and A. Levy. The ALLM parameterization of $\sigma_{tot}(\gamma^* p)$: An Update. hep-ph/9712415, 1997, 9712.415. (Cited on pages 65, 94.)

[91] V. Andrieux. Private comunication. (Cited on page 70.)

[92] J. Koivuniemi. Private comunication. (Cited on page 70.)

[93] V.Yu. Alexakhin *et al.* (COMPASS Collaboration). Spin asymmetry A_1^d and the spin-dependent structure function g_1^d of the deuteron at low values of x and Q^2. *Phys.Lett. B*, 647:330, 2007. (Cited on pages 70, 73, 114, 116.)

[94] M. Stolarski. *Spin structure of the nucleon at low x and low Q^2 in the COMPASS experiment at CERN*. PhD thesis, Warsaw University, 2006. (Cited on page 70.)

[95] COMPASS stability page, http://wwwcompass.cern.ch/compass/software/offline/input/stab/index.html, visited on September 2013. (Cited on pages 71, 71, 73.)

[96] COMPASS Transversity group. Collins and sivers asymmetries from 2007 proton transverse run. COMPASS note 2008-10. (Cited on page 71.)

[97] O.A. Rondon-Aramayo. Corrections to nucleon spin structure asymmetries measured on nuclear polarized targets. *Phys. Rev.*, C60:035201, 1999. (Cited on page 85.)

[98] B. Adeva *et al.* (Spin Muon Collaboration). Measurement of proton and nitrogen polarization in ammonia and a test of equal spin temperature. *Nucl. Instrum. Meth.*, A419:60–82, 1998. (Cited on page 85.)

[99] J. J. Aubert et al. The ratio of the nucleon structure functions $F2_n$ for iron and deuterium. *Phys. Lett.*, 123B:275–278, 1983. (Cited on page 85.)

[100] B. Badełek. COMPASS webpage on F_2, http://wwwcompass.cern.ch/compass/software/offline/input/F2R/F2/, visited on September 2013. (Cited on page 87.)

[101] B. Badełek and J. Kwieciński. Electroproduction structure function F_2 in the low Q^2, low x region. *Phys.Lett. B*, 295:263, 1992. (Cited on page 87.)

[102] M.Alekseev *et al.* (COMPASS Collaboration). Double spin asymmetry in exclusive ρ^0 muoproduction at COMPASS. *Eur.Phys.J.C*, 52:255, 2007. (Cited on page 87.)

[103] I. Akushevich, A. Ilyichev, N. Shumeiko, A. Soroko, and A. Tolkachev. POLARD 2.0 FORTRAN code for the radiative corrections calculation to deep inelastic scattering of polarized particles. *Comput. Phys. Commun.*, 104:201–244, 1997, hep-ph/9706516. (Cited on page 87.)

[104] A.S. Nunes, M. Wilfert, V. Andrieux, and B. Badełek. Extraction of A_1^p and of g_1^p for $Q^2 < 1$ (GeV/c)^2 from 2007 and 2011 longitudinal data. September 2013. (Cited on pages 89, 107.)

[105] HEPDATA (Durham High Energy Physics Database). (Cited on page 94.)

[106] K. Abe *et al.* (E143 Collaboration). Measurements of the proton and deuteron spin structure functions g_1 and g_2. *Phys.Rev. D*, 58, 1998. (Cited on page 94.)

[107] J. Ruan. Private comunication. (Cited on pages xviii, 104, 105, 125.)

[108] M Stolarski B. Badelek A.S. Nunes, M. Wilfert and the SIDIS subgroup. Release note "Extraction of A_1^p and g_1^p for $Q^2 < 1$ (GeV/c)^2 in two-dimensional bins from the 2007 and 2011 longitudinal data". November 2015. (Cited on page 108.)

[109] A. Accardi et al. Electron Ion Collider: The Next QCD Frontier. *Eur. Phys. J.*, A52(9):268, 2016, 1212.1701. (Cited on page 130.)

[110] J. Barth, J. Bernhard, E.M. Kabuss, N. du Fresne and B. Veit. Trigger configuration summary, 2002-2012. COMPASS note 2016-4. (Cited on page 139.)

Appendix A

Data-taking Conditions

In this Appendix, details about the conditions of the COMPASS data taking, and in particular the longitudinally polarised proton data-taking campaigns of 2007 and 2011, are presented.

In Table A.1 there is information that is specific for the programs with polarised beams and polarised targets, for the years of 2007 and 2011.

Year	Beam		Target			
	Particles	Energy (GeV)	Material	Cells	Magnetic field (T)	Acceptance (mrad)
2007	$\overrightarrow{\mu}^+$	160	proton (NH_3)	3	long. ±1.0; transv. 0.63	±180
2011	$\overrightarrow{\mu}^+$	200	proton (NH_3)	3	long. ±2.5	±180

Table A.1: Polarised target conditions for data taking of COMPASS with a polarised muon beam and a polarised target in 2007 and 2011. The target magnetic field is the one in place during the physical measurements (the solenoid for the longitudinal target polarisation and the dipole for the transverse field polarisation), while during the polarisation build-up the solenoid field of 2.5 T was always used. The last column indicates the polar angle of the target cylindrical barrel, as measured from the most upstream point in the axis of the target volume.

A general description of the trigger elements and logic is given in Ref. [68]. The details on the triggers used during the 2007 longitudinal data taking and the 2011 data taking can be found in Ref. [110].

A summary of the beam characteristics and dead times is presented in Table A.2. Note the reduction by a factor of the order of 10^{-5} of the proton flux impinging in the T6 primary beryllium target and the positive muon flux that reaches the COMPASS hall. The quantity denoted by Δt_{spill} is the duration of the slow extraction of protons of the SPS to the North Area experiments, the so called "flat top", during which the magnets of the SPS maintain their maximum nominal current.

The DAQ dead times are mainly constrained by the time gates programmed at the level of the front ends of some of the detectors, whereas the veto dead times are related to the time that it takes to process events triggered by the hodoscopes of the Veto system (intended to reject events that would otherwise be triggered halo muons and recorded).

The composition of each trigger, *i.e.* the elements entering its logics, for the 2007 data-

Year	rough p flux (spill^{-1})	rough μ^+ flux (spill^{-1})	Δt_{spill} (s)	Δt_{SC} (s)	DT_{DAQ}	DT_{Veto}	Programm
2007	$1.4 \cdot 10^{13}$	$2.0 \cdot 10^{8}$	4.8	16.8	13 %	19 %	L/T
2011	$2.4 \cdot 10^{13}$	$1.0 \cdot 10^{8}$	9.6	46.8	6 %	11 %	L

Table A.2: Beam intensity and dead times during the years 2007 and 2011 (L=longitudinal, T=transverse). The proton flux indicated is the one impinging at the T6 beryllium target, which may be a fraction of the total extracted from the SPS, because this may be distributed to other fixed target experiments; DT stands for dead time; Δt_{spill} is the duration of the slow extraction ("flat top") from the SPS; Δt_{SC} is the duration of the SPS super-cycle. During the two years, a NH_3 target was used.

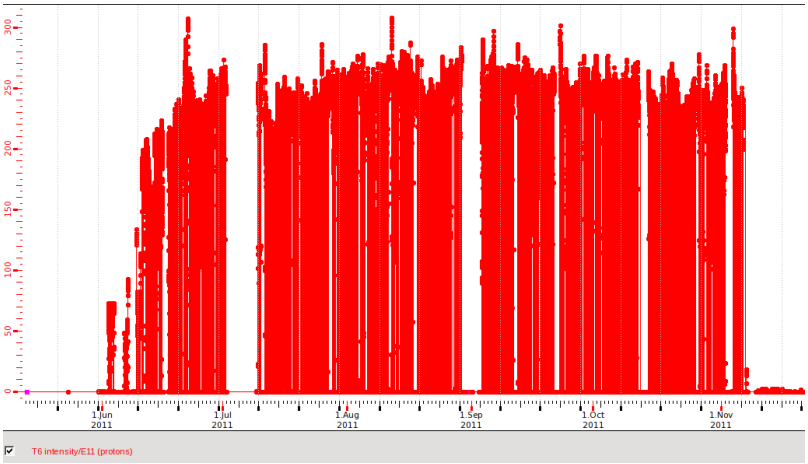

Figure A.1: Proton beam intensity per spill impinging in the T6 primary target in 2011, as recorded by the Detector Control System. The average proton beam intensity was about 2.4×10^{13} protons per spill.

General:	
Veto	VI01 || VI02 || Vbl || VO1 || Vupdown
x	matrix condition
Inclusive triggers:	
MTincl	(HM04 x HM05) && !Veto
OT	(HO03 x HO04) && !Veto
Semi-inclusive triggers:	
IT	(HI04 x HI05) && (HCAL1$_{\text{low thr}}$ || HCAL2$_{\text{low thr}}$ || ECAL1$_{\text{low thr}}$) ~~&& !Veto~~
MT	MTincl && (HCAL1$_{\text{low thr}}$ || HCAL2$_{\text{low thr}}$ || ECAL1$_{\text{low thr}}$)
LT	(HL04 x HL05) && (HCAL1$_{\text{low thr}}$ || HCAL2$_{\text{low thr}}$ || ECAL1$_{\text{low thr}}$) && !Veto
Calorimetric trigger:	
CT	(HCAL1$_{\text{high thr}}$ || HCAL2$_{\text{high thr}}$ || ECAL1$_{\text{high thr}}$)

Table A.3: Trigger composition for the 2007 longitudinal proton run. The short names of the triggers were introduced in Table 3.2 whereas the location of the individual trigger hodoscopes in the experiment is indicated in Fig. 3.12. The matrix conditions are illustrated in 3.13. Each matrix represents in its columns and lines, respectively, two sets of slabs of two hodoscope planes from one trigger system; in red are the coincidences that give rise to a trigger, that is, for which an event is recorded.

taking, is shown in Table A.3. The elements can be hodoscopes, vetos and calorimeters.

The Large Q^2 Trigger (LargeQ2) was not used in the production of the data. The thresholds for the Calorimeter Trigger (CT) components were: 3(4) MIPS for HCAL1(HCAL2) and 4 GeV for ECAL1 (Note 2008-07, p.6). In 2007, the inclusive triggers (*i.e.* without the calorimeters in the trigger condition) were: Outer Trigger (OT) and Inclusive Middle Trigger (inclMT). In 2011, the Ladder Trigger (LT) was changed to become an inclusive trigger, *i.e.* the calorimeter condition was removed from its definition.

Appendix B

Detectors

In Table B.1, the detectors of the COMPASS experiment are listed, grouped by their positions and functions in the spectrometer.

Station	# of dets.	Planes per det.	# of ch. per det.	Active area $X \times Y$ (cm^2)	Resolution
			Beam detectors		
BM01-04	4	Y	64	$6-12 \times 9-23$	$\sigma_s = 1.3-2.5$ mm, $\sigma_t = 0.3$ ns
BM05	2	Y	64	12×16	$\sigma_s = 0.7$ mm, $\sigma_t = 0.5$ ns
BM06	2	Y	128	12×16	$\sigma_s = 0.4$ mm, $\sigma_t = 0.5$ ns
SciFi 1,2	2	XY	192	3.9×3.9	$\sigma_s = 130\,\mu$m, $\sigma_t = 0.4$ ns
Silicon	2	$XYUV$	2304	5×7	$\sigma_s = 8-11\,\mu$m, $\sigma_t = 2.5$ ns
			Large angle spectrometer		
SciFi 3,4	2	XYU	384	5.3×5.3	$\sigma_s = 130\,\mu$m, $\sigma_t = 0.4$ ns
Micromegas	12	$X/Y/U/V$	1024	40×40	$\sigma_s = 90\,\mu$m, $\sigma_t = 9$ ns
DC	3	$XYUV$	1408	180×127	$\sigma_s = 190\,\mu$m
Straw	9	$X/Y/U/V$	892	323×280	$\sigma_s = 190\,\mu$m [a]
GEM 1-4	8	XY/UV	1536	31×31	$\sigma_s = 70\,\mu$m, $\sigma_t = 12$ ns
SciFi 5	1	XY	320	8.4×8.4	$\sigma_s = 170\,\mu$m, $\sigma_t = 0.4$ ns
RICH-1	8	1 (pads)	10368	60×120	$\sigma_{ph} = 1.2$ mrad $\sigma_{ring} = 0.55$ mrad (for $\beta = 1$)
MWPC A*	1	$XUVY$	2768	178×120	$\sigma_s = 1.6$ mm
HCAL1	1	1	480	420×300	$\Delta E/E = 0.59/\sqrt{E/\mathrm{GeV}} \oplus 0.08$
MW1	8	X/Y	1184/928	473×405	$\sigma_s = 3$ mm
			Small angle spectrometer		
GEM 5-11	14	XY/UV	1536	31×31	$\sigma_s = 70\,\mu$m, $\sigma_t = 12$ ns
MWPC A	7	XUV	2256	178×120	$\sigma_s = 1.6$ mm
SciFi 6	1	XYU	462	10×10	$\sigma_s = 210\,\mu$m, $\sigma_t = 0.4$ ns
SciFi 7	1	XY	286	10×10	$\sigma_s = 210\,\mu$m, $\sigma_t = 0.4$ ns
SciFi 8	1	XY	352	12.3×12.3	$\sigma_s = 210\,\mu$m, $\sigma_t = 0.4$ ns
Straw	6	$X/Y/U/V$	892	323×280	$\sigma_s = 190\,\mu$m [a]
Large area DC	6	$XY/XU/XV$	500	500×250	$\sigma_s = 0.5$ mm
ECAL2	1	1	2972	245×184	$\Delta E/E = 0.06/\sqrt{E/\mathrm{GeV}} \oplus 0.02$
HCAL2	1	1	216	440×200	$\Delta E/E = 0.66/\sqrt{E/\mathrm{GeV}} \oplus 0.05$
MWPC B	6	XU/XV	1504	178×90	$\sigma_s = 1.6$ mm
MW2	2	XYV	840	447×202	$\sigma_s = 0.6-0.9$ mm

[a] Resolution measured for 6 mm straw tubes only, corresponding to an active area of $110 \times 350\,\mathrm{cm}^2$

Table B.1: Overview of detectors used in COMPASS, together with their respective main parameters, grouped according to their geometrical positions along the beam line (stations) and functions in the spectrometer.

Appendix C

Systematic Studies

In this Appendix, the results of the tests done for the search of possible sources of false asymmetries are shown. From Fig. C.1 to Fig. C.16, the tests done on $A_1^p(x)$ from 2007 data are presented; the tests done on $A_1^p(nu)$ from 2007 data are shown from Fig. C.17 to Fig. C.32. The test done on $A_1^p(x)$ from 2011 data are show from Fig. C.33 to Fig. C.48 and the tests for $A_1^p(\nu)$ from 2011 data are in Fig. C.49 to Fig. C.64. The tests explanation is detailed in 6.7.2. With respect to the tests done, the results are ordered

- Different methods of asymmetry extraction. The results of the tests are sho Figs. C.1, C.17, C.33 and C.49.
- Global vs. consecutive configurations. The results of the tests are shown in Figs. C.2, C.18, C.34 and C.50, the results using the global and the consecutive configuration are shown.
- Fake configurations. The results of the tests are shown in Figs. C.3, C.19, C.35 and C.51.
- C-C/U-D.The results of the tests are shown in Figs. C.4, C.20, C.36 and C.52.
- Day/night. The results of the tests are show in Figs C.5, C.21, C.38 and C.53.
- Microwave settings. The results of the tests are show in Figs C.7, C.23, C.39 and C.55.
- Top/bottom μ'. The results of the tests are show in Figs C.9, C.25, C.41 and C.57.
- Left/right μ'. The results of the tests are show in Figs C.11, C.27, C.43 and C.59.
- Inner/outer PV. The results of the tests are show in Figs C.13, C.29, C.45 and C.61.
- Upstream/downstream PV. The results of the tests are show in Figs C.15, C.31, C.47 and C.63.

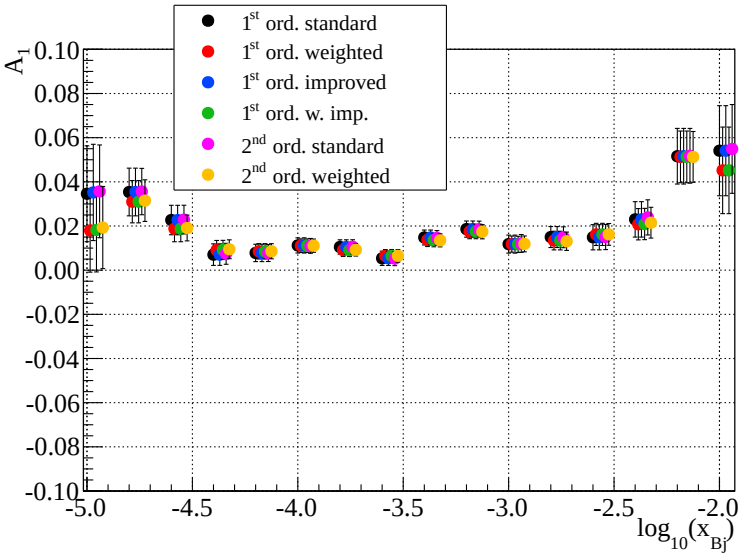

Figure C.1: Experimental $A_1^p(x)$ obtained from 2007 data, using six methods of asymmetry extraction.

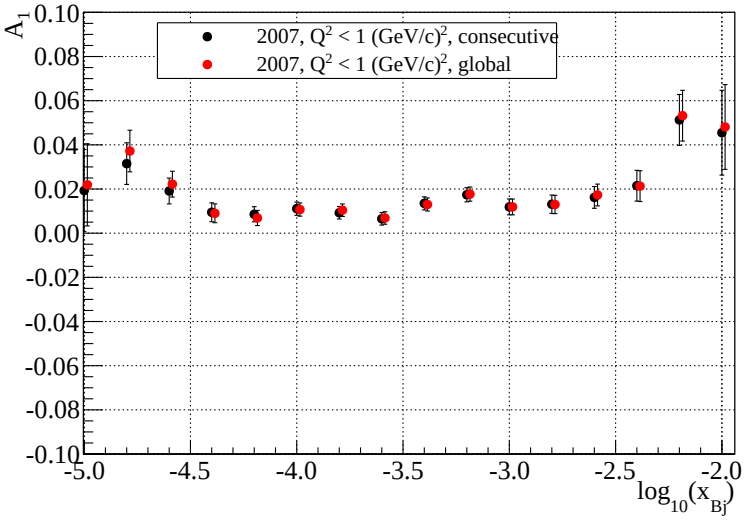

Figure C.2: Experimental $A_1^p(x)$ obtained from 2007 data, using the global and the consecutive configurations.

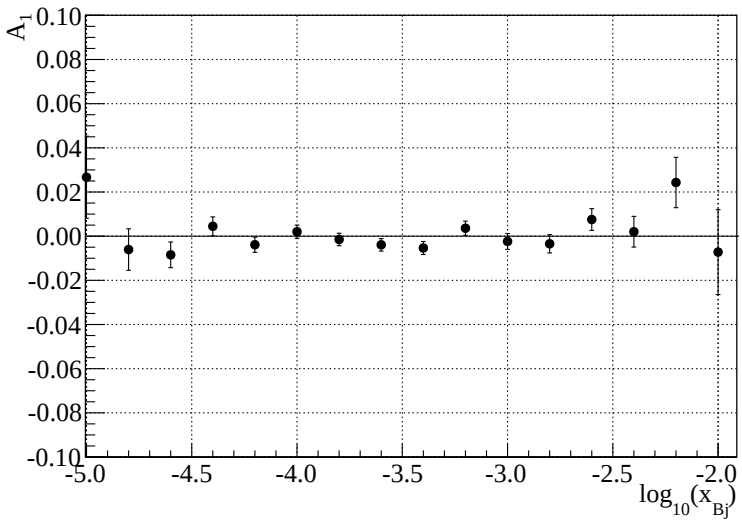

Figure C.3: Experimental $A_1^p(x)$ obtained from 2007 data, using data grouped according to fake configurations.

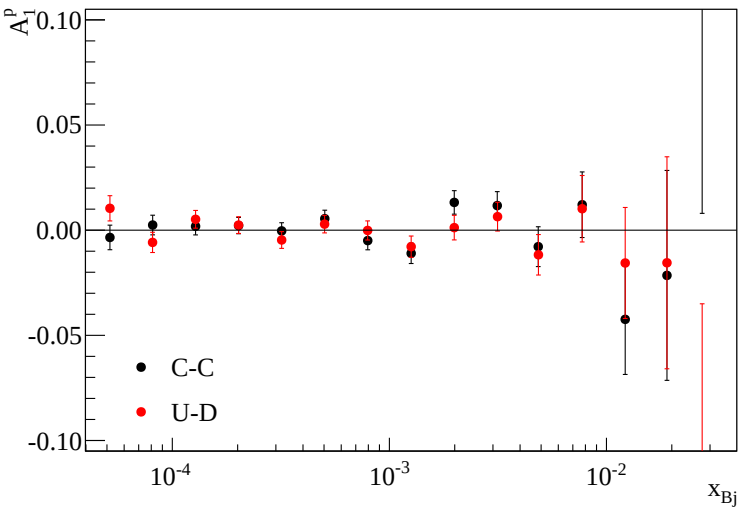

Figure C.4: Experimental $A_1^p(x)$ obtained from 2007 data, using data from the upstream and downstream target cells or the two halves of the central target cell.

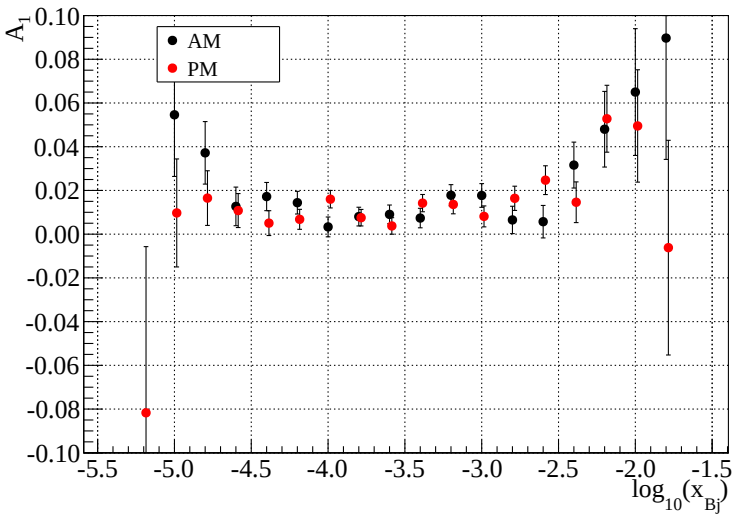

Figure C.5: Experimental $A_1^p(x)$ obtained from 2007 data, using data taken during the "day" and the "night".

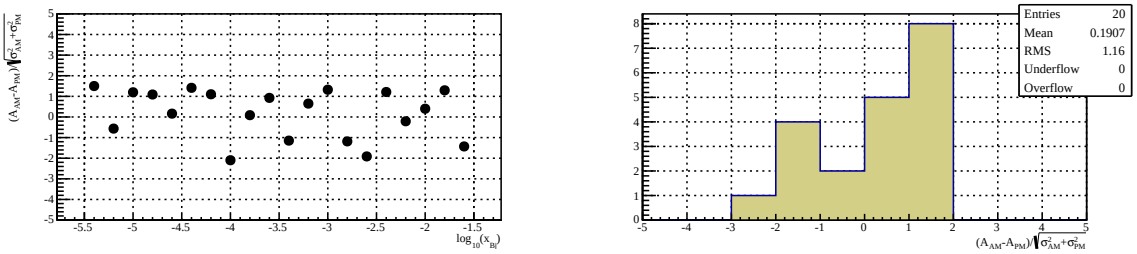

Figure C.6: Pulls of the experimental $A_1^p(x)$ obtained from 2007 data, using data taken during the "day" and the "night".

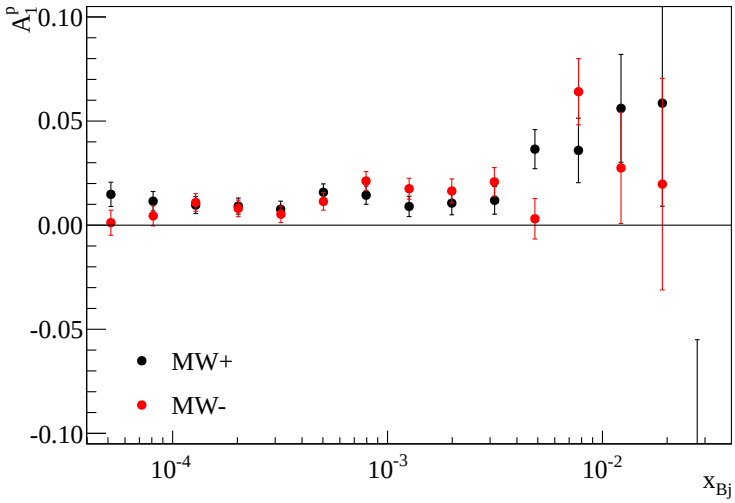

Figure C.7: Experimental $A_1^p(x)$ obtained from 2007 data, using the two microwave settings.

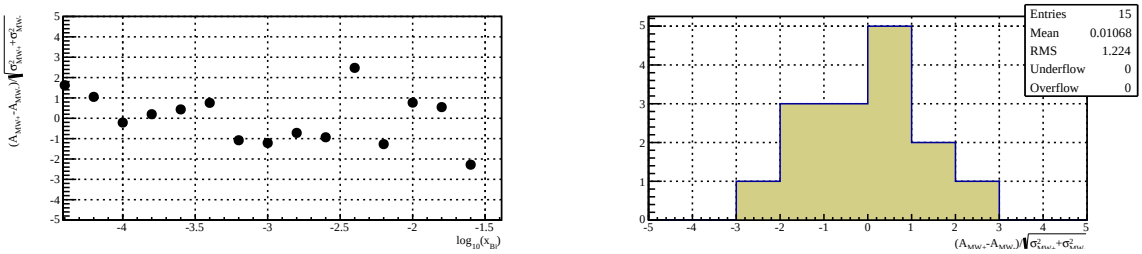

Figure C.8: Pulls of the experimental $A_1^p(x)$ obtained from 2007 data, using the two microwave settings.

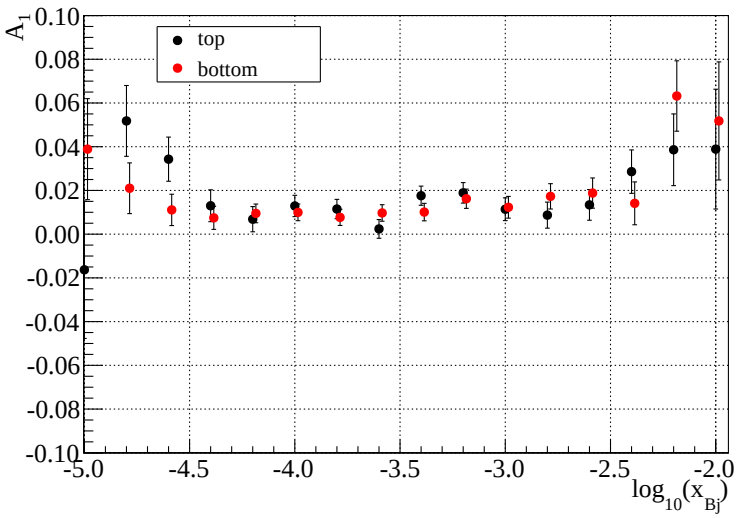

Figure C.9: Experimental $A_1^p(x)$ obtained from 2007 data, using data with the scattered muon directed to the top or the bottom part of the spectrometer.

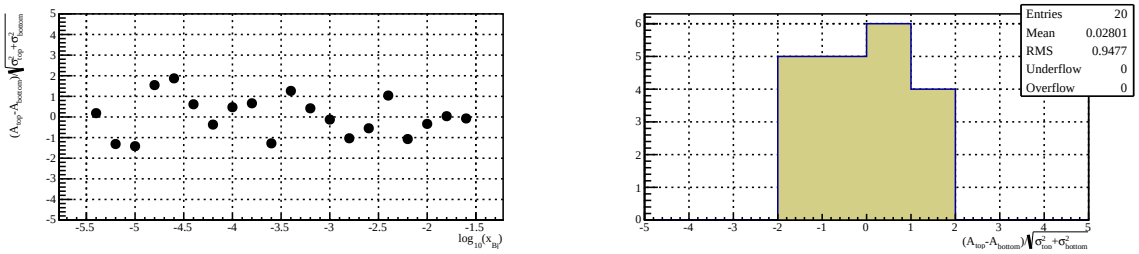

Figure C.10: Pulls of the experimental $A_1^p(x)$ obtained from 2007 data, using data with the scattered muon directed to the top or the bottom part of the spectrometer.

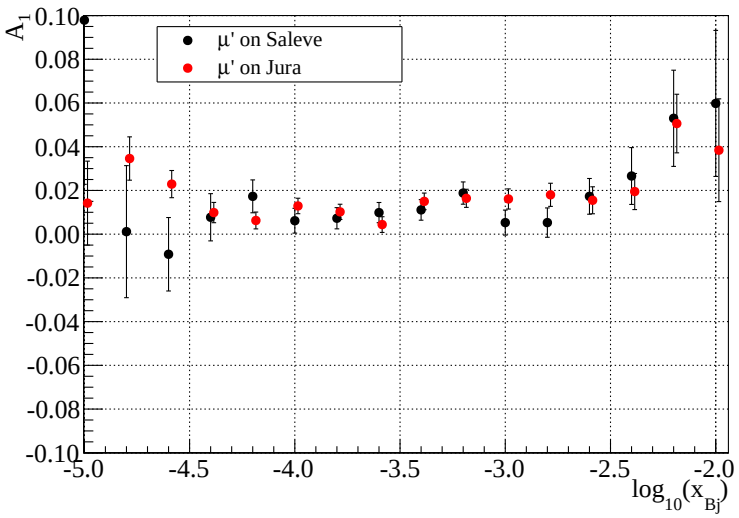

Figure C.11: Experimental $A_1^p(x)$ obtained from 2007 data, using data with the scattered muon directed to the left or the right part of the spectrometer.

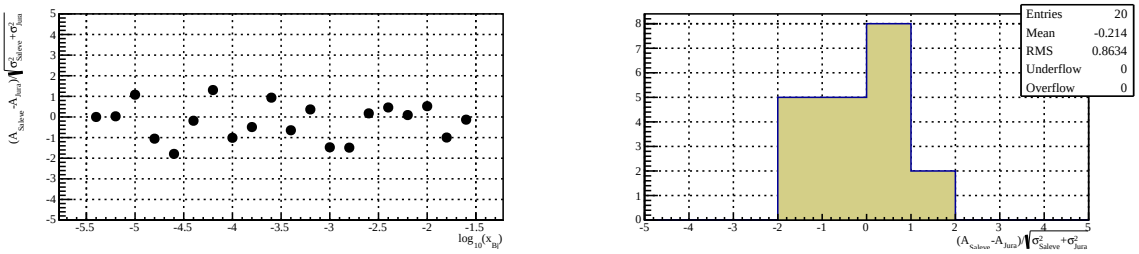

Figure C.12: Pulls of the experimental $A_1^p(x)$ obtained from 2007 data, using data with the scattered muon directed to the left or the right part of the spectrometer.

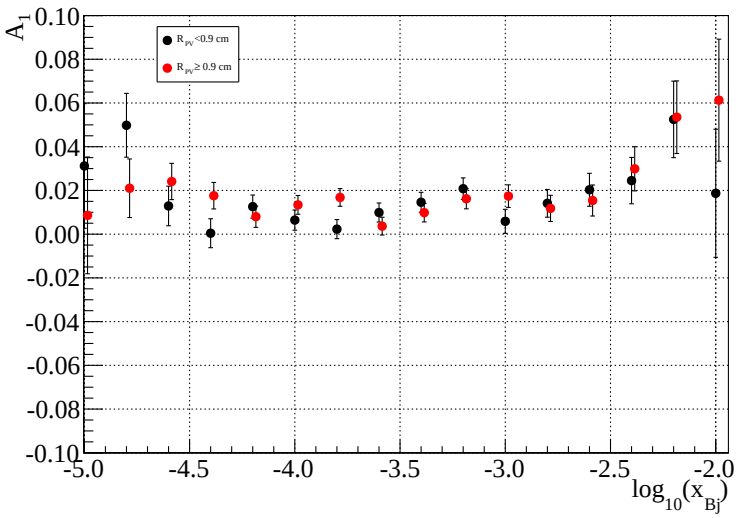

Figure C.13: Experimental $A_1^p(x)$ obtained from 2007 data, using data with a primary vertex in the inner or the outer part of the target.

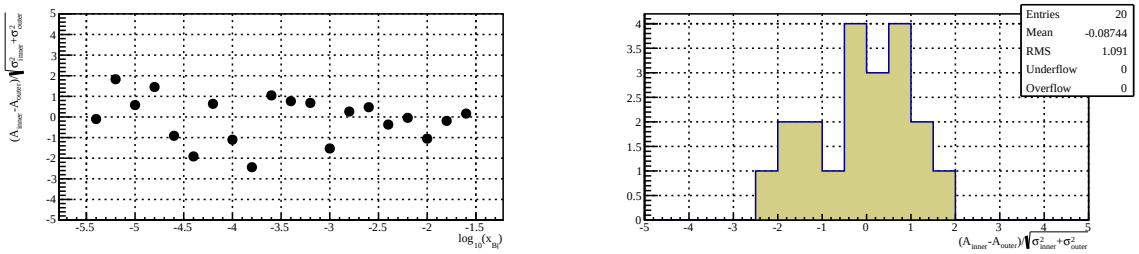

Figure C.14: Pulls of experimental $A_1^p(x)$ obtained from 2007 data, using data with a primary vertex in the inner or the outer part of the target.

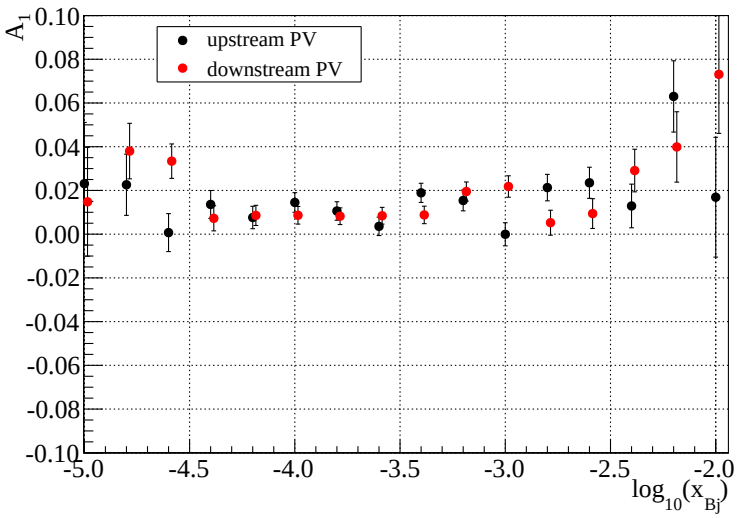

Figure C.15: Experimental $A_1^p(x)$ obtained from 2007 data, using data with a primary vertex in the upstream or the downstream half of the target.

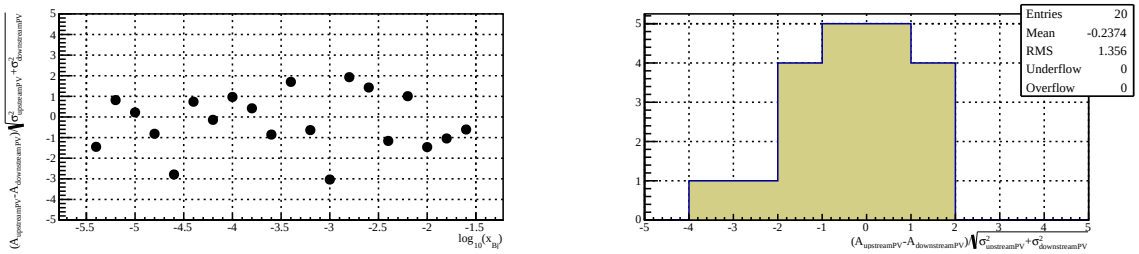

Figure C.16: Pulls of the experimental $A_1^p(x)$ obtained from 2007 data, using data with a primary vertex in the upstream or the downstream half of the target.

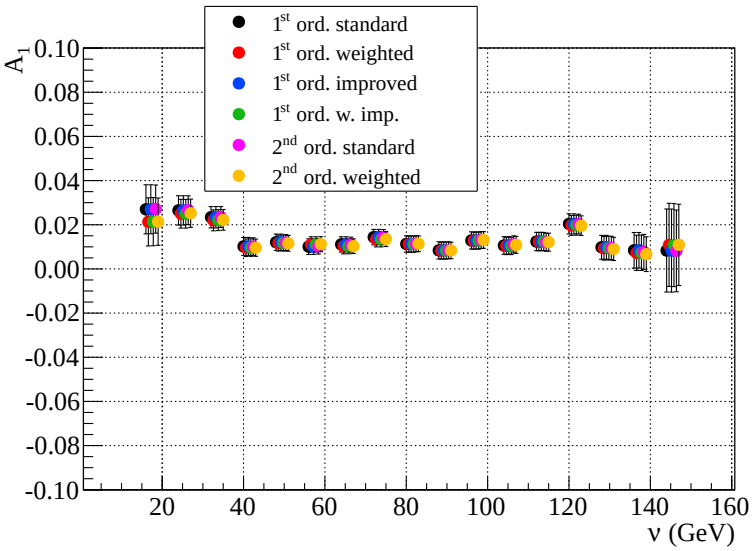

Figure C.17: Experimental $A_1^p(\nu)$ obtained from 2007 data, using six methods of asymmetry extraction.

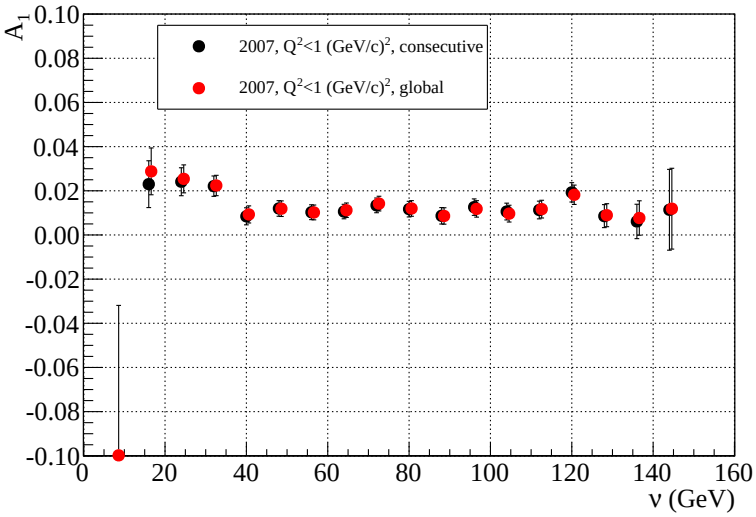

Figure C.18: Experimental $A_1^p(\nu)$ obtained from 2007 data, using the global and consecutive configurations.

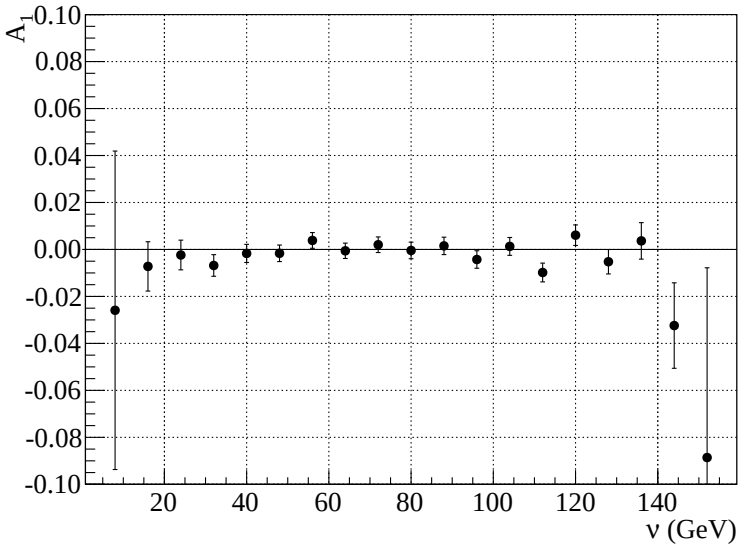

Figure C.19: Experimental $A_1^p(\nu)$ obtained from 2007 data, using data grouped according to fake configurations.

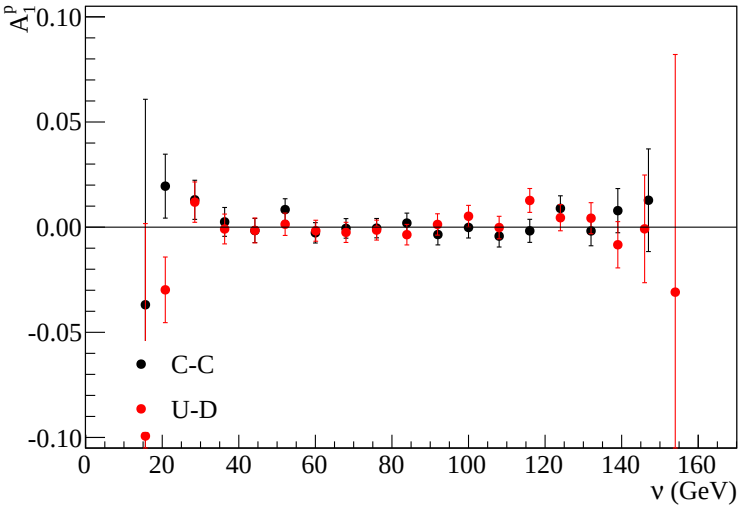

Figure C.20: Experimental $A_1^p(\nu)$ obtained from 2007 data, calculating the asymmetries either from the upstream and the downstream target cells, or from the two upstream and downstream halves of the central target cell.

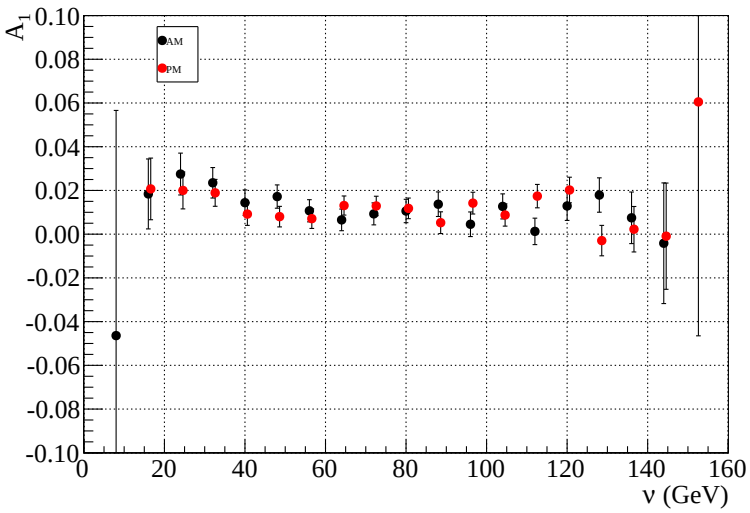

Figure C.21: Experimental $A_1^p(\nu)$ obtained from 2007 data, using data taken during the "day" and the "night".

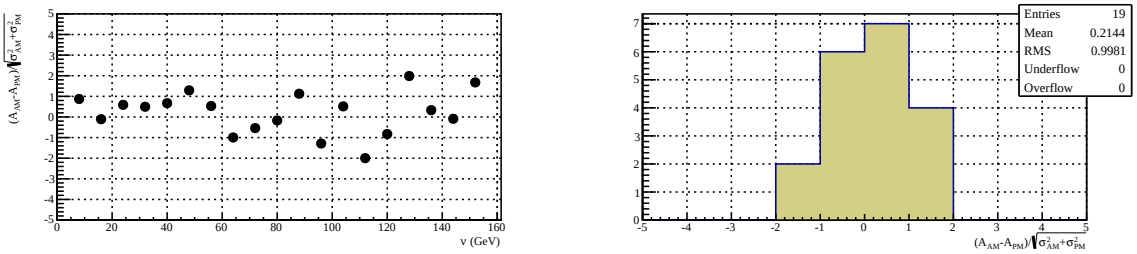

Figure C.22: Pulls of the experimental $A_1^p(\nu)$ obtained from 2007 data, using data taken during the "day" and the "night".

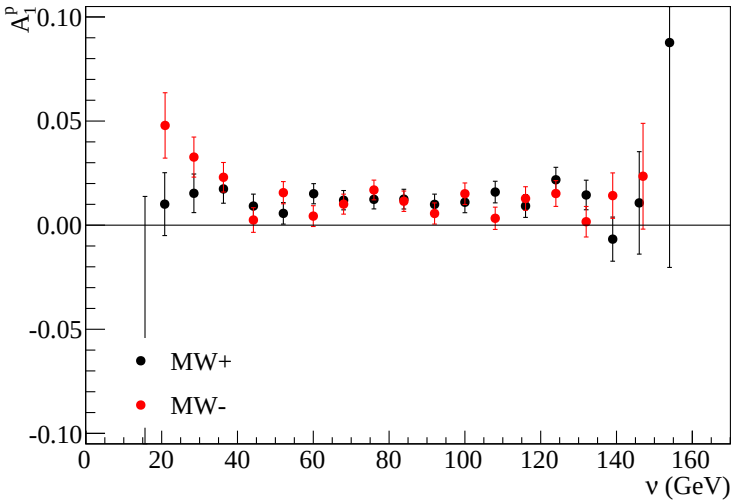

Figure C.23: Experimental $A_1^p(\nu)$ obtained from 2007 data, using the two different microwave settings. No significant false asymmetry is observed.

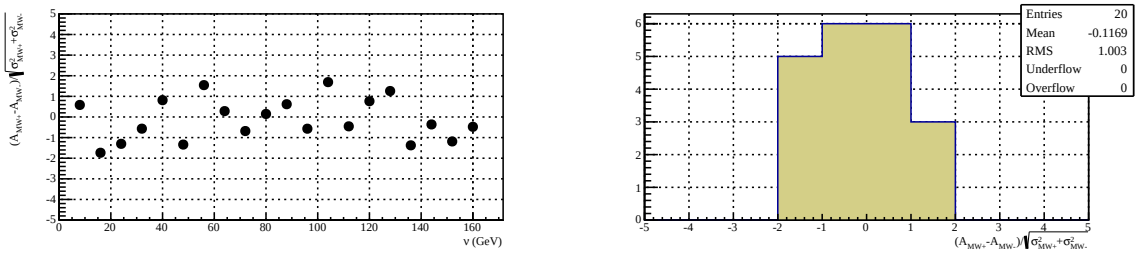

Figure C.24: Pulls of the experimental $A_1^p(\nu)$ obtained from 2007 data, using the two different microwave settings.

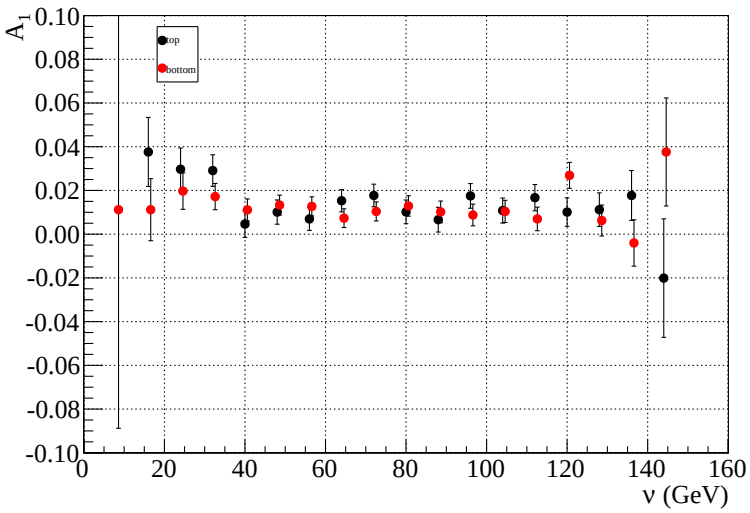

Figure C.25: Experimental $A_1^p(\nu)$ obtained from 2007 data, using data with the scattered muon directed to the top or the bottom part of the spectrometer.

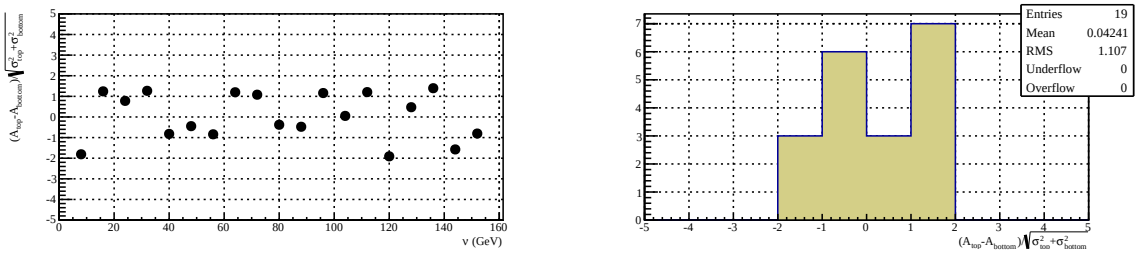

Figure C.26: Pulls of the experimental $A_1^p(\nu)$ obtained from 2007 data, using data with the scattered muon directed to the top or the bottom part of the spectrometer.

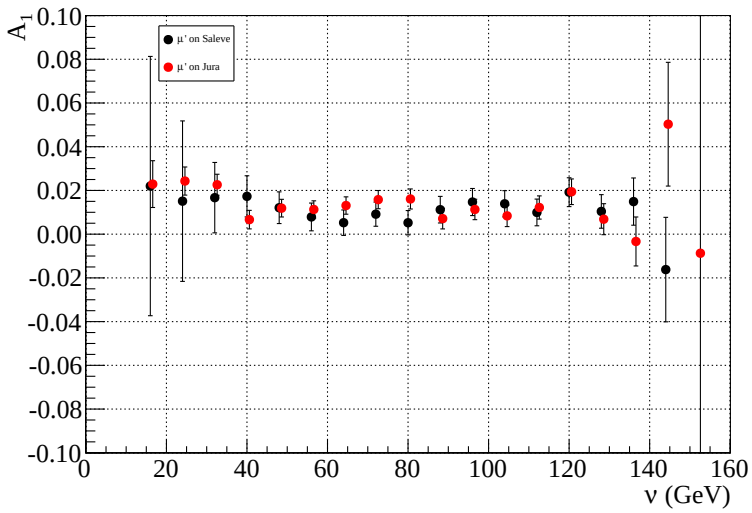

Figure C.27: Experimental $A_1^p(\nu)$ obtained from 2007 data, using data with the scattered muon directed to the left or to the right part of the spectrometer.

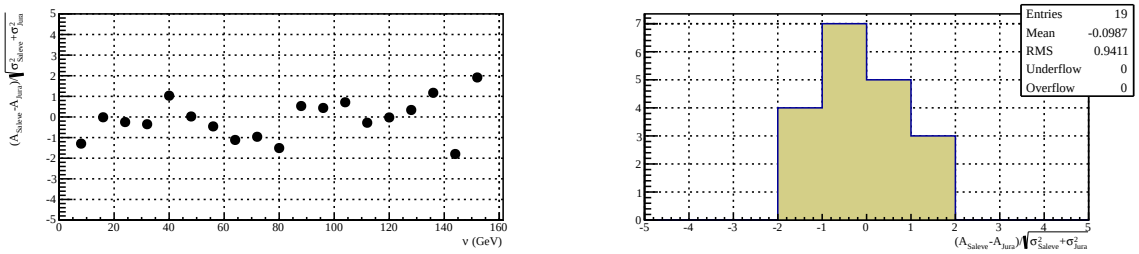

Figure C.28: Pulls of the experimental $A_1^p(\nu)$ obtained from 2007 data, using data with the scattered muon directed to the left or to the right part of the spectrometer.

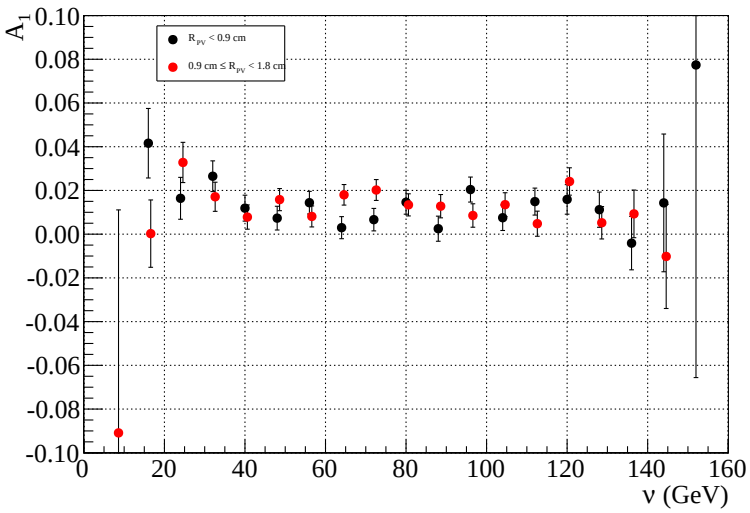

Figure C.29: Experimental $A_1^p(\nu)$ obtained from 2007 data, using data with the primary vertex from the inner or the outer part of the target volume.

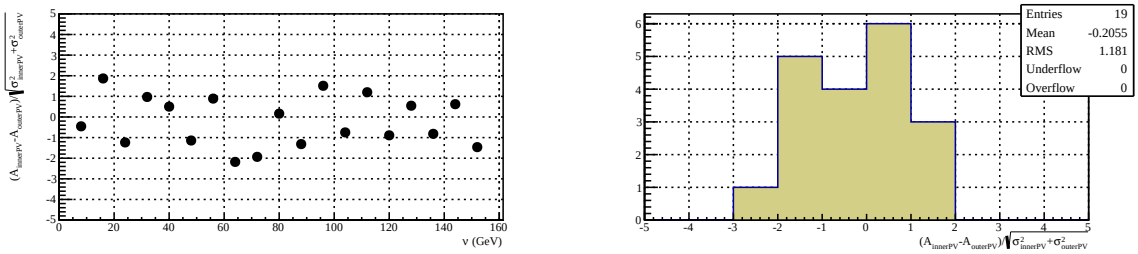

Figure C.30: Pulls of the experimental $A_1^p(\nu)$ obtained from 2007 data, using data with the primary vertex from the inner or the outer part of the target volume.

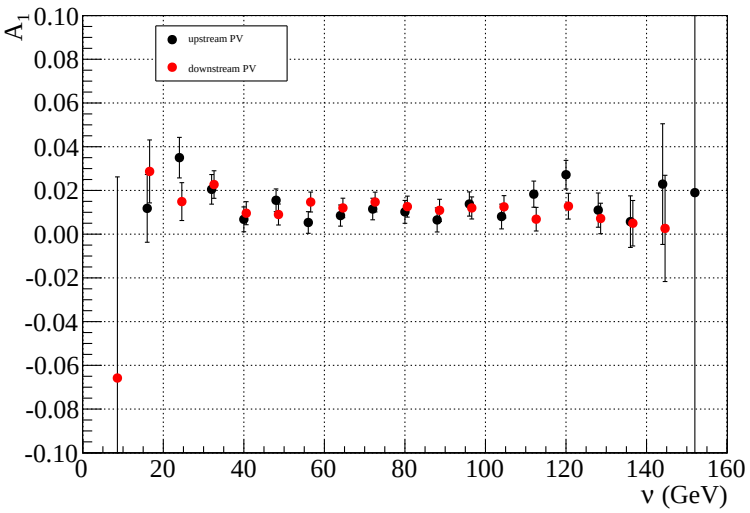

Figure C.31: Experimental $A_1^p(\nu)$ obtained from 2007 data, using data with the primary vertex in the upstream or the downstream half of the target volume.

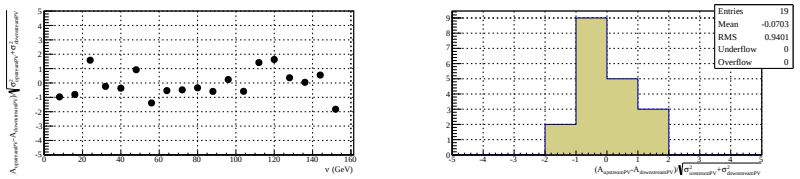

Figure C.32: Pulls of the experimental $A_1^p(\nu)$ obtained from 2007 data, using data with the primary vertex in the upstream or the downstream half of the target volume.

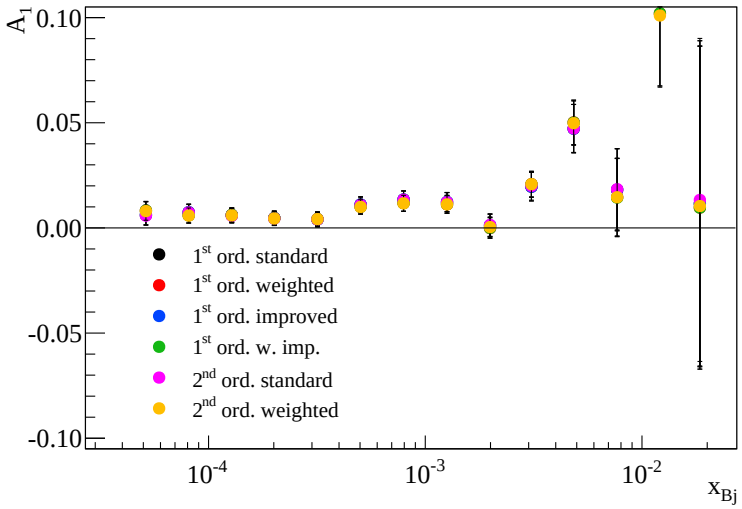

Figure C.33: Experimental $A_1^p(x)$ obtained from 2011 data, using six methods of asymmetry extraction.

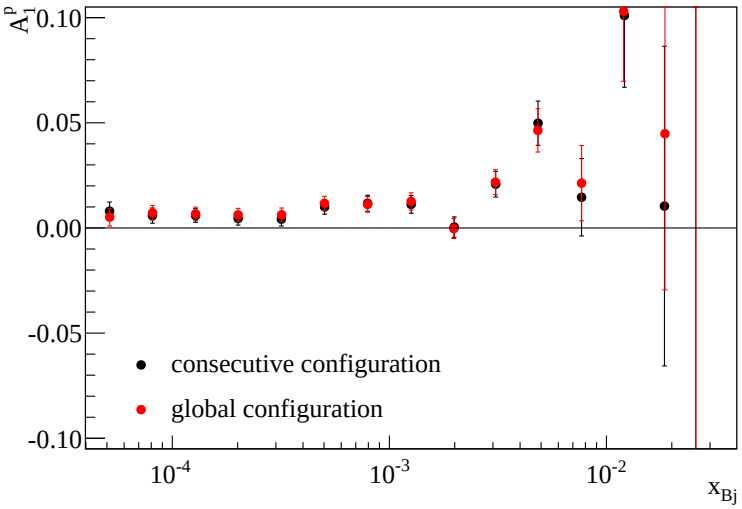

Figure C.34: Experimental $A_1^p(x)$ obtained from 2011 data, in the global and consecutive configurations.

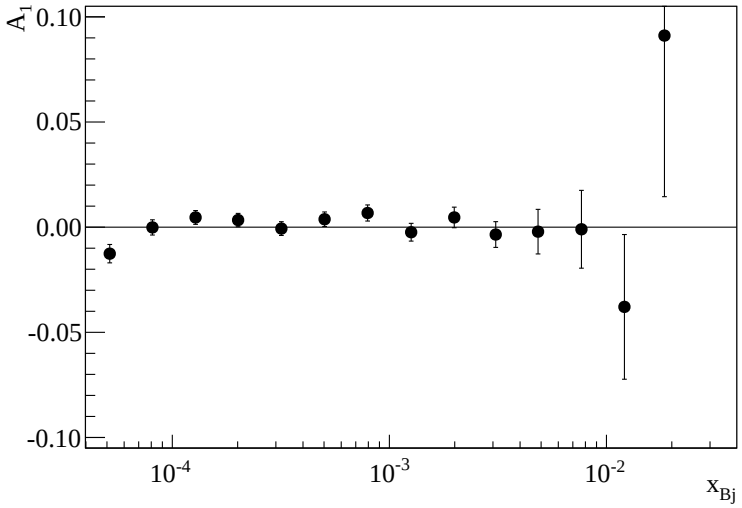

Figure C.35: Experimental $A_1^p(x)$ obtained from 2011 data, using data grouped according to fake configurations.

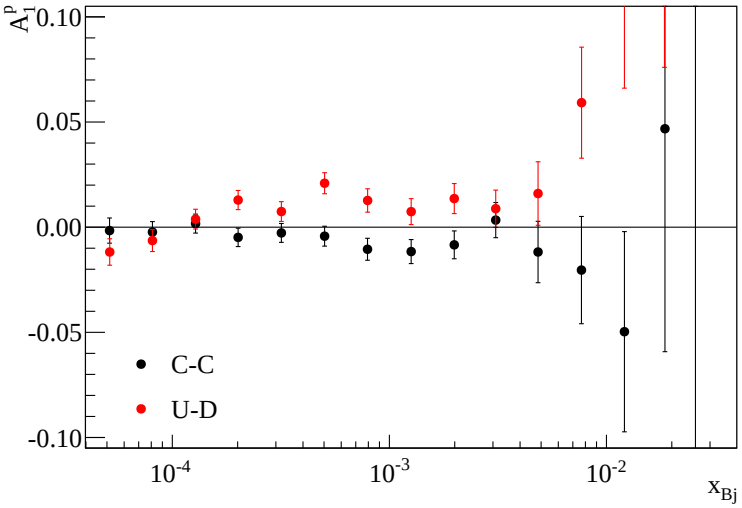

Figure C.36: Experimental $A_1^p(x)$ obtained from 2011 data, using data from the upstream and downstream target cells or the two halves of the central target cell.

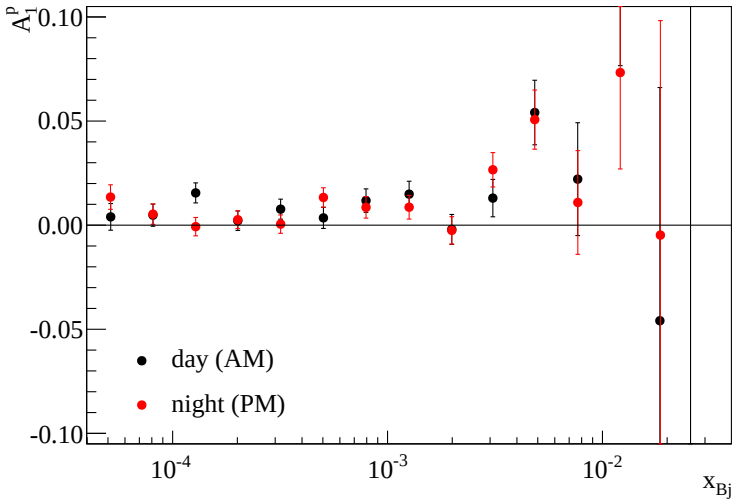

Figure C.37: Experimental $A_1^p(x)$ obtained from 2011 data, using data taken during the "day" and the "night".

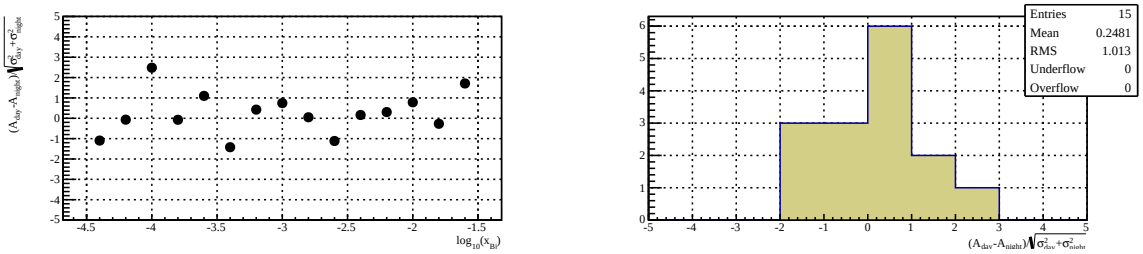

Figure C.38: Pulls of the experimental $A_1^p(x)$ obtained from 2011 data, using data taken during the "day" and the "night".

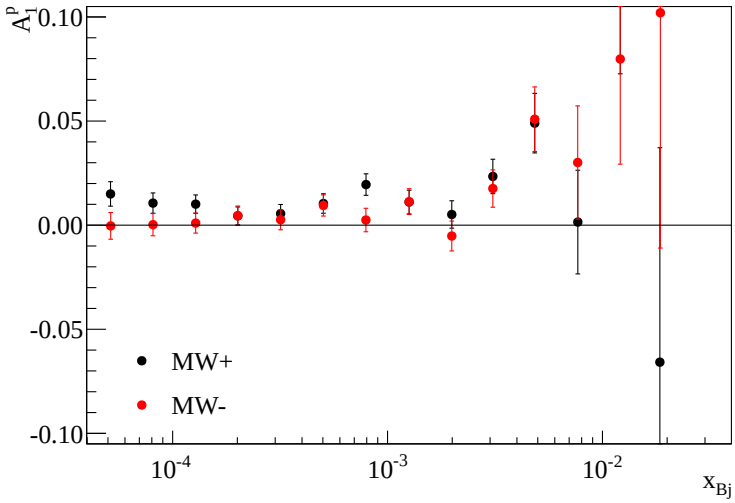

Figure C.39: Experimental $A_1^p(x)$ obtained from 2011 data, using the two different microwave settings. For the three first points, one gets $\chi^2/\mathrm{NDF} = 0.760453/3$, with a probability $p = 0.858901$.

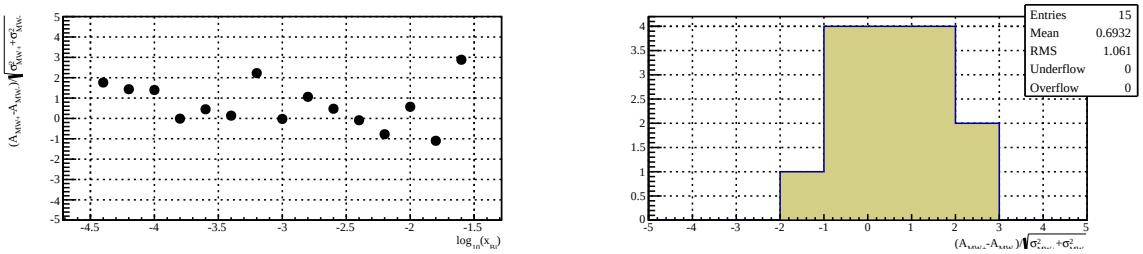

Figure C.40: Pulls for experimental $A_1^p(x)$ obtained from 2011 data, using the two different microwave settings.

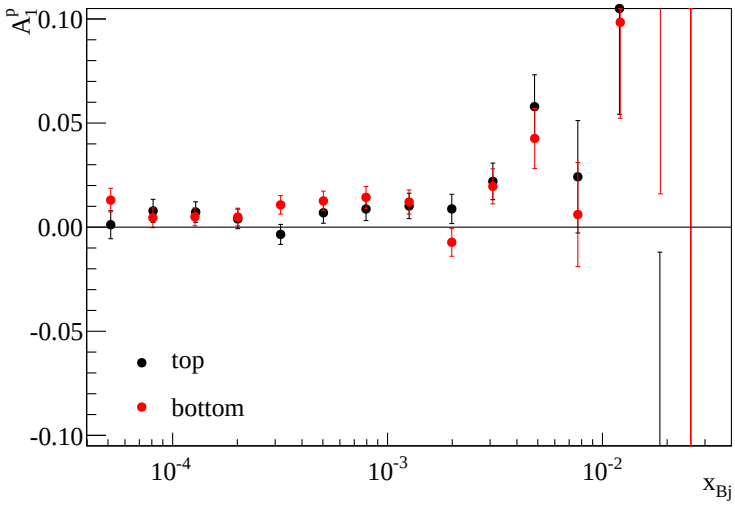

Figure C.41: Experimental $A_1^p(x)$ obtained from 2011 data, using data with the scattered muon directed to the top or the bottom part of the spectrometer.

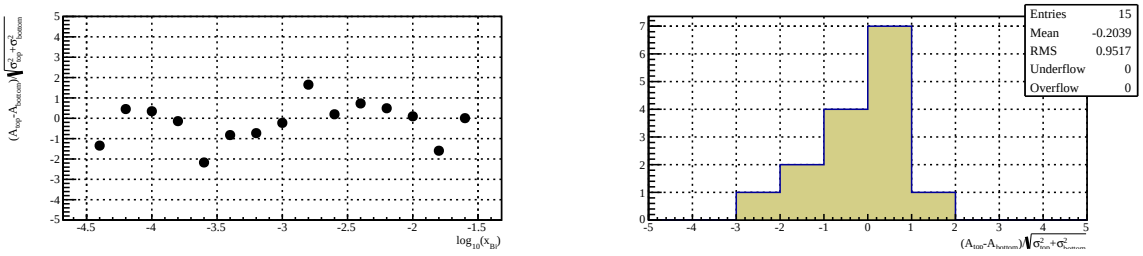

Figure C.42: Pulls of the experimental $A_1^p(x)$ obtained from 2011 data, using data with the scattered muon directed to the top or the bottom part of the spectrometer.

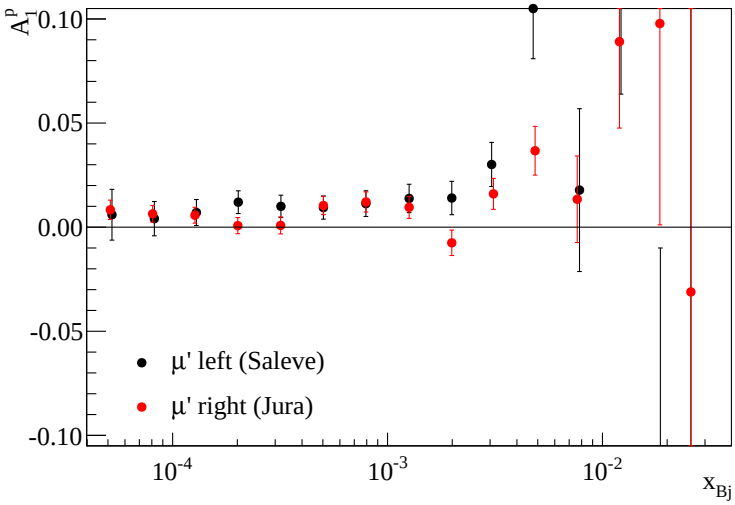

Figure C.43: Experimental $A_1^p(x)$ obtained from 2011 data, using events with the scattered muon directed to the left and the right part of the spectrometer.

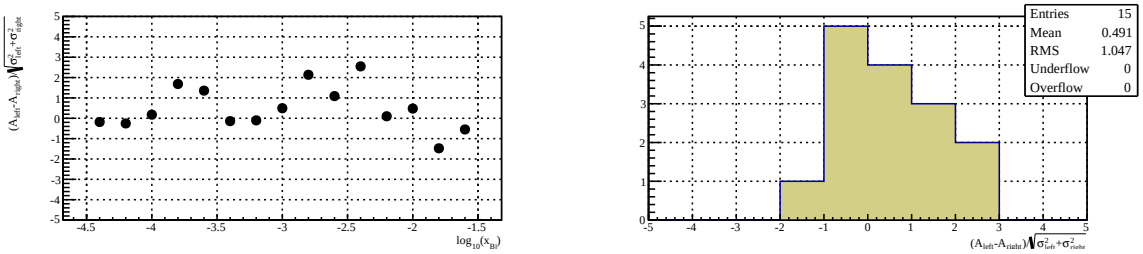

Figure C.44: Pulls for experimental $A_1^p(x)$ obtained from 2011 data, using events with the scattered muon directed to the left and the right part of the spectrometer.

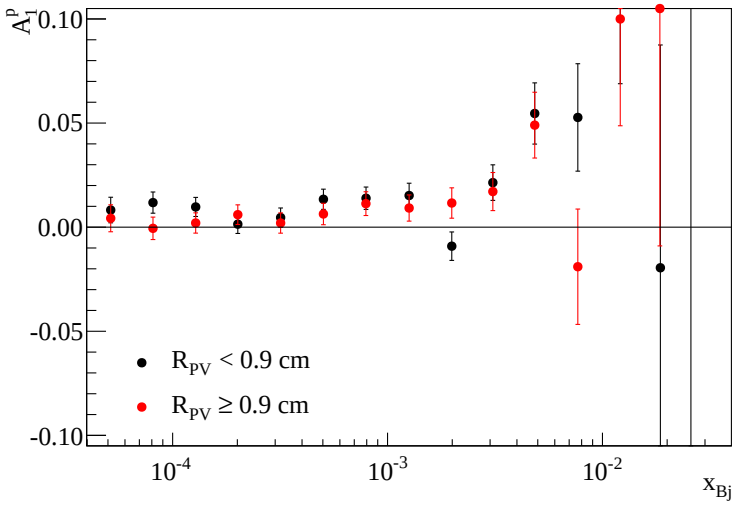

Figure C.45: Experimental $A_1^p(x)$ obtained from 2011 data, using data with a primary vertex in the inner or the outer part of the target.

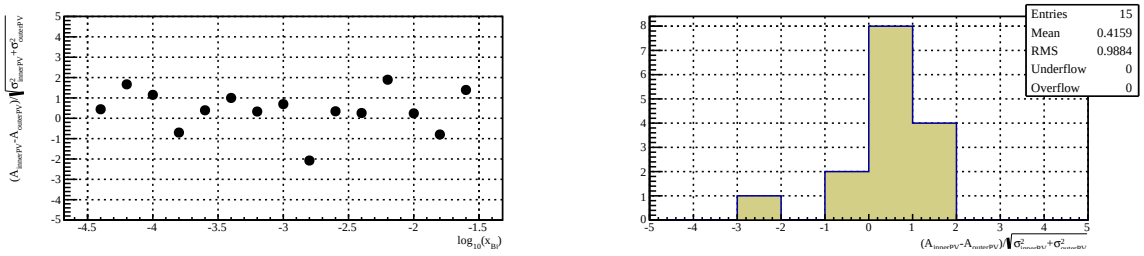

Figure C.46: Pulls of experimental $A_1^p(x)$ obtained from 2011 data, using data with a primary vertex in the inner or the outer part of the target.

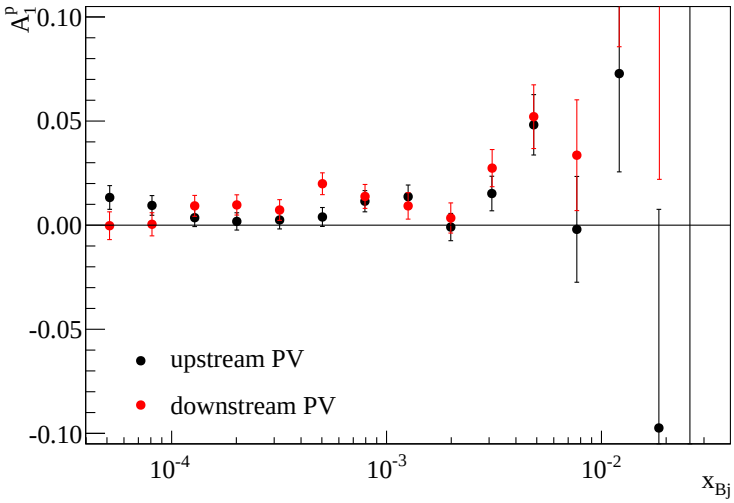

Figure C.47: Experimental $A_1^p(x)$ obtained from 2011 data, using data with a primary vertex in the upstream or the downstream half of the target.

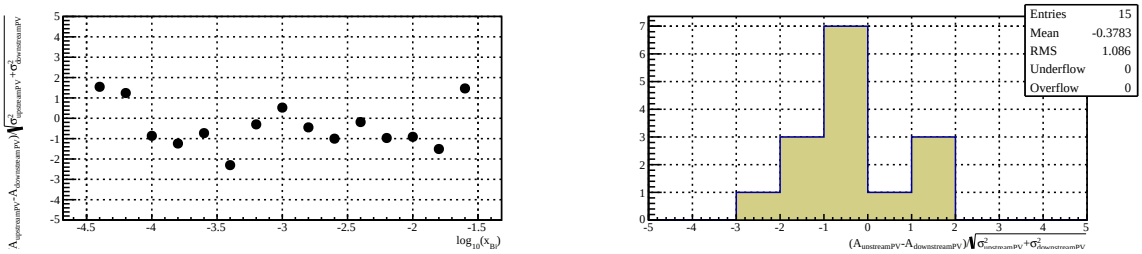

Figure C.48: Pulls of the experimental $A_1^p(x)$ obtained from 2011 data, using data with a primary vertex in the upstream or the downstream half of the target.

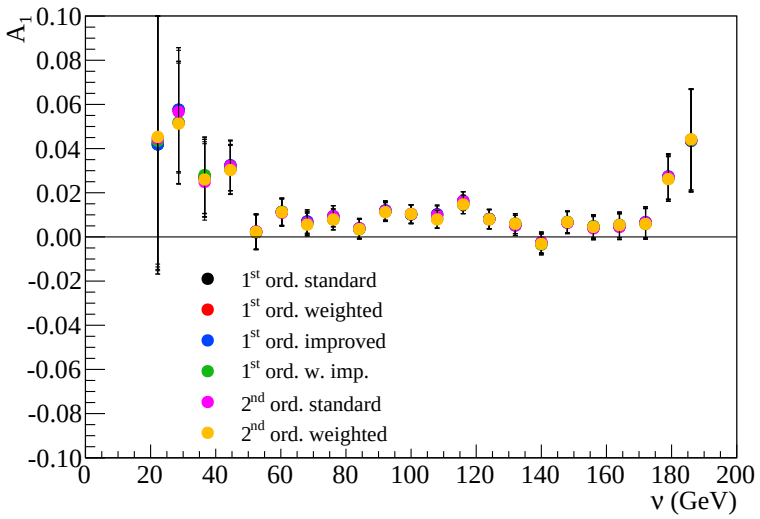

Figure C.49: Experimental $A_1^p(\nu)$ obtained from 2011 data, using six methods of asymmetry extraction.

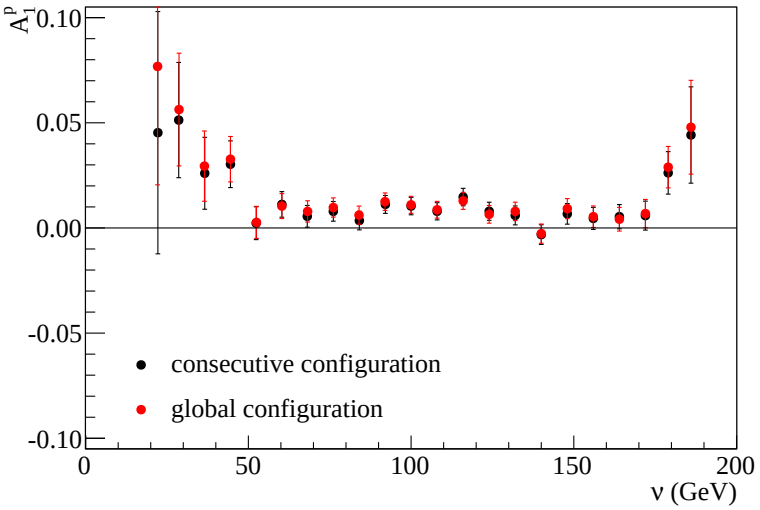

Figure C.50: Experimental $A_1^p(\nu)$ obtained from 2011 data, in the global and consecutive configurations.

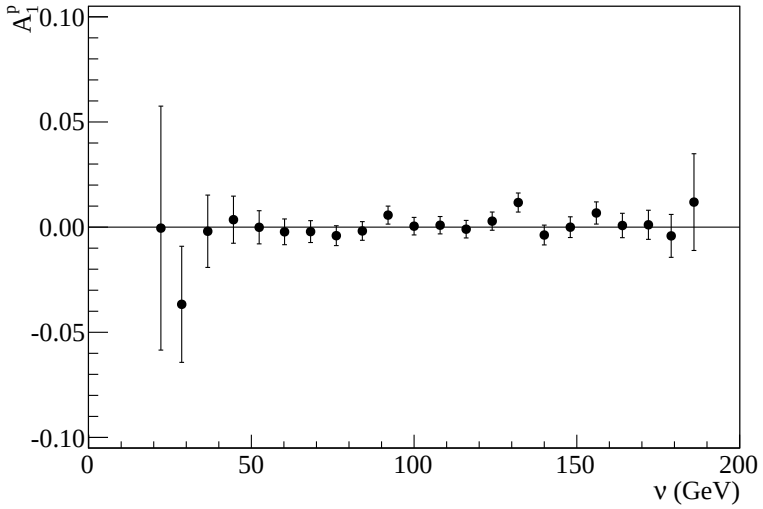

Figure C.51: Experimental $A_1^p(\nu)$ obtained from 2011 data, using data grouped according to fake configurations.

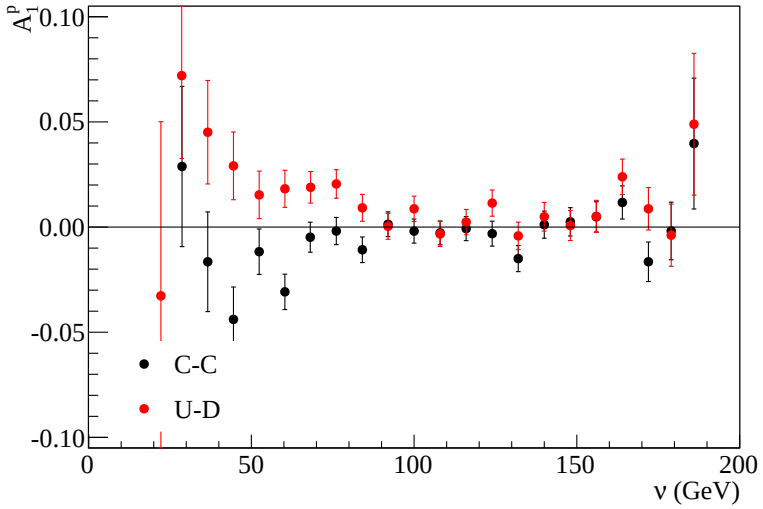

Figure C.52: Experimental $A_1^p(\nu)$ obtained from 2011 data, calculating the asymmetries either from the upstream and the downstream target cells, or from the two upstream and downstream halves of the central target cell.

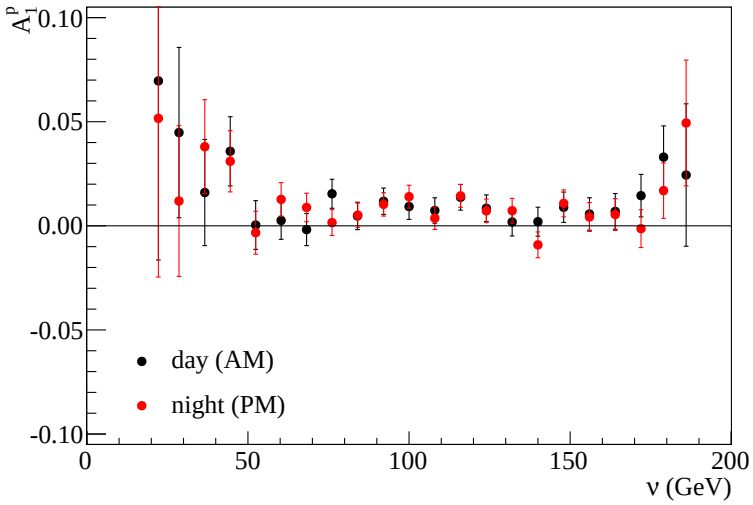

Figure C.53: Experimental $A_1^p(\nu)$ obtained from 2011 data, using data taken during the "day" and the "night".

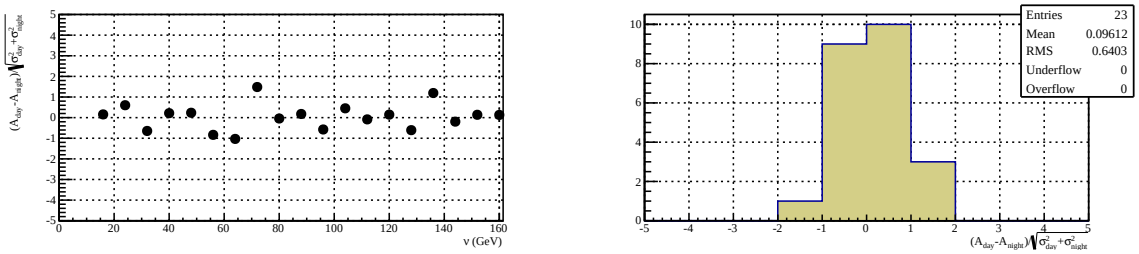

Figure C.54: Pulls of the experimental $A_1^p(\nu)$ obtained from 2011 data, using data taken during the "day" and the "night".

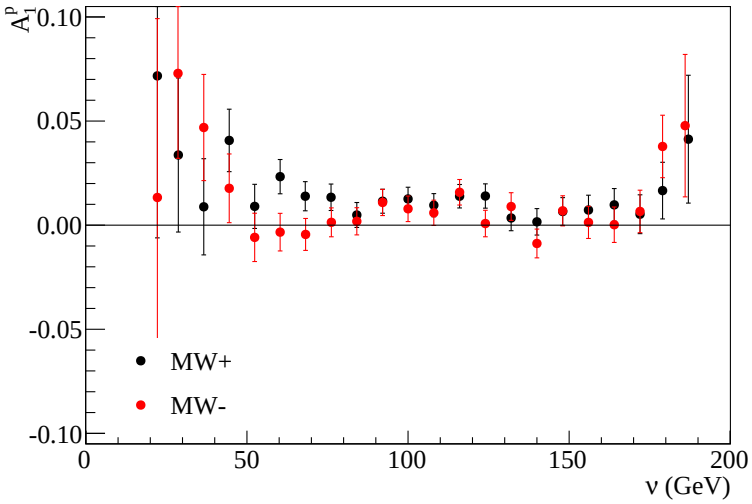

Figure C.55: Experimental $A_1^p(\nu)$ obtained from 2011 data, using the two different microwave settings.

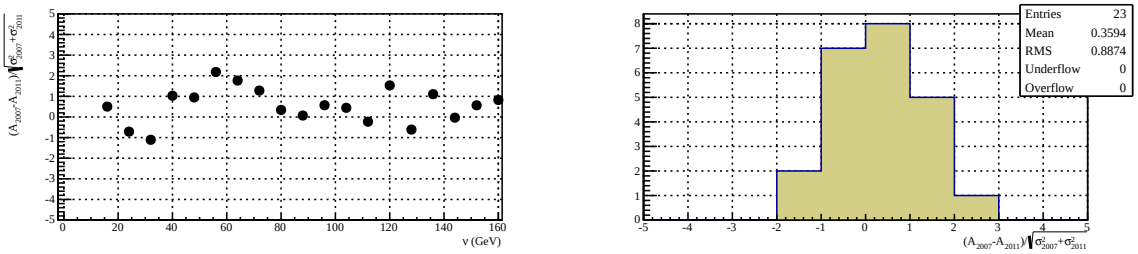

Figure C.56: Pulls for experimental $A_1^p(\nu)$ obtained from 2011 data, using the two different microwave settings.

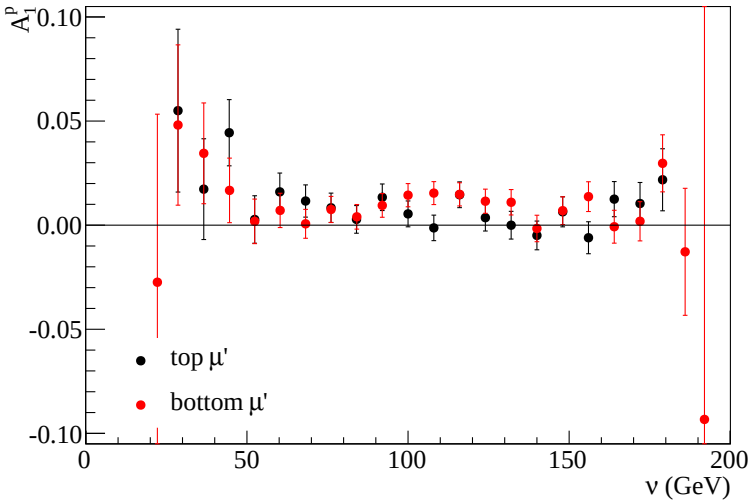

Figure C.57: Experimental $A_1^p(\nu)$ obtained from 2011 data, using data with the scattered muon directed to the top or the bottom part of the spectrometer.

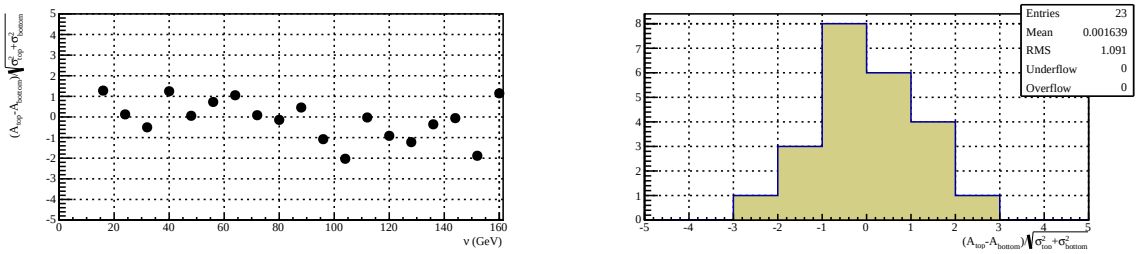

Figure C.58: Pulls of the experimental $A_1^p(\nu)$ obtained from 2011 data, using data with the scattered muon directed to the top or the bottom part of the spectrometer.

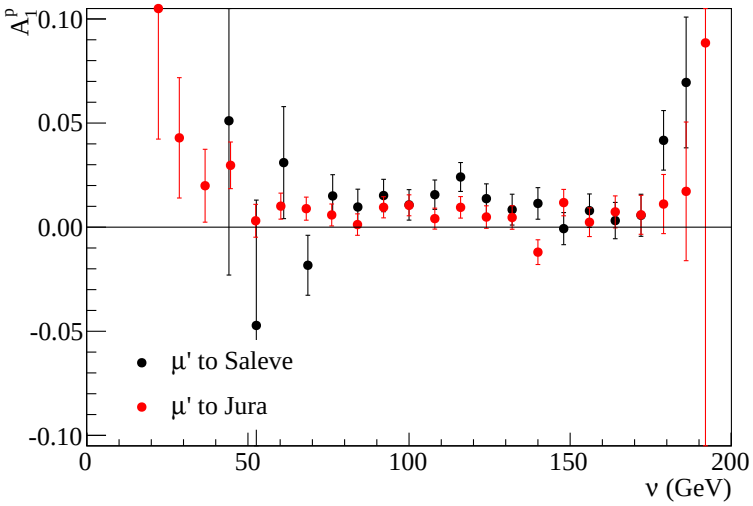

Figure C.59: Experimental $A_1^p(\nu)$ obtained from 2011 data, using events with the scattered muon directed to the left of to the right of the spectrometer, at the primary vertex.

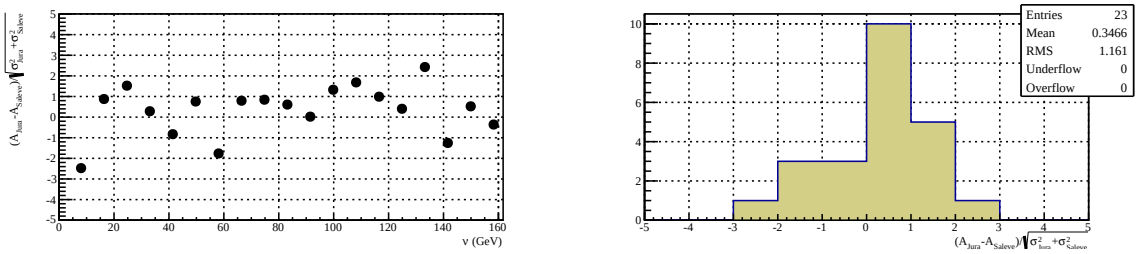

Figure C.60: Pulls for experimental $A_1^p(\nu)$ obtained from 2011 data, using events with the scattered muon directed to the left of to the right of the spectrometer, at the primary vertex.

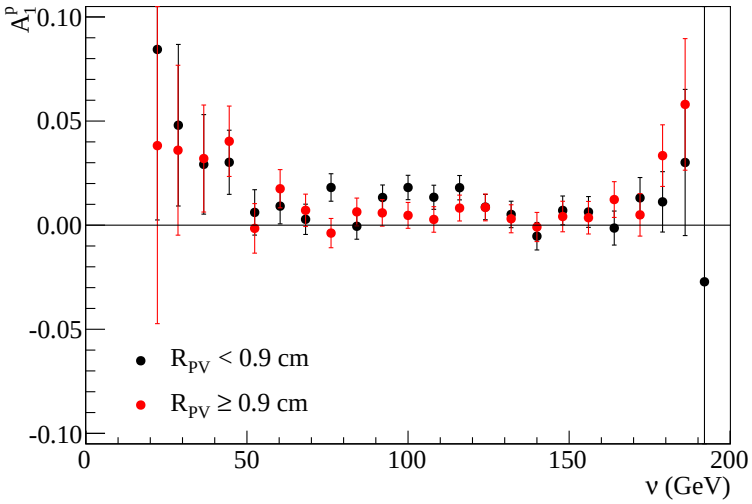

Figure C.61: Experimental $A_1^p(\nu)$ obtained from 2011 data, using data with the primary vertex from the inner or the outer part of the target volume.

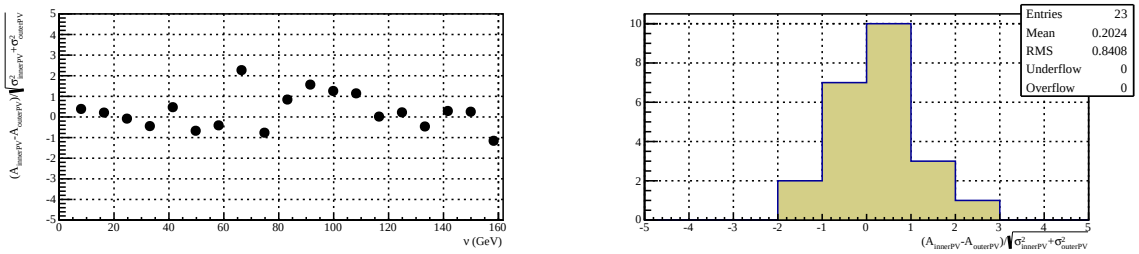

Figure C.62: Pulls of the experimental $A_1^p(\nu)$ obtained from 2011 data, using data with the primary vertex from the inner or the outer part of the target volume.

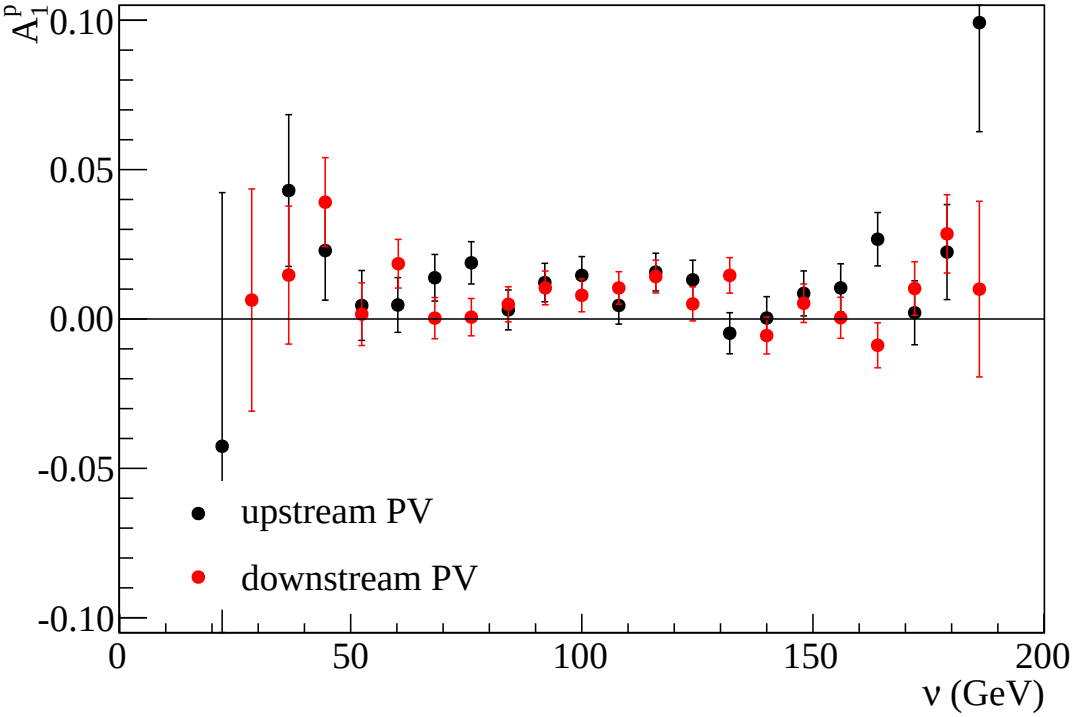

Figure C.63: Experimental $A_1^p(\nu)$ obtained from 2011 data, using data with the primary vertex in the upstream or the downstream half of the target volume.

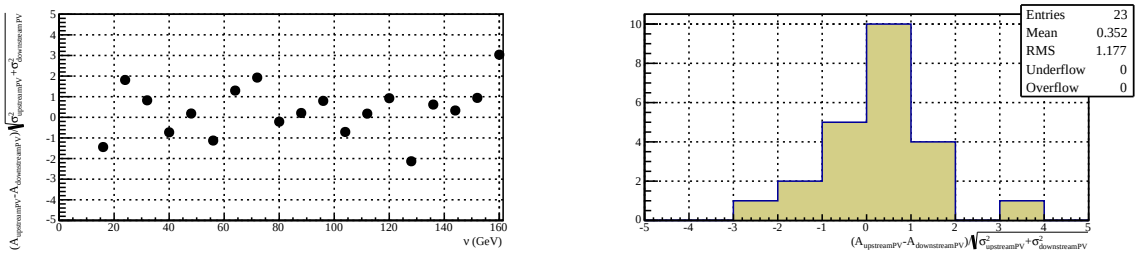

Figure C.64: Pulls of the experimental $A_1^p(\nu)$ obtained from 2011 data, using data with the primary vertex in the upstream or the downstream half of the target volume.

Appendix D

Pulls for the One-dimensional analyses

The plots of pulls for the estimation of false asymmetries, as defined by Eq. 6.7, are presented in this Appendix. The fraction of the statistical uncertainty that is considered for the false asymmetry contribution of the systematic uncertainty is indicated as "limit", given by Eq. 6.8.

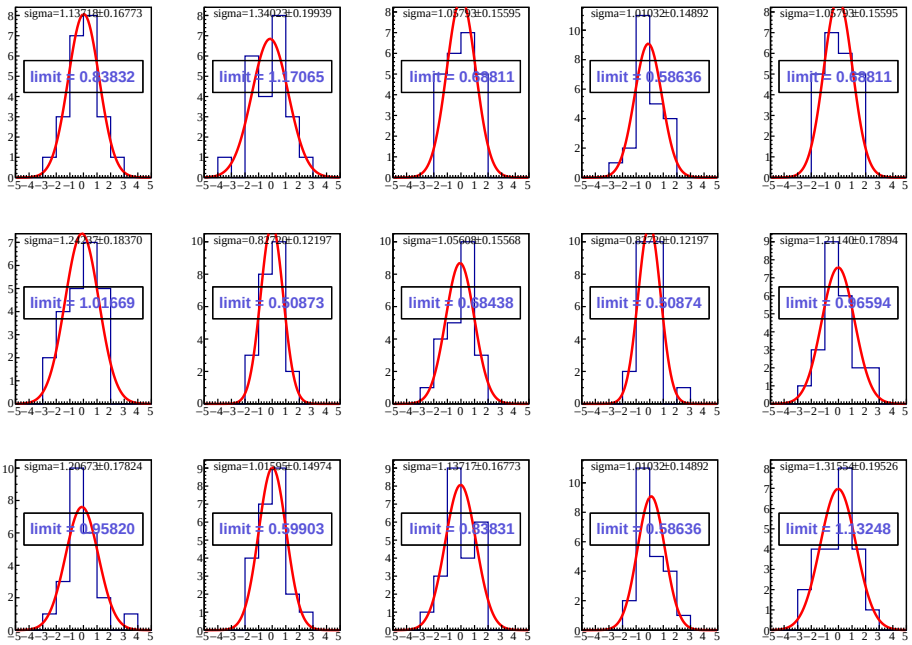

Figure D.1: Pulls for 2007, $A(x_{Bj})$.

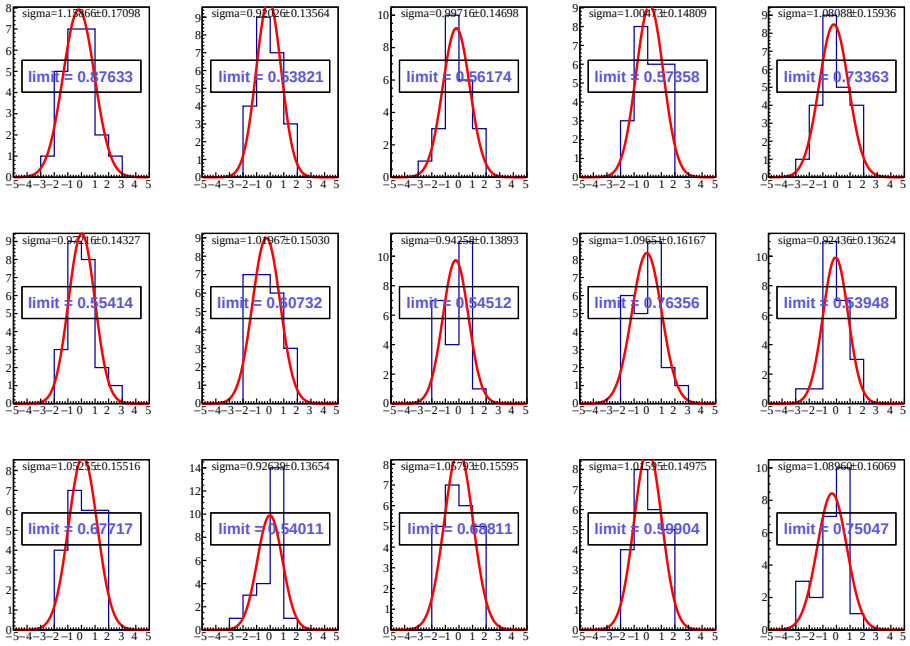

Figure D.2: Pulls for 2011, $A(x_{Bj})$.

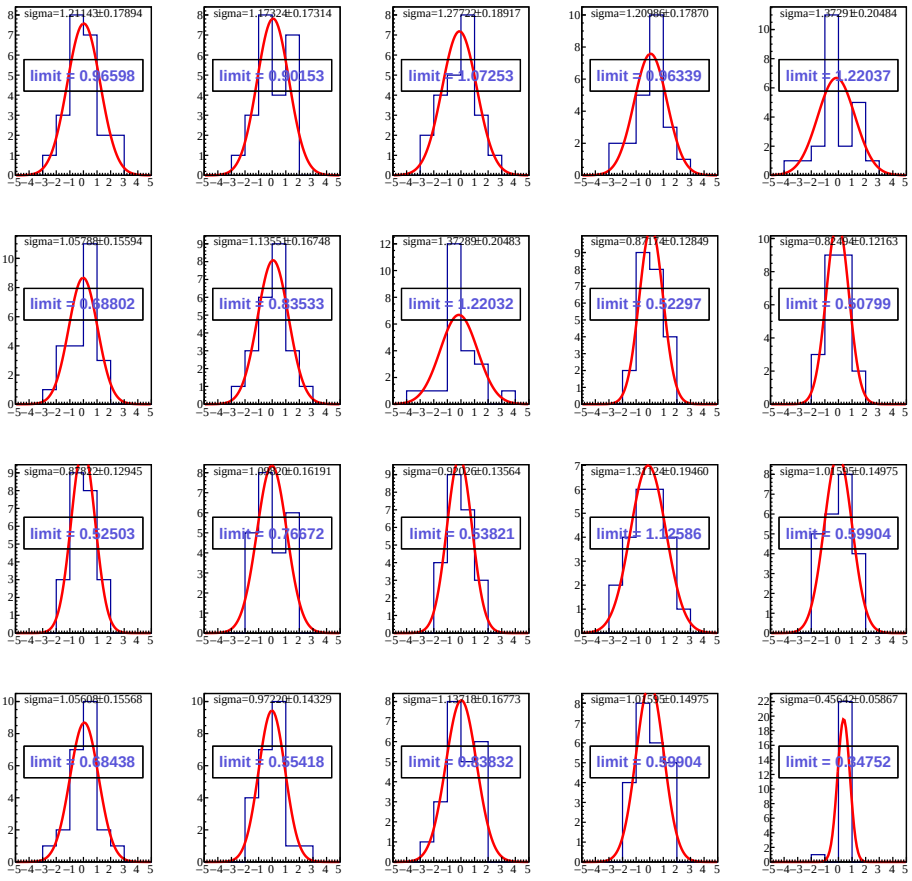

Figure D.3: Pulls for 2007, $A(\nu)$.

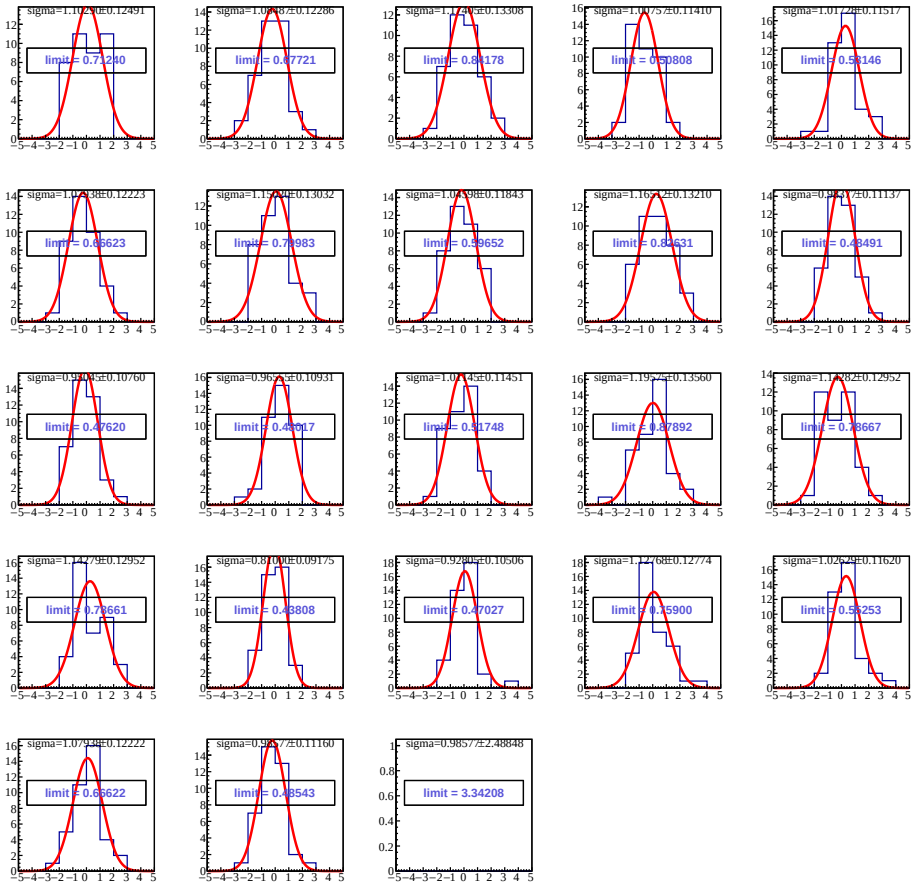

Figure D.4: Pulls for 2011, $A(\nu)$.

Appendix E

Pulls Distributions for the Two-dimensional Analyses

The plots of pulls for the estimation of false asymmetries, as defined by Eq. 6.7, are presented in the following way: for each of the bins of the first independent kinematic variable, 3 or 5 bins of the second independent kinematic variable were used (#0 to #2 or #0 to #4); the bins thereby labeled #0, #1, etc. are grouped together. The fraction of the statistical uncertainty that is considered for the false asymmetry contribution of the systematic uncertainty is indicated as "limit", given by Eq. 6.8.

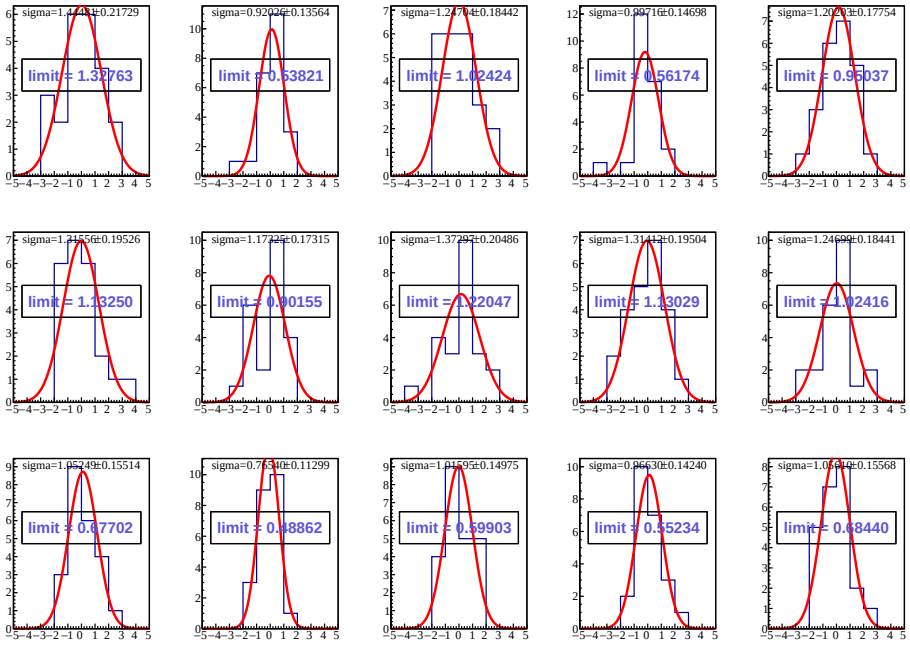

Figure E.1: Pulls for 2007, $A(x_{Bj}, Q^2)$, set of bins #0.

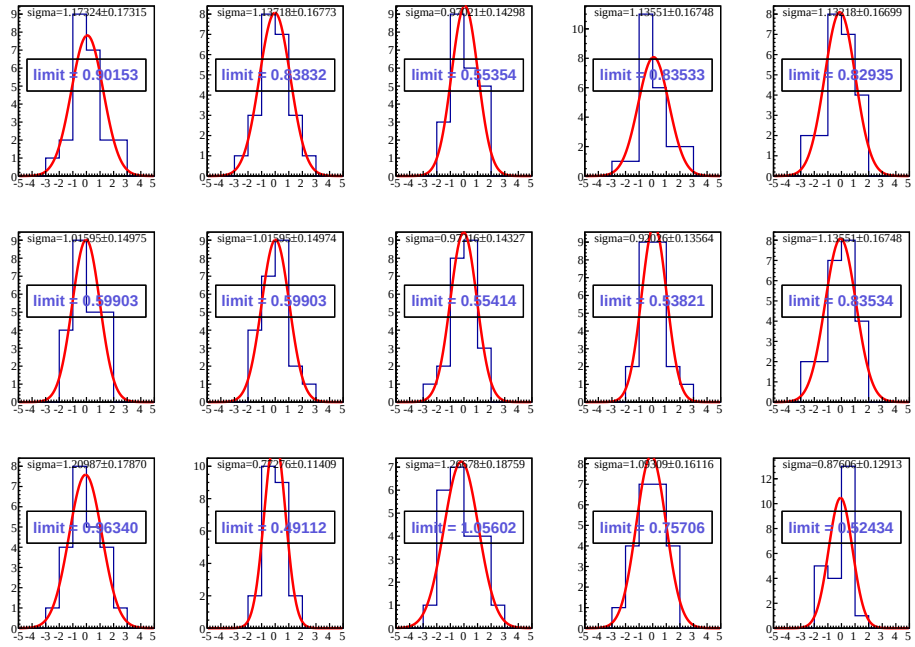

Figure E.2: Pulls for 2007, $A(x_{Bj}, Q^2)$, set of bins #1.

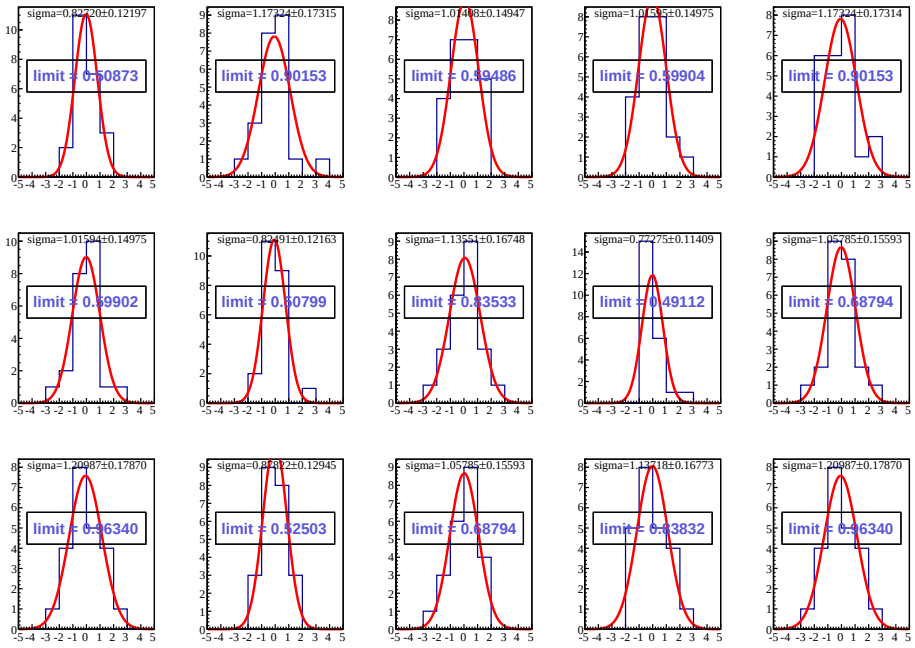

Figure E.3: Pulls for 2007, $A(x_{Bj}, Q^2)$, set of bins #2.

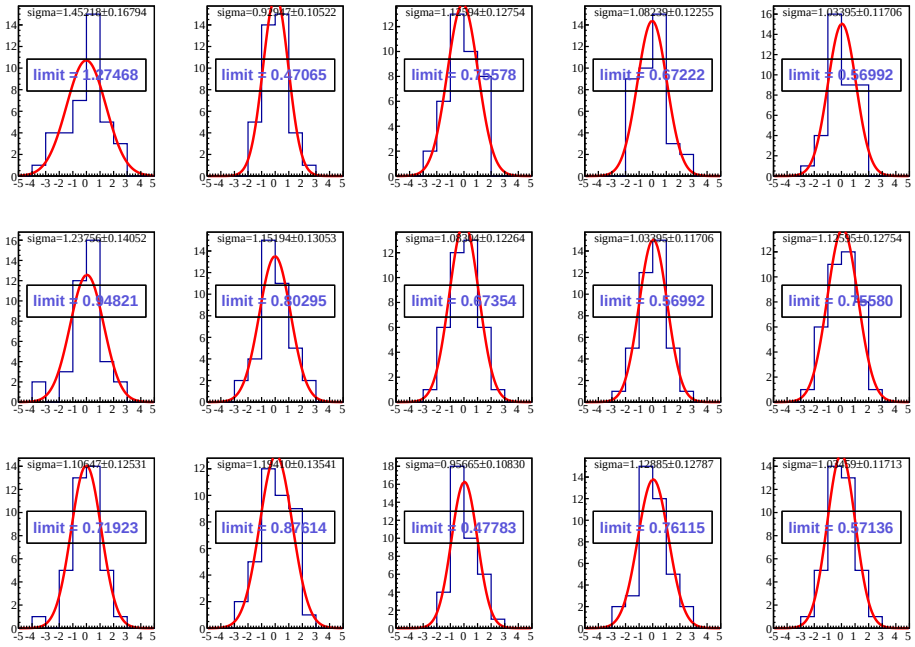

Figure E.4: Pulls for 2011, $A(x_{Bj}, Q^2)$, set of bins #0.

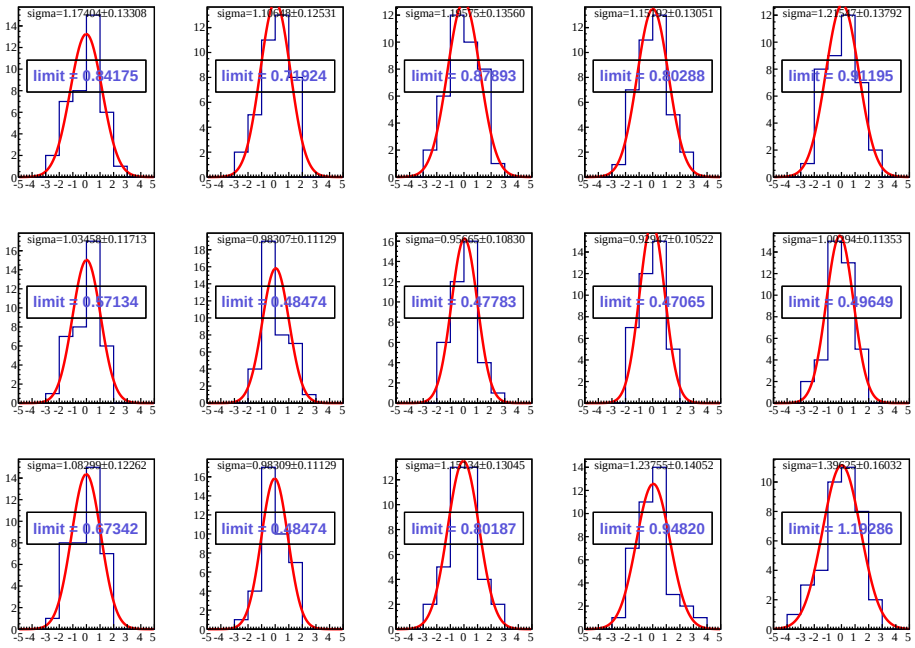

Figure E.5: Pulls for 2011, $A(x_{Bj}, Q^2)$, set of bins #1.

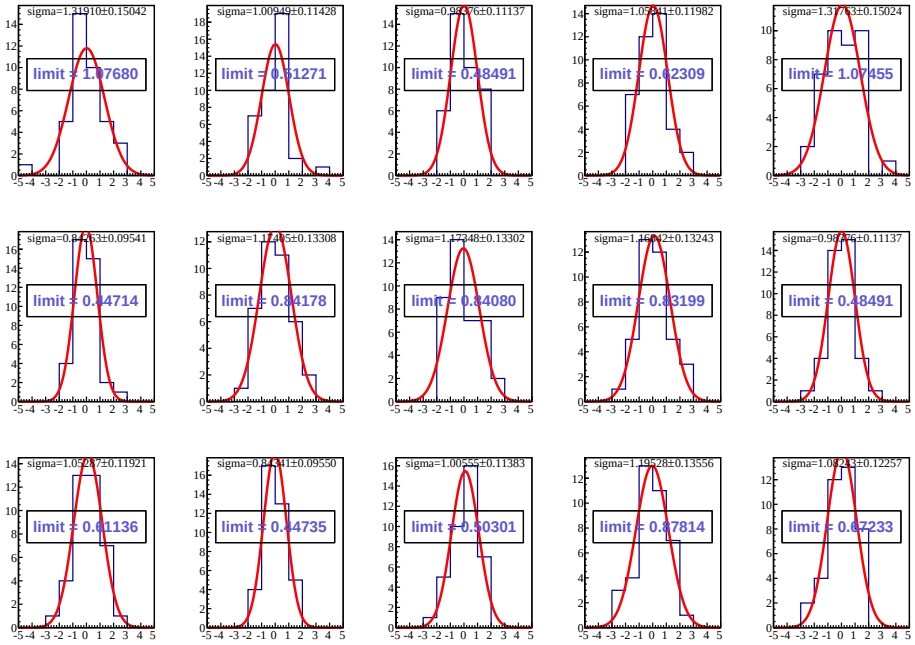

Figure E.6: Pulls for 2011, $A(x_{Bj}, Q^2)$, set of bins #2.

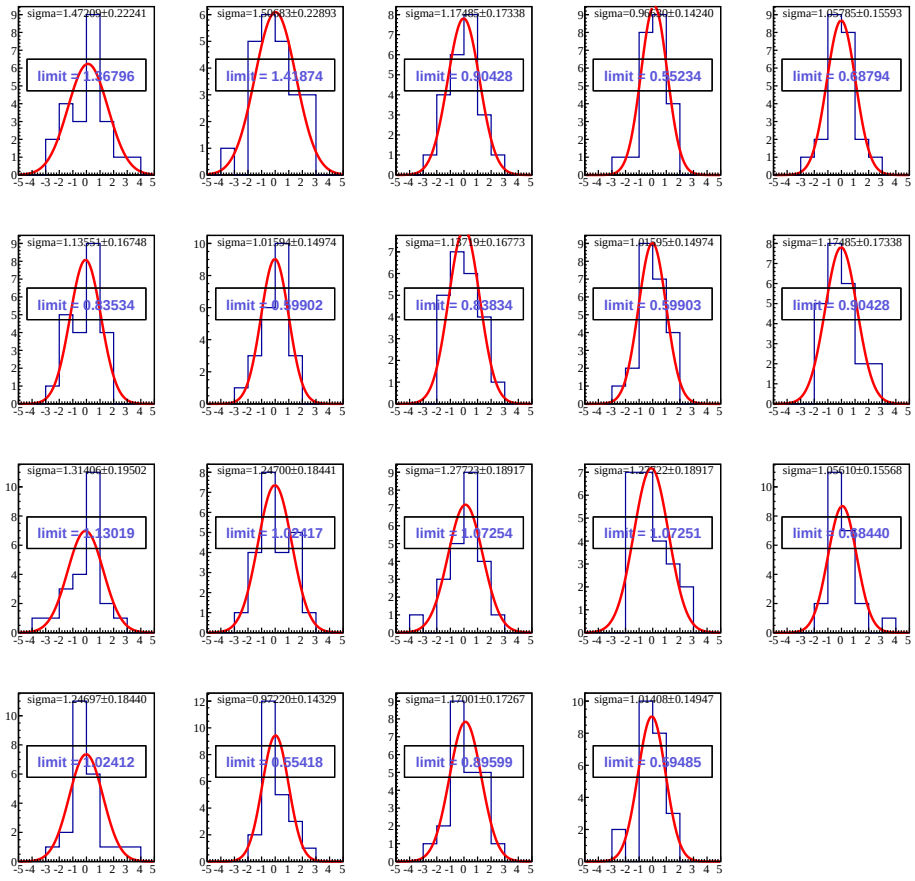

Figure E.7: Pulls for 2007, $A(\nu, Q^2)$, set of bins #0.

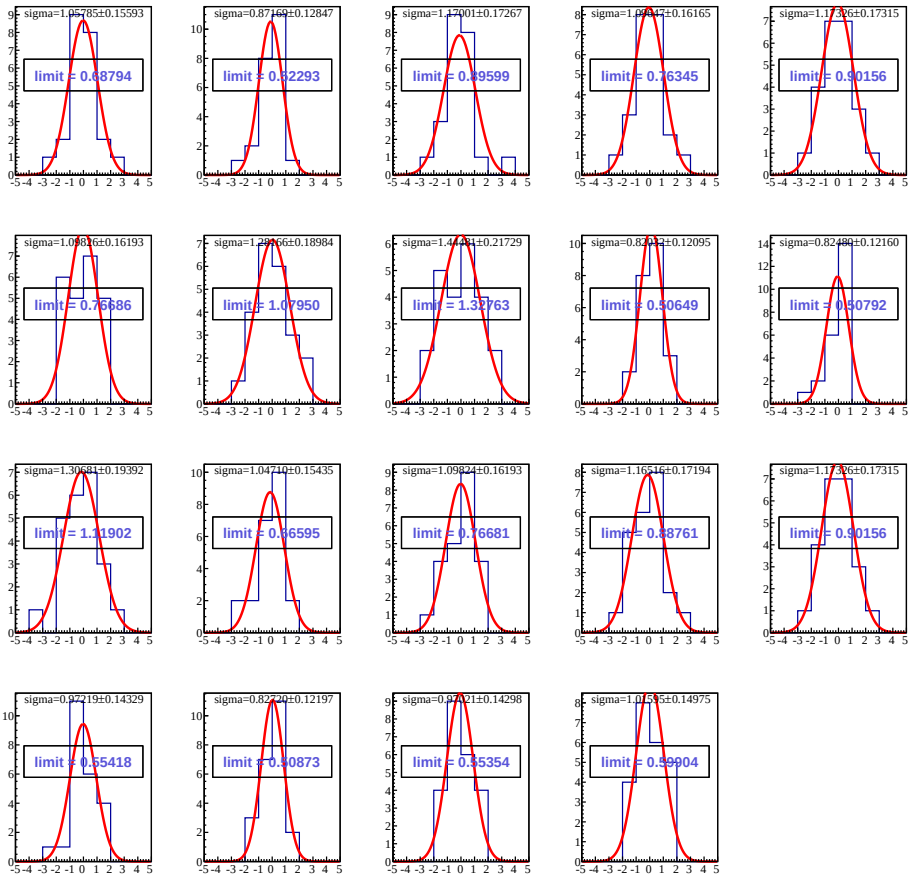

Figure E.8: Pulls for 2007, $A(\nu, Q^2)$, set of bins #1.

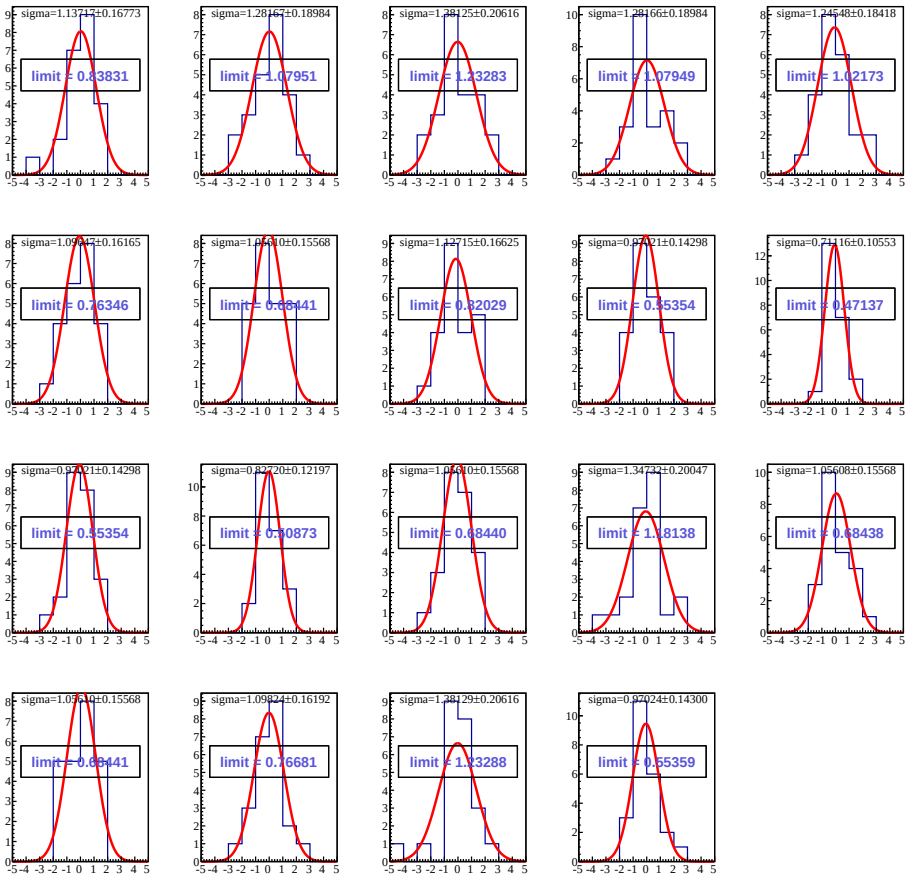

Figure E.9: Pulls for 2007, $A(\nu, Q^2)$, set of bins #2.

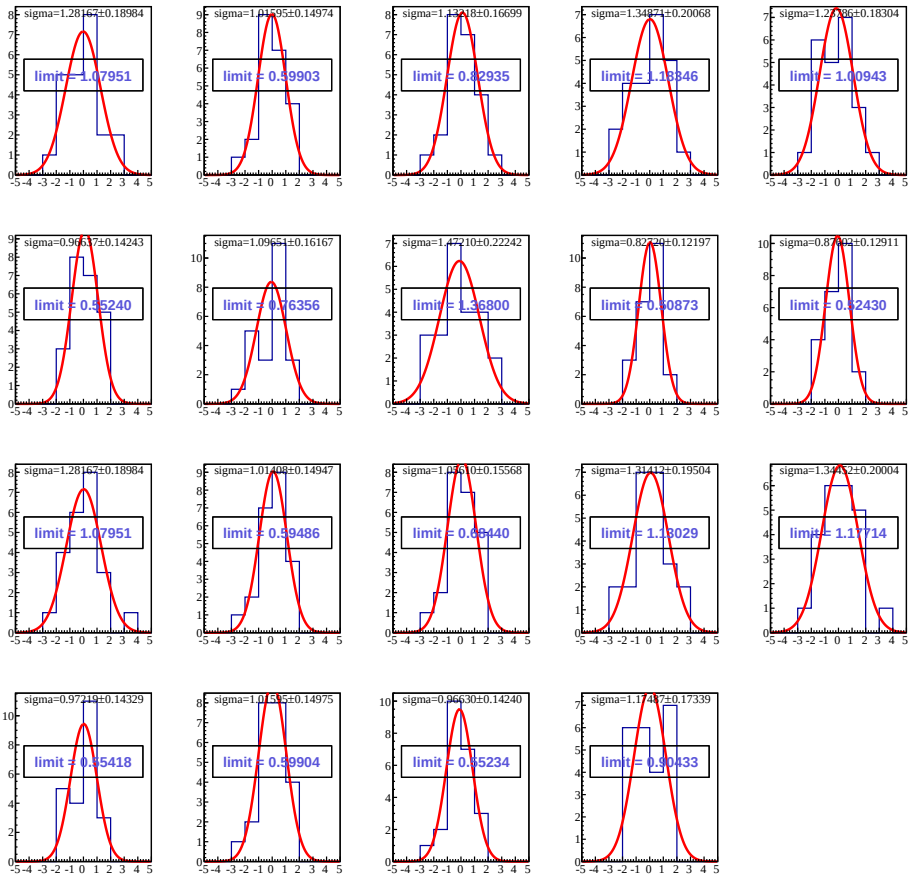

Figure E.10: Pulls for 2007, $A(\nu, Q^2)$, set of bins #3.

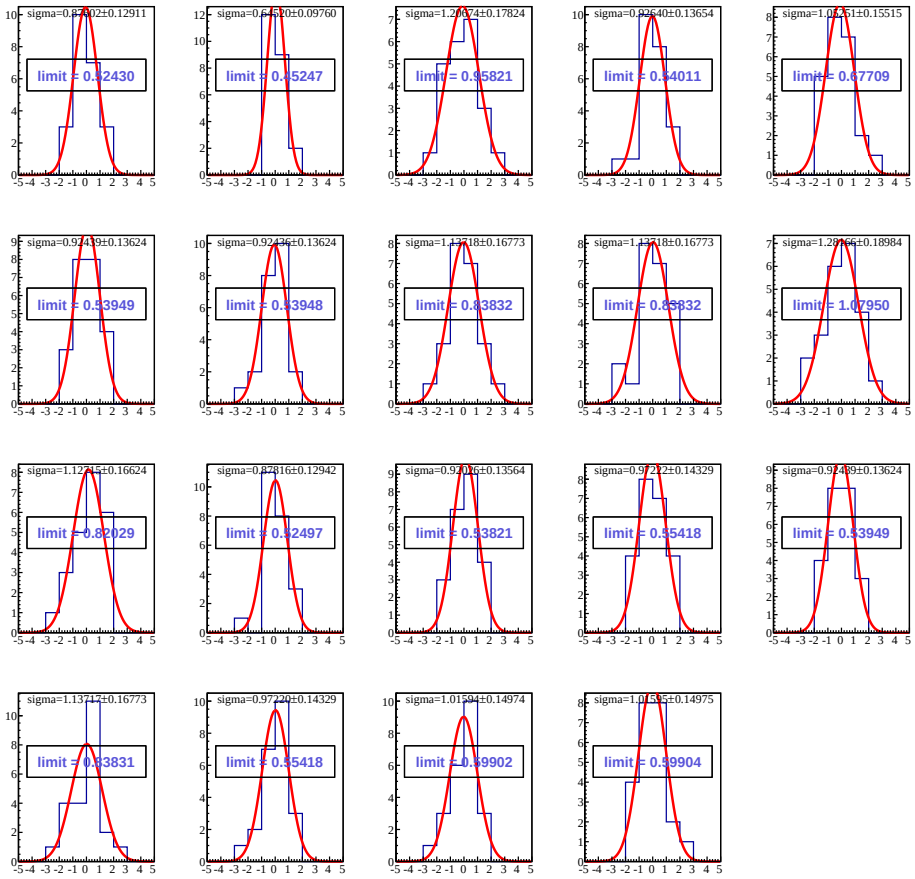

Figure E.11: Pulls for 2007, $A(\nu, Q^2)$, set of bins #4.

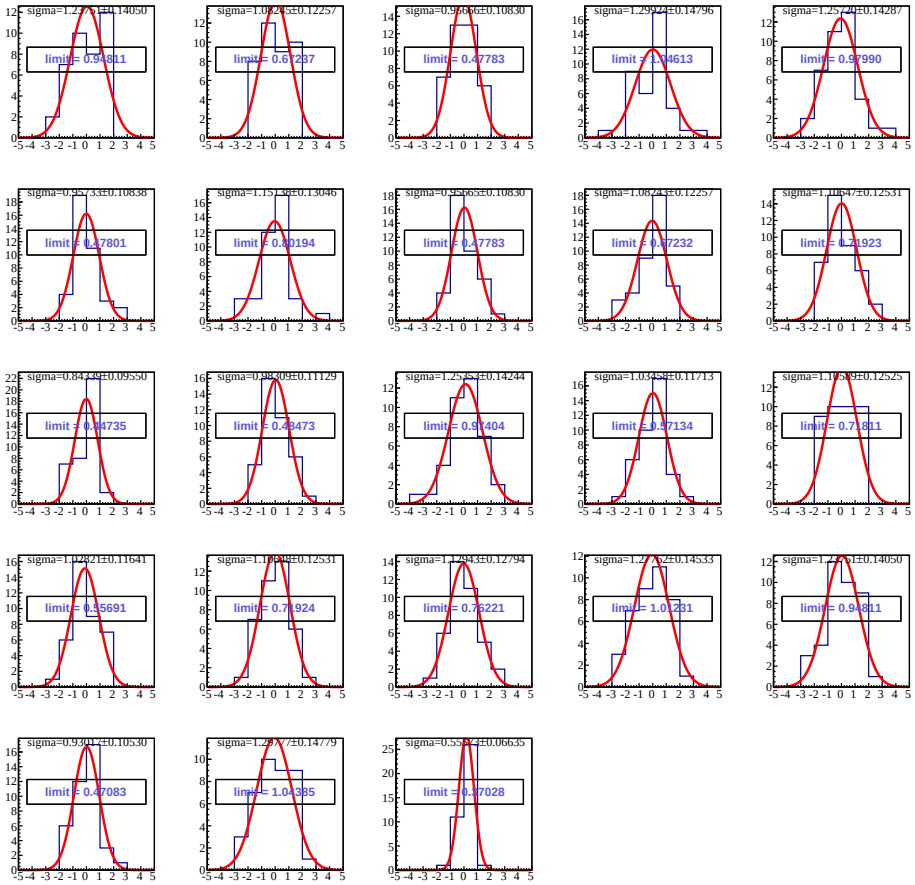

Figure E.12: Pulls for 2011, $A(\nu, Q^2)$, set of bins #0.

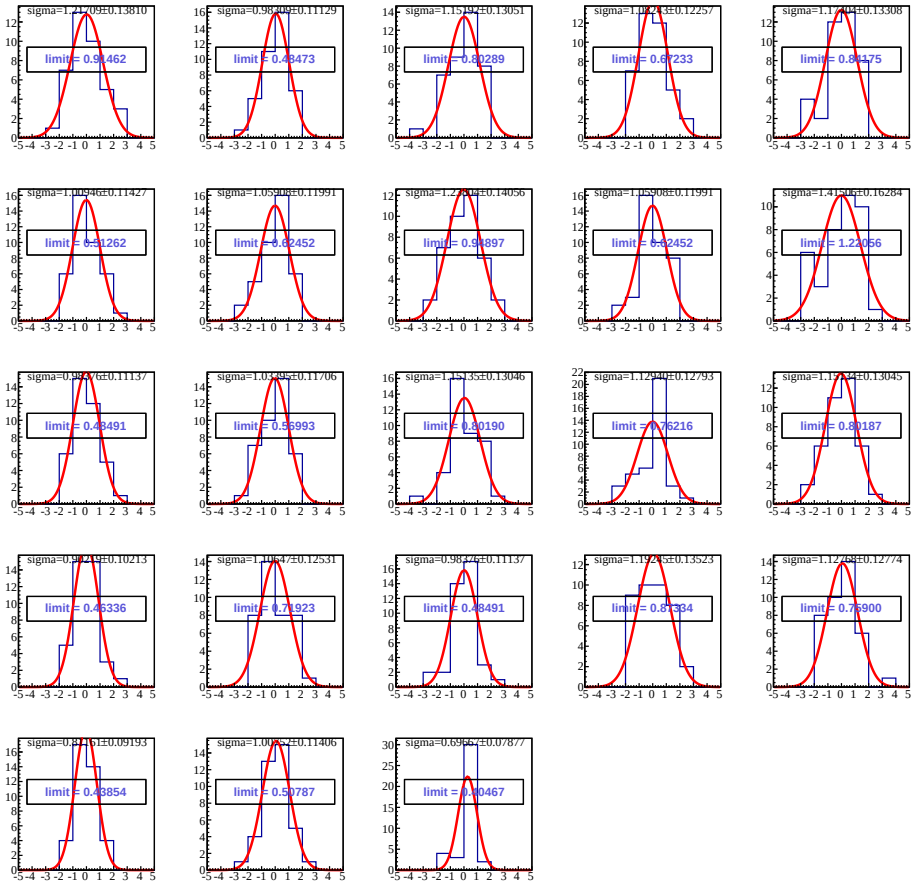

Figure E.13: Pulls for 2011, $A(\nu, Q^2)$, set of bins #1.

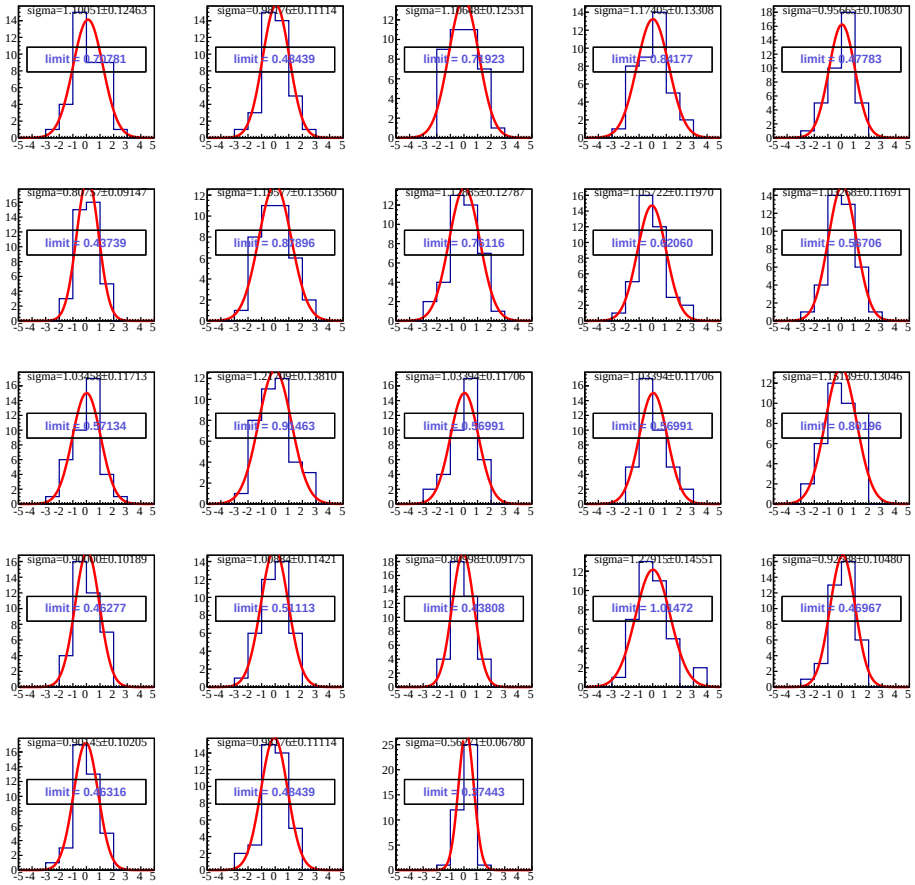

Figure E.14: Pulls for 2011, $A(\nu, Q^2)$, set of bins #2.

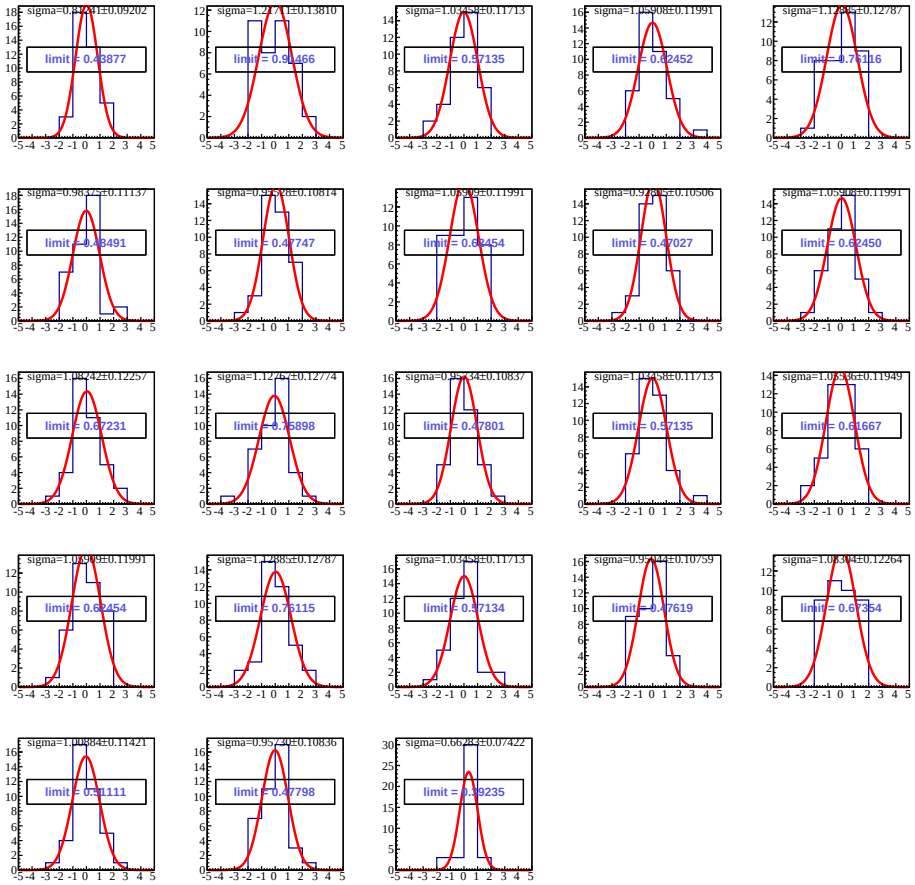

Figure E.15: Pulls for 2011, $A(\nu, Q^2)$, set of bins #3.

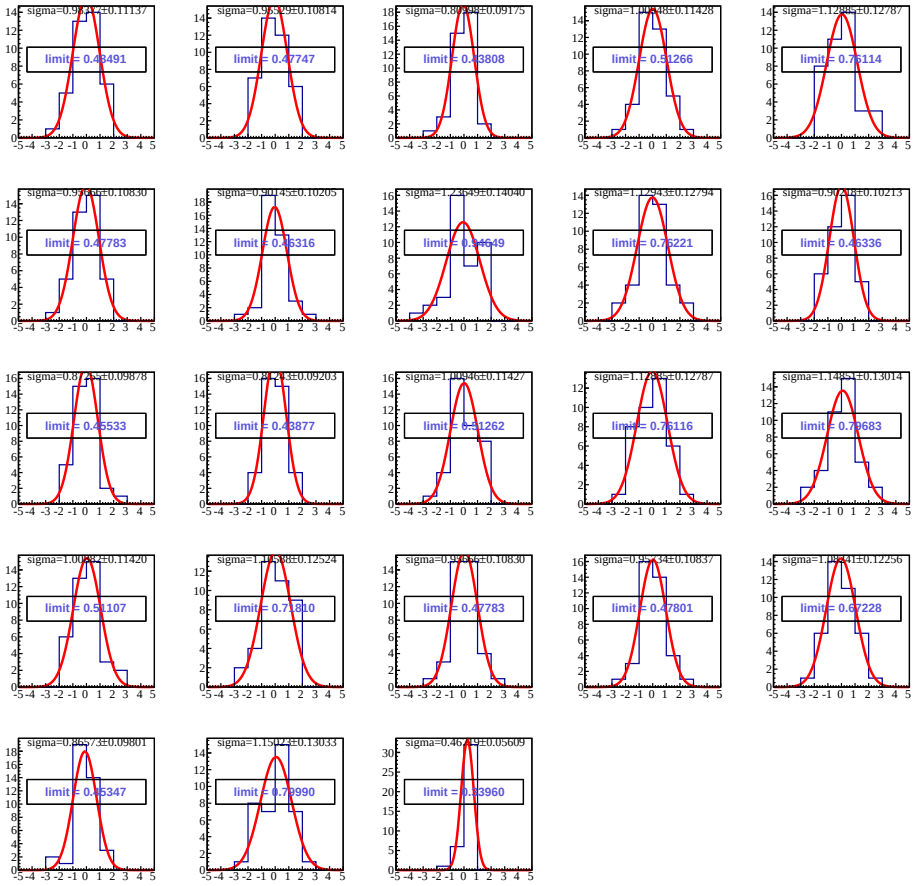

Figure E.16: Pulls for 2011, $A(\nu, Q^2)$, set of bins #4.

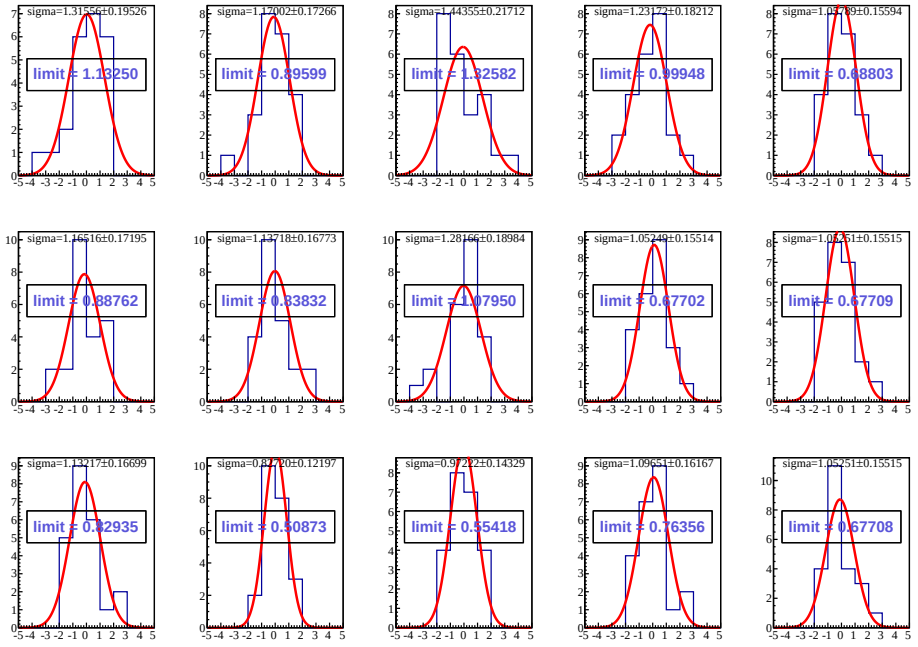

Figure E.17: Pulls for 2007, $A(x_{Bj}, \nu)$, set of bins #0.

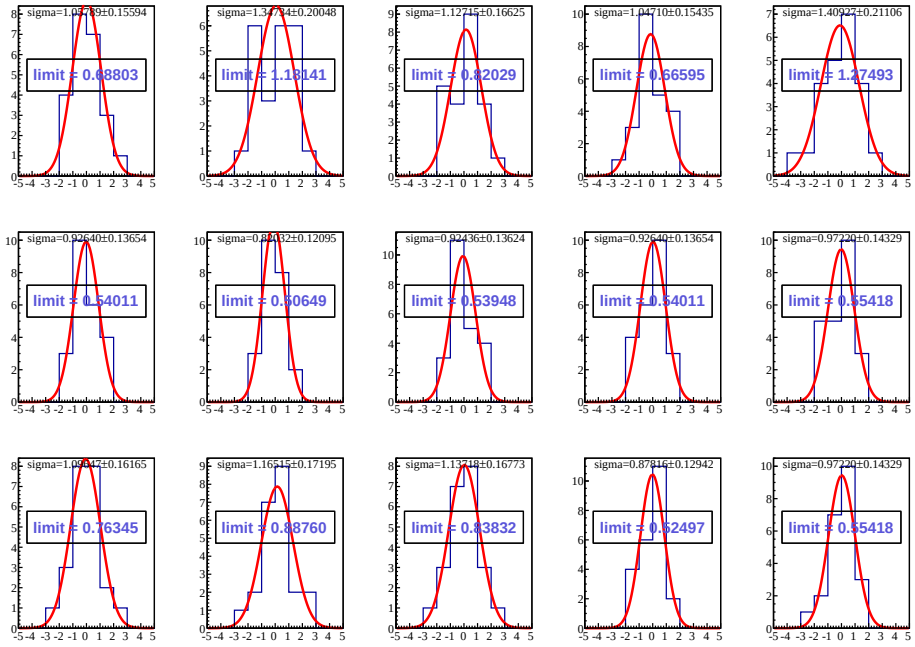

Figure E.18: Pulls for 2007, $A(x_{Bj}, \nu)$, set of bins #1.

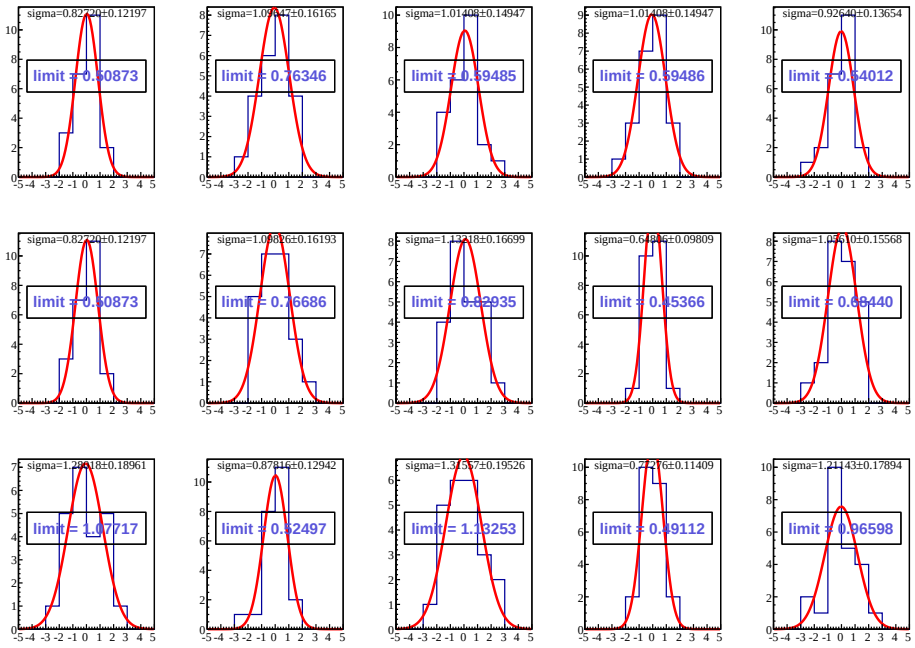

Figure E.19: Pulls for 2007, $A(x_{Bj}, \nu)$, set of bins #2.

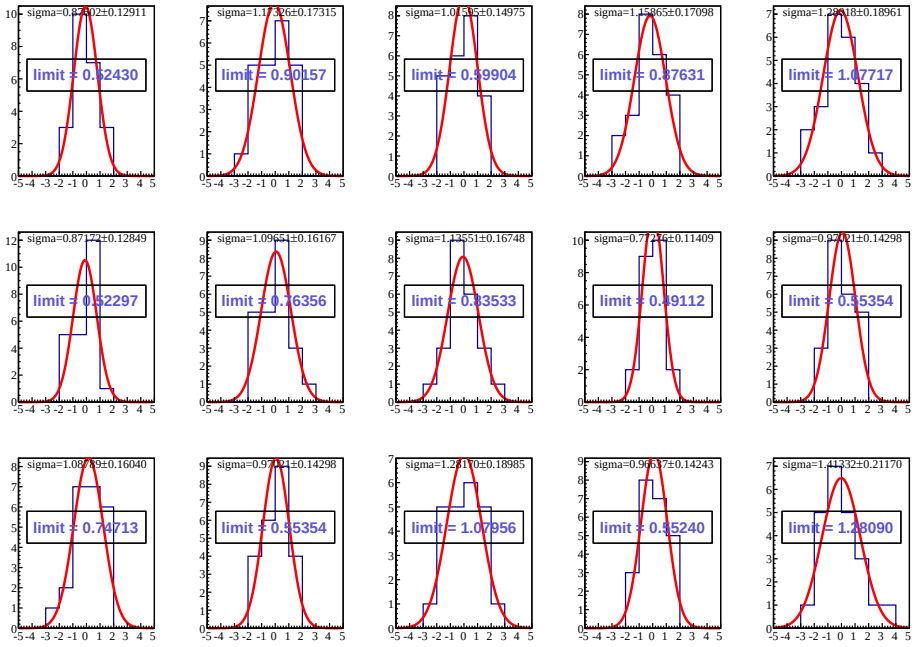

Figure E.20: Pulls for 2007, $A(x_{Bj}, \nu)$, set of bins #3.

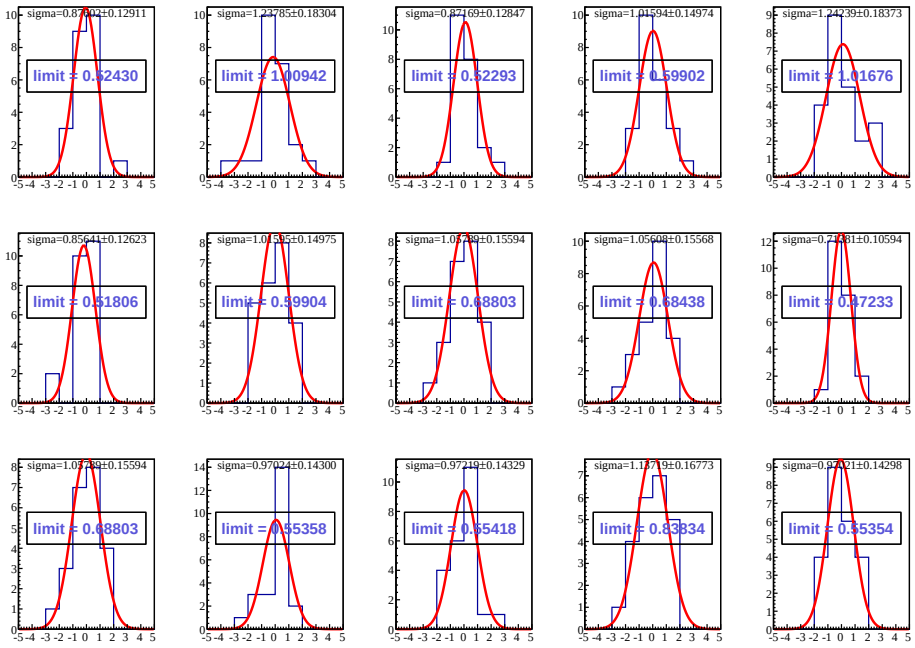

Figure E.21: Pulls for 2007, $A(x_{Bj}, \nu)$, set of bins #4.

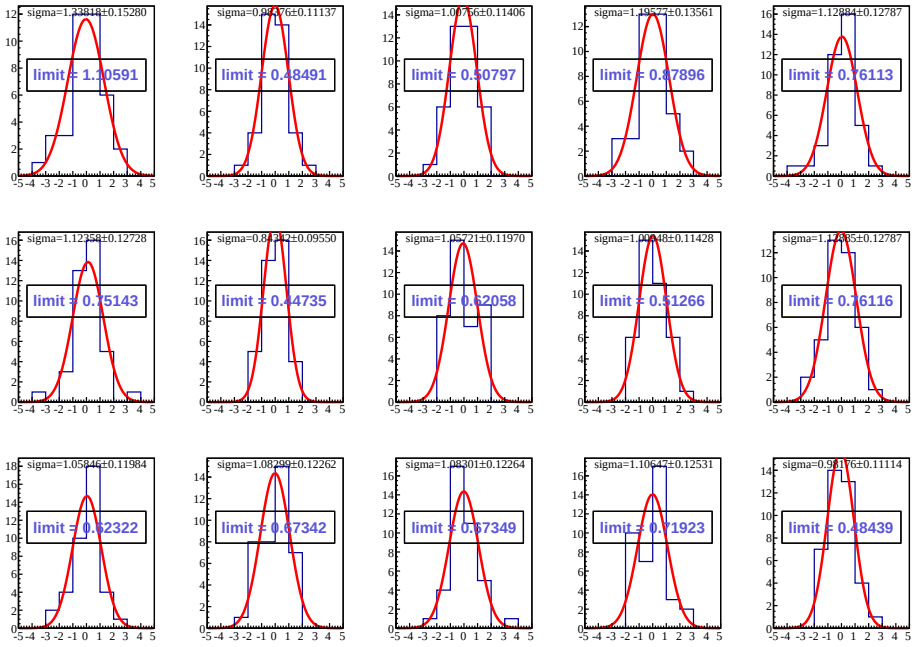

Figure E.22: Pulls for 2011, $A(x_{Bj}, \nu)$, set of bins #0.

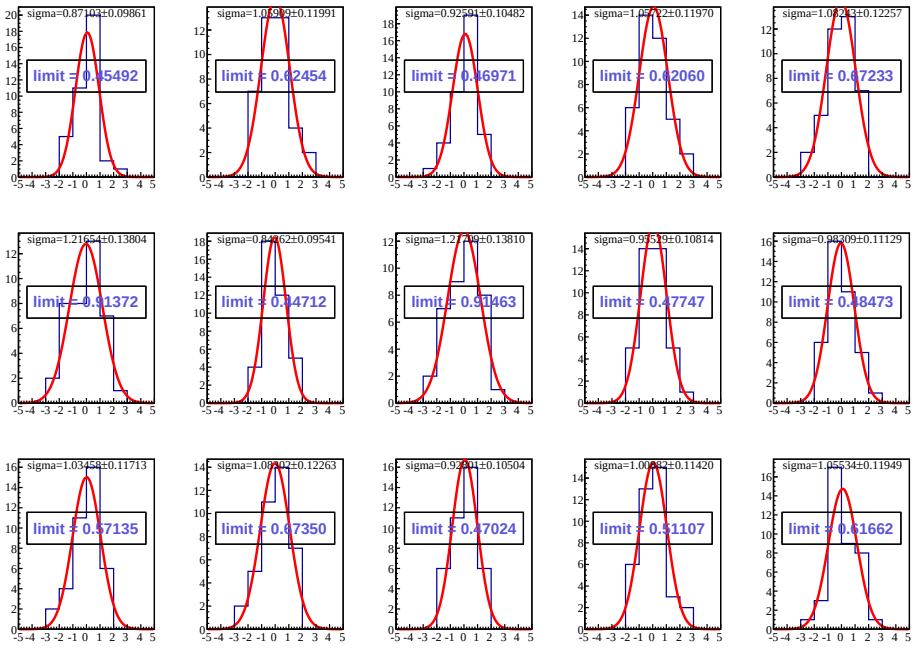

Figure E.23: Pulls for 2011, $A(x_{Bj}, \nu)$, set of bins #1.

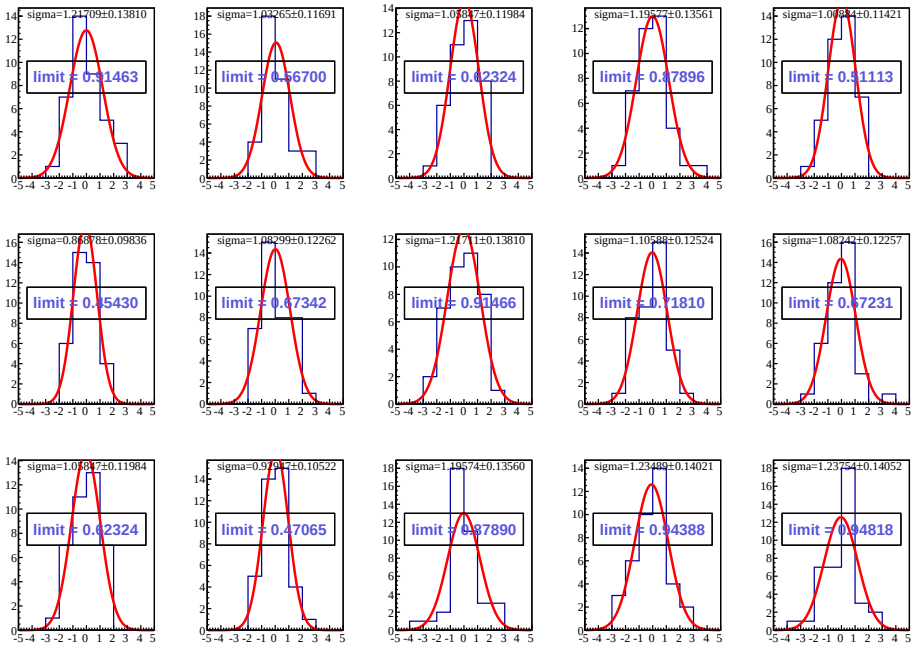

Figure E.24: Pulls for 2011, $A(x_{Bj}, \nu)$, set of bins #2.

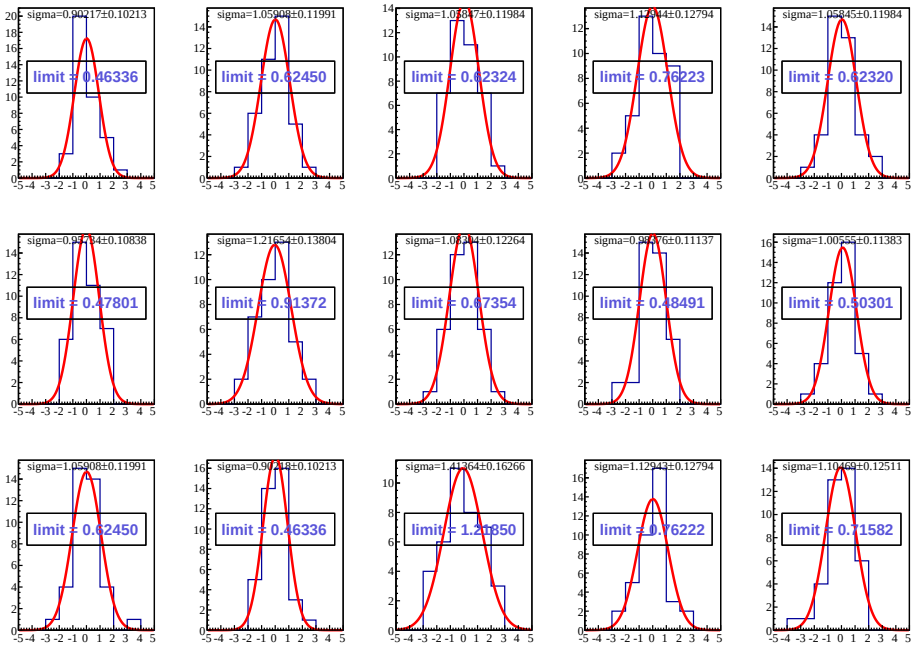

Figure E.25: Pulls for 2011, $A(x_{Bj}, \nu)$, set of bins #3.

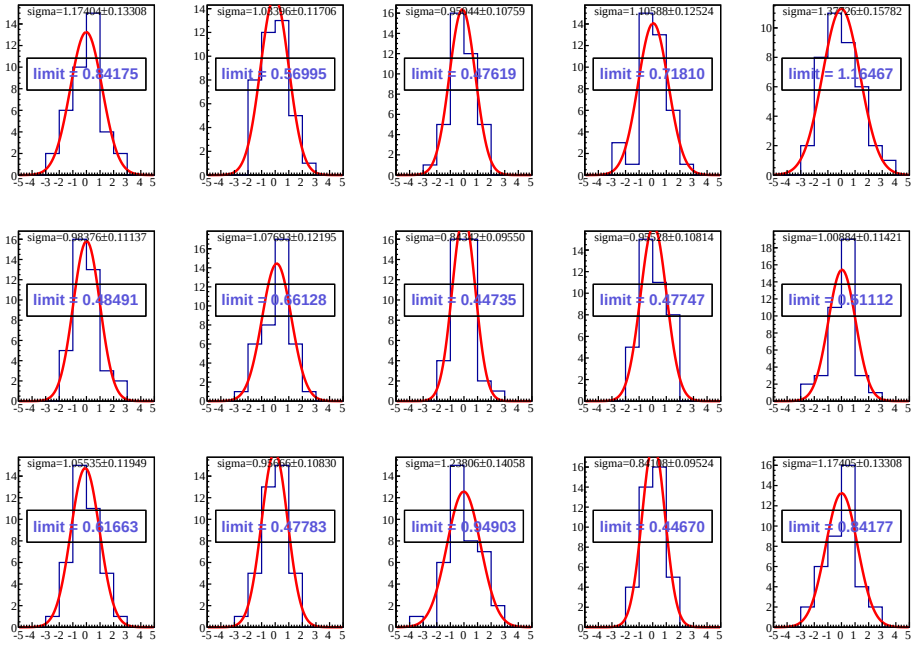

Figure E.26: Pulls for 2011, $A(x_{Bj}, \nu)$, set of bins #4.

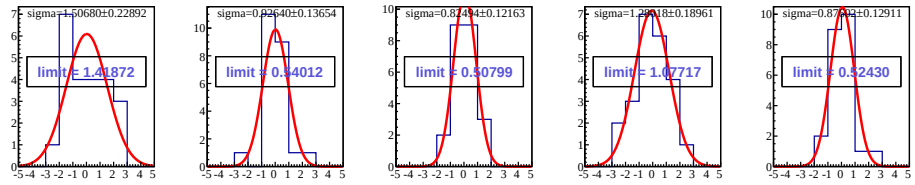

Figure E.27: Pulls for 2007, $A(Q^2, x_{Bj})$, set of bins #0.

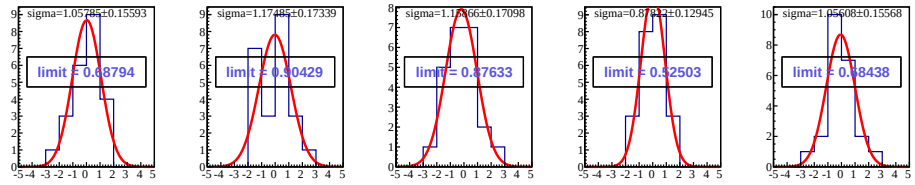

Figure E.28: Pulls for 2007, $A(Q^2, x_{Bj})$, set of bins #1.

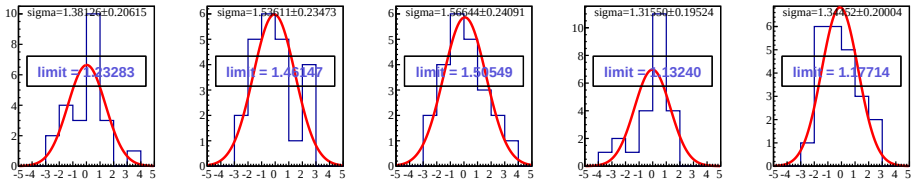

Figure E.29: Pulls for 2007, $A(Q^2, x_{Bj})$, set of bins #2.

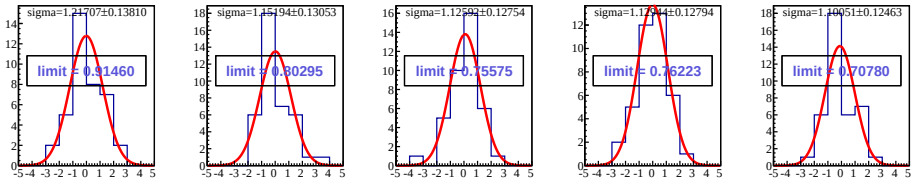

Figure E.30: Pulls for 2011, $A(Q^2, x_{Bj})$, set of bins #0.

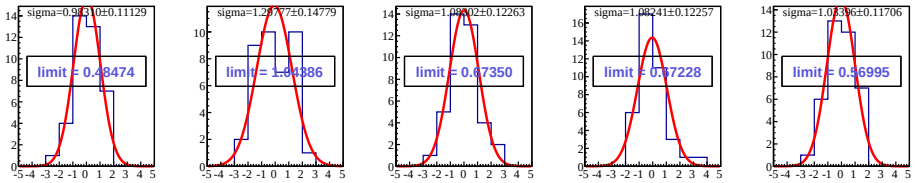

Figure E.31: Pulls for 2011, $A(Q^2, x_{Bj})$, set of bins #1.

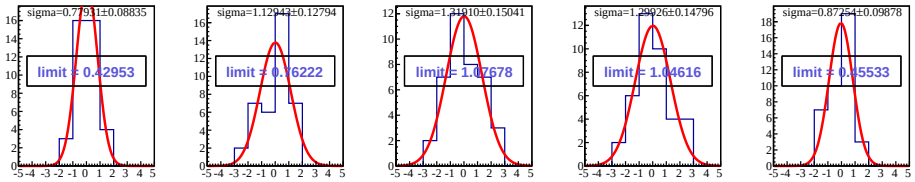

Figure E.32: Pulls for 2011, $A(Q^2, x_{Bj})$, set of bins #2.

Appendix F

Results

In this Appendix, the extracted results of A_1^p and g_1^p are presented in the referred tables:

Table(s)	Results
F.1	$A_1^p(x)$ from 2007 data
F.2	$A_1^p(\nu)$ from 2007 data
F.3	$A_1^p(x)$ from 2011 data
F.4	$A_1^p(\nu)$ from 2011 data
F.5	$g_1^p(x)$ from 2007 data
F.7	$g_1^p(\nu)$ from 2007 data
F.6	$g_1^p(x)$ from 2011 data
F.8	$g_1^p(\nu)$ from 2011 data
F.9	$A_1^p(x, Q^2)$ from 2007 data
F.10	$A_1^p(x, Q^2)$ from 2011 data
F.11 and F.12	$A_1^p(\nu, Q^2)$ from 2007 data
F.13 and F.14	$A_1^p(\nu, Q^2)$ from 2011 data
F.15 and F.16	$A_1^p(x, \nu)$ from 2007 data
F.17 and F.18	$A_1^p(x, \nu)$ from 2011 data
F.19	$A_1^p(Q^2, x)$ from 2007 data
F.20	$A_1^p(Q^2, x)$ from 2011 data
F.21	$g_1^p(x, Q^2)$ from 2007 data
F.22	$g_1^p(x, Q^2)$ from 2011 data
F.23 and F.24	$g_1^p(\nu, Q^2)$ from 2007 data
F.25 and F.26	$g_1^p(\nu, Q^2)$ from 2011 data
F.27	$g_1^p(x, \nu)$ from 2007 data
F.28	$g_1^p(x, \nu)$ from 2011 data
F.29	$g_1^p(Q^2, x)$ from 2007 data
F.30	$g_1^p(Q^2, x)$ from 2011 data.

$\log_{10}(x)$		$\langle x \rangle$	$\langle Q^2 \rangle$	$\langle \nu \rangle$	$\langle y \rangle$	$A_1^{p,exp}$	F_2^p	F_2^d	$\Delta A_1^{^{14}N}$	ΔA_1^{RC}	$A_1^{p\gamma}$	$\sigma_{stat}(A_1^p)$	$\sigma_{syst}(A_1^p)$
−4.4	−4.2	5.16×10^{-5}	6.19×10^{-3}	63.6	0.397	$+8.19 \times 10^{-3}$	7.324×10^{-3}	7.30×10^{-3}	-1.13×10^{-6}	0.00085	$+7.34 \times 10^{-3}$	4.2×10^{-3}	4.7×10^{-3}
−4.2	−4.0	8.11×10^{-5}	1.10×10^{-2}	72.0	0.450	$+8.08 \times 10^{-3}$	1.286×10^{-2}	1.28×10^{-2}	-1.77×10^{-6}	0.00061	$+7.47 \times 10^{-3}$	3.4×10^{-3}	4.4×10^{-3}
−4.0	−3.8	1.28×10^{-4}	1.90×10^{-2}	79.0	0.494	$+1.03 \times 10^{-2}$	2.179×10^{-2}	2.17×10^{-2}	-2.79×10^{-6}	0.00047	$+9.83 \times 10^{-3}$	2.9×10^{-3}	3.2×10^{-3}
−3.8	−3.6	2.02×10^{-4}	3.19×10^{-2}	84.1	0.526	$+8.62 \times 10^{-3}$	3.546×10^{-2}	3.53×10^{-2}	-4.37×10^{-6}	0.00040	$+8.22 \times 10^{-3}$	2.8×10^{-3}	2.2×10^{-3}
−3.6	−3.4	3.18×10^{-4}	5.18×10^{-2}	86.7	0.542	$+6.49 \times 10^{-3}$	5.491×10^{-2}	5.47×10^{-2}	-6.80×10^{-6}	0.00038	$+6.12 \times 10^{-3}$	2.8×10^{-3}	2.7×10^{-3}
−3.4	−3.2	5.03×10^{-4}	8.25×10^{-2}	87.4	0.547	$+1.37 \times 10^{-2}$	8.152×10^{-2}	8.13×10^{-2}	-1.06×10^{-5}	0.00040	$+1.33 \times 10^{-2}$	2.9×10^{-3}	3.6×10^{-3}
−3.2	−3.0	7.94×10^{-4}	1.30×10^{-1}	87.2	0.546	$+1.77 \times 10^{-2}$	1.161×10^{-1}	1.16×10^{-1}	-1.62×10^{-5}	0.00047	$+1.72 \times 10^{-2}$	3.2×10^{-3}	3.1×10^{-3}
−3.0	−2.8	1.26×10^{-3}	2.07×10^{-1}	87.7	0.549	$+1.31 \times 10^{-2}$	9.872×10^{-2}	9.84×10^{-2}	-2.45×10^{-5}	0.00058	$+1.25 \times 10^{-2}$	3.5×10^{-3}	3.0×10^{-3}
−2.8	−2.6	1.99×10^{-3}	3.29×10^{-1}	88.1	0.551	$+1.34 \times 10^{-2}$	1.517×10^{-1}	1.51×10^{-1}	-3.57×10^{-5}	0.00086	$+1.26 \times 10^{-2}$	4.0×10^{-3}	2.7×10^{-3}
−2.6	−2.4	3.14×10^{-3}	5.19×10^{-1}	88.0	0.552	$+1.62 \times 10^{-2}$	2.054×10^{-1}	2.03×10^{-1}	-4.93×10^{-5}	0.00120	$+1.50 \times 10^{-2}$	4.8×10^{-3}	4.9×10^{-3}
−2.4	−2.2	4.85×10^{-3}	6.56×10^{-1}	73.0	0.458	$+2.04 \times 10^{-2}$	2.302×10^{-1}	2.27×10^{-1}	-6.18×10^{-5}	0.00154	$+1.89 \times 10^{-2}$	6.7×10^{-3}	6.7×10^{-3}
−2.2	−2.0	7.73×10^{-3}	6.93×10^{-1}	48.5	0.304	$+4.96 \times 10^{-2}$	2.350×10^{-1}	2.30×10^{-1}	-6.70×10^{-5}	0.00182	$+4.78 \times 10^{-2}$	1.1×10^{-2}	8.1×10^{-3}
−2.0	−1.8	1.22×10^{-2}	7.43×10^{-1}	33.0	0.207	$+4.22 \times 10^{-2}$	2.463×10^{-1}	2.40×10^{-1}	-4.89×10^{-5}	0.00209	$+4.02 \times 10^{-2}$	1.9×10^{-2}	1.6×10^{-2}
−1.8	−1.6	1.90×10^{-2}	8.12×10^{-1}	23.0	0.145	$+3.96 \times 10^{-2}$	2.627×10^{-1}	2.55×10^{-1}	$+1.00 \times 10^{-5}$	0.00231	$+3.73 \times 10^{-2}$	3.5×10^{-2}	2.4×10^{-2}
−1.6	−1.4	2.76×10^{-2}	9.14×10^{-1}	17.7	0.112	$+3.54 \times 10^{-2}$	2.809×10^{-1}	2.71×10^{-1}	$+1.06 \times 10^{-4}$	0.00251	$+3.28 \times 10^{-2}$	1.1×10^{-1}	1.3×10^{-1}

Table F.1: $A_1^p(x)$ from 2007 data.

ν (GeV)		$\langle x \rangle$	$\langle Q^2 \rangle$	$\langle \nu \rangle$	$\langle y \rangle$	$A_1^{p,exp}$	F_2^p	F_2^d	$\Delta A_1^{^{14}N}$	ΔA_1^{RC}	$A_1^{p\gamma}$	$\sigma_{stat}(A_1^p)$	$\sigma_{syst}(A_1^p)$
8	16	4.25×10^{-3}	1.25×10^{-1}	15.6	0.103	-1.22×10^{-1}	1.162×10^{-1}	1.15×10^{-1}	-5.86×10^{-5}	0.00037	-1.22×10^{-1}	7.0×10^{-2}	6.9×10^{-2}
16	24	3.53×10^{-3}	1.35×10^{-1}	20.9	0.133	$+2.82 \times 10^{-2}$	1.214×10^{-1}	1.20×10^{-1}	-5.30×10^{-5}	0.00045	$+2.78 \times 10^{-2}$	1.1×10^{-2}	1.1×10^{-2}
24	32	1.86×10^{-3}	9.84×10^{-2}	28.5	0.181	$+2.37 \times 10^{-2}$	9.451×10^{-2}	9.38×10^{-2}	-3.38×10^{-5}	0.00047	$+2.33 \times 10^{-2}$	6.7×10^{-3}	8.5×10^{-3}
32	40	1.22×10^{-3}	8.23×10^{-2}	36.3	0.229	$+2.01 \times 10^{-2}$	8.143×10^{-2}	8.09×10^{-2}	-2.37×10^{-5}	0.00048	$+1.96 \times 10^{-2}$	4.9×10^{-3}	6.8×10^{-3}
40	48	9.40×10^{-4}	7.77×10^{-2}	44.2	0.278	$+5.93 \times 10^{-3}$	7.743×10^{-2}	7.70×10^{-2}	-1.89×10^{-5}	0.00046	$+5.49 \times 10^{-3}$	4.1×10^{-3}	5.3×10^{-3}
48	56	8.09×10^{-4}	7.90×10^{-2}	52.1	0.327	$+1.05 \times 10^{-2}$	7.838×10^{-2}	7.80×10^{-2}	-1.65×10^{-5}	0.00045	$+1.01 \times 10^{-2}$	3.7×10^{-3}	4.5×10^{-3}
56	64	7.40×10^{-4}	8.34×10^{-2}	60.1	0.377	$+9.89 \times 10^{-3}$	8.192×10^{-2}	8.15×10^{-2}	-1.52×10^{-5}	0.00044	$+9.47 \times 10^{-3}$	3.5×10^{-3}	5.0×10^{-3}
64	72	7.01×10^{-4}	8.94×10^{-2}	68.0	0.427	$+1.11 \times 10^{-2}$	8.671×10^{-2}	8.64×10^{-2}	-1.44×10^{-5}	0.00043	$+1.07 \times 10^{-2}$	3.3×10^{-3}	6.6×10^{-3}
72	80	6.92×10^{-4}	9.86×10^{-2}	76.0	0.476	$+1.46 \times 10^{-2}$	9.383×10^{-2}	9.35×10^{-2}	-1.43×10^{-5}	0.00043	$+1.42 \times 10^{-2}$	3.3×10^{-3}	8.0×10^{-3}
80	88	7.24×10^{-4}	1.14×10^{-1}	83.9	0.525	$+1.20 \times 10^{-2}$	1.051×10^{-1}	1.05×10^{-1}	-1.49×10^{-5}	0.00044	$+1.16 \times 10^{-2}$	3.4×10^{-3}	7.3×10^{-3}
88	96	7.59×10^{-4}	1.31×10^{-1}	92.0	0.576	$+7.87 \times 10^{-3}$	1.169×10^{-1}	1.16×10^{-1}	-1.55×10^{-5}	0.00046	$+7.43 \times 10^{-3}$	3.5×10^{-3}	5.3×10^{-3}
96	104	7.56×10^{-4}	1.42×10^{-1}	100	0.627	$+1.30 \times 10^{-2}$	1.241×10^{-1}	1.24×10^{-1}	-1.55×10^{-5}	0.00046	$+1.26 \times 10^{-2}$	3.6×10^{-3}	9.5×10^{-3}
104	112	7.64×10^{-4}	1.55×10^{-1}	108	0.676	$+9.80 \times 10^{-3}$	1.323×10^{-1}	1.32×10^{-1}	-1.56×10^{-5}	0.00047	$+9.35 \times 10^{-3}$	3.7×10^{-3}	7.5×10^{-3}
112	120	7.97×10^{-4}	1.74×10^{-1}	116	0.725	$+1.10 \times 10^{-2}$	1.436×10^{-1}	1.43×10^{-1}	-1.63×10^{-5}	0.00049	$+1.05 \times 10^{-2}$	3.9×10^{-3}	9.7×10^{-3}
120	128	8.52×10^{-4}	1.98×10^{-1}	124	0.774	$+1.86 \times 10^{-2}$	1.566×10^{-1}	1.56×10^{-1}	-1.73×10^{-5}	0.00052	$+1.81 \times 10^{-2}$	4.3×10^{-3}	1.6×10^{-2}
128	136	9.20×10^{-4}	2.27×10^{-1}	132	0.817	$+8.28 \times 10^{-3}$	1.157×10^{-1}	1.16×10^{-1}	-1.87×10^{-5}	0.00054	$+7.76 \times 10^{-3}$	5.1×10^{-3}	7.7×10^{-3}
136	144	1.02×10^{-3}	2.66×10^{-1}	139	0.850	$+3.41 \times 10^{-3}$	1.356×10^{-1}	1.36×10^{-1}	-2.05×10^{-5}	0.00060	$+2.83 \times 10^{-3}$	7.6×10^{-3}	4.9×10^{-3}
144	152	1.13×10^{-3}	3.11×10^{-1}	147	0.873	$+1.69 \times 10^{-2}$	1.557×10^{-1}	1.56×10^{-1}	-2.24×10^{-5}	0.00068	$+1.62 \times 10^{-2}$	1.8×10^{-2}	2.1×10^{-2}
152	160	1.16×10^{-3}	3.34×10^{-1}	154	0.882	$+1.75 \times 10^{-1}$	1.655×10^{-1}	1.66×10^{-1}	-2.30×10^{-5}	0.00068	$+1.74 \times 10^{-1}$	7.9×10^{-2}	1.7×10^{-1}
160	168	1.23×10^{-3}	3.71×10^{-1}	161	0.895	-6.81×10^{-1}	1.797×10^{-1}	1.80×10^{-1}	-2.42×10^{-5}	0.00075	-6.82×10^{-1}	$1.4 \times 10^{+0}$	8.0×10^{-1}

Table F.2: $A_1^p(\nu)$ from 2007 data.

$\log_{10}(x)$		$\langle x \rangle$	$\langle Q^2 \rangle$	$\langle \nu \rangle$	$\langle y \rangle$	$A_1^{p,exp}$	F_2^p	F_2^d	$\Delta A_1^{^{14}N}$	ΔA_1^{RC}	$A_1^{p\gamma}$	$\sigma_{stat}(A_1^p)$	$\sigma_{syst}(A_1^p)$
−4.4	−4.2	5.14×10^{-5}	9.06×10^{-3}	93.4	0.461	$+7.99 \times 10^{-3}$	1.069×10^{-2}	1.07×10^{-2}	-1.13×10^{-6}	0.00061	$+7.38 \times 10^{-3}$	4.3×10^{-3}	4.4×10^{-3}
−4.2	−4.0	8.10×10^{-5}	1.57×10^{-2}	103	0.508	$+5.88 \times 10^{-3}$	1.825×10^{-2}	1.82×10^{-2}	-1.77×10^{-6}	0.00045	$+5.43 \times 10^{-3}$	3.6×10^{-3}	2.3×10^{-3}
−4.0	−3.8	1.28×10^{-4}	2.64×10^{-2}	110	0.544	$+5.96 \times 10^{-3}$	2.991×10^{-2}	2.99×10^{-2}	-2.79×10^{-6}	0.00037	$+5.59 \times 10^{-3}$	3.3×10^{-3}	2.1×10^{-3}
−3.8	−3.6	2.01×10^{-4}	4.34×10^{-2}	115	0.567	$+4.49 \times 10^{-3}$	4.724×10^{-2}	4.71×10^{-2}	-4.35×10^{-6}	0.00034	$+4.15 \times 10^{-3}$	3.2×10^{-3}	1.9×10^{-3}
−3.6	−3.4	3.18×10^{-4}	6.97×10^{-2}	117	0.576	$+4.18 \times 10^{-3}$	7.138×10^{-2}	7.11×10^{-2}	-6.81×10^{-6}	0.00035	$+3.84 \times 10^{-3}$	3.3×10^{-3}	2.5×10^{-3}
−3.4	−3.2	5.03×10^{-4}	1.11×10^{-1}	117	0.580	$+9.97 \times 10^{-3}$	1.039×10^{-1}	1.03×10^{-1}	-1.06×10^{-5}	0.00028	$+9.70 \times 10^{-3}$	3.4×10^{-3}	2.4×10^{-3}
−3.2	−3.0	7.94×10^{-4}	1.74×10^{-1}	117	0.578	$+1.17 \times 10^{-2}$	1.436×10^{-1}	1.43×10^{-1}	-1.62×10^{-5}	0.00048	$+1.12 \times 10^{-2}$	3.8×10^{-3}	2.8×10^{-3}
−3.0	−2.8	1.26×10^{-3}	2.81×10^{-1}	119	0.588	$+1.12 \times 10^{-2}$	1.388×10^{-1}	1.39×10^{-1}	-2.46×10^{-5}	0.00065	$+1.06 \times 10^{-2}$	4.2×10^{-3}	2.7×10^{-3}
−2.8	−2.6	1.99×10^{-3}	4.44×10^{-1}	119	0.588	$+4.01 \times 10^{-4}$	1.932×10^{-1}	1.93×10^{-1}	-3.58×10^{-5}	0.00093	-4.93×10^{-4}	4.9×10^{-3}	3.7×10^{-3}
−2.6	−2.4	3.09×10^{-3}	6.46×10^{-1}	112	0.557	$+2.08 \times 10^{-2}$	2.360×10^{-1}	2.34×10^{-1}	-4.88×10^{-5}	0.00120	$+1.96 \times 10^{-2}$	6.1×10^{-3}	3.8×10^{-3}
−2.4	−2.2	4.84×10^{-3}	7.09×10^{-1}	79.3	0.393	$+4.98 \times 10^{-2}$	2.403×10^{-1}	2.37×10^{-1}	-6.18×10^{-5}	0.00150	$+4.84 \times 10^{-2}$	1.1×10^{-2}	8.6×10^{-3}
−2.2	−2.0	7.68×10^{-3}	7.57×10^{-1}	53.3	0.264	$+1.46 \times 10^{-2}$	2.454×10^{-1}	2.40×10^{-1}	-6.70×10^{-5}	0.00177	$+1.29 \times 10^{-2}$	1.8×10^{-2}	1.0×10^{-2}
−2.0	−1.8	1.21×10^{-2}	8.01×10^{-1}	35.9	0.178	$+1.01 \times 10^{-1}$	2.542×10^{-1}	2.48×10^{-1}	-4.95×10^{-5}	0.00201	$+9.90 \times 10^{-2}$	3.4×10^{-2}	2.5×10^{-2}
−1.8	−1.6	1.85×10^{-2}	8.74×10^{-1}	25.3	0.126	$+1.04 \times 10^{-2}$	2.692×10^{-1}	2.61×10^{-1}	$+4.98 \times 10^{-6}$	0.00221	$+8.19 \times 10^{-3}$	7.6×10^{-2}	4.6×10^{-2}
−1.6	−1.4	2.58×10^{-2}	9.76×10^{-1}	20.2	0.103	-4.44×10^{-1}	2.851×10^{-1}	2.75×10^{-1}	$+8.48 \times 10^{-5}$	0.00240	-4.46×10^{-1}	8.1×10^{-1}	6.1×10^{-1}

Table F.3: $A_1^p(x)$ 2011 data.

ν (GeV)		$\langle x \rangle$	$\langle Q^2 \rangle$	$\langle \nu \rangle$	$\langle y \rangle$	$A_1^{p,exp}$	F_2^p	F_2^d	$\Delta A_1^{^{14}N}$	ΔA_1^{RC}	$A_1^{p\gamma}$	$\sigma_{stat}(A_1^p)$	$\sigma_{syst}(A_1^p)$
16	24	9.55×10^{-3}	3.96×10^{-1}	22.2	0.111	$+4.53 \times 10^{-2}$	1.738×10^{-1}	1.70×10^{-1}	-6.27×10^{-5}	0.00107	$+4.43 \times 10^{-2}$	5.8×10^{-2}	4.1×10^{-2}
24	32	5.96×10^{-3}	3.16×10^{-1}	28.6	0.144	$+5.13 \times 10^{-2}$	1.421×10^{-1}	1.39×10^{-1}	-6.59×10^{-5}	0.00085	$+5.05 \times 10^{-2}$	2.7×10^{-2}	2.0×10^{-2}
32	40	3.19×10^{-3}	2.17×10^{-1}	36.6	0.184	$+2.60 \times 10^{-2}$	9.755×10^{-2}	9.62×10^{-2}	-4.96×10^{-5}	0.00060	$+2.54 \times 10^{-2}$	1.7×10^{-2}	1.5×10^{-2}
40	48	1.81×10^{-3}	1.50×10^{-1}	44.5	0.224	$+3.03 \times 10^{-2}$	1.282×10^{-1}	1.28×10^{-1}	-3.31×10^{-5}	0.00050	$+2.98 \times 10^{-2}$	1.1×10^{-2}	9.0×10^{-3}
48	56	1.15×10^{-3}	1.13×10^{-1}	52.4	0.262	$+2.27 \times 10^{-3}$	1.041×10^{-1}	1.03×10^{-1}	-2.26×10^{-5}	0.00046	$+1.83 \times 10^{-3}$	7.8×10^{-3}	4.2×10^{-3}
56	64	8.36×10^{-4}	9.43×10^{-2}	60.3	0.301	$+1.12 \times 10^{-2}$	9.043×10^{-2}	9.00×10^{-2}	-1.70×10^{-5}	0.00044	$+1.08 \times 10^{-2}$	6.1×10^{-3}	5.4×10^{-3}
64	72	6.87×10^{-4}	8.78×10^{-2}	68.1	0.339	$+5.53 \times 10^{-3}$	8.546×10^{-2}	8.51×10^{-2}	-1.42×10^{-5}	0.00042	$+5.12 \times 10^{-3}$	5.2×10^{-3}	4.6×10^{-3}
72	80	6.21×10^{-4}	8.86×10^{-2}	76.1	0.378	$+7.90 \times 10^{-3}$	8.618×10^{-2}	8.58×10^{-2}	-1.29×10^{-5}	0.00041	$+7.50 \times 10^{-3}$	4.7×10^{-3}	4.2×10^{-3}
80	88	5.93×10^{-4}	9.35×10^{-2}	84.1	0.417	$+3.51 \times 10^{-3}$	9.011×10^{-2}	8.97×10^{-2}	-1.23×10^{-5}	0.00041	$+3.11 \times 10^{-3}$	4.4×10^{-3}	3.9×10^{-3}
88	96	5.79×10^{-4}	1.00×10^{-1}	92.1	0.456	$+1.12 \times 10^{-2}$	9.519×10^{-2}	9.49×10^{-2}	-1.21×10^{-5}	0.00040	$+1.08 \times 10^{-2}$	4.3×10^{-3}	6.0×10^{-3}
96	104	5.69×10^{-4}	1.07×10^{-1}	100	0.495	$+1.04 \times 10^{-2}$	1.005×10^{-1}	1.00×10^{-1}	-1.19×10^{-5}	0.00040	$+1.00 \times 10^{-2}$	4.1×10^{-3}	6.1×10^{-3}
104	112	5.63×10^{-4}	1.14×10^{-1}	108	0.534	$+7.92 \times 10^{-3}$	1.057×10^{-1}	1.05×10^{-1}	-1.18×10^{-5}	0.00040	$+7.53 \times 10^{-3}$	4.1×10^{-3}	5.1×10^{-3}
112	120	5.71×10^{-4}	1.24×10^{-1}	116	0.573	$+1.47 \times 10^{-2}$	1.129×10^{-1}	1.13×10^{-1}	-1.19×10^{-5}	0.00041	$+1.43 \times 10^{-2}$	4.1×10^{-3}	9.8×10^{-3}
120	128	5.97×10^{-4}	1.39×10^{-1}	124	0.613	$+7.94 \times 10^{-3}$	1.230×10^{-1}	1.23×10^{-1}	-1.24×10^{-5}	0.00042	$+7.53 \times 10^{-3}$	4.3×10^{-3}	6.6×10^{-3}
128	136	6.17×10^{-4}	1.53×10^{-1}	132	0.652	$+5.97 \times 10^{-3}$	1.320×10^{-1}	1.31×10^{-1}	-1.28×10^{-5}	0.00045	$+5.53 \times 10^{-3}$	4.5×10^{-3}	5.5×10^{-3}
136	144	6.25×10^{-4}	1.64×10^{-1}	140	0.692	-3.16×10^{-3}	1.389×10^{-1}	1.39×10^{-1}	-1.30×10^{-5}	0.00043	-3.58×10^{-3}	4.7×10^{-3}	4.6×10^{-3}
144	152	6.43×10^{-4}	1.78×10^{-1}	148	0.731	$+6.71 \times 10^{-3}$	1.471×10^{-1}	1.47×10^{-1}	-1.33×10^{-5}	0.00044	$+6.28 \times 10^{-3}$	4.9×10^{-3}	5.6×10^{-3}
152	160	6.83×10^{-4}	2.00×10^{-1}	156	0.770	$+4.54 \times 10^{-3}$	1.592×10^{-1}	1.59×10^{-1}	-1.41×10^{-5}	0.00046	$+4.09 \times 10^{-3}$	5.2×10^{-3}	4.2×10^{-3}
160	168	7.38×10^{-4}	2.27×10^{-1}	164	0.807	$+5.37 \times 10^{-3}$	1.202×10^{-1}	1.72×10^{-1}	-2.18×10^{-5}	0.00049	$+4.90 \times 10^{-3}$	5.8×10^{-3}	6.1×10^{-3}
168	176	8.21×10^{-4}	2.65×10^{-1}	172	0.841	$+5.87 \times 10^{-3}$	1.402×10^{-1}	1.89×10^{-1}	-2.26×10^{-5}	0.00054	$+5.35 \times 10^{-3}$	6.9×10^{-3}	6.1×10^{-3}
176	184	9.21×10^{-4}	3.10×10^{-1}	179	0.866	$+2.62 \times 10^{-2}$	1.607×10^{-1}	1.62×10^{-1}	-1.88×10^{-5}	0.00061	$+2.56 \times 10^{-2}$	1.0×10^{-2}	2.4×10^{-2}
184	192	1.04×10^{-3}	3.63×10^{-1}	186	0.885	$+4.42 \times 10^{-2}$	1.814×10^{-1}	1.83×10^{-1}	-2.09×10^{-5}	0.00071	$+4.35 \times 10^{-2}$	2.3×10^{-2}	4.2×10^{-2}
192	200	1.15×10^{-3}	4.15×10^{-1}	192	0.898	-4.12×10^{-1}	1.991×10^{-1}	2.01×10^{-1}	-2.28×10^{-5}	0.00048	-4.12×10^{-1}	2.7×10^{-1}	9.9×10^{-1}

Table F.4: $A_1^p(\nu)$ from 2011 data.

$\log_{10}(x)$		$\langle x \rangle$	$\langle Q^2 \rangle$	$\langle \nu \rangle$	R	$\sigma(R)$	g_1^p	$\sigma_{stat}(g_1^p)$	$\sigma_{syst}(g_1^p)$
−4.4	−4.2	5.16×10^{-5}	63.6	6.19×10^{-3}	1.039×10^{-2}	2.000×10^{-1}	$+5.16 \times 10^{-1}$	2.9×10^{-1}	2.9×10^{-1}
−4.2	−4.0	8.11×10^{-5}	72.0	1.10×10^{-2}	1.817×10^{-2}	2.000×10^{-1}	$+5.82 \times 10^{-1}$	2.6×10^{-1}	3.1×10^{-1}
−4.0	−3.8	1.28×10^{-4}	79.0	1.90×10^{-2}	3.071×10^{-2}	2.000×10^{-1}	$+8.12 \times 10^{-1}$	2.4×10^{-1}	2.2×10^{-1}
−3.8	−3.6	2.02×10^{-4}	84.1	3.19×10^{-2}	5.001×10^{-2}	2.000×10^{-1}	$+6.87 \times 10^{-1}$	2.3×10^{-1}	1.5×10^{-1}
−3.6	−3.4	3.18×10^{-4}	86.7	5.18×10^{-2}	7.782×10^{-2}	2.000×10^{-1}	$+4.90 \times 10^{-1}$	2.2×10^{-1}	2.1×10^{-1}
−3.4	−3.2	5.03×10^{-4}	87.4	8.25×10^{-2}	1.166×10^{-1}	2.000×10^{-1}	$+9.65 \times 10^{-1}$	2.1×10^{-1}	2.4×10^{-1}
−3.2	−3.0	7.94×10^{-4}	87.2	1.30×10^{-1}	1.681×10^{-1}	2.000×10^{-1}	$+1.08 \times 10^{+0}$	2.0×10^{-1}	1.6×10^{-1}
−3.0	−2.8	1.26×10^{-3}	87.7	2.07×10^{-1}	2.340×10^{-1}	2.000×10^{-1}	$+3.97 \times 10^{-1}$	1.1×10^{-1}	1.5×10^{-1}
−2.8	−2.6	1.99×10^{-3}	88.1	3.29×10^{-1}	3.060×10^{-1}	2.000×10^{-1}	$+3.68 \times 10^{-1}$	1.2×10^{-1}	9.5×10^{-2}
−2.6	−2.4	3.14×10^{-3}	88.0	5.19×10^{-1}	3.687×10^{-1}	6.703×10^{-2}	$+3.58 \times 10^{-1}$	1.1×10^{-1}	1.2×10^{-1}
−2.4	−2.2	4.85×10^{-3}	73.0	6.56×10^{-1}	3.901×10^{-1}	6.109×10^{-2}	$+3.23 \times 10^{-1}$	1.2×10^{-1}	1.2×10^{-1}
−2.2	−2.0	7.73×10^{-3}	48.5	6.93×10^{-1}	3.911×10^{-1}	6.076×10^{-2}	$+5.22 \times 10^{-1}$	1.2×10^{-1}	9.6×10^{-2}
−2.0	−1.8	1.22×10^{-2}	33.0	7.43×10^{-1}	3.920×10^{-1}	6.060×10^{-2}	$+2.92 \times 10^{-1}$	1.3×10^{-1}	1.2×10^{-1}
−1.8	−1.6	1.90×10^{-2}	23.0	8.12×10^{-1}	3.918×10^{-1}	6.019×10^{-2}	$+1.85 \times 10^{-1}$	1.8×10^{-1}	1.2×10^{-1}
−1.6	−1.4	2.76×10^{-2}	17.7	9.14×10^{-1}	3.895×10^{-1}	5.926×10^{-2}	$+1.20 \times 10^{-1}$	4.0×10^{-1}	4.8×10^{-1}

Table F.5: $g_1^p(x)$ from 2007 data.

ν	(GeV)	$\langle x \rangle$	$\langle Q^2 \rangle$	$\langle \nu \rangle$	R	$\sigma(R)$	g_1^p	$\sigma_{stat}(g_1^p)$	$\sigma_{syst}(g_1^p)$
8	16	4.25×10^{-3}	15.6	1.25×10^{-1}	1.590×10^{-1}	2.000×10^{-1}	$-1.44 \times 10^{+0}$	8.3×10^{-1}	8.4×10^{-1}
16	24	3.53×10^{-3}	20.9	1.35×10^{-1}	1.693×10^{-1}	2.000×10^{-1}	$+4.09 \times 10^{-1}$	1.6×10^{-1}	1.6×10^{-1}
24	32	1.86×10^{-3}	28.5	9.84×10^{-2}	1.326×10^{-1}	2.000×10^{-1}	$+5.23 \times 10^{-1}$	1.5×10^{-1}	1.8×10^{-1}
32	40	1.22×10^{-3}	36.3	8.23×10^{-2}	1.148×10^{-1}	2.000×10^{-1}	$+5.87 \times 10^{-1}$	1.5×10^{-1}	1.7×10^{-1}
40	48	9.40×10^{-4}	44.2	7.77×10^{-2}	1.097×10^{-1}	2.000×10^{-1}	$+2.04 \times 10^{-1}$	1.5×10^{-1}	1.9×10^{-1}
48	56	8.09×10^{-4}	52.1	7.90×10^{-2}	1.115×10^{-1}	2.000×10^{-1}	$+4.40 \times 10^{-1}$	1.6×10^{-1}	1.3×10^{-1}
56	64	7.40×10^{-4}	60.1	8.34×10^{-2}	1.170×10^{-1}	2.000×10^{-1}	$+4.69 \times 10^{-1}$	1.7×10^{-1}	1.6×10^{-1}
64	72	7.01×10^{-4}	68.0	8.94×10^{-2}	1.242×10^{-1}	2.000×10^{-1}	$+5.89 \times 10^{-1}$	1.8×10^{-1}	2.4×10^{-1}
72	80	6.92×10^{-4}	76.0	9.86×10^{-2}	1.348×10^{-1}	2.000×10^{-1}	$+8.48 \times 10^{-1}$	2.0×10^{-1}	1.7×10^{-1}
80	88	7.24×10^{-4}	83.9	1.14×10^{-1}	1.517×10^{-1}	2.000×10^{-1}	$+7.31 \times 10^{-1}$	2.1×10^{-1}	1.5×10^{-1}
88	96	7.59×10^{-4}	92.0	1.31×10^{-1}	1.692×10^{-1}	2.000×10^{-1}	$+4.89 \times 10^{-1}$	2.3×10^{-1}	1.4×10^{-1}
96	104	7.56×10^{-4}	100	1.42×10^{-1}	1.801×10^{-1}	2.000×10^{-1}	$+8.76 \times 10^{-1}$	2.5×10^{-1}	2.2×10^{-1}
104	112	7.64×10^{-4}	108	1.55×10^{-1}	1.923×10^{-1}	2.000×10^{-1}	$+6.79 \times 10^{-1}$	2.7×10^{-1}	1.7×10^{-1}
112	120	7.97×10^{-4}	116	1.74×10^{-1}	2.090×10^{-1}	2.000×10^{-1}	$+7.82 \times 10^{-1}$	2.9×10^{-1}	3.4×10^{-1}
120	128	8.52×10^{-4}	124	1.98×10^{-1}	2.285×10^{-1}	2.000×10^{-1}	$+1.35 \times 10^{+0}$	3.2×10^{-1}	2.5×10^{-1}
128	136	9.20×10^{-4}	132	2.27×10^{-1}	2.497×10^{-1}	2.000×10^{-1}	$+3.90 \times 10^{-1}$	2.6×10^{-1}	2.0×10^{-1}
136	144	1.02×10^{-3}	139	2.66×10^{-1}	2.748×10^{-1}	2.000×10^{-1}	$+1.48 \times 10^{-1}$	4.0×10^{-1}	2.2×10^{-1}
144	152	1.13×10^{-3}	147	3.11×10^{-1}	2.996×10^{-1}	2.000×10^{-1}	$+8.59 \times 10^{-1}$	9.4×10^{-1}	8.0×10^{-1}
152	160	1.16×10^{-3}	154	3.34×10^{-1}	3.108×10^{-1}	2.000×10^{-1}	$+9.47 \times 10^{+0}$	$4.3 \times 10^{+0}$	$3.1 \times 10^{+0}$
160	168	1.23×10^{-3}	161	3.71×10^{-1}	3.269×10^{-1}	2.000×10^{-1}	$-3.75 \times 10^{+1}$	$7.7 \times 10^{+1}$	$2.7 \times 10^{+1}$

Table F.6: $g_1^p(\nu)$ from 2007 data.

$\log_{10}(x)$		$\langle x \rangle$	$\langle Q^2 \rangle$	$\langle \nu \rangle$	R	$\sigma(R)$	g_1^p	$\sigma_{stat}(g_1^p)$	$\sigma_{syst}(g_1^p)$
−4.4	−4.2	5.14×10^{-5}	93.4	9.06×10^{-3}	1.513×10^{-2}	2.000×10^{-1}	$+7.56 \times 10^{-1}$	4.4×10^{-1}	4.0×10^{-1}
−4.2	−4.0	8.10×10^{-5}	103	1.57×10^{-2}	2.571×10^{-2}	2.000×10^{-1}	$+5.96 \times 10^{-1}$	4.0×10^{-1}	2.2×10^{-1}
−4.0	−3.8	1.28×10^{-4}	110	2.64×10^{-2}	4.210×10^{-2}	2.000×10^{-1}	$+6.27 \times 10^{-1}$	3.6×10^{-1}	2.2×10^{-1}
−3.8	−3.6	2.01×10^{-4}	115	4.34×10^{-2}	6.666×10^{-2}	2.000×10^{-1}	$+4.57 \times 10^{-1}$	3.5×10^{-1}	2.1×10^{-1}
−3.6	−3.4	3.18×10^{-4}	117	6.97×10^{-2}	1.014×10^{-1}	2.000×10^{-1}	$+3.91 \times 10^{-1}$	3.3×10^{-1}	2.5×10^{-1}
−3.4	−3.2	5.03×10^{-4}	117	1.11×10^{-1}	1.493×10^{-1}	2.000×10^{-1}	$+8.72 \times 10^{-1}$	3.1×10^{-1}	2.0×10^{-1}
−3.2	−3.0	7.94×10^{-4}	117	1.74×10^{-1}	2.090×10^{-1}	2.000×10^{-1}	$+8.38 \times 10^{-1}$	2.8×10^{-1}	2.0×10^{-1}
−3.0	−2.8	1.26×10^{-3}	119	2.81×10^{-1}	2.828×10^{-1}	2.000×10^{-1}	$+4.55 \times 10^{-1}$	1.8×10^{-1}	1.4×10^{-1}
−2.8	−2.6	1.99×10^{-3}	119	4.44×10^{-1}	3.507×10^{-1}	2.000×10^{-1}	-1.77×10^{-2}	1.7×10^{-1}	1.3×10^{-1}
−2.6	−2.4	3.09×10^{-3}	112	6.46×10^{-1}	3.916×10^{-1}	6.224×10^{-2}	$+5.38 \times 10^{-1}$	1.7×10^{-1}	1.1×10^{-1}
−2.4	−2.2	4.84×10^{-3}	79.3	7.09×10^{-1}	3.954×10^{-1}	6.348×10^{-2}	$+8.61 \times 10^{-1}$	1.9×10^{-1}	1.6×10^{-1}
−2.2	−2.0	7.68×10^{-3}	53.3	7.57×10^{-1}	3.959×10^{-1}	6.357×10^{-2}	$+1.48 \times 10^{-1}$	2.1×10^{-1}	1.2×10^{-1}
−2.0	−1.8	1.21×10^{-2}	35.9	8.01×10^{-1}	3.950×10^{-1}	6.272×10^{-2}	$+7.45 \times 10^{-1}$	2.6×10^{-1}	1.9×10^{-1}
−1.8	−1.6	1.85×10^{-2}	25.3	8.74×10^{-1}	3.935×10^{-1}	6.176×10^{-2}	$+4.28 \times 10^{-2}$	4.0×10^{-1}	2.4×10^{-1}
−1.6	−1.4	2.58×10^{-2}	20.2	9.76×10^{-1}	3.902×10^{-1}	6.019×10^{-2}	$-1.77 \times 10^{+0}$	$3.2 \times 10^{+0}$	$2.4 \times 10^{+0}$

Table F.7: $g_1^p(x)$ from 2011 data.

ν (GeV)		$\langle x \rangle$	$\langle Q^2 \rangle$	$\langle \nu \rangle$	R	$\sigma(R)$	g_1^p	$\sigma_{stat}(g_1^p)$	$\sigma_{syst}(g_1^p)$
16	24	9.55×10^{-3}	22.2	3.96×10^{-1}	3.266×10^{-1}	2.000×10^{-1}	$+3.04 \times 10^{-1}$	4.0×10^{-1}	2.9×10^{-1}
24	32	5.96×10^{-3}	28.6	3.16×10^{-1}	2.948×10^{-1}	2.000×10^{-1}	$+4.65 \times 10^{-1}$	2.5×10^{-1}	2.0×10^{-1}
32	40	3.19×10^{-3}	36.6	2.17×10^{-1}	2.381×10^{-1}	2.000×10^{-1}	$+3.14 \times 10^{-1}$	2.1×10^{-1}	2.1×10^{-1}
40	48	1.81×10^{-3}	44.5	1.50×10^{-1}	1.852×10^{-1}	2.000×10^{-1}	$+8.90 \times 10^{-1}$	3.3×10^{-1}	2.1×10^{-1}
48	56	1.15×10^{-3}	52.4	1.13×10^{-1}	1.496×10^{-1}	2.000×10^{-1}	$+7.20 \times 10^{-2}$	3.1×10^{-1}	1.6×10^{-1}
56	64	8.36×10^{-4}	60.3	9.43×10^{-2}	1.295×10^{-1}	2.000×10^{-1}	$+5.17 \times 10^{-1}$	2.9×10^{-1}	2.1×10^{-1}
64	72	6.87×10^{-4}	68.1	8.78×10^{-2}	1.223×10^{-1}	2.000×10^{-1}	$+2.84 \times 10^{-1}$	2.9×10^{-1}	2.3×10^{-1}
72	80	6.21×10^{-4}	76.1	8.86×10^{-2}	1.235×10^{-1}	2.000×10^{-1}	$+4.63 \times 10^{-1}$	2.9×10^{-1}	1.8×10^{-1}
80	88	5.93×10^{-4}	84.1	9.35×10^{-2}	1.293×10^{-1}	2.000×10^{-1}	$+2.09 \times 10^{-1}$	3.0×10^{-1}	2.5×10^{-1}
88	96	5.79×10^{-4}	92.1	1.00×10^{-1}	1.368×10^{-1}	2.000×10^{-1}	$+7.81 \times 10^{-1}$	3.1×10^{-1}	1.8×10^{-1}
96	104	5.69×10^{-4}	100	1.07×10^{-1}	1.446×10^{-1}	2.000×10^{-1}	$+7.72 \times 10^{-1}$	3.2×10^{-1}	1.8×10^{-1}
104	112	5.63×10^{-4}	108	1.14×10^{-1}	1.523×10^{-1}	2.000×10^{-1}	$+6.13 \times 10^{-1}$	3.3×10^{-1}	1.8×10^{-1}
112	120	5.71×10^{-4}	116	1.24×10^{-1}	1.628×10^{-1}	2.000×10^{-1}	$+1.22 \times 10^{+0}$	3.5×10^{-1}	2.4×10^{-1}
120	128	5.97×10^{-4}	124	1.39×10^{-1}	1.778×10^{-1}	2.000×10^{-1}	$+6.59 \times 10^{-1}$	3.8×10^{-1}	3.4×10^{-1}
128	136	6.17×10^{-4}	132	1.53×10^{-1}	1.910×10^{-1}	2.000×10^{-1}	$+4.97 \times 10^{-1}$	4.0×10^{-1}	3.2×10^{-1}
136	144	6.25×10^{-4}	140	1.64×10^{-1}	2.010×10^{-1}	2.000×10^{-1}	-3.31×10^{-1}	4.3×10^{-1}	3.4×10^{-1}
144	152	6.43×10^{-4}	148	1.78×10^{-1}	2.131×10^{-1}	2.000×10^{-1}	$+5.92 \times 10^{-1}$	4.6×10^{-1}	2.1×10^{-1}
152	160	6.83×10^{-4}	156	2.00×10^{-1}	2.308×10^{-1}	2.000×10^{-1}	$+3.87 \times 10^{-1}$	5.0×10^{-1}	2.4×10^{-1}
160	168	7.38×10^{-4}	164	2.27×10^{-1}	2.506×10^{-1}	2.000×10^{-1}	$+3.19 \times 10^{-1}$	3.8×10^{-1}	2.9×10^{-1}
168	176	8.21×10^{-4}	172	2.65×10^{-1}	2.751×10^{-1}	2.000×10^{-1}	$+3.58 \times 10^{-1}$	4.6×10^{-1}	2.6×10^{-1}
176	184	9.21×10^{-4}	179	3.10×10^{-1}	3.000×10^{-1}	2.000×10^{-1}	$+1.72 \times 10^{+0}$	6.8×10^{-1}	5.5×10^{-1}
184	192	1.04×10^{-3}	186	3.63×10^{-1}	3.243×10^{-1}	2.000×10^{-1}	$+2.86 \times 10^{+0}$	$1.5 \times 10^{+0}$	8.7×10^{-1}
192	200	1.15×10^{-3}	192	4.15×10^{-1}	3.439×10^{-1}	2.000×10^{-1}	$-2.65 \times 10^{+1}$	$1.8 \times 10^{+1}$	$5.9 \times 10^{+1}$

Table F.8: $g_1^p(\nu)$ from 2011 data.

$\log_{10}(x)$		$\langle x \rangle$	$\langle Q^2 \rangle$	$\langle \nu \rangle$	$\langle y \rangle$	$A_1^{p,exp}$	F_2^p	F_2^d	$\Delta A_1^{^{14}N}$	ΔA_1^{RC}	$A_1^{p\gamma}$	$\sigma_{stat}(A_1^p)$	$\sigma_{syst}(A_1^p)$
−4.4	−4.2	4.73×10^{-5}	2.92×10^{-3}	3.33×10^{1}	2.12×10^{-1}	$+1.38 \times 10^{-2}$	3.51×10^{-3}	3.49×10^{-3}	$+1.04 \times 10^{-6}$	1.55×10^{-3}	$+1.22 \times 10^{-2}$	1.4×10^{-2}	1.9×10^{-2}
−4.4	−4.2	4.90×10^{-5}	4.38×10^{-3}	4.85×10^{1}	3.04×10^{-1}	$+3.98 \times 10^{-3}$	5.22×10^{-3}	5.19×10^{-3}	$+1.07 \times 10^{-6}$	1.10×10^{-3}	$+2.87 \times 10^{-3}$	8.6×10^{-3}	6.8×10^{-3}
−4.4	−4.2	5.31×10^{-5}	7.25×10^{-3}	7.29×10^{1}	4.54×10^{-1}	$+8.96 \times 10^{-3}$	8.56×10^{-3}	8.53×10^{-3}	$+1.16 \times 10^{-6}$	7.70×10^{-4}	$+8.19 \times 10^{-3}$	5.1×10^{-3}	1.1×10^{-2}
−4.2	−4.0	7.49×10^{-5}	4.80×10^{-3}	3.45×10^{1}	2.19×10^{-1}	-9.96×10^{-3}	5.73×10^{-3}	5.70×10^{-3}	$+1.64 \times 10^{-6}$	1.25×10^{-3}	-1.12×10^{-2}	1.2×10^{-2}	7.0×10^{-3}
−4.2	−4.0	7.75×10^{-5}	7.43×10^{-3}	5.19×10^{1}	3.26×10^{-1}	$+1.61 \times 10^{-2}$	8.77×10^{-3}	8.73×10^{-3}	$+1.69 \times 10^{-6}$	8.40×10^{-4}	$+1.53 \times 10^{-2}$	7.0×10^{-3}	1.1×10^{-2}
−4.2	−4.0	8.32×10^{-5}	1.30×10^{-2}	8.33×10^{1}	5.19×10^{-1}	$+7.54 \times 10^{-3}$	1.51×10^{-2}	1.51×10^{-2}	$+1.82 \times 10^{-6}$	5.40×10^{-4}	$+7.00 \times 10^{-3}$	4.0×10^{-3}	1.3×10^{-2}
−4.0	−3.8	1.19×10^{-4}	7.82×10^{-3}	3.55×10^{1}	2.25×10^{-1}	$+1.40 \times 10^{-2}$	9.27×10^{-3}	9.21×10^{-3}	$+2.58 \times 10^{-6}$	1.00×10^{-3}	$+1.29 \times 10^{-2}$	1.0×10^{-2}	1.3×10^{-2}
−4.0	−3.8	1.23×10^{-4}	1.24×10^{-2}	5.50×10^{1}	3.45×10^{-1}	$+7.56 \times 10^{-3}$	1.45×10^{-2}	1.44×10^{-2}	$+2.67 \times 10^{-6}$	6.50×10^{-4}	$+6.90 \times 10^{-3}$	6.1×10^{-3}	1.7×10^{-2}
−4.0	−3.8	1.31×10^{-4}	2.25×10^{-2}	9.19×10^{1}	5.74×10^{-1}	$+1.07 \times 10^{-2}$	2.56×10^{-2}	2.55×10^{-2}	$+2.85 \times 10^{-6}$	4.20×10^{-4}	$+1.02 \times 10^{-2}$	3.5×10^{-3}	1.9×10^{-2}
−3.8	−3.6	1.88×10^{-4}	1.26×10^{-2}	3.60×10^{1}	2.28×10^{-1}	$+1.98 \times 10^{-2}$	1.47×10^{-2}	1.46×10^{-2}	$+4.07 \times 10^{-6}$	8.10×10^{-4}	$+1.90 \times 10^{-2}$	1.0×10^{-2}	2.2×10^{-2}
−3.8	−3.6	1.94×10^{-4}	2.04×10^{-2}	5.70×10^{1}	3.58×10^{-1}	$+9.27 \times 10^{-3}$	2.33×10^{-2}	2.32×10^{-2}	$+4.19 \times 10^{-6}$	5.30×10^{-4}	$+8.74 \times 10^{-3}$	5.8×10^{-3}	1.8×10^{-2}
−3.8	−3.6	2.06×10^{-4}	3.77×10^{-2}	9.81×10^{1}	6.13×10^{-1}	$+7.20 \times 10^{-3}$	4.14×10^{-2}	4.13×10^{-2}	$+4.45 \times 10^{-6}$	3.60×10^{-4}	$+6.84 \times 10^{-3}$	3.3×10^{-3}	2.0×10^{-2}
−3.6	−3.4	2.99×10^{-4}	1.99×10^{-2}	3.60×10^{1}	2.28×10^{-1}	$+1.31 \times 10^{-2}$	2.29×10^{-2}	2.28×10^{-2}	$+6.40 \times 10^{-6}$	6.70×10^{-4}	$+1.24 \times 10^{-2}$	1.0×10^{-2}	3.3×10^{-2}
−3.6	−3.4	3.07×10^{-4}	3.30×10^{-2}	5.81×10^{1}	3.65×10^{-1}	$+1.64 \times 10^{-3}$	3.64×10^{-2}	3.63×10^{-2}	$+6.56 \times 10^{-6}$	4.60×10^{-4}	$+1.17 \times 10^{-3}$	5.8×10^{-3}	4.3×10^{-2}
−3.6	−3.4	3.24×10^{-4}	6.14×10^{-2}	1.01×10^{2}	6.34×10^{-1}	$+7.44 \times 10^{-3}$	6.38×10^{-2}	6.36×10^{-2}	$+6.94 \times 10^{-6}$	3.60×10^{-4}	$+7.07 \times 10^{-3}$	3.3×10^{-3}	1.4×10^{-1}
−3.4	−3.2	4.75×10^{-4}	3.10×10^{-2}	3.53×10^{1}	2.23×10^{-1}	$+1.98 \times 10^{-2}$	3.47×10^{-2}	3.45×10^{-2}	$+9.98 \times 10^{-6}$	5.70×10^{-4}	$+1.92 \times 10^{-2}$	1.1×10^{-2}	7.8×10^{-3}
−3.4	−3.2	4.85×10^{-4}	5.25×10^{-2}	5.86×10^{1}	3.68×10^{-1}	$+1.05 \times 10^{-2}$	5.54×10^{-2}	5.51×10^{-2}	$+1.02 \times 10^{-5}$	4.30×10^{-4}	$+1.01 \times 10^{-2}$	6.0×10^{-3}	7.0×10^{-3}
−3.4	−3.2	5.13×10^{-4}	9.80×10^{-2}	1.02×10^{2}	6.40×10^{-1}	$+1.41 \times 10^{-2}$	9.39×10^{-2}	9.36×10^{-2}	$+1.08 \times 10^{-5}$	4.00×10^{-4}	$+1.37 \times 10^{-2}$	3.5×10^{-3}	3.7×10^{-3}
−3.2	−3.0	7.54×10^{-4}	4.77×10^{-2}	3.42×10^{1}	2.16×10^{-1}	$+3.62 \times 10^{-2}$	5.12×10^{-2}	5.09×10^{-2}	$+1.54 \times 10^{-5}$	5.10×10^{-4}	$+3.57 \times 10^{-2}$	1.2×10^{-2}	5.2×10^{-3}
−3.2	−3.0	7.66×10^{-4}	8.26×10^{-2}	5.84×10^{1}	3.67×10^{-1}	$+1.43 \times 10^{-2}$	8.13×10^{-2}	8.09×10^{-2}	$+1.56 \times 10^{-5}$	4.40×10^{-4}	$+1.39 \times 10^{-2}$	6.5×10^{-3}	4.8×10^{-3}
−3.2	−3.0	8.08×10^{-4}	1.55×10^{-1}	1.02×10^{2}	6.41×10^{-1}	$+1.69 \times 10^{-2}$	1.32×10^{-1}	1.31×10^{-1}	$+1.65 \times 10^{-5}$	4.80×10^{-4}	$+1.65 \times 10^{-2}$	3.8×10^{-3}	4.1×10^{-3}
−3.0	−2.8	1.20×10^{-3}	7.24×10^{-2}	3.27×10^{1}	2.06×10^{-1}	$+1.84 \times 10^{-2}$	7.34×10^{-2}	7.30×10^{-2}	$+2.33 \times 10^{-5}$	4.80×10^{-4}	$+1.79 \times 10^{-2}$	1.3×10^{-2}	4.6×10^{-3}
−3.0	−2.8	1.21×10^{-3}	1.29×10^{-1}	5.75×10^{1}	3.62×10^{-1}	$+8.70 \times 10^{-3}$	1.15×10^{-1}	1.14×10^{-1}	$+2.36 \times 10^{-5}$	5.00×10^{-4}	$+8.18 \times 10^{-3}$	7.3×10^{-3}	4.3×10^{-3}
−3.0	−2.8	1.28×10^{-3}	2.46×10^{-1}	1.03×10^{2}	6.44×10^{-1}	$+1.41 \times 10^{-2}$	1.20×10^{-1}	1.20×10^{-1}	$+2.49 \times 10^{-5}$	6.20×10^{-4}	$+1.35 \times 10^{-2}$	4.2×10^{-3}	5.0×10^{-3}
−2.8	−2.6	1.90×10^{-3}	1.08×10^{-1}	3.07×10^{1}	1.94×10^{-1}	$+3.58 \times 10^{-2}$	1.01×10^{-1}	1.01×10^{-1}	$+3.43 \times 10^{-5}$	4.90×10^{-4}	$+3.53 \times 10^{-2}$	1.6×10^{-2}	9.6×10^{-3}
−2.8	−2.6	1.92×10^{-3}	1.96×10^{-1}	5.52×10^{1}	3.47×10^{-1}	$+9.50 \times 10^{-3}$	1.53×10^{-1}	1.52×10^{-1}	$+3.47 \times 10^{-5}$	6.10×10^{-4}	$+8.85 \times 10^{-3}$	8.8×10^{-3}	1.5×10^{-2}
−2.8	−2.6	2.02×10^{-3}	3.88×10^{-1}	1.03×10^{2}	6.44×10^{-1}	$+1.26 \times 10^{-2}$	1.74×10^{-1}	1.73×10^{-1}	$+3.61 \times 10^{-5}$	9.40×10^{-4}	$+1.16 \times 10^{-2}$	4.7×10^{-3}	1.2×10^{-2}
−2.6	−2.4	3.00×10^{-3}	1.59×10^{-1}	2.85×10^{1}	1.80×10^{-1}	$+1.21 \times 10^{-2}$	1.35×10^{-1}	1.33×10^{-1}	$+4.80 \times 10^{-5}$	5.40×10^{-4}	$+1.15 \times 10^{-2}$	1.9×10^{-2}	3.6×10^{-2}
−2.6	−2.4	3.05×10^{-3}	2.92×10^{-1}	5.18×10^{1}	3.26×10^{-1}	$+1.98 \times 10^{-2}$	1.32×10^{-1}	1.30×10^{-1}	$+4.83 \times 10^{-5}$	8.50×10^{-4}	$+1.89 \times 10^{-2}$	1.1×10^{-2}	4.8×10^{-2}
−2.6	−2.4	3.18×10^{-3}	6.06×10^{-1}	1.02×10^{2}	6.39×10^{-1}	$+1.57 \times 10^{-2}$	2.26×10^{-1}	2.24×10^{-1}	$+4.97 \times 10^{-5}$	1.27×10^{-3}	$+1.44 \times 10^{-2}$	5.5×10^{-3}	1.0×10^{-1}
−2.4	−2.2	4.75×10^{-3}	2.31×10^{-1}	2.62×10^{1}	1.65×10^{-1}	$+2.79 \times 10^{-2}$	1.06×10^{-1}	1.04×10^{-1}	$+6.12 \times 10^{-5}$	6.50×10^{-4}	$+2.72 \times 10^{-2}$	2.5×10^{-2}	3.9×10^{-3}
−2.4	−2.2	4.85×10^{-3}	4.03×10^{-1}	4.50×10^{1}	2.82×10^{-1}	$+2.09 \times 10^{-2}$	1.69×10^{-1}	1.67×10^{-1}	$+6.18 \times 10^{-5}$	1.19×10^{-3}	$+1.96 \times 10^{-2}$	1.5×10^{-2}	4.1×10^{-3}
−2.4	−2.2	4.87×10^{-3}	7.66×10^{-1}	8.52×10^{1}	5.35×10^{-1}	$+1.95 \times 10^{-2}$	2.50×10^{-1}	2.47×10^{-1}	$+6.19 \times 10^{-5}$	1.65×10^{-3}	$+1.78 \times 10^{-2}$	7.9×10^{-3}	3.0×10^{-3}
−2.2	−2.0	7.52×10^{-3}	3.34×10^{-1}	2.40×10^{1}	1.51×10^{-1}	$+6.48 \times 10^{-2}$	1.51×10^{-1}	1.48×10^{-1}	$+6.72 \times 10^{-5}$	9.90×10^{-4}	$+6.37 \times 10^{-2}$	3.4×10^{-2}	2.3×10^{-3}
−2.2	−2.0	7.72×10^{-3}	5.27×10^{-1}	3.70×10^{1}	2.32×10^{-1}	$+4.92 \times 10^{-2}$	2.03×10^{-1}	1.99×10^{-1}	$+6.70 \times 10^{-5}$	1.53×10^{-3}	$+4.76 \times 10^{-2}$	2.2×10^{-2}	3.2×10^{-3}
−2.2	−2.0	7.77×10^{-3}	8.22×10^{-1}	5.73×10^{1}	3.60×10^{-1}	$+4.71 \times 10^{-2}$	2.55×10^{-1}	2.50×10^{-1}	$+6.69 \times 10^{-5}$	2.00×10^{-3}	$+4.51 \times 10^{-2}$	1.4×10^{-2}	2.9×10^{-3}
−2.0	−1.8	1.18×10^{-2}	4.66×10^{-1}	2.12×10^{1}	1.34×10^{-1}	$+1.29 \times 10^{-1}$	1.96×10^{-1}	1.91×10^{-1}	$+5.13 \times 10^{-5}$	1.39×10^{-3}	$+1.28 \times 10^{-1}$	4.6×10^{-2}	3.0×10^{-3}
−2.0	−1.8	1.22×10^{-2}	6.51×10^{-1}	2.90×10^{1}	1.82×10^{-1}	$+3.65 \times 10^{-2}$	2.32×10^{-1}	2.27×10^{-1}	$+4.90 \times 10^{-5}$	1.90×10^{-3}	$+3.46 \times 10^{-2}$	3.4×10^{-2}	3.9×10^{-3}
−2.0	−1.8	1.22×10^{-2}	8.75×10^{-1}	3.88×10^{1}	2.43×10^{-1}	$+1.95 \times 10^{-2}$	2.64×10^{-1}	2.57×10^{-1}	$+4.86 \times 10^{-5}$	2.32×10^{-3}	$+1.71 \times 10^{-2}$	2.5×10^{-2}	2.7×10^{-3}
−1.8	−1.6	1.81×10^{-2}	6.34×10^{-1}	1.88×10^{1}	1.19×10^{-1}	$+1.65 \times 10^{-1}$	2.38×10^{-1}	2.31×10^{-1}	-5.63×10^{-7}	1.83×10^{-3}	$+1.63 \times 10^{-1}$	7.3×10^{-2}	4.0×10^{-3}
−1.8	−1.6	1.92×10^{-2}	7.84×10^{-1}	2.21×10^{1}	1.39×10^{-1}	$+1.90 \times 10^{-2}$	2.60×10^{-1}	2.52×10^{-1}	-1.22×10^{-5}	2.24×10^{-3}	$+1.68 \times 10^{-2}$	6.3×10^{-2}	7.8×10^{-3}
−1.8	−1.6	1.93×10^{-2}	9.26×10^{-1}	2.60×10^{1}	1.63×10^{-1}	-1.19×10^{-2}	2.75×10^{-1}	2.67×10^{-1}	-1.34×10^{-5}	2.56×10^{-3}	-1.45×10^{-2}	5.3×10^{-2}	8.3×10^{-3}
−1.6	−1.4	2.66×10^{-2}	8.35×10^{-1}	1.68×10^{1}	1.07×10^{-1}	-1.62×10^{-2}	2.72×10^{-1}	2.63×10^{-1}	-9.41×10^{-5}	2.30×10^{-3}	-1.84×10^{-2}	2.0×10^{-1}	1.7×10^{-2}
−1.6	−1.4	2.76×10^{-2}	9.17×10^{-1}	1.77×10^{1}	1.12×10^{-1}	$+2.63 \times 10^{-3}$	2.81×10^{-1}	2.72×10^{-1}	-1.06×10^{-4}	2.50×10^{-3}	$+2.34 \times 10^{-4}$	1.9×10^{-1}	4.5×10^{-2}
−1.6	−1.4	2.83×10^{-2}	9.74×10^{-1}	1.84×10^{1}	1.16×10^{-1}	$+1.08 \times 10^{-1}$	2.87×10^{-1}	2.77×10^{-1}	-1.15×10^{-4}	2.64×10^{-3}	$+1.05 \times 10^{-1}$	1.8×10^{-1}	1.8×10^{-1}

Table F.9: $A_1^p(x, Q^2)$ from 2007 data.

$\log_{10}(x)$		$\langle x \rangle$	$\langle Q^2 \rangle$	$\langle \nu \rangle$	$\langle y \rangle$	$A_1^{p,exp}$	F_2^p	F_2^d	ΔA_1^{14N}	ΔA_1^{RC}	$A_1^{p\gamma}$	$\sigma_{stat}(A_1^p)$	$\sigma_{syst}(A_1^p)$
−4.4	−4.2	4.66×10^{-5}	5.37×10^{-3}	6.21×10^{1}	3.10×10^{-1}	-8.30×10^{-3}	6.37×10^{-3}	6.34×10^{-3}	$+1.02 \times 10^{-6}$	9.00×10^{-4}	-9.20×10^{-3}	1.2×10^{-2}	1.5×10^{-2}
−4.4	−4.2	4.90×10^{-5}	7.36×10^{-3}	8.13×10^{1}	4.03×10^{-1}	$+1.51 \times 10^{-3}$	8.69×10^{-3}	8.67×10^{-3}	$+1.08 \times 10^{-6}$	7.00×10^{-4}	$+8.04 \times 10^{-4}$	8.1×10^{-3}	5.5×10^{-3}
−4.4	−4.2	5.39×10^{-5}	1.08×10^{-2}	1.07×10^{2}	5.27×10^{-1}	$+1.50 \times 10^{-2}$	1.27×10^{-2}	1.27×10^{-2}	$+1.18 \times 10^{-6}$	5.40×10^{-4}	$+1.44 \times 10^{-2}$	5.7×10^{-3}	6.9×10^{-3}
−4.2	−4.0	7.40×10^{-5}	8.75×10^{-3}	6.37×10^{1}	3.17×10^{-1}	$+1.30 \times 10^{-2}$	1.03×10^{-2}	1.02×10^{-2}	$+1.62 \times 10^{-6}$	7.20×10^{-4}	$+1.23 \times 10^{-2}$	9.9×10^{-3}	6.0×10^{-3}
−4.2	−4.0	7.77×10^{-5}	1.23×10^{-2}	8.60×10^{1}	4.26×10^{-1}	$+4.98 \times 10^{-3}$	1.44×10^{-2}	1.44×10^{-2}	$+1.70 \times 10^{-6}$	5.30×10^{-4}	$+4.44 \times 10^{-3}$	6.8×10^{-3}	5.3×10^{-3}
−4.2	−4.0	8.42×10^{-5}	1.88×10^{-2}	1.20×10^{2}	5.89×10^{-1}	$+4.39 \times 10^{-3}$	2.18×10^{-2}	2.17×10^{-2}	$+1.84 \times 10^{-6}$	4.00×10^{-4}	$+3.98 \times 10^{-3}$	4.7×10^{-3}	9.6×10^{-3}
−4.0	−3.8	1.18×10^{-4}	1.41×10^{-2}	6.48×10^{1}	3.23×10^{-1}	$+2.95 \times 10^{-3}$	1.64×10^{-2}	1.63×10^{-2}	$+2.56 \times 10^{-6}$	5.90×10^{-4}	$+2.36 \times 10^{-3}$	9.1×10^{-3}	9.8×10^{-3}
−4.0	−3.8	1.23×10^{-4}	2.04×10^{-2}	8.99×10^{1}	4.45×10^{-1}	-1.63×10^{-3}	2.34×10^{-2}	2.33×10^{-2}	$+2.68 \times 10^{-6}$	4.30×10^{-4}	-2.06×10^{-3}	6.2×10^{-3}	8.9×10^{-3}
−4.0	−3.8	1.32×10^{-4}	3.19×10^{-2}	1.29×10^{2}	6.38×10^{-1}	$+1.04 \times 10^{-2}$	3.58×10^{-2}	3.57×10^{-2}	$+2.88 \times 10^{-6}$	3.30×10^{-4}	$+1.01 \times 10^{-2}$	4.2×10^{-3}	1.0×10^{-2}
−3.8	−3.6	1.87×10^{-4}	2.26×10^{-2}	6.51×10^{1}	3.24×10^{-1}	$+2.76 \times 10^{-3}$	2.56×10^{-2}	2.55×10^{-2}	$+4.04 \times 10^{-6}$	4.90×10^{-4}	$+2.27 \times 10^{-3}$	8.9×10^{-3}	1.7×10^{-2}
−3.8	−3.6	1.94×10^{-4}	3.31×10^{-2}	9.23×10^{1}	4.57×10^{-1}	$+2.12 \times 10^{-3}$	3.68×10^{-2}	3.67×10^{-2}	$+4.21 \times 10^{-6}$	3.80×10^{-4}	$+1.73 \times 10^{-3}$	6.0×10^{-3}	2.4×10^{-2}
−3.8	−3.6	2.08×10^{-4}	5.25×10^{-2}	1.36×10^{2}	6.69×10^{-1}	$+5.99 \times 10^{-3}$	5.62×10^{-2}	5.60×10^{-2}	$+4.49 \times 10^{-6}$	3.10×10^{-4}	$+5.67 \times 10^{-3}$	4.1×10^{-3}	4.5×10^{-2}
−3.6	−3.4	2.96×10^{-4}	3.53×10^{-2}	6.43×10^{1}	3.20×10^{-1}	$+2.55 \times 10^{-3}$	3.88×10^{-2}	3.87×10^{-2}	$+6.34 \times 10^{-6}$	4.40×10^{-4}	$+2.10 \times 10^{-3}$	9.3×10^{-3}	3.9×10^{-2}
−3.6	−3.4	3.07×10^{-4}	5.28×10^{-2}	9.30×10^{1}	4.60×10^{-1}	$+4.98 \times 10^{-3}$	5.59×10^{-2}	5.57×10^{-2}	$+6.58 \times 10^{-6}$	3.60×10^{-4}	$+4.61 \times 10^{-3}$	6.2×10^{-3}	1.1×10^{-1}
−3.6	−3.4	3.27×10^{-4}	8.43×10^{-2}	1.38×10^{2}	6.82×10^{-1}	$+4.25 \times 10^{-3}$	8.40×10^{-2}	8.38×10^{-2}	$+7.01 \times 10^{-6}$	3.40×10^{-4}	$+3.90 \times 10^{-3}$	4.2×10^{-3}	8.5×10^{-1}
−3.4	−3.2	4.71×10^{-4}	5.48×10^{-2}	6.29×10^{1}	3.13×10^{-1}	$+6.13 \times 10^{-3}$	5.75×10^{-2}	5.73×10^{-2}	$+9.91 \times 10^{-6}$	4.10×10^{-4}	$+5.71 \times 10^{-3}$	1.0×10^{-2}	6.8×10^{-3}
−3.4	−3.2	4.85×10^{-4}	8.40×10^{-2}	9.38×10^{1}	4.65×10^{-1}	$+9.27 \times 10^{-3}$	8.28×10^{-2}	8.26×10^{-2}	$+1.02 \times 10^{-5}$	3.80×10^{-4}	$+8.88 \times 10^{-3}$	6.5×10^{-3}	5.0×10^{-3}
−3.4	−3.2	5.18×10^{-4}	1.34×10^{-1}	1.39×10^{2}	6.86×10^{-1}	$+1.09 \times 10^{-2}$	1.20×10^{-1}	1.20×10^{-1}	$+1.09 \times 10^{-5}$	4.00×10^{-4}	$+1.05 \times 10^{-2}$	4.4×10^{-3}	5.5×10^{-3}
−3.2	−3.0	7.48×10^{-4}	8.36×10^{-2}	6.04×10^{1}	3.01×10^{-1}	$+1.86 \times 10^{-2}$	8.20×10^{-2}	8.17×10^{-2}	$+1.53 \times 10^{-5}$	4.30×10^{-4}	$+1.82 \times 10^{-2}$	1.1×10^{-2}	4.8×10^{-3}
−3.2	−3.0	7.64×10^{-4}	1.31×10^{-1}	9.26×10^{1}	4.59×10^{-1}	$+1.67 \times 10^{-2}$	1.17×10^{-1}	1.16×10^{-1}	$+1.56 \times 10^{-5}$	4.40×10^{-4}	$+1.62 \times 10^{-2}$	7.1×10^{-3}	5.7×10^{-3}
−3.2	−3.0	8.16×10^{-4}	2.11×10^{-1}	1.39×10^{2}	6.86×10^{-1}	$+7.77 \times 10^{-3}$	1.08×10^{-1}	1.63×10^{-1}	$+2.52 \times 10^{-5}$	4.90×10^{-4}	$+7.25 \times 10^{-3}$	4.9×10^{-3}	4.0×10^{-3}
−3.0	−2.8	1.19×10^{-3}	1.26×10^{-1}	5.72×10^{1}	2.85×10^{-1}	-3.53×10^{-3}	1.13×10^{-1}	1.12×10^{-1}	$+2.32 \times 10^{-5}$	4.70×10^{-4}	-4.02×10^{-3}	1.3×10^{-2}	4.4×10^{-3}
−3.0	−2.8	1.21×10^{-3}	2.05×10^{-1}	9.16×10^{1}	4.54×10^{-1}	$+1.18 \times 10^{-2}$	9.78×10^{-2}	9.75×10^{-2}	$+2.36 \times 10^{-5}$	5.40×10^{-4}	$+1.13 \times 10^{-2}$	8.0×10^{-3}	4.2×10^{-3}
−3.0	−2.8	1.29×10^{-3}	3.39×10^{-1}	1.41×10^{2}	6.96×10^{-1}	$+1.27 \times 10^{-2}$	1.65×10^{-1}	1.65×10^{-1}	$+2.51 \times 10^{-5}$	7.30×10^{-4}	$+1.20 \times 10^{-2}$	5.3×10^{-3}	4.7×10^{-3}
−2.8	−2.6	1.89×10^{-3}	1.83×10^{-1}	5.24×10^{1}	2.61×10^{-1}	$+2.35 \times 10^{-2}$	1.47×10^{-1}	1.46×10^{-1}	$+3.42 \times 10^{-5}$	5.50×10^{-4}	$+2.29 \times 10^{-2}$	1.7×10^{-2}	6.7×10^{-3}
−2.8	−2.6	1.91×10^{-3}	3.10×10^{-1}	8.77×10^{1}	4.35×10^{-1}	-5.87×10^{-3}	1.44×10^{-1}	1.43×10^{-1}	$+3.46 \times 10^{-5}$	7.60×10^{-4}	-6.67×10^{-3}	9.7×10^{-3}	1.4×10^{-2}
−2.8	−2.6	2.03×10^{-3}	5.30×10^{-1}	1.40×10^{2}	6.90×10^{-1}	-1.39×10^{-4}	2.18×10^{-1}	2.18×10^{-1}	$+3.64 \times 10^{-5}$	9.70×10^{-4}	-1.15×10^{-3}	6.0×10^{-3}	1.6×10^{-2}
−2.6	−2.4	2.99×10^{-3}	2.59×10^{-1}	4.67×10^{1}	2.32×10^{-1}	$+4.44 \times 10^{-3}$	1.18×10^{-1}	1.16×10^{-1}	$+4.76 \times 10^{-5}$	6.90×10^{-4}	$+3.71 \times 10^{-3}$	2.2×10^{-2}	5.0×10^{-2}
−2.6	−2.4	3.04×10^{-3}	4.43×10^{-1}	7.90×10^{1}	3.92×10^{-1}	$+1.72 \times 10^{-2}$	1.85×10^{-1}	1.83×10^{-1}	$+4.82 \times 10^{-5}$	1.04×10^{-3}	$+1.61 \times 10^{-2}$	1.3×10^{-2}	1.3×10^{-1}
−2.6	−2.4	3.12×10^{-3}	7.59×10^{-1}	1.31×10^{2}	6.49×10^{-1}	$+2.39 \times 10^{-2}$	2.59×10^{-1}	2.57×10^{-1}	$+4.92 \times 10^{-5}$	1.31×10^{-3}	$+2.25 \times 10^{-2}$	7.3×10^{-3}	$1.7 \times 10^{+0}$
−2.4	−2.2	4.74×10^{-3}	3.39×10^{-1}	3.87×10^{1}	1.92×10^{-1}	$+1.66 \times 10^{-3}$	1.49×10^{-1}	1.47×10^{-1}	$+6.12 \times 10^{-5}$	9.30×10^{-4}	$+6.73 \times 10^{-4}$	3.3×10^{-2}	7.6×10^{-3}
−2.4	−2.2	4.81×10^{-3}	5.49×10^{-1}	6.17×10^{1}	3.06×10^{-1}	$+2.86 \times 10^{-2}$	2.08×10^{-1}	2.04×10^{-1}	$+6.16 \times 10^{-5}$	1.30×10^{-3}	$+2.73 \times 10^{-2}$	2.0×10^{-2}	2.6×10^{-3}
−2.4	−2.2	4.86×10^{-3}	8.34×10^{-1}	9.29×10^{1}	4.61×10^{-1}	$+6.56 \times 10^{-2}$	2.62×10^{-1}	2.58×10^{-1}	$+6.19 \times 10^{-5}$	1.61×10^{-3}	$+6.39 \times 10^{-2}$	1.3×10^{-2}	2.7×10^{-3}
−2.2	−2.0	7.54×10^{-3}	4.47×10^{-1}	3.20×10^{1}	1.59×10^{-1}	$+8.74 \times 10^{-2}$	1.84×10^{-1}	1.80×10^{-1}	$+6.72 \times 10^{-5}$	1.22×10^{-3}	$+8.62 \times 10^{-2}$	4.9×10^{-2}	2.7×10^{-3}
−2.2	−2.0	7.65×10^{-3}	6.63×10^{-1}	4.69×10^{1}	2.33×10^{-1}	-1.59×10^{-2}	2.30×10^{-1}	2.25×10^{-1}	$+6.71 \times 10^{-5}$	1.63×10^{-3}	-1.76×10^{-2}	3.3×10^{-2}	4.5×10^{-3}
−2.2	−2.0	7.73×10^{-3}	8.85×10^{-1}	6.20×10^{1}	3.07×10^{-1}	$+1.48 \times 10^{-2}$	2.64×10^{-1}	2.59×10^{-1}	$+6.70 \times 10^{-5}$	1.92×10^{-3}	$+1.29 \times 10^{-2}$	2.5×10^{-2}	2.4×10^{-3}
−2.0	−1.8	1.18×10^{-2}	5.76×10^{-1}	2.63×10^{1}	1.31×10^{-1}	$+1.45 \times 10^{-1}$	2.18×10^{-1}	2.13×10^{-1}	$+5.17 \times 10^{-5}$	1.53×10^{-3}	$+1.44 \times 10^{-1}$	7.7×10^{-2}	4.2×10^{-3}
−2.0	−1.8	1.21×10^{-2}	7.57×10^{-1}	3.39×10^{1}	1.68×10^{-1}	$+1.55 \times 10^{-1}$	2.48×10^{-1}	2.42×10^{-1}	$+4.95 \times 10^{-5}$	1.93×10^{-3}	$+1.53 \times 10^{-1}$	6.0×10^{-2}	4.7×10^{-3}
−2.0	−1.8	1.21×10^{-2}	9.22×10^{-1}	4.11×10^{1}	2.04×10^{-1}	$+4.66 \times 10^{-2}$	2.69×10^{-1}	2.62×10^{-1}	$+4.92 \times 10^{-5}$	2.19×10^{-3}	$+4.44 \times 10^{-2}$	4.9×10^{-2}	5.0×10^{-3}
−1.8	−1.6	1.76×10^{-2}	7.51×10^{-1}	2.29×10^{1}	1.14×10^{-1}	$+2.02 \times 10^{-2}$	2.54×10^{-1}	2.46×10^{-1}	$+4.27 \times 10^{-6}$	1.92×10^{-3}	$+1.83 \times 10^{-2}$	1.4×10^{-1}	4.0×10^{-3}
−1.8	−1.6	1.87×10^{-2}	8.75×10^{-1}	2.53×10^{1}	1.26×10^{-1}	$+1.79 \times 10^{-1}$	2.69×10^{-1}	2.61×10^{-1}	-6.54×10^{-6}	2.19×10^{-3}	$+1.77 \times 10^{-1}$	1.3×10^{-1}	9.9×10^{-3}
−1.8	−1.6	1.92×10^{-2}	9.61×10^{-1}	2.72×10^{1}	1.35×10^{-1}	-1.39×10^{-1}	2.79×10^{-1}	2.70×10^{-1}	-1.18×10^{-5}	2.37×10^{-3}	-1.41×10^{-1}	1.2×10^{-1}	1.1×10^{-2}
−1.6	−1.4	2.56×10^{-2}	9.52×10^{-1}	1.98×10^{1}	1.02×10^{-1}	-4.98×10^{-1}	2.83×10^{-1}	2.73×10^{-1}	-8.22×10^{-5}	2.35×10^{-3}	-5.00×10^{-1}	$1.5 \times 10^{+0}$	2.5×10^{-2}
−1.6	−1.4	2.58×10^{-2}	9.79×10^{-1}	2.02×10^{1}	1.03×10^{-1}	-9.58×10^{-1}	2.85×10^{-1}	2.76×10^{-1}	-8.44×10^{-5}	2.38×10^{-3}	-9.60×10^{-1}	$1.4 \times 10^{+0}$	1.1×10^{-1}
−1.6	−1.4	2.59×10^{-2}	9.94×10^{-1}	2.05×10^{1}	1.03×10^{-1}	$+2.52 \times 10^{-2}$	2.87×10^{-1}	2.77×10^{-1}	-8.59×10^{-5}	2.41×10^{-3}	$+2.29 \times 10^{-2}$	$1.4 \times 10^{+0}$	9.1×10^{-1}

Table F.10: $A_1^p(x, Q^2)$ from 2011 data.

ν (GeV)		$\langle x \rangle$	$\langle Q^2 \rangle$	$\langle \nu \rangle$	$\langle y \rangle$	$A_1^{p,exp}$	F_2^p	F_2^d	$\Delta A_1^{^{14}N}$	ΔA_1^{RC}	$A_1^{p\gamma}$	$\sigma_{stat}(A_1^p)$	$\sigma_{syst}(A_1^p)$
8	16	1.26×10^{-4}	3.69×10^{-3}	1.56×10^{1}	1.03×10^{-1}	-1.41×10^{-1}	4.57×10^{-3}	4.53×10^{-3}	$+2.74 \times 10^{-6}$	2.00×10^{-3}	-1.43×10^{-1}	1.4×10^{-1}	1.9×10^{-1}
8	16	2.07×10^{-3}	6.08×10^{-2}	1.56×10^{1}	1.03×10^{-1}	-1.77×10^{-1}	6.52×10^{-2}	6.46×10^{-2}	$+3.67 \times 10^{-5}$	4.70×10^{-4}	-1.77×10^{-1}	1.5×10^{-1}	3.0×10^{-2}
8	16	2.16×10^{-2}	6.34×10^{-1}	1.57×10^{1}	1.02×10^{-1}	-1.05×10^{-1}	2.42×10^{-1}	2.35×10^{-1}	-3.75×10^{-5}	1.83×10^{-3}	-1.06×10^{-1}	2.0×10^{-1}	1.3×10^{-2}
8	16	5.87×10^{-4}	1.72×10^{-2}	1.56×10^{1}	1.03×10^{-1}	-1.82×10^{-1}	2.05×10^{-2}	2.04×10^{-2}	$+1.22 \times 10^{-5}$	9.70×10^{-4}	-1.83×10^{-1}	1.4×10^{-1}	5.4×10^{-3}
8	16	6.76×10^{-3}	1.98×10^{-1}	1.56×10^{1}	1.03×10^{-1}	$+5.44 \times 10^{-2}$	1.59×10^{-1}	1.58×10^{-1}	$+6.76 \times 10^{-5}$	4.40×10^{-4}	$+5.39 \times 10^{-2}$	1.8×10^{-1}	5.6×10^{-3}
16	24	1.35×10^{-4}	5.26×10^{-3}	2.10×10^{1}	1.36×10^{-1}	-8.09×10^{-3}	6.39×10^{-3}	6.34×10^{-3}	$+2.92 \times 10^{-6}$	1.53×10^{-3}	-9.62×10^{-3}	2.1×10^{-2}	6.8×10^{-3}
16	24	1.72×10^{-2}	6.55×10^{-1}	2.05×10^{1}	1.29×10^{-1}	$+7.97 \times 10^{-2}$	2.40×10^{-1}	2.33×10^{-1}	$+7.54 \times 10^{-6}$	1.91×10^{-3}	$+7.78 \times 10^{-2}$	3.2×10^{-2}	4.4×10^{-3}
16	24	1.99×10^{-3}	7.67×10^{-2}	2.08×10^{1}	1.32×10^{-1}	$+5.97 \times 10^{-2}$	7.82×10^{-2}	7.76×10^{-2}	$+3.56 \times 10^{-5}$	4.60×10^{-4}	$+5.92 \times 10^{-2}$	2.4×10^{-2}	5.5×10^{-3}
16	24	5.94×10^{-3}	2.28×10^{-1}	2.07×10^{1}	1.31×10^{-1}	$+2.02 \times 10^{-2}$	1.06×10^{-1}	1.04×10^{-1}	$+6.58 \times 10^{-5}$	5.90×10^{-4}	$+1.96 \times 10^{-2}$	2.8×10^{-2}	4.9×10^{-3}
16	24	6.17×10^{-4}	2.40×10^{-2}	2.10×10^{1}	1.34×10^{-1}	$+2.15 \times 10^{-2}$	2.78×10^{-2}	2.75×10^{-2}	$+1.28 \times 10^{-5}$	7.50×10^{-4}	$+2.07 \times 10^{-2}$	2.2×10^{-2}	7.3×10^{-3}
24	32	1.01×10^{-2}	5.33×10^{-1}	2.83×10^{1}	1.78×10^{-1}	$+5.17 \times 10^{-2}$	2.07×10^{-1}	2.03×10^{-1}	$+6.04 \times 10^{-5}$	1.58×10^{-3}	$+5.00 \times 10^{-2}$	2.0×10^{-2}	7.4×10^{-3}
24	32	2.63×10^{-3}	1.39×10^{-1}	2.84×10^{1}	1.79×10^{-1}	$+2.70 \times 10^{-2}$	1.23×10^{-1}	1.22×10^{-1}	$+4.38 \times 10^{-5}$	5.10×10^{-4}	$+2.65 \times 10^{-2}$	1.6×10^{-2}	6.8×10^{-3}
24	32	2.85×10^{-4}	1.52×10^{-2}	2.86×10^{1}	1.82×10^{-1}	$+2.05 \times 10^{-2}$	1.78×10^{-2}	1.77×10^{-2}	$+6.09 \times 10^{-6}$	8.30×10^{-4}	$+1.96 \times 10^{-2}$	1.4×10^{-2}	7.5×10^{-3}
24	32	8.49×10^{-4}	4.51×10^{-2}	2.85×10^{1}	1.80×10^{-1}	$+1.12 \times 10^{-2}$	4.90×10^{-2}	4.86×10^{-2}	$+1.72 \times 10^{-5}$	5.30×10^{-4}	$+1.07 \times 10^{-2}$	1.4×10^{-2}	8.2×10^{-3}
24	32	8.83×10^{-5}	4.72×10^{-3}	2.86×10^{1}	1.83×10^{-1}	$+2.19 \times 10^{-2}$	5.67×10^{-3}	5.63×10^{-3}	$+1.93 \times 10^{-6}$	1.39×10^{-3}	$+2.05 \times 10^{-2}$	1.3×10^{-2}	5.9×10^{-3}
32	40	1.55×10^{-3}	1.05×10^{-1}	3.63×10^{1}	2.29×10^{-1}	$+5.36 \times 10^{-3}$	9.91×10^{-2}	9.84×10^{-2}	$+2.92 \times 10^{-5}$	4.90×10^{-4}	$+4.84 \times 10^{-3}$	1.2×10^{-2}	1.0×10^{-2}
32	40	1.96×10^{-4}	1.33×10^{-2}	3.64×10^{1}	2.30×10^{-1}	$+1.69 \times 10^{-2}$	1.56×10^{-2}	1.55×10^{-2}	$+4.24 \times 10^{-6}$	7.90×10^{-4}	$+1.61 \times 10^{-2}$	1.0×10^{-2}	8.4×10^{-3}
32	40	5.18×10^{-4}	3.52×10^{-2}	3.64×10^{1}	2.30×10^{-1}	$+3.81 \times 10^{-2}$	3.89×10^{-2}	3.86×10^{-2}	$+1.08 \times 10^{-5}$	5.40×10^{-4}	$+3.75 \times 10^{-2}$	1.1×10^{-2}	3.3×10^{-2}
32	40	6.71×10^{-3}	4.54×10^{-1}	3.62×10^{1}	2.28×10^{-1}	$+4.89 \times 10^{-2}$	1.85×10^{-1}	1.81×10^{-1}	$+6.71 \times 10^{-5}$	1.34×10^{-3}	$+4.75 \times 10^{-2}$	1.5×10^{-2}	9.5×10^{-2}
32	40	7.43×10^{-5}	5.04×10^{-3}	3.63×10^{1}	2.29×10^{-1}	$+4.72 \times 10^{-3}$	6.02×10^{-3}	5.98×10^{-3}	$+1.62 \times 10^{-6}$	1.20×10^{-3}	$+3.52 \times 10^{-3}$	9.7×10^{-3}	1.0×10^{-1}
40	48	1.16×10^{-3}	9.63×10^{-2}	4.42×10^{1}	2.79×10^{-1}	$+2.47 \times 10^{-2}$	9.21×10^{-2}	9.15×10^{-2}	$+2.28 \times 10^{-5}$	4.80×10^{-4}	$+2.42 \times 10^{-2}$	9.9×10^{-3}	1.2×10^{-2}
40	48	1.76×10^{-4}	1.46×10^{-2}	4.42×10^{1}	2.79×10^{-1}	$+3.42 \times 10^{-3}$	1.69×10^{-2}	1.68×10^{-2}	$+3.81 \times 10^{-6}$	6.90×10^{-4}	$+2.72 \times 10^{-3}$	8.5×10^{-3}	1.3×10^{-2}
40	48	4.22×10^{-4}	3.50×10^{-2}	4.43×10^{1}	2.79×10^{-1}	-6.43×10^{-3}	3.85×10^{-2}	3.83×10^{-2}	$+8.92 \times 10^{-6}$	5.10×10^{-4}	-6.95×10^{-3}	8.9×10^{-3}	8.4×10^{-3}
40	48	5.01×10^{-3}	4.14×10^{-1}	4.42×10^{1}	2.77×10^{-1}	$+1.96 \times 10^{-2}$	1.73×10^{-1}	1.70×10^{-1}	$+6.26 \times 10^{-5}$	1.20×10^{-3}	$+1.84 \times 10^{-2}$	1.2×10^{-2}	7.7×10^{-3}
40	48	7.18×10^{-5}	5.92×10^{-3}	4.41×10^{1}	2.77×10^{-1}	-7.11×10^{-4}	7.03×10^{-3}	6.99×10^{-3}	$+1.57 \times 10^{-6}$	1.01×10^{-3}	-1.72×10^{-3}	8.1×10^{-3}	6.5×10^{-3}
48	56	1.02×10^{-3}	9.99×10^{-2}	5.22×10^{1}	3.29×10^{-1}	$+1.21 \times 10^{-2}$	9.46×10^{-2}	9.41×10^{-2}	$+2.03 \times 10^{-5}$	4.70×10^{-4}	$+1.16 \times 10^{-2}$	8.9×10^{-3}	8.1×10^{-3}
48	56	1.79×10^{-4}	1.75×10^{-2}	5.21×10^{1}	3.27×10^{-1}	$+1.42 \times 10^{-2}$	2.01×10^{-2}	2.01×10^{-2}	$+3.89 \times 10^{-6}$	5.90×10^{-4}	$+1.36 \times 10^{-2}$	7.6×10^{-3}	9.3×10^{-3}
48	56	4.07×10^{-4}	3.98×10^{-2}	5.22×10^{1}	3.28×10^{-1}	$+2.98 \times 10^{-3}$	4.33×10^{-2}	4.31×10^{-2}	$+8.63 \times 10^{-6}$	4.60×10^{-4}	$+2.51 \times 10^{-3}$	8.1×10^{-3}	3.7×10^{-3}
48	56	4.15×10^{-3}	4.05×10^{-1}	5.21×10^{1}	3.27×10^{-1}	$+8.64 \times 10^{-3}$	1.70×10^{-1}	1.68×10^{-1}	$+5.76 \times 10^{-5}$	1.15×10^{-3}	$+7.43 \times 10^{-3}$	1.1×10^{-2}	3.7×10^{-3}
48	56	7.36×10^{-5}	7.17×10^{-3}	5.20×10^{1}	3.26×10^{-1}	$+1.27 \times 10^{-2}$	8.46×10^{-3}	8.42×10^{-3}	$+1.61 \times 10^{-6}$	8.60×10^{-4}	$+1.19 \times 10^{-2}$	7.2×10^{-3}	8.4×10^{-3}
56	64	1.87×10^{-4}	2.10×10^{-2}	6.01×10^{1}	3.77×10^{-1}	$+1.19 \times 10^{-2}$	2.39×10^{-2}	2.38×10^{-2}	$+4.04 \times 10^{-6}$	5.20×10^{-4}	$+1.14 \times 10^{-2}$	7.2×10^{-3}	6.1×10^{-3}
56	64	3.64×10^{-3}	4.09×10^{-1}	6.01×10^{1}	3.78×10^{-1}	$+7.28 \times 10^{-3}$	1.73×10^{-1}	1.70×10^{-1}	$+5.37 \times 10^{-5}$	1.12×10^{-3}	$+6.10 \times 10^{-3}$	1.0×10^{-2}	6.2×10^{-3}
56	64	4.15×10^{-4}	4.67×10^{-2}	6.01×10^{1}	3.77×10^{-1}	$+1.94 \times 10^{-2}$	5.00×10^{-2}	4.98×10^{-2}	$+8.79 \times 10^{-6}$	4.30×10^{-4}	$+1.89 \times 10^{-2}$	7.7×10^{-3}	7.4×10^{-3}
56	64	7.56×10^{-5}	8.50×10^{-3}	6.00×10^{1}	3.76×10^{-1}	$+7.37 \times 10^{-3}$	1.00×10^{-2}	9.96×10^{-3}	$+1.65 \times 10^{-6}$	7.40×10^{-4}	$+6.63 \times 10^{-3}$	6.7×10^{-3}	8.3×10^{-3}
56	64	9.76×10^{-4}	1.10×10^{-1}	6.02×10^{1}	3.78×10^{-1}	$+1.35 \times 10^{-3}$	1.02×10^{-1}	1.01×10^{-1}	$+1.95 \times 10^{-5}$	4.70×10^{-4}	$+8.62 \times 10^{-4}$	8.4×10^{-3}	6.0×10^{-3}
64	72	1.92×10^{-4}	2.45×10^{-2}	6.80×10^{1}	4.27×10^{-1}	$+7.15 \times 10^{-3}$	2.77×10^{-2}	2.76×10^{-2}	$+4.16 \times 10^{-6}$	4.60×10^{-4}	$+6.69 \times 10^{-3}$	6.9×10^{-3}	8.2×10^{-3}
64	72	3.31×10^{-3}	4.22×10^{-1}	6.81×10^{1}	4.28×10^{-1}	$+2.37 \times 10^{-2}$	1.77×10^{-1}	1.75×10^{-1}	$+5.09 \times 10^{-5}$	1.11×10^{-3}	$+2.25 \times 10^{-2}$	9.7×10^{-3}	2.1×10^{-2}
64	72	4.24×10^{-4}	5.41×10^{-2}	6.80×10^{1}	4.27×10^{-1}	$+1.06 \times 10^{-2}$	5.69×10^{-2}	5.67×10^{-2}	$+8.98 \times 10^{-6}$	4.10×10^{-4}	$+1.02 \times 10^{-2}$	7.4×10^{-3}	1.1×10^{-1}
64	72	7.75×10^{-5}	9.87×10^{-3}	6.80×10^{1}	4.26×10^{-1}	$+5.89 \times 10^{-3}$	1.16×10^{-2}	1.15×10^{-2}	$+1.69 \times 10^{-6}$	6.60×10^{-4}	$+5.23 \times 10^{-3}$	6.3×10^{-3}	1.3×10^{-1}
64	72	9.73×10^{-4}	1.24×10^{-1}	6.81×10^{1}	4.28×10^{-1}	$+1.71 \times 10^{-2}$	1.12×10^{-1}	1.11×10^{-1}	$+1.95 \times 10^{-5}$	4.80×10^{-4}	$+1.66 \times 10^{-2}$	8.2×10^{-3}	2.8×10^{-2}
72	80	1.02×10^{-3}	1.45×10^{-1}	7.61×10^{1}	4.77×10^{-1}	$+1.59 \times 10^{-2}$	1.25×10^{-1}	1.25×10^{-1}	$+2.03 \times 10^{-5}$	5.00×10^{-4}	$+1.54 \times 10^{-2}$	8.2×10^{-3}	1.8×10^{-2}
72	80	2.03×10^{-4}	2.89×10^{-2}	7.60×10^{1}	4.76×10^{-1}	$+7.20 \times 10^{-3}$	3.23×10^{-2}	3.22×10^{-2}	$+4.39 \times 10^{-6}$	4.20×10^{-4}	$+6.78 \times 10^{-3}$	6.9×10^{-3}	1.4×10^{-2}
72	80	3.15×10^{-3}	4.50×10^{-1}	7.61×10^{1}	4.79×10^{-1}	$+3.18 \times 10^{-2}$	1.86×10^{-1}	1.84×10^{-1}	$+4.94 \times 10^{-5}$	1.13×10^{-3}	$+3.06 \times 10^{-2}$	9.6×10^{-3}	9.2×10^{-3}
72	80	4.48×10^{-4}	6.39×10^{-2}	7.60×10^{1}	4.76×10^{-1}	$+1.58 \times 10^{-2}$	6.57×10^{-2}	6.54×10^{-2}	$+9.46 \times 10^{-6}$	4.00×10^{-4}	$+1.54 \times 10^{-2}$	7.4×10^{-3}	6.2×10^{-3}
72	80	8.05×10^{-5}	1.15×10^{-2}	7.59×10^{1}	4.75×10^{-1}	$+1.18 \times 10^{-2}$	1.34×10^{-2}	1.33×10^{-2}	$+1.76 \times 10^{-6}$	5.90×10^{-4}	$+1.13 \times 10^{-2}$	6.1×10^{-3}	6.4×10^{-3}

Table F.11: $A_1^p(\nu, Q^2)$ from 2007 data (1/2).

ν (GeV)		$\langle x \rangle$	$\langle Q^2 \rangle$	$\langle \nu \rangle$	$\langle y \rangle$	$A_1^{p,exp}$	F_2^p	F_2^d	$\Delta A_1^{^{14}N}$	ΔA_1^{RC}	$A_1^{p\gamma}$	$\sigma_{stat}(A_1^p)$	$\sigma_{syst}(A_1^p)$
80	88	1.12×10^{-3}	1.76×10^{-1}	8.40×10^{1}	5.27×10^{-1}	$+6.70 \times 10^{-3}$	1.43×10^{-1}	1.43×10^{-1}	$+2.20 \times 10^{-5}$	5.40×10^{-4}	$+6.14 \times 10^{-3}$	8.5×10^{-3}	6.4×10^{-3}
80	88	2.30×10^{-4}	3.61×10^{-2}	8.39×10^{1}	5.25×10^{-1}	$+4.87 \times 10^{-3}$	3.97×10^{-2}	3.96×10^{-2}	$+4.95 \times 10^{-6}$	3.90×10^{-4}	$+4.48 \times 10^{-3}$	7.1×10^{-3}	4.9×10^{-3}
80	88	3.13×10^{-3}	4.94×10^{-1}	8.41×10^{1}	5.29×10^{-1}	$+2.27 \times 10^{-2}$	1.99×10^{-1}	1.97×10^{-1}	$+4.92 \times 10^{-5}$	1.17×10^{-3}	$+2.15 \times 10^{-2}$	9.9×10^{-3}	4.0×10^{-3}
80	88	5.02×10^{-4}	7.91×10^{-2}	8.40×10^{1}	5.26×10^{-1}	$+1.03 \times 10^{-2}$	7.87×10^{-2}	7.84×10^{-2}	$+1.06 \times 10^{-5}$	4.00×10^{-4}	$+9.87 \times 10^{-3}$	7.7×10^{-3}	4.5×10^{-3}
80	88	8.89×10^{-5}	1.40×10^{-2}	8.38×10^{1}	5.23×10^{-1}	$+1.73 \times 10^{-2}$	1.63×10^{-2}	1.62×10^{-2}	$+1.94 \times 10^{-6}$	5.20×10^{-4}	$+1.67 \times 10^{-2}$	6.2×10^{-3}	5.0×10^{-3}
88	96	1.01×10^{-4}	1.74×10^{-2}	9.19×10^{1}	5.75×10^{-1}	$+3.92 \times 10^{-3}$	2.01×10^{-2}	2.00×10^{-2}	$+2.21 \times 10^{-6}$	4.60×10^{-4}	$+3.45 \times 10^{-3}$	6.5×10^{-3}	5.8×10^{-3}
88	96	1.20×10^{-3}	2.06×10^{-1}	9.20×10^{1}	5.76×10^{-1}	$+1.65 \times 10^{-2}$	9.89×10^{-2}	9.87×10^{-2}	$+2.34 \times 10^{-5}$	5.70×10^{-4}	$+1.59 \times 10^{-2}$	8.9×10^{-3}	1.0×10^{-2}
88	96	2.52×10^{-4}	4.34×10^{-2}	9.20×10^{1}	5.77×10^{-1}	$+7.33 \times 10^{-3}$	4.70×10^{-2}	4.68×10^{-2}	$+5.42 \times 10^{-6}$	3.70×10^{-4}	$+6.96 \times 10^{-3}$	7.4×10^{-3}	7.2×10^{-3}
88	96	3.12×10^{-3}	5.39×10^{-1}	9.21×10^{1}	5.78×10^{-1}	$+1.19 \times 10^{-2}$	2.11×10^{-1}	2.08×10^{-1}	$+4.91 \times 10^{-5}$	1.21×10^{-3}	$+1.07 \times 10^{-2}$	1.0×10^{-2}	8.0×10^{-3}
88	96	5.44×10^{-4}	9.38×10^{-2}	9.20×10^{1}	5.76×10^{-1}	$+4.90 \times 10^{-3}$	9.05×10^{-2}	9.02×10^{-2}	$+1.14 \times 10^{-5}$	4.10×10^{-4}	$+4.48 \times 10^{-3}$	8.0×10^{-3}	1.3×10^{-2}
96	104	1.11×10^{-4}	2.08×10^{-2}	9.99×10^{1}	6.24×10^{-1}	$+1.53 \times 10^{-3}$	2.39×10^{-2}	2.38×10^{-2}	$+2.43 \times 10^{-6}$	4.20×10^{-4}	$+1.11 \times 10^{-3}$	6.6×10^{-3}	5.0×10^{-2}
96	104	1.18×10^{-3}	2.22×10^{-1}	1.00×10^{2}	6.27×10^{-1}	$+1.81 \times 10^{-2}$	1.08×10^{-1}	1.08×10^{-1}	$+2.32 \times 10^{-5}$	5.80×10^{-4}	$+1.75 \times 10^{-2}$	9.1×10^{-3}	1.0×10^{-1}
96	104	2.58×10^{-4}	4.84×10^{-2}	1.00×10^{2}	6.28×10^{-1}	$+2.15 \times 10^{-2}$	5.19×10^{-2}	5.17×10^{-2}	$+5.56 \times 10^{-6}$	3.60×10^{-4}	$+2.12 \times 10^{-2}$	7.5×10^{-3}	1.9×10^{-1}
96	104	3.02×10^{-3}	5.67×10^{-1}	1.00×10^{2}	6.28×10^{-1}	$+8.36 \times 10^{-3}$	2.18×10^{-1}	2.16×10^{-1}	$+4.81 \times 10^{-5}$	1.21×10^{-3}	$+7.10 \times 10^{-3}$	1.0×10^{-2}	1.7×10^{-2}
96	104	5.40×10^{-4}	1.01×10^{-1}	1.00×10^{2}	6.28×10^{-1}	$+1.93 \times 10^{-2}$	9.63×10^{-2}	9.60×10^{-2}	$+1.13 \times 10^{-5}$	4.10×10^{-4}	$+1.89 \times 10^{-2}$	8.2×10^{-3}	1.4×10^{-2}
104	112	1.15×10^{-3}	2.34×10^{-1}	1.08×10^{2}	6.78×10^{-1}	$+1.99 \times 10^{-2}$	1.16×10^{-1}	1.16×10^{-1}	$+2.27 \times 10^{-5}$	5.90×10^{-4}	$+1.93 \times 10^{-2}$	9.4×10^{-3}	1.4×10^{-2}
104	112	1.29×10^{-4}	2.61×10^{-2}	1.08×10^{2}	6.71×10^{-1}	$+6.18 \times 10^{-3}$	2.95×10^{-2}	2.95×10^{-2}	$+2.81 \times 10^{-6}$	3.80×10^{-4}	$+5.80 \times 10^{-3}$	6.9×10^{-3}	1.1×10^{-2}
104	112	2.81×10^{-4}	5.70×10^{-2}	1.08×10^{2}	6.77×10^{-1}	$+1.19 \times 10^{-2}$	6.00×10^{-2}	5.98×10^{-2}	$+6.05 \times 10^{-6}$	3.50×10^{-4}	$+1.15 \times 10^{-2}$	7.8×10^{-3}	5.4×10^{-3}
104	112	2.87×10^{-3}	5.82×10^{-1}	1.08×10^{2}	6.77×10^{-1}	$+1.42 \times 10^{-2}$	2.23×10^{-1}	2.21×10^{-1}	$+4.66 \times 10^{-5}$	1.20×10^{-3}	$+1.30 \times 10^{-2}$	1.0×10^{-2}	6.4×10^{-3}
104	112	5.56×10^{-4}	1.13×10^{-1}	1.08×10^{2}	6.78×10^{-1}	$+1.69 \times 10^{-3}$	1.05×10^{-1}	1.04×10^{-1}	$+1.16 \times 10^{-5}$	4.10×10^{-4}	$+1.27 \times 10^{-3}$	8.4×10^{-3}	1.2×10^{-2}
112	120	1.18×10^{-3}	2.56×10^{-1}	1.16×10^{2}	7.28×10^{-1}	$+2.81 \times 10^{-2}$	1.28×10^{-1}	1.28×10^{-1}	$+2.32 \times 10^{-5}$	6.20×10^{-4}	$+2.75 \times 10^{-2}$	9.9×10^{-3}	4.9×10^{-3}
112	120	1.55×10^{-4}	3.37×10^{-2}	1.16×10^{2}	7.19×10^{-1}	$+1.08 \times 10^{-2}$	3.76×10^{-2}	3.75×10^{-2}	$+3.38 \times 10^{-6}$	3.60×10^{-4}	$+1.04 \times 10^{-2}$	7.5×10^{-3}	4.6×10^{-3}
112	120	2.74×10^{-3}	5.97×10^{-1}	1.16×10^{2}	7.28×10^{-1}	$+7.69 \times 10^{-3}$	2.28×10^{-1}	2.26×10^{-1}	$+4.52 \times 10^{-5}$	1.18×10^{-3}	$+6.46 \times 10^{-3}$	1.1×10^{-2}	9.9×10^{-3}
112	120	3.20×10^{-4}	6.96×10^{-2}	1.16×10^{2}	7.27×10^{-1}	$+5.50 \times 10^{-3}$	7.13×10^{-2}	7.11×10^{-2}	$+6.85 \times 10^{-6}$	3.50×10^{-4}	$+5.14 \times 10^{-3}$	8.3×10^{-3}	5.9×10^{-3}
112	120	6.01×10^{-4}	1.31×10^{-1}	1.16×10^{2}	7.28×10^{-1}	$+6.85 \times 10^{-3}$	1.17×10^{-1}	1.17×10^{-1}	$+1.25 \times 10^{-5}$	4.30×10^{-4}	$+6.41 \times 10^{-3}$	8.9×10^{-3}	6.9×10^{-3}
120	128	1.23×10^{-3}	2.87×10^{-1}	1.24×10^{2}	7.76×10^{-1}	$+2.83 \times 10^{-2}$	1.42×10^{-1}	1.42×10^{-1}	$+2.42 \times 10^{-5}$	6.70×10^{-4}	$+2.76 \times 10^{-2}$	1.1×10^{-2}	1.2×10^{-2}
120	128	1.90×10^{-4}	4.42×10^{-2}	1.24×10^{2}	7.66×10^{-1}	$+1.24 \times 10^{-2}$	4.81×10^{-2}	4.80×10^{-2}	$+4.13 \times 10^{-6}$	3.50×10^{-4}	$+1.20 \times 10^{-2}$	8.3×10^{-3}	1.3×10^{-2}
120	128	2.69×10^{-3}	6.25×10^{-1}	1.24×10^{2}	7.76×10^{-1}	$+1.99 \times 10^{-2}$	2.35×10^{-1}	2.33×10^{-1}	$+4.45 \times 10^{-5}$	1.17×10^{-3}	$+1.86 \times 10^{-2}$	1.1×10^{-2}	7.1×10^{-3}
120	128	3.67×10^{-4}	8.54×10^{-2}	1.24×10^{2}	7.75×10^{-1}	$+1.05 \times 10^{-2}$	8.46×10^{-2}	8.44×10^{-2}	$+7.83 \times 10^{-6}$	3.60×10^{-4}	$+1.01 \times 10^{-2}$	9.1×10^{-3}	1.1×10^{-2}
120	128	6.55×10^{-4}	1.52×10^{-1}	1.24×10^{2}	7.76×10^{-1}	$+2.69 \times 10^{-2}$	1.31×10^{-1}	1.31×10^{-1}	$+1.36 \times 10^{-5}$	4.50×10^{-4}	$+2.64 \times 10^{-2}$	9.6×10^{-3}	2.3×10^{-2}
128	136	1.31×10^{-3}	3.24×10^{-1}	1.32×10^{2}	8.21×10^{-1}	$+1.80 \times 10^{-2}$	1.58×10^{-1}	1.58×10^{-1}	$+2.55 \times 10^{-5}$	7.30×10^{-4}	$+1.73 \times 10^{-2}$	1.2×10^{-2}	1.7×10^{-1}
128	136	2.34×10^{-4}	5.77×10^{-2}	1.31×10^{2}	8.09×10^{-1}	$+1.98 \times 10^{-3}$	6.09×10^{-2}	6.08×10^{-2}	$+5.05 \times 10^{-6}$	3.50×10^{-4}	$+1.63 \times 10^{-3}$	1.0×10^{-2}	1.1×10^{-1}
128	136	2.66×10^{-3}	6.57×10^{-1}	1.32×10^{2}	8.21×10^{-1}	$+7.96 \times 10^{-3}$	2.42×10^{-1}	2.41×10^{-1}	$+4.42 \times 10^{-5}$	1.17×10^{-3}	$+6.75 \times 10^{-3}$	1.3×10^{-2}	1.6×10^{-2}
128	136	4.29×10^{-4}	1.06×10^{-1}	1.32×10^{2}	8.18×10^{-1}	$+7.90 \times 10^{-3}$	1.01×10^{-1}	1.00×10^{-1}	$+9.08 \times 10^{-6}$	3.90×10^{-4}	$+7.50 \times 10^{-3}$	1.1×10^{-2}	2.0×10^{-2}
128	136	7.34×10^{-4}	1.81×10^{-1}	1.32×10^{2}	8.20×10^{-1}	$+1.10 \times 10^{-2}$	1.48×10^{-1}	1.48×10^{-1}	$+1.51 \times 10^{-5}$	4.80×10^{-4}	$+1.05 \times 10^{-2}$	1.2×10^{-2}	1.0×10^{-2}
136	144	1.44×10^{-3}	3.77×10^{-1}	1.39×10^{2}	8.56×10^{-1}	$+2.91 \times 10^{-2}$	1.78×10^{-1}	1.78×10^{-1}	$+2.76 \times 10^{-5}$	8.00×10^{-4}	$+2.82 \times 10^{-2}$	1.8×10^{-2}	8.5×10^{-3}
136	144	2.66×10^{-3}	6.96×10^{-1}	1.39×10^{2}	8.56×10^{-1}	$+1.26 \times 10^{-2}$	2.51×10^{-1}	2.49×10^{-1}	$+4.43 \times 10^{-5}$	1.16×10^{-3}	$+1.14 \times 10^{-2}$	1.9×10^{-2}	5.9×10^{-3}
136	144	2.82×10^{-4}	7.36×10^{-2}	1.39×10^{2}	8.41×10^{-1}	$+6.05 \times 10^{-3}$	7.52×10^{-2}	7.50×10^{-2}	$+6.07 \times 10^{-6}$	3.70×10^{-4}	$+5.67 \times 10^{-3}$	1.5×10^{-2}	5.5×10^{-3}
136	144	5.15×10^{-4}	1.34×10^{-1}	1.39×10^{2}	8.49×10^{-1}	-1.32×10^{-2}	1.21×10^{-1}	1.20×10^{-1}	$+1.08 \times 10^{-5}$	4.20×10^{-4}	-1.36×10^{-2}	1.6×10^{-2}	8.7×10^{-3}
136	144	8.62×10^{-4}	2.25×10^{-1}	1.39×10^{2}	8.53×10^{-1}	-8.74×10^{-3}	1.16×10^{-1}	1.70×10^{-1}	$+2.57 \times 10^{-5}$	5.30×10^{-4}	-9.30×10^{-3}	1.7×10^{-2}	9.0×10^{-3}
144	152	1.01×10^{-3}	2.78×10^{-1}	1.47×10^{2}	8.75×10^{-1}	-3.29×10^{-2}	1.42×10^{-1}	1.43×10^{-1}	$+2.03 \times 10^{-5}$	6.10×10^{-4}	-3.35×10^{-2}	4.1×10^{-2}	1.1×10^{-2}
144	152	1.58×10^{-3}	4.34×10^{-1}	1.47×10^{2}	8.76×10^{-1}	-4.49×10^{-2}	1.96×10^{-1}	1.96×10^{-1}	$+2.98 \times 10^{-5}$	8.50×10^{-4}	-4.58×10^{-2}	4.2×10^{-2}	8.4×10^{-3}
144	152	2.67×10^{-3}	7.35×10^{-1}	1.47×10^{2}	8.77×10^{-1}	$+7.13 \times 10^{-2}$	2.59×10^{-1}	2.57×10^{-1}	$+4.44 \times 10^{-5}$	1.16×10^{-3}	$+7.01 \times 10^{-2}$	4.4×10^{-2}	5.4×10^{-3}
144	152	3.38×10^{-4}	9.28×10^{-2}	1.46×10^{2}	8.63×10^{-1}	$+1.03 \times 10^{-1}$	9.10×10^{-2}	9.08×10^{-2}	$+7.23 \times 10^{-6}$	3.90×10^{-4}	$+1.03 \times 10^{-1}$	3.5×10^{-2}	5.7×10^{-3}
144	152	6.23×10^{-4}	1.71×10^{-1}	1.46×10^{2}	8.72×10^{-1}	-2.66×10^{-2}	1.43×10^{-1}	1.43×10^{-1}	$+1.29 \times 10^{-5}$	4.70×10^{-4}	-2.71×10^{-2}	3.8×10^{-2}	5.9×10^{-3}
152	160	1.05×10^{-3}	3.03×10^{-1}	1.54×10^{2}	8.83×10^{-1}	$+2.49 \times 10^{-2}$	1.54×10^{-1}	1.55×10^{-1}	$+2.10 \times 10^{-5}$	6.40×10^{-4}	$+2.42 \times 10^{-2}$	1.8×10^{-1}	6.3×10^{-3}
152	160	1.60×10^{-3}	4.63×10^{-1}	1.54×10^{2}	8.84×10^{-1}	$+1.12 \times 10^{-1}$	2.05×10^{-1}	2.06×10^{-1}	$+3.02 \times 10^{-5}$	8.50×10^{-4}	$+1.11 \times 10^{-1}$	1.8×10^{-1}	1.1×10^{-2}
152	160	2.61×10^{-3}	7.54×10^{-1}	1.54×10^{2}	8.85×10^{-1}	$+3.14 \times 10^{-1}$	2.63×10^{-1}	2.62×10^{-1}	$+4.37 \times 10^{-5}$	1.14×10^{-3}	$+3.13 \times 10^{-1}$	1.9×10^{-1}	1.1×10^{-2}
152	160	3.62×10^{-4}	1.05×10^{-1}	1.54×10^{2}	8.76×10^{-1}	-9.17×10^{-2}	1.00×10^{-1}	1.00×10^{-1}	$+7.72 \times 10^{-6}$	4.10×10^{-4}	-9.21×10^{-2}	1.6×10^{-1}	2.7×10^{-2}
152	160	6.58×10^{-4}	1.90×10^{-1}	1.54×10^{2}	8.82×10^{-1}	$+5.34 \times 10^{-1}$	1.54×10^{-1}	1.54×10^{-1}	$+1.36 \times 10^{-5}$	4.90×10^{-4}	$+5.33 \times 10^{-1}$	1.7×10^{-1}	1.2×10^{-1}

Table F.12: $A_1^p(\nu, Q^2)$ from 2007 data (2/2).

ν (GeV)		$\langle x \rangle$	$\langle Q^2 \rangle$	$\langle \nu \rangle$	$\langle y \rangle$	$A_1^{p,exp}$	F_2^p	F_2^d	$\Delta A_1^{^{14}N}$	ΔA_1^{RC}	$A_1^{p\gamma}$	$\sigma_{stat}(A_1^p)$	$\sigma_{syst}(A_1^p)$
16	24	1.01×10^{-2}	4.20×10^{-1}	2.22×10^{1}	1.10×10^{-1}	-6.43×10^{-2}	1.81×10^{-1}	1.78×10^{-1}	$+6.04 \times 10^{-5}$	1.12×10^{-3}	-6.55×10^{-2}	1.4×10^{-1}	8.8×10^{-2}
16	24	1.55×10^{-2}	6.45×10^{-1}	2.22×10^{1}	1.10×10^{-1}	-6.34×10^{-3}	2.36×10^{-1}	2.29×10^{-1}	$+2.30 \times 10^{-5}$	1.67×10^{-3}	-8.03×10^{-3}	1.4×10^{-1}	3.5×10^{-2}
16	24	1.94×10^{-3}	8.06×10^{-2}	2.22×10^{1}	1.13×10^{-1}	-1.62×10^{-2}	8.12×10^{-2}	8.06×10^{-2}	$+3.49 \times 10^{-5}$	4.30×10^{-4}	-1.67×10^{-2}	1.1×10^{-1}	1.7×10^{-2}
16	24	2.12×10^{-2}	8.80×10^{-1}	2.22×10^{1}	1.10×10^{-1}	$+1.27 \times 10^{-1}$	2.72×10^{-1}	2.64×10^{-1}	-3.35×10^{-5}	2.18×10^{-3}	$+1.25 \times 10^{-1}$	1.4×10^{-1}	2.0×10^{-2}
16	24	5.56×10^{-3}	2.31×10^{-1}	2.22×10^{1}	1.11×10^{-1}	$+1.99 \times 10^{-1}$	1.07×10^{-1}	1.05×10^{-1}	$+6.47 \times 10^{-5}$	5.30×10^{-4}	$+1.98 \times 10^{-1}$	1.3×10^{-1}	1.3×10^{-2}
24	32	1.06×10^{-2}	5.62×10^{-1}	2.84×10^{1}	1.41×10^{-1}	$+2.15 \times 10^{-1}$	2.14×10^{-1}	2.09×10^{-1}	$+5.80 \times 10^{-5}$	1.49×10^{-3}	$+2.13 \times 10^{-1}$	7.0×10^{-2}	6.0×10^{-3}
24	32	1.61×10^{-2}	8.47×10^{-1}	2.83×10^{1}	1.40×10^{-1}	$+1.96 \times 10^{-2}$	2.64×10^{-1}	2.56×10^{-1}	$+1.85 \times 10^{-5}$	2.12×10^{-3}	$+1.75 \times 10^{-2}$	7.2×10^{-2}	6.4×10^{-3}
24	32	2.94×10^{-3}	1.57×10^{-1}	2.86×10^{1}	1.43×10^{-1}	$+1.78 \times 10^{-2}$	1.33×10^{-1}	1.32×10^{-1}	$+4.73 \times 10^{-5}$	4.80×10^{-4}	$+1.72 \times 10^{-2}$	5.8×10^{-2}	6.4×10^{-3}
24	32	5.99×10^{-3}	3.18×10^{-1}	2.85×10^{1}	1.42×10^{-1}	$+7.02 \times 10^{-2}$	1.43×10^{-1}	1.40×10^{-1}	$+6.59 \times 10^{-5}$	8.30×10^{-4}	$+6.93 \times 10^{-2}$	6.5×10^{-2}	5.8×10^{-3}
24	32	8.51×10^{-4}	4.59×10^{-2}	2.90×10^{1}	1.48×10^{-1}	-2.53×10^{-3}	4.97×10^{-2}	4.94×10^{-2}	$+1.72 \times 10^{-5}$	5.20×10^{-4}	-3.07×10^{-3}	5.0×10^{-2}	5.4×10^{-3}
32	40	1.13×10^{-3}	7.71×10^{-2}	3.66×10^{1}	1.84×10^{-1}	$+4.44 \times 10^{-2}$	7.72×10^{-2}	7.67×10^{-2}	$+2.21 \times 10^{-5}$	4.50×10^{-4}	$+4.39 \times 10^{-2}$	3.5×10^{-2}	5.1×10^{-3}
32	40	1.14×10^{-2}	7.74×10^{-1}	3.62×10^{1}	1.80×10^{-1}	$+5.38 \times 10^{-2}$	2.50×10^{-1}	2.44×10^{-1}	$+5.37 \times 10^{-5}$	1.93×10^{-3}	$+5.18 \times 10^{-2}$	4.7×10^{-2}	4.5×10^{-3}
32	40	2.66×10^{-3}	1.81×10^{-1}	3.65×10^{1}	1.82×10^{-1}	$+2.16 \times 10^{-2}$	1.46×10^{-1}	1.45×10^{-1}	$+4.42 \times 10^{-5}$	5.40×10^{-4}	$+2.10 \times 10^{-2}$	3.9×10^{-2}	6.2×10^{-3}
32	40	2.70×10^{-4}	1.87×10^{-2}	3.69×10^{1}	1.89×10^{-1}	$+3.55 \times 10^{-2}$	2.15×10^{-2}	2.14×10^{-2}	$+5.80 \times 10^{-6}$	6.90×10^{-4}	$+3.48 \times 10^{-2}$	3.1×10^{-2}	5.4×10^{-3}
32	40	5.84×10^{-3}	3.97×10^{-1}	3.63×10^{1}	1.81×10^{-1}	-4.03×10^{-2}	1.68×10^{-1}	1.65×10^{-1}	$+6.56 \times 10^{-5}$	1.09×10^{-3}	-4.15×10^{-2}	4.5×10^{-2}	5.3×10^{-3}
40	48	1.21×10^{-3}	1.00×10^{-1}	4.44×10^{1}	2.22×10^{-1}	$+2.25 \times 10^{-2}$	9.50×10^{-2}	9.44×10^{-2}	$+2.35 \times 10^{-5}$	4.50×10^{-4}	$+2.20 \times 10^{-2}$	2.5×10^{-2}	5.1×10^{-3}
40	48	1.21×10^{-4}	1.02×10^{-2}	4.48×10^{1}	2.27×10^{-1}	$+3.45 \times 10^{-2}$	1.19×10^{-2}	1.19×10^{-2}	$+2.64 \times 10^{-6}$	8.10×10^{-4}	$+3.37 \times 10^{-2}$	2.1×10^{-2}	5.6×10^{-3}
40	48	3.01×10^{-3}	2.50×10^{-1}	4.43×10^{1}	2.21×10^{-1}	$+3.48 \times 10^{-2}$	1.14×10^{-1}	1.12×10^{-1}	$+4.78 \times 10^{-5}$	6.70×10^{-4}	$+3.41 \times 10^{-2}$	2.8×10^{-2}	6.6×10^{-3}
40	48	4.54×10^{-4}	3.78×10^{-2}	4.46×10^{1}	2.24×10^{-1}	$+1.62 \times 10^{-2}$	4.14×10^{-2}	4.12×10^{-2}	$+9.56 \times 10^{-6}$	4.90×10^{-4}	$+1.57 \times 10^{-2}$	2.2×10^{-2}	6.9×10^{-3}
40	48	8.07×10^{-3}	6.67×10^{-1}	4.42×10^{1}	2.20×10^{-1}	$+5.76 \times 10^{-2}$	2.31×10^{-1}	2.26×10^{-1}	$+6.66 \times 10^{-5}$	1.64×10^{-3}	$+5.59 \times 10^{-2}$	3.2×10^{-2}	1.1×10^{-2}
48	56	1.72×10^{-3}	1.68×10^{-1}	5.23×10^{1}	2.60×10^{-1}	-4.48×10^{-3}	1.39×10^{-1}	1.38×10^{-1}	$+3.17 \times 10^{-5}$	5.30×10^{-4}	-5.04×10^{-3}	2.0×10^{-2}	8.8×10^{-3}
48	56	2.38×10^{-4}	2.34×10^{-2}	5.25×10^{1}	2.63×10^{-1}	-7.81×10^{-3}	2.65×10^{-2}	2.64×10^{-2}	$+5.12 \times 10^{-6}$	5.40×10^{-4}	-8.35×10^{-3}	1.6×10^{-2}	4.2×10^{-2}
48	56	5.73×10^{-3}	5.60×10^{-1}	5.22×10^{1}	2.59×10^{-1}	$+7.93 \times 10^{-3}$	2.09×10^{-1}	2.06×10^{-1}	$+6.53 \times 10^{-5}$	1.37×10^{-3}	$+6.49 \times 10^{-3}$	2.3×10^{-2}	2.3×10^{-1}
48	56	6.30×10^{-4}	6.18×10^{-2}	5.24×10^{1}	2.61×10^{-1}	$+3.76 \times 10^{-4}$	6.38×10^{-2}	6.35×10^{-2}	$+1.31 \times 10^{-5}$	4.30×10^{-4}	-6.74×10^{-5}	1.7×10^{-2}	1.2×10^{-1}
48	56	8.14×10^{-5}	8.02×10^{-3}	5.25×10^{1}	2.65×10^{-1}	$+1.50 \times 10^{-2}$	9.44×10^{-3}	9.40×10^{-3}	$+1.78 \times 10^{-6}$	8.30×10^{-4}	$+1.42 \times 10^{-2}$	1.5×10^{-2}	2.8×10^{-2}
56	64	1.15×10^{-3}	1.29×10^{-1}	6.02×10^{1}	2.99×10^{-1}	$+7.21 \times 10^{-3}$	1.15×10^{-1}	1.15×10^{-1}	$+2.25 \times 10^{-5}$	4.70×10^{-4}	$+6.71 \times 10^{-3}$	1.5×10^{-2}	2.9×10^{-2}
56	64	1.70×10^{-4}	1.92×10^{-2}	6.03×10^{1}	3.01×10^{-1}	$+6.58 \times 10^{-3}$	2.19×10^{-2}	2.19×10^{-2}	$+3.68 \times 10^{-6}$	5.40×10^{-4}	$+6.04 \times 10^{-3}$	1.2×10^{-2}	1.5×10^{-2}
56	64	4.16×10^{-4}	4.70×10^{-2}	6.03×10^{1}	3.00×10^{-1}	$+1.65 \times 10^{-2}$	5.02×10^{-2}	5.00×10^{-2}	$+8.81 \times 10^{-6}$	4.30×10^{-4}	$+1.60 \times 10^{-2}$	1.3×10^{-2}	1.3×10^{-2}
56	64	4.32×10^{-3}	4.87×10^{-1}	6.02×10^{1}	2.99×10^{-1}	$+1.36 \times 10^{-2}$	1.93×10^{-1}	1.90×10^{-1}	$+5.88 \times 10^{-5}$	1.18×10^{-3}	$+1.24 \times 10^{-2}$	1.8×10^{-2}	6.5×10^{-3}
56	64	6.91×10^{-5}	7.80×10^{-3}	6.03×10^{1}	3.01×10^{-1}	$+1.26 \times 10^{-2}$	9.20×10^{-3}	9.16×10^{-3}	$+1.51 \times 10^{-6}$	7.80×10^{-4}	$+1.19 \times 10^{-2}$	1.2×10^{-2}	6.7×10^{-3}
64	72	1.52×10^{-4}	1.94×10^{-2}	6.82×10^{1}	3.39×10^{-1}	-4.21×10^{-3}	2.22×10^{-2}	2.21×10^{-2}	$+3.30 \times 10^{-6}$	5.10×10^{-4}	-4.73×10^{-3}	1.1×10^{-2}	9.3×10^{-3}
64	72	3.45×10^{-4}	4.41×10^{-2}	6.82×10^{1}	3.39×10^{-1}	-4.98×10^{-3}	4.75×10^{-2}	4.73×10^{-2}	$+7.36 \times 10^{-6}$	4.10×10^{-4}	-5.40×10^{-3}	1.1×10^{-2}	5.7×10^{-3}
64	72	3.51×10^{-3}	4.48×10^{-1}	6.81×10^{1}	3.38×10^{-1}	$+5.67 \times 10^{-3}$	1.84×10^{-1}	1.82×10^{-1}	$+5.27 \times 10^{-5}$	1.07×10^{-3}	$+4.55 \times 10^{-3}$	1.5×10^{-2}	1.1×10^{-2}
64	72	6.64×10^{-5}	8.48×10^{-3}	6.81×10^{1}	3.38×10^{-1}	-3.17×10^{-4}	9.98×10^{-3}	9.94×10^{-3}	$+1.45 \times 10^{-6}$	7.10×10^{-4}	-1.03×10^{-3}	1.0×10^{-2}	5.2×10^{-3}
64	72	9.11×10^{-4}	1.16×10^{-1}	6.82×10^{1}	3.39×10^{-1}	$+4.12 \times 10^{-2}$	1.07×10^{-1}	1.06×10^{-1}	$+1.83 \times 10^{-5}$	4.50×10^{-4}	$+4.07 \times 10^{-2}$	1.3×10^{-2}	5.0×10^{-3}
72	80	1.53×10^{-4}	2.19×10^{-2}	7.61×10^{1}	3.77×10^{-1}	$+9.06 \times 10^{-3}$	2.49×10^{-2}	2.48×10^{-2}	$+3.33 \times 10^{-6}$	4.60×10^{-4}	$+8.60 \times 10^{-3}$	9.7×10^{-3}	6.9×10^{-3}
72	80	3.03×10^{-3}	4.33×10^{-1}	7.61×10^{1}	3.78×10^{-1}	$+5.22 \times 10^{-3}$	1.82×10^{-1}	1.80×10^{-1}	$+4.82 \times 10^{-5}$	1.02×10^{-3}	$+4.15 \times 10^{-3}$	1.4×10^{-2}	7.4×10^{-3}
72	80	3.34×10^{-4}	4.77×10^{-2}	7.62×10^{1}	3.78×10^{-1}	$+2.60 \times 10^{-2}$	5.09×10^{-2}	5.08×10^{-2}	$+7.13 \times 10^{-6}$	3.90×10^{-4}	$+2.56 \times 10^{-2}$	1.0×10^{-2}	7.7×10^{-3}
72	80	6.75×10^{-5}	9.62×10^{-3}	7.60×10^{1}	3.76×10^{-1}	-1.79×10^{-2}	1.13×10^{-2}	1.13×10^{-2}	$+1.48 \times 10^{-6}$	6.40×10^{-4}	-1.85×10^{-2}	9.0×10^{-3}	4.7×10^{-3}
72	80	8.26×10^{-4}	1.18×10^{-1}	7.62×10^{1}	3.78×10^{-1}	$+2.70 \times 10^{-2}$	1.08×10^{-1}	1.07×10^{-1}	$+1.68 \times 10^{-5}$	4.40×10^{-4}	$+2.65 \times 10^{-2}$	1.1×10^{-2}	7.4×10^{-3}
80	88	1.61×10^{-4}	2.54×10^{-2}	8.41×10^{1}	4.16×10^{-1}	$+1.94 \times 10^{-3}$	2.87×10^{-2}	2.86×10^{-2}	$+3.51 \times 10^{-6}$	4.20×10^{-4}	$+1.52 \times 10^{-3}$	9.1×10^{-3}	5.5×10^{-3}
80	88	2.75×10^{-3}	4.34×10^{-1}	8.41×10^{1}	4.17×10^{-1}	$+1.49 \times 10^{-2}$	1.84×10^{-1}	1.82×10^{-1}	$+4.52 \times 10^{-5}$	1.00×10^{-3}	$+1.38 \times 10^{-2}$	1.3×10^{-2}	1.1×10^{-2}
80	88	3.48×10^{-4}	5.48×10^{-2}	8.41×10^{1}	4.17×10^{-1}	-4.86×10^{-3}	5.77×10^{-2}	5.75×10^{-2}	$+7.42 \times 10^{-6}$	3.80×10^{-4}	-5.25×10^{-3}	9.8×10^{-3}	1.1×10^{-2}
80	88	6.96×10^{-5}	1.10×10^{-2}	8.40×10^{1}	4.16×10^{-1}	$+7.83 \times 10^{-3}$	1.28×10^{-2}	1.28×10^{-2}	$+1.52 \times 10^{-6}$	5.70×10^{-4}	$+7.26 \times 10^{-3}$	8.4×10^{-3}	9.6×10^{-3}
80	88	8.12×10^{-4}	1.28×10^{-1}	8.41×10^{1}	4.18×10^{-1}	$+5.33 \times 10^{-4}$	1.15×10^{-1}	1.14×10^{-1}	$+1.65 \times 10^{-5}$	4.50×10^{-4}	$+6.68 \times 10^{-5}$	1.1×10^{-2}	2.7×10^{-2}
88	96	1.70×10^{-4}	2.93×10^{-2}	9.20×10^{1}	4.56×10^{-1}	$+1.06 \times 10^{-2}$	3.29×10^{-2}	3.28×10^{-2}	$+3.69 \times 10^{-6}$	3.90×10^{-4}	$+1.02 \times 10^{-2}$	8.8×10^{-3}	3.0×10^{-1}
88	96	2.57×10^{-3}	4.44×10^{-1}	9.21×10^{1}	4.57×10^{-1}	$+8.38 \times 10^{-3}$	1.88×10^{-1}	1.86×10^{-1}	$+4.32 \times 10^{-5}$	9.90×10^{-4}	$+7.35 \times 10^{-3}$	1.2×10^{-2}	9.7×10^{-2}
88	96	3.66×10^{-4}	6.32×10^{-2}	9.21×10^{1}	4.56×10^{-1}	$+1.17 \times 10^{-2}$	6.53×10^{-2}	6.51×10^{-2}	$+7.80 \times 10^{-6}$	3.70×10^{-4}	$+1.13 \times 10^{-2}$	9.5×10^{-3}	3.4×10^{-2}
88	96	7.16×10^{-5}	1.24×10^{-2}	9.20×10^{1}	4.55×10^{-1}	$+7.38 \times 10^{-3}$	1.44×10^{-2}	1.44×10^{-2}	$+1.57 \times 10^{-6}$	5.20×10^{-4}	$+6.86 \times 10^{-3}$	8.0×10^{-3}	2.9×10^{-2}
88	96	8.23×10^{-4}	1.42×10^{-1}	9.21×10^{1}	4.57×10^{-1}	$+2.03 \times 10^{-2}$	1.24×10^{-1}	1.23×10^{-1}	$+1.67 \times 10^{-5}$	4.60×10^{-4}	$+1.98 \times 10^{-2}$	1.0×10^{-2}	2.1×10^{-2}
96	104	1.76×10^{-4}	3.31×10^{-2}	1.00×10^{2}	4.95×10^{-1}	$+1.66 \times 10^{-2}$	3.68×10^{-2}	3.67×10^{-2}	$+3.83 \times 10^{-6}$	3.70×10^{-4}	$+1.63 \times 10^{-2}$	8.6×10^{-3}	8.2×10^{-3}
96	104	2.46×10^{-3}	4.62×10^{-1}	1.00×10^{2}	4.96×10^{-1}	$+1.65 \times 10^{-2}$	1.94×10^{-1}	1.93×10^{-1}	$+4.18 \times 10^{-5}$	9.90×10^{-4}	$+1.54 \times 10^{-2}$	1.2×10^{-2}	6.6×10^{-3}
96	104	3.79×10^{-4}	7.11×10^{-2}	1.00×10^{2}	4.95×10^{-1}	-1.34×10^{-3}	7.22×10^{-2}	7.20×10^{-2}	$+8.06 \times 10^{-6}$	3.60×10^{-4}	-1.70×10^{-3}	9.3×10^{-3}	1.0×10^{-2}
96	104	7.33×10^{-5}	1.38×10^{-2}	1.00×10^{2}	4.95×10^{-1}	$+1.54 \times 10^{-2}$	1.60×10^{-2}	1.60×10^{-2}	$+1.61 \times 10^{-6}$	4.80×10^{-4}	$+1.49 \times 10^{-2}$	7.7×10^{-3}	9.3×10^{-3}
96	104	8.34×10^{-4}	1.57×10^{-1}	1.00×10^{2}	4.96×10^{-1}	$+2.71 \times 10^{-3}$	1.33×10^{-1}	1.32×10^{-1}	$+1.69 \times 10^{-5}$	4.70×10^{-4}	$+2.22 \times 10^{-3}$	1.0×10^{-2}	6.1×10^{-3}

Table F.13: $A_1^p(\nu, Q^2)$ from 2011 data (1/2).

ν (GeV)		$\langle x \rangle$	$\langle Q^2 \rangle$	$\langle \nu \rangle$	$\langle y \rangle$	$A_1^{p,exp}$	F_2^p	F_2^d	$\Delta A_1^{^{14}N}$	ΔA_1^{RC}	$A_1^{p\gamma}$	$\sigma_{stat}(A_1^p)$	$\sigma_{syst}(A_1^p)$
104	112	1.81×10^{-4}	3.66×10^{-2}	1.08×10^{2}	5.35×10^{-1}	$+5.91 \times 10^{-3}$	4.04×10^{-2}	4.03×10^{-2}	$+3.92 \times 10^{-6}$	3.50×10^{-4}	$+5.56 \times 10^{-3}$	8.5×10^{-3}	5.8×10^{-3}
104	112	2.40×10^{-3}	4.86×10^{-1}	1.08×10^{2}	5.36×10^{-1}	$+3.28 \times 10^{-2}$	2.02×10^{-1}	2.00×10^{-1}	$+4.11 \times 10^{-5}$	1.00×10^{-3}	$+3.18 \times 10^{-2}$	1.2×10^{-2}	5.3×10^{-3}
104	112	3.88×10^{-4}	7.87×10^{-2}	1.08×10^{2}	5.35×10^{-1}	$+6.32 \times 10^{-3}$	7.88×10^{-2}	7.86×10^{-2}	$+8.26 \times 10^{-6}$	3.60×10^{-4}	$+5.95 \times 10^{-3}$	9.3×10^{-3}	8.5×10^{-3}
104	112	7.47×10^{-5}	1.51×10^{-2}	1.08×10^{2}	5.34×10^{-1}	-1.02×10^{-2}	1.76×10^{-2}	1.76×10^{-2}	$+1.64 \times 10^{-6}$	4.50×10^{-4}	-1.07×10^{-2}	7.5×10^{-3}	5.7×10^{-3}
104	112	8.51×10^{-4}	1.72×10^{-1}	1.08×10^{2}	5.35×10^{-1}	$+2.81 \times 10^{-2}$	1.42×10^{-1}	1.42×10^{-1}	$+1.73 \times 10^{-5}$	4.80×10^{-4}	$+2.76 \times 10^{-2}$	1.0×10^{-2}	5.7×10^{-3}
112	120	1.90×10^{-4}	4.13×10^{-2}	1.16×10^{2}	5.73×10^{-1}	$+3.35 \times 10^{-3}$	4.52×10^{-2}	4.51×10^{-2}	$+4.12 \times 10^{-6}$	3.30×10^{-4}	$+3.02 \times 10^{-3}$	8.6×10^{-3}	8.2×10^{-3}
112	120	2.38×10^{-3}	5.18×10^{-1}	1.16×10^{2}	5.75×10^{-1}	$+3.39 \times 10^{-2}$	2.11×10^{-1}	2.10×10^{-1}	$+4.09 \times 10^{-5}$	1.02×10^{-3}	$+3.28 \times 10^{-2}$	1.2×10^{-2}	5.9×10^{-3}
112	120	4.06×10^{-4}	8.83×10^{-2}	1.16×10^{2}	5.74×10^{-1}	$+1.11 \times 10^{-2}$	8.68×10^{-2}	8.65×10^{-2}	$+8.62 \times 10^{-6}$	3.60×10^{-4}	$+1.08 \times 10^{-2}$	9.4×10^{-3}	5.7×10^{-3}
112	120	7.82×10^{-5}	1.70×10^{-2}	1.16×10^{2}	5.72×10^{-1}	$+9.02 \times 10^{-3}$	1.97×10^{-2}	1.97×10^{-2}	$+1.71 \times 10^{-6}$	4.20×10^{-4}	$+8.60 \times 10^{-3}$	7.6×10^{-3}	5.2×10^{-3}
112	120	8.81×10^{-4}	1.92×10^{-1}	1.16×10^{2}	5.74×10^{-1}	$+3.25 \times 10^{-2}$	1.53×10^{-1}	1.53×10^{-1}	$+1.78 \times 10^{-5}$	4.90×10^{-4}	$+3.20 \times 10^{-2}$	1.1×10^{-2}	1.3×10^{-2}
120	128	2.05×10^{-4}	4.78×10^{-2}	1.24×10^{2}	6.13×10^{-1}	$+1.68 \times 10^{-2}$	5.16×10^{-2}	5.15×10^{-2}	$+4.45 \times 10^{-6}$	3.20×10^{-4}	$+1.64 \times 10^{-2}$	9.0×10^{-3}	7.4×10^{-3}
120	128	2.39×10^{-3}	5.55×10^{-1}	1.24×10^{2}	6.14×10^{-1}	$+1.36 \times 10^{-2}$	2.21×10^{-1}	2.20×10^{-1}	$+4.10 \times 10^{-5}$	1.05×10^{-3}	$+1.25 \times 10^{-2}$	1.2×10^{-2}	1.2×10^{-2}
120	128	4.35×10^{-4}	1.01×10^{-1}	1.24×10^{2}	6.13×10^{-1}	$+9.85 \times 10^{-3}$	9.69×10^{-2}	9.66×10^{-2}	$+9.21 \times 10^{-6}$	3.70×10^{-4}	$+9.47 \times 10^{-3}$	9.8×10^{-3}	2.5×10^{-2}
120	128	8.61×10^{-5}	2.00×10^{-2}	1.24×10^{2}	6.10×10^{-1}	$+5.40 \times 10^{-3}$	2.31×10^{-2}	2.31×10^{-2}	$+1.88 \times 10^{-6}$	3.90×10^{-4}	$+5.01 \times 10^{-3}$	7.9×10^{-3}	2.9×10^{-1}
120	128	9.34×10^{-4}	2.17×10^{-1}	1.24×10^{2}	6.13×10^{-1}	-7.84×10^{-3}	1.10×10^{-1}	1.10×10^{-1}	$+1.89 \times 10^{-5}$	5.20×10^{-4}	-8.38×10^{-3}	1.1×10^{-2}	6.2×10^{-2}
128	136	2.18×10^{-4}	5.40×10^{-2}	1.32×10^{2}	6.53×10^{-1}	$+9.39 \times 10^{-3}$	5.76×10^{-2}	5.74×10^{-2}	$+4.72 \times 10^{-6}$	3.20×10^{-4}	$+9.07 \times 10^{-3}$	9.4×10^{-3}	6.8×10^{-2}
128	136	2.37×10^{-3}	5.87×10^{-1}	1.32×10^{2}	6.53×10^{-1}	$+6.46 \times 10^{-3}$	2.29×10^{-1}	2.28×10^{-1}	$+4.08 \times 10^{-5}$	1.06×10^{-3}	$+5.36 \times 10^{-3}$	1.3×10^{-2}	2.6×10^{-2}
128	136	4.49×10^{-4}	1.11×10^{-1}	1.32×10^{2}	6.53×10^{-1}	$+7.67 \times 10^{-3}$	1.04×10^{-1}	1.04×10^{-1}	$+9.49 \times 10^{-6}$	3.70×10^{-4}	$+7.29 \times 10^{-3}$	1.0×10^{-2}	1.9×10^{-2}
128	136	9.57×10^{-4}	2.37×10^{-1}	1.32×10^{2}	6.53×10^{-1}	-8.40×10^{-3}	1.21×10^{-1}	1.21×10^{-1}	$+1.93 \times 10^{-5}$	5.40×10^{-4}	-8.96×10^{-3}	1.1×10^{-2}	1.5×10^{-2}
128	136	9.61×10^{-5}	2.38×10^{-2}	1.32×10^{2}	6.50×10^{-1}	$+1.01 \times 10^{-2}$	2.73×10^{-2}	2.72×10^{-2}	$+2.10 \times 10^{-6}$	3.60×10^{-4}	$+9.77 \times 10^{-3}$	8.3×10^{-3}	7.3×10^{-3}
136	144	1.08×10^{-4}	2.83×10^{-2}	1.40×10^{2}	6.89×10^{-1}	-4.84×10^{-3}	3.22×10^{-2}	3.21×10^{-2}	$+2.36 \times 10^{-6}$	3.40×10^{-4}	-5.18×10^{-3}	8.8×10^{-3}	9.5×10^{-3}
136	144	2.29×10^{-3}	6.01×10^{-1}	1.40×10^{2}	6.92×10^{-1}	$+8.90 \times 10^{-3}$	2.34×10^{-1}	2.33×10^{-1}	$+3.98 \times 10^{-5}$	1.06×10^{-3}	$+7.80 \times 10^{-3}$	1.3×10^{-2}	8.6×10^{-3}
136	144	2.31×10^{-4}	6.08×10^{-2}	1.40×10^{2}	6.93×10^{-1}	-9.10×10^{-3}	6.39×10^{-2}	6.38×10^{-2}	$+5.00 \times 10^{-6}$	3.10×10^{-4}	-9.42×10^{-3}	9.8×10^{-3}	5.1×10^{-3}
136	144	4.57×10^{-4}	1.20×10^{-1}	1.40×10^{2}	6.93×10^{-1}	-2.32×10^{-2}	1.11×10^{-1}	1.11×10^{-1}	$+9.66 \times 10^{-6}$	3.80×10^{-4}	-2.35×10^{-2}	1.1×10^{-2}	7.4×10^{-3}
136	144	9.46×10^{-4}	2.48×10^{-1}	1.40×10^{2}	6.93×10^{-1}	$+2.27 \times 10^{-2}$	1.28×10^{-1}	1.28×10^{-1}	$+1.92 \times 10^{-5}$	5.50×10^{-4}	$+2.21 \times 10^{-2}$	1.2×10^{-2}	6.9×10^{-3}
144	152	1.24×10^{-4}	3.44×10^{-2}	1.48×10^{2}	7.27×10^{-1}	$+1.93 \times 10^{-2}$	3.86×10^{-2}	3.85×10^{-2}	$+2.71 \times 10^{-6}$	3.20×10^{-4}	$+1.89 \times 10^{-2}$	9.3×10^{-3}	9.0×10^{-3}
144	152	2.19×10^{-3}	6.09×10^{-1}	1.48×10^{2}	7.33×10^{-1}	-2.02×10^{-3}	2.37×10^{-1}	2.36×10^{-1}	$+3.86 \times 10^{-5}$	1.04×10^{-3}	-3.10×10^{-3}	1.3×10^{-2}	7.0×10^{-3}
144	152	2.55×10^{-4}	7.07×10^{-2}	1.48×10^{2}	7.32×10^{-1}	-6.27×10^{-3}	7.28×10^{-2}	7.27×10^{-2}	$+5.49 \times 10^{-6}$	3.20×10^{-4}	-6.59×10^{-3}	1.0×10^{-2}	6.4×10^{-3}
144	152	4.84×10^{-4}	1.34×10^{-1}	1.48×10^{2}	7.32×10^{-1}	$+3.26 \times 10^{-3}$	1.21×10^{-1}	1.21×10^{-1}	$+1.02 \times 10^{-5}$	3.90×10^{-4}	$+2.86 \times 10^{-3}$	1.1×10^{-2}	7.1×10^{-3}
144	152	9.59×10^{-4}	2.66×10^{-1}	1.48×10^{2}	7.33×10^{-1}	$+1.55 \times 10^{-2}$	1.37×10^{-1}	1.38×10^{-1}	$+1.94 \times 10^{-5}$	5.70×10^{-4}	$+1.49 \times 10^{-2}$	1.2×10^{-2}	7.9×10^{-3}
152	160	1.01×10^{-3}	2.97×10^{-1}	1.56×10^{2}	7.71×10^{-1}	-2.31×10^{-3}	1.51×10^{-1}	1.52×10^{-1}	$+2.04 \times 10^{-5}$	6.10×10^{-4}	-2.94×10^{-3}	1.3×10^{-2}	9.5×10^{-3}
152	160	1.46×10^{-4}	4.28×10^{-2}	1.56×10^{2}	7.64×10^{-1}	$+9.52 \times 10^{-3}$	4.71×10^{-2}	4.70×10^{-2}	$+3.19 \times 10^{-6}$	3.10×10^{-4}	$+9.21 \times 10^{-3}$	1.0×10^{-2}	7.4×10^{-3}
152	160	2.16×10^{-3}	6.34×10^{-1}	1.56×10^{2}	7.72×10^{-1}	$+5.32 \times 10^{-3}$	2.43×10^{-1}	2.43×10^{-1}	$+3.82 \times 10^{-5}$	1.04×10^{-3}	$+4.25 \times 10^{-3}$	1.4×10^{-2}	6.8×10^{-3}
152	160	2.88×10^{-4}	8.41×10^{-2}	1.56×10^{2}	7.71×10^{-1}	$+1.18 \times 10^{-2}$	8.43×10^{-2}	8.41×10^{-2}	$+6.18 \times 10^{-6}$	3.30×10^{-4}	$+1.15 \times 10^{-2}$	1.1×10^{-2}	1.1×10^{-2}
152	160	5.27×10^{-4}	1.54×10^{-1}	1.56×10^{2}	7.71×10^{-1}	-6.30×10^{-3}	1.34×10^{-1}	1.33×10^{-1}	$+1.11 \times 10^{-5}$	4.00×10^{-4}	-6.71×10^{-3}	1.2×10^{-2}	1.3×10^{-2}
160	168	1.08×10^{-3}	3.33×10^{-1}	1.64×10^{2}	8.10×10^{-1}	-6.49×10^{-3}	1.67×10^{-1}	1.68×10^{-1}	$+2.16 \times 10^{-5}$	6.70×10^{-4}	-7.18×10^{-3}	1.4×10^{-2}	2.8×10^{-2}
160	168	1.77×10^{-4}	5.43×10^{-2}	1.64×10^{2}	8.01×10^{-1}	$+6.95 \times 10^{-3}$	5.83×10^{-2}	5.82×10^{-2}	$+3.84 \times 10^{-6}$	3.10×10^{-4}	$+6.64 \times 10^{-3}$	1.1×10^{-2}	3.3×10^{-1}
160	168	2.16×10^{-3}	6.66×10^{-1}	1.64×10^{2}	8.10×10^{-1}	-1.61×10^{-2}	2.51×10^{-1}	2.50×10^{-1}	$+3.82 \times 10^{-5}$	1.05×10^{-3}	-1.72×10^{-2}	1.5×10^{-2}	7.0×10^{-2}
160	168	3.33×10^{-4}	1.02×10^{-1}	1.64×10^{2}	8.09×10^{-1}	$+1.76 \times 10^{-2}$	9.88×10^{-2}	9.86×10^{-2}	$+7.12 \times 10^{-6}$	3.40×10^{-4}	$+1.73 \times 10^{-2}$	1.2×10^{-2}	3.4×10^{-2}
160	168	5.87×10^{-4}	1.81×10^{-1}	1.64×10^{2}	8.10×10^{-1}	$+1.59 \times 10^{-2}$	1.49×10^{-1}	1.49×10^{-1}	$+1.22 \times 10^{-5}$	4.30×10^{-4}	$+1.55 \times 10^{-2}$	1.3×10^{-2}	2.1×10^{-2}
168	176	1.20×10^{-3}	3.87×10^{-1}	1.72×10^{2}	8.46×10^{-1}	$+1.91 \times 10^{-2}$	1.87×10^{-1}	1.88×10^{-1}	$+2.37 \times 10^{-5}$	7.30×10^{-4}	$+1.83 \times 10^{-2}$	1.7×10^{-2}	1.7×10^{-2}
168	176	2.17×10^{-4}	6.97×10^{-2}	1.71×10^{2}	8.34×10^{-1}	$+2.02 \times 10^{-3}$	7.24×10^{-2}	7.23×10^{-2}	$+4.69 \times 10^{-6}$	3.20×10^{-4}	$+1.70 \times 10^{-3}$	1.4×10^{-2}	1.7×10^{-2}
168	176	2.19×10^{-3}	7.05×10^{-1}	1.72×10^{2}	8.46×10^{-1}	$+2.47 \times 10^{-2}$	2.59×10^{-1}	2.59×10^{-1}	$+3.85 \times 10^{-5}$	1.05×10^{-3}	$+2.36 \times 10^{-2}$	1.7×10^{-2}	8.7×10^{-3}
168	176	4.03×10^{-4}	1.30×10^{-1}	1.72×10^{2}	8.41×10^{-1}	-7.74×10^{-3}	1.19×10^{-1}	1.18×10^{-1}	$+8.56 \times 10^{-6}$	3.70×10^{-4}	-8.12×10^{-3}	1.4×10^{-2}	7.1×10^{-3}
168	176	6.95×10^{-4}	2.24×10^{-1}	1.72×10^{2}	8.44×10^{-1}	-1.97×10^{-4}	1.20×10^{-1}	1.71×10^{-1}	$+2.06 \times 10^{-5}$	4.80×10^{-4}	-6.98×10^{-4}	1.6×10^{-2}	1.3×10^{-2}
176	184	1.33×10^{-3}	4.47×10^{-1}	1.79×10^{2}	8.71×10^{-1}	$+2.96 \times 10^{-2}$	2.06×10^{-1}	2.07×10^{-1}	$+2.58 \times 10^{-5}$	7.70×10^{-4}	$+2.88 \times 10^{-2}$	2.4×10^{-2}	9.9×10^{-3}
176	184	2.21×10^{-3}	7.45×10^{-1}	1.79×10^{2}	8.72×10^{-1}	$+1.54 \times 10^{-2}$	2.67×10^{-1}	2.67×10^{-1}	$+3.88 \times 10^{-5}$	1.05×10^{-3}	$+1.43 \times 10^{-2}$	2.5×10^{-2}	5.7×10^{-3}
176	184	2.63×10^{-4}	8.83×10^{-2}	1.79×10^{2}	8.59×10^{-1}	$+7.44 \times 10^{-3}$	8.82×10^{-2}	8.81×10^{-2}	$+5.66 \times 10^{-6}$	3.40×10^{-4}	$+7.10 \times 10^{-3}$	2.0×10^{-2}	5.8×10^{-3}
176	184	4.95×10^{-4}	1.66×10^{-1}	1.79×10^{2}	8.66×10^{-1}	$+2.09 \times 10^{-2}$	1.42×10^{-1}	1.42×10^{-1}	$+1.04 \times 10^{-5}$	4.10×10^{-4}	$+2.05 \times 10^{-2}$	2.1×10^{-2}	6.5×10^{-3}
176	184	8.35×10^{-4}	2.81×10^{-1}	1.79×10^{2}	8.69×10^{-1}	$+6.16 \times 10^{-2}$	1.49×10^{-1}	1.96×10^{-1}	$+2.25 \times 10^{-5}$	5.60×10^{-4}	$+6.10 \times 10^{-2}$	2.3×10^{-2}	7.1×10^{-3}
184	192	1.46×10^{-3}	5.11×10^{-1}	1.87×10^{2}	8.87×10^{-1}	$+1.18 \times 10^{-1}$	2.24×10^{-1}	2.24×10^{-1}	$+2.80 \times 10^{-5}$	8.10×10^{-4}	$+1.17 \times 10^{-1}$	5.4×10^{-2}	9.4×10^{-3}
184	192	2.24×10^{-3}	7.83×10^{-1}	1.87×10^{2}	8.87×10^{-1}	-3.84×10^{-2}	2.75×10^{-1}	2.74×10^{-1}	$+3.92 \times 10^{-5}$	1.06×10^{-3}	-3.95×10^{-2}	5.6×10^{-2}	1.0×10^{-2}
184	192	3.30×10^{-4}	1.15×10^{-1}	1.86×10^{2}	8.81×10^{-1}	$+2.05 \times 10^{-2}$	1.09×10^{-1}	1.09×10^{-1}	$+7.06 \times 10^{-6}$	3.80×10^{-4}	$+2.01 \times 10^{-2}$	4.6×10^{-2}	6.6×10^{-3}
184	192	6.15×10^{-4}	2.15×10^{-1}	1.86×10^{2}	8.85×10^{-1}	$+1.09 \times 10^{-1}$	1.16×10^{-1}	1.68×10^{-1}	$+1.85 \times 10^{-5}$	4.70×10^{-4}	$+1.09 \times 10^{-1}$	5.0×10^{-2}	9.5×10^{-3}
184	192	9.88×10^{-4}	3.46×10^{-1}	1.86×10^{2}	8.86×10^{-1}	-1.56×10^{-3}	1.75×10^{-1}	1.77×10^{-1}	$+2.00 \times 10^{-5}$	6.50×10^{-4}	-2.23×10^{-3}	5.2×10^{-2}	6.6×10^{-3}
192	200	1.13×10^{-3}	4.08×10^{-1}	1.93×10^{2}	8.98×10^{-1}	$+2.50 \times 10^{-1}$	1.97×10^{-1}	1.98×10^{-1}	$+2.25 \times 10^{-5}$	7.20×10^{-4}	$+2.50 \times 10^{-1}$	7.6×10^{-1}	7.3×10^{-3}
192	200	1.61×10^{-3}	5.80×10^{-1}	1.92×10^{2}	8.98×10^{-1}	-1.20×10^{-1}	2.40×10^{-1}	2.41×10^{-1}	$+3.03 \times 10^{-5}$	8.60×10^{-4}	-1.21×10^{-1}	8.3×10^{-1}	1.2×10^{-2}
192	200	2.26×10^{-3}	8.18×10^{-1}	1.93×10^{2}	8.98×10^{-1}	-4.63×10^{-1}	2.81×10^{-1}	2.80×10^{-1}	$+3.95 \times 10^{-5}$	1.06×10^{-3}	-4.64×10^{-1}	8.2×10^{-1}	1.1×10^{-2}
192	200	4.06×10^{-4}	1.47×10^{-1}	1.92×10^{2}	8.98×10^{-1}	$+5.45 \times 10^{-1}$	1.30×10^{-1}	1.30×10^{-1}	$+8.62 \times 10^{-6}$	4.10×10^{-4}	$+5.45 \times 10^{-1}$	6.4×10^{-1}	4.5×10^{-2}
192	200	7.31×10^{-4}	2.64×10^{-1}	1.92×10^{2}	8.98×10^{-1}	-3.36×10^{-1}	1.43×10^{-1}	1.90×10^{-1}	$+2.01 \times 10^{-5}$	5.30×10^{-4}	-3.36×10^{-1}	7.4×10^{-1}	2.8×10^{-1}

Table F.14: $A_1^p(\nu, Q^2)$ from 2011 data (2/2).

$\log_{10}(x)$		$\langle x \rangle$	$\langle Q^2 \rangle$	$\langle \nu \rangle$	$\langle y \rangle$	$A_1^{p,exp}$	F_2^p	F_2^d	$\Delta A_1^{^{14}N}$	ΔA_1^{RC}	$A_1^{p\gamma}$	$\sigma_{stat}(A_1^p)$	$\sigma_{syst}(A_1^p)$
−4.4	−4.2	5.10×10^{-5}	3.65×10^{-3}	3.81×10^{1}	2.41×10^{-1}	-3.37×10^{-3}	4.37×10^{-3}	4.34×10^{-3}	$+1.12 \times 10^{-6}$	1.34×10^{-3}	-4.72×10^{-3}	9.3×10^{-3}	1.1×10^{-2}
−4.4	−4.2	5.10×10^{-5}	6.19×10^{-3}	6.46×10^{1}	4.05×10^{-1}	$+1.10 \times 10^{-2}$	7.32×10^{-3}	7.30×10^{-3}	$+1.12 \times 10^{-6}$	8.50×10^{-4}	$+1.01 \times 10^{-2}$	9.4×10^{-3}	6.7×10^{-3}
−4.4	−4.2	5.10×10^{-5}	5.11×10^{-3}	5.34×10^{1}	3.35×10^{-1}	$+2.75 \times 10^{-3}$	6.07×10^{-3}	6.04×10^{-3}	$+1.12 \times 10^{-6}$	9.90×10^{-4}	$+1.76 \times 10^{-3}$	9.3×10^{-3}	9.0×10^{-3}
−4.4	−4.2	5.11×10^{-5}	7.18×10^{-3}	7.49×10^{1}	4.68×10^{-1}	$+1.11 \times 10^{-2}$	8.48×10^{-3}	8.45×10^{-3}	$+1.12 \times 10^{-6}$	7.70×10^{-4}	$+1.03 \times 10^{-2}$	9.4×10^{-3}	6.8×10^{-3}
−4.4	−4.2	5.39×10^{-5}	8.90×10^{-3}	8.78×10^{1}	5.41×10^{-1}	$+1.99 \times 10^{-2}$	1.05×10^{-2}	1.05×10^{-2}	$+1.18 \times 10^{-6}$	7.10×10^{-4}	$+1.92 \times 10^{-2}$	9.4×10^{-3}	4.3×10^{-3}
−4.2	−4.0	8.05×10^{-5}	6.15×10^{-3}	4.07×10^{1}	2.57×10^{-1}	$+4.19 \times 10^{-3}$	7.30×10^{-3}	7.26×10^{-3}	$+1.76 \times 10^{-6}$	1.04×10^{-3}	$+3.15 \times 10^{-3}$	7.5×10^{-3}	6.4×10^{-3}
−4.2	−4.0	8.05×10^{-5}	8.86×10^{-3}	5.86×10^{1}	3.68×10^{-1}	$+1.63 \times 10^{-2}$	1.04×10^{-2}	1.04×10^{-2}	$+1.76 \times 10^{-6}$	7.40×10^{-4}	$+1.56 \times 10^{-2}$	7.5×10^{-3}	7.5×10^{-3}
−4.2	−4.0	8.06×10^{-5}	1.09×10^{-2}	7.20×10^{1}	4.51×10^{-1}	$+1.51 \times 10^{-2}$	1.27×10^{-2}	1.27×10^{-2}	$+1.76 \times 10^{-6}$	6.20×10^{-4}	$+1.44 \times 10^{-2}$	7.6×10^{-3}	8.7×10^{-3}
−4.2	−4.0	8.07×10^{-5}	1.29×10^{-2}	8.54×10^{1}	5.34×10^{-1}	$+6.30 \times 10^{-3}$	1.51×10^{-2}	1.50×10^{-2}	$+1.77 \times 10^{-6}$	5.40×10^{-4}	$+5.76 \times 10^{-3}$	7.6×10^{-3}	6.4×10^{-3}
−4.2	−4.0	8.35×10^{-5}	1.60×10^{-2}	1.02×10^{2}	6.33×10^{-1}	-6.47×10^{-4}	1.86×10^{-2}	1.86×10^{-2}	$+1.83 \times 10^{-6}$	4.80×10^{-4}	-1.13×10^{-3}	7.3×10^{-3}	7.5×10^{-3}
−4.0	−3.8	1.27×10^{-4}	1.02×10^{-2}	4.29×10^{1}	2.70×10^{-1}	$+1.16 \times 10^{-2}$	1.20×10^{-2}	1.19×10^{-2}	$+2.76 \times 10^{-6}$	8.20×10^{-4}	$+1.07 \times 10^{-2}$	6.6×10^{-3}	1.4×10^{-2}
−4.0	−3.8	1.27×10^{-4}	1.51×10^{-2}	6.31×10^{1}	3.96×10^{-1}	$+1.13 \times 10^{-2}$	1.74×10^{-2}	1.74×10^{-2}	$+2.77 \times 10^{-6}$	5.70×10^{-4}	$+1.07 \times 10^{-2}$	6.6×10^{-3}	1.5×10^{-2}
−4.0	−3.8	1.27×10^{-4}	1.88×10^{-2}	7.87×10^{1}	4.92×10^{-1}	$+9.94 \times 10^{-3}$	2.16×10^{-2}	2.15×10^{-2}	$+2.77 \times 10^{-6}$	4.70×10^{-4}	$+9.47 \times 10^{-3}$	6.6×10^{-3}	2.5×10^{-2}
−4.0	−3.8	1.27×10^{-4}	2.28×10^{-2}	9.55×10^{1}	5.99×10^{-1}	$+5.72 \times 10^{-3}$	2.60×10^{-2}	2.59×10^{-2}	$+2.78 \times 10^{-6}$	4.10×10^{-4}	$+5.31 \times 10^{-3}$	6.6×10^{-3}	6.2×10^{-2}
−4.0	−3.8	1.30×10^{-4}	2.79×10^{-2}	1.14×10^{2}	7.07×10^{-1}	$+1.26 \times 10^{-2}$	3.16×10^{-2}	3.15×10^{-2}	$+2.84 \times 10^{-6}$	3.80×10^{-4}	$+1.22 \times 10^{-2}$	6.5×10^{-3}	1.6×10^{-1}
−3.8	−3.6	2.01×10^{-4}	1.67×10^{-2}	4.44×10^{1}	2.80×10^{-1}	$+1.35 \times 10^{-2}$	1.93×10^{-2}	1.92×10^{-2}	$+4.34 \times 10^{-6}$	6.50×10^{-4}	$+1.28 \times 10^{-2}$	6.2×10^{-3}	6.4×10^{-3}
−3.8	−3.6	2.01×10^{-4}	3.87×10^{-2}	1.03×10^{2}	6.44×10^{-1}	$+9.87 \times 10^{-3}$	4.25×10^{-2}	4.23×10^{-2}	$+4.35 \times 10^{-6}$	3.60×10^{-4}	$+9.51 \times 10^{-3}$	6.2×10^{-3}	9.7×10^{-3}
−3.8	−3.6	2.01×10^{-4}	2.50×10^{-2}	6.61×10^{1}	4.15×10^{-1}	$+7.17 \times 10^{-3}$	2.82×10^{-2}	2.80×10^{-2}	$+4.35 \times 10^{-6}$	4.70×10^{-4}	$+6.70 \times 10^{-3}$	6.2×10^{-3}	5.9×10^{-3}
−3.8	−3.6	2.01×10^{-4}	3.16×10^{-2}	8.37×10^{1}	5.24×10^{-1}	$+4.28 \times 10^{-3}$	3.51×10^{-2}	3.50×10^{-2}	$+4.35 \times 10^{-6}$	4.00×10^{-4}	$+3.87 \times 10^{-3}$	6.2×10^{-3}	4.4×10^{-3}
−3.8	−3.6	2.04×10^{-4}	4.73×10^{-2}	1.23×10^{2}	7.64×10^{-1}	$+8.14 \times 10^{-3}$	5.11×10^{-2}	5.09×10^{-2}	$+4.42 \times 10^{-6}$	3.40×10^{-4}	$+7.80 \times 10^{-3}$	6.2×10^{-3}	8.3×10^{-3}
−3.6	−3.4	3.18×10^{-4}	4.02×10^{-2}	6.74×10^{1}	4.23×10^{-1}	$+1.05 \times 10^{-2}$	4.37×10^{-2}	4.35×10^{-2}	$+6.80 \times 10^{-6}$	4.20×10^{-4}	$+1.00 \times 10^{-2}$	6.3×10^{-3}	4.7×10^{-3}
−3.6	−3.4	3.18×10^{-4}	2.68×10^{-2}	4.49×10^{1}	2.83×10^{-1}	$+2.43 \times 10^{-3}$	3.01×10^{-2}	3.00×10^{-2}	$+6.79 \times 10^{-6}$	5.50×10^{-4}	$+1.87 \times 10^{-3}$	6.2×10^{-3}	4.1×10^{-3}
−3.6	−3.4	3.18×10^{-4}	6.34×10^{-2}	1.06×10^{2}	6.66×10^{-1}	$+1.51 \times 10^{-2}$	6.57×10^{-2}	6.55×10^{-2}	$+6.81 \times 10^{-6}$	3.60×10^{-4}	$+1.48 \times 10^{-2}$	6.1×10^{-3}	4.4×10^{-3}
−3.6	−3.4	3.19×10^{-4}	5.14×10^{-2}	8.61×10^{1}	5.39×10^{-1}	$+4.63 \times 10^{-3}$	5.46×10^{-2}	5.44×10^{-2}	$+6.81 \times 10^{-6}$	3.80×10^{-4}	$+4.25 \times 10^{-3}$	6.2×10^{-3}	6.1×10^{-3}
−3.6	−3.4	3.19×10^{-4}	7.62×10^{-2}	1.27×10^{2}	7.90×10^{-1}	-1.99×10^{-4}	7.72×10^{-2}	7.70×10^{-2}	$+6.84 \times 10^{-6}$	3.60×10^{-4}	-5.66×10^{-4}	6.2×10^{-3}	7.8×10^{-3}
−3.4	−3.2	5.03×10^{-4}	4.25×10^{-2}	4.50×10^{1}	2.84×10^{-1}	$+1.46 \times 10^{-2}$	4.59×10^{-2}	4.57×10^{-2}	$+1.05 \times 10^{-5}$	4.80×10^{-4}	$+1.41 \times 10^{-2}$	6.5×10^{-3}	1.2×10^{-2}
−3.4	−3.2	5.03×10^{-4}	1.01×10^{-1}	1.07×10^{2}	6.71×10^{-1}	$+7.09 \times 10^{-3}$	9.62×10^{-2}	9.59×10^{-2}	$+1.06 \times 10^{-5}$	4.00×10^{-4}	$+6.68 \times 10^{-3}$	6.3×10^{-3}	2.3×10^{-2}
−3.4	−3.2	5.03×10^{-4}	8.19×10^{-2}	8.67×10^{1}	5.43×10^{-1}	$+1.11 \times 10^{-2}$	8.10×10^{-2}	8.07×10^{-2}	$+1.06 \times 10^{-5}$	4.00×10^{-4}	$+1.07 \times 10^{-2}$	6.5×10^{-3}	3.6×10^{-2}
−3.4	−3.2	5.04×10^{-4}	6.45×10^{-2}	6.82×10^{1}	4.28×10^{-1}	$+1.76 \times 10^{-2}$	6.62×10^{-2}	6.59×10^{-2}	$+1.06 \times 10^{-5}$	4.10×10^{-4}	$+1.72 \times 10^{-2}$	6.6×10^{-3}	4.1×10^{-2}
−3.4	−3.2	5.04×10^{-4}	1.21×10^{-1}	1.28×10^{2}	7.96×10^{-1}	$+1.83 \times 10^{-2}$	1.11×10^{-1}	1.11×10^{-1}	$+1.06 \times 10^{-5}$	4.00×10^{-4}	$+1.79 \times 10^{-2}$	6.5×10^{-3}	1.4×10^{-1}
−3.2	−3.0	7.93×10^{-4}	1.91×10^{-1}	1.29×10^{2}	7.99×10^{-1}	$+1.18 \times 10^{-2}$	1.53×10^{-1}	1.53×10^{-1}	$+1.62 \times 10^{-5}$	4.90×10^{-4}	$+1.13 \times 10^{-2}$	7.0×10^{-3}	5.8×10^{-3}
−3.2	−3.0	7.93×10^{-4}	1.59×10^{-1}	1.07×10^{2}	6.71×10^{-1}	$+2.42 \times 10^{-2}$	1.35×10^{-1}	1.34×10^{-1}	$+1.62 \times 10^{-5}$	4.80×10^{-4}	$+2.37 \times 10^{-2}$	7.0×10^{-3}	6.9×10^{-3}
−3.2	−3.0	7.94×10^{-4}	1.02×10^{-1}	6.83×10^{1}	4.29×10^{-1}	$+1.16 \times 10^{-2}$	9.62×10^{-2}	9.58×10^{-2}	$+1.62 \times 10^{-5}$	4.50×10^{-4}	$+1.11 \times 10^{-2}$	7.1×10^{-3}	4.5×10^{-3}
−3.2	−3.0	7.96×10^{-4}	6.64×10^{-2}	4.45×10^{1}	2.81×10^{-1}	$+2.45 \times 10^{-2}$	6.79×10^{-2}	6.76×10^{-2}	$+1.62 \times 10^{-5}$	4.60×10^{-4}	$+2.41 \times 10^{-2}$	7.1×10^{-3}	3.8×10^{-3}
−3.2	−3.0	7.96×10^{-4}	1.30×10^{-1}	8.69×10^{1}	5.45×10^{-1}	$+1.64 \times 10^{-2}$	1.16×10^{-1}	1.15×10^{-1}	$+1.62 \times 10^{-5}$	4.60×10^{-4}	$+1.59 \times 10^{-2}$	7.1×10^{-3}	3.4×10^{-3}

Table F.15: $A_1^p(x, \nu)$ from 2007 data (1/2).

$\log_{10}(x)$		$\langle x \rangle$	$\langle Q^2 \rangle$	$\langle \nu \rangle$	$\langle y \rangle$	$A_1^{p,exp}$	F_2^p	F_2^d	$\Delta A_1^{^{14}N}$	ΔA_1^{RC}	$A_1^{p\gamma}$	$\sigma_{stat}(A_1^p)$	$\sigma_{syst}(A_1^p)$
−3.0	−2.8	1.25×10^{-3}	1.61×10^{-1}	6.84×10^{1}	4.30×10^{-1}	$+6.89 \times 10^{-3}$	1.35×10^{-1}	1.34×10^{-1}	$+2.44 \times 10^{-5}$	5.40×10^{-4}	$+6.33 \times 10^{-3}$	8.0×10^{-3}	3.8×10^{-3}
−3.0	−2.8	1.26×10^{-3}	1.02×10^{-1}	4.34×10^{1}	2.73×10^{-1}	$+1.07 \times 10^{-2}$	9.66×10^{-2}	9.60×10^{-2}	$+2.44 \times 10^{-5}$	4.80×10^{-4}	$+1.02 \times 10^{-2}$	7.9×10^{-3}	6.0×10^{-3}
−3.0	−2.8	1.26×10^{-3}	2.06×10^{-1}	8.70×10^{1}	5.46×10^{-1}	$+8.01 \times 10^{-3}$	9.78×10^{-2}	9.75×10^{-2}	$+2.45 \times 10^{-5}$	5.80×10^{-4}	$+7.40 \times 10^{-3}$	7.9×10^{-3}	6.7×10^{-3}
−3.0	−2.8	1.26×10^{-3}	3.05×10^{-1}	1.29×10^{2}	8.02×10^{-1}	$+2.66 \times 10^{-2}$	1.50×10^{-1}	1.50×10^{-1}	$+2.46 \times 10^{-5}$	6.90×10^{-4}	$+2.59 \times 10^{-2}$	7.7×10^{-3}	4.2×10^{-3}
−3.0	−2.8	1.26×10^{-3}	2.52×10^{-1}	1.07×10^{2}	6.69×10^{-1}	$+1.32 \times 10^{-2}$	1.24×10^{-1}	1.24×10^{-1}	$+2.46 \times 10^{-5}$	6.30×10^{-4}	$+1.26 \times 10^{-2}$	7.7×10^{-3}	7.4×10^{-3}
−2.8	−2.6	1.98×10^{-3}	2.57×10^{-1}	6.91×10^{1}	4.34×10^{-1}	$+2.32 \times 10^{-2}$	1.20×10^{-1}	1.19×10^{-1}	$+3.55 \times 10^{-5}$	7.10×10^{-4}	$+2.25 \times 10^{-2}$	9.2×10^{-3}	1.6×10^{-2}
−2.8	−2.6	1.99×10^{-3}	3.32×10^{-1}	8.89×10^{1}	5.58×10^{-1}	$+9.27 \times 10^{-3}$	1.53×10^{-1}	1.52×10^{-1}	$+3.57 \times 10^{-5}$	8.60×10^{-4}	$+8.37 \times 10^{-3}$	8.9×10^{-3}	1.3×10^{-2}
−2.8	−2.6	1.99×10^{-3}	4.84×10^{-1}	1.29×10^{2}	8.05×10^{-1}	$+1.20 \times 10^{-2}$	2.06×10^{-1}	2.05×10^{-1}	$+3.58 \times 10^{-5}$	9.60×10^{-4}	$+1.10 \times 10^{-2}$	8.9×10^{-3}	4.9×10^{-2}
−2.8	−2.6	1.99×10^{-3}	1.57×10^{-1}	4.21×10^{1}	2.65×10^{-1}	$+9.17 \times 10^{-3}$	1.33×10^{-1}	1.32×10^{-1}	$+3.57 \times 10^{-5}$	5.50×10^{-4}	$+8.59 \times 10^{-3}$	9.1×10^{-3}	4.0×10^{-2}
−2.8	−2.6	1.99×10^{-3}	4.04×10^{-1}	1.08×10^{2}	6.78×10^{-1}	$+1.49 \times 10^{-2}$	1.80×10^{-1}	1.79×10^{-1}	$+3.58 \times 10^{-5}$	9.50×10^{-4}	$+1.40 \times 10^{-2}$	9.0×10^{-3}	2.4×10^{-1}
−2.6	−2.4	3.14×10^{-3}	7.60×10^{-1}	1.29×10^{2}	8.04×10^{-1}	$+1.51 \times 10^{-2}$	2.59×10^{-1}	2.57×10^{-1}	$+4.93 \times 10^{-5}$	1.32×10^{-3}	$+1.37 \times 10^{-2}$	1.1×10^{-2}	6.3×10^{-3}
−2.6	−2.4	3.14×10^{-3}	4.08×10^{-1}	6.92×10^{1}	4.35×10^{-1}	$+3.53 \times 10^{-2}$	1.73×10^{-1}	1.71×10^{-1}	$+4.93 \times 10^{-5}$	1.09×10^{-3}	$+3.41 \times 10^{-2}$	1.1×10^{-2}	7.0×10^{-3}
−2.6	−2.4	3.14×10^{-3}	5.30×10^{-1}	8.99×10^{1}	5.65×10^{-1}	$+1.23 \times 10^{-2}$	2.08×10^{-1}	2.06×10^{-1}	$+4.93 \times 10^{-5}$	1.20×10^{-3}	$+1.11 \times 10^{-2}$	1.1×10^{-2}	4.1×10^{-3}
−2.6	−2.4	3.15×10^{-3}	2.42×10^{-1}	4.09×10^{1}	2.57×10^{-1}	$+1.17 \times 10^{-2}$	1.10×10^{-1}	1.08×10^{-1}	$+4.92 \times 10^{-5}$	7.10×10^{-4}	$+1.10 \times 10^{-2}$	1.1×10^{-2}	5.7×10^{-3}
−2.6	−2.4	3.15×10^{-3}	6.41×10^{-1}	1.08×10^{2}	6.79×10^{-1}	$+7.64 \times 10^{-3}$	2.34×10^{-1}	2.32×10^{-1}	$+4.95 \times 10^{-5}$	1.29×10^{-3}	$+6.30 \times 10^{-3}$	1.0×10^{-2}	7.0×10^{-3}
−2.4	−2.2	4.42×10^{-3}	9.00×10^{-1}	1.09×10^{2}	6.83×10^{-1}	$+1.05 \times 10^{-2}$	2.74×10^{-1}	2.70×10^{-1}	$+5.95 \times 10^{-5}$	1.68×10^{-3}	$+8.78 \times 10^{-3}$	1.5×10^{-2}	3.4×10^{-3}
−2.4	−2.2	4.86×10^{-3}	8.10×10^{-1}	8.89×10^{1}	5.59×10^{-1}	$+3.00 \times 10^{-2}$	2.58×10^{-1}	2.54×10^{-1}	$+6.19 \times 10^{-5}$	1.68×10^{-3}	$+2.82 \times 10^{-2}$	1.5×10^{-2}	6.2×10^{-3}
−2.4	−2.2	5.01×10^{-3}	6.88×10^{-1}	7.33×10^{1}	4.61×10^{-1}	$+2.43 \times 10^{-2}$	2.36×10^{-1}	2.32×10^{-1}	$+6.26 \times 10^{-5}$	1.58×10^{-3}	$+2.26 \times 10^{-2}$	1.5×10^{-2}	6.7×10^{-3}
−2.4	−2.2	5.01×10^{-3}	3.23×10^{-1}	3.44×10^{1}	2.16×10^{-1}	$+3.82 \times 10^{-2}$	1.43×10^{-1}	1.41×10^{-1}	$+6.25 \times 10^{-5}$	9.60×10^{-4}	$+3.71 \times 10^{-2}$	1.5×10^{-2}	4.7×10^{-3}
−2.4	−2.2	5.01×10^{-3}	5.27×10^{-1}	5.61×10^{1}	3.52×10^{-1}	-9.40×10^{-4}	2.02×10^{-1}	1.99×10^{-1}	$+6.26 \times 10^{-5}$	1.38×10^{-3}	-2.38×10^{-3}	1.5×10^{-2}	5.8×10^{-3}
−2.2	−2.0	6.97×10^{-3}	9.09×10^{-1}	6.98×10^{1}	4.38×10^{-1}	$+6.76 \times 10^{-2}$	2.68×10^{-1}	2.63×10^{-1}	$+6.72 \times 10^{-5}$	2.02×10^{-3}	$+6.56 \times 10^{-2}$	2.5×10^{-2}	1.1×10^{-2}
−2.2	−2.0	7.69×10^{-3}	8.29×10^{-1}	5.74×10^{1}	3.60×10^{-1}	$+4.06 \times 10^{-2}$	2.56×10^{-1}	2.51×10^{-1}	$+6.70 \times 10^{-5}$	1.99×10^{-3}	$+3.85 \times 10^{-2}$	2.5×10^{-2}	1.4×10^{-2}
−2.2	−2.0	7.99×10^{-3}	3.99×10^{-1}	2.66×10^{1}	1.68×10^{-1}	$+4.75 \times 10^{-2}$	1.72×10^{-1}	1.68×10^{-1}	$+6.67 \times 10^{-5}$	1.22×10^{-3}	$+4.62 \times 10^{-2}$	2.5×10^{-2}	4.5×10^{-2}
−2.2	−2.0	8.00×10^{-3}	7.30×10^{-1}	4.86×10^{1}	3.05×10^{-1}	$+2.19 \times 10^{-2}$	2.41×10^{-1}	2.36×10^{-1}	$+6.67 \times 10^{-5}$	1.87×10^{-3}	$+2.00 \times 10^{-2}$	2.4×10^{-2}	4.5×10^{-2}
−2.2	−2.0	8.00×10^{-3}	5.88×10^{-1}	3.92×10^{1}	2.46×10^{-1}	$+7.14 \times 10^{-2}$	2.16×10^{-1}	2.12×10^{-1}	$+6.67 \times 10^{-5}$	1.64×10^{-3}	$+6.97 \times 10^{-2}$	2.5×10^{-2}	3.3×10^{-1}
−2.0	−1.8	1.09×10^{-2}	9.18×10^{-1}	4.49×10^{1}	2.82×10^{-1}	-2.91×10^{-3}	2.68×10^{-1}	2.62×10^{-1}	$+5.65 \times 10^{-5}$	2.31×10^{-3}	-5.28×10^{-3}	4.1×10^{-2}	9.2×10^{-3}
−2.0	−1.8	1.19×10^{-2}	8.43×10^{-1}	3.77×10^{1}	2.37×10^{-1}	-2.29×10^{-2}	2.60×10^{-1}	2.53×10^{-1}	$+5.07 \times 10^{-5}$	2.24×10^{-3}	-2.52×10^{-2}	4.1×10^{-2}	7.4×10^{-3}
−2.0	−1.8	1.26×10^{-2}	7.76×10^{-1}	3.28×10^{1}	2.06×10^{-1}	$+1.10 \times 10^{-1}$	2.51×10^{-1}	2.45×10^{-1}	$+4.62 \times 10^{-5}$	2.14×10^{-3}	$+1.08 \times 10^{-1}$	4.2×10^{-2}	4.1×10^{-3}
−2.0	−1.8	1.27×10^{-2}	6.64×10^{-1}	2.79×10^{1}	1.75×10^{-1}	$+5.46 \times 10^{-2}$	2.35×10^{-1}	2.29×10^{-1}	$+4.57 \times 10^{-5}$	1.91×10^{-3}	$+5.27 \times 10^{-2}$	4.2×10^{-2}	3.9×10^{-3}
−2.0	−1.8	1.27×10^{-2}	5.06×10^{-1}	2.12×10^{1}	1.34×10^{-1}	$+7.65 \times 10^{-2}$	2.06×10^{-1}	2.01×10^{-1}	$+4.53 \times 10^{-5}$	1.49×10^{-3}	$+7.50 \times 10^{-2}$	4.2×10^{-2}	6.3×10^{-3}
−1.8	−1.6	1.70×10^{-2}	9.33×10^{-1}	2.93×10^{1}	1.84×10^{-1}	-7.06×10^{-2}	2.74×10^{-1}	2.66×10^{-1}	$+9.54 \times 10^{-6}$	2.52×10^{-3}	-7.32×10^{-2}	8.0×10^{-2}	3.9×10^{-3}
−1.8	−1.6	1.82×10^{-2}	8.72×10^{-1}	2.55×10^{1}	1.60×10^{-1}	-3.84×10^{-2}	2.69×10^{-1}	2.61×10^{-1}	-2.38×10^{-6}	2.41×10^{-3}	-4.08×10^{-2}	8.1×10^{-2}	4.4×10^{-3}
−1.8	−1.6	1.93×10^{-2}	8.28×10^{-1}	2.29×10^{1}	1.44×10^{-1}	$+1.02 \times 10^{-1}$	2.65×10^{-1}	2.57×10^{-1}	-1.31×10^{-5}	2.32×10^{-3}	$+1.00 \times 10^{-1}$	8.0×10^{-2}	5.9×10^{-3}
−1.8	−1.6	2.01×10^{-2}	7.70×10^{-1}	2.04×10^{1}	1.29×10^{-1}	$+5.62 \times 10^{-2}$	2.59×10^{-1}	2.51×10^{-1}	-2.14×10^{-5}	2.17×10^{-3}	$+5.41 \times 10^{-2}$	7.7×10^{-2}	6.2×10^{-3}
−1.8	−1.6	2.02×10^{-2}	6.65×10^{-1}	1.76×10^{1}	1.11×10^{-1}	$+1.45 \times 10^{-1}$	2.45×10^{-1}	2.38×10^{-1}	-2.24×10^{-5}	1.88×10^{-3}	$+1.43 \times 10^{-1}$	7.9×10^{-2}	5.1×10^{-3}
−1.6	−1.4	2.61×10^{-2}	9.63×10^{-1}	1.97×10^{1}	1.24×10^{-1}	$+2.86 \times 10^{-1}$	2.84×10^{-1}	2.75×10^{-1}	-8.82×10^{-5}	2.61×10^{-3}	$+2.84 \times 10^{-1}$	2.4×10^{-1}	1.0×10^{-2}
−1.6	−1.4	2.70×10^{-2}	9.33×10^{-1}	1.84×10^{1}	1.16×10^{-1}	-8.53×10^{-2}	2.82×10^{-1}	2.72×10^{-1}	-9.84×10^{-5}	2.53×10^{-3}	-8.77×10^{-2}	2.6×10^{-1}	1.5×10^{-2}
−1.6	−1.4	2.76×10^{-2}	9.12×10^{-1}	1.76×10^{1}	1.11×10^{-1}	-4.79×10^{-2}	2.81×10^{-1}	2.71×10^{-1}	-1.06×10^{-4}	2.47×10^{-3}	-5.03×10^{-2}	2.4×10^{-1}	2.3×10^{-2}
−1.6	−1.4	2.82×10^{-2}	8.93×10^{-1}	1.69×10^{1}	1.06×10^{-1}	$+9.39 \times 10^{-2}$	2.79×10^{-1}	2.70×10^{-1}	-1.13×10^{-4}	2.41×10^{-3}	$+9.16 \times 10^{-2}$	2.5×10^{-1}	6.7×10^{-2}
−1.6	−1.4	2.90×10^{-2}	8.70×10^{-1}	1.60×10^{1}	1.03×10^{-1}	-8.44×10^{-2}	2.78×10^{-1}	2.68×10^{-1}	-1.22×10^{-4}	2.39×10^{-3}	-8.66×10^{-2}	2.4×10^{-1}	1.4×10^{-1}

Table F.16: $A_1^p(x, \nu)$ from 2007 data (2/2).

$\log_{10}(x)$		$\langle x \rangle$	$\langle Q^2 \rangle$	$\langle \nu \rangle$	$\langle y \rangle$	$A_1^{p,exp}$	F_2^p	F_2^d	$\Delta A_1^{^{14}N}$	ΔA_1^{RC}	$A_1^{p\gamma}$	$\sigma_{stat}(A_1^p)$	$\sigma_{syst}(A_1^p)$
−4.4	−4.2	5.09×10^{-5}	5.98×10^{-3}	6.26×10^{1}	3.12×10^{-1}	$+1.17 \times 10^{-3}$	7.07×10^{-3}	7.05×10^{-3}	$+1.12 \times 10^{-6}$	8.60×10^{-4}	$+3.14 \times 10^{-4}$	9.7×10^{-3}	1.1×10^{-2}
−4.4	−4.2	5.09×10^{-5}	7.66×10^{-3}	8.02×10^{1}	3.97×10^{-1}	-4.40×10^{-3}	9.05×10^{-3}	9.02×10^{-3}	$+1.12 \times 10^{-6}$	6.90×10^{-4}	-5.09×10^{-3}	9.8×10^{-3}	4.3×10^{-3}
−4.4	−4.2	5.09×10^{-5}	8.95×10^{-3}	9.37×10^{1}	4.63×10^{-1}	$+9.50 \times 10^{-3}$	1.06×10^{-2}	1.05×10^{-2}	$+1.12 \times 10^{-6}$	6.10×10^{-4}	$+8.89 \times 10^{-3}$	9.9×10^{-3}	4.0×10^{-3}
−4.4	−4.2	5.09×10^{-5}	1.02×10^{-2}	1.06×10^{2}	5.27×10^{-1}	$+1.27 \times 10^{-2}$	1.20×10^{-2}	1.20×10^{-2}	$+1.12 \times 10^{-6}$	5.60×10^{-4}	$+1.21 \times 10^{-2}$	9.6×10^{-3}	6.2×10^{-3}
−4.4	−4.2	5.35×10^{-5}	1.23×10^{-2}	1.22×10^{2}	5.97×10^{-1}	$+1.94 \times 10^{-2}$	1.45×10^{-2}	1.44×10^{-2}	$+1.17 \times 10^{-6}$	5.10×10^{-4}	$+1.89 \times 10^{-2}$	9.4×10^{-3}	5.6×10^{-3}
−4.2	−4.0	8.03×10^{-5}	9.85×10^{-3}	6.54×10^{1}	3.25×10^{-1}	$+8.21 \times 10^{-3}$	1.15×10^{-2}	1.15×10^{-2}	$+1.76 \times 10^{-6}$	6.80×10^{-4}	$+7.53 \times 10^{-3}$	8.1×10^{-3}	6.1×10^{-3}
−4.2	−4.0	8.04×10^{-5}	1.30×10^{-2}	8.63×10^{1}	4.27×10^{-1}	$+4.97 \times 10^{-3}$	1.52×10^{-2}	1.51×10^{-2}	$+1.76 \times 10^{-6}$	5.30×10^{-4}	$+4.44 \times 10^{-3}$	8.1×10^{-3}	5.5×10^{-3}
−4.2	−4.0	8.05×10^{-5}	1.56×10^{-2}	1.04×10^{2}	5.12×10^{-1}	$+6.64 \times 10^{-3}$	1.82×10^{-2}	1.81×10^{-2}	$+1.76 \times 10^{-6}$	4.50×10^{-4}	$+6.19 \times 10^{-3}$	7.8×10^{-3}	5.9×10^{-3}
−4.2	−4.0	8.05×10^{-5}	1.81×10^{-2}	1.20×10^{2}	5.92×10^{-1}	$+1.80 \times 10^{-3}$	2.10×10^{-2}	2.09×10^{-2}	$+1.76 \times 10^{-6}$	4.00×10^{-4}	$+1.40 \times 10^{-3}$	8.3×10^{-3}	5.9×10^{-3}
−4.2	−4.0	8.33×10^{-5}	2.18×10^{-2}	1.39×10^{2}	6.82×10^{-1}	$+6.73 \times 10^{-3}$	2.51×10^{-2}	2.51×10^{-2}	$+1.82 \times 10^{-6}$	3.70×10^{-4}	$+6.36 \times 10^{-3}$	8.0×10^{-3}	1.1×10^{-2}
−4.0	−3.8	1.27×10^{-4}	1.61×10^{-2}	6.75×10^{1}	3.36×10^{-1}	$+6.95 \times 10^{-3}$	1.85×10^{-2}	1.85×10^{-2}	$+2.76 \times 10^{-6}$	5.50×10^{-4}	$+6.40 \times 10^{-3}$	7.3×10^{-3}	1.5×10^{-2}
−4.0	−3.8	1.27×10^{-4}	2.18×10^{-2}	9.12×10^{1}	4.52×10^{-1}	-1.27×10^{-3}	2.48×10^{-2}	2.48×10^{-2}	$+2.77 \times 10^{-6}$	4.20×10^{-4}	-1.69×10^{-3}	7.2×10^{-3}	2.9×10^{-2}
−4.0	−3.8	1.27×10^{-4}	2.64×10^{-2}	1.10×10^{2}	5.46×10^{-1}	$+8.92 \times 10^{-3}$	2.99×10^{-2}	2.98×10^{-2}	$+2.77 \times 10^{-6}$	3.70×10^{-4}	$+8.55 \times 10^{-3}$	7.2×10^{-3}	5.3×10^{-2}
−4.0	−3.8	1.27×10^{-4}	3.10×10^{-2}	1.30×10^{2}	6.42×10^{-1}	$+7.69 \times 10^{-3}$	3.49×10^{-2}	3.48×10^{-2}	$+2.77 \times 10^{-6}$	3.30×10^{-4}	$+7.35 \times 10^{-3}$	7.4×10^{-3}	1.2×10^{-1}
−4.0	−3.8	1.30×10^{-4}	3.71×10^{-2}	1.52×10^{2}	7.47×10^{-1}	$+8.43 \times 10^{-3}$	4.14×10^{-2}	4.13×10^{-2}	$+2.83 \times 10^{-6}$	3.20×10^{-4}	$+8.11 \times 10^{-3}$	7.3×10^{-3}	8.9×10^{-1}
−3.8	−3.6	2.01×10^{-4}	2.58×10^{-2}	6.86×10^{1}	3.41×10^{-1}	$+2.55 \times 10^{-3}$	2.91×10^{-2}	2.90×10^{-2}	$+4.34 \times 10^{-6}$	4.60×10^{-4}	$+2.09 \times 10^{-3}$	7.1×10^{-3}	4.7×10^{-3}
−3.8	−3.6	2.01×10^{-4}	5.14×10^{-2}	1.36×10^{2}	6.75×10^{-1}	$+3.67 \times 10^{-3}$	5.52×10^{-2}	5.51×10^{-2}	$+4.35 \times 10^{-6}$	3.10×10^{-4}	$+3.36 \times 10^{-3}$	7.0×10^{-3}	5.1×10^{-3}
−3.8	−3.6	2.01×10^{-4}	3.56×10^{-2}	9.44×10^{1}	4.67×10^{-1}	$+8.33 \times 10^{-3}$	3.93×10^{-2}	3.92×10^{-2}	$+4.35 \times 10^{-6}$	3.70×10^{-4}	$+7.95 \times 10^{-3}$	6.9×10^{-3}	3.4×10^{-3}
−3.8	−3.6	2.01×10^{-4}	4.33×10^{-2}	1.15×10^{2}	5.68×10^{-1}	$+4.14 \times 10^{-3}$	4.71×10^{-2}	4.70×10^{-2}	$+4.35 \times 10^{-6}$	3.30×10^{-4}	$+3.80 \times 10^{-3}$	7.1×10^{-3}	4.6×10^{-3}
−3.8	−3.6	2.03×10^{-4}	6.14×10^{-2}	1.61×10^{2}	7.92×10^{-1}	$+3.66 \times 10^{-3}$	6.48×10^{-2}	6.47×10^{-2}	$+4.40 \times 10^{-6}$	3.10×10^{-4}	$+3.34 \times 10^{-3}$	7.2×10^{-3}	5.1×10^{-3}
−3.6	−3.4	3.17×10^{-4}	5.69×10^{-2}	9.55×10^{1}	4.73×10^{-1}	$+8.12 \times 10^{-3}$	5.97×10^{-2}	5.95×10^{-2}	$+6.79 \times 10^{-6}$	3.60×10^{-4}	$+7.76 \times 10^{-3}$	7.3×10^{-3}	7.0×10^{-3}
−3.6	−3.4	3.18×10^{-4}	4.11×10^{-2}	6.89×10^{1}	3.43×10^{-1}	$+5.64 \times 10^{-3}$	4.45×10^{-2}	4.44×10^{-2}	$+6.79 \times 10^{-6}$	4.10×10^{-4}	$+5.22 \times 10^{-3}$	7.2×10^{-3}	4.1×10^{-3}
−3.6	−3.4	3.18×10^{-4}	6.98×10^{-2}	1.17×10^{2}	5.78×10^{-1}	$+8.16 \times 10^{-3}$	7.14×10^{-2}	7.13×10^{-2}	$+6.81 \times 10^{-6}$	3.40×10^{-4}	$+7.81 \times 10^{-3}$	7.2×10^{-3}	8.6×10^{-3}
−3.6	−3.4	3.18×10^{-4}	8.33×10^{-2}	1.39×10^{2}	6.90×10^{-1}	-8.02×10^{-3}	8.32×10^{-2}	8.30×10^{-2}	$+6.82 \times 10^{-6}$	3.30×10^{-4}	-8.36×10^{-3}	7.3×10^{-3}	5.3×10^{-3}
−3.6	−3.4	3.19×10^{-4}	9.81×10^{-2}	1.64×10^{2}	8.06×10^{-1}	$+7.14 \times 10^{-3}$	9.56×10^{-2}	9.54×10^{-2}	$+6.83 \times 10^{-6}$	3.40×10^{-4}	$+6.80 \times 10^{-3}$	7.4×10^{-3}	6.9×10^{-3}
−3.4	−3.2	5.02×10^{-4}	6.44×10^{-2}	6.84×10^{1}	3.40×10^{-1}	$+1.08 \times 10^{-2}$	6.61×10^{-2}	6.58×10^{-2}	$+1.05 \times 10^{-5}$	4.00×10^{-4}	$+1.04 \times 10^{-2}$	7.7×10^{-3}	1.4×10^{-2}
−3.4	−3.2	5.02×10^{-4}	1.32×10^{-1}	1.40×10^{2}	6.92×10^{-1}	$+3.81 \times 10^{-3}$	1.19×10^{-1}	1.19×10^{-1}	$+1.06 \times 10^{-5}$	3.90×10^{-4}	$+3.41 \times 10^{-3}$	7.6×10^{-3}	2.8×10^{-2}
−3.4	−3.2	5.03×10^{-4}	1.11×10^{-1}	1.17×10^{2}	5.80×10^{-1}	$+1.85 \times 10^{-2}$	1.04×10^{-1}	1.03×10^{-1}	$+1.06 \times 10^{-5}$	3.90×10^{-4}	$+1.81 \times 10^{-2}$	7.7×10^{-3}	3.7×10^{-2}
−3.4	−3.2	5.03×10^{-4}	1.56×10^{-1}	1.65×10^{2}	8.12×10^{-1}	$+1.26 \times 10^{-2}$	1.35×10^{-1}	1.35×10^{-1}	$+1.06 \times 10^{-5}$	4.00×10^{-4}	$+1.22 \times 10^{-2}$	7.8×10^{-3}	8.9×10^{-2}
−3.4	−3.2	5.03×10^{-4}	9.10×10^{-2}	9.64×10^{1}	4.77×10^{-1}	$+3.95 \times 10^{-3}$	8.84×10^{-2}	8.81×10^{-2}	$+1.06 \times 10^{-5}$	3.90×10^{-4}	$+3.55 \times 10^{-3}$	7.7×10^{-3}	$1.0 \times 10^{+0}$
−3.2	−3.0	7.92×10^{-4}	1.74×10^{-1}	1.17×10^{2}	5.81×10^{-1}	$+1.59 \times 10^{-2}$	1.44×10^{-1}	1.43×10^{-1}	$+1.62 \times 10^{-5}$	4.70×10^{-4}	$+1.54 \times 10^{-2}$	8.6×10^{-3}	9.4×10^{-3}
−3.2	−3.0	7.92×10^{-4}	2.08×10^{-1}	1.40×10^{2}	6.92×10^{-1}	$+5.89 \times 10^{-3}$	1.07×10^{-1}	1.62×10^{-1}	$+2.46 \times 10^{-5}$	4.90×10^{-4}	$+5.37 \times 10^{-3}$	8.5×10^{-3}	4.7×10^{-3}
−3.2	−3.0	7.93×10^{-4}	1.43×10^{-1}	9.62×10^{1}	4.77×10^{-1}	$+1.07 \times 10^{-2}$	1.25×10^{-1}	1.24×10^{-1}	$+1.62 \times 10^{-5}$	4.50×10^{-4}	$+1.03 \times 10^{-2}$	8.4×10^{-3}	4.8×10^{-3}
−3.2	−3.0	7.96×10^{-4}	1.00×10^{-1}	6.74×10^{1}	3.35×10^{-1}	$+2.23 \times 10^{-2}$	9.51×10^{-2}	9.47×10^{-2}	$+1.62 \times 10^{-5}$	4.30×10^{-4}	$+2.19 \times 10^{-2}$	8.5×10^{-3}	6.3×10^{-3}
−3.2	−3.0	7.96×10^{-4}	2.47×10^{-1}	1.66×10^{2}	8.15×10^{-1}	$+2.78 \times 10^{-3}$	1.31×10^{-1}	1.81×10^{-1}	$+2.26 \times 10^{-5}$	5.10×10^{-4}	$+2.25 \times 10^{-3}$	8.6×10^{-3}	3.9×10^{-3}

Table F.17: $A_1^p(x, \nu)$ from 2011 data (1/2).

$\log_{10}(x)$		$\langle x \rangle$	$\langle Q^2 \rangle$	$\langle \nu \rangle$	$\langle y \rangle$	$A_1^{p,exp}$	F_2^p	F_2^d	$\Delta A_1^{^{14}N}$	ΔA_1^{RC}	$A_1^{p\gamma}$	$\sigma_{stat}(A_1^p)$	$\sigma_{syst}(A_1^p)$
−3.0	−2.8	1.25×10^{-3}	2.29×10^{-1}	9.75×10^{1}	4.83×10^{-1}	$+6.21 \times 10^{-3}$	1.12×10^{-1}	1.12×10^{-1}	$+2.44 \times 10^{-5}$	5.70×10^{-4}	$+5.62 \times 10^{-3}$	9.4×10^{-3}	4.5×10^{-3}
−3.0	−2.8	1.26×10^{-3}	3.37×10^{-1}	1.43×10^{2}	7.08×10^{-1}	$+9.78 \times 10^{-3}$	1.65×10^{-1}	1.65×10^{-1}	$+2.46 \times 10^{-5}$	7.20×10^{-4}	$+9.03 \times 10^{-3}$	9.3×10^{-3}	6.2×10^{-3}
−3.0	−2.8	1.26×10^{-3}	1.56×10^{-1}	6.62×10^{1}	3.29×10^{-1}	$+6.03 \times 10^{-3}$	1.32×10^{-1}	1.31×10^{-1}	$+2.44 \times 10^{-5}$	5.00×10^{-4}	$+5.51 \times 10^{-3}$	9.4×10^{-3}	8.9×10^{-3}
−3.0	−2.8	1.26×10^{-3}	3.97×10^{-1}	1.68×10^{2}	8.26×10^{-1}	$+1.47 \times 10^{-2}$	1.89×10^{-1}	1.90×10^{-1}	$+2.46 \times 10^{-5}$	7.50×10^{-4}	$+1.40 \times 10^{-2}$	9.4×10^{-3}	7.8×10^{-3}
−3.0	−2.8	1.26×10^{-3}	2.83×10^{-1}	1.20×10^{2}	5.94×10^{-1}	$+1.78 \times 10^{-2}$	1.40×10^{-1}	1.40×10^{-1}	$+2.46 \times 10^{-5}$	6.40×10^{-4}	$+1.71 \times 10^{-2}$	9.4×10^{-3}	9.7×10^{-3}
−2.8	−2.6	1.98×10^{-3}	3.64×10^{-1}	9.77×10^{1}	4.85×10^{-1}	$+8.95 \times 10^{-3}$	1.65×10^{-1}	1.64×10^{-1}	$+3.56 \times 10^{-5}$	8.60×10^{-4}	$+8.05 \times 10^{-3}$	1.1×10^{-2}	1.5×10^{-2}
−2.8	−2.6	1.99×10^{-3}	4.52×10^{-1}	1.21×10^{2}	6.00×10^{-1}	$+5.69 \times 10^{-3}$	1.96×10^{-1}	1.95×10^{-1}	$+3.57 \times 10^{-5}$	9.20×10^{-4}	$+4.74 \times 10^{-3}$	1.1×10^{-2}	1.9×10^{-2}
−2.8	−2.6	1.99×10^{-3}	6.28×10^{-1}	1.68×10^{2}	8.27×10^{-1}	$+9.61 \times 10^{-4}$	2.45×10^{-1}	2.44×10^{-1}	$+3.58 \times 10^{-5}$	9.80×10^{-4}	-5.47×10^{-5}	1.1×10^{-2}	6.9×10^{-2}
−2.8	−2.6	1.99×10^{-3}	5.36×10^{-1}	1.43×10^{2}	7.09×10^{-1}	-3.78×10^{-3}	2.21×10^{-1}	2.20×10^{-1}	$+3.58 \times 10^{-5}$	9.70×10^{-4}	-4.78×10^{-3}	1.1×10^{-2}	1.6×10^{-1}
−2.8	−2.6	1.99×10^{-3}	2.40×10^{-1}	6.42×10^{1}	3.19×10^{-1}	-9.75×10^{-3}	1.11×10^{-1}	1.10×10^{-1}	$+3.56 \times 10^{-5}$	6.30×10^{-4}	-1.04×10^{-2}	1.1×10^{-2}	$1.6 \times 10^{+0}$
−2.6	−2.4	2.89×10^{-3}	8.69×10^{-1}	1.61×10^{2}	7.93×10^{-1}	$+3.03 \times 10^{-3}$	2.81×10^{-1}	2.79×10^{-1}	$+4.68 \times 10^{-5}$	1.29×10^{-3}	$+1.69 \times 10^{-3}$	1.4×10^{-2}	5.9×10^{-3}
−2.6	−2.4	3.11×10^{-3}	7.92×10^{-1}	1.36×10^{2}	6.71×10^{-1}	$+1.84 \times 10^{-2}$	2.65×10^{-1}	2.63×10^{-1}	$+4.91 \times 10^{-5}$	1.32×10^{-3}	$+1.71 \times 10^{-2}$	1.4×10^{-2}	5.2×10^{-3}
−2.6	−2.4	3.14×10^{-3}	6.83×10^{-1}	1.16×10^{2}	5.74×10^{-1}	$+4.03 \times 10^{-2}$	2.43×10^{-1}	2.41×10^{-1}	$+4.93 \times 10^{-5}$	1.25×10^{-3}	$+3.90 \times 10^{-2}$	1.4×10^{-2}	4.8×10^{-3}
−2.6	−2.4	3.15×10^{-3}	5.45×10^{-1}	9.24×10^{1}	4.58×10^{-1}	$+2.35 \times 10^{-2}$	2.12×10^{-1}	2.10×10^{-1}	$+4.94 \times 10^{-5}$	1.14×10^{-3}	$+2.23 \times 10^{-2}$	1.3×10^{-2}	5.3×10^{-3}
−2.6	−2.4	3.16×10^{-3}	3.53×10^{-1}	5.96×10^{1}	2.96×10^{-1}	$+1.82 \times 10^{-2}$	1.55×10^{-1}	1.53×10^{-1}	$+4.94 \times 10^{-5}$	9.20×10^{-4}	$+1.73 \times 10^{-2}$	1.4×10^{-2}	4.7×10^{-3}
−2.4	−2.2	4.34×10^{-3}	9.18×10^{-1}	1.13×10^{2}	5.60×10^{-1}	$+5.46 \times 10^{-2}$	2.77×10^{-1}	2.73×10^{-1}	$+5.90 \times 10^{-5}$	1.60×10^{-3}	$+5.29 \times 10^{-2}$	2.4×10^{-2}	3.6×10^{-3}
−2.4	−2.2	4.76×10^{-3}	8.37×10^{-1}	9.39×10^{1}	4.65×10^{-1}	$+6.31 \times 10^{-2}$	2.62×10^{-1}	2.59×10^{-1}	$+6.14 \times 10^{-5}$	1.59×10^{-3}	$+6.15 \times 10^{-2}$	2.3×10^{-2}	7.8×10^{-3}
−2.4	−2.2	5.01×10^{-3}	7.54×10^{-1}	8.02×10^{1}	3.97×10^{-1}	$+4.27 \times 10^{-2}$	2.48×10^{-1}	2.44×10^{-1}	$+6.26 \times 10^{-5}$	1.54×10^{-3}	$+4.11 \times 10^{-2}$	2.3×10^{-2}	6.4×10^{-3}
−2.4	−2.2	5.02×10^{-3}	6.23×10^{-1}	6.61×10^{1}	3.28×10^{-1}	$+5.98 \times 10^{-2}$	2.23×10^{-1}	2.20×10^{-1}	$+6.26 \times 10^{-5}$	1.40×10^{-3}	$+5.83 \times 10^{-2}$	2.3×10^{-2}	5.3×10^{-3}
−2.4	−2.2	5.03×10^{-3}	4.26×10^{-1}	4.51×10^{1}	2.24×10^{-1}	$+2.65 \times 10^{-2}$	1.76×10^{-1}	1.73×10^{-1}	$+6.27 \times 10^{-5}$	1.12×10^{-3}	$+2.53 \times 10^{-2}$	2.3×10^{-2}	7.0×10^{-3}
−2.2	−2.0	6.86×10^{-3}	9.23×10^{-1}	7.19×10^{1}	3.56×10^{-1}	$+6.23 \times 10^{-2}$	2.70×10^{-1}	2.65×10^{-1}	$+6.72 \times 10^{-5}$	1.88×10^{-3}	$+6.04 \times 10^{-2}$	4.1×10^{-2}	1.5×10^{-2}
−2.2	−2.0	7.47×10^{-3}	8.54×10^{-1}	6.10×10^{1}	3.02×10^{-1}	-4.14×10^{-2}	2.60×10^{-1}	2.55×10^{-1}	$+6.72 \times 10^{-5}$	1.85×10^{-3}	-4.33×10^{-2}	4.0×10^{-2}	1.9×10^{-2}
−2.2	−2.0	7.97×10^{-3}	7.98×10^{-1}	5.34×10^{1}	2.65×10^{-1}	-1.20×10^{-2}	2.52×10^{-1}	2.46×10^{-1}	$+6.67 \times 10^{-5}$	1.82×10^{-3}	-1.39×10^{-2}	4.1×10^{-2}	9.3×10^{-2}
−2.2	−2.0	8.06×10^{-3}	6.90×10^{-1}	4.56×10^{1}	2.26×10^{-1}	$+2.26 \times 10^{-2}$	2.34×10^{-1}	2.30×10^{-1}	$+6.66 \times 10^{-5}$	1.67×10^{-3}	$+2.09 \times 10^{-2}$	4.1×10^{-2}	1.3×10^{-1}
−2.2	−2.0	8.07×10^{-3}	5.01×10^{-1}	3.31×10^{1}	1.65×10^{-1}	$+5.13 \times 10^{-2}$	1.98×10^{-1}	1.94×10^{-1}	$+6.66 \times 10^{-5}$	1.33×10^{-3}	$+4.99 \times 10^{-2}$	4.2×10^{-2}	$1.6 \times 10^{+0}$
−2.0	−1.8	1.07×10^{-2}	9.35×10^{-1}	4.65×10^{1}	2.31×10^{-1}	$+2.28 \times 10^{-2}$	2.70×10^{-1}	2.64×10^{-1}	$+5.74 \times 10^{-5}$	2.14×10^{-3}	$+2.06 \times 10^{-2}$	7.6×10^{-2}	1.0×10^{-2}
−2.0	−1.8	1.16×10^{-2}	8.74×10^{-1}	4.03×10^{1}	2.00×10^{-1}	$+1.83 \times 10^{-1}$	2.63×10^{-1}	2.57×10^{-1}	$+5.28 \times 10^{-5}$	2.08×10^{-3}	$+1.81 \times 10^{-1}$	7.5×10^{-2}	4.7×10^{-3}
−2.0	−1.8	1.24×10^{-2}	8.29×10^{-1}	3.57×10^{1}	1.77×10^{-1}	$+4.22 \times 10^{-2}$	2.58×10^{-1}	2.52×10^{-1}	$+4.77 \times 10^{-5}$	2.04×10^{-3}	$+4.01 \times 10^{-2}$	7.8×10^{-2}	3.7×10^{-3}
−2.0	−1.8	1.28×10^{-2}	7.56×10^{-1}	3.14×10^{1}	1.56×10^{-1}	$+1.14 \times 10^{-1}$	2.49×10^{-1}	2.42×10^{-1}	$+4.46 \times 10^{-5}$	1.91×10^{-3}	$+1.12 \times 10^{-1}$	7.6×10^{-2}	5.2×10^{-3}
−2.0	−1.8	1.28×10^{-2}	6.06×10^{-1}	2.51×10^{1}	1.25×10^{-1}	$+1.37 \times 10^{-1}$	2.25×10^{-1}	2.20×10^{-1}	$+4.46 \times 10^{-5}$	1.59×10^{-3}	$+1.35 \times 10^{-1}$	7.7×10^{-2}	8.6×10^{-3}
−1.8	−1.6	1.67×10^{-2}	9.50×10^{-1}	3.03×10^{1}	1.50×10^{-1}	-2.82×10^{-1}	2.76×10^{-1}	2.68×10^{-1}	$+1.22 \times 10^{-5}$	2.31×10^{-3}	-2.84×10^{-1}	1.7×10^{-1}	4.0×10^{-3}
−1.8	−1.6	1.77×10^{-2}	9.04×10^{-1}	2.73×10^{1}	1.35×10^{-1}	$+2.18 \times 10^{-1}$	2.72×10^{-1}	2.64×10^{-1}	$+3.11 \times 10^{-6}$	2.23×10^{-3}	$+2.16 \times 10^{-1}$	1.7×10^{-1}	5.7×10^{-3}
−1.8	−1.6	1.85×10^{-2}	8.71×10^{-1}	2.50×10^{1}	1.24×10^{-1}	$+4.04 \times 10^{-2}$	2.69×10^{-1}	2.61×10^{-1}	-5.43×10^{-6}	2.16×10^{-3}	$+3.82 \times 10^{-2}$	1.7×10^{-1}	4.4×10^{-3}
−1.8	−1.6	1.94×10^{-2}	8.41×10^{-1}	2.31×10^{1}	1.15×10^{-1}	$+8.94 \times 10^{-3}$	2.66×10^{-1}	2.58×10^{-1}	-1.44×10^{-5}	2.10×10^{-3}	$+6.86 \times 10^{-3}$	1.7×10^{-1}	5.2×10^{-3}
−1.8	−1.6	2.03×10^{-2}	8.05×10^{-1}	2.11×10^{1}	1.06×10^{-1}	$+7.26 \times 10^{-2}$	2.63×10^{-1}	2.55×10^{-1}	-2.36×10^{-5}	2.02×10^{-3}	$+7.06 \times 10^{-2}$	1.7×10^{-1}	7.0×10^{-3}
−1.6	−1.4	2.53×10^{-2}	9.92×10^{-1}	2.09×10^{1}	1.04×10^{-1}	-5.50×10^{-1}	2.86×10^{-1}	2.77×10^{-1}	-7.93×10^{-5}	2.39×10^{-3}	-5.53×10^{-1}	$2.0 \times 10^{+0}$	1.6×10^{-2}
−1.6	−1.4	2.55×10^{-2}	9.86×10^{-1}	2.06×10^{1}	1.03×10^{-1}	$-2.74 \times 10^{+0}$	2.86×10^{-1}	2.76×10^{-1}	-8.14×10^{-5}	2.38×10^{-3}	$-2.75 \times 10^{+0}$	$2.2 \times 10^{+0}$	2.0×10^{-2}
−1.6	−1.4	2.57×10^{-2}	9.80×10^{-1}	2.03×10^{1}	1.03×10^{-1}	$-1.47 \times 10^{+0}$	2.85×10^{-1}	2.76×10^{-1}	-8.31×10^{-5}	2.38×10^{-3}	$-1.48 \times 10^{+0}$	$1.7 \times 10^{+0}$	7.2×10^{-2}
−1.6	−1.4	2.59×10^{-2}	9.72×10^{-1}	2.00×10^{1}	1.02×10^{-1}	$+2.77 \times 10^{+0}$	2.85×10^{-1}	2.75×10^{-1}	-8.57×10^{-5}	2.38×10^{-3}	$+2.76 \times 10^{+0}$	$1.6 \times 10^{+0}$	8.1×10^{-2}
−1.6	−1.4	2.62×10^{-2}	9.60×10^{-1}	1.95×10^{1}	1.01×10^{-1}	$-2.39 \times 10^{+0}$	2.84×10^{-1}	2.74×10^{-1}	-8.97×10^{-5}	2.39×10^{-3}	$-2.39 \times 10^{+0}$	$1.8 \times 10^{+0}$	$1.7 \times 10^{+0}$

Table F.18: $A_1^p(x, \nu)$ from 2011 data (2/2).

$\log_{10}(x)$		$\langle x \rangle$	$\langle Q^2 \rangle$	$\langle \nu \rangle$	$\langle y \rangle$	$A_1^{p,exp}$	F_2^p	F_2^d	$\Delta A_1^{^{14}N}$	ΔA_1^{RC}	$A_1^{p\gamma}$	$\sigma_{stat}(A_1^p)$	$\sigma_{syst}(A_1^p)$
-3.0	-2.4	4.25×10^{-5}	3.19×10^{-3}	4.00×10^{1}	2.52×10^{-1}	$+9.55 \times 10^{-3}$	3.81×10^{-3}	3.79×10^{-3}	$+9.32 \times 10^{-7}$	1.38×10^{-3}	$+8.17 \times 10^{-3}$	1.6×10^{-2}	2.3×10^{-2}
-3.0	-2.4	4.88×10^{-5}	3.27×10^{-3}	3.58×10^{1}	2.26×10^{-1}	$+1.74 \times 10^{-3}$	3.92×10^{-3}	3.90×10^{-3}	$+1.07 \times 10^{-6}$	1.44×10^{-3}	$+2.99 \times 10^{-4}$	2.0×10^{-2}	3.2×10^{-3}
-3.0	-2.4	6.44×10^{-5}	3.37×10^{-3}	2.86×10^{1}	1.83×10^{-1}	$+2.22 \times 10^{-3}$	4.07×10^{-3}	4.05×10^{-3}	$+1.41 \times 10^{-6}$	1.57×10^{-3}	$+6.47 \times 10^{-4}$	1.8×10^{-2}	2.5×10^{-3}
-2.4	-1.8	1.38×10^{-4}	1.20×10^{-2}	4.92×10^{1}	3.10×10^{-1}	$+1.08 \times 10^{-2}$	1.41×10^{-2}	1.40×10^{-2}	$+3.00 \times 10^{-6}$	6.90×10^{-4}	$+1.01 \times 10^{-2}$	4.2×10^{-3}	3.7×10^{-3}
-2.4	-1.8	5.55×10^{-5}	7.17×10^{-3}	6.87×10^{1}	4.28×10^{-1}	$+8.17 \times 10^{-3}$	8.46×10^{-3}	8.43×10^{-3}	$+1.22 \times 10^{-6}$	7.80×10^{-4}	$+7.39 \times 10^{-3}$	4.0×10^{-3}	3.3×10^{-3}
-2.4	-1.8	8.22×10^{-5}	1.05×10^{-2}	6.82×10^{1}	4.27×10^{-1}	$+8.49 \times 10^{-3}$	1.23×10^{-2}	1.22×10^{-2}	$+1.80 \times 10^{-6}$	6.40×10^{-4}	$+7.84 \times 10^{-3}$	4.1×10^{-3}	1.4×10^{-2}
-1.8	-1.2	1.38×10^{-4}	2.41×10^{-2}	9.34×10^{1}	5.83×10^{-1}	$+1.04 \times 10^{-2}$	2.73×10^{-2}	2.72×10^{-2}	$+3.01 \times 10^{-6}$	4.10×10^{-4}	$+9.97 \times 10^{-3}$	2.9×10^{-3}	4.2×10^{-3}
-1.8	-1.2	2.25×10^{-4}	3.66×10^{-2}	8.67×10^{1}	5.43×10^{-1}	$+7.42 \times 10^{-3}$	4.02×10^{-2}	4.01×10^{-2}	$+4.87 \times 10^{-6}$	3.80×10^{-4}	$+7.03 \times 10^{-3}$	3.0×10^{-3}	2.9×10^{-3}
-1.8	-1.2	4.20×10^{-4}	4.49×10^{-2}	6.19×10^{1}	3.89×10^{-1}	$+1.04 \times 10^{-2}$	4.83×10^{-2}	4.80×10^{-2}	$+8.88 \times 10^{-6}$	4.30×10^{-4}	$+9.99 \times 10^{-3}$	3.0×10^{-3}	2.7×10^{-3}
-1.2	-0.6	1.44×10^{-3}	1.71×10^{-1}	6.98×10^{1}	4.38×10^{-1}	$+1.02 \times 10^{-2}$	1.40×10^{-1}	1.40×10^{-1}	$+2.75 \times 10^{-5}$	5.80×10^{-4}	$+9.64 \times 10^{-3}$	3.3×10^{-3}	3.6×10^{-3}
-1.2	-0.6	4.29×10^{-4}	8.68×10^{-2}	1.10×10^{2}	6.83×10^{-1}	$+1.16 \times 10^{-2}$	8.53×10^{-2}	8.51×10^{-2}	$+9.08 \times 10^{-6}$	3.80×10^{-4}	$+1.12 \times 10^{-2}$	3.2×10^{-3}	2.2×10^{-2}
-1.2	-0.6	7.30×10^{-4}	1.27×10^{-1}	9.34×10^{1}	5.84×10^{-1}	$+1.47 \times 10^{-2}$	1.15×10^{-1}	1.14×10^{-1}	$+1.50 \times 10^{-5}$	4.50×10^{-4}	$+1.43 \times 10^{-2}$	3.2×10^{-3}	6.5×10^{-3}
-0.6	$+0.0$	1.56×10^{-3}	3.30×10^{-1}	1.14×10^{2}	7.11×10^{-1}	$+1.96 \times 10^{-2}$	1.57×10^{-1}	1.56×10^{-1}	$+2.95 \times 10^{-5}$	8.00×10^{-4}	$+1.88 \times 10^{-2}$	4.6×10^{-3}	4.9×10^{-3}
-0.6	$+0.0$	2.66×10^{-3}	4.84×10^{-1}	9.76×10^{1}	6.11×10^{-1}	$+1.70 \times 10^{-2}$	1.99×10^{-1}	1.97×10^{-1}	$+4.41 \times 10^{-5}$	1.10×10^{-3}	$+1.59 \times 10^{-2}$	4.6×10^{-3}	4.0×10^{-3}
-0.6	$+0.0$	5.84×10^{-3}	6.77×10^{-1}	7.11×10^{1}	4.46×10^{-1}	$+2.56 \times 10^{-2}$	2.33×10^{-1}	2.29×10^{-1}	$+6.56 \times 10^{-5}$	1.76×10^{-3}	$+2.37 \times 10^{-2}$	4.7×10^{-3}	6.0×10^{-3}

Table F.19: $A_1^p(Q^2, x)$ from 2007 data.

$\log_{10}(x)$		$\langle x \rangle$	$\langle Q^2 \rangle$	$\langle \nu \rangle$	$\langle y \rangle$	$A_1^{p,exp}$	F_2^p	F_2^d	$\Delta A_1^{^{14}N}$	ΔA_1^{RC}	$A_1^{p\gamma}$	$\sigma_{stat}(A_1^p)$	$\sigma_{syst}(A_1^p)$
-3.0	-2.4	4.11×10^{-5}	3.58×10^{-3}	4.64×10^{1}	2.36×10^{-1}	$+3.63 \times 10^{-2}$	4.27×10^{-3}	4.25×10^{-3}	$+9.01 \times 10^{-7}$	1.23×10^{-3}	$+3.51 \times 10^{-2}$	8.4×10^{-2}	7.8×10^{-2}
-3.0	-2.4	4.40×10^{-5}	3.58×10^{-3}	4.34×10^{1}	2.22×10^{-1}	$+4.74 \times 10^{-2}$	4.28×10^{-3}	4.26×10^{-3}	$+9.65 \times 10^{-7}$	1.27×10^{-3}	$+4.61 \times 10^{-2}$	1.1×10^{-1}	5.0×10^{-3}
-3.0	-2.4	5.16×10^{-5}	3.59×10^{-3}	3.76×10^{1}	1.93×10^{-1}	$+1.36 \times 10^{-1}$	4.30×10^{-3}	4.28×10^{-3}	$+1.13 \times 10^{-6}$	1.36×10^{-3}	$+1.35 \times 10^{-1}$	9.9×10^{-2}	2.5×10^{-3}
-2.4	-1.8	4.81×10^{-5}	8.36×10^{-3}	9.24×10^{1}	4.56×10^{-1}	$+8.22 \times 10^{-3}$	9.87×10^{-3}	9.84×10^{-3}	$+1.06 \times 10^{-6}$	6.40×10^{-4}	$+7.58 \times 10^{-3}$	5.2×10^{-3}	2.8×10^{-3}
-2.4	-1.8	6.44×10^{-5}	1.13×10^{-2}	9.36×10^{1}	4.63×10^{-1}	$+5.52 \times 10^{-3}$	1.32×10^{-2}	1.32×10^{-2}	$+1.41 \times 10^{-6}$	5.40×10^{-4}	$+4.98 \times 10^{-3}$	5.4×10^{-3}	3.7×10^{-3}
-2.4	-1.8	9.57×10^{-5}	1.28×10^{-2}	7.35×10^{1}	3.65×10^{-1}	$+6.75 \times 10^{-3}$	1.49×10^{-2}	1.49×10^{-2}	$+2.09 \times 10^{-6}$	5.70×10^{-4}	$+6.18 \times 10^{-3}$	5.6×10^{-3}	5.5×10^{-2}
-1.8	-1.2	1.06×10^{-4}	2.36×10^{-2}	1.19×10^{2}	5.88×10^{-1}	$+1.93 \times 10^{-3}$	2.70×10^{-2}	2.69×10^{-2}	$+2.32 \times 10^{-6}$	3.70×10^{-4}	$+1.56 \times 10^{-3}$	3.3×10^{-3}	5.8×10^{-3}
-1.8	-1.2	1.71×10^{-4}	3.66×10^{-2}	1.14×10^{2}	5.63×10^{-1}	$+9.98 \times 10^{-3}$	4.05×10^{-2}	4.03×10^{-2}	$+3.72 \times 10^{-6}$	3.40×10^{-4}	$+9.64 \times 10^{-3}$	3.4×10^{-3}	2.9×10^{-3}
-1.8	-1.2	2.95×10^{-4}	4.71×10^{-2}	8.95×10^{1}	4.44×10^{-1}	$+4.72 \times 10^{-3}$	5.04×10^{-2}	5.03×10^{-2}	$+6.33 \times 10^{-6}$	3.70×10^{-4}	$+4.35 \times 10^{-3}$	3.5×10^{-3}	2.5×10^{-3}
-1.2	-0.6	1.04×10^{-3}	1.77×10^{-1}	9.74×10^{1}	4.83×10^{-1}	$+1.29 \times 10^{-2}$	1.44×10^{-1}	1.44×10^{-1}	$+2.07 \times 10^{-5}$	5.10×10^{-4}	$+1.24 \times 10^{-2}$	3.7×10^{-3}	2.9×10^{-3}
-1.2	-0.6	3.30×10^{-4}	8.55×10^{-2}	1.40×10^{2}	6.90×10^{-1}	$+5.48 \times 10^{-3}$	8.50×10^{-2}	8.48×10^{-2}	$+7.06 \times 10^{-6}$	3.40×10^{-4}	$+5.13 \times 10^{-3}$	3.6×10^{-3}	5.4×10^{-2}
-1.2	-0.6	5.54×10^{-4}	1.26×10^{-1}	1.22×10^{2}	6.01×10^{-1}	$+5.99 \times 10^{-3}$	1.14×10^{-1}	1.14×10^{-1}	$+1.16 \times 10^{-5}$	4.00×10^{-4}	$+5.58 \times 10^{-3}$	3.5×10^{-3}	4.5×10^{-3}
-0.6	$+0.0$	1.23×10^{-3}	3.33×10^{-1}	1.46×10^{2}	7.18×10^{-1}	$+1.37 \times 10^{-2}$	1.63×10^{-1}	1.64×10^{-1}	$+2.42 \times 10^{-5}$	7.10×10^{-4}	$+1.30 \times 10^{-2}$	4.8×10^{-3}	3.9×10^{-3}
-0.6	$+0.0$	2.05×10^{-3}	4.85×10^{-1}	1.27×10^{2}	6.26×10^{-1}	-7.03×10^{-4}	2.05×10^{-1}	2.04×10^{-1}	$+3.66 \times 10^{-5}$	9.50×10^{-4}	-1.69×10^{-3}	5.0×10^{-3}	4.4×10^{-3}
-0.6	$+0.0$	4.21×10^{-3}	6.91×10^{-1}	9.85×10^{1}	4.88×10^{-1}	$+3.15 \times 10^{-2}$	2.39×10^{-1}	2.36×10^{-1}	$+5.81 \times 10^{-5}$	1.47×10^{-3}	$+2.99 \times 10^{-2}$	5.2×10^{-3}	3.9×10^{-3}

Table F.20: $A_1^p(Q^2, x)$ from 2011 data.

$\log_{10}(x)$		$\langle x \rangle$	$\langle Q^2 \rangle$	$\langle \nu \rangle$	R	$\sigma(R)$	g_1^p	$\sigma_{stat}(g_1^p)$	$\sigma_{syst}(g_1^p)$
−4.4	−4.2	4.73×10^{-5}	2.92×10^{-3}	$3.33 \times 10^{+1}$	4.94×10^{-3}	2.00×10^{-1}	$+4.52 \times 10^{-1}$	5.2×10^{-1}	6.9×10^{-1}
−4.4	−4.2	4.90×10^{-5}	4.38×10^{-3}	$4.85 \times 10^{+1}$	7.39×10^{-3}	2.00×10^{-1}	$+1.52 \times 10^{-1}$	4.6×10^{-1}	2.4×10^{-1}
−4.4	−4.2	5.31×10^{-5}	7.25×10^{-3}	$7.29 \times 10^{+1}$	1.21×10^{-2}	2.00×10^{-1}	$+6.53 \times 10^{-1}$	4.1×10^{-1}	4.2×10^{-1}
−4.2	−4.0	7.49×10^{-5}	4.80×10^{-3}	$3.45 \times 10^{+1}$	8.02×10^{-3}	2.00×10^{-1}	-4.26×10^{-1}	4.4×10^{-1}	2.3×10^{-1}
−4.2	−4.0	7.75×10^{-5}	7.43×10^{-3}	$5.19 \times 10^{+1}$	1.24×10^{-2}	2.00×10^{-1}	$+8.53 \times 10^{-1}$	3.9×10^{-1}	3.9×10^{-1}
−4.2	−4.0	8.32×10^{-5}	1.30×10^{-2}	$8.33 \times 10^{+1}$	2.13×10^{-2}	2.00×10^{-1}	$+6.23 \times 10^{-1}$	3.6×10^{-1}	4.5×10^{-1}
−4.0	−3.8	1.19×10^{-4}	7.82×10^{-3}	$3.55 \times 10^{+1}$	1.29×10^{-2}	2.00×10^{-1}	$+4.98 \times 10^{-1}$	4.0×10^{-1}	3.7×10^{-1}
−4.0	−3.8	1.23×10^{-4}	1.24×10^{-2}	$5.50 \times 10^{+1}$	2.04×10^{-2}	2.00×10^{-1}	$+4.00 \times 10^{-1}$	3.6×10^{-1}	4.8×10^{-1}
−4.0	−3.8	1.31×10^{-4}	2.25×10^{-2}	$9.19 \times 10^{+1}$	3.61×10^{-2}	2.00×10^{-1}	$+9.67 \times 10^{-1}$	3.3×10^{-1}	4.3×10^{-1}
−3.8	−3.6	1.88×10^{-4}	1.26×10^{-2}	$3.60 \times 10^{+1}$	2.04×10^{-2}	2.00×10^{-1}	$+7.25 \times 10^{-1}$	3.9×10^{-1}	4.1×10^{-1}
−3.8	−3.6	1.94×10^{-4}	2.04×10^{-2}	$5.70 \times 10^{+1}$	3.27×10^{-2}	2.00×10^{-1}	$+5.08 \times 10^{-1}$	3.4×10^{-1}	1.7×10^{-1}
−3.8	−3.6	2.06×10^{-4}	3.77×10^{-2}	$9.81 \times 10^{+1}$	5.85×10^{-2}	2.00×10^{-1}	$+6.51 \times 10^{-1}$	3.2×10^{-1}	1.6×10^{-1}
−3.6	−3.4	2.99×10^{-4}	1.99×10^{-2}	$3.60 \times 10^{+1}$	3.18×10^{-2}	2.00×10^{-1}	$+4.62 \times 10^{-1}$	3.8×10^{-1}	2.1×10^{-1}
−3.6	−3.4	3.07×10^{-4}	3.30×10^{-2}	$5.81 \times 10^{+1}$	5.12×10^{-2}	2.00×10^{-1}	$+6.63 \times 10^{-2}$	3.3×10^{-1}	2.1×10^{-1}
−3.6	−3.4	3.24×10^{-4}	6.14×10^{-2}	$1.01 \times 10^{+2}$	9.07×10^{-2}	2.00×10^{-1}	$+6.38 \times 10^{-1}$	3.0×10^{-1}	5.1×10^{-1}
−3.4	−3.2	4.75×10^{-4}	3.10×10^{-2}	$3.53 \times 10^{+1}$	4.81×10^{-2}	2.00×10^{-1}	$+6.70 \times 10^{-1}$	3.7×10^{-1}	4.1×10^{-1}
−3.4	−3.2	4.85×10^{-4}	5.25×10^{-2}	$5.86 \times 10^{+1}$	7.83×10^{-2}	2.00×10^{-1}	$+5.33 \times 10^{-1}$	3.2×10^{-1}	3.4×10^{-1}
−3.4	−3.2	5.13×10^{-4}	9.80×10^{-2}	$1.02 \times 10^{+2}$	1.35×10^{-1}	2.00×10^{-1}	$+1.11 \times 10^{+0}$	2.8×10^{-1}	2.0×10^{-1}
−3.2	−3.0	7.54×10^{-4}	4.77×10^{-2}	$3.42 \times 10^{+1}$	7.12×10^{-2}	2.00×10^{-1}	$+1.13 \times 10^{+0}$	3.7×10^{-1}	2.9×10^{-1}
−3.2	−3.0	7.66×10^{-4}	8.26×10^{-2}	$5.84 \times 10^{+1}$	1.16×10^{-1}	2.00×10^{-1}	$+6.60 \times 10^{-1}$	3.1×10^{-1}	2.7×10^{-1}
−3.2	−3.0	8.08×10^{-4}	1.55×10^{-1}	$1.02 \times 10^{+2}$	1.92×10^{-1}	2.00×10^{-1}	$+1.13 \times 10^{+0}$	2.6×10^{-1}	2.0×10^{-1}
−3.0	−2.8	1.20×10^{-3}	7.24×10^{-2}	$3.27 \times 10^{+1}$	1.03×10^{-1}	2.00×10^{-1}	$+4.99 \times 10^{-1}$	3.7×10^{-1}	2.0×10^{-1}
−3.0	−2.8	1.21×10^{-3}	1.29×10^{-1}	$5.75 \times 10^{+1}$	1.66×10^{-1}	2.00×10^{-1}	$+3.32 \times 10^{-1}$	3.0×10^{-1}	1.7×10^{-1}
−3.0	−2.8	1.28×10^{-3}	2.46×10^{-1}	$1.03 \times 10^{+2}$	2.61×10^{-1}	2.00×10^{-1}	$+5.03 \times 10^{-1}$	1.6×10^{-1}	1.6×10^{-1}
−2.8	−2.6	1.90×10^{-3}	1.08×10^{-1}	$3.07 \times 10^{+1}$	1.43×10^{-1}	2.00×10^{-1}	$+8.24 \times 10^{-1}$	3.7×10^{-1}	1.7×10^{-1}
−2.8	−2.6	1.92×10^{-3}	1.96×10^{-1}	$5.52 \times 10^{+1}$	2.24×10^{-1}	2.00×10^{-1}	$+2.88 \times 10^{-1}$	2.9×10^{-1}	2.0×10^{-1}
−2.8	−2.6	2.02×10^{-3}	3.88×10^{-1}	$1.03 \times 10^{+2}$	3.31×10^{-1}	2.00×10^{-1}	$+3.75 \times 10^{-1}$	1.5×10^{-1}	1.2×10^{-1}
−2.6	−2.4	3.00×10^{-3}	1.59×10^{-1}	$2.85 \times 10^{+1}$	1.92×10^{-1}	2.00×10^{-1}	$+2.16 \times 10^{-1}$	3.6×10^{-1}	2.5×10^{-1}
−2.6	−2.4	3.05×10^{-3}	2.92×10^{-1}	$5.18 \times 10^{+1}$	2.85×10^{-1}	2.00×10^{-1}	$+3.17 \times 10^{-1}$	1.8×10^{-1}	2.3×10^{-1}
−2.6	−2.4	3.18×10^{-3}	6.06×10^{-1}	$1.02 \times 10^{+2}$	3.86×10^{-1}	6.12×10^{-2}	$+3.70 \times 10^{-1}$	1.4×10^{-1}	3.7×10^{-1}
−2.4	−2.2	4.75×10^{-3}	2.31×10^{-1}	$2.62 \times 10^{+1}$	2.46×10^{-1}	2.00×10^{-1}	$+2.42 \times 10^{-1}$	2.3×10^{-1}	2.2×10^{-1}
−2.4	−2.2	4.85×10^{-3}	4.03×10^{-1}	$4.50 \times 10^{+1}$	3.32×10^{-1}	2.00×10^{-1}	$+2.57 \times 10^{-1}$	2.0×10^{-1}	3.3×10^{-1}
−2.4	−2.2	4.87×10^{-3}	7.66×10^{-1}	$8.52 \times 10^{+1}$	3.99×10^{-1}	6.62×10^{-2}	$+3.27 \times 10^{-1}$	1.5×10^{-1}	2.2×10^{-1}
−2.2	−2.0	7.52×10^{-3}	3.34×10^{-1}	$2.40 \times 10^{+1}$	3.02×10^{-1}	2.00×10^{-1}	$+4.91 \times 10^{-1}$	2.6×10^{-1}	2.0×10^{-1}
−2.2	−2.0	7.72×10^{-3}	5.27×10^{-1}	$3.70 \times 10^{+1}$	3.66×10^{-1}	6.46×10^{-2}	$+4.59 \times 10^{-1}$	2.1×10^{-1}	2.8×10^{-1}
−2.2	−2.0	7.77×10^{-3}	8.22×10^{-1}	$5.73 \times 10^{+1}$	3.99×10^{-1}	6.59×10^{-2}	$+5.29 \times 10^{-1}$	1.6×10^{-1}	2.1×10^{-1}
−2.0	−1.8	1.18×10^{-2}	4.66×10^{-1}	$2.12 \times 10^{+1}$	3.48×10^{-1}	2.00×10^{-1}	$+7.86 \times 10^{-1}$	2.8×10^{-1}	1.9×10^{-1}
−2.0	−1.8	1.22×10^{-2}	6.51×10^{-1}	$2.90 \times 10^{+1}$	3.84×10^{-1}	5.75×10^{-2}	$+2.38 \times 10^{-1}$	2.4×10^{-1}	1.8×10^{-1}
−2.0	−1.8	1.22×10^{-2}	8.75×10^{-1}	$3.88 \times 10^{+1}$	3.97×10^{-1}	6.46×10^{-2}	$+1.32 \times 10^{-1}$	1.9×10^{-1}	1.0×10^{-1}
−1.8	−1.6	1.81×10^{-2}	6.34×10^{-1}	$1.88 \times 10^{+1}$	3.79×10^{-1}	5.56×10^{-2}	$+7.78 \times 10^{-1}$	3.5×10^{-1}	1.1×10^{-1}
−1.8	−1.6	1.92×10^{-2}	7.84×10^{-1}	$2.21 \times 10^{+1}$	3.91×10^{-1}	5.93×10^{-2}	$+8.17 \times 10^{-2}$	3.1×10^{-1}	1.4×10^{-1}
−1.8	−1.6	1.93×10^{-2}	9.26×10^{-1}	$2.60 \times 10^{+1}$	3.93×10^{-1}	6.21×10^{-2}	-7.40×10^{-2}	2.7×10^{-1}	1.0×10^{-1}
−1.6	−1.4	2.66×10^{-2}	8.35×10^{-1}	$1.68 \times 10^{+1}$	3.89×10^{-1}	5.84×10^{-2}	-6.80×10^{-2}	7.5×10^{-1}	1.3×10^{-1}
−1.6	−1.4	2.76×10^{-2}	9.17×10^{-1}	$1.77 \times 10^{+1}$	3.90×10^{-1}	5.93×10^{-2}	$+8.58 \times 10^{-4}$	7.0×10^{-1}	2.3×10^{-1}
−1.6	−1.4	2.83×10^{-2}	9.74×10^{-1}	$1.84 \times 10^{+1}$	3.89×10^{-1}	5.94×10^{-2}	$+3.83 \times 10^{-1}$	6.6×10^{-1}	6.4×10^{-1}

Table F.21: $g_1^p(x, Q^2)$ from 2007 data.

$\log_{10}(x)$		$\langle x \rangle$	$\langle Q^2 \rangle$	$\langle \nu \rangle$	R	$\sigma(R)$	g_1^p	$\sigma_{stat}(g_1^p)$	$\sigma_{syst}(g_1^p)$
−4.4	−4.2	4.66×10^{-5}	5.37×10^{-3}	$6.21 \times 10^{+1}$	9.04×10^{-3}	2.00×10^{-1}	-6.24×10^{-1}	7.8×10^{-1}	$1.0 \times 10^{+0}$
−4.4	−4.2	4.90×10^{-5}	7.36×10^{-3}	$8.13 \times 10^{+1}$	1.23×10^{-2}	2.00×10^{-1}	$+7.05 \times 10^{-2}$	7.1×10^{-1}	3.3×10^{-1}
−4.4	−4.2	5.39×10^{-5}	1.08×10^{-2}	$1.07 \times 10^{+2}$	1.80×10^{-2}	2.00×10^{-1}	$+1.67 \times 10^{+0}$	6.6×10^{-1}	4.7×10^{-1}
−4.2	−4.0	7.40×10^{-5}	8.75×10^{-3}	$6.37 \times 10^{+1}$	1.45×10^{-2}	2.00×10^{-1}	$+8.40 \times 10^{-1}$	6.8×10^{-1}	4.0×10^{-1}
−4.2	−4.0	7.77×10^{-5}	1.23×10^{-2}	$8.60 \times 10^{+1}$	2.04×10^{-2}	2.00×10^{-1}	$+4.04 \times 10^{-1}$	6.2×10^{-1}	3.3×10^{-1}
−4.2	−4.0	8.42×10^{-5}	1.88×10^{-2}	$1.20 \times 10^{+2}$	3.06×10^{-2}	2.00×10^{-1}	$+5.00 \times 10^{-1}$	5.9×10^{-1}	5.4×10^{-1}
−4.0	−3.8	1.18×10^{-4}	1.41×10^{-2}	$6.48 \times 10^{+1}$	2.31×10^{-2}	2.00×10^{-1}	$+1.61 \times 10^{-1}$	6.2×10^{-1}	4.7×10^{-1}
−4.0	−3.8	1.23×10^{-4}	2.04×10^{-2}	$8.99 \times 10^{+1}$	3.29×10^{-2}	2.00×10^{-1}	-1.90×10^{-1}	5.7×10^{-1}	3.6×10^{-1}
−4.0	−3.8	1.32×10^{-4}	3.19×10^{-2}	$1.29 \times 10^{+2}$	5.03×10^{-2}	2.00×10^{-1}	$+1.30 \times 10^{+0}$	5.4×10^{-1}	3.2×10^{-1}
−3.8	−3.6	1.87×10^{-4}	2.26×10^{-2}	$6.51 \times 10^{+1}$	3.60×10^{-2}	2.00×10^{-1}	$+1.50 \times 10^{-1}$	5.9×10^{-1}	2.6×10^{-1}
−3.8	−3.6	1.94×10^{-4}	3.31×10^{-2}	$9.23 \times 10^{+1}$	5.19×10^{-2}	2.00×10^{-1}	$+1.56 \times 10^{-1}$	5.4×10^{-1}	2.9×10^{-1}
−3.8	−3.6	2.08×10^{-4}	5.25×10^{-2}	$1.36 \times 10^{+2}$	7.92×10^{-2}	2.00×10^{-1}	$+7.12 \times 10^{-1}$	5.1×10^{-1}	4.1×10^{-1}
−3.6	−3.4	2.96×10^{-4}	3.53×10^{-2}	$6.43 \times 10^{+1}$	5.47×10^{-2}	2.00×10^{-1}	$+1.31 \times 10^{-1}$	5.8×10^{-1}	2.8×10^{-1}
−3.6	−3.4	3.07×10^{-4}	5.28×10^{-2}	$9.30 \times 10^{+1}$	7.92×10^{-2}	2.00×10^{-1}	$+3.89 \times 10^{-1}$	5.2×10^{-1}	5.7×10^{-1}
−3.6	−3.4	3.27×10^{-4}	8.43×10^{-2}	$1.38 \times 10^{+2}$	1.20×10^{-1}	2.00×10^{-1}	$+4.47 \times 10^{-1}$	4.8×10^{-1}	$3.4 \times 10^{+0}$
−3.4	−3.2	4.71×10^{-4}	5.48×10^{-2}	$6.29 \times 10^{+1}$	8.15×10^{-2}	2.00×10^{-1}	$+3.23 \times 10^{-1}$	5.7×10^{-1}	6.0×10^{-1}
−3.4	−3.2	4.85×10^{-4}	8.40×10^{-2}	$9.38 \times 10^{+1}$	1.18×10^{-1}	2.00×10^{-1}	$+6.78 \times 10^{-1}$	4.9×10^{-1}	4.5×10^{-1}
−3.4	−3.2	5.18×10^{-4}	1.34×10^{-1}	$1.39 \times 10^{+2}$	1.73×10^{-1}	2.00×10^{-1}	$+1.04 \times 10^{+0}$	4.4×10^{-1}	5.0×10^{-1}
−3.2	−3.0	7.48×10^{-4}	8.36×10^{-2}	$6.04 \times 10^{+1}$	1.17×10^{-1}	2.00×10^{-1}	$+8.94 \times 10^{-1}$	5.6×10^{-1}	4.3×10^{-1}
−3.2	−3.0	7.64×10^{-4}	1.31×10^{-1}	$9.26 \times 10^{+1}$	1.69×10^{-1}	2.00×10^{-1}	$+1.06 \times 10^{+0}$	4.6×10^{-1}	4.8×10^{-1}
−3.2	−3.0	8.16×10^{-4}	2.11×10^{-1}	$1.39 \times 10^{+2}$	2.39×10^{-1}	2.00×10^{-1}	$+3.89 \times 10^{-1}$	2.6×10^{-1}	2.9×10^{-1}
−3.0	−2.8	1.19×10^{-3}	1.26×10^{-1}	$5.72 \times 10^{+1}$	1.63×10^{-1}	2.00×10^{-1}	-1.64×10^{-1}	5.4×10^{-1}	2.6×10^{-1}
−3.0	−2.8	1.21×10^{-3}	2.05×10^{-1}	$9.16 \times 10^{+1}$	2.32×10^{-1}	2.00×10^{-1}	$+3.70 \times 10^{-1}$	2.6×10^{-1}	1.7×10^{-1}
−3.0	−2.8	1.29×10^{-3}	3.39×10^{-1}	$1.41 \times 10^{+2}$	3.13×10^{-1}	2.00×10^{-1}	$+5.83 \times 10^{-1}$	2.6×10^{-1}	1.4×10^{-1}
−2.8	−2.6	1.89×10^{-3}	1.83×10^{-1}	$5.24 \times 10^{+1}$	2.14×10^{-1}	2.00×10^{-1}	$+7.33 \times 10^{-1}$	5.3×10^{-1}	1.5×10^{-1}
−2.8	−2.6	1.91×10^{-3}	3.10×10^{-1}	$8.77 \times 10^{+1}$	2.97×10^{-1}	2.00×10^{-1}	-1.94×10^{-1}	2.8×10^{-1}	2.2×10^{-1}
−2.8	−2.6	2.03×10^{-3}	5.30×10^{-1}	$1.40 \times 10^{+2}$	3.74×10^{-1}	6.61×10^{-2}	-4.48×10^{-2}	2.3×10^{-1}	1.8×10^{-1}
−2.6	−2.4	2.99×10^{-3}	2.59×10^{-1}	$4.67 \times 10^{+1}$	2.66×10^{-1}	2.00×10^{-1}	$+5.75 \times 10^{-2}$	3.4×10^{-1}	3.8×10^{-1}
−2.6	−2.4	3.04×10^{-3}	4.43×10^{-1}	$7.90 \times 10^{+1}$	3.48×10^{-1}	2.00×10^{-1}	$+3.64 \times 10^{-1}$	2.8×10^{-1}	6.5×10^{-1}
−2.6	−2.4	3.12×10^{-3}	7.59×10^{-1}	$1.31 \times 10^{+2}$	4.02×10^{-1}	6.78×10^{-2}	$+6.66 \times 10^{-1}$	2.2×10^{-1}	$6.7 \times 10^{+0}$
−2.4	−2.2	4.74×10^{-3}	3.39×10^{-1}	$3.87 \times 10^{+1}$	3.07×10^{-1}	2.00×10^{-1}	$+8.09 \times 10^{-3}$	4.0×10^{-1}	7.4×10^{-1}
−2.4	−2.2	4.81×10^{-3}	5.49×10^{-1}	$6.17 \times 10^{+1}$	3.73×10^{-1}	6.26×10^{-2}	$+4.28 \times 10^{-1}$	3.2×10^{-1}	3.1×10^{-1}
−2.4	−2.2	4.86×10^{-3}	8.34×10^{-1}	$9.29 \times 10^{+1}$	4.02×10^{-1}	6.87×10^{-2}	$+1.23 \times 10^{+0}$	2.5×10^{-1}	3.0×10^{-1}
−2.2	−2.0	7.54×10^{-3}	4.47×10^{-1}	$3.20 \times 10^{+1}$	3.45×10^{-1}	2.00×10^{-1}	$+7.81 \times 10^{-1}$	4.5×10^{-1}	3.3×10^{-1}
−2.2	−2.0	7.65×10^{-3}	6.63×10^{-1}	$4.69 \times 10^{+1}$	3.88×10^{-1}	5.96×10^{-2}	-1.90×10^{-1}	3.6×10^{-1}	5.2×10^{-1}
−2.2	−2.0	7.73×10^{-3}	8.85×10^{-1}	$6.20 \times 10^{+1}$	4.00×10^{-1}	6.76×10^{-2}	$+1.57 \times 10^{-1}$	3.0×10^{-1}	2.3×10^{-1}
−2.0	−1.8	1.18×10^{-2}	5.76×10^{-1}	$2.63 \times 10^{+1}$	3.73×10^{-1}	5.86×10^{-2}	$+9.71 \times 10^{-1}$	5.2×10^{-1}	2.5×10^{-1}
−2.0	−1.8	1.21×10^{-2}	7.57×10^{-1}	$3.39 \times 10^{+1}$	3.93×10^{-1}	6.12×10^{-2}	$+1.12 \times 10^{+0}$	4.4×10^{-1}	2.4×10^{-1}
−2.0	−1.8	1.21×10^{-2}	9.22×10^{-1}	$4.11 \times 10^{+1}$	3.97×10^{-1}	6.54×10^{-2}	$+3.52 \times 10^{-1}$	3.9×10^{-1}	1.9×10^{-1}
−1.8	−1.6	1.76×10^{-2}	7.51×10^{-1}	$2.29 \times 10^{+1}$	3.90×10^{-1}	5.88×10^{-2}	$+9.50 \times 10^{-2}$	7.5×10^{-1}	1.3×10^{-1}
−1.8	−1.6	1.87×10^{-2}	8.75×10^{-1}	$2.53 \times 10^{+1}$	3.93×10^{-1}	6.17×10^{-2}	$+9.18 \times 10^{-1}$	6.8×10^{-1}	2.0×10^{-1}
−1.8	−1.6	1.92×10^{-2}	9.61×10^{-1}	$2.72 \times 10^{+1}$	3.93×10^{-1}	6.25×10^{-2}	-7.36×10^{-1}	6.4×10^{-1}	1.4×10^{-1}
−1.6	−1.4	2.56×10^{-2}	9.52×10^{-1}	$1.98 \times 10^{+1}$	3.90×10^{-1}	6.02×10^{-2}	$-1.99 \times 10^{+0}$	$5.9 \times 10^{+0}$	2.0×10^{-1}
−1.6	−1.4	2.58×10^{-2}	9.79×10^{-1}	$2.02 \times 10^{+1}$	3.90×10^{-1}	6.02×10^{-2}	$-3.82 \times 10^{+0}$	$5.6 \times 10^{+0}$	5.7×10^{-1}
−1.6	−1.4	2.59×10^{-2}	9.94×10^{-1}	$2.05 \times 10^{+1}$	3.90×10^{-1}	6.02×10^{-2}	$+9.11 \times 10^{-2}$	$5.4 \times 10^{+0}$	$3.6 \times 10^{+0}$

Table F.22: $g_1^p(x, Q^2)$ from 2011 data.

ν		$\langle x \rangle$	$\langle Q^2 \rangle$	$\langle \nu \rangle$	R	$\sigma(R)$	g_1^p	$\sigma_{stat}(g_1^p)$	$\sigma_{syst}(g_1^p)$
8	16	1.26×10^{-4}	3.69×10^{-3}	$1.56 \times 10^{+1}$	6.13×10^{-3}	2.00×10^{-1}	$-2.57 \times 10^{+0}$	$2.5 \times 10^{+0}$	$3.4 \times 10^{+0}$
8	16	2.07×10^{-3}	6.08×10^{-2}	$1.56 \times 10^{+1}$	8.74×10^{-2}	2.00×10^{-1}	$-2.57 \times 10^{+0}$	$2.2 \times 10^{+0}$	7.0×10^{-1}
8	16	2.16×10^{-2}	6.34×10^{-1}	$1.57 \times 10^{+1}$	3.77×10^{-1}	5.49×10^{-2}	-4.34×10^{-1}	8.3×10^{-1}	4.0×10^{-1}
8	16	5.87×10^{-4}	1.72×10^{-2}	$1.56 \times 10^{+1}$	2.72×10^{-2}	2.00×10^{-1}	$-3.12 \times 10^{+0}$	$2.4 \times 10^{+0}$	2.2×10^{-1}
8	16	6.76×10^{-3}	1.98×10^{-1}	$1.56 \times 10^{+1}$	2.22×10^{-1}	2.00×10^{-1}	$+5.20 \times 10^{-1}$	$1.7 \times 10^{+0}$	2.7×10^{-1}
16	24	1.35×10^{-4}	5.26×10^{-3}	$2.10 \times 10^{+1}$	8.71×10^{-3}	2.00×10^{-1}	-2.26×10^{-1}	4.9×10^{-1}	3.7×10^{-1}
16	24	1.72×10^{-2}	6.55×10^{-1}	$2.05 \times 10^{+1}$	3.81×10^{-1}	5.60×10^{-2}	$+3.92 \times 10^{-1}$	1.6×10^{-1}	2.8×10^{-1}
16	24	1.99×10^{-3}	7.67×10^{-2}	$2.08 \times 10^{+1}$	1.07×10^{-1}	2.00×10^{-1}	$+1.05 \times 10^{+0}$	4.2×10^{-1}	4.0×10^{-1}
16	24	5.94×10^{-3}	2.28×10^{-1}	$2.07 \times 10^{+1}$	2.43×10^{-1}	2.00×10^{-1}	$+1.41 \times 10^{-1}$	2.0×10^{-1}	3.8×10^{-1}
16	24	6.17×10^{-4}	2.40×10^{-2}	$2.10 \times 10^{+1}$	3.75×10^{-2}	2.00×10^{-1}	$+4.49 \times 10^{-1}$	4.7×10^{-1}	6.3×10^{-1}
24	32	1.01×10^{-2}	5.33×10^{-1}	$2.83 \times 10^{+1}$	3.65×10^{-1}	6.32×10^{-2}	$+3.76 \times 10^{-1}$	1.5×10^{-1}	7.1×10^{-1}
24	32	2.63×10^{-3}	1.39×10^{-1}	$2.84 \times 10^{+1}$	1.74×10^{-1}	2.00×10^{-1}	$+5.26 \times 10^{-1}$	3.3×10^{-1}	7.0×10^{-1}
24	32	2.85×10^{-4}	1.52×10^{-2}	$2.86 \times 10^{+1}$	2.44×10^{-2}	2.00×10^{-1}	$+5.98 \times 10^{-1}$	4.1×10^{-1}	8.2×10^{-1}
24	32	8.49×10^{-4}	4.51×10^{-2}	$2.85 \times 10^{+1}$	6.76×10^{-2}	2.00×10^{-1}	$+2.89 \times 10^{-1}$	3.9×10^{-1}	9.3×10^{-1}
24	32	8.83×10^{-5}	4.72×10^{-3}	$2.86 \times 10^{+1}$	7.87×10^{-3}	2.00×10^{-1}	$+6.53 \times 10^{-1}$	4.2×10^{-1}	6.9×10^{-1}
32	40	1.55×10^{-3}	1.05×10^{-1}	$3.63 \times 10^{+1}$	1.41×10^{-1}	2.00×10^{-1}	$+1.35 \times 10^{-1}$	3.3×10^{-1}	$1.2 \times 10^{+0}$
32	40	1.96×10^{-4}	1.33×10^{-2}	$3.64 \times 10^{+1}$	2.16×10^{-2}	2.00×10^{-1}	$+6.26 \times 10^{-1}$	3.9×10^{-1}	$1.0 \times 10^{+0}$
32	40	5.18×10^{-4}	3.52×10^{-2}	$3.64 \times 10^{+1}$	5.40×10^{-2}	2.00×10^{-1}	$+1.34 \times 10^{+0}$	3.8×10^{-1}	$4.1 \times 10^{+0}$
32	40	6.71×10^{-3}	4.54×10^{-1}	$3.62 \times 10^{+1}$	3.48×10^{-1}	2.00×10^{-1}	$+4.85 \times 10^{-1}$	1.5×10^{-1}	$1.2 \times 10^{+1}$
32	40	7.43×10^{-5}	5.04×10^{-3}	$3.63 \times 10^{+1}$	8.43×10^{-3}	2.00×10^{-1}	$+1.41 \times 10^{-1}$	3.9×10^{-1}	$1.7 \times 10^{+0}$
40	48	1.16×10^{-3}	9.63×10^{-2}	$4.42 \times 10^{+1}$	1.31×10^{-1}	2.00×10^{-1}	$+8.47 \times 10^{-1}$	3.5×10^{-1}	2.6×10^{-1}
40	48	1.76×10^{-4}	1.46×10^{-2}	$4.42 \times 10^{+1}$	2.36×10^{-2}	2.00×10^{-1}	$+1.28 \times 10^{-1}$	4.0×10^{-1}	3.8×10^{-1}
40	48	4.22×10^{-4}	3.50×10^{-2}	$4.43 \times 10^{+1}$	5.39×10^{-2}	2.00×10^{-1}	-3.01×10^{-1}	3.9×10^{-1}	3.2×10^{-1}
40	48	5.01×10^{-3}	4.14×10^{-1}	$4.42 \times 10^{+1}$	3.36×10^{-1}	2.00×10^{-1}	$+2.37 \times 10^{-1}$	1.5×10^{-1}	3.6×10^{-1}
40	48	7.18×10^{-5}	5.92×10^{-3}	$4.41 \times 10^{+1}$	9.89×10^{-3}	2.00×10^{-1}	-8.35×10^{-2}	3.9×10^{-1}	3.4×10^{-1}
48	56	1.02×10^{-3}	9.99×10^{-2}	$5.22 \times 10^{+1}$	1.35×10^{-1}	2.00×10^{-1}	$+4.74 \times 10^{-1}$	3.6×10^{-1}	4.9×10^{-1}
48	56	1.79×10^{-4}	1.75×10^{-2}	$5.21 \times 10^{+1}$	2.83×10^{-2}	2.00×10^{-1}	$+7.41 \times 10^{-1}$	4.2×10^{-1}	6.4×10^{-1}
48	56	4.07×10^{-4}	3.98×10^{-2}	$5.22 \times 10^{+1}$	6.09×10^{-2}	2.00×10^{-1}	$+1.26 \times 10^{-1}$	4.1×10^{-1}	2.8×10^{-1}
48	56	4.15×10^{-3}	4.05×10^{-1}	$5.21 \times 10^{+1}$	3.34×10^{-1}	2.00×10^{-1}	$+1.14 \times 10^{-1}$	1.7×10^{-1}	3.0×10^{-1}
48	56	7.36×10^{-5}	7.17×10^{-3}	$5.20 \times 10^{+1}$	1.19×10^{-2}	2.00×10^{-1}	$+6.75 \times 10^{-1}$	4.1×10^{-1}	7.3×10^{-1}
56	64	1.87×10^{-4}	2.10×10^{-2}	$6.01 \times 10^{+1}$	3.36×10^{-2}	2.00×10^{-1}	$+7.08 \times 10^{-1}$	4.5×10^{-1}	5.3×10^{-1}
56	64	3.64×10^{-3}	4.09×10^{-1}	$6.01 \times 10^{+1}$	3.36×10^{-1}	2.00×10^{-1}	$+1.08 \times 10^{-1}$	1.8×10^{-1}	6.0×10^{-1}
56	64	4.15×10^{-4}	4.67×10^{-2}	$6.01 \times 10^{+1}$	7.06×10^{-2}	2.00×10^{-1}	$+1.07 \times 10^{+0}$	4.3×10^{-1}	7.4×10^{-1}
56	64	7.56×10^{-5}	8.50×10^{-3}	$6.00 \times 10^{+1}$	1.41×10^{-2}	2.00×10^{-1}	$+4.32 \times 10^{-1}$	4.3×10^{-1}	8.5×10^{-1}
56	64	9.76×10^{-4}	1.10×10^{-1}	$6.02 \times 10^{+1}$	1.47×10^{-1}	2.00×10^{-1}	$+3.93 \times 10^{-2}$	3.8×10^{-1}	6.2×10^{-1}
64	72	1.92×10^{-4}	2.45×10^{-2}	$6.80 \times 10^{+1}$	3.90×10^{-2}	2.00×10^{-1}	$+4.64 \times 10^{-1}$	4.8×10^{-1}	8.3×10^{-1}
64	72	3.31×10^{-3}	4.22×10^{-1}	$6.81 \times 10^{+1}$	3.41×10^{-1}	2.00×10^{-1}	$+4.51 \times 10^{-1}$	1.9×10^{-1}	$2.0 \times 10^{+0}$
64	72	4.24×10^{-4}	5.41×10^{-2}	$6.80 \times 10^{+1}$	8.06×10^{-2}	2.00×10^{-1}	$+6.31 \times 10^{-1}$	4.6×10^{-1}	$1.2 \times 10^{+1}$
64	72	7.75×10^{-5}	9.87×10^{-3}	$6.80 \times 10^{+1}$	1.64×10^{-2}	2.00×10^{-1}	$+3.85 \times 10^{-1}$	4.6×10^{-1}	$1.9 \times 10^{+0}$
64	72	9.73×10^{-4}	1.24×10^{-1}	$6.81 \times 10^{+1}$	1.62×10^{-1}	2.00×10^{-1}	$+8.19 \times 10^{-1}$	4.0×10^{-1}	4.9×10^{-1}
72	80	1.02×10^{-3}	1.45×10^{-1}	$7.61 \times 10^{+1}$	1.82×10^{-1}	2.00×10^{-1}	$+8.04 \times 10^{-1}$	4.3×10^{-1}	4.8×10^{-1}
72	80	2.03×10^{-4}	2.89×10^{-2}	$7.60 \times 10^{+1}$	4.56×10^{-2}	2.00×10^{-1}	$+5.16 \times 10^{-1}$	5.2×10^{-1}	4.6×10^{-1}
72	80	3.15×10^{-3}	4.50×10^{-1}	$7.61 \times 10^{+1}$	3.50×10^{-1}	2.00×10^{-1}	$+6.70 \times 10^{-1}$	2.1×10^{-1}	4.0×10^{-1}
72	80	4.48×10^{-4}	6.39×10^{-2}	$7.60 \times 10^{+1}$	9.34×10^{-2}	2.00×10^{-1}	$+1.03 \times 10^{+0}$	5.0×10^{-1}	3.1×10^{-1}
72	80	8.05×10^{-5}	1.15×10^{-2}	$7.59 \times 10^{+1}$	1.89×10^{-2}	2.00×10^{-1}	$+9.18 \times 10^{-1}$	5.0×10^{-1}	3.3×10^{-1}
80	88	1.12×10^{-3}	1.76×10^{-1}	$8.40 \times 10^{+1}$	2.09×10^{-1}	2.00×10^{-1}	$+3.26 \times 10^{-1}$	4.5×10^{-1}	3.9×10^{-1}
80	88	2.30×10^{-4}	3.61×10^{-2}	$8.39 \times 10^{+1}$	5.61×10^{-2}	2.00×10^{-1}	$+3.67 \times 10^{-1}$	5.8×10^{-1}	3.0×10^{-1}
80	88	3.13×10^{-3}	4.94×10^{-1}	$8.41 \times 10^{+1}$	3.63×10^{-1}	2.00×10^{-1}	$+5.01 \times 10^{-1}$	2.3×10^{-1}	2.7×10^{-1}
80	88	5.02×10^{-4}	7.91×10^{-2}	$8.40 \times 10^{+1}$	1.12×10^{-1}	2.00×10^{-1}	$+6.95 \times 10^{-1}$	5.4×10^{-1}	3.3×10^{-1}

Table F.23: $g_1^p(\nu, Q^2)$ from 2007 data (1/2).

ν		$\langle x \rangle$	$\langle Q^2 \rangle$	$\langle \nu \rangle$	R	$\sigma(R)$	g_1^p	$\sigma_{stat}(g_1^p)$	$\sigma_{syst}(g_1^p)$
80	88	8.89×10^{-5}	1.40×10^{-2}	$8.38 \times 10^{+1}$	2.29×10^{-2}	2.00×10^{-1}	$+1.50 \times 10^{+0}$	5.5×10^{-1}	3.7×10^{-1}
88	96	1.01×10^{-4}	1.74×10^{-2}	$9.19 \times 10^{+1}$	2.83×10^{-2}	2.00×10^{-1}	$+3.34 \times 10^{-1}$	6.3×10^{-1}	4.7×10^{-1}
88	96	1.20×10^{-3}	2.06×10^{-1}	$9.20 \times 10^{+1}$	2.34×10^{-1}	2.00×10^{-1}	$+5.35 \times 10^{-1}$	3.0×10^{-1}	8.8×10^{-1}
88	96	2.52×10^{-4}	4.34×10^{-2}	$9.20 \times 10^{+1}$	6.64×10^{-2}	2.00×10^{-1}	$+6.09 \times 10^{-1}$	6.5×10^{-1}	6.2×10^{-1}
88	96	3.12×10^{-3}	5.39×10^{-1}	$9.21 \times 10^{+1}$	3.73×10^{-1}	6.44×10^{-2}	$+2.62 \times 10^{-1}$	2.5×10^{-1}	6.7×10^{-1}
88	96	5.44×10^{-4}	9.38×10^{-2}	$9.20 \times 10^{+1}$	1.30×10^{-1}	2.00×10^{-1}	$+3.30 \times 10^{-1}$	5.9×10^{-1}	7.3×10^{-1}
96	104	1.11×10^{-4}	2.08×10^{-2}	$9.99 \times 10^{+1}$	3.36×10^{-2}	2.00×10^{-1}	$+1.15 \times 10^{-1}$	6.8×10^{-1}	$2.8 \times 10^{+0}$
96	104	1.18×10^{-3}	2.22×10^{-1}	$1.00 \times 10^{+2}$	2.45×10^{-1}	2.00×10^{-1}	$+6.45 \times 10^{-1}$	3.4×10^{-1}	$5.7 \times 10^{+0}$
96	104	2.58×10^{-4}	4.84×10^{-2}	$1.00 \times 10^{+2}$	7.34×10^{-2}	2.00×10^{-1}	$+1.98 \times 10^{+0}$	7.1×10^{-1}	$1.8 \times 10^{+0}$
96	104	3.02×10^{-3}	5.67×10^{-1}	$1.00 \times 10^{+2}$	3.79×10^{-1}	6.22×10^{-2}	$+1.86 \times 10^{-1}$	2.7×10^{-1}	1.3×10^{-1}
96	104	5.40×10^{-4}	1.01×10^{-1}	$1.00 \times 10^{+2}$	1.38×10^{-1}	2.00×10^{-1}	$+1.48 \times 10^{+0}$	6.4×10^{-1}	2.8×10^{-1}
104	112	1.15×10^{-3}	2.34×10^{-1}	$1.08 \times 10^{+2}$	2.53×10^{-1}	2.00×10^{-1}	$+7.71 \times 10^{-1}$	3.8×10^{-1}	3.9×10^{-1}
104	112	1.29×10^{-4}	2.61×10^{-2}	$1.08 \times 10^{+2}$	4.16×10^{-2}	2.00×10^{-1}	$+6.38 \times 10^{-1}$	7.6×10^{-1}	3.7×10^{-1}
104	112	2.81×10^{-4}	5.70×10^{-2}	$1.08 \times 10^{+2}$	8.50×10^{-2}	2.00×10^{-1}	$+1.13 \times 10^{+0}$	7.6×10^{-1}	2.1×10^{-1}
104	112	2.87×10^{-3}	5.82×10^{-1}	$1.08 \times 10^{+2}$	3.82×10^{-1}	6.17×10^{-2}	$+3.64 \times 10^{-1}$	2.9×10^{-1}	2.9×10^{-1}
104	112	5.56×10^{-4}	1.13×10^{-1}	$1.08 \times 10^{+2}$	1.51×10^{-1}	2.00×10^{-1}	$+1.04 \times 10^{-1}$	6.9×10^{-1}	5.6×10^{-1}
112	120	1.18×10^{-3}	2.56×10^{-1}	$1.16 \times 10^{+2}$	2.68×10^{-1}	2.00×10^{-1}	$+1.17 \times 10^{+0}$	4.2×10^{-1}	2.4×10^{-1}
112	120	1.55×10^{-4}	3.37×10^{-2}	$1.16 \times 10^{+2}$	5.29×10^{-2}	2.00×10^{-1}	$+1.20 \times 10^{+0}$	8.6×10^{-1}	2.4×10^{-1}
112	120	2.74×10^{-3}	5.97×10^{-1}	$1.16 \times 10^{+2}$	3.85×10^{-1}	6.16×10^{-2}	$+1.94 \times 10^{-1}$	3.2×10^{-1}	3.6×10^{-1}
112	120	3.20×10^{-4}	6.96×10^{-2}	$1.16 \times 10^{+2}$	1.01×10^{-1}	2.00×10^{-1}	$+5.20 \times 10^{-1}$	8.4×10^{-1}	2.7×10^{-1}
112	120	6.01×10^{-4}	1.31×10^{-1}	$1.16 \times 10^{+2}$	1.70×10^{-1}	2.00×10^{-1}	$+5.35 \times 10^{-1}$	7.4×10^{-1}	3.3×10^{-1}
120	128	1.23×10^{-3}	2.87×10^{-1}	$1.24 \times 10^{+2}$	2.86×10^{-1}	2.00×10^{-1}	$+1.24 \times 10^{+0}$	4.8×10^{-1}	5.5×10^{-1}
120	128	1.90×10^{-4}	4.42×10^{-2}	$1.24 \times 10^{+2}$	6.78×10^{-2}	2.00×10^{-1}	$+1.42 \times 10^{+0}$	9.8×10^{-1}	6.2×10^{-1}
120	128	2.69×10^{-3}	6.25×10^{-1}	$1.24 \times 10^{+2}$	3.90×10^{-1}	6.20×10^{-2}	$+5.86 \times 10^{-1}$	3.6×10^{-1}	3.6×10^{-1}
120	128	3.67×10^{-4}	8.54×10^{-2}	$1.24 \times 10^{+2}$	1.21×10^{-1}	2.00×10^{-1}	$+1.04 \times 10^{+0}$	9.3×10^{-1}	5.6×10^{-1}
120	128	6.55×10^{-4}	1.52×10^{-1}	$1.24 \times 10^{+2}$	1.90×10^{-1}	2.00×10^{-1}	$+2.22 \times 10^{+0}$	8.1×10^{-1}	$1.1 \times 10^{+0}$
128	136	1.31×10^{-3}	3.24×10^{-1}	$1.32 \times 10^{+2}$	3.05×10^{-1}	2.00×10^{-1}	$+7.97 \times 10^{-1}$	5.7×10^{-1}	$7.9 \times 10^{+0}$
128	136	2.34×10^{-4}	5.77×10^{-2}	$1.31 \times 10^{+2}$	8.61×10^{-2}	2.00×10^{-1}	$+1.95 \times 10^{-1}$	$1.2 \times 10^{+0}$	4.4×10^{-1}
128	136	2.66×10^{-3}	6.57×10^{-1}	$1.32 \times 10^{+2}$	3.94×10^{-1}	6.32×10^{-2}	$+2.21 \times 10^{-1}$	4.3×10^{-1}	8.4×10^{-2}
128	136	4.29×10^{-4}	1.06×10^{-1}	$1.32 \times 10^{+2}$	1.44×10^{-1}	2.00×10^{-1}	$+7.69 \times 10^{-1}$	$1.1 \times 10^{+0}$	1.5×10^{-1}
128	136	7.34×10^{-4}	1.81×10^{-1}	$1.32 \times 10^{+2}$	2.16×10^{-1}	2.00×10^{-1}	$+8.70 \times 10^{-1}$	9.6×10^{-1}	1.1×10^{-1}
136	144	1.44×10^{-3}	3.77×10^{-1}	$1.39 \times 10^{+2}$	3.28×10^{-1}	2.00×10^{-1}	$+1.31 \times 10^{+0}$	8.5×10^{-1}	1.1×10^{-1}
136	144	2.66×10^{-3}	6.96×10^{-1}	$1.39 \times 10^{+2}$	3.98×10^{-1}	6.52×10^{-2}	$+3.84 \times 10^{-1}$	6.5×10^{-1}	9.2×10^{-2}
136	144	2.82×10^{-4}	7.36×10^{-2}	$1.39 \times 10^{+2}$	1.07×10^{-1}	2.00×10^{-1}	$+6.83 \times 10^{-1}$	$1.8 \times 10^{+0}$	9.9×10^{-2}
136	144	5.15×10^{-4}	1.34×10^{-1}	$1.39 \times 10^{+2}$	1.74×10^{-1}	2.00×10^{-1}	$-1.36 \times 10^{+0}$	$1.6 \times 10^{+0}$	1.8×10^{-1}
136	144	8.62×10^{-4}	2.25×10^{-1}	$1.39 \times 10^{+2}$	2.49×10^{-1}	2.00×10^{-1}	-5.01×10^{-1}	9.3×10^{-1}	2.1×10^{-1}
144	152	1.01×10^{-3}	2.78×10^{-1}	$1.47 \times 10^{+2}$	2.82×10^{-1}	2.00×10^{-1}	$-1.84 \times 10^{+0}$	$2.2 \times 10^{+0}$	2.6×10^{-1}
144	152	1.58×10^{-3}	4.34×10^{-1}	$1.47 \times 10^{+2}$	3.49×10^{-1}	2.00×10^{-1}	$-2.11 \times 10^{+0}$	$1.9 \times 10^{+0}$	2.1×10^{-1}
144	152	2.67×10^{-3}	7.35×10^{-1}	$1.47 \times 10^{+2}$	4.01×10^{-1}	6.73×10^{-2}	$+2.42 \times 10^{+0}$	$1.5 \times 10^{+0}$	1.4×10^{-1}
144	152	3.38×10^{-4}	9.28×10^{-2}	$1.46 \times 10^{+2}$	1.30×10^{-1}	2.00×10^{-1}	$+1.23 \times 10^{+1}$	$4.2 \times 10^{+0}$	1.6×10^{-1}
144	152	6.23×10^{-4}	1.71×10^{-1}	$1.46 \times 10^{+2}$	2.07×10^{-1}	2.00×10^{-1}	$-2.58 \times 10^{+0}$	$3.6 \times 10^{+0}$	1.8×10^{-1}
152	160	1.05×10^{-3}	3.03×10^{-1}	$1.54 \times 10^{+2}$	2.96×10^{-1}	2.00×10^{-1}	$+1.37 \times 10^{+0}$	$1.0 \times 10^{+1}$	2.1×10^{-1}
152	160	1.60×10^{-3}	4.63×10^{-1}	$1.54 \times 10^{+2}$	3.58×10^{-1}	2.00×10^{-1}	$+5.23 \times 10^{+0}$	$8.7 \times 10^{+0}$	3.6×10^{-1}
152	160	2.61×10^{-3}	7.54×10^{-1}	$1.54 \times 10^{+2}$	4.03×10^{-1}	6.84×10^{-2}	$+1.13 \times 10^{+1}$	$6.9 \times 10^{+0}$	3.6×10^{-1}
152	160	3.62×10^{-4}	1.05×10^{-1}	$1.54 \times 10^{+2}$	1.43×10^{-1}	2.00×10^{-1}	$-1.12 \times 10^{+1}$	$1.9 \times 10^{+1}$	9.4×10^{-1}
152	160	6.58×10^{-4}	1.90×10^{-1}	$1.54 \times 10^{+2}$	2.23×10^{-1}	2.00×10^{-1}	$+5.10 \times 10^{+1}$	$1.6 \times 10^{+1}$	$4.3 \times 10^{+0}$

Table F.24: $g_1^p(\nu, Q^2)$ from 2007 data (2/2).

ν		$\langle x \rangle$	$\langle Q^2 \rangle$	$\langle \nu \rangle$	R	$\sigma(R)$	g_1^p	$\sigma_{stat}(g_1^p)$	$\sigma_{syst}(g_1^p)$
16	24	1.01×10^{-2}	4.20×10^{-1}	$2.22 \times 10^{+1}$	3.35×10^{-1}	2.00×10^{-1}	-4.39×10^{-1}	9.1×10^{-1}	$1.7 \times 10^{+0}$
16	24	1.55×10^{-2}	6.45×10^{-1}	$2.22 \times 10^{+1}$	3.81×10^{-1}	5.63×10^{-2}	-4.41×10^{-2}	7.8×10^{-1}	9.5×10^{-1}
16	24	1.94×10^{-3}	8.06×10^{-2}	$2.22 \times 10^{+1}$	1.12×10^{-1}	2.00×10^{-1}	-3.13×10^{-1}	$2.0 \times 10^{+0}$	6.1×10^{-1}
16	24	2.12×10^{-2}	8.80×10^{-1}	$2.22 \times 10^{+1}$	3.92×10^{-1}	6.09×10^{-2}	$+5.75 \times 10^{-1}$	6.6×10^{-1}	9.5×10^{-1}
16	24	5.56×10^{-3}	2.31×10^{-1}	$2.22 \times 10^{+1}$	2.46×10^{-1}	2.00×10^{-1}	$+1.53 \times 10^{+0}$	9.7×10^{-1}	7.5×10^{-1}
24	32	1.06×10^{-2}	5.62×10^{-1}	$2.84 \times 10^{+1}$	3.71×10^{-1}	5.99×10^{-2}	$+1.57 \times 10^{+0}$	5.1×10^{-1}	3.8×10^{-1}
24	32	1.61×10^{-2}	8.47×10^{-1}	$2.83 \times 10^{+1}$	3.94×10^{-1}	6.22×10^{-2}	$+1.03 \times 10^{-1}$	4.2×10^{-1}	4.7×10^{-1}
24	32	2.94×10^{-3}	1.57×10^{-1}	$2.86 \times 10^{+1}$	1.90×10^{-1}	2.00×10^{-1}	$+3.29 \times 10^{-1}$	$1.1 \times 10^{+0}$	4.7×10^{-1}
24	32	5.99×10^{-3}	3.18×10^{-1}	$2.85 \times 10^{+1}$	2.96×10^{-1}	2.00×10^{-1}	$+6.37 \times 10^{-1}$	6.0×10^{-1}	5.2×10^{-1}
24	32	8.51×10^{-4}	4.59×10^{-2}	$2.90 \times 10^{+1}$	6.87×10^{-2}	2.00×10^{-1}	-8.39×10^{-2}	$1.4 \times 10^{+0}$	5.3×10^{-1}
32	40	1.13×10^{-3}	7.71×10^{-2}	$3.66 \times 10^{+1}$	1.09×10^{-1}	2.00×10^{-1}	$+1.36 \times 10^{+0}$	$1.1 \times 10^{+0}$	4.9×10^{-1}
32	40	1.14×10^{-2}	7.74×10^{-1}	$3.62 \times 10^{+1}$	3.94×10^{-1}	6.21×10^{-2}	$+4.06 \times 10^{-1}$	3.7×10^{-1}	4.9×10^{-1}
32	40	2.66×10^{-3}	1.81×10^{-1}	$3.65 \times 10^{+1}$	2.11×10^{-1}	2.00×10^{-1}	$+4.76 \times 10^{-1}$	8.9×10^{-1}	7.4×10^{-1}
32	40	2.70×10^{-4}	1.87×10^{-2}	$3.69 \times 10^{+1}$	2.98×10^{-2}	2.00×10^{-1}	$+1.34 \times 10^{+0}$	$1.2 \times 10^{+0}$	7.0×10^{-1}
32	40	5.84×10^{-3}	3.97×10^{-1}	$3.63 \times 10^{+1}$	3.29×10^{-1}	2.00×10^{-1}	-4.49×10^{-1}	4.8×10^{-1}	7.0×10^{-1}
40	48	1.21×10^{-3}	1.00×10^{-1}	$4.44 \times 10^{+1}$	1.36×10^{-1}	2.00×10^{-1}	$+7.64 \times 10^{-1}$	8.6×10^{-1}	7.2×10^{-1}
40	48	1.21×10^{-4}	1.02×10^{-2}	$4.48 \times 10^{+1}$	1.67×10^{-2}	2.00×10^{-1}	$+1.63 \times 10^{+0}$	$1.0 \times 10^{+0}$	7.7×10^{-1}
40	48	3.01×10^{-3}	2.50×10^{-1}	$4.43 \times 10^{+1}$	2.60×10^{-1}	2.00×10^{-1}	$+5.10 \times 10^{-1}$	4.2×10^{-1}	9.9×10^{-1}
40	48	4.54×10^{-4}	3.78×10^{-2}	$4.46 \times 10^{+1}$	5.80×10^{-2}	2.00×10^{-1}	$+6.80 \times 10^{-1}$	9.7×10^{-1}	$1.0 \times 10^{+0}$
40	48	8.07×10^{-3}	6.67×10^{-1}	$4.42 \times 10^{+1}$	3.88×10^{-1}	5.96×10^{-2}	$+5.75 \times 10^{-1}$	3.3×10^{-1}	$1.7 \times 10^{+0}$
48	56	1.72×10^{-3}	1.68×10^{-1}	$5.23 \times 10^{+1}$	2.02×10^{-1}	2.00×10^{-1}	-1.69×10^{-1}	6.6×10^{-1}	$1.3 \times 10^{+0}$
48	56	2.38×10^{-4}	2.34×10^{-2}	$5.25 \times 10^{+1}$	3.71×10^{-2}	2.00×10^{-1}	-4.48×10^{-1}	8.5×10^{-1}	$6.0 \times 10^{+0}$
48	56	5.73×10^{-3}	5.60×10^{-1}	$5.22 \times 10^{+1}$	3.74×10^{-1}	6.13×10^{-2}	$+8.62 \times 10^{-2}$	3.0×10^{-1}	$3.3 \times 10^{+1}$
48	56	6.30×10^{-4}	6.18×10^{-2}	$5.24 \times 10^{+1}$	9.03×10^{-2}	2.00×10^{-1}	-3.13×10^{-3}	7.9×10^{-1}	$1.0 \times 10^{+0}$
48	56	8.14×10^{-5}	8.02×10^{-3}	$5.25 \times 10^{+1}$	1.33×10^{-2}	2.00×10^{-1}	$+8.11 \times 10^{-1}$	8.6×10^{-1}	5.4×10^{-1}
56	64	1.15×10^{-3}	1.29×10^{-1}	$6.02 \times 10^{+1}$	1.67×10^{-1}	2.00×10^{-1}	$+2.89 \times 10^{-1}$	6.4×10^{-1}	8.9×10^{-1}
56	64	1.70×10^{-4}	1.92×10^{-2}	$6.03 \times 10^{+1}$	3.08×10^{-2}	2.00×10^{-1}	$+3.79 \times 10^{-1}$	7.8×10^{-1}	6.6×10^{-1}
56	64	4.16×10^{-4}	4.70×10^{-2}	$6.03 \times 10^{+1}$	7.09×10^{-2}	2.00×10^{-1}	$+9.04 \times 10^{-1}$	7.5×10^{-1}	7.2×10^{-1}
56	64	4.32×10^{-3}	4.87×10^{-1}	$6.02 \times 10^{+1}$	3.59×10^{-1}	2.00×10^{-1}	$+2.04 \times 10^{-1}$	2.9×10^{-1}	4.0×10^{-1}
56	64	6.91×10^{-5}	7.80×10^{-3}	$6.03 \times 10^{+1}$	1.30×10^{-2}	2.00×10^{-1}	$+7.79 \times 10^{-1}$	7.7×10^{-1}	4.7×10^{-1}
64	72	1.52×10^{-4}	1.94×10^{-2}	$6.82 \times 10^{+1}$	3.12×10^{-2}	2.00×10^{-1}	-3.35×10^{-1}	7.5×10^{-1}	7.3×10^{-1}
64	72	3.45×10^{-4}	4.41×10^{-2}	$6.82 \times 10^{+1}$	6.71×10^{-2}	2.00×10^{-1}	-3.48×10^{-1}	7.3×10^{-1}	4.9×10^{-1}
64	72	3.51×10^{-3}	4.48×10^{-1}	$6.81 \times 10^{+1}$	3.49×10^{-1}	2.00×10^{-1}	$+8.86 \times 10^{-2}$	3.0×10^{-1}	$1.0 \times 10^{+0}$
64	72	6.64×10^{-5}	8.48×10^{-3}	$6.81 \times 10^{+1}$	1.41×10^{-2}	2.00×10^{-1}	-7.62×10^{-2}	7.4×10^{-1}	4.7×10^{-1}
64	72	9.11×10^{-4}	1.16×10^{-1}	$6.82 \times 10^{+1}$	1.54×10^{-1}	2.00×10^{-1}	$+2.06 \times 10^{+0}$	6.4×10^{-1}	5.2×10^{-1}
72	80	1.53×10^{-4}	2.19×10^{-2}	$7.61 \times 10^{+1}$	3.51×10^{-2}	2.00×10^{-1}	$+6.75 \times 10^{-1}$	7.6×10^{-1}	7.8×10^{-1}
72	80	3.03×10^{-3}	4.33×10^{-1}	$7.61 \times 10^{+1}$	3.45×10^{-1}	2.00×10^{-1}	$+9.23 \times 10^{-2}$	3.0×10^{-1}	8.4×10^{-1}
72	80	3.34×10^{-4}	4.77×10^{-2}	$7.62 \times 10^{+1}$	7.21×10^{-2}	2.00×10^{-1}	$+1.82 \times 10^{+0}$	7.3×10^{-1}	9.3×10^{-1}
72	80	6.75×10^{-5}	9.62×10^{-3}	$7.60 \times 10^{+1}$	1.60×10^{-2}	2.00×10^{-1}	$-1.52 \times 10^{+0}$	7.4×10^{-1}	5.9×10^{-1}
72	80	8.26×10^{-4}	1.18×10^{-1}	$7.62 \times 10^{+1}$	1.56×10^{-1}	2.00×10^{-1}	$+1.50 \times 10^{+0}$	6.4×10^{-1}	9.6×10^{-1}
80	88	1.61×10^{-4}	2.54×10^{-2}	$8.41 \times 10^{+1}$	4.05×10^{-2}	2.00×10^{-1}	$+1.30 \times 10^{-1}$	7.8×10^{-1}	7.2×10^{-1}
80	88	2.75×10^{-3}	4.34×10^{-1}	$8.41 \times 10^{+1}$	3.46×10^{-1}	2.00×10^{-1}	$+3.43 \times 10^{-1}$	3.2×10^{-1}	$1.4 \times 10^{+0}$
80	88	3.48×10^{-4}	5.48×10^{-2}	$8.41 \times 10^{+1}$	8.18×10^{-2}	2.00×10^{-1}	-4.03×10^{-1}	7.5×10^{-1}	$1.4 \times 10^{+0}$
80	88	6.96×10^{-5}	1.10×10^{-2}	$8.40 \times 10^{+1}$	1.81×10^{-2}	2.00×10^{-1}	$+6.58 \times 10^{-1}$	7.6×10^{-1}	$1.2 \times 10^{+0}$
80	88	8.12×10^{-4}	1.28×10^{-1}	$8.41 \times 10^{+1}$	1.66×10^{-1}	2.00×10^{-1}	$+4.05 \times 10^{-3}$	6.5×10^{-1}	$2.9 \times 10^{+0}$
88	96	1.70×10^{-4}	2.93×10^{-2}	$9.20 \times 10^{+1}$	4.63×10^{-2}	2.00×10^{-1}	$+9.40 \times 10^{-1}$	8.1×10^{-1}	$2.4 \times 10^{+1}$
88	96	2.57×10^{-3}	4.44×10^{-1}	$9.21 \times 10^{+1}$	3.50×10^{-1}	2.00×10^{-1}	$+1.99 \times 10^{-1}$	3.3×10^{-1}	6.5×10^{-1}
88	96	3.66×10^{-4}	6.32×10^{-2}	$9.21 \times 10^{+1}$	9.29×10^{-2}	2.00×10^{-1}	$+9.23 \times 10^{-1}$	7.7×10^{-1}	3.2×10^{-1}
88	96	7.16×10^{-5}	1.24×10^{-2}	$9.20 \times 10^{+1}$	2.04×10^{-2}	2.00×10^{-1}	$+6.78 \times 10^{-1}$	7.9×10^{-1}	6.5×10^{-1}
88	96	8.23×10^{-4}	1.42×10^{-1}	$9.21 \times 10^{+1}$	1.80×10^{-1}	2.00×10^{-1}	$+1.27 \times 10^{+0}$	6.7×10^{-1}	7.3×10^{-1}
96	104	1.76×10^{-4}	3.31×10^{-2}	$1.00 \times 10^{+2}$	5.19×10^{-2}	2.00×10^{-1}	$+1.61 \times 10^{+0}$	8.5×10^{-1}	3.8×10^{-1}
96	104	2.46×10^{-3}	4.62×10^{-1}	$1.00 \times 10^{+2}$	3.55×10^{-1}	2.00×10^{-1}	$+4.49 \times 10^{-1}$	3.5×10^{-1}	3.5×10^{-1}
96	104	3.79×10^{-4}	7.11×10^{-2}	$1.00 \times 10^{+2}$	1.03×10^{-1}	2.00×10^{-1}	-1.47×10^{-1}	8.1×10^{-1}	6.4×10^{-1}
96	104	7.33×10^{-5}	1.38×10^{-2}	$1.00 \times 10^{+2}$	2.26×10^{-2}	2.00×10^{-1}	$+1.60 \times 10^{+0}$	8.3×10^{-1}	6.1×10^{-1}
96	104	8.34×10^{-4}	1.57×10^{-1}	$1.00 \times 10^{+2}$	1.93×10^{-1}	2.00×10^{-1}	$+1.49 \times 10^{-1}$	6.9×10^{-1}	4.7×10^{-1}
104	112	1.81×10^{-4}	3.66×10^{-2}	$1.08 \times 10^{+2}$	5.70×10^{-2}	2.00×10^{-1}	$+5.88 \times 10^{-1}$	9.0×10^{-1}	4.5×10^{-1}
104	112	2.40×10^{-3}	4.86×10^{-1}	$1.08 \times 10^{+2}$	3.62×10^{-1}	2.00×10^{-1}	$+9.82 \times 10^{-1}$	3.6×10^{-1}	4.6×10^{-1}

Table F.25: $g_1^p(\nu, Q^2)$ from 2011 data (1/2).

ν		$\langle x \rangle$	$\langle Q^2 \rangle$	$\langle \nu \rangle$	R	$\sigma(R)$	g_1^p	$\sigma_{stat}(g_1^p)$	$\sigma_{syst}(g_1^p)$
104	112	3.88×10^{-4}	7.87×10^{-2}	$1.08 \times 10^{+2}$	1.12×10^{-1}	2.00×10^{-1}	$+5.43 \times 10^{-1}$	8.4×10^{-1}	7.7×10^{-1}
104	112	7.47×10^{-5}	1.51×10^{-2}	$1.08 \times 10^{+2}$	2.48×10^{-2}	2.00×10^{-1}	$-1.23 \times 10^{+0}$	8.7×10^{-1}	5.2×10^{-1}
104	112	8.51×10^{-4}	1.72×10^{-1}	$1.08 \times 10^{+2}$	2.07×10^{-1}	2.00×10^{-1}	$+1.91 \times 10^{+0}$	7.2×10^{-1}	5.5×10^{-1}
112	120	1.90×10^{-4}	4.13×10^{-2}	$1.16 \times 10^{+2}$	6.38×10^{-2}	2.00×10^{-1}	$+3.37 \times 10^{-1}$	9.7×10^{-1}	8.3×10^{-1}
112	120	2.38×10^{-3}	5.18×10^{-1}	$1.16 \times 10^{+2}$	3.70×10^{-1}	6.76×10^{-2}	$+1.06 \times 10^{+0}$	3.8×10^{-1}	5.8×10^{-1}
112	120	4.06×10^{-4}	8.83×10^{-2}	$1.16 \times 10^{+2}$	1.24×10^{-1}	2.00×10^{-1}	$+1.02 \times 10^{+0}$	9.0×10^{-1}	6.0×10^{-1}
112	120	7.82×10^{-5}	1.70×10^{-2}	$1.16 \times 10^{+2}$	2.78×10^{-2}	2.00×10^{-1}	$+1.06 \times 10^{+0}$	9.3×10^{-1}	5.6×10^{-1}
112	120	8.81×10^{-4}	1.92×10^{-1}	$1.16 \times 10^{+2}$	2.23×10^{-1}	2.00×10^{-1}	$+2.27 \times 10^{+0}$	7.5×10^{-1}	$1.4 \times 10^{+0}$
120	128	2.05×10^{-4}	4.78×10^{-2}	$1.24 \times 10^{+2}$	7.28×10^{-2}	2.00×10^{-1}	$+1.92 \times 10^{+0}$	$1.0 \times 10^{+0}$	5.1×10^{-1}
120	128	2.39×10^{-3}	5.55×10^{-1}	$1.24 \times 10^{+2}$	3.78×10^{-1}	6.34×10^{-2}	$+4.19 \times 10^{-1}$	4.1×10^{-1}	$1.2 \times 10^{+0}$
120	128	4.35×10^{-4}	1.01×10^{-1}	$1.24 \times 10^{+2}$	1.39×10^{-1}	2.00×10^{-1}	$+9.26 \times 10^{-1}$	9.5×10^{-1}	$1.7 \times 10^{+0}$
120	128	8.61×10^{-5}	2.00×10^{-2}	$1.24 \times 10^{+2}$	3.25×10^{-2}	2.00×10^{-1}	$+6.51 \times 10^{-1}$	$1.0 \times 10^{+0}$	$1.9 \times 10^{+1}$
120	128	9.34×10^{-4}	2.17×10^{-1}	$1.24 \times 10^{+2}$	2.43×10^{-1}	2.00×10^{-1}	-3.95×10^{-1}	5.2×10^{-1}	3.4×10^{-1}
128	136	2.18×10^{-4}	5.40×10^{-2}	$1.32 \times 10^{+2}$	8.13×10^{-2}	2.00×10^{-1}	$+1.11 \times 10^{+0}$	$1.1 \times 10^{+0}$	5.1×10^{-1}
128	136	2.37×10^{-3}	5.87×10^{-1}	$1.32 \times 10^{+2}$	3.84×10^{-1}	6.20×10^{-2}	$+1.87 \times 10^{-1}$	4.4×10^{-1}	2.9×10^{-1}
128	136	4.49×10^{-4}	1.11×10^{-1}	$1.32 \times 10^{+2}$	1.50×10^{-1}	2.00×10^{-1}	$+7.37 \times 10^{-1}$	$1.0 \times 10^{+0}$	3.0×10^{-1}
128	136	9.57×10^{-4}	2.37×10^{-1}	$1.32 \times 10^{+2}$	2.56×10^{-1}	2.00×10^{-1}	-4.50×10^{-1}	5.7×10^{-1}	5.0×10^{-1}
128	136	9.61×10^{-5}	2.38×10^{-2}	$1.32 \times 10^{+2}$	3.83×10^{-2}	2.00×10^{-1}	$+1.33 \times 10^{+0}$	$1.1 \times 10^{+0}$	3.1×10^{-1}
136	144	1.08×10^{-4}	2.83×10^{-2}	$1.40 \times 10^{+2}$	4.51×10^{-2}	2.00×10^{-1}	-7.39×10^{-1}	$1.2 \times 10^{+0}$	4.0×10^{-1}
136	144	2.29×10^{-3}	6.01×10^{-1}	$1.40 \times 10^{+2}$	3.87×10^{-1}	6.21×10^{-2}	$+2.87 \times 10^{-1}$	4.7×10^{-1}	4.4×10^{-1}
136	144	2.31×10^{-4}	6.08×10^{-2}	$1.40 \times 10^{+2}$	9.03×10^{-2}	2.00×10^{-1}	$-1.19 \times 10^{+0}$	$1.2 \times 10^{+0}$	3.1×10^{-1}
136	144	4.57×10^{-4}	1.20×10^{-1}	$1.40 \times 10^{+2}$	1.59×10^{-1}	2.00×10^{-1}	$-2.46 \times 10^{+0}$	$1.1 \times 10^{+0}$	4.4×10^{-1}
136	144	9.46×10^{-4}	2.48×10^{-1}	$1.40 \times 10^{+2}$	2.64×10^{-1}	2.00×10^{-1}	$+1.18 \times 10^{+0}$	6.3×10^{-1}	4.6×10^{-1}
144	152	1.24×10^{-4}	3.44×10^{-2}	$1.48 \times 10^{+2}$	5.41×10^{-2}	2.00×10^{-1}	$+2.79 \times 10^{+0}$	$1.4 \times 10^{+0}$	5.9×10^{-1}
144	152	2.19×10^{-3}	6.09×10^{-1}	$1.48 \times 10^{+2}$	3.88×10^{-1}	6.22×10^{-2}	-1.21×10^{-1}	5.1×10^{-1}	4.4×10^{-1}
144	152	2.55×10^{-4}	7.07×10^{-2}	$1.48 \times 10^{+2}$	1.03×10^{-1}	2.00×10^{-1}	-8.55×10^{-1}	$1.3 \times 10^{+0}$	3.2×10^{-1}
144	152	4.84×10^{-4}	1.34×10^{-1}	$1.48 \times 10^{+2}$	1.74×10^{-1}	2.00×10^{-1}	$+3.04 \times 10^{-1}$	$1.2 \times 10^{+0}$	3.7×10^{-1}
144	152	9.59×10^{-4}	2.66×10^{-1}	$1.48 \times 10^{+2}$	2.75×10^{-1}	2.00×10^{-1}	$+8.35 \times 10^{-1}$	6.9×10^{-1}	4.8×10^{-1}
152	160	1.01×10^{-3}	2.97×10^{-1}	$1.56 \times 10^{+2}$	2.92×10^{-1}	2.00×10^{-1}	-1.70×10^{-1}	7.5×10^{-1}	5.5×10^{-1}
152	160	1.46×10^{-4}	4.28×10^{-2}	$1.56 \times 10^{+2}$	6.61×10^{-2}	2.00×10^{-1}	$+1.39 \times 10^{+0}$	$1.5 \times 10^{+0}$	4.3×10^{-1}
152	160	2.16×10^{-3}	6.34×10^{-1}	$1.56 \times 10^{+2}$	3.92×10^{-1}	6.29×10^{-2}	$+1.71 \times 10^{-1}$	5.6×10^{-1}	4.0×10^{-1}
152	160	2.88×10^{-4}	8.41×10^{-2}	$1.56 \times 10^{+2}$	1.20×10^{-1}	2.00×10^{-1}	$+1.51 \times 10^{+0}$	$1.4 \times 10^{+0}$	6.8×10^{-1}
152	160	5.27×10^{-4}	1.54×10^{-1}	$1.56 \times 10^{+2}$	1.93×10^{-1}	2.00×10^{-1}	-7.14×10^{-1}	$1.3 \times 10^{+0}$	7.5×10^{-1}
160	168	1.08×10^{-3}	3.33×10^{-1}	$1.64 \times 10^{+2}$	3.11×10^{-1}	2.00×10^{-1}	-4.22×10^{-1}	8.3×10^{-1}	$1.7 \times 10^{+0}$
160	168	1.77×10^{-4}	5.43×10^{-2}	$1.64 \times 10^{+2}$	8.19×10^{-2}	2.00×10^{-1}	$+1.01 \times 10^{+0}$	$1.7 \times 10^{+0}$	$1.8 \times 10^{+1}$
160	168	2.16×10^{-3}	6.66×10^{-1}	$1.64 \times 10^{+2}$	3.96×10^{-1}	6.43×10^{-2}	-7.14×10^{-1}	6.2×10^{-1}	3.3×10^{-1}
160	168	3.33×10^{-4}	1.02×10^{-1}	$1.64 \times 10^{+2}$	1.41×10^{-1}	2.00×10^{-1}	$+2.25 \times 10^{+0}$	$1.6 \times 10^{+0}$	2.0×10^{-1}
160	168	5.87×10^{-4}	1.81×10^{-1}	$1.64 \times 10^{+2}$	2.16×10^{-1}	2.00×10^{-1}	$+1.62 \times 10^{+0}$	$1.4 \times 10^{+0}$	1.7×10^{-1}
168	176	1.20×10^{-3}	3.87×10^{-1}	$1.72 \times 10^{+2}$	3.33×10^{-1}	2.00×10^{-1}	$+1.07 \times 10^{+0}$	9.7×10^{-1}	1.8×10^{-1}
168	176	2.17×10^{-4}	6.97×10^{-2}	$1.71 \times 10^{+2}$	1.02×10^{-1}	2.00×10^{-1}	$+2.58 \times 10^{-1}$	$2.0 \times 10^{+0}$	2.3×10^{-1}
168	176	2.19×10^{-3}	7.05×10^{-1}	$1.72 \times 10^{+2}$	4.00×10^{-1}	6.64×10^{-2}	$+1.00 \times 10^{+0}$	7.4×10^{-1}	1.4×10^{-1}
168	176	4.03×10^{-4}	1.30×10^{-1}	$1.72 \times 10^{+2}$	1.70×10^{-1}	2.00×10^{-1}	$-1.02 \times 10^{+0}$	$1.8 \times 10^{+0}$	1.4×10^{-1}
168	176	6.95×10^{-4}	2.24×10^{-1}	$1.72 \times 10^{+2}$	2.49×10^{-1}	2.00×10^{-1}	-4.81×10^{-2}	$1.1 \times 10^{+0}$	2.9×10^{-1}
176	184	1.33×10^{-3}	4.47×10^{-1}	$1.79 \times 10^{+2}$	3.54×10^{-1}	2.00×10^{-1}	$+1.65 \times 10^{+0}$	$1.4 \times 10^{+0}$	2.5×10^{-1}
176	184	2.21×10^{-3}	7.45×10^{-1}	$1.79 \times 10^{+2}$	4.03×10^{-1}	6.86×10^{-2}	$+6.16 \times 10^{-1}$	$1.1 \times 10^{+0}$	1.6×10^{-1}
176	184	2.63×10^{-4}	8.83×10^{-2}	$1.79 \times 10^{+2}$	1.25×10^{-1}	2.00×10^{-1}	$+1.06 \times 10^{+0}$	$3.0 \times 10^{+0}$	1.7×10^{-1}
176	184	4.95×10^{-4}	1.66×10^{-1}	$1.79 \times 10^{+2}$	2.04×10^{-1}	2.00×10^{-1}	$+2.44 \times 10^{+0}$	$2.5 \times 10^{+0}$	2.1×10^{-1}
176	184	8.35×10^{-4}	2.81×10^{-1}	$1.79 \times 10^{+2}$	2.85×10^{-1}	2.00×10^{-1}	$+4.22 \times 10^{+0}$	$1.6 \times 10^{+0}$	2.4×10^{-1}
184	192	1.46×10^{-3}	5.11×10^{-1}	$1.87 \times 10^{+2}$	3.71×10^{-1}	6.93×10^{-2}	$+6.52 \times 10^{+0}$	$3.0 \times 10^{+0}$	3.2×10^{-1}
184	192	2.24×10^{-3}	7.83×10^{-1}	$1.87 \times 10^{+2}$	4.05×10^{-1}	7.04×10^{-2}	$-1.73 \times 10^{+0}$	$2.4 \times 10^{+0}$	3.5×10^{-1}
184	192	3.30×10^{-4}	1.15×10^{-1}	$1.86 \times 10^{+2}$	1.55×10^{-1}	2.00×10^{-1}	$+2.87 \times 10^{+0}$	$6.5 \times 10^{+0}$	2.4×10^{-1}
184	192	6.15×10^{-4}	2.15×10^{-1}	$1.86 \times 10^{+2}$	2.43×10^{-1}	2.00×10^{-1}	$+8.31 \times 10^{+0}$	$3.8 \times 10^{+0}$	3.7×10^{-1}
184	192	9.88×10^{-4}	3.46×10^{-1}	$1.86 \times 10^{+2}$	3.17×10^{-1}	2.00×10^{-1}	-1.50×10^{-1}	$3.5 \times 10^{+0}$	2.7×10^{-1}
192	200	1.13×10^{-3}	4.08×10^{-1}	$1.93 \times 10^{+2}$	3.42×10^{-1}	2.00×10^{-1}	$+1.62 \times 10^{+1}$	$4.9 \times 10^{+1}$	3.1×10^{-1}
192	200	1.61×10^{-3}	5.80×10^{-1}	$1.92 \times 10^{+2}$	3.85×10^{-1}	6.31×10^{-2}	$-6.54 \times 10^{+0}$	$4.5 \times 10^{+1}$	5.1×10^{-1}
192	200	2.26×10^{-3}	8.18×10^{-1}	$1.93 \times 10^{+2}$	4.06×10^{-1}	7.18×10^{-2}	$-2.05 \times 10^{+1}$	$3.6 \times 10^{+1}$	4.9×10^{-1}
192	200	4.06×10^{-4}	1.47×10^{-1}	$1.92 \times 10^{+2}$	1.86×10^{-1}	2.00×10^{-1}	$+7.38 \times 10^{+1}$	$8.7 \times 10^{+1}$	$2.0 \times 10^{+0}$
192	200	7.31×10^{-4}	2.64×10^{-1}	$1.92 \times 10^{+2}$	2.75×10^{-1}	2.00×10^{-1}	$-2.57 \times 10^{+1}$	$5.7 \times 10^{+1}$	$1.2 \times 10^{+1}$

Table F.26: $g_1^p(\nu, Q^2)$ from 2011 data (2/2).

$\log_{10}(x)$		$\langle x \rangle$	$\langle Q^2 \rangle$	$\langle \nu \rangle$	R	$\sigma(R)$	g_1^p	$\sigma_{stat}(g_1^p)$	$\sigma_{syst}(g_1^p)$
−4.4	−4.2	5.10×10^{-5}	3.65×10^{-3}	$3.81 \times 10^{+1}$	6.16×10^{-3}	2.00×10^{-1}	-2.01×10^{-1}	4.0×10^{-1}	4.5×10^{-1}
−4.4	−4.2	5.10×10^{-5}	6.19×10^{-3}	$6.46 \times 10^{+1}$	1.04×10^{-2}	2.00×10^{-1}	$+7.20 \times 10^{-1}$	6.7×10^{-1}	3.0×10^{-1}
−4.4	−4.2	5.10×10^{-5}	5.11×10^{-3}	$5.34 \times 10^{+1}$	8.60×10^{-3}	2.00×10^{-1}	$+1.04 \times 10^{-1}$	5.5×10^{-1}	4.1×10^{-1}
−4.4	−4.2	5.11×10^{-5}	7.18×10^{-3}	$7.49 \times 10^{+1}$	1.20×10^{-2}	2.00×10^{-1}	$+8.44 \times 10^{-1}$	7.7×10^{-1}	3.0×10^{-1}
−4.4	−4.2	5.39×10^{-5}	8.90×10^{-3}	$8.78 \times 10^{+1}$	1.48×10^{-2}	2.00×10^{-1}	$+1.84 \times 10^{+0}$	9.1×10^{-1}	2.0×10^{-1}
−4.2	−4.0	8.05×10^{-5}	6.15×10^{-3}	$4.07 \times 10^{+1}$	1.03×10^{-2}	2.00×10^{-1}	$+1.41 \times 10^{-1}$	3.4×10^{-1}	2.6×10^{-1}
−4.2	−4.0	8.05×10^{-5}	8.86×10^{-3}	$5.86 \times 10^{+1}$	1.47×10^{-2}	2.00×10^{-1}	$+9.92 \times 10^{-1}$	4.8×10^{-1}	2.6×10^{-1}
−4.2	−4.0	8.06×10^{-5}	1.09×10^{-2}	$7.20 \times 10^{+1}$	1.80×10^{-2}	2.00×10^{-1}	$+1.12 \times 10^{+0}$	5.9×10^{-1}	2.9×10^{-1}
−4.2	−4.0	8.07×10^{-5}	1.29×10^{-2}	$8.54 \times 10^{+1}$	2.13×10^{-2}	2.00×10^{-1}	$+5.27 \times 10^{-1}$	6.9×10^{-1}	1.8×10^{-1}
−4.2	−4.0	8.35×10^{-5}	1.60×10^{-2}	$1.02 \times 10^{+2}$	2.62×10^{-2}	2.00×10^{-1}	-1.23×10^{-1}	7.9×10^{-1}	1.1×10^{-1}
−4.0	−3.8	1.27×10^{-4}	1.02×10^{-2}	$4.29 \times 10^{+1}$	1.68×10^{-2}	2.00×10^{-1}	$+4.98 \times 10^{-1}$	3.0×10^{-1}	1.7×10^{-1}
−4.0	−3.8	1.27×10^{-4}	1.51×10^{-2}	$6.31 \times 10^{+1}$	2.45×10^{-2}	2.00×10^{-1}	$+7.14 \times 10^{-1}$	4.4×10^{-1}	1.2×10^{-1}
−4.0	−3.8	1.27×10^{-4}	1.88×10^{-2}	$7.87 \times 10^{+1}$	3.04×10^{-2}	2.00×10^{-1}	$+7.78 \times 10^{-1}$	5.5×10^{-1}	1.5×10^{-1}
−4.0	−3.8	1.27×10^{-4}	2.28×10^{-2}	$9.55 \times 10^{+1}$	3.66×10^{-2}	2.00×10^{-1}	$+5.23 \times 10^{-1}$	6.5×10^{-1}	2.8×10^{-1}
−4.0	−3.8	1.30×10^{-4}	2.79×10^{-2}	$1.14 \times 10^{+2}$	4.44×10^{-2}	2.00×10^{-1}	$+1.42 \times 10^{+0}$	7.5×10^{-1}	5.7×10^{-1}
−3.8	−3.6	2.01×10^{-4}	1.67×10^{-2}	$4.44 \times 10^{+1}$	2.70×10^{-2}	2.00×10^{-1}	$+5.99 \times 10^{-1}$	2.9×10^{-1}	3.8×10^{-1}
−3.8	−3.6	2.01×10^{-4}	3.87×10^{-2}	$1.03 \times 10^{+2}$	5.99×10^{-2}	2.00×10^{-1}	$+9.48 \times 10^{-1}$	6.2×10^{-1}	5.8×10^{-1}
−3.8	−3.6	2.01×10^{-4}	2.50×10^{-2}	$6.61 \times 10^{+1}$	3.96×10^{-2}	2.00×10^{-1}	$+4.51 \times 10^{-1}$	4.2×10^{-1}	3.7×10^{-1}
−3.8	−3.6	2.01×10^{-4}	3.16×10^{-2}	$8.37 \times 10^{+1}$	4.96×10^{-2}	2.00×10^{-1}	$+3.22 \times 10^{-1}$	5.2×10^{-1}	2.8×10^{-1}
−3.8	−3.6	2.04×10^{-4}	4.73×10^{-2}	$1.23 \times 10^{+2}$	7.21×10^{-2}	2.00×10^{-1}	$+9.09 \times 10^{-1}$	7.2×10^{-1}	5.3×10^{-1}
−3.6	−3.4	3.18×10^{-4}	4.02×10^{-2}	$6.74 \times 10^{+1}$	6.17×10^{-2}	2.00×10^{-1}	$+6.50 \times 10^{-1}$	4.1×10^{-1}	2.4×10^{-1}
−3.6	−3.4	3.18×10^{-4}	2.68×10^{-2}	$4.49 \times 10^{+1}$	4.21×10^{-2}	2.00×10^{-1}	$+8.51 \times 10^{-2}$	2.8×10^{-1}	2.0×10^{-1}
−3.6	−3.4	3.18×10^{-4}	6.34×10^{-2}	$1.06 \times 10^{+2}$	9.33×10^{-2}	2.00×10^{-1}	$+1.39 \times 10^{+0}$	5.8×10^{-1}	2.0×10^{-1}
−3.6	−3.4	3.19×10^{-4}	5.14×10^{-2}	$8.61 \times 10^{+1}$	7.73×10^{-2}	2.00×10^{-1}	$+3.38 \times 10^{-1}$	4.9×10^{-1}	1.9×10^{-1}
−3.6	−3.4	3.19×10^{-4}	7.62×10^{-2}	$1.27 \times 10^{+2}$	1.10×10^{-1}	2.00×10^{-1}	-6.16×10^{-2}	6.8×10^{-1}	1.8×10^{-1}
−3.4	−3.2	5.03×10^{-4}	4.25×10^{-2}	$4.50 \times 10^{+1}$	6.44×10^{-2}	2.00×10^{-1}	$+6.03 \times 10^{-1}$	2.8×10^{-1}	1.7×10^{-1}
−3.4	−3.2	5.03×10^{-4}	1.01×10^{-1}	$1.07 \times 10^{+2}$	1.38×10^{-1}	2.00×10^{-1}	$+5.61 \times 10^{-1}$	5.3×10^{-1}	2.3×10^{-1}
−3.4	−3.2	5.03×10^{-4}	8.19×10^{-2}	$8.67 \times 10^{+1}$	1.16×10^{-1}	2.00×10^{-1}	$+7.73 \times 10^{-1}$	4.7×10^{-1}	2.4×10^{-1}
−3.4	−3.2	5.04×10^{-4}	6.45×10^{-2}	$6.82 \times 10^{+1}$	9.40×10^{-2}	2.00×10^{-1}	$+1.03 \times 10^{+0}$	4.0×10^{-1}	1.9×10^{-1}
−3.4	−3.2	5.04×10^{-4}	1.21×10^{-1}	$1.28 \times 10^{+2}$	1.60×10^{-1}	2.00×10^{-1}	$+1.70 \times 10^{+0}$	6.2×10^{-1}	4.9×10^{-1}
−3.2	−3.0	7.93×10^{-4}	1.91×10^{-1}	$1.29 \times 10^{+2}$	2.23×10^{-1}	2.00×10^{-1}	$+8.93 \times 10^{-1}$	5.5×10^{-1}	3.5×10^{-1}
−3.2	−3.0	7.93×10^{-4}	1.59×10^{-1}	$1.07 \times 10^{+2}$	1.96×10^{-1}	2.00×10^{-1}	$+1.69 \times 10^{+0}$	5.0×10^{-1}	4.7×10^{-1}
−3.2	−3.0	7.94×10^{-4}	1.02×10^{-1}	$6.83 \times 10^{+1}$	1.38×10^{-1}	2.00×10^{-1}	$+5.91 \times 10^{-1}$	3.8×10^{-1}	3.4×10^{-1}
−3.2	−3.0	7.96×10^{-4}	6.64×10^{-2}	$4.45 \times 10^{+1}$	9.59×10^{-2}	2.00×10^{-1}	$+9.37 \times 10^{-1}$	2.7×10^{-1}	3.1×10^{-1}
−3.2	−3.0	7.96×10^{-4}	1.30×10^{-1}	$8.69 \times 10^{+1}$	1.68×10^{-1}	2.00×10^{-1}	$+9.90 \times 10^{-1}$	4.4×10^{-1}	2.7×10^{-1}
−3.0	−2.8	1.25×10^{-3}	1.61×10^{-1}	$6.84 \times 10^{+1}$	1.96×10^{-1}	2.00×10^{-1}	$+2.84 \times 10^{-1}$	3.6×10^{-1}	2.5×10^{-1}
−3.0	−2.8	1.26×10^{-3}	1.02×10^{-1}	$4.34 \times 10^{+1}$	1.38×10^{-1}	2.00×10^{-1}	$+3.45 \times 10^{-1}$	2.7×10^{-1}	3.6×10^{-1}
−3.0	−2.8	1.26×10^{-3}	2.06×10^{-1}	$8.70 \times 10^{+1}$	2.33×10^{-1}	2.00×10^{-1}	$+2.33 \times 10^{-1}$	2.5×10^{-1}	2.2×10^{-1}
−3.0	−2.8	1.26×10^{-3}	3.05×10^{-1}	$1.29 \times 10^{+2}$	2.96×10^{-1}	2.00×10^{-1}	$+1.19 \times 10^{+0}$	3.5×10^{-1}	1.3×10^{-1}
−3.0	−2.8	1.26×10^{-3}	2.52×10^{-1}	$1.07 \times 10^{+2}$	2.65×10^{-1}	2.00×10^{-1}	$+4.89 \times 10^{-1}$	3.0×10^{-1}	1.8×10^{-1}
−2.8	−2.6	1.98×10^{-3}	2.57×10^{-1}	$6.91 \times 10^{+1}$	2.66×10^{-1}	2.00×10^{-1}	$+5.36 \times 10^{-1}$	2.2×10^{-1}	2.8×10^{-1}
−2.8	−2.6	1.99×10^{-3}	3.32×10^{-1}	$8.89 \times 10^{+1}$	3.07×10^{-1}	2.00×10^{-1}	$+2.46 \times 10^{-1}$	2.6×10^{-1}	1.4×10^{-1}
−2.8	−2.6	1.99×10^{-3}	4.84×10^{-1}	$1.29 \times 10^{+2}$	3.62×10^{-1}	2.00×10^{-1}	$+4.17 \times 10^{-1}$	3.4×10^{-1}	3.5×10^{-1}
−2.8	−2.6	1.99×10^{-3}	1.57×10^{-1}	$4.21 \times 10^{+1}$	1.92×10^{-1}	2.00×10^{-1}	$+2.40 \times 10^{-1}$	2.5×10^{-1}	2.0×10^{-1}
−2.8	−2.6	1.99×10^{-3}	4.04×10^{-1}	$1.08 \times 10^{+2}$	3.37×10^{-1}	2.00×10^{-1}	$+4.71 \times 10^{-1}$	3.0×10^{-1}	8.7×10^{-1}
−2.6	−2.4	3.14×10^{-3}	7.60×10^{-1}	$1.29 \times 10^{+2}$	4.02×10^{-1}	6.79×10^{-2}	$+4.04 \times 10^{-1}$	3.1×10^{-1}	4.2×10^{-1}
−2.6	−2.4	3.14×10^{-3}	4.08×10^{-1}	$6.92 \times 10^{+1}$	3.36×10^{-1}	2.00×10^{-1}	$+7.05 \times 10^{-1}$	2.2×10^{-1}	6.3×10^{-1}
−2.6	−2.4	3.14×10^{-3}	5.30×10^{-1}	$8.99 \times 10^{+1}$	3.71×10^{-1}	6.54×10^{-2}	$+2.67 \times 10^{-1}$	2.6×10^{-1}	3.9×10^{-1}
−2.6	−2.4	3.15×10^{-3}	2.42×10^{-1}	$4.09 \times 10^{+1}$	2.55×10^{-1}	2.00×10^{-1}	$+1.52 \times 10^{-1}$	1.5×10^{-1}	5.5×10^{-1}
−2.6	−2.4	3.15×10^{-3}	6.41×10^{-1}	$1.08 \times 10^{+2}$	3.91×10^{-1}	6.20×10^{-2}	$+1.68 \times 10^{-1}$	2.8×10^{-1}	6.4×10^{-1}
−2.4	−2.2	4.42×10^{-3}	9.00×10^{-1}	$1.09 \times 10^{+2}$	4.04×10^{-1}	7.09×10^{-2}	$+1.94 \times 10^{-1}$	3.3×10^{-1}	2.9×10^{-1}
−2.4	−2.2	4.86×10^{-3}	8.10×10^{-1}	$8.89 \times 10^{+1}$	4.01×10^{-1}	6.79×10^{-2}	$+5.34 \times 10^{-1}$	2.8×10^{-1}	4.3×10^{-1}
−2.4	−2.2	5.01×10^{-3}	6.88×10^{-1}	$7.33 \times 10^{+1}$	3.93×10^{-1}	6.24×10^{-2}	$+3.83 \times 10^{-1}$	2.5×10^{-1}	2.8×10^{-1}
−2.4	−2.2	5.01×10^{-3}	3.23×10^{-1}	$3.44 \times 10^{+1}$	2.99×10^{-1}	2.00×10^{-1}	$+4.09 \times 10^{-1}$	1.7×10^{-1}	1.7×10^{-1}
−2.4	−2.2	5.01×10^{-3}	5.27×10^{-1}	$5.61 \times 10^{+1}$	3.68×10^{-1}	6.51×10^{-2}	-3.51×10^{-2}	2.3×10^{-1}	1.6×10^{-1}
−2.2	−2.0	6.97×10^{-3}	9.09×10^{-1}	$6.98 \times 10^{+1}$	4.01×10^{-1}	6.86×10^{-2}	$+9.00 \times 10^{-1}$	3.4×10^{-1}	2.2×10^{-1}
−2.2	−2.0	7.69×10^{-3}	8.29×10^{-1}	$5.74 \times 10^{+1}$	3.99×10^{-1}	6.62×10^{-2}	$+4.58 \times 10^{-1}$	2.9×10^{-1}	1.7×10^{-1}
−2.2	−2.0	7.99×10^{-3}	3.99×10^{-1}	$2.66 \times 10^{+1}$	3.29×10^{-1}	2.00×10^{-1}	$+3.74 \times 10^{-1}$	2.0×10^{-1}	3.5×10^{-1}
−2.2	−2.0	8.00×10^{-3}	7.30×10^{-1}	$4.86 \times 10^{+1}$	3.94×10^{-1}	6.22×10^{-2}	$+2.16 \times 10^{-1}$	2.6×10^{-1}	2.4×10^{-1}
−2.2	−2.0	8.00×10^{-3}	5.88×10^{-1}	$3.92 \times 10^{+1}$	3.77×10^{-1}	5.90×10^{-2}	$+6.83 \times 10^{-1}$	2.4×10^{-1}	$1.2 \times 10^{+0}$
−2.0	−1.8	1.09×10^{-2}	9.18×10^{-1}	$4.49 \times 10^{+1}$	3.98×10^{-1}	6.60×10^{-2}	-4.64×10^{-2}	3.6×10^{-1}	5.3×10^{-1}
−2.0	−1.8	1.19×10^{-2}	8.43×10^{-1}	$3.77 \times 10^{+1}$	3.96×10^{-1}	6.40×10^{-2}	-1.96×10^{-1}	3.2×10^{-1}	8.0×10^{-1}
−2.0	−1.8	1.26×10^{-2}	7.76×10^{-1}	$3.28 \times 10^{+1}$	3.94×10^{-1}	6.16×10^{-2}	$+7.74 \times 10^{-1}$	3.0×10^{-1}	4.2×10^{-1}
−2.0	−1.8	1.27×10^{-2}	6.64×10^{-1}	$2.79 \times 10^{+1}$	3.85×10^{-1}	5.76×10^{-2}	$+3.52 \times 10^{-1}$	2.8×10^{-1}	4.5×10^{-1}
−2.0	−1.8	1.27×10^{-2}	5.06×10^{-1}	$2.12 \times 10^{+1}$	3.58×10^{-1}	6.76×10^{-2}	$+4.47 \times 10^{-1}$	2.5×10^{-1}	6.9×10^{-1}
−1.8	−1.6	1.70×10^{-2}	9.33×10^{-1}	$2.93 \times 10^{+1}$	3.95×10^{-1}	6.32×10^{-2}	-4.23×10^{-1}	4.6×10^{-1}	3.9×10^{-1}
−1.8	−1.6	1.82×10^{-2}	8.72×10^{-1}	$2.55 \times 10^{+1}$	3.94×10^{-1}	6.18×10^{-2}	-2.16×10^{-1}	4.3×10^{-1}	3.5×10^{-1}
−1.8	−1.6	1.93×10^{-2}	8.28×10^{-1}	$2.29 \times 10^{+1}$	3.92×10^{-1}	6.05×10^{-2}	$+4.93 \times 10^{-1}$	4.0×10^{-1}	3.5×10^{-1}
−1.8	−1.6	2.01×10^{-2}	7.70×10^{-1}	$2.04 \times 10^{+1}$	3.89×10^{-1}	5.86×10^{-2}	$+2.51 \times 10^{-1}$	3.6×10^{-1}	2.4×10^{-1}
−1.8	−1.6	2.02×10^{-2}	6.65×10^{-1}	$1.76 \times 10^{+1}$	3.81×10^{-1}	5.55×10^{-2}	$+6.30 \times 10^{-1}$	3.5×10^{-1}	1.5×10^{-1}
−1.6	−1.4	2.61×10^{-2}	9.63×10^{-1}	$1.97 \times 10^{+1}$	3.90×10^{-1}	6.01×10^{-2}	$+1.11 \times 10^{+0}$	9.5×10^{-1}	2.3×10^{-1}
−1.6	−1.4	2.70×10^{-2}	9.33×10^{-1}	$1.84 \times 10^{+1}$	3.90×10^{-1}	5.96×10^{-2}	-3.30×10^{-1}	9.7×10^{-1}	2.1×10^{-1}
−1.6	−1.4	2.76×10^{-2}	9.12×10^{-1}	$1.76 \times 10^{+1}$	3.90×10^{-1}	5.92×10^{-2}	-1.84×10^{-1}	9.0×10^{-1}	2.0×10^{-1}
−1.6	−1.4	2.82×10^{-2}	8.93×10^{-1}	$1.69 \times 10^{+1}$	3.89×10^{-1}	5.88×10^{-2}	$+3.26 \times 10^{-1}$	8.9×10^{-1}	3.9×10^{-1}
−1.6	−1.4	2.90×10^{-2}	8.70×10^{-1}	$1.60 \times 10^{+1}$	3.88×10^{-1}	5.83×10^{-2}	-2.99×10^{-1}	8.4×10^{-1}	5.4×10^{-1}

Table F.27: $g_1^p(x, \nu)$ from 2007 data.

$\log_{10}(x)$		$\langle x \rangle$	$\langle Q^2 \rangle$	$\langle \nu \rangle$	R	$\sigma(R)$	g_1^p	$\sigma_{stat}(g_1^p)$	$\sigma_{syst}(g_1^p)$
−4.4	−4.2	5.09×10^{-5}	5.98×10^{-3}	$6.26 \times 10^{+1}$	1.00×10^{-2}	2.00×10^{-1}	$+2.16 \times 10^{-2}$	6.7×10^{-1}	7.4×10^{-1}
−4.4	−4.2	5.09×10^{-5}	7.66×10^{-3}	$8.02 \times 10^{+1}$	1.28×10^{-2}	2.00×10^{-1}	-4.47×10^{-1}	8.6×10^{-1}	2.8×10^{-1}
−4.4	−4.2	5.09×10^{-5}	8.95×10^{-3}	$9.37 \times 10^{+1}$	1.49×10^{-2}	2.00×10^{-1}	$+9.08 \times 10^{-1}$	$1.0 \times 10^{+0}$	2.7×10^{-1}
−4.4	−4.2	5.09×10^{-5}	1.02×10^{-2}	$1.06 \times 10^{+2}$	1.70×10^{-2}	2.00×10^{-1}	$+1.40 \times 10^{+0}$	$1.1 \times 10^{+0}$	4.3×10^{-1}
−4.4	−4.2	5.35×10^{-5}	1.23×10^{-2}	$1.22 \times 10^{+2}$	2.04×10^{-2}	2.00×10^{-1}	$+2.51 \times 10^{+0}$	$1.3 \times 10^{+0}$	3.7×10^{-1}
−4.2	−4.0	8.03×10^{-5}	9.85×10^{-3}	$6.54 \times 10^{+1}$	1.63×10^{-2}	2.00×10^{-1}	$+5.32 \times 10^{-1}$	5.7×10^{-1}	3.6×10^{-1}
−4.2	−4.0	8.04×10^{-5}	1.30×10^{-2}	$8.63 \times 10^{+1}$	2.14×10^{-2}	2.00×10^{-1}	$+4.10 \times 10^{-1}$	7.5×10^{-1}	2.4×10^{-1}
−4.2	−4.0	8.05×10^{-5}	1.56×10^{-2}	$1.04 \times 10^{+2}$	2.56×10^{-2}	2.00×10^{-1}	$+6.81 \times 10^{-1}$	8.6×10^{-1}	2.6×10^{-1}
−4.2	−4.0	8.05×10^{-5}	1.81×10^{-2}	$1.20 \times 10^{+2}$	2.95×10^{-2}	2.00×10^{-1}	$+1.78 \times 10^{-1}$	$1.1 \times 10^{+0}$	1.4×10^{-1}
−4.2	−4.0	8.33×10^{-5}	2.18×10^{-2}	$1.39 \times 10^{+2}$	3.52×10^{-2}	2.00×10^{-1}	$+9.27 \times 10^{-1}$	$1.2 \times 10^{+0}$	2.0×10^{-1}
−4.0	−3.8	1.27×10^{-4}	1.61×10^{-2}	$6.75 \times 10^{+1}$	2.61×10^{-2}	2.00×10^{-1}	$+4.55 \times 10^{-1}$	5.2×10^{-1}	2.0×10^{-1}
−4.0	−3.8	1.27×10^{-4}	2.18×10^{-2}	$9.12 \times 10^{+1}$	3.50×10^{-2}	2.00×10^{-1}	-1.60×10^{-1}	6.8×10^{-1}	2.6×10^{-1}
−4.0	−3.8	1.27×10^{-4}	2.64×10^{-2}	$1.10 \times 10^{+2}$	4.20×10^{-2}	2.00×10^{-1}	$+9.64 \times 10^{-1}$	8.1×10^{-1}	3.5×10^{-1}
−4.0	−3.8	1.27×10^{-4}	3.10×10^{-2}	$1.30 \times 10^{+2}$	4.90×10^{-2}	2.00×10^{-1}	$+9.62 \times 10^{-1}$	9.6×10^{-1}	5.6×10^{-1}
−4.0	−3.8	1.30×10^{-4}	3.71×10^{-2}	$1.52 \times 10^{+2}$	5.80×10^{-2}	2.00×10^{-1}	$+1.22 \times 10^{+0}$	$1.1 \times 10^{+0}$	$3.5 \times 10^{+0}$
−3.8	−3.6	2.01×10^{-4}	2.58×10^{-2}	$6.86 \times 10^{+1}$	4.10×10^{-2}	2.00×10^{-1}	$+1.45 \times 10^{-1}$	4.9×10^{-1}	3.9×10^{-1}
−3.8	−3.6	2.01×10^{-4}	5.14×10^{-2}	$1.36 \times 10^{+2}$	7.78×10^{-2}	2.00×10^{-1}	$+4.28 \times 10^{-1}$	8.9×10^{-1}	4.7×10^{-1}
−3.8	−3.6	2.01×10^{-4}	3.56×10^{-2}	$9.44 \times 10^{+1}$	5.54×10^{-2}	2.00×10^{-1}	$+7.36 \times 10^{-1}$	6.4×10^{-1}	3.2×10^{-1}
−3.8	−3.6	2.01×10^{-4}	4.33×10^{-2}	$1.15 \times 10^{+2}$	6.65×10^{-2}	2.00×10^{-1}	$+4.18 \times 10^{-1}$	7.8×10^{-1}	4.1×10^{-1}
−3.8	−3.6	2.03×10^{-4}	6.14×10^{-2}	$1.61 \times 10^{+2}$	9.13×10^{-2}	2.00×10^{-1}	$+4.90 \times 10^{-1}$	$1.1 \times 10^{+0}$	4.3×10^{-1}
−3.6	−3.4	3.17×10^{-4}	5.69×10^{-2}	$9.55 \times 10^{+1}$	8.47×10^{-2}	2.00×10^{-1}	$+6.72 \times 10^{-1}$	6.3×10^{-1}	5.5×10^{-1}
−3.6	−3.4	3.18×10^{-4}	4.11×10^{-2}	$6.89 \times 10^{+1}$	6.29×10^{-2}	2.00×10^{-1}	$+3.44 \times 10^{-1}$	4.8×10^{-1}	2.6×10^{-1}
−3.6	−3.4	3.18×10^{-4}	6.98×10^{-2}	$1.17 \times 10^{+2}$	1.02×10^{-1}	2.00×10^{-1}	$+7.97 \times 10^{-1}$	7.3×10^{-1}	3.1×10^{-1}
−3.6	−3.4	3.18×10^{-4}	8.33×10^{-2}	$1.39 \times 10^{+2}$	1.18×10^{-1}	2.00×10^{-1}	-9.77×10^{-1}	8.5×10^{-1}	1.7×10^{-1}
−3.6	−3.4	3.19×10^{-4}	9.81×10^{-2}	$1.64 \times 10^{+2}$	1.36×10^{-1}	2.00×10^{-1}	$+8.98 \times 10^{-1}$	9.8×10^{-1}	1.8×10^{-1}
−3.4	−3.2	5.02×10^{-4}	6.44×10^{-2}	$6.84 \times 10^{+1}$	9.40×10^{-2}	2.00×10^{-1}	$+6.25 \times 10^{-1}$	4.6×10^{-1}	2.5×10^{-1}
−3.4	−3.2	5.02×10^{-4}	1.32×10^{-1}	$1.40 \times 10^{+2}$	1.71×10^{-1}	2.00×10^{-1}	$+3.45 \times 10^{-1}$	7.6×10^{-1}	2.9×10^{-1}
−3.4	−3.2	5.03×10^{-4}	1.11×10^{-1}	$1.17 \times 10^{+2}$	1.49×10^{-1}	2.00×10^{-1}	$+1.62 \times 10^{+0}$	6.9×10^{-1}	2.6×10^{-1}
−3.4	−3.2	5.03×10^{-4}	1.56×10^{-1}	$1.65 \times 10^{+2}$	1.94×10^{-1}	2.00×10^{-1}	$+1.37 \times 10^{+0}$	8.8×10^{-1}	4.4×10^{-1}
−3.4	−3.2	5.03×10^{-4}	9.10×10^{-2}	$9.64 \times 10^{+1}$	1.27×10^{-1}	2.00×10^{-1}	$+2.77 \times 10^{-1}$	6.0×10^{-1}	$4.0 \times 10^{+0}$
−3.2	−3.0	7.92×10^{-4}	1.74×10^{-1}	$1.17 \times 10^{+2}$	2.09×10^{-1}	2.00×10^{-1}	$+1.16 \times 10^{+0}$	6.4×10^{-1}	9.3×10^{-1}
−3.2	−3.0	7.92×10^{-4}	2.08×10^{-1}	$1.40 \times 10^{+2}$	2.36×10^{-1}	2.00×10^{-1}	$+2.92 \times 10^{-1}$	4.6×10^{-1}	4.9×10^{-1}
−3.2	−3.0	7.93×10^{-4}	1.43×10^{-1}	$9.62 \times 10^{+1}$	1.81×10^{-1}	2.00×10^{-1}	$+6.83 \times 10^{-1}$	5.6×10^{-1}	5.2×10^{-1}
−3.2	−3.0	7.96×10^{-4}	1.00×10^{-1}	$6.74 \times 10^{+1}$	1.37×10^{-1}	2.00×10^{-1}	$+1.15 \times 10^{+0}$	4.5×10^{-1}	6.9×10^{-1}
−3.2	−3.0	7.96×10^{-4}	2.47×10^{-1}	$1.66 \times 10^{+2}$	2.64×10^{-1}	2.00×10^{-1}	$+1.47 \times 10^{-1}$	5.6×10^{-1}	3.8×10^{-1}
−3.0	−2.8	1.25×10^{-3}	2.29×10^{-1}	$9.75 \times 10^{+1}$	2.50×10^{-1}	2.00×10^{-1}	$+2.00 \times 10^{-1}$	3.3×10^{-1}	3.6×10^{-1}
−3.0	−2.8	1.26×10^{-3}	3.37×10^{-1}	$1.43 \times 10^{+2}$	3.12×10^{-1}	2.00×10^{-1}	$+4.51 \times 10^{-1}$	4.6×10^{-1}	4.5×10^{-1}
−3.0	−2.8	1.26×10^{-3}	1.56×10^{-1}	$6.62 \times 10^{+1}$	1.92×10^{-1}	2.00×10^{-1}	$+2.42 \times 10^{-1}$	4.1×10^{-1}	4.0×10^{-1}
−3.0	−2.8	1.26×10^{-3}	3.97×10^{-1}	$1.68 \times 10^{+2}$	3.37×10^{-1}	2.00×10^{-1}	$+7.85 \times 10^{-1}$	5.3×10^{-1}	2.8×10^{-1}
−3.0	−2.8	1.26×10^{-3}	2.83×10^{-1}	$1.20 \times 10^{+2}$	2.84×10^{-1}	2.00×10^{-1}	$+7.41 \times 10^{-1}$	4.1×10^{-1}	2.8×10^{-1}
−2.8	−2.6	1.98×10^{-3}	3.64×10^{-1}	$9.77 \times 10^{+1}$	3.22×10^{-1}	2.00×10^{-1}	$+2.54 \times 10^{-1}$	3.4×10^{-1}	2.7×10^{-1}
−2.8	−2.6	1.99×10^{-3}	4.52×10^{-1}	$1.21 \times 10^{+2}$	3.53×10^{-1}	2.00×10^{-1}	$+1.72 \times 10^{-1}$	3.9×10^{-1}	2.2×10^{-1}
−2.8	−2.6	1.99×10^{-3}	6.28×10^{-1}	$1.68 \times 10^{+2}$	3.92×10^{-1}	6.30×10^{-2}	-2.42×10^{-3}	4.8×10^{-1}	5.1×10^{-1}
−2.8	−2.6	1.99×10^{-3}	5.36×10^{-1}	$1.43 \times 10^{+2}$	3.75×10^{-1}	6.55×10^{-2}	-1.93×10^{-1}	4.4×10^{-1}	8.2×10^{-1}
−2.8	−2.6	1.99×10^{-3}	2.40×10^{-1}	$6.42 \times 10^{+1}$	2.56×10^{-1}	2.00×10^{-1}	-2.32×10^{-1}	2.4×10^{-1}	$6.6 \times 10^{+0}$
−2.6	−2.4	2.89×10^{-3}	8.69×10^{-1}	$1.61 \times 10^{+2}$	4.06×10^{-1}	7.23×10^{-2}	$+5.87 \times 10^{-2}$	4.8×10^{-1}	5.4×10^{-1}
−2.6	−2.4	3.11×10^{-3}	7.92×10^{-1}	$1.36 \times 10^{+2}$	4.03×10^{-1}	6.93×10^{-2}	$+5.18 \times 10^{-1}$	4.1×10^{-1}	6.6×10^{-1}
−2.6	−2.4	3.14×10^{-3}	6.83×10^{-1}	$1.16 \times 10^{+2}$	3.96×10^{-1}	6.39×10^{-2}	$+1.08 \times 10^{+0}$	3.8×10^{-1}	6.1×10^{-1}
−2.6	−2.4	3.15×10^{-3}	5.45×10^{-1}	$9.24 \times 10^{+1}$	3.75×10^{-1}	6.37×10^{-2}	$+5.47 \times 10^{-1}$	3.3×10^{-1}	6.8×10^{-1}
−2.6	−2.4	3.16×10^{-3}	3.53×10^{-1}	$5.96 \times 10^{+1}$	3.15×10^{-1}	2.00×10^{-1}	$+3.22 \times 10^{-1}$	2.5×10^{-1}	5.4×10^{-1}
−2.4	−2.2	4.34×10^{-3}	9.18×10^{-1}	$1.13 \times 10^{+2}$	4.04×10^{-1}	7.13×10^{-2}	$+1.20 \times 10^{+0}$	5.5×10^{-1}	3.7×10^{-1}
−2.4	−2.2	4.76×10^{-3}	8.37×10^{-1}	$9.39 \times 10^{+1}$	4.02×10^{-1}	6.89×10^{-2}	$+1.21 \times 10^{+0}$	4.6×10^{-1}	4.3×10^{-1}
−2.4	−2.2	5.01×10^{-3}	7.54×10^{-1}	$8.02 \times 10^{+1}$	3.98×10^{-1}	6.55×10^{-2}	$+7.28 \times 10^{-1}$	4.2×10^{-1}	3.2×10^{-1}
−2.4	−2.2	5.02×10^{-3}	6.23×10^{-1}	$6.61 \times 10^{+1}$	3.86×10^{-1}	6.01×10^{-2}	$+9.35 \times 10^{-1}$	3.7×10^{-1}	2.1×10^{-1}
−2.4	−2.2	5.03×10^{-3}	4.26×10^{-1}	$4.51 \times 10^{+1}$	3.40×10^{-1}	2.00×10^{-1}	$+3.30 \times 10^{-1}$	3.1×10^{-1}	2.1×10^{-1}
−2.2	−2.0	6.86×10^{-3}	9.23×10^{-1}	$7.19 \times 10^{+1}$	4.01×10^{-1}	6.89×10^{-2}	$+8.48 \times 10^{-1}$	5.7×10^{-1}	3.1×10^{-1}
−2.2	−2.0	7.47×10^{-3}	8.54×10^{-1}	$6.10 \times 10^{+1}$	4.00×10^{-1}	6.70×10^{-2}	-5.38×10^{-1}	5.0×10^{-1}	2.4×10^{-1}
−2.2	−2.0	7.97×10^{-3}	7.98×10^{-1}	$5.34 \times 10^{+1}$	3.98×10^{-1}	6.50×10^{-2}	-1.57×10^{-1}	4.6×10^{-1}	7.6×10^{-1}
−2.2	−2.0	8.06×10^{-3}	6.90×10^{-1}	$4.56 \times 10^{+1}$	3.91×10^{-1}	6.04×10^{-2}	$+2.18 \times 10^{-1}$	4.3×10^{-1}	7.3×10^{-1}
−2.2	−2.0	8.07×10^{-3}	5.01×10^{-1}	$3.31 \times 10^{+1}$	3.59×10^{-1}	6.91×10^{-2}	$+4.50 \times 10^{-1}$	3.8×10^{-1}	$6.6 \times 10^{+0}$
−2.0	−1.8	1.07×10^{-2}	9.35×10^{-1}	$4.65 \times 10^{+1}$	3.98×10^{-1}	6.63×10^{-2}	$+1.86 \times 10^{-1}$	6.8×10^{-1}	$1.1 \times 10^{+0}$
−2.0	−1.8	1.16×10^{-2}	8.74×10^{-1}	$4.03 \times 10^{+1}$	3.97×10^{-1}	6.49×10^{-2}	$+1.47 \times 10^{+0}$	6.1×10^{-1}	6.7×10^{-1}
−2.0	−1.8	1.24×10^{-2}	8.29×10^{-1}	$3.57 \times 10^{+1}$	3.96×10^{-1}	6.34×10^{-2}	$+3.00 \times 10^{-1}$	5.8×10^{-1}	5.4×10^{-1}
−2.0	−1.8	1.28×10^{-2}	7.56×10^{-1}	$3.14 \times 10^{+1}$	3.92×10^{-1}	6.08×10^{-2}	$+7.81 \times 10^{-1}$	5.3×10^{-1}	7.6×10^{-1}
−2.0	−1.8	1.28×10^{-2}	6.06×10^{-1}	$2.51 \times 10^{+1}$	3.77×10^{-1}	5.71×10^{-2}	$+8.61 \times 10^{-1}$	4.9×10^{-1}	$1.1 \times 10^{+0}$
−1.8	−1.6	1.67×10^{-2}	9.50×10^{-1}	$3.03 \times 10^{+1}$	3.95×10^{-1}	6.34×10^{-2}	$-1.68 \times 10^{+0}$	$1.0 \times 10^{+0}$	4.7×10^{-1}
−1.8	−1.6	1.77×10^{-2}	9.04×10^{-1}	$2.73 \times 10^{+1}$	3.94×10^{-1}	6.25×10^{-2}	$+1.19 \times 10^{+0}$	9.4×10^{-1}	3.7×10^{-1}
−1.8	−1.6	1.85×10^{-2}	8.71×10^{-1}	$2.50 \times 10^{+1}$	3.93×10^{-1}	6.17×10^{-2}	$+1.99 \times 10^{-1}$	8.7×10^{-1}	2.7×10^{-1}
−1.8	−1.6	1.94×10^{-2}	8.41×10^{-1}	$2.31 \times 10^{+1}$	3.92×10^{-1}	6.08×10^{-2}	$+3.38 \times 10^{-2}$	8.6×10^{-1}	2.3×10^{-1}
−1.8	−1.6	2.03×10^{-2}	8.05×10^{-1}	$2.11 \times 10^{+1}$	3.91×10^{-1}	5.96×10^{-2}	$+3.29 \times 10^{-1}$	7.8×10^{-1}	2.4×10^{-1}
−1.6	−1.4	2.53×10^{-2}	9.92×10^{-1}	$2.09 \times 10^{+1}$	3.90×10^{-1}	6.04×10^{-2}	$-2.25 \times 10^{+0}$	$8.1 \times 10^{+0}$	3.6×10^{-1}
−1.6	−1.4	2.55×10^{-2}	9.86×10^{-1}	$2.06 \times 10^{+1}$	3.90×10^{-1}	6.03×10^{-2}	$-1.11 \times 10^{+1}$	$9.0 \times 10^{+0}$	2.9×10^{-1}
−1.6	−1.4	2.57×10^{-2}	9.80×10^{-1}	$2.03 \times 10^{+1}$	3.90×10^{-1}	6.02×10^{-2}	$-5.91 \times 10^{+0}$	$6.9 \times 10^{+0}$	6.5×10^{-1}
−1.6	−1.4	2.59×10^{-2}	9.72×10^{-1}	$2.00 \times 10^{+1}$	3.90×10^{-1}	6.02×10^{-2}	$+1.09 \times 10^{+1}$	$6.2 \times 10^{+0}$	4.8×10^{-1}
−1.6	−1.4	2.62×10^{-2}	9.60×10^{-1}	$1.95 \times 10^{+1}$	3.90×10^{-1}	6.00×10^{-2}	$-9.33 \times 10^{+0}$	$6.9 \times 10^{+0}$	$6.8 \times 10^{+0}$

Table F.28: $g_1^p(x, \nu)$ from 2011 data.

$\log_{10}(Q^2)$		$\langle x \rangle$	$\langle Q^2 \rangle$	$\langle \nu \rangle$	R	$\sigma(R)$	g_1^p	$\sigma_{stat}(g_1^p)$	$\sigma_{syst}(g_1^p)$
-3.0	-2.4	4.25×10^{-5}	3.19×10^{-3}	$4.00 \times 10^{+1}$	5.39×10^{-3}	2.00×10^{-1}	$+3.65 \times 10^{-1}$	7.2×10^{-1}	$1.0 \times 10^{+0}$
-3.0	-2.4	4.88×10^{-5}	3.27×10^{-3}	$3.58 \times 10^{+1}$	5.52×10^{-3}	2.00×10^{-1}	$+1.19 \times 10^{-2}$	7.9×10^{-1}	1.7×10^{-1}
-3.0	-2.4	6.44×10^{-5}	3.37×10^{-3}	$2.86 \times 10^{+1}$	5.67×10^{-3}	2.00×10^{-1}	$+2.03 \times 10^{-2}$	5.6×10^{-1}	1.7×10^{-1}
-2.4	-1.8	1.38×10^{-4}	1.20×10^{-2}	$4.92 \times 10^{+1}$	1.97×10^{-2}	2.00×10^{-1}	$+5.04 \times 10^{-1}$	2.1×10^{-1}	3.2×10^{-1}
-2.4	-1.8	5.55×10^{-5}	7.17×10^{-3}	$6.87 \times 10^{+1}$	1.20×10^{-2}	2.00×10^{-1}	$+5.57 \times 10^{-1}$	3.0×10^{-1}	1.7×10^{-1}
-2.4	-1.8	8.22×10^{-5}	1.05×10^{-2}	$6.82 \times 10^{+1}$	1.73×10^{-2}	2.00×10^{-1}	$+5.75 \times 10^{-1}$	3.0×10^{-1}	5.4×10^{-1}
-1.8	-1.2	1.38×10^{-4}	2.41×10^{-2}	$9.34 \times 10^{+1}$	3.85×10^{-2}	2.00×10^{-1}	$+9.47 \times 10^{-1}$	2.8×10^{-1}	2.8×10^{-1}
-1.8	-1.2	2.25×10^{-4}	3.66×10^{-2}	$8.67 \times 10^{+1}$	5.68×10^{-2}	2.00×10^{-1}	$+5.94 \times 10^{-1}$	2.5×10^{-1}	2.3×10^{-1}
-1.8	-1.2	4.20×10^{-4}	4.49×10^{-2}	$6.19 \times 10^{+1}$	6.81×10^{-2}	2.00×10^{-1}	$+5.38 \times 10^{-1}$	1.6×10^{-1}	1.6×10^{-1}
-1.2	-0.6	1.44×10^{-3}	1.71×10^{-1}	$6.98 \times 10^{+1}$	2.05×10^{-1}	2.00×10^{-1}	$+3.89 \times 10^{-1}$	1.3×10^{-1}	1.1×10^{-1}
-1.2	-0.6	4.29×10^{-4}	8.68×10^{-2}	$1.10 \times 10^{+2}$	1.22×10^{-1}	2.00×10^{-1}	$+9.97 \times 10^{-1}$	2.8×10^{-1}	6.9×10^{-1}
-1.2	-0.6	7.30×10^{-4}	1.27×10^{-1}	$9.34 \times 10^{+1}$	1.66×10^{-1}	2.00×10^{-1}	$+9.60 \times 10^{-1}$	2.1×10^{-1}	3.1×10^{-1}
-0.6	$+0.0$	1.56×10^{-3}	3.30×10^{-1}	$1.14 \times 10^{+2}$	3.07×10^{-1}	2.00×10^{-1}	$+7.20 \times 10^{-1}$	1.7×10^{-1}	2.5×10^{-1}
-0.6	$+0.0$	2.66×10^{-3}	4.84×10^{-1}	$9.76 \times 10^{+1}$	3.61×10^{-1}	2.00×10^{-1}	$+4.37 \times 10^{-1}$	1.3×10^{-1}	1.6×10^{-1}
-0.6	$+0.0$	5.84×10^{-3}	6.77×10^{-1}	$7.11 \times 10^{+1}$	3.91×10^{-1}	6.12×10^{-2}	$+3.40 \times 10^{-1}$	6.8×10^{-2}	9.0×10^{-2}

Table F.29: $g_1^p(Q^2, x)$ from 2007 data.

$\log_{10}(Q^2)$		$\langle x \rangle$	$\langle Q^2 \rangle$	$\langle \nu \rangle$	R	$\sigma(R)$	g_1^p	$\sigma_{stat}(g_1^p)$	$\sigma_{syst}(g_1^p)$
-3.0	-2.4	4.11×10^{-5}	3.58×10^{-3}	$4.64 \times 10^{+1}$	6.05×10^{-3}	2.00×10^{-1}	$+1.81 \times 10^{+0}$	$4.3 \times 10^{+0}$	$4.0 \times 10^{+0}$
-3.0	-2.4	4.40×10^{-5}	3.58×10^{-3}	$4.34 \times 10^{+1}$	6.06×10^{-3}	2.00×10^{-1}	$+2.23 \times 10^{+0}$	$5.4 \times 10^{+0}$	4.3×10^{-1}
-3.0	-2.4	5.16×10^{-5}	3.59×10^{-3}	$3.76 \times 10^{+1}$	6.06×10^{-3}	2.00×10^{-1}	$+5.57 \times 10^{+0}$	$4.1 \times 10^{+0}$	3.1×10^{-1}
-2.4	-1.8	4.81×10^{-5}	8.36×10^{-3}	$9.24 \times 10^{+1}$	1.40×10^{-2}	2.00×10^{-1}	$+7.67 \times 10^{-1}$	5.2×10^{-1}	3.2×10^{-1}
-2.4	-1.8	6.44×10^{-5}	1.13×10^{-2}	$9.36 \times 10^{+1}$	1.87×10^{-2}	2.00×10^{-1}	$+5.02 \times 10^{-1}$	5.4×10^{-1}	2.1×10^{-1}
-2.4	-1.8	9.57×10^{-5}	1.28×10^{-2}	$7.35 \times 10^{+1}$	2.10×10^{-2}	2.00×10^{-1}	$+4.71 \times 10^{-1}$	4.2×10^{-1}	$2.6 \times 10^{+0}$
-1.8	-1.2	1.06×10^{-4}	2.36×10^{-2}	$1.19 \times 10^{+2}$	3.79×10^{-2}	2.00×10^{-1}	$+1.91 \times 10^{-1}$	4.0×10^{-1}	5.7×10^{-1}
-1.8	-1.2	1.71×10^{-4}	3.66×10^{-2}	$1.14 \times 10^{+2}$	5.70×10^{-2}	2.00×10^{-1}	$+1.08 \times 10^{+0}$	3.8×10^{-1}	2.8×10^{-1}
-1.8	-1.2	2.95×10^{-4}	4.71×10^{-2}	$8.95 \times 10^{+1}$	7.14×10^{-2}	2.00×10^{-1}	$+3.47 \times 10^{-1}$	2.8×10^{-1}	2.2×10^{-1}
-1.2	-0.6	1.04×10^{-3}	1.77×10^{-1}	$9.74 \times 10^{+1}$	2.11×10^{-1}	2.00×10^{-1}	$+7.07 \times 10^{-1}$	2.1×10^{-1}	1.1×10^{-1}
-1.2	-0.6	3.30×10^{-4}	8.55×10^{-2}	$1.40 \times 10^{+2}$	1.21×10^{-1}	2.00×10^{-1}	$+5.89 \times 10^{-1}$	4.1×10^{-1}	$1.9 \times 10^{+0}$
-1.2	-0.6	5.54×10^{-4}	1.26×10^{-1}	$1.22 \times 10^{+2}$	1.65×10^{-1}	2.00×10^{-1}	$+4.95 \times 10^{-1}$	3.1×10^{-1}	3.3×10^{-1}
-0.6	$+0.0$	1.23×10^{-3}	3.33×10^{-1}	$1.46 \times 10^{+2}$	3.10×10^{-1}	2.00×10^{-1}	$+6.58 \times 10^{-1}$	2.4×10^{-1}	3.1×10^{-1}
-0.6	$+0.0$	2.05×10^{-3}	4.85×10^{-1}	$1.27 \times 10^{+2}$	3.62×10^{-1}	2.00×10^{-1}	-6.21×10^{-2}	1.9×10^{-1}	2.4×10^{-1}
-0.6	$+0.0$	4.21×10^{-3}	6.91×10^{-1}	$9.85 \times 10^{+1}$	3.95×10^{-1}	6.31×10^{-2}	$+6.09 \times 10^{-1}$	1.1×10^{-1}	8.8×10^{-2}

Table F.30: $g_1^p(Q^2, x)$ from 2011 data.